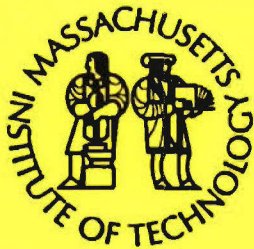


**Massachusetts Institute of Technology  
Woods Hole Oceanographic Institution**



**Joint Program  
in Oceanography/  
Applied Ocean Science  
and Engineering**



---

**DOCTORAL DISSERTATION**

The Influence of Ridge Geometry at the  
Ultraslow-Spreading Southwest Indian Ridge (9°-25°E):  
Basalt Composition Sensitivity to Variations in Source  
and Process

by

Jared Jeffrey Standish

**DISTRIBUTION STATEMENT A**  
Approved for Public Release  
Distribution Unlimited

February 2006



MIT/WHOI

2006-02

**The Influence of Ridge Geometry at the Ultraslow-Spreading Southwest Indian Ridge  
(9°-25°E): Basalt Composition Sensitivity to Variations in Source and Process**

by

Jared Jeffrey Standish

Massachusetts Institute of Technology  
Cambridge, Massachusetts 02139

and

Woods Hole Oceanographic Institution  
Woods Hole, Massachusetts 02543

February 2006

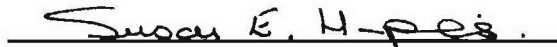
DOCTORAL DISSERTATION

Funding was provided by grants from the National Science Foundation: grants OCE 9907630, OCE 0137325, EAR 9804891, OCE 9416620, and OCE 0096634.

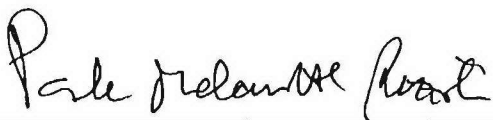
Reproduction in whole or in part is permitted for any purpose of the United States Government. This thesis should be cited as: Jared Jeffrey Standish, 2006. The Influence of Ridge Geometry at the Ultraslow-Spreading Southwest Indian Ridge (9°-25°E): Basalt Composition Sensitivity to Variations in Source and Process. Ph.D. Thesis. MIT/WHOI. 2006-02.

Approved for publication; distribution unlimited.

Approved for Distribution:



Susan E. Humphris, Chair  
Department of Geology and Geophysics



Paola Malanotte-Rizzoli  
MIT Director of JointProgram



James A. Yoder  
WHOI Dean of Graduate Studies

***The Influence of Ridge Geometry at the Ultraslow-Spreading  
Southwest Indian Ridge (9°-25°E): Basalt Composition  
Sensitivity to Variations in Source and Process***

by

**JARED JEFFREY STANDISH**

B.A., Geology, Colgate University, 1992  
M.S., Geology, University of Idaho, 1996

Submitted in partial fulfillment of the requirements for the degree of

**Doctor of Philosophy**

at the

**MASSACHUSETTS INSTITUTE OF TECHNOLOGY**

and the

**WOODS HOLE OCEANOGRAPHIC INSTITUTION**

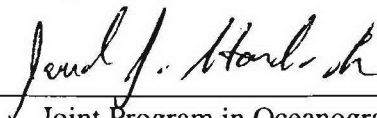
on

**February 2006**

© Jared Jeffrey Standish, 2006  
All rights reserved.

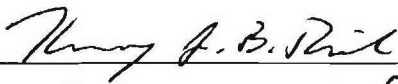
The author hereby grants to WHOI permission to reproduce and to distribute paper and electronic copies of this thesis in whole or in part.

Signature of the author



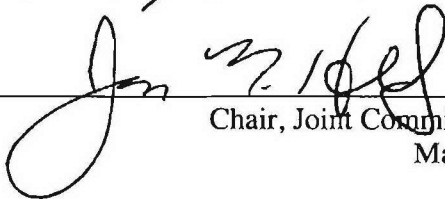
Joint Program in Oceanography, Massachusetts Institute of  
Technology and Woods Hole Oceanographic Institution  
February 2006

Certified by



Henry J.B. Dick, Thesis Supervisor

Accepted by



Chair, Joint Committee for Marine Geology & Geophysics,  
Massachusetts Institute of Technology and  
Woods Hole Oceanographic Institution

***The Influence of Ridge Geometry at the Ultraslow-Spreading  
Southwest Indian Ridge (9°-25°E): Basalt Composition  
Sensitivity to Variations in Source and Process***

by  
Jared Jeffrey Standish

Submitted in partial fulfillment of the requirements for the degree of  
**Doctor of Philosophy**

to the

**DEPARTMENT OF EARTH, ATMOSPHERIC, AND PLANETARY SCIENCES,  
MASSACHUSETTS INSTITUTE OF TECHNOLOGY**

and the

**DEPARTMENT OF GEOLOGY AND GEOPHYSICS,  
WOODS HOLE OCEANOGRAPHIC INSTITUTION**

**February 2006**

***Abstract***

Between 9°-25° E on the ultraslow-spreading Southwest Indian Ridge lie two sharply contrasting supersegments. One 630 km long supersegment erupts N-MORB that is progressively enriched in incompatible element concentrations from east to west. The second 400 km long supersegment contains three separate volcanic centers erupting E-MORB and connected by long amagmatic accretionary segments, where mantle is emplaced directly to the seafloor with only scattered N-MORB and E-MORB erupted. Rather than a major break in mantle composition at the discontinuity between the supersegments, this sharp contrast in geometry, physiography, and chemistry reflects “source” versus “process” dominated generation of basalt.

Robust along-axis correlation of ridge characteristics (i.e. morphology, upwelling rate, lithospheric thickness), basalt chemistry, and crustal thickness (estimated from gravity) provides a unique opportunity to compare the influence of spreading geometry and rate on MORB generation. What had not been well established until now is the importance of melting processes rather than source at spreading rates < 20 mm/yr. Along the orthogonally spreading supersegment (14 mm/yr) moderate degrees of partial melting effectively sample the bulk mantle source, while on the obliquely spreading supersegment (7-14 mm/yr) suppression of mantle melting to low degrees means that the bulk source is not uniformly sampled, and thus “process” rather than “source” dominates melt chemistry.

Thesis Supervisor: Henry J.B. Dick  
Senior Scientist, W.H.O.I.



## ***Acknowledgements***

There are so many people to thank when reaching a milestone such as this, so let me start with those that have had the most recent impact on this accomplishment, my thesis committee; Henry Dick, Stan Hart, Ken Sims, Fred Frey, Anton le Roex, Mark Kurz, Jian Lin, and my thesis defense chairperson, Hans Schouten. With both Hans and Jian I have gained a new appreciation for and understanding of real-time seagoing geophysics, and I think all four of us (including Henry) have witnessed some pretty amazing human efforts and as a result grown together as people and scientists during the many days bouncing around the South Atlantic. Mark's analytical expertise, continuing support and encouraging words, and attention to detail, has kept my path over the last 6 years straight and narrow, and in the right direction. Anton has been a great source of information both regarding trace elements and more importantly the SW Indian Ridge. As one of the first geochemists to study the South Atlantic spreading ridges in detail, his early work through the 80's and 90's set the bar (and quite a high bar it was) for which all of my work will be gauged. It is a shame that our schedules did not coincide so that he could be here at WHOI for the defense, but I know much discussion will come from my work. Learning trace element geochemistry from Fred Frey was special. Fred's ability to get back to the basics and stress the importance to understanding "why" in the most fundamental terms is important in geochemistry. I very much appreciated his willingness to make the trip to WHOI for committee meetings, and I thank you for your guidance and support. Ken Sims eternal positive attitude is a model by which we should all live and conduct science. His friendship over the past 5 years and guidance in U-series and geochemistry in general have been greatly appreciated and I look forward to many exciting discoveries in future joint work. Ken, thanks so much for your unending support. Stan R. Hart is such an amazing mentor, scientist, and great person to have as a friend. Being able to watch and learn how Stan's mind works and analyzes a problem has been a treat and I only hope that some day I can pick apart a manuscript or talk with the same ease, efficiency, and understanding. His friendship has been much appreciated and I thank you Stan for your patience and guidance. Henry "Hank" Dick, you have been the most gracious and kind-hearted advisor a student could want. Your generosity as a supporting advisor, as a friend, and as a colleague has been tremendous. Your guidance both in the lab and at sea have been much appreciated and the opportunities that you have presented me are unequalled and unbelievable...I never would have thought standing on the North Pole would occur in graduate career or life for that matter. You have been able to get the best out of me and I thank you for that. I look forward to continued friendship and scientific investigation as an official colleague of yours.

Of course the Joint Program would not be as amazing and successful as it is without 1) my fellow students, and 2) the Academic Programs Office (APO). The APO has been under the astute guidance of John Farrington. The ultimate dean, John is a great friend, a super dean, and yet a stickler for the rules, and each one of those aspects are greatly appreciated. Judy McDowell, Marsha Gomes, Julia Westwater, and their supporting

crew are such amazing people and friends. It is their fervor for science education, and the student's well-being that serves as the foundation for the Joint Program. I thank you all very much for your unending effort and support over the past 6 years. There are so many JP students that I have learned from, admired, and befriended that it is not possible to remember all the names. So if you are not included here, that does not mean you haven't influenced my graduate career and life. First of all, let me sincerely thank the ladies of McGregor/Katy's Hatch...Rhea, Linda, and Margaret. You have been great friends and tremendous colleagues for the past 6 years and hopefully well into the future. I hope our paths cross often. Other sixth year fellow JPers includes Mea, Heidi, Rose, Matt, Chris R., Charlie, and Fabian. Other JPers such as Jessica "ica-ica" Warren, "Phat" Matt Jackson, Paul "Slim" Craddock, Luke, Carlos, Claire, Dave L., Brian "the martian" deMartin, and a host of others.

I have not forgotten the best JPer of them all, Cara, to whom I owe so much. Her support throughout the past 3 years has been consistent and unending and in the past 3 months has been enduring. From her I have gained so much, including a bit of knowledge about "geo-micro-biology" (I think that is the right order)! Cara, thank you for your support, friendship, and love, from the bottom of my heart and whole of my brain!

And lastly, I have to thank my family. Mom and dad have been truly great supporters of my seemingly unending desire to be a student. Their mental and financial support (at times) have been greatly appreciated and probably have gone un-thanked a number of times. Well, to make up for those missed opportunities and to thank you and tell you what wonderful parents you have been, are, and always will be...I love you and thank you for being my parents in the fullest sense of the term! I also owe a great deal of thanks to both my sisters, who have continued to encourage me to strive for the stars, just as they do. Kimmer and Scooter you are the best sisters ever and I thank you so much for your support, encouragement, and willingness to be a sounding board for all sorts of science and non-science issues.

This work has been supported financially by three main grants from NSF. The main body of work consisting of major element, trace element, and isotopic data acquisition and interpretation (Chapter 2 & 3) was funded by H. Dick's grant from the National Science Foundation-OCE 9907630. National Science Foundation-OCE 0137325 supported the U-series work described in Chapter 4. The published work of Chapter 5 was funded by National Science Foundation-EAR 9804891, NSF-OCE 9416620, and NSF-OCE 0096634.

## ***Biographical Note***

**Jared Jeffrey Standish**

### **EDUCATION**

1993-1996 M.S. – Geology, University of Idaho  
1988-1992 B.A. – Geology, Colgate University

### **TEACHING EXPERIENCE**

2003 Teaching Assistant (2 terms), Sea Education Association  
1994-1996 Graduate Teaching Assistant, University of Idaho

### **FIELD RESEARCH**

2003 Petrologist, SW Indian Ridge (9-25° E), R/V Melville  
2002 Field Assistant, Ta'u Island, American Samoa  
2001 Petrologist, Arctic Mid-Ocean Ridge Expedition, USCG Icebreaker Healy  
2001 Petrologist/Rock Curator, SW Indian Ridge (9-25° E), R/V Knorr  
1995 Watch Stander, SE Indian Ridge, R/V Melville  
1994 Volcanologist/Field Assistant, Galapagos Islands, PI – D. Geist

### **PUBLICATIONS**

Geist, D., T. Naumann, **J.J. Standish**, M. Kurz, K. Harpp, William M. White, and D. Fornari, Wolf Volcano, Galápagos Archipelago: Melting and Magmatic Evolution at the Margins of a Mantle Plume, *Journal of Petrology* (in press).  
**Standish, J.J.**, S.R. Hart, J. Blusztajn, H.J.B. Dick, and K.L. Lee, Abyssal Peridotite Osmium Isotopic Compositions from Cr-spinel, *Geochemistry, Geophysics, Geosystems*, Vol. 3, No. 1, p. 24, 2002.  
**Standish, J.**, D. Geist, K. Harpp, and M.D. Kurz, The Emergence of a Galapagos shield volcano, Roca Redonda, *Contrib. Mineral. Petrol.*, Vol. 133, pp. 136-148, 1998.  
Seaman, S.J., E.E. Scherer, and **J.J. Standish**, Multi-stage magma mixing and mingling and the origin of flow banding in the Aliso Lava Dome, Tumacacori Mountains, Southern Arizona, *Journal of Geophysical Research*, Vol. 100, pp. 8381-8398, 1995.  
**Standish, J.J.**, H.J.B. Dick, W. Melson, P. J. Michael, and T. O'Hearn, The influence of ridge geometry on magma chemistry at ultraslow-spreading rates (Southwest Indian Ridge from 9°-25°E): A tectonomagmatic model for origin of non-hotspot E-MORB, (submitted G-cubed).



## *Table of Contents*

<b>ABSTRACT .....</b>	<b>3</b>
<b>ACKNOWLEDGEMENTS .....</b>	<b>4</b>
<b>BIOGRAPHICAL NOTE.....</b>	<b>6</b>
<b>CHAPTER 1. INTRODUCTION.....</b>	<b>11</b>
REFERENCES .....	14
<b>CHAPTER 2. THE INFLUENCE OF RIDGE GEOMETRY ON MAJOR ELEMENT CHEMISTRY AT THE ULTRASLOW-SPREADING SOUTHWEST INDIAN RIDGE (9°-25°E): THE ROLE OF PROCESS VERSUS SOURCE DURING MORB GENERATION .....</b>	<b>15</b>
ABSTRACT .....	17
1. INTRODUCTION .....	18
2. TECTONICS AND RIDGE CHARACTERISTICS .....	20
2.1. <i>Regional setting</i> .....	20
2.2. <i>Local setting</i> .....	21
3. DATA COLLECTION & METHODS.....	25
3.1. <i>Bathymetry</i> .....	25
3.2. <i>Dredging and Rock Curation</i> .....	25
3.3. <i>Chemical Analysis</i> .....	26
4. RESULTS .....	27
4.1. <i>Lithologic Distribution</i> .....	27
4.2. <i>Basalt Modal Abundance</i> .....	27
4.3. <i>Major Element Chemistry</i> .....	28
4.4. <i>Dissolved Water and Carbon Dioxide Abundance</i> .....	31
5. DISCUSSION.....	31
5.1. <i>Major Element Petrogenesis - Fractional crystallization</i> .....	31
5.2. <i>Variation in Parental Melt Compositions</i> .....	36
5.3. <i>MORB Source Mantle</i> .....	41
6. TECTONOMAGMATIC MODEL .....	44
6.1. <i>Origin and nature of the mantle heterogeneity</i> .....	44
6.2. <i>Bimodal melting</i> .....	47
6.3. <i>Extraction of mafic melts from host peridotite</i> .....	48
6.4. <i>Segmentation, upwelling, and melt focusing</i> .....	49
6.5. <i>Off-axis versus on-axis heterogeneity</i> .....	50
7. MODEL SUMMARY.....	52
8. CONCLUSIONS .....	54
ACKNOWLEDGEMENTS .....	55
APPENDIX 1. ....	56
REFERENCES .....	57

<b>CHAPTER 3. TRACE ELEMENT MODELING AND ISOTOPIC CONSTRAINTS ON THE IMPORTANCE OF MELTING PROCESSES VERSUS SOURCE AT THE ULTRASLOW-SPREADING SOUTHWEST INDIAN RIDGE (9°-25°E).....</b>	<b>101</b>
1. INTRODUCTION .....	103
2. TECTONIC SETTING.....	104
3. ANALYTICAL METHODS.....	105
3.1. <i>Trace Element Measurements</i> .....	105
3.2. <i>Isotope Measurements</i> .....	105
Sample Preparation .....	105
Measurement Techniques .....	106
4. RESULTS & OBSERVATIONS.....	107
4.1. <i>Trace Element Composition</i> .....	107
4.2. <i>Isotopic Composition</i> .....	110
5. PETROGENESIS.....	112
5.1. <i>Effects of Fractional Crystallization on Trace Elements</i> .....	112
5.2. <i>Along-Axis Variations</i> .....	114
Isotopic Compositions – Local Mantle Heterogeneity? .....	114
Trace Element Concentrations and Ratios.....	115
5.3. <i>Trace element modeling</i> .....	118
Generation of N-MORB from depleted MORB mantle (DMM).....	119
Melting modified-DMM to produce E-MORB.....	121
Necessity of garnet in the mantle source .....	122
Multi-lithology mantle compositions .....	123
DMM mixed with continental crust .....	124
Enriched mantle II composition.....	124
5.4. <i>Garnet-bearing mantle lithology</i> .....	125
Can eclogite explain the Narrowgate segment lavas? .....	126
Idealized melt modeling of eclogite/peridotite multi-lithology source.....	127
5.5. <i>Regional isotopic variations – Is this Bouvet material?</i> .....	130
<sup>3</sup> He/ <sup>4</sup> He variation.....	131
6. CONCLUSIONS .....	132
ACKNOWLEDGEMENTS .....	134
APPENDIX A: SAMPLE DIGESTION & COLUMN CHEMISTRY .....	135
REFERENCES.....	138
<b>CHAPTER 4. THE GENERATION OF <sup>238</sup>U-<sup>230</sup>Th-<sup>226</sup>Ra DISEQUILIBRIA ON THE ULTRASLOW-SPREADING SOUTHWEST INDIAN RIDGE (9°-25°E): SPATIALLY AND TEMPORALLY VARIABLE VOLCANISM .....</b>	<b>187</b>
ABSTRACT .....	189
1. INTRODUCTION .....	190
2. TECTONIC SETTING, SPREADING RATES, AND SAMPLE LOCATIONS .....	191
3. METHODS.....	193

3.1. Leaching.....	193
3.2. Dissolution and fuming.....	193
3.3. Spiking .....	194
3.4. Column chemistry.....	194
3.5. Mass spectrometry methods .....	195
4. RESULTS .....	195
4.1. Major and Trace Elements.....	195
4.2. Sr, Nd, Pb, Hf, and He Isotopic Compositions .....	196
4.3. U-Series Disequilibria Measurements.....	196
5. U-TH-RA DISEQUILIBRIUM DISCUSSION .....	198
5.1. Age constraints: coeval lavas beyond the axis of rifting .....	198
5.2. Effects of melting processes on U-series disequilibria.....	204
5.3. Global & local U-Th systematics .....	211
5.4. Amount of pyroxenite in MORB source .....	212
5.5. Global Observations.....	213
6. CONCLUSIONS .....	214
ACKNOWLEDGEMENTS .....	216
APPENDIX A. ....	217
APPENDIX B. ....	222
REFERENCES .....	223

## CHAPTER 5. ABYSSAL PERIDOTITE OSMIUM ISOTOPIC COMPOSITIONS FROM CR-SPINEL..... 257

ABSTRACT .....	259
1. INTRODUCTION .....	260
2. GEOLOGY AND SAMPLE DESCRIPTION .....	261
3. SAMPLE PREPARATION AND LEACHING .....	262
3.1. Whole Rock .....	262
3.2. Spinel .....	263
3.3. Leaching.....	263
3.4. Leachates .....	264
4. ANALYTICAL METHODS .....	264
4.1. Mineral Dat.....	264
4.2. Sparging.....	264
5. RESULTS .....	266
5.1. Mineralogical and Petrographic Analysis.....	266
5.2. Osmium Isotopes .....	271
6. DISCUSSION.....	272
6.1. Whole Rock Osmium.....	272
6.2. Small-Scale Os Isotope Heterogeneity .....	272
6.3. Regional Os Heterogeneity .....	275
6.4. Cr-Spinel and Serpentinization .....	276
6.5. Cr-Spinel Osmium .....	276
6.6. Cr-Spinel Versus Whole Rock Osmium .....	278



6. CONCLUSIONS .....	279
ACKNOWLEDGEMENTS .....	279
REFERENCES .....	280
<b>CHAPTER 6. SUMMARY .....</b>	<b>283</b>
REFERENCES .....	286

## Chapter 1. Introduction

Volcanoes erupt every day, whether above sea level at ocean islands like Hawaii, or deep beneath the Earth's oceans along what is termed the "mid-ocean ridge spreading system". Analogous to the seams of a baseball, this generally linear chain of submerged volcanic mountains winds around the Earth's surface demarcating diverging plates, and continually producing oceanic crust, which incidentally accounts for 60% of the Earth's surface [Cogley, 1984]. The sheer volume of crust produced together with the inherently high heat budget associated with mid-ocean ridges, means that the ridge system is a global regulator of ocean chemistry; hydrothermal circulation at ridges is estimated to pump the equivalent of an entire ocean's worth of water through the mid-ocean ridge hydrothermal systems every 10 million years or so [Elderfield and Schultz, 1996]. Therefore, knowledge of the composition of Earth's oceanic crust and evolution across time and space may potentially aid in the prediction of changing ocean chemistry and everything related (i.e. climate change).

The Earth's ocean crust is dominantly basaltic, and compared with other volcanic settings (i.e. ocean islands, island arcs) it is chemically homogeneous. Yet, comparison of mid-ocean ridge basalt (MORB) erupted from ridges in each of the major ocean basins, namely the Pacific, Atlantic, and Indian Oceans, finds significant diversity. Because MORB is produced by decompression melting of the underlying mantle, compositional heterogeneity is a function of either initial source or melting processes, or both. The overarching question(s) that we address are; How is mid-ocean ridge basalt generated, transported, and erupted? How is the geochemical diversity of MORB controlled by "source" versus "process"? It would be nearsighted and foolish of us to attempt to answer these questions by focusing only on the geochemical data available, thus this thesis strives to incorporate geophysical, geological, and geochemical observations and constraints to develop a self-consistent model of MORB generation that considers the effects of both source variation and changes in melting process.

The Earth's divergent plate boundaries, usually called spreading centers, are dynamic. The process of creating new ocean crust theoretically splits "zero-age" crust in half, and spreads it apart (usually orthogonal to the trend of the ridge) at a rate proportional to the spreading rate. Commonly referred to as "crustal accretion", this process is accommodated by both magmatic and tectonic mechanisms, with the proportion that each contributes to lithospheric architecture depending on the seafloor spreading-rate. Fast-spreading ridges ( $> 80 \text{ mm yr}^{-1}$ ) like the East Pacific Rise have high heat budgets and large magma fluxes to the seafloor. On the other end of the spectrum, ultraslow-spreading ridges ( $< 20 \text{ mm yr}^{-1}$ ) are presumed cooler and to generate less magma [Reid and Jackson, 1981]. Few studies of ultraslow-spreading ridges have occurred, but the findings presented here illustrate the important role that tectonic controls play in crustal accretion at ultraslow-spreading rates, thereby supporting model predictions. Most noticeable is the influence that tectonics have on the erupted magma chemistry. The interaction of tectonic and magmatic accretionary processes is fundamentally different

than at fast- or even slow-spreading ridges, and this is highlighted by the differences in magma chemistry.

Chapters 2, 3, and 4 of this dissertation focus on basalt geochemistry along a portion of the ultraslow-spreading Southwest Indian Ridge from 9°-25°E. We present a sizable amount of data ranging from major and trace element analyses, to isotope compositions, to U-series disequilibrium measurements. Each geochemical genre is useful in addressing separate, but related petrogenetic questions. Major element data provides critical information regarding source composition, melting conditions (i.e. temperature, pressure, etc.), and the differentiation history of magmas, as they migrate from mantle to ocean floor. In much the same way trace element data can address many of those issues, but because they behave much differently than major elements due to their high incompatibility in most basaltic phases, they are often used as indicators of source enrichment, style of melting, and extent of melting. On the other hand, long-lived radiogenic isotope ratios serve as an indicator of source composition and provenance. A lavas isotopic signature is a geochemical fingerprint that links magmas to any number of mantle source reservoirs. Isotopic data also provides valuable age information that is directly dependent on the parent/daughter fractionation reflected by trace element analysis. In this way, U-series disequilibrium measurements are used to provide time constraints on petrologic processes such as melt transport and eruption, and to gain insight into the source lithology, melting style, and melt migration mechanisms. Below we briefly outline how all this geochemical data is used in conjunction with geophysical, geodynamic, and geologic observations to develop a model for MORB generation at the Southwest Indian Ridge.

Chapter 2 presents first order geologic, morphologic, tectonic, and geophysical observations, along with basalt major element abundances (including H<sub>2</sub>O and CO<sub>2</sub>), that show striking along-axis correlations, consistent with basalt chemistry and accretion largely controlled by spreading rate and spreading geometry (i.e. tectonics). The petrologic model we propose attributes variations in basalt chemistry, ridge segmentation, and relative crustal thickness, among other observations, to the influence of ridge geometry on mantle upwelling rate and thus on lithospheric thickness. The inferred along-axis lithospheric topography subsequently affects melting parameters and transport processes such as, the height of the mantle melting column, 3D melt focusing, and depletion of the shallow mantle. These processes indicate that at ridge segments with upwelling rates < 20 mm/yr the importance and influence of melting processes and parameters over source composition is significantly increased. The diminished volume of melt beneath these segments means perturbations to the melting process that would ordinarily be overwhelmed by the shear volume of melt on fast-spreading ridges, would play a vital role in melt chemistry in this magma starved environment. The model presented within illustrates that basalt compositions generated in an environment of highly variable upwelling rates, lithospheric thickness, and melt focusing, as seen on the oblique supersegment are dominated by “process” relative to the orthogonal supersegment where the above parameters are generally constant, despite spreading rates below 20 mm/yr.



Within Chapter 3, we use trace element and isotope measurements to more rigorously define our model by investigating the source composition beneath the ridge. Using a mantle melting algorithm we calculate trace element melt compositions from different initial sources and attempt to match the model melts with measured lava compositions. At the same time, along-axis isotopic variations (e.g. Sr, Nd, Pb, Hf, and He) of our end-member lavas enable “fingerprinting” of their source from a different line of evidence, helping us rule out potential source reservoirs and better define others. By successfully matching the modeled and measured melt compositions and the isotopic signatures we non-uniquely determine the trace element composition of the MORB mantle source responsible for the lavas we observe along the ridge. However, not to be misled, it is the style of melting or the “process” that dominantly controls the final basalt composition. In the end, evaluation of the data presented in this chapter provides critical constraints on the Southwest Indian Ridge MORB source, showing it to be generally consistent with the model we present in Chapter 2.

In order to gain insight into the temporal and spatial variability of crustal accretion at an ultraslow-spreading ridge and to better constrain the MORB source lithology, we measured U-series disequilibrium in 12 glasses. In Chapter 4, we present U-Th and Th-Ra disequilibrium data, which reveals anomalously young lavas scattered throughout the rift valley. This illustrates the complexity of ultraslow-spreading crustal accretion. Petrologically our U-series data is not easily explained, as it is not consistent with previously proposed models of disequilibrium generation. We briefly discuss an alternative model.

We have presented a strong case implicating “process” as the dominant control on basalt chemistry at the ultraslow-spreading Southwest Indian Ridge, however, source lithology and composition still play a vital roles in MORB generation and basalt heterogeneity – more so at faster spreading ridges where melting may be limited more by phase constraints than available heat. In Chapters 2-4 our investigation explores the MORB generation process by looking at the variations in basalt chemistry and working backwards to constrain a source composition. In the final chapter, Chapter 5, we take a different tack and analyze the residues of mantle melting at mid-ocean ridges - abyssal peridotites. This chapter is included in the thesis as a published manuscript in the journal *Geochemistry, Geophysics, and Geosystems* (G-Cubed) with the following reference [Standish *et al.*, 2002]. Specifically, we separated chromium-spinel, the most resistant mineral to post-melting alteration, from the host peridotite and analyzed their osmium isotopic composition. Even though the samples analyzed in Chapter 5 are unrelated to the study area discussed above, the characterization of the  $^{187}\text{Os}/^{188}\text{Os}$  isotopic signature in the residue of MORB melting allows further and better constraint of the depleted MORB mantle.

We gain considerable insight into the MORB generation processes at ultraslow-spreading rates, realizing the significant influence that upwelling rate and lithospheric thickness have on the final chemistry of the basalts. Many unanswered questions remain, some of which will be addressed with further investigation and interpretation of the data

in hand, and others that will require additional data collection. For example, why is U-Th disequilibrium so different between N-MORB and E-MORB, or is it? How thick is the crust along the oblique supersegment? Are basalts commonly erupting from the crests of the rift valley walls? We do know from the work presented here, that ultraslow-spreading ridges must be viewed differently than fast or slow-spreading ridges, as the influence of melting style becomes more important the slower the upwelling rate.

## References

- Cogley, J. G. (1984), Continental margins and the extent and number of the continents, *Review of Geophysics and Space Physics*, 22, 101-122.
- Elderfield, H., and A. Schultz (1996), Mid-ocean ridge hydrothermal fluxes and the chemical composition of the ocean, *Annu. Rev. Earth Planet. Sci.*, 24, 191-224.
- Reid, I., and H. R. Jackson (1981), Oceanic spreading rate and crustal thickness, *Marine Geophysical Researches*, 5, 165-172.
- Standish, J. J., S. R. Hart, J. Blusztajn, H. J. B. Dick, and K. L. Lee (2002), Abyssal peridotite osmium isotopic compositions from Cr-spinel, *Geochemistry, Geophysics, Geosystems*, 3, 24.

***Chapter 2. The influence of ridge geometry on major element chemistry at the ultraslow-spreading Southwest Indian Ridge (9°-25°E): The role of process versus source during MORB generation***

# **The influence of ridge geometry on major element chemistry at the ultraslow-spreading Southwest Indian Ridge (9°-25°E): The role of process versus source during MORB generation**

Jared J. Standish

MIT/WHOI Joint Program in Oceanography, Woods Hole, MA.

Henry J.B. Dick

Geology and Geophysics, Woods Hole Oceanographic Institution, Woods Hole, MA.

Peter J. Michael

Department of Geosciences, The University of Tulsa, Tulsa, OK.

William G. Melson, Timothy O'Hearn

Department of Mineral Sciences, U.S. National Museum of Natural History, Washington, D.C

## **Abstract**

Between 9°-25° E on the ultraslow-spreading Southwest Indian Ridge lie two sharply contrasting supersegments. One 630 km long supersegment erupts N-MORB that is progressively enriched in incompatible element concentrations from east to west towards the Bouvet Hotspot. Despite being over 1000 km from the current plume location, these established “global” geochemical and geophysical trends reflect ridge/hotspot interaction. The second 400 km long supersegment consists of three separate volcanic centers erupting alkali basalt and E-MORB and connected by long amagmatic accretionary segments, where the mantle is emplaced directly to the seafloor with only scattered N-MORB and E-MORB erupted. Rather than a major break in mantle composition at the discontinuity between the two supersegments, this sharp contrast in physiography and chemistry reflects “source” versus “process” dominated generation of basalt. Along the orthogonal supersegment moderate degrees of partial melting effectively sample the bulk mantle source, while on the oblique supersegment suppression of mantle melting to low degrees means that the bulk source is not uniformly sampled and thus “process” rather than “source” dominates melt chemistry. To assess the influence of “process” we define four distinct tectonomagmatic provinces based on ridge characteristics, geophysics, and chemistry: 1) the 16°-25°E orthogonal accretionary supersegment, 2) the Narrowgate accretionary segment at 14°40'E, 3) Joseph Mayes Seamount at 11°20'E, and 4) the amagmatic accretionary segments that lie between Joseph Mayes Seamount and the Narrowgate segment, and between the Narrowgate segment and the orthogonal supersegment.

Much of the local major element heterogeneity can be explained by polybaric fractional crystallization in the presence of varying amounts of H<sub>2</sub>O. The remaining major element

variation, specifically the elevated  $K_2O$  contents of the E-MORBs, is attributed to mixing partial melts of an eclogite lithology in varying proportions with partial melts of depleted peridotite. Locally we also find significant differences between on- and off-axis basalt suites at the orthogonal supersegment demonstrating that even at a “normal” ocean ridge, melting environment “process” can be important in determining melt composition. The substantial role of “process” at the oblique supersegment is attributed to variable spreading geometry and thus inferred upwelling rates, which drop as low as 7 mm/yr (relative to 14.5 mm/yr on the orthogonal supersegment) along portions of the amagmatic accretionary segments thereby allowing conductive cooling of the lithosphere from above to penetrate much deeper than on adjacent magmatic segments, like the Narrowgate segment and Joseph Mayes Seamount. The increased lithospheric thickness and resulting along-axis lithospheric topography therefore influences local melting dynamics, including but not limited to the following effects, 1) lower extents of melting due to a locally shortened melting column, 2) enhanced melt focusing from areas of thicker lithosphere toward areas of thinner lithosphere, 3) enhanced mantle depletion (decreased clinopyroxene) of local residual column, all of which impact local melt chemistry. Our proposed model of MORB generation illustrates the dramatic effect that “process” can have on melt chemistry beneath ridges spreading at rates  $< 20$  mm/yr, and if consistent with trace element and isotopic data suggests the importance of spreading geometry and upwelling rate for MORB generation.

## 1. Introduction

We present major element glass analyses (including  $H_2O$  &  $CO_2$ ), dredge statistics, and bathymetry data collected aboard RV Knorr, expedition 162 legs 7-9 and RV Melville, expedition Vancouver 07 from two ultraslow-spreading supersegments between  $9^{\circ}56'$  and  $25^{\circ}$  E ( $\sim 1050$  km in length). Both accretionary supersegments were densely sampled and show highly contrasting morphology, segmentation, tectonics, and lava chemistry. The supersegments are broadly delineated by their general axial trend relative to spreading direction, which between  $\sim 17^{\circ}$  -  $25^{\circ}$  E is nearly orthogonal, but then begins to bend to the southwest at  $\sim 17^{\circ}$  E, becoming highly oblique. The eastern 600 km long supersegment spreads orthogonally along normal magmatic segments linked by short non-transform offsets, not unlike the well-characterized slow-spreading MAR. This “orthogonal” supersegment is dominated by “normal” mid-ocean ridge basalt (N-MORB), but shows a systematic major element enrichment trend from east to west. To the west of  $17^{\circ}$  E the ridge takes on a completely different appearance as the axial trend becomes highly oblique (up to  $\sim 56^{\circ}$ ) to spreading, magmatism abruptly dwindles, segmentation patterns change, and unique ultraslow-spreading accretionary tectonics becomes stable [Dick et al., 2003]. Basalt compositions along the “oblique” supersegment are heterogeneous with both N-MORB and anomalously elevated E-MORB occurring together within the axis of rifting, but vary along-axis according to tectonomagmatic province.

Generation of new ocean crust at mid-ocean ridge spreading centers incorporates magmatic, tectonic, and hydrothermal processes. Over fifty years of investigation and

sampling the ocean ridges has documented variations in mid-ocean ridge basalt compositions on both the regional “ocean basin” scale and the local “ridge segment” scale. These often correlate with the composition of residual abyssal mantle [Dick and Fisher, 1984; Dick et al., 1984], which together with theoretical [Klein and Langmuir, 1987; McKenzie and Bickle, 1988] and experimental work [Baker and Stolper, 1994; Hirose and Kushiro, 1993; Jaques and Green, 1980; Walter, 1998] clearly show that ‘normal’ mid-ocean ridge basalt (N-MORB) is produced by partial melting of a peridotitic mantle. Subtle variations seen in N-MORB major element compositions between ocean basins are commonly attributed to proximity of mantle hotspots [Schilling et al., 1983], increasing degree of mantle melting near hotspots [Dick et al., 1984], differences in mantle potential temperature and extent of melting [Klein and Langmuir, 1987; McKenzie and Bickle, 1988], and in some cases source compositional differences [Shen and Forsyth, 1995] or variations in the depth of mantle upwelling and melting as related to ridge migration [Small and Danyushevsky, 2003]. However, localized segment-scale variations in major and trace element compositions are often difficult to explain using regional mechanisms, thus another explanation is warranted. Originally recognized on ridges located in close proximity to hotspots, this phenomenon was generally explained by upwelling of deep-seated plume material mixing with ambient depleted upper mantle [Allègre et al., 1984; Batiza and Vanko, 1984; Schilling, 1973]. However, enriched mid-ocean ridge basalt (E-MORB) together with depleted mid-ocean ridge basalt (N-MORB) on ridges far from hotspots is more contentious. The presence of E-MORB on fast- and slow-spreading ridges far from hotspots may be related to differences in degree of melting [Kinzler and Grove, 1992b; Langmuir et al., 1992; le Roex et al., 1992], hydrous melting and differentiation [Asimow et al., 2004; Asimow and Langmuir, 2003; Gaetani and Grove, 1998; Michael and Chase, 1987], prior source enrichment [Donnelly et al., 2004], and or source heterogeneity [Castillo, 2000; Hanson, 1977; le Roex, 1985; le Roex et al., 1983; Meyzen et al., 2003]. We present MORB compositions that reflect post-generation processes in addition to heterogeneity within the initial source material.

Various factors including, spreading geometry, conductive cooling, upwelling rate, mantle flow, and lithospheric thickness govern the complex continuum of processes from melt generation in the mantle to melt emplacement beneath MOR. Away from mantle hotspots and large transform offsets, crustal thickness, and therefore mantle melting, is relatively constant down to a spreading rate of 20 mm/yr, assuming constant potential temperature and source composition. At slower spreading rates, crustal thickness drops off irregularly but dramatically [Bown and White, 1994; Jackson et al., 1982; Jokat et al., 2003; Reid and Jackson, 1981; White et al., 1992; White et al., 2001], often with significant effects on melt chemistry and tectonics [Dick et al., 2003]. Recent studies of ultraslow-spreading ridges have documented significant differences in crustal accretion from faster spreading ridges [Cannat et al., 1999; Dick et al., 2003; Michael et al., 2003; Sauter et al., 2004b; Sauter et al., 2001]. Specifically, investigations of the Southwest Indian Ridge, the Gakkel Ridge, and Lena Trough have revealed anomalous yet correlated morphologic, tectonic, geophysical, and geochemical features [Cannat et al.,



2003; Dick et al., 2003; Gauger et al., 2004; Jokat et al., 2003; Mendel et al., 2003; Meyzen et al., 2003; Michael et al., 2003; Sauter et al., 2004a; Sauter et al., 2004b; Snow et al., 2004; Standish and Dick, 2004]. Detailed study of the Southwest Indian Ridge (9-25° E) provides added insight into the accretionary processes controlling major element chemistry, morphology, segmentation, and geology, within an ultraslow-spreading environment. The observation that changes in basalt compositions are correlated with changes in accretionary style appears to be unique to the slowest end of the mid-ocean ridge spectrum. This suggests the importance of the mid-ocean ridge thermal regime, both perpendicular and parallel to the axis of rifting. The along-axis correlations among chemistry, effective spreading rate, and inferred lithospheric thickness indicate that below 20 mm/yr spreading rate “process” may have a greater influence on MORB composition than “source”.

## 2. Tectonics and ridge characteristics

### 2.1. Regional setting

Situated between the African and Antarctic plates, the Southwest Indian Ridge (SWIR) is one of the slowest spreading mid-ocean ridges in the global ridge system, with an average full rate of 14-15 mm/yr [DeMets et al., 1990; Menke, 2005]. The SW Indian Ridge measures 7700 km in length from the Bouvet Triple Junction (55° S, 0° E) to the Rodrigues Triple Junction (25° S, 70° E) and maintains a highly oblique (~60°) SW-NE orientation relative to the plate spreading direction. Numerous studies have observed variations in segmentation pattern and geochemistry along axis, leading to the division of the SWIR into three regional sections. The eastern SW Indian Ridge from 46° E to 70° E [Cannat et al., 1999; Mendel and Sauter, 1997; Mendel et al., 2003; Sauter et al., 2004a; Sauter et al., 2004b; Seyler et al., 2003] is characterized by sections having a segmentation pattern typical of slow spreading ridges contrasted with highly oblique sections devoid of transform offsets [Sauter et al., 2004a]. The central SW Indian ridge from 25° E to 46° E [Hamelin and Allègre, 1985; le Roex et al., 1989; Mahoney et al., 1992] is strongly influenced by the Marion Hotspot and contains many large transform offsets. The western SW Indian Ridge [le Roex et al., 1985; le Roex et al., 1992] between the Bouvet Triple Junction (~0°) and 25° E has an overall E-W trend, thereby lacking the extreme 1<sup>st</sup> order obliquity of the rest of the ridge. From 0° to 10° E the western SWIR contains numerous transform offsets linking orthogonal magmatic accretionary segments; while for 1050 km from 9°-25° E (see Figure 1 *inset*) it has no transforms, consisting of two distinctly different but directly linked oblique and orthogonal supersegments.

Much of the SW Indian Ridge shows typical slow-spreading ridge segmentation, characterized by second-order magmatic segmentation [Sinton et al., 1991] linked by transform offsets and smaller non-transform discontinuities. Other sections, notably portions of the eastern SWIR [Sauter et al., 2004a] and our study area in western SWIR between 9°-25° E, completely lack transforms and instead have sub-orthogonal magmatic accretionary segments linked by obliquely spreading amagmatic accretionary segments

(also referred to as amagmatic troughs owing to their physiography). Although segmentation and crustal architecture would appear to be directly related to spreading rate, the mechanism(s) responsible for stability of these contrasting segmentation patterns remain poorly understood. Geometrically, as the obliquity of the ridge axis increases so too does ridge length per unit lithosphere created, and thus mantle upwelling must decrease proportionately (Figure 1, *inset*). The amount that mantle upwelling slows is calculated as the effective spreading rate (ESR), which is simply the spreading component perpendicular to the ridge axis. These transitions in style of segmentation have also been observed on the Knipovich Ridge [Okino et al., 2002], the Lena Trough [Snow et al., 2004], and Gakkel Ridge [Cochran et al., 2003; Jokat et al., 2003; Michael et al., 2003] where it is also linked to decreasing spreading rate [Dick et al., 2003]. Based on observations from all these ridges, Dick et al., [2003] suggested that the transition to linked magmatic and amagmatic accretionary segments, “ultraslow-spreading accretionary ridge tectonics”, replacing transform faults occurs at ESR full rates of  $\sim 12$  mm/yr or less.

Here we restrict an “ultraslow-spreading ridge” to a portion of the mid-ocean ridge system that has a full spreading rate below 20 mm/yr, and thus is defined solely by spreading rate. The rate at which a ridge diverges does not exclusively determine its’ morphologic, tectonic, or geochemical characteristics, thus fast-, slow-, and ultraslow-spreading ridges alike, can and often do display variable ridge characteristics. The term “ultraslow-spreading accretionary tectonics” [Dick et al., 2003] refers to the ridge characteristics largely restricted to ultraslow-spreading ridges [Cannat et al., 1999; Dick et al., 2003; Michael et al., 2003; Sauter et al., 2004b; Sauter et al., 2001], but found to occur stably at effective spreading rates  $\leq 12$  mm/yr [Dick et al., 2003]. The term “ultraslow-spreading accretionary tectonics” is defined by orthogonally spreading magmatic accretionary segments linked, without transform offset, by obliquely spreading amagmatic accretionary segments. This contrasts with slow-spreading ridge accretionary tectonics in two main ways, 1) ultraslow-spreading accretionary tectonics accommodate ridge offset via oblique amagmatic accretionary segments rather than transforms, and 2) crustal thickness variations are much more pronounced relative to slow-spreading accretionary tectonics. Below 20 mm/yr variations in spreading geometry and upwelling rate have a greater relative effect on conductive cooling and lithospheric thickening, and thus on the melting regime and the composition of magmas. Therefore, it is possible to have slow-spreading accretionary tectonics on an ultraslow-spreading ridge, but ultraslow-spreading accretionary tectonics appear to be observed and stable largely at spreading rates  $\leq 12$  mm/yr. In this way, a spreading rate below 20 mm/yr is a necessary, but not a sufficient reason for ultraslow-spreading ridge accretionary tectonics to occur.

## 2.2. Local setting

At the eastern end of the 1050 km long ridge section between the Shaka Fracture Zone at  $\sim 9^\circ$  E and the Du Toit Fracture Zone at  $25^\circ$  E (Figure 1), the “orthogonal supersegment” maintains an overall axial orientation nearly perpendicular relative to the spreading direction from  $25^\circ$  to  $\sim 16^\circ$  E. At  $16^\circ$  E the rift valley floor drops nearly 500 m,

and the morphology, physiography, lithology, and segmentation pattern of the ridge changes. From 16° E, for nearly 420 km, the western or oblique supersegment maintains a general southwesterly trend, reaching an maximum obliquity relative to the spreading direction of ~57°, and intersects the Shaka Fracture Zone at about 9°50' E. Comparison of along-axis morphology, physiography, lithology, and segmentation pattern between and within each supersegment shows four distinct tectonomagmatic provinces (Figure 2 & 3). Table 1 summarizes the specific ridge characteristics for each of the following tectonomagmatic provinces.

### ***Orthogonal Accretionary Supersegment***

The 630 km long orthogonal accretionary supersegment (15°45' -25° E) mapped by *Grindlay and Madsen [1998]* has typical slow-spreading ridge morphology and geology, with 290 and 220 km orthogonal spreading sections linked by a 120 km long slightly oblique (~10°) section around 20°-22°E. Similar to the slow-spreading MAR this tectonomagmatic province (Figure 2a) is characterized by short (10-15 km) to moderate length (20-35 km) 'secondary' magmatic segments [*Grindlay et al., 1998; Sinton et al., 1991*]. *Dulaney [2002]* and *Grindlay et al., [2000]* define seventeen individual magmatic segments, with en-echelon left stepping segmentation accommodated by short (<10 km) non-transform offsets. The overall axial trend of the orthogonal supersegment begins to bend to the southwest at ~17°E, reflecting increased en-echelon left stepping of the individual magmatic accretionary segments. Thus, as the overall ridge trend increases in obliquity west of 17°E, each magmatic accretionary segment remains nearly perpendicular to the spreading direction to the western terminus of the orthogonal supersegment at 15°45'E. This equates to effective spreading rates on each individual segment similar to the average calculated full spreading rate of 14.5 mm/yr [*Menke, 2005*].

The along-axis rift mountain topography of the supersegment is rough but relatively symmetrical (Figure 2b). Similarities between the profiles exist in the total rift valley relief (measured from rift valley floor to crest of bounding wall) of 1500-2000 meters and the distinctive staircase, normal faulting present in the wall morphology. 12 of 17 magmatic segments are topographically elevated at their midpoints with the other 5 showing irregular, asymmetrical along-axis segment profiles [*Dulaney, 2002*]. The majority of the segments display lineated axial volcanic ridges (AVRs) suggesting focused melt flow to a narrow zone along the axis of the rift valley, although bathymetric features throughout the rift valley suggest recent volcanic activity may be highly dispersed, as documented on other slow-spreading ridges [*Perfit and Chadwick, 1998*]. Along-axis relative crustal thickness is presented in Figure 4 as both gravity-derived crustal thickness (grey field) [*Dulaney, 2002; Grindlay et al., 2000*] and bathymetry compensated relative crustal thickness (red curve)(see figure caption for details). Both techniques illustrate distinct segmentation, with a 1-1.5 km increase in inferred crustal thickness from east to west along the orthogonal supersegment. The total range in relative crustal thickness from gravity inversion (assuming a constant 6 km thick oceanic crust) is from -2.7 to +0.8 km, while bathymetrically compensated relative crustal thickness generally agrees. Dredge statistics (Table 1) show that 85% of recovered

samples are basalt, and only 5 rift mountain dredges recovered peridotite and/or gabbro. Intra-rift valley dredges were all basalt, mostly fresh, glassy pillow lavas. This together with estimated crustal thickness measurements typical of slow spreading ridges indicate modest magmatic output, although somewhat less than typical mid-ocean ridge crustal thickness of  $6.3 \pm 0.9$  km, at full spreading rates of 20 mm/yr and above [Bown and White, 1994; Jackson et al., 1982; Reid and Jackson, 1981; White et al., 1992; White et al., 2001].

### ***Oblique Accretionary Supersegment***

#### ***Amagmatic Accretionary Segments***

Within the oblique supersegment are three ‘amagmatic’ accretionary segments. For clarification we prefer the term ‘amagmatic’ rather than ‘avolcanic’ (as suggested by M. Cannat via personal communication) to describe specific segments of the SW Indian Ridge based on multiple observations including, 1) the high proportion of dredged abyssal peridotite versus basalt, 2) the striking lack of gabbro in numerous dredges, 3) gravity anomalies, and 4) the increased bathymetric depths and distinctive rift valley morphology. While other locations may be better characterized as ‘avolcanic’, we feel the geologic and geophysical observations are supportive of an ‘amagmatic’ environment. These amagmatic troughs are an integral part of ultraslow-spreading ridge accretionary tectonics [Dick et al., 2003], and isolated, they represent unique tectonomagmatic settings. Profiles B-B’ and D-D’ illustrate similar characteristics relative to the Narrowgate segment or the orthogonal supersegment (Figure 3d). Profile B-B’ has a wide rift valley (> 50 km) and inner valley floor width (19.5 km) with gently sloping walls and fairly subdued rift mountain topography. Comparatively, profile D-D’ has a 29 km wide rift valley, a 12.5 km inner rift valley width, steep rift valley walls, and heavily faulted rift mountain topography. Both profiles have rift valley relief similar to the orthogonal supersegment, but average rift valley floor depths ~500 meters greater. Gently dipping rift valley walls in profile B-B’ are largely attributed to low-angle faults that expose massive peridotite blocks rather than high-angle normal faults exposing extrusives. Since peridotites were also dredged from both rift walls near profile D-D’, it is likely that given the narrower rift valley width their steeper slopes reflect an initial high-angle dip that progressively flattens with continual extension and fault growth.

The most prominent of the three amagmatic sections extends from 11°35’E to 14°15’E (Figure 3c), linking Narrowgate Segment and Joseph Mayes Seamount. This segment is separated by a short magmatic segment at a sharp 22 km deviation in the trend of the rift valley to sub-orthogonal centered at 12°55’E. There, a 25 km wide rift valley contains several apparently volcanic sub-orthogonal ridges where dredges KN 162-9-48 and -49 recovered abundant fresh to moderately weathered glassy pillow basalt. To the NNE and SSW, parallel the spreading directions are topographically elevated regions with lineated terrain perpendicular to the spreading direction. This terrain flanks the western side of a long NNE trending deep in the northern rift mountains: together these features mark the trace of a now extinct transform fault and an adjacent robust magmatic segment. The geophysical signal of the present day vestigial segment consists of a negative mantle



Bouguer anomaly (<15 mGal) and a small (~5 Am/m) positive magnetic anomaly that contrasts to the more robust negative gravity (20-30 mGal) and strong positive magnetic anomalies (~15 Am/m) found associated with the large Joseph Mayes and Narrowgate volcanic centers. The elevated terrain in the rift mountains is believed to constitute a cross-axis volcanic high centered on the vestigial rift segment that becomes progressively narrower and less pronounced towards the ridge axis. It is interrupted entirely on the northern side of the rift valley, where a large oblique peridotite block has been emplaced. Thus, this segment is believed to be dying out and of little consequence to the surrounding tectonomagmatic province.

Varying obliquity exists along the amagmatic accretionary segments, reaching a maximum of ~57° between 11°35'E and 12°50'E, and resulting in an effective spreading rate (proportional to mantle upwelling rate) as low as 7.5 mm/yr. The distribution of rock types also differs quite strikingly between tectonomagmatic provinces, as 47% of the dredged material on the amagmatic accretionary segments was peridotite, compared to 4% on the orthogonal supersegment and 0% on both Joseph Mayes Seamount and the Narrowgate segment (Table 2). Peridotite and its alteration products [Bach et al., 2003] were dredged directly from the rift valley floor at many of these locations. This, and the lack of recovered gabbro (1% by weight), implies a thin to locally absent basaltic crust [Dick et al., 2003]. This inference from dredging is supported by calculations of the relative crustal thickness required to compensate local topography (Figure 4), noting that where magmatic crust is entirely absent, a non-zero calculated crustal thickness is likely due to serpentinization of the shallow mantle [Cannat, 1996; Cannat et al., 2003; Mével et al., 1997].

#### *Narrowgate Segment*

Narrowgate segment (14°15'-14°54' E; Figure 3a) is a robust, orthogonally spreading magmatic accretionary segment located between two amagmatic accretionary segments. It has a narrow rift valley ~20 km across with steep walls. Despite oblique spreading amagmatic segments to the east and west, Narrowgate segment is oriented nearly perpendicular to the spreading direction with an effective spreading rate (ESR) equal to portions of the orthogonal supersegment (14.2 mm/yr). The cross-axis profile C-C' (Figure 3d) illustrates elevated off-axis bathymetry, relative to other profiles, as well as morphologic symmetry in the rift mountains. Relief within the rift valley is ~1500 meters and the inner width of the rift valley (measured at the base of the bounding faults) is 8-9 km. Current volcanic activity appears to be focused along a lineated, 45 km long, axial volcanic high, corroborated by our surface topography, magnetic, dredging, and gravity data to be the locus of recent activity. A cross-axis volcanic plateau forming a V-shaped trace sub-parallel (5° to 15°) to the spreading direction extends ~100 km into the rift mountains to the NNE and at least 200 km to the SW, suggesting robust magmatic activity at the Narrowgate segment for at least 8-9 Ma. All seven dredges conducted within the domain of the Narrowgate accretionary segment tectonomagmatic province recovered fresh, glassy pillow lavas. This is particularly interesting since dredges KN162-9-61 and VAN7-89 are both located near the crests of the north and south rift valley walls, respectively, rather than the axial ridge. Bathymetry compensated relative

crustal thicknesses (Figure 4) show Narrowgate segment to have 1-2 km thicker crust than the amagmatic accretionary segments to either side.

#### *Joseph Mayes Seamount*

Joseph Mayes Seamount [Standish and Dick, 2004] is a point source axial volcano without off-axis extensions located between 11°-11°35' E (Figure 3a). It shoals to ~1000 m water depth from the adjacent amagmatic trough to the east, prominently displaying a double peaked axial summit (Figure 3b, profile A-A' in 3d). One of the largest, if not the largest, non-hotspot volcanoes on the global ridge system, Joseph Mayes Seamount is bounded to the north and south by pre-existing peridotite blocks (see Figure 3b)(verified by dredging, morphology, gravity, and magnetics) rifted 20 km apart by the volcano. Based on the orientation of the summit axial ridges, Joseph Mayes Seamount is spreading sub-orthogonally, with an effective spreading rate just over 13 mm/yr. The age of Joseph Mayes Seamount is constrained using this rate and the width of the rift between the peridotite blocks to be less than 1.3 Ma. The segment does not contain a single linear volcanic ridge, but has two prominent curved segments (arms) extending from the two summit peaks to the NW and SE (Figure 3b), respectively, overlapping near the summit. Several linear volcanic ridges oriented nearly perpendicular to the spreading direction also extend to the NW and SE from the saddle between the two peaks. The length of the segment is ~50 km, with the northern summit peak a few hundred meters higher than the southern peak. Sampling indicates it is robust, erupting moderately to highly evolved basalts, some highly vesicular. Joseph Mayes Seamount is an area of voluminous magmatic activity based on bathymetry compensated relative crustal thickness that is over 5 km greater than surrounding segments and nearly 3 km thicker than any segment in the study area (Figure 4). Although details of volcanic construction and evolution are different, both the Narrowgate segment and Joseph Mayes Seamount tectonomagmatic provinces are areas of focused magmatic activity, with well-defined, negative mantle Bouguer anomalies and positive magnetic signatures [Dick et al., 2003; Lin et al., 2003].

### **3. Data Collection & Methods**

#### **3.1. Bathymetry**

Bathymetric data presented in Figures 1-3 for the oblique supersegment (9°-16° E) was collected during legs 7&9 of the RV Knorr 162 expedition using a 12 kHz SEABEAM Series 2100 multibeam sonar system meshed with the ships GPS navigation code. The orthogonal supersegment between 16°-25°E was previously mapped [Grindlay et al., 1998].

#### **3.2. Dredging and Rock Curation**

Dredge sampling was completed on the Knorr 162 and Melville (VAN7) expeditions. A Miniature Autonomous Plume Recorder (MAPR) attached 2 meters above the pinger, provided a direct measurement of both starting and final dredge depths along the track. GPS latitude and longitude as well as dredge depth (Table 2) were recorded when the dredge was “on bottom”, taken to be the maximum depth. Track lengths ranged from 500



m to 3000 m. Typically a dredge targeting a steep wall location would be shorter than one targeting a low-angle volcanic feature. Rocks were sorted by lithology at sea, and up to 70 or 80 samples (per dredge) were cut, resorted, and described. After description on a standardized form, initial sampling for thin sections, XRF analysis, and glass chipping was done onboard.

### 3.3. Chemical Analysis

#### *Electron Microprobe*

Major element basalt glass analyses were conducted on a five-wavelength-spectrometer JEOL JXA-8900R electron microprobe at the Smithsonian Institute using JEOL software with ZAF corrections. Each glass sample was analyzed for 10 elements with a 24 by 17 micron rastering beam at 15 kV and 20 nano-amps. Count times for major elements were 10 seconds on peak and 5 seconds off peak for background correction, except for  $K_2O$ ,  $MnO$  and  $P_2O_5$ , which had slightly longer count times. The internal basalt glass standard was VG-2 [Melson et al., 2001], plus three mineral standards: apatite, microcline, and magnetite. To monitor for instrumental variation VG-2 was run at the beginning of each 45-sample mount and after every 10 samples. A minimum of five spots comprised each glass data analysis. Analyses having sums less than 98.5% and greater than 100.5% were deleted and rerun. If  $1\sigma$  for the unknown sample is not less than the  $2\sigma$  for all VG-2 analyses, the sample was rerun. Analytical details are further discussed in *Melson et al., [2001]*.

#### *Fourier Transform Infrared Spectroscopy (FTIR)*

Volatile concentrations in basalt glasses were measured at the University of Tulsa using micro-FTIR methods. Visibly unaltered glass shards were chosen from a representative subset of the total sample suite. In all 40 glasses were selected to be measured for  $CO_3^{2-}$ , molecular  $CO_2$ , molecular  $H_2O$  ( $H_2O_m$ ), and  $OH^-$ . Glass shards were mounted in Buehler Transoptic® and then polished on both sides to a wafer thickness of 40–300  $\mu m$ . Thickness measurements were made using a digital micrometer ( $\pm 1 \mu m$  precision) and mapped on photographs for later reference. Samples were analyzed using previously published methods [Dixon et al., 1988; Dixon et al., 1995a; Michael, 1999; Michael, 1995].

Absorbance was measured for dissolved water ( $3535 \text{ cm}^{-1}$ ), molecular water ( $1630 \text{ cm}^{-1}$ ), and carbonate bands ( $1515$  and  $1430 \text{ cm}^{-1}$ ) at two points on each wafer, and from two different wafers for each sample. Dissolved water concentrations for most samples represent the average of four spot measurements, with an average reproducibility for all samples equal to 4% and most samples less than 3%.

Carbonate bands ( $1435$  and  $1515 \text{ cm}^{-1}$ ) and molecular water ( $1630 \text{ cm}^{-1}$ ) absorbance spectra were corrected for background spectrum by subtracting a devolatilized basalt glass [Dixon et al., 1988]. The carbonate doublet and molecular water peaks were fit to this background level and subjectively adjusted using methods described in [Dixon and Stolper, 1995b; Dixon et al., 1988].  $CO_2$  reproducibility is generally 15-20% due to the uncertainty in the compositional dependence of the molar absorptivity for dissolved

carbon in silicate glass and the uncertainty in the background correction methods. Degassing corrections are discussed in the results section.

## **4. Results**

### **4.1. Lithologic Distribution**

Between 9°-25°E we made a total of ninety-six dredges and a single gravity core. Overall recovery was high, although a handful of dredges came up empty - mostly on the oblique supersegment. Each dredge haul was classified by rock type and the individual rock types were combined into one of seven lithologic groups. Total rock recovered included, 67% pillow basalt/basalt, 18% peridotite/dunite, and 5% hydrothermal/volcanoclastic rocks. Dredge statistics (Table 2) show marked differences in percent lithology for the different tectonomagmatic provinces. Dredge information for PS4 is not included, but can be found in *le Roex et al.*, [1992].

57 dredges from the orthogonal supersegment recovered 4044.8 kg of rock; the vast majority of which is basalt/pillow basalt (85%). The rest is 5% diabase, 4% peridotite/dunite, 3% gabbro, and 2% hydrothermal/volcanoclastics. Of 57 dredges, 14 were in the Rift Mountains and the rest were on the axial ridge or rift valley floor. A similar total weight of rock was recovered from the oblique supersegment (4048.3 kg), in contrast the oblique supersegment yielded 50% basalt/pillow basalt, 32% peridotite/dunite, 8% hydrothermal/volcanoclastics, and 5% erratics, but little gabbro (1%) or diabase (5%).

Three lithologically variable tectonomagmatic provinces comprise the oblique supersegment. 1) Narrowgate segment yielded primarily basalt/pillow basalt (74%). Dredging on the steep, heavily faulted rift valley walls recovered 11% diabase, more than in any other province, and 13% hydrothermal/volcanoclastic rocks. 2) Joseph Mayes Seamount dredges were dominated by extrusives, with 97% of 316 kg of total recovered rock being basalt/pillow basalt. The remaining 3% consisted of 2% diabase and 1% erratics. 3) The amagmatic accretionary segments are strikingly different. Forty-four dredges were completed, with 8 dredges empty and 7 additional rift valley floor locations recovering peridotite or hydrothermal clays (after serpentinites). The frequency of empty dredges on the rift valley floor forced us to dredge the rift valley walls. In all we found 46% peridotite/dunite, only 37% basalt/pillow basalt, 7% hydrothermal/volcanoclastics and erratics, 2% diabase, and 1% gabbro, for a total recovery of 2810 kg of rock from the amagmatic accretionary segments. The lack of gabbro and diabase indicate that these segments are not just simply avolcanic like the 15°20'N region of the MAR where numerous gabbro plugs occur over large regions coincident with exposed mantle peridotite [e.g. Cannat, 1996; Kelemen et al., 2004], but are truly amagmatic.

### **4.2. Basalt Modal Abundance**

Classification and description of individual hand samples includes estimated modal phenocryst and vesicle abundances. Modal phenocryst percentages and percent vesicularity are listed in Table 2 as averages for each dredge. Detailed visual inspection

of basalts from both supersegments found little evidence of alteration or weathering for nearly all near-axis lavas, however off-axis lavas (rift mountain) more commonly display weathered surfaces. In general, manganese coatings were thin when present, indicating relatively young eruptions ages.

Joseph Mayes Seamount has the highest average percent plagioclase phenocrysts at 13% and the highest average vesicularity at 11%. The Narrowgate segment has 8% plagioclase phenocrysts, although this average value is quite unrepresentative of the range seen in individual lavas. It also has 7% average vesicularity, while the lavas from the amagmatic troughs have 4% plagioclase phenocrysts and 7% vesicularity. The orthogonal supersegment tectonomagmatic province, by contrast, has only 2% plagioclase phenocrysts and 2% vesicularity in its lavas. The high vesicularity, particularly in the basalts from Joseph Mayes Seamount and Narrowgate segment correlate with volatile content (Figure 7) and dredge depth. Analysis of select sample thin sections finds the estimated modal percentages to largely correspond to petrographically estimated megacryst/phenocryst proportions. However, hand sample estimates cannot account for mineral modes (i.e. plagioclase) as microphenocrysts, thus some samples from the Narrowgate segment and amagmatic accretionary segment (e.g. 48-21, 49-13, 26-23) may have significantly higher modal abundances than reflected by the reported dredge averages.

#### 4.3. Major Element Chemistry

Over 350 fresh basalt glasses from between 9-25° E on the SW Indian Ridge were analyzed for major element concentrations (Table 3). These samples were collected during the Knorr 162 (KN162 prefix) and Melville “Vancouver 07” (VAN7 prefix) dredging expeditions and are presented in Table 3. Also included in the table are unpublished major element glass data from the ANT IV/4 (PS4) and Agulhas 22 expeditions. Much of the ANT IV/4 PS4 data was previously published in [le Roex et al., 1992].

Basalt compositions range from hypersthene-normative tholeiitic basalts to nepheline-normative alkali basalts similar to the range reported by [le Roex et al., 1992] for a subset of basalts from the oblique supersegment. Tholeiites are concentrated on the orthogonal supersegment while alkali olivine basalts dominate the oblique supersegment. MgO ranges from rare undifferentiated parental-type liquids with 10.02 wt%, largely from the amagmatic accretionary segments, to highly evolved liquids with 3.5 wt%, suggesting crystal fractionation as an important compositional control. Corresponding Mg#s (where  $Mg\# = 100 * (Mg^{2+}) / (Mg^{2+} + Fe^{2+})$ ; with  $Fe_2O_3/FeO = 0.15$ ) also span a wide range from 72.7 down to 40.7. Major element compositions show a large range from depleted N-MORB to E-MORB (Figure 5a).  $K_2O$  concentrations as high as 2.2 wt% occur and as a result K/Ti values range from 0.04 up to 0.80. The K/Ti vs. MgO plot in Figure 5a allows classification and discrimination of the lavas from the different tectonomagmatic provinces, where N-MORB has  $K/Ti < 0.09$ , T-MORB has  $K/Ti$  from 0.09 to 0.15, and E-MORB has  $K/Ti > 0.15$  and  $K_2O > 0.2$  wt% [Cushman et al., 2004; Langmuir et al., 1992; Schilling et al., 1983; Sinton et al., 1991]. A positive linear trend is also present

for K/Ti versus H<sub>2</sub>O (Figure 5b), further depicting distinct compositions for each tectonomagmatic province and illustrating the variation in enrichment within and among the provinces.

Basalts from Joseph Mayes Seamount show well-defined differentiation trends, while lavas from the amagmatic accretionary segments display significant scatter in most oxide vs. MgO plots (Figure 6). The Narrowgate segment and orthogonal supersegment lavas show variable amounts of scatter and correlation, with general negative correlations for FeO\*, Na<sub>2</sub>O, and K<sub>2</sub>O, and positive correlations for Al<sub>2</sub>O<sub>3</sub> and CaO. The discrimination between Joseph Mayes Seamount and Narrowgate segment lavas (i.e. FeO\*, Al<sub>2</sub>O<sub>3</sub>, K/Ti) suggests fundamental differences in the character of their primary magmas and/or differentiation histories. Comparison of lavas from the orthogonal supersegment to the global “Normal”-MORB averages from the EPR, MAR, and Indian Ocean [Su and Langmuir, 2002] in Figure 6 finds the orthogonal supersegment basalts to have higher Al<sub>2</sub>O<sub>3</sub> and Na<sub>2</sub>O, lower CaO, FeO\*, and CaO/Al<sub>2</sub>O<sub>3</sub>, and similar SiO<sub>2</sub> and K<sub>2</sub>O, at a given MgO. Yet, an average N-MORB composition calculated using data from this study with K/Ti < 0.09 has various characteristics similar to all four ocean basin averages, but is most similar to N-MORB from the Indian Ocean (Table 4). Average ‘normal’-MORB from the Mid-Cayman Rise, which has a full spreading rate of 20 mm/yr [Macdonald and Holcombe, 1978], lies well separated from the other ocean basins at lower MgO and oxide compositions much more similar to the alkali basalts and E-MORB of the Narrowgate segment, Joseph Mayes Seamount, and the amagmatic accretionary segments. Below we briefly describe some of the compositional characteristics of each tectonomagmatic province from east to west along-axis.

### ***Orthogonal Supersegment***

The orthogonal supersegment lavas (16°-25° E) are most depleted on the eastern end of the ridge, with K/Ti averaging ~ 0.05, typical of N-MORB globally (Figure 6). The majority of the basalts are depleted tholeiites. Sample KN162-7 26-23 from the far eastern end of the ridge is an extreme example with a maximum normative quartz of ~ 16.9%. Mg# ranges from 53.7-69.5 and has a smooth average trend from less evolved in the east to more evolved in the west (Figure 7). This is opposite the variation in estimated crustal thickness, thus more evolved basalts are associated with thicker inferred crust, as might be expected. Variation of Al<sub>2</sub>O<sub>3</sub> is similar to Mg# with a decreasing trend from east to west. FeO\*, K/Ti, and H<sub>2</sub>O all show systematic increasing trends from east to west, with SiO<sub>2</sub> and Na<sub>2</sub>O holding relatively constant, but with much less variance than lavas west of 16°E. A bit of scatter in many of the oxide trends exists on the eastern end of the supersegment and may indicate the influence (possibly amplified at ultraslow-spreading rates) of the Du Toit Fracture Zone on the thermal regime beneath the ridge [Georgen et al., 1998].

### ***Oblique Supersegment***

At ~16° E the SW Indian Ridge transitions from the final magmatic segment of the orthogonal supersegment to the easternmost amagmatic accretionary segment (14°54' E - 15°45' E). Despite 8 dredge attempts and a single gravity core we recovered mostly

peridotite and only a small, altered basalt fragment that could not be analyzed. Therefore, the next along-axis glass data is from Narrowgate segment (14°15'-14°54' E), and discussion of the lavas from the other amagmatic accretionary segments will follow.

#### *Narrowgate segment*

The Narrowgate segment has erupted significant volumes of nepheline normative alkali olivine basalt. Silica-under saturation reaches an extreme of 9.9% normative nepheline in sample VAN7 90-52, dredged from the western edge of the province. Lavas from the Narrowgate segment have strikingly elevated K/Ti and H<sub>2</sub>O, with values up to 0.8 and 1.1 wt%, respectively. These high K/Ti and H<sub>2</sub>O values distinguish the Narrowgate segment lavas from the other tectonomagmatic provinces. The Narrowgate segment lavas show a large range in Mg# (65.6-44.5), with some of the most evolved basalts sampled in the entire 9°-25°E region. They also deviate substantially from the systematic oxide trends of the orthogonal supersegment lavas, with on average lower FeO\*, higher Al<sub>2</sub>O<sub>3</sub> and Na<sub>2</sub>O, and more variable SiO<sub>2</sub> (Figure 7). A handful of lavas from the Narrowgate segment have elevated Al<sub>2</sub>O<sub>3</sub> at low MgO contents, suggesting the possibility of plagioclase involvement during melting or more likely fractional crystallization.

#### *Amagmatic accretionary segments*

In stark contrast to the highly enriched basalts from the Narrowgate segment, lavas from the amagmatic accretionary segments (specifically 11°35'-14°15' E) include some of the most depleted (K/Ti = 0.04) basalts in our study area. Yet, this tectonomagmatic province displays a large compositional range from quartz normative tholeiitic basalts to nepheline normative alkaline basalts and hawaiites. The amagmatic accretionary segment lavas are most strongly distinguished from those in the other tectonomagmatic provinces by their significant variation in silica, relative to Mg# (Figure 7). Amagmatic accretionary segment lavas extend from primitive MgO concentrations (9.82 wt%) to moderately evolved MgO contents (5.70 wt%), with largely primitive Mg# between 72.7 and 53.3, similar to lavas in the eastern orthogonal supersegment where the crust is thinnest. K/Ti and H<sub>2</sub>O show a range, but are generally elevated, with relatively constant Mg# compared to Joseph Mayes Seamount and the Narrowgate segment (Figure 7), implying that the variation in K/Ti and H<sub>2</sub>O is not correlated with extent of fractional crystallization. Other oxides show a large range in abundance variation, with Al<sub>2</sub>O<sub>3</sub> generally higher and FeO\* generally lower, relative to the orthogonal supersegment lavas. SiO<sub>2</sub> and Na<sub>2</sub>O display ranges significantly larger than the orthogonal supersegment lavas. Basalts dredged from the amagmatic accretionary trough between Joseph Mayes Seamount and the Shaka Fracture Zone (10°-11°E) have major element and volatile compositions similar to the lavas discussed here, despite erupting from a highly confused morphologic and tectonic portion of the oblique supersegment.

#### *Joseph Mayes Seamount*

Although values of K/Ti (0.2 – 0.35) and Mg# (64.2-40.7) overlap with other segments, Joseph Mayes Seamount (11°-11°45' E) is chemically distinct from the other tectonomagmatic provinces. While not as enriched as the Narrowgate segment lavas, Joseph Mayes Seamount lavas lie above the projected trends of orthogonal supersegment



lavas for K/Ti, H<sub>2</sub>O and Na<sub>2</sub>O. FeO\* abundances are the highest for Joseph Mayes Seamount lavas and extend down to values that overlap with the amagmatic accretionary segment lavas. Al<sub>2</sub>O<sub>3</sub> is consistently lower than other provinces, likely indicative of significant plagioclase crystallization. SiO<sub>2</sub> is constant and similar to the orthogonal supersegment lavas.

#### 4.4. Dissolved Water and Carbon Dioxide Abundance

Total dissolved H<sub>2</sub>O concentrations range from 0.15 to 1.04 wt% and CO<sub>2</sub> concentrations range from 141 to 256 ppm (Table 3). Although there is no correlated variation between water and carbon dioxide content, the lavas are noticeably separated by tectonomagmatic province according to H<sub>2</sub>O content, whereas the range in CO<sub>2</sub> content is similar for all provinces (Figure 8a). Water and carbon dioxide concentrations are plotted against each other along with contours of equilibration pressure (solid black lines) and mole fraction of water in the vapor (dashed black lines; X<sub>H<sub>2</sub>O</sub>). Equilibration pressures and vapor compositions for each glass were calculated based on the solubility model of *Dixon et al., [1995a]*. Southwest Indian Ridge glasses have equilibration pressures between 330 and 550 bars, corresponding to vapor compositions with H<sub>2</sub>O fractions “X<sub>H<sub>2</sub>O</sub>” between 0.004 and 0.264. The majority of the glasses have X<sub>H<sub>2</sub>O</sub> less than 0.1. Figure 8b plots calculated equilibration pressures versus estimated eruption pressures. Estimated eruption pressures reflect the depth at the start of the dredge, and since the majority of the glasses are from the rift valley floor, these represent the maximum eruption pressure. Of the 40 glasses measured, 7 are from outside the rift valley (all on the oblique supersegment) where an increased potential exists that tectonic uplift has moved these lavas to lower pressures than their eruption pressures. Variable vesicle contents (Table 2) plus super-saturation of nearly all the glasses in Figure 8b (above the 1:1 line) means the lavas were degassing volatiles upon eruption. However, because of the relative solubilities of H<sub>2</sub>O and CO<sub>2</sub> in basaltic melts, the vapor compositions in equilibrium with these glasses were CO<sub>2</sub>-rich (Figure 8a) and thus insignificant amounts of H<sub>2</sub>O were lost due to pre-eruption degassing. To verify this for highly vesicular glasses, we calculated the percent water contained in the vesicles of each sample (using dredge averaged vesicularity from Table 1 and the dredge depths as eruption pressures). We found that the largest percentage of H<sub>2</sub>O lost by any sample (KN162-7-33-49) due to degassing was 3.6% of the measured H<sub>2</sub>O concentration, which is less than the internal error (4%) for the initial absorbance measurement. No statistically significant amounts of H<sub>2</sub>O, therefore, have been lost from any of our glasses.

### 5. Discussion

#### 5.1. Major Element Petrogenesis - Fractional crystallization

The cooling of magma as it ascends buoyantly to shallower levels inevitably leads to crystallization and differentiation at a range of pressures. Here we discuss the major element variation observed along the SW Indian Ridge, between 9° – 25°E, and compare



it with modeled liquid lines of descent (LLDs) to assess the amount of chemical heterogeneity that can be accounted for by fractional crystallization.

When grouped in their respective tectonomagmatic provinces the lavas define reasonably linear trends (Figure 6). Lavas from all four provinces show decreasing  $\text{Al}_2\text{O}_3$  and CaO, and increasing  $\text{FeO}^*$ ,  $\text{Na}_2\text{O}$ , and  $\text{K}_2\text{O}$  with decreasing MgO, that is typical of liquid evolution resulting from phase saturation of olivine and plagioclase  $\pm$  clinopyroxene. One exception exists, that being the Narrowgate segment lavas with a flat to slightly negative slope for  $\text{Al}_2\text{O}_3$  versus MgO. This could be the result of a number of processes including plagioclase resorption, suppression of plagioclase and clinopyroxene crystallization, or variable parental melt compositions and thus variable LLDs. Most of these compositional trends are supported by the presence of varying proportions of olivine and plagioclase phenocrysts (Table 2). Despite little if any observed augite in hand sample or thin section, as is commonly the situation for MORB, [e.g. Grove et al., 1992; le Roux et al., 2002b; Reynolds and Langmuir, 1997; Thompson et al., 1980] a phase is required to explain decreasing CaO with decreasing MgO or Mg#. The majority of MORB petrogenetic studies show major and trace element compositional variations that also require the participation of augite (along with olivine and plagioclase) as a crystallizing phase [e.g. le Roux et al., 2002b], and our basalt suite is no different. The most common explanation for this discrepancy is higher-pressure crystallization of clinopyroxene [Grove et al., 1992; Schilling et al., 1983] followed by subsequent resorption, or at least cessation of crystallization, as the melt moves to lower pressures. To investigate the importance and absence of augite and also constrain the amount of heterogeneity that can be accounted for by fractional crystallization, we used the recently released “Adiabat\_1ph” program [Smith, 2005] to quantitatively forward model liquid lines of descent for parental liquid compositions. Details regarding the setup and use of “Adiabat\_1ph” and MELTS [Ghiorso and Sack, 1995] are discussed in Appendix 1.

### ***Low-pressure crystallization***

As a starting point we selected one of the most primitive lavas in our suite (KN162 48-21), with 9.82% MgO, as our parental liquid in forward models. This makes the technically unrealistic assumption that all of our lavas evolved from similar MgO contents. Basaltic mid-ocean ridge liquids typically follow the fractionating assemblage of olivine ( $\pm$  spinel), olivine + plagioclase, and olivine + plagioclase + clinopyroxene as the liquid moves to lower temperature and pressure, although clinopyroxene crystallization is often associated with higher-pressures [Bryan, 1983; Bryan and Moore, 1977; Grove et al., 1992; Thompson et al., 1980]. Using MELTS we model the evolution path of KN162 48-21 in order to assess the crystallization history of a typical parental liquid from our study area.

Figure 6 shows a series of liquid lines of descent (LLDs) that trace the compositional course of parental liquid 48-21 as it cools. Each of the four LLDs represents a different combination of pressure - 1 kbar (thin lines) or 3 kbar (thick lines), and  $\text{H}_2\text{O}$  content - 0.18 wt% (red lines) or 0.6 wt% (blue lines), with the same major element starting composition. The 1 kbar LLD with 0.18 wt% water does overlap large portions of the

major element compositional variation (i.e.  $\text{SiO}_2$ ,  $\text{Na}_2\text{O}$ ,  $\text{CaO}$ ), yet it is clear that more major element heterogeneity exists than can be accounted for by differentiation of this single parental melt composition. In most of the oxide versus  $\text{MgO}$  plots, the LLDs display subtle to sharp kinks, particularly  $\text{Al}_2\text{O}_3$ ,  $\text{CaO}$ , and  $\text{FeO}^*$  that reflect changes in the crystallizing assemblage with decreasing temperature. Specific to the 1 kbar (0.18 wt%  $\text{H}_2\text{O}$ ) LLD, saturation of plagioclase at  $\text{MgO}$  of 9.37 wt% and  $1232^\circ\text{C}$  is followed by saturation of Cpx at 7.56%  $\text{MgO}$  and  $1191^\circ\text{C}$ . The simple fact that these modeled liquid lines of descent overlap some of our data does not prove phase saturation, or the specific  $\text{MgO}$  contents and temperatures.

The overall trend of decreasing  $\text{Al}_2\text{O}_3$  with decreasing  $\text{MgO}$  that is displayed by Joseph Mayes Seamount, the orthogonal supersegment, and the amagmatic accretionary segment lavas are consistent with crystallization of Plag + Oliv + Cpx. Based on our modeled 1 kbar liquid line of descent together with observed slopes of high- $\text{MgO}$  lavas in  $\text{Al}_2\text{O}_3$  versus  $\text{MgO}$  and  $\text{CaO}/\text{Al}_2\text{O}_3$  versus  $\text{MgO}$  (Figure 6), we infer that lavas with  $\text{MgO}$  contents greater than 7.56 wt% (augite saturation point) may not have crystallized clinopyroxene, if they crystallized solely at 1 kbar.

Indeed the general negative trends displayed by high  $\text{MgO}$  lavas in  $\text{CaO}/\text{Al}_2\text{O}_3$  versus  $\text{MgO}$  and also for Sc versus  $\text{MgO}$  (Figure 9) suggest little to no involvement of Cpx during differentiation, especially for the orthogonal supersegment lavas. However, we have highlighted individual dredges from both the orthogonal supersegment and the amagmatic accretionary segment (small red and blue dots, respectively in Figure 9) to illustrate local differentiation trends. In both  $\text{CaO}/\text{Al}_2\text{O}_3$  versus  $\text{MgO}$  and Sc versus  $\text{MgO}$  these individual dredges have differentiation trends that are flat (constant  $\text{CaO}/\text{Al}_2\text{O}_3$  or Sc) or positively sloped, implying saturation of Cpx. Furthermore, both individual dredges have lavas with  $\text{MgO}$  contents above 7.56 wt%, indicating that augite saturation at 1 kbar may occur at higher  $\text{MgO}$  contents than indicated by MELTS modeling, or Cpx is in the crystallizing assemblage at higher pressures, as suggested by the modeled LLD at 3 kbar (Figure 6).

### ***High-pressure, polybaric crystallization***

From numerous basalt studies at mid-ocean ridge settings [e.g. Elthon, 1989; Grove et al., 1992; Herzberg, 2004; e.g. Kushiro, 1964; Kushiro, 1973; Michael and Cornell, 1998; O'Hara, 1968] crystallization pressures in excess of 10 kbar have been inferred. At higher pressures the augite stability field increases at the expense of the olivine stability field [Bender et al., 1978; Elthon, 1989; Kushiro, 1964, 1973; O'Hara, 1968], leading to augite saturation at higher temperatures, relative to olivine and plagioclase. Is it likely that fractional crystallization of MORB on an ultraslow spreading ridge would occur at pressures above 3 kbar ( $\sim 9$  km) [Michael and Cornell, 1998]. We investigate this issue in a number of ways, but first we forward model the same parental composition ( $\text{H}_2\text{O} = 0.18$  wt%) at 3 kbar. The representative LLD (Figure 6, thick red line) shows augite joining the fractionating phase assemblage at  $1231^\circ\text{C}$  and 8.78%  $\text{MgO}$ , significantly earlier than augite saturation at 1 kbar (7.56%  $\text{MgO}$  and a temperature of  $1191^\circ\text{C}$ ). The elevated pressure during crystallization also leads to higher  $\text{Al}_2\text{O}_3$  in the melt at a given

MgO, and thus a large portion of the variability in  $\text{Al}_2\text{O}_3$  and CaO can be modeled by polybaric crystal fractionation at pressures starting above 3 kbar and extending down to and below 1 kbar.

Partial crystallization pressures for ol + plag + cpx within the global MORB database have been suggested to range between 1 atm. - 1 GPa [Herzberg, 2004]. Assuming 3-phase saturation of olivine, plagioclase, and clinopyroxene at some early phase in their crystallization history above 3 kbar, basalt compositions are recalculated and projected into a CMAS pseudoternary diagram [Grove et al., 1992], illustrating estimated partial crystallization pressures relative to experimentally determined saturation boundaries. In Figure 10a & b we show lavas from each tectonomagmatic province relative to the olivine, plagioclase, augite, low-Ca pyroxene, and melt saturation boundary (OPALM; green X's), and the olivine, plagioclase, augite, and melt saturation boundary (OPAM; black lines), plotted at various pressures ranging from 0.001 to 10 kbars [Grove et al., 1992]. They span a range of saturation pressures, with orthogonal supersegment and amagmatic accretionary segment lavas plotting at pressures generally between 4-8 kbar and Joseph Mayes Seamount and Narrowgate segment lavas at pressures between 1 atm. and 4 kbar. Despite the overall range displayed by the entire suite, each tectonomagmatic province is distinct, suggesting along-axis variations in initial 3-phase saturation pressure are quite dramatic, and by inference may indicate local differences in lithospheric thickness, re-equilibration depths, melt extraction pathways, and mantle melting column heights.

Separately, we calculated partial crystallization pressures using equation 6 in Herzberg [2004], finding good agreement with pressures displayed in Figure 10a & b. Lavas from the orthogonal supersegment span a large range between 2-8 kbars, with the bulk of the basalts falling between 4-7 kbars (Figure 10c). In general the shallowest pressures lie to the west and the deepest proximal to the Du Toit FZ, where the majority of lavas from the easternmost dredge are between 7-8 kbars. This along-axis trend correlates with the slight increase in gravity-inferred crustal thickness, consistent with greater conductive cooling toward Du Toit FZ. The glasses from the amagmatic accretionary segment show the largest range in partial crystallization pressure from 2 to ~ 11 kbar, with the N-MORB compositions ( $\text{K/Ti} < 0.1$ ; blue triangles) plotting below 6 kbar (Figure 10c). This is not surprising as these depleted lavas are from the portion of the amagmatic trough with the greatest obliquity ( $11^\circ 45' - 13^\circ$ ), thus likely have the thickest lithosphere. These pressures are much higher, with minimal overlap, than lavas from the bordering Narrowgate segment and Joseph Mayes Seamount. Both the Narrowgate segment and Joseph Mayes Seamount lavas plot at pressures less than 4 kbar, also much shallower than the orthogonal supersegment lavas, despite having similar effective spreading rates (i.e. upwelling rates). These two tectonomagmatic provinces reflect partial crystallization pressures more in line with fast-spreading EPR type environments [Herzberg, 2004; Michael and Cornell, 1998], yet their inferred upwelling rates are only 14.2 and 13.3 mm/yr, respectively. Large variations of partial crystallization pressures within a single dredge indicate substantially different polybaric crystallization histories for individual lavas, similar to lavas on the Mid-Atlantic Ridge [Herzberg, 2004].

One explanation for the low pressures of crystallization may be increased thermal or melt flux [Michael and Cornell, 1998], resulting from melt focusing toward magmatically robust segments, and away from the amagmatic accretionary segments. Just as fast-spreading ridges have a higher magma supply and heat flux relative to slow-spreading ridges, the orthogonally spreading volcanic segments (i.e. JMS and the Narrowgate segment) must experience higher melt flux than the neighboring oblique amagmatic accretionary segments. Segment-scale variations in melt focusing and melt flux are likely attributable to the changing lithospheric thicknesses along-axis, supported by the differences in predicted pressures of partial crystallization among tectonomagmatic provinces (Figure 10c). 3-D numerical modeling of heat flow beneath a ridge segment suggests there would be significant temperature differences extending below 30 km depth as a function of spreading geometry. A ridge segment with an obliquity of 60° (relative to spreading direction, and comparable to our study area) is modeled to have a temperature ~ 100° cooler at 30 km depth compared to an orthogonal spreading ridge segment [Barry, 2005]. It is possible that along-axis fluctuations in partial crystallization pressures and the related thermal variations could be associated with buoyant 3-D mantle upwelling, however, this preliminary modeling and the resulting range in temperatures was modeled using a 2-D passive flow regime [Barry, 2005]. This indicates that changes in along-axis spreading geometry (i.e. mantle upwelling rate) can have dramatic effects on the depth to which conductive cooling penetrates, and thus lithospheric thickness. These findings are consistent with observed correlations between partial crystallization pressures and ridge segmentation [Dmitriev, 1998].

The top of the melting regime is bounded by the termination of mantle melting and presumably is closely associated with the initiation of partial crystallization. While predicted pressures of partial crystallization [Herzberg, 2004] cannot directly constrain the depth at which melting ceases, initiation of partial crystallization does provide an upper limit to the melting regime. Therefore the variable pressures of partial crystallization imply significant along-axis topography to the top of the melting regime, which by inference suggests variation in lithospheric thickness, and potentially different mean pressures of melting within each tectonomagmatic province. Indeed, shallow melting relative to deep melting of the same composition should produce higher SiO<sub>2</sub> [Jaques and Green, 1980]. Yet the observation from Figure 10a that many of the Narrowgate segment, Joseph Mayes Seamount, and amagmatic segment lavas are nepheline normative is thus a bit counter intuitive. What we have not considered yet is the importance and affect that melt-rock interaction can have on the major element composition of melt generated at depth that must traverse through significant peridotite before erupting. Owing to the significant leverage that peridotite has on SiO<sub>2</sub> (as well as FeO and MgO), varying extents of re-equilibration between melt and host peridotite could make a large difference. By contrast, low-silica alkali basalts commonly erupt bearing mantle xenoliths - a testament to their rapid ascent from deep in the mantle with little equilibration.



## 5.2. Variation in Parental Melt Compositions

### *Fractionation correction*

In order to quantify the major element variation in parental melt compositions it is necessary to remove the effects of low-pressure crystal fractionation. To accomplish this we correct our lava compositions to an MgO content of 8.0 wt% [Klein and Langmuir, 1987]. Following the methods of *Cushman et al.*, [2004], we fit linear regressions to SiO<sub>2</sub>, FeO\*, CaO, and Al<sub>2</sub>O<sub>3</sub>, and power law regressions to Na<sub>2</sub>O, K<sub>2</sub>O, P<sub>2</sub>O<sub>5</sub>, TiO<sub>2</sub>, and H<sub>2</sub>O. The regressions match well the modeled liquid line of descent for a single parental composition and are therefore held to represent the differentiation path resulting from three-phase saturation (olivine, plagioclase, and clinopyroxene). Individual regressions were fit to each of the tectonomagmatic provinces when statistically significant. Alternatively, provinces were combined and regressed as a single group. Fractionation corrections were only applied to lavas with MgO contents between 3.5 and 8.5 wt%, and corrected elemental values are specifically designated with subscripts (e.g. Fe<sub>8</sub>, Na<sub>8</sub>, K/Ti<sub>8</sub>).

### *Along-axis variations*

One of the most striking features of our data is the systematic compositional behavior observed along the orthogonal supersegment compared to the high level of variability on the oblique supersegment (Figure 11). The oblique supersegment lavas scatter about the projected trends of the orthogonal supersegment lavas for Na<sub>8</sub> and (Ca/Al)<sub>8</sub>, lie dominantly above the trend for (Si/Fe)<sub>8</sub>, (K/Ti)<sub>8</sub>, and H<sub>2</sub>O<sub>8</sub>, and below the trend for Fe<sub>8</sub>. Yet the apparent randomness of the fractionation-corrected compositions between 9°-16°E become much more systematic when grouped into their respective tectonomagmatic provinces. The individual lava compositions from each province generally overlap with lavas from other provinces, but average compositions for each province illustrate distinctly different chemistry (Table 4). Here we discuss major element fractionation-corrected abundances and ratios and what the observations indicate with regard to various melting parameters, e.g. degree of melting (Na<sub>8</sub>, (Ca/Al)<sub>8</sub>) and pressure of melting (Fe<sub>8</sub> and (Si/Fe)<sub>8</sub>). We also assess variations in (K/Ti)<sub>8</sub> and H<sub>2</sub>O<sub>8</sub> and discuss possible explanations for the overall range and province specific variations.

The orthogonal supersegment lavas display generally tight, systematic along-axis compositional variation, as seen in Figure 11 for Na<sub>8</sub>, Fe<sub>8</sub>, (Si/Fe)<sub>8</sub>, and (K/Ti)<sub>8</sub>, and less so for (Ca/Al)<sub>8</sub>. Na<sub>8</sub> values (higher values approximate low mean extent of melting of a homogeneous source composition) are nearly constant from east to west across the orthogonal supersegment (avg. = 3.13), with only a slight decreasing trend on the western portion of the ridge. (Ca/Al)<sub>8</sub> values (higher values approximate high mean extent of melting, after Niu & Batiza, [1991]) are more variable along-axis, but also maintain a relatively constant level at 0.69. It is an altogether different story on the oblique supersegment, where the Narrowgate segment lavas have (Ca/Al)<sub>8</sub> from 0.75-0.87 (with only a single lava outside that range at 0.67) and the Joseph Mayes Seamount lavas range from 0.81-0.88. Both magmatically robust segments have (Ca/Al)<sub>8</sub> indicative of high mean degree of melting, relative to the orthogonal supersegment. This would insinuate that Na<sub>8</sub> for Joseph Mayes Seamount and the Narrowgate segment lavas should

be lower than the orthogonal supersegment, but values are nearly identical (within standard deviation; Table 4 & Figure 11).  $\text{Na}_8$  for the amagmatic accretionary segments ranges from 2.61-4.06, with a majority of the N-MORBs having the highest  $\text{Na}_8$ . This is counterintuitive to conventional melting models, which associate N-MORB generation with high mean extent of melting and E-MORB generation with low mean extent of melting.  $(\text{Ca}/\text{Al})_8$  in the amagmatic accretionary segment lavas also suggest low mean extent of melting, as most of the lavas fall below the generally constant value for the orthogonal supersegment of 0.69.

Major element indicators of partial melting pressure ( $\text{Fe}_8$  and  $(\text{Si}/\text{Fe})_8$ ) are also quite different east and west of  $16^\circ\text{E}$ . The orthogonal province lavas display systematic trends of increasing  $\text{Fe}_8$  and decreasing  $(\text{Si}/\text{Fe})_8$  from east to west, similarly indicating higher mean pressures of partial melting to the west. The western most volcanic segment of the orthogonal supersegment deviates from the overall trend, with lavas having mostly lower  $\text{Fe}_8$  and higher  $(\text{Si}/\text{Fe})_8$ . Average  $\text{Fe}_8$  and  $(\text{Si}/\text{Fe})_8$  values for the orthogonal supersegment are 8.84 and 5.72, respectively. Lavas from the oblique supersegment, with the exception of a handful of amagmatic accretionary segment lavas, have lower  $\text{Fe}_8$  and higher  $(\text{Si}/\text{Fe})_8$  relative to the orthogonal supersegment lavas, suggesting lower mean pressures of partial melting. The Narrowgate segment glasses have the lowest average  $\text{Fe}_8$  (6.36) and highest  $(\text{Si}/\text{Fe})_8$  (7.93) for any of the tectonomagmatic provinces, while Joseph Mayes Seamount basalts are tightly clustered with average  $\text{Fe}_8$  of 7.75 and  $(\text{Si}/\text{Fe})_8$  of 6.46. The amagmatic accretionary segment lavas are highly variable, spanning nearly the full range from the highest  $\text{Fe}_8$  and lowest  $(\text{Si}/\text{Fe})_8$  of the orthogonal supersegment province to the lowest  $\text{Fe}_8$  and highest  $(\text{Si}/\text{Fe})_8$  of the Narrowgate segment.

As we briefly discussed in section 4.3, variations in  $\text{Mg}\#$  correlate with the estimated crustal thickness measurements for each province. The Narrowgate segment and Joseph Mayes Seamount lavas have the largest range in  $\text{Mg}\#$  and the most evolved basalts, together with the thickest estimated crust and for Joseph Mayes Seamount the shallowest depth. The depth to the axis of rifting for the Narrowgate segment is similar to other orthogonal supersegment segments (Figure 11), although the off-axis depth associated with Narrowgate segment is much shallower than other volcanic segments (Figure 4). The orthogonal supersegment similarly shows decreasing  $\text{Mg}\#$  from east to west correlated with increasing crustal thickness, although overall depths remains constant. Tracers of pressure of partial melting are a bit anomalous for the amagmatic accretionary segment lavas, where we would expect thin crust and low extents of melting to signify higher mean pressures of melting (i.e. high  $\text{Fe}_8$  and low  $(\text{Si}/\text{Fe})_8$ ). This may indicate shallow re-equilibration of melts during transport, especially considering the low volume flux of melt in the amagmatic accretionary segments. Low  $\text{Fe}_8$  and high  $(\text{Si}/\text{Fe})_8$ , particularly for the Narrowgate segment glasses can be attributed to higher extents of melting (high  $(\text{Ca}/\text{Al})_8$ ), and assuming constant mantle potential temperature would result in lower mean partial melting pressures.

$(\text{Ca}/\text{Al})_8$  for the Narrowgate segment and Joseph Mayes Seamount is significantly higher than either the amagmatic accretionary segment or orthogonal supersegment lavas,



and thus requires a brief discussion. The disagreement between  $(\text{Ca}/\text{Al})_8$  and  $\text{Na}_8$ , both indicators of degree of melting, lends support to a heterogeneous mantle source, especially considering the elevated and variable  $(\text{K}/\text{Ti})_8$ . With parental melts having such elevated  $(\text{Ca}/\text{Al})_8$  the possibility exists for shallow melting of spinel harzburgite, as orthopyroxene has a  $\text{CaO}/\text{Al}_2\text{O}_3 \approx 1$  and pressures of partial crystallization for both provinces are inferred to indicate partial melting to low pressures (Figure 10). Of course shallow re-equilibration of deeply formed melts with shallow cpx-free depleted peridotite would have similar effects on  $\text{CaO}/\text{Al}_2\text{O}_3$ . Certainly further investigation of this striking difference in  $(\text{Ca}/\text{Al})_8$  is needed, but at the present we have not reached an acceptable explanation. Although it is presumed that the source is not homogeneous it is still interesting to note that the high mean extent of melting indicated by high  $(\text{Ca}/\text{Al})_8$  at Joseph Mayes Seamount and the Narrowgate segment coincides with thicker than normal crust, and the low mean extent of melting (low  $(\text{Ca}/\text{Al})_8$ ) for the amagmatic accretionary segments is associated with significantly thinned crust.

Figure 11 also plots  $(\text{K}/\text{Ti})_8$  and  $\text{H}_2\text{O}_8$ , showing abrupt enrichment between the western end of the orthogonal supersegment and the Narrowgate segment lavas. The orthogonal supersegment again shows systematic compositional behavior with slightly increasing trends for both  $(\text{K}/\text{Ti})_8$  (0.04 – 0.26) and  $\text{H}_2\text{O}_8$  (0.14–0.3 wt%) from east to west.  $(\text{K}/\text{Ti})_8$  shows a sharp increase at the Narrowgate segment with values between ~ 0.2 and 0.8. Joseph Mayes Seamount lavas contain elevated  $(\text{K}/\text{Ti})_8$  ranging from 0.14–0.31 and  $\text{H}_2\text{O}_8$  from 0.27–0.44 wt%. In between these two magmatic segments, the amagmatic accretionary segment has highly variable  $(\text{K}/\text{Ti})_8$  and  $\text{H}_2\text{O}_8$ , ranging from 0.03 to 0.44 and 0.21 to 0.58 wt%, respectively. While fractional crystallization can affect both  $(\text{K}/\text{Ti})_8$  and  $\text{H}_2\text{O}_8$ , the large range observed along-axis among the tectonomagmatic provinces is a function of something other than low-pressure fractionation. This is exemplified by the significant variation of  $(\text{K}/\text{Ti})_8$  and  $\text{H}_2\text{O}_8$ , and the subsequent strong correlation between  $(\text{K}/\text{Ti})_8$  and  $\text{H}_2\text{O}_8$ . The range in fractionation corrected  $\text{H}_2\text{O}_8$  content illustrates substantial variation in primary lava composition, both between and within each province, and also suggests that  $\text{H}_2\text{O}$  content may play an important role during magma differentiation. Figure 5b clearly shows that each tectonomagmatic province occupies a distinct area of  $\text{K}/\text{Ti}$  vs.  $\text{H}_2\text{O}$  space, with the exception of the amagmatic accretionary segment lavas, which span nearly the entire range from depleted to enriched. The distinct nature of each province suggests that the mechanisms controlling MORB chemistry (i.e. source composition and/or process) are highly variable along this portion of the Southwest Indian Ridge.

### ***Influence of $\text{H}_2\text{O}$***

Dissolved  $\text{H}_2\text{O}$  content of the melt can substantially influence the low-pressure evolution of magma by suppression of plagioclase saturation relative to clinopyroxene and olivine [Kushiro, 1972, 1975; Michael and Chase, 1987; Yoder and Tilley, 1962]. A number of recent MORB petrogenetic studies [e.g. Asimow et al., 2004; Asimow and Langmuir, 2003; Christie et al., 2005; Cushman et al., 2004; Danyushevsky, 2001] have revisited this issue, showing a range of effects due to increased  $\text{H}_2\text{O}$  during fractional crystallization (and melting). Most recently *Asimow et al.*, [2004] concluded that major

element variability at a given MgO content (for Azores basalts) is dominantly created by the effect of H<sub>2</sub>O on low-pressure fractionation rather than melting.

Basalts from our study area range from 0.15 to 1.06 wt% H<sub>2</sub>O, and as seen in Figure 7 & 8. H<sub>2</sub>O content correlates well with other indices of source enrichment (K/Ti) and is systematically segregated between tectonomagmatic provinces, forming a fairly continuous gradation from typical N-MORB concentrations (~ 0.2 wt%) to E-MORB concentrations (~ 1.0 wt%). This observed range in H<sub>2</sub>O content allows us to assess the influence of water on low-pressure fractionation, by modeling and comparing liquid lines of descent for two compositionally identical parental melts; one containing the lowest fractionation-corrected H<sub>2</sub>O content (0.18 wt.%) and a second with the highest fractionation-corrected H<sub>2</sub>O content (0.60 wt.%). We presume a linear dependence between H<sub>2</sub>O content and its influence on major element chemistry [Asimow et al., 2004], and we apply graphical methods to constrain the absolute variation of major element abundances as a function of H<sub>2</sub>O content.

Figure 6 shows the LLDs (both at 3 kbars) for the parental melt with 0.18 wt% (H<sub>2</sub>O)<sub>8</sub> (thick red curve) compared to the parental melt with 0.6 wt% (H<sub>2</sub>O)<sub>8</sub> (thick blue curve). The suppression of plagioclase crystallization caused by higher H<sub>2</sub>O leads to large differences in melt composition at the same MgO content, especially lower FeO and higher Al<sub>2</sub>O<sub>3</sub>. SiO<sub>2</sub> and Na<sub>2</sub>O are only slightly higher while CaO is slightly lower. Differences in K<sub>2</sub>O and TiO<sub>2</sub> trends are not discernable, showing that the variable conditions during crystallization cannot account for the significant range in K<sub>2</sub>O or K/Ti.

#### ***Global variations in Na<sub>8</sub> & Fe<sub>8</sub>***

Comparison of our individual tectonomagmatic provinces to the “global array” of regional MORB averages [Klein and Langmuir, 1987] finds the orthogonal supersegment glasses lie within the global array (Figure 12), but at lower Fe<sub>8</sub> and higher Na<sub>8</sub> than averages for normal-MORB from the MAR, EPR, and the Indian Ocean [Su and Langmuir, 2002], and at higher Fe<sub>8</sub> and lower Na<sub>8</sub> than the Mid-Cayman Rise [Elthon et al., 1995](Table 4). The position of the orthogonal supersegment within the global array is consistent with the slow-spreading architecture of the Southwest Indian Ridge and the relatively deep axial valley (~4000 meters). Inferred crustal thicknesses of between 4 and 6 km correspond to the global trend of crustal thickness versus Na<sub>8</sub> [Klein and Langmuir, 1987]. However, very slow spreading ridges may be greatly influenced by top-down conductive cooling compared to faster spreading ridges [Reid and Jackson, 1981], which would alter the thermal regime. Theoretically then, the oblique amagmatic accretionary segments with lower inferred upwelling rates should incur greater conductive cooling of the lithosphere and thus deeper cessation of melting.

The other tectonomagmatic groups lie off the global array at higher Na<sub>8</sub> and lower Fe<sub>8</sub> at a given ridge depth (Figure 12a & b), conventionally interpreted to reflect lower mean extents and pressures of melting. The amagmatic accretionary segment lavas are quite variable (blue fields, Figure 10), with average Fe<sub>8</sub> and Na<sub>8</sub> slightly lower than the global array, but similar to Mid-Cayman Rise lavas (Figure 12c). Based on the average ridge depths of Narrowgate segment and Joseph Mayes Seamount lavas, and to a lesser extent

those of the amagmatic accretionary segments,  $Fe_8$  sits well below the global array, suggesting much lower mean melt extraction pressures than ridges at similar depths. However, the anomalously low  $Fe_8$  compared to the global array could be the result of increased  $H_2O$  in the melt, thus changing the LLD and  $Fe_8$  [Asimow et al., 2004]. Indeed, the deviation of  $Fe_8$  from the global array is correlated with the  $H_2O$  content of the parental melt. In other words, if  $H_2O$  varies by  $\sim 0.4$  wt%, this is equivalent to a difference in  $FeO^*$  of  $\sim 2$  wt%, at a given  $MgO$  of 7.6 – arrived at graphically by comparing the 1 kbar LLDs in Figure 6. Therefore, the influence of  $H_2O$  on differentiation of parental melts is substantial, and accounts for most of the difference in  $Fe_8$  between the orthogonal supersegment and the Narrowgate segment averages.

$Na_8$  is only slightly affected by elevated  $H_2O$  and since  $Na_8$  is fairly constant along-axis any adjustments will have little impact on interpretation. However, adjustment of  $Fe_8$  based on the water content of the lavas would shift the Narrowgate segment and Joseph Mayes Seamount lavas closer to the global array (at a constant  $Na_8$ ), and thus only the amagmatic accretionary segment lavas would have a higher  $Na_8$ , as might be expected based on conductive cooling arguments. Because higher  $H_2O$  contents delay the crystallization of plagioclase the  $Al_2O_3$  content of the melt will be higher. Thus, at a constant  $MgO$ ,  $Al_8$  is elevated by  $\sim 1.5$  wt% for lavas that have high water contents. One might also expect a significant effect on  $CaO$  abundances, but because plagioclase is suppressed to a larger extent than clinopyroxene the effect of elevated  $H_2O$  on  $Ca_8$  is only 0.5 wt%. This means that the influence of  $H_2O$  on  $CaO/Al_2O_3$  is measurable for those lavas with significant  $H_2O$  content.

It is also important to note that once suppression of plagioclase and clinopyroxene extends below 8%  $MgO$ ,  $Fe_8$  and other “element-8” values will no longer be influenced, even though suppression of plagioclase may continue to influence the LLD [Asimow et al., 2004]. They determined this point to occur at 0.7 wt%  $(H_2O)_8$  for the Azores, which is higher than the maximum  $(H_2O)_8$  for our suite (0.61 wt%). However, the influence of  $H_2O$  on low-pressure fractional crystallization prior to this point provides an explanation for the anomalously low  $Fe_8$  and high  $Al_8$  (Figure 11) at a given  $MgO$  in volatile-rich lavas, particularly from the Narrowgate segment and Joseph Mayes Seamount.

Preliminary numerical modeling [Barry, 2005] shows substantial differences in the temperature at a given depth beneath an orthogonal spreading segment versus a segment spreading  $60^\circ$  oblique to the spreading direction (equivalent to the maximum obliquity on the oblique supersegment). For example, at 10 km beneath the ridge axis the temperature varies  $\sim 300^\circ$  C between an orthogonally oriented segment and a highly oblique one, and even at 50 km depth there is a temperature difference of  $\sim 14^\circ$  C. In addition, enhanced conductive cooling as a function of upwelling rate has a significant influence on the cessation of melting, extent of melting, and the mean pressure of melting, thereby complicating the interpretation of  $Na_8$  and  $Fe_8$ .

### 5.3. MORB Source Mantle

#### ***“Normal” - MORB***

A significant portion of the major element variation can be explained by polybaric fractional crystallization with variable parental H<sub>2</sub>O contents. However, many of the observed relationships among the fractionation-corrected abundances, for example the covariation of Fe<sub>8</sub>, (Si/Fe)<sub>8</sub>, and (K/Ti)<sub>8</sub> on the orthogonal supersegment cannot be explained by low-pressure crystallization, and therefore must be generated by variations in melting process and/or source composition. The differences in major element chemistry between the tectonomagmatic provinces suggest either significant variation of melting parameters (i.e. extent of melting, mean melting pressure) along-axis or the MORB source composition is variable, or both. However, before we attempt to explain the variation to highly enriched compositions, let us first focus on modeling the generation of typical depleted N-MORB, which dominates the orthogonal supersegment and sporadically erupts within the amagmatic accretionary segments.

The orthogonal supersegment lavas, especially the eastern-most lavas, have K/Ti values characteristic of N-MORB, and overall their major element compositions are very similar to segment averaged “normal”-MORB compositions for the EPR, MAR, and Indian Ocean [Su and Langmuir, 2002]. Over the past decades numerous major element experimental studies [Gaetani and Grove, 1998; Kinzler and Grove, 1992a; Pickering-Witter and Johnston, 2000; Wasylenki et al., 2003] and petrologic models [Kinzler and Grove, 1992b; Klein and Langmuir, 1987; Langmuir et al., 1992; Shen and Forsyth, 1995] have attempted to generate the compositional range observed in global MORB data. Kinzler [1997] used experimental results of spinel lherzolite melting between 1.5 and 2.3 GPa to parameterize a melting model which presents polybaric, near-fractional aggregate magma compositions over a range of pressure intervals, assuming both a triangular melting regime [Plank and Langmuir, 1992] and a columnar melting regime [Kinzler and Grove, 1992b]. While more recent experimental work and modeling efforts have been published, the straightforward nature of her methodology provides a useful array of aggregate melt compositions for depleted spinel lherzolite. We have adopted these compositions as a proxy for aggregate melt compositions produced by melting of the ambient depleted MORB mantle beneath this portion of the Southwest Indian Ridge. Kinzler's [1997] starting mantle composition was derived by depleting the primitive upper mantle composition estimated by Hart and Zindler [1986], and thus may be more fertile than other depleted peridotite compositions.

The modeled aggregate liquid compositions [Kinzler, 1997] are derived assuming passive upwelling and a triangular melting regime, and hence have a larger contribution from deeper, small degree melts, relative to a columnar shaped regime. The primitive depleted mantle melts are plotted in Figure 13 (as black diamonds), at higher Mg# from 71 to 76 than the most magnesium-rich N-MORBs from the SWIR. The aggregate

compositions form a smooth melting array representing 4%, 7%, 9%, 11%, and 13% melt fractions. The array covers a range of oxide concentrations, with the exception of  $K_2O$  and  $TiO_2$ , as is expected based on compatibility in fractionating phases.

Multiple liquid lines of descent have been modeled from various aggregate melt compositions (e.g. variable  $F$ ) in an attempt to account for the range in major element concentrations of the SWIR data. It is apparent from the various LLDs (same descriptions as Figure 6) that a range in aggregate melt compositions, pressures of crystallization, and  $H_2O$  content of the melts is required to adequately model the full major element compositional variation. For  $SiO_2$ ,  $FeO^*$ ,  $CaO$ ,  $Na_2O$ , and  $TiO_2$  the compositional range of the orthogonal supersegment lavas can be modeled by near-fractional melting of depleted spinel lherzolite, followed by low-pressure fractionation involving Oliv  $\pm$  Plag  $\pm$  Cpx. Thin red lines ( $H_2O = 0.18$  wt%) in Figure 13 represent the modeled fractionation trends, at 100 bars, of aggregate melt compositions produced by 7% and 9% partial melting. The large range in  $Al_2O_3$  is not sufficiently constrained by this partial melting and crystal fractionation sequence. Low-pressure modeled trends have  $Al_2O_3$  abundances lower than the orthogonal supersegment data. However, calculated pressures of partial crystallization indicate that the orthogonal supersegment lavas likely begin crystallizing at pressures  $> 4$  kbar (Figure 10c). Further modeling finds that fractional crystallization of a 7% partial melt of depleted peridotite at 3 kbar, provides an upper concentration limit for the N-MORBs, suggesting polybaric fractional crystallization. Polybaric crystallization is further insinuated from the range in pressures calculated for initiation of 3-phase partial crystallization. Therefore the N-MORBs from the orthogonal supersegment and those N-MORBs from the amagmatic accretionary segment can be quantitatively modeled by 7% to 9% partial melting of depleted spinel lherzolite followed by polybaric fractional crystallization initiating at 3 kbar but likely greater, and continuing to nearly atmospheric pressures.

#### ***“Enriched” – MORB from depleted peridotite***

Fractional crystallization of a 7-9% near-fractional melt of depleted peridotite does not sufficiently account for the range in major element abundances within the E-MORBs, especially in terms of  $K_2O$ . As previously described, the E-MORBs from the westernmost orthogonal supersegment have  $K/Ti$  above 1.5 and elevated  $K_2O$  (0.22-0.53 wt%) similar to E-MORBs from Joseph Mayes Seamount and the amagmatic accretionary segment. These elevated abundances are higher than abundances modeled by the 100 bar LLD of even a 4% peridotite melt (Figure 13), and thus require either lower extents of melting or a more fertile initial source composition, both of which would result in aggregate melts with higher  $K_2O$ . Reverting to a more fertile initial composition is unlikely as the source composition adopted from Kinzler [1997] is derived by melting the estimated primitive upper mantle composition only 1%, and is thus minimally depleted. On the other hand, in accordance with traditional models of MORB generation, more enriched compositions are usually produced by lower degree melts of the same source mantle that produces N-MORB. Although a smaller degree melt, maybe 2 or 3%, of spinel lherzolite would at least satisfy  $K_2O$  concentrations, it is obvious that this composition parental melt would not constrain many of the other oxide compositions.



Furthermore, by proposing that E-MORBs from the orthogonal supersegment, Joseph Mayes Seamount, and amagmatic accretionary segment be petrogenetically related through differentiation to a 2-3% aggregate partial melt of depleted spinel lherzolite, implies that the extreme  $K_2O$  enrichment of the Narrowgate segment lavas must result from spinel lherzolite melting  $< 1\%$ . Despite the fact that extraction of melt quantities less than a fraction of a percent from the peridotite matrix may [Faul, 1997; Jha et al., 1994; Johnson et al., 1990; McKenzie, 1989] or may not [Zhu and Hirth, 2003] realistically occur in nature, a number of other observations provide substantial evidence in opposition of E-MORB generation being the result of lower degrees of peridotite melting. To begin with, Table 6b of [Kinzler, 1997] reports that 4% melting of depleted spinel lherzolite is associated with a pressure range of 1.0-0.3 GPa, a temperature range of 1221°-1056° C, and a “melt generated” crustal thickness of 1 km (this assumes 100% extraction and aggregation of melt). Estimated crustal thickness derived from gravity data [Grindlay et al., 1998] for the westernmost segment of the orthogonal supersegment is ~ 6 km (Figure 4), with thicknesses for Joseph Mayes Seamount and the Narrowgate segment even greater. If the calculated crustal thickness of 1 km for 4% peridotite melting [Kinzler, 1997] is taken as an upper limit (based on the 100% extraction and aggregation assumption), then melting to even lower extents will generate less crust.

In addition,  $Na_8$  shows little variation among N-MORBs from the orthogonal supersegment and E-MORBs from the Narrowgate segment (Figure 11). Assuming a homogeneous MORB source beneath the ridge, nearly constant  $Na_8$  would indicate little to no variation in extent of melting. Of course this is in direct contrast to the variable  $K/Ti$ , which under the auspices of a conventional melting model and homogeneous mantle suggests variable degrees of melting (Figure 13).  $(Ca/Al)_8$ , also used as an indicator of degree of melting “ $F$ ” as suggested by [Niu and Batiza, 1991] - with high  $(Ca/Al)_8$  approximating high mean extent of melting, is well correlated with  $K/Ti$  along the ridge, with elevated  $(Ca/Al)_8$  at Joseph Mayes Seamount and the Narrowgate segment relative to the orthogonal supersegment (Figure 11). This however suggests a higher degree of melting where  $(Ca/Al)_8$  is elevated, which is again opposite the signal of low  $F$  from  $K/Ti$ . For that matter  $Fe_8$  and  $(Si/Fe)_8$  do not behave in an intuitive manner if the E-MORBs are created by lower degrees of melting of a depleted peridotite. The two are complementary with increasing  $Fe_8$  (decreasing  $(Si/Fe)_8$ ) from east to west along the orthogonal supersegment and lower  $Fe_8$  (higher  $(Si/Fe)_8$ ) for the E-MORBs, suggesting lower mean pressures of melting for the E-MORBs, thus assuming a constant mantle temperature the E-MORBs melted at shallower depths, but to a lower extent than the N-MORBs. This petrogenetic/geophysical scenario is difficult to envision without variation of mantle temperature, upwelling and melting regime, or mantle composition. Regardless of the pressure of melting, the lack of agreement between indicators of degree of melting ( $Na_8$ ,  $(Ca/Al)_8$ , and  $K/Ti$ ) must be justified by an alternative model.

O'Hara [1985] was one of the first to propose the idea that aggregate melts pooled from throughout the melting regime may reflect the “shape” of the melting regime. This was later transformed into a more quantitative model of MORB generation by Plank and Langmuir [1992], who introduced the idea of “extra source volumes” for low degree deep



melts, which if accumulated in large enough volumes could influence the aggregate melt composition. In a 2-D passive upwelling regime the ‘source volume’ is dependent on the difference between the peridotite + volatiles solidus and the dry peridotite solidus, where the former occurs at lower T and thus allows low-degree peridotite melts to form in the “wings” of the melting regime [Galer and O’Nions, 1986]. Other geophysical mechanisms control the importance of these incompatible element enriched low degree melts, but assuming favorable conditions *Plank and Langmuir* [1992] proposed that up to 5 extra source volumes were available at a typical passive upwelling ridge environment. Even with the potential of adding to the volume by expanding the source volume to 3-D upwelling and melt focusing, the amount of extra volumes from which low degree melts could be generated is constrained by the difference in solidi. Since K<sub>2</sub>O abundances for the orthogonal supersegment lavas and the Narrowgate segment lavas differ on average by a factor of 8.5, it is unlikely that focusing of enough low degree melts could account for the K-rich lavas from the Narrowgate segment.

#### ***“Enriched”-MORB from heterogeneous mantle***

While the disagreement among major element indicators of melting supplies sufficient evidence for MORB source heterogeneity, variation of radiogenic isotope compositions (i.e. Sr, Nd, Pb, Hf) along the orthogonal supersegment and within the oblique supersegment, provides definitive evidence of mantle heterogeneity [Standish et al., 2005b]. Recognition of basaltic isotopic variation in this region was previously documented on a much broader scale from isolated samples [Janney et al., 2005; le Roex et al., 1989; le Roex et al., 1992]. Variation in K/Ti is well correlated with isotopic composition and other trace element ratios such as, (La/Sm)<sub>n</sub> and (Sm/Yb)<sub>n</sub>, which are commonly used as tracers of source heterogeneity. This conclusively indicates that K/Ti variation is a function of both source and process. If variation in K/Ti is indicative of changing source composition, then by correlation (Ca/Al)<sub>8</sub> and (Si/Fe)<sub>8</sub> may also be reflecting major element source variation.

Major element mantle heterogeneity is also suggested by K/Ti and K<sub>2</sub>O, illustrating a clear division between the N-MORBs from the orthogonal supersegment and amagmatic accretionary segment and the E-MORBs from Joseph Mayes Seamount and the amagmatic accretionary segment, with the Narrowgate segment lavas further separated. No discernable difference in TiO<sub>2</sub> exists among the provinces at a given MgO, but Na<sub>2</sub>O, Al<sub>2</sub>O<sub>3</sub>, and FeO\* show varying extents of separation (Figure 6), which may be partially attributable to source differences. Yet although much of the variation can be modeled by fractional crystallization under varying conditions, the range in K<sub>2</sub>O is not explainable this way nor is it consistent with lower degrees of peridotite melting.

## **6. Tectonomagmatic Model**

### **6.1. Origin and nature of the mantle heterogeneity**

Over the years, various studies of MORB geochemistry have documented the existence of trace element and isotopic heterogeneity [e.g. Zindler and Hart, 1986], as well major element variation [e.g. Melson et al., 1976; Schilling et al., 1983] in the MORB source

region. Correlations among major element, trace element, and isotopic basalt compositions from the tectonomagmatic provinces, together with observed relationships between geochemistry and geophysics, provide convincing evidence of a heterogeneous MORB source. What is not as well known or constrained is the nature of this mantle enrichment. At the heart of this issue is the question of whether the heterogeneity is present as a variably enriched single lithology peridotite (i.e. metasomatism), or a multi-lithology assemblage with depleted peridotite as the host for veins, layers, “plums”, etc.

Pyroxene-rich rocks have been sampled from many types of mantle including xenoliths [e.g. Frey et al., 1980; Irving, 1980], ophiolites [e.g. Boudier and Coleman, 1981; Quick, 1981], orogenic peridotites [Pearson et al., 1993; Suen and Frey, 1987], and abyssal peridotites [e.g. Dick et al., 1984; Ross and Elthon, 1993], yet direct evidence of “pyroxenite” in the convecting asthenosphere is sparse. The existence of lithologically heterogeneous or veined mantle source regions has been inferred from MORB geochemistry [e.g. Zindler et al., 1984], and numerous studies have sighted the potential importance of mafic lithologies (i.e. pyroxenite or eclogite) during MORB [e.g. Hanson, 1977; Hirschmann et al., 2002; Hirschmann and Stolper, 1996; Kogiso, 2004; le Roex et al., 1983; Pertermann and Hirschmann, 2003a; Prinzhofer et al., 1989; Sleep, 1984; Sun and McDonough, 1989; Sun and Hanson, 1975] and OIB [e.g. Allègre et al., 1984; Hart, 1988; Ito and Mahoney, 2004; Weaver, 1991] generation.

Ongoing complementary study of the abyssal peridotites dredged between 9°-25°E on the Southwest Indian Ridge recently discovered layered pyroxene-rich bands in a number of samples from the western end of the oblique supersegment [Warren et al., 2004]. These pyroxene-rich lithologies may or may not turn out to be primary, but the existence of pyroxenite in association with an amagmatic accretionary segment is significant, as the occurrence of residual pyroxenite would intuitively be associated with segments that have experienced the lowest extents of melting. Additionally, comparison of basalt and abyssal peridotite compositions along the oblique supersegment [Salters and Dick, 2002] concludes that a lithology other than peridotite, one with a lower melting temperature such as pyroxenite or eclogite, was required to explain the low Nd isotopic compositions of the basalts and their lack of overlap with peridotite Nd compositions. Independent evidence from Hf isotopic compositions and trace element fractionation in basalts further supports the likelihood of a pyroxenite source component beneath 13°-15°E on the Southwest Indian Ridge [Janney et al., 2005].

Present day plume-ridge interaction is unrealistic, as the Bouvet hotspot is currently located near the Bouvet Triple Junction, over 500 km away and offset from the study area by the large ~200 km Shaka Fracture Zone [Georgen et al., 2001]. However, based on plate reconstruction calculations [*H. Schouten*, personal communication] and the trajectory of the Bouvet hotspot trace (along the NW edge of the Shaka FZ trace), the Bouvet hotspot would have been positioned adjacent to the current oblique supersegment between 20-30 Ma. Upwelling of buoyant plume material will, at an unspecified depth, generate low degree partial melts near the base of the melting zone, effectively metasomatising the surrounding depleted mantle [Donnelly et al., 2004] in the form of

enriched veins or diffuse reactive flow. The resulting low degree melts would be greatly enhanced in incompatible trace element concentration [Ito and Mahoney, 2004] and possibly major element concentrations as well, thus providing an enriched source lithology within the upwelling MORB source with elevated  $K_2O$ . Using estimated crustal thickness measurements for the Narrowgate segment and the peridotite melting parameterization of *Hirschmann* [2000], the percentage of pyroxenite (eclogite) present in the mantle beneath the Narrowgate segment is estimated to be  $\sim 5\%$  (6 km crustal thickness and peridotite solidus of 50 km; see Figure 7 of [Pertermann and Hirschmann, 2003a]). With 5% eclogite existing in the upwelling source volume, further calculation based on the difference in temperature between peridotite and eclogite solidi, indicates that approximately 25% of the total melt volume produced comes from the eclogite source volume.

Similar two-stage melting models involving an initial melting event that enriches the ambient depleted peridotite followed by a second event that produces a range of enriched and depleted MORB compositions by melting the veined or metasomatised source mantle, have been proposed recently for the southern MAR, near the Shona and Discovery hotspots [le Roux et al., 2002a], and as a broad model of global E-MORB generation [Donnelly et al., 2004]. As *le Roux and coworkers* [2002a] show in their study of the Discovery and Shona Hotspot-influenced southern Mid-Atlantic Ridge, partial melting of pyroxenitic lithologies can account for a portion of the major element variation in MORB. While much of the variation in the Southwest Indian Ridge major element concentrations is consistent with, but does not require, partial melting of a mafic lithology, the highly elevated  $K_2O$  of the Narrowgate segment lavas are the exception. In order to petrogenetically model the range in  $K_2O$  exhibited by the Narrowgate segment lavas, parental melt compositions with abundances near 1 wt% and Mg# similar to the aggregate peridotite melts are required. Natural pyroxenites span a large range in major element space and generally lie between fields for mantle peridotite and MORB. The term pyroxenite is often used generically to represent pyroxene-rich rocks, which incidentally cover a great deal of lithologic variability from eclogites to olivine- and orthopyroxene-bearing rocks. Eclogites also can vary quite significantly in major element composition, but largely reflect basaltic compositions. A few examples of eclogitic lithologies that have elevated  $K_2O$  abundances are found in the experimental literature [Kogiso, 2004; Pertermann and Hirschmann, 2003b; Yaxley and Green, 1998].

The “G2” composition is derived from natural garnet, clinopyroxene, quartz, kyanite, and synthetic  $TiO_2$ , and was chosen to represent present-day mid-ocean ridge crust [Pertermann and Hirschmann, 2003a]. Glass compositions measured from experimental melting of “G2” (green diamonds) and “G2K” (green and orange diamonds; elevated  $K_2O$  and renormalized oxide concentrations relative to “G2”) starting compositions are plotted in Figure 13, with degree of melting noted in percent. Of importance is the range in  $K_2O$  covered by the 14% melt and 51% melt of “G2K”, illustrating that low to moderate degree melts of K-rich eclogite ( $> 0.2$  wt%) provide enough leverage to generate MORB compositions similar to the Narrowgate segment lavas. In theory, the elevated  $K_2O$  signature of the eclogite melts is passed along to the aggregate melts by

mixing large volumes of early formed enriched end-member melt with depleted peridotite melt. The reason that the other major element abundances do not reflect the influence of eclogite melting as distinctly as  $K_2O$  is because of re-equilibration of the enriched eclogite melt with ambient depleted peridotite. Re-equilibration of the eclogite melt with depleted peridotite beneath the Narrowgate segment does not affect the incompatible element content of the enriched melt because there is little to no cpx remaining in the residual mantle column, as the Narrowgate magmatic segment represents a continuous 6-8 Ma melting history that would leave the shallow mantle stripped of cpx. Thus, while  $SiO_2$ ,  $FeO^*$ , etc. of the eclogite melt undergo reactive re-equilibration with the depleted peridotite host,  $K_2O$  is unaffected, since the residual phases of the host peridotite do not preferentially partition K. This process results in parental melts for the Narrowgate segment MORB that have elevated  $K_2O$  and Mg# similar to the aggregate peridotite melts, and effectively remove any significant major element signature of eclogite melting, leaving instead the typical depleted harzburgite signature.

## 6.2. Bimodal melting

Whether the enriched mafic lithology is pyroxenitic or eclogitic (natural compositions largely overlap, although pyroxenites extend to more MgO-rich compositions), experimental studies at pressures between 1 and 3 GPa [Kogiso, 2004; Pertermann and Hirschmann, 2003a; Rapp and Watson, 1995; Yaxley and Green, 1998] place the solidus for anhydrous compositions on average 100 to 150° C lower than depleted peridotite solidi. The eclogitic composition “G2” is even more discrepant from the peridotite solidi, as [Pertermann and Hirschmann, 2003a] recorded the “G2” solidus at 2 and 3 GPa respectively, to be  $190 \pm 25^\circ C$  and  $170 \pm 25^\circ C$  cooler than the depleted peridotite solidus [Herzberg et al., 2000; Hirschmann, 2000; Walter, 1998]. Using the peridotite solidus parameterization of Hirschmann [Hirschmann, 2000], which is based on experimental peridotite melting data [Walter, 1998], this difference in temperature equates to an eclogite lithology 60% molten by the time the 3 GPa ‘dry’ peridotite solidus is reached [Pertermann and Hirschmann, 2003a].

The difference in the depth of initial melting for eclogite lithologies versus peridotite lithologies is estimated to be ~ 50 km based on an adiabatic gradient of  $10^\circ C/GPa$  [Pertermann and Hirschmann, 2003a]. Assuming passive upwelling, the difference in solidi equates to a much larger source volume for eclogite melt generation relative to peridotite melt generation. This means that the volume of mantle crossing the pyroxenite solidus is greater than the volume crossing the peridotite solidus, as put forth for a typical triangular melting regime [e.g. McKenzie and Bickle, 1988; Plank and Langmuir, 1992]. Even if the peridotite was hydrous and started melting deeper, the amount of melt produced in that region would be small (Asimow and Langmuir, 2004) and would not diminish the relative contribution of melt from the eclogite component. Overall, the contribution of the eclogite lithology to the aggregate MORB melt will still be significant, as the proportion of eclogite-derived melt contributed to the crust can be 5 to >10 times the proportion of eclogite in the effective source [Pertermann and Hirschmann, 2003a].



### 6.3. Extraction of mafic melts from host peridotite

Deep partial melts of eclogite/pyroxenite have been shown to span a large range in composition from silica-saturated to silica-undersaturated [Kogiso, 2004; Pertermann and Hirschmann, 2003a; Rapp and Watson, 1995; Yaxley and Green, 1998]. As a result of chemical disequilibrium and subsequent reaction with the host peridotite, Yaxley [2000] and Yaxley and Green, [1998] concluded that silica-saturated mafic partial melts not in equilibrium with olivine would likely crystallize upon reaction with the surrounding host mantle. Despite the silica-saturated nature of the “G2K” partial melts, solidification due to chemical disequilibrium is not a foregone conclusion, as few constraints exist on the fate of mafic partial melts at depth in a peridotitic host. If opx-rich subsolidus reaction skarns develop prior to melting [Kogiso et al., 2000] as a consequence of the disequilibrium between silica-saturated mafic lithologies and depleted peridotite [Pertermann and Hirschmann, 2003a], siliceous melt should be well enough insulated to avoid reaction with olivine until segregation. Field observations of dunites show relationships between pyroxenite veins, replacive dunites, and host peridotites that suggest vein melting incorporates a limited volume of surrounding peridotite. This mechanism may serve to bring mafic melts into equilibrium with mantle olivine in a narrow region, thereby facilitating extraction through harzburgite and/or dunite channels. Zones of fertilized peridotite created by reaction of eclogite melt with non-fertilized peridotite can armor a conduit through which an eclogite melt can be extracted without equilibrating with the host peridotite [Takahashi and Nakajima, 2002].

With ~5% mafic veins within the mantle and a melt productivity near the eclogite solidus of ~ 15%/GPa [Pertermann and Hirschmann, 2003a], it is reasonable that a substantial volume of melt would be generated quickly enough that extraction of these deep, enriched melts into coalescing dunite conduits could prevent significant reaction with the surrounding peridotite. Not to mention that based on earlier discussion of eclogite melting, the enriched compositions are not limited to low-degree melts, but will also exist in moderate-degree eclogite melts. Extraction of low-volume partial melts from the surrounding peridotite may proceed primarily as focused flow in melt conduits [Kelemen et al., 1997], rather than reactive porous flow through the host peridotite [Aharonov et al., 1995; Dick, 1989; Elthon, 1992; Kelemen and Dick, 1995]. Spatial distribution of dunite bodies in ophiolites [Kelemen et al., 2000] indicates melt conduits on the order of 0.1 to 1 meters wide, which form initially as a result of reactive dissolution, and then coalesce into much larger dunites. Melt separation from a molten peridotite matrix at  $F < 1\%$  may be possible [Faul, 1997; Jha et al., 1994; Johnson et al., 1990; McKenzie, 1989], but could be inhibited by grain-scale heterogeneity [Zhu and Hirth, 2003], where the addition of significant proportions of pyroxene could result in decreased permeability relative to a homogeneous (i.e. olivine dominated) molten peridotite. Yet, even at that scale of 0.1 to 1 m, analysis by Kogiso [2000] suggests that chemically isolated pyroxenite partial melts can escape their host via dunite channels without equilibration with olivine.

The ability of pyroxenite-derived melts to ascend without reaction may also be enhanced beneath the Narrowgate segment and to a lesser degree beneath Joseph Mayes



Seamount, as it is likely that the melting column is highly depleted, with little clinopyroxene remaining, as a result of continuous reactive-porous flow of melt from depth and melt focusing. A paucity of clinopyroxene within the melting column diminishes the trace element buffering capacity of the mantle column, resulting in a greater volume of incompatible element enriched basalt. Variable melt-rock reaction based on the depletion history of the local mantle column may significantly influence parental magma compositions, where the depletion history is largely a function of mantle melting and melt focusing. Furthermore, the difference in local depletion histories and thus basalt compositions between the Narrowgate segment and Joseph Mayes Seamount may likely be attributable to the youth of Joseph Mayes Seamount, which has only been erupting for  $\sim 1$  Ma, versus 8 Ma for the Narrowgate segment.

#### **6.4. Segmentation, upwelling, and melt focusing**

The complex segmentation along the oblique supersegment implies significant changes in the rates of mantle upwelling and crustal production consistent with the observed calculated crustal thickness, and basalt chemistry. Laboratory modeling of 3-D buoyant instabilities in a low-viscosity melt-region [Crane, 1985; Kincaid et al., 1996; Whitehead et al., 1984] offered the possibility that mantle diapirs might define ridge segmentation, and that mantle Bouguer anomaly (MBA) bull's-eye lows, which reflect enhanced crustal thickness, were the result of associated increased melt production [Kuo and Forsyth, 1988; Lin et al., 1990]. Mapping of residual mantle Bouguer anomalies on both the orthogonal supersegment [Grindlay et al., 1998] and oblique supersegment [Lin et al., 2003] find moderate amplitude bull's eye lows associated with thickened crust at the western end of the orthogonal supersegment and well-defined bull's eye lows with thick crust at Narrowgate segment and Joseph Mayes Seamount. However, the wavelengths that are modeled for convective instabilities and resulting mantle diapirs [Jha et al., 1994; Parmentier and Phipps Morgan, 1990; Sparks and Parmentier, 1993] are still much longer than the segment lengths of the study area and of MOR segments in general. Segmentation may however be related to 3-D focused melt flow imposed by the segmentation pattern at ultraslow-spreading rates [e.g. Dick et al., 2003; Michael et al., 2003], as well as inferred buoyant mantle upwelling.

Buoyancy and viscosity effects of partial melting, namely increased viscosity due to dehydration melting [Braun et al., 2000; Hirth and Kohlstedt, 1996], can result in pressure gradients causing three dimensional melt focusing [e.g. Buck and Su, 1989; Magde and Sparks, 1997; Parmentier and Phipps Morgan, 1990; Scott and Stevenson, 1989; Spiegelman and Reynolds, 1999] in both 2-D and 3-D mantle flow structures. The stability of buoyant upwelling to shallower depths, plus 3-D melt focusing should create locally thicker crust. Estimated crustal thicknesses are greatest at Narrowgate segment and Joseph Mayes Seamount, suggesting the possibility of buoyant upwelling at depth and, but certainly focused melt flow in the shallow mantle and lower crust. At this stage we have few constraints on the mantle flow regime, other than preliminary numerical modeling [Barry, 2005], which indicates that 2-D passive flow can account for many of

the ridge characteristics observed. Therefore, we assume 2-D passive corner flow and further investigate the effects of melt focusing.

Increased conductive cooling at highly segmented, slow-spreading ridges together with decreased plate-driven upwelling may reduce crustal thicknesses as much as 75% [Magde and Sparks, 1997]. While estimated crustal thicknesses for the amagmatic segments do not indicate a 75% reduction relative to active upwelling segments, the presence of serpentinized mantle peridotite could lead to overestimates of the basaltic thickness which may be 1 km or less. This would be consistent with forward modeling of igneous crustal thickness [Bown and White, 1994; White et al., 2001] generated by partial melting of anhydrous peridotite at a typical mantle temperature of 1300° C, but with the melting column cut off at 30 km depth due to conductive cooling from above. Thickened lithosphere at the amagmatic accretionary segments will then play an important role in MORB generation, as the total extent of melting will be diminished (relative to surrounding segments) and melt focusing will be enhanced. In general the variation in melting “process” as a function of conductive cooling, will make the aggregate melt composition much more sensitive to changes in the relative proportion of eclogite/pyroxenite in the effective source region [e.g. Ito and Mahoney, 2004].

At ultraslow-spreading rates where conductive cooling and thus lithospheric topography are inferred to be highly variable, the enriched nature of E-MORB from both the oblique and orthogonal supersegment can be largely attributed to along-axis melt focusing of high proportions of eclogitic melt toward volcanic segments (Figure 15). A number of variables will influence the efficiency and the length-scale over which melt focusing occurs, including, along-axis conductive cooling, mantle flow, viscosity, and permeability. One mechanism for lateral transport of melt towards a ridge is melt focusing along an impermeable boundary, such as the top of the melting region [Sparks and Parmentier, 1991; Sparks and Parmentier, 1993; Spiegelman and Elliot, 1993] or the base of the rheologic lithosphere or rheologic boundary layer [Hall and Parmentier, 2000; Hall and Kincaid, 2003; Ito et al., 1999]. Based on the upwelling rate, crustal thickness, and the segmentation pattern along-axis, variations in the top of the melting column and lithospheric thickness should be substantial along the oblique supersegment. This predicted lithospheric topography together with passive upwelling would result in enhanced melt focusing from the amagmatic accretionary segments toward the neighboring volcanic segments. In addition to enhanced melt focusing, the combination of conductive cooling and passive upwelling is also responsible for variations in the degree of local mantle depletion, similar to the effects of the “transform edge effect” [Ghose et al., 1996; Langmuir and Bender, 1984; Magde and Sparks, 1997; Phipps Morgan and Forsyth, 1988].

### **6.5. Off-axis versus on-axis heterogeneity**

The vast majority of MORB have been collected on or near the axial ridge, and as a result relatively few studies [Bryan, 1979; Hekinian et al., 1989; Karsten et al., 1990; Reynolds et al., 1992; Smith et al., 1994] have systematically examined temporal and spatial variations of on-axis and off-axis lava compositions. However, recognition and

understanding of the compositional differences between on-axis and off-axis lavas is fundamental to understanding ocean crust accretion [Perfit and Chadwick, 1998]. With half-spreading rates along the Southwest Indian Ridge of 7-8 mm/yr, typically only about 2 million years of MORB evolutionary information is accessible within the rift valley - much less than at faster spreading ridges. To gain a more complete picture of potential temporal and spatial variation of the ridge chemistry, dredges were collected from the rift valley walls and rift valley floor along the Southwest Indian Ridge from 9° to 25°E.

The rift valley wall basalts (henceforth termed off-axis basalts unless noted; black circles) generally overlap compositionally with rift valley floor basalts (Figure 14) (henceforth termed on-axis basalts unless noted; red circles), but specific differences do exist. Along most parts of the ridge, off-axis basalts extend systematically to higher  $Fe_8$ , and in a few cases lower  $(K/Ti)_8$  than axial basalts.  $Na_8$  is generally higher for off-axis lavas along the orthogonal supersegment.  $Fe_8$ ,  $Na_8$ , and to a lesser extent  $(K/Ti)_8$  are similar for axial and off-axis basalts from Narrowgate segment and Joseph Mayes Seamount, both robust volcanic segments, suggesting little to no temporal variation at these segments (out to 2 Ma), even though inferred crustal thickness is markedly different. Below, we briefly investigate potential mechanisms to explain the compositional differences between off-axis and on-axis lavas within our study area.

Eruption of zero age basalt may not be confined to morphologically distinct linear axial ridges, but instead may be widely distributed, as documented by U-Th-Ra disequilibria in 12 glasses from our study area that indicate young volcanism throughout the rift valley and its walls [Standish et al., 2005a]. Multibeam bathymetric maps of the amagmatic accretionary segments within the study area, depict multiple, disperse linear and cone shaped volcanic zones scattered throughout the rift valley. Although very little is known about the mechanisms controlling off-axis volcanism, the complex tectonic environment coupled with the wide temporal and spatial distribution of dredged lavas suggests that “zero-age” volcanism on an ultraslow-spreading ridge may represent a much different suite of lavas than on the EPR. However, investigation of basalt compositions from a single ~50 km segment on the East Pacific Rise [Reynolds et al., 1992] found the volume and chemistry of zero age basalts to vary both temporally and spatially along-axis.

Perhaps the differences in off-axis and on-axis compositions are a function of accretionary cycles related to transient melt focusing as modeled by Cannat et al., [2003] for the easternmost SWIR. It is places with thin crust (amagmatic accretionary segments and eastern end of the orthogonal supersegment) that show the greatest differences between on-axis and off-axis compositions. Elevated  $Fe_8$  and depressed  $Na_8$  in off-axis basalt from the amagmatic accretionary segments may reflect a change in the melting regime beneath the ridge, where the off-axis lavas were the product of relatively high degree melts that started deep. More recently, the amagmatic accretionary segments have produced less melt (higher  $Na_8$ ) at lower mean pressures (low  $Fe_8$ ), as evidenced by highly thinned crust, the lack of dredged gabbro, and the abundance of mantle outcropping on the seafloor. This suggests that crustal thickness may play an important

role, or may be a telltale indication of variable melting regimes and general differences in melt generation.

There are additional ways that melt focusing could account for differences in off-axis versus on-axis composition. Continued focusing of large volumes of melt beneath the Narrowgate segment and Joseph Mayes Seamount would tend to uniformly deplete a broad mantle column, therefore melts traveling through any portion of the column would likely reflect similar extents of melt-rock reaction and re-equilibration at shallow depths, regardless of where in the rift valley they were erupted. On the other hand, the ridge segments experiencing removal of melt that is focused away to neighboring robust segments, could have a spatially heterogeneous mantle column, in which the residual mantle directly beneath the rift axis would likely be more depleted than off-axis. Thus, elevated  $\text{Fe}_8$  and  $\text{Na}_8$  on the eastern end of the orthogonal supersegment and elevated  $\text{Fe}_8$  at the amagmatic accretionary segment could be attributed to melts equilibrating with a more fertile mantle. This also then assumes that the off-axis and on-axis lavas are erupted contemporaneously, as is suggested from U-series disequilibria. From the variety of potential explanations, it is apparent that few constraints exist on temporal and spatial variability of lithospheric accretion, especially at ultraslow-spreading ridge environments where tectonic processes have a significant influence on ridge architecture.

## 7. Model Summary

Major element relationships (i.e.  $(\text{K/Ti})_8$ ,  $\text{Na}_8$ ,  $\text{Fe}_8$ ) within and among each of the tectonomagmatic provinces, plus the correlations among chemistry, ridge segmentation, geology, and crustal thickness cannot be explained by variable degrees of melting of a homogeneous peridotite lithology. To account for the significant variation in major element abundances, particularly  $\text{K}_2\text{O}$ , it is necessary to call upon an eclogitic lithology, likely originating from recycled ocean crust upwelling beneath the Bouvet plume. The combination of enriched and depleted end-member melts provides the overall range in compositional space exhibited by the basalts, but melting systematics control the distribution of MORB compositions along the ridge. Variations in upwelling rate have a significant influence on the depth of penetration of conductive cooling, the depth at which melting shuts off, the effectiveness of melt focusing, and thus by inference the degree of depletion of the residual mantle column, which affects the extent of re-equilibration of upward percolating melts. There is little doubt that at spreading rates this slow even the smallest perturbation in spreading geometry, thermal regime, or melting dynamics in general will have a noticeable effect on MORB chemistry. Below we briefly summarize the key aspects of this tectonomagmatic model (schematically illustrated in Figure 15) for generation of a range of mid-ocean ridge basalt compositions.

At 30 Ma the Bouvet plume was sitting adjacent to the current position of the oblique supersegment. Low to moderate degree melts of the upwelling plume material infiltrated the surrounding asthenosphere and created a small proportion of incompatible element enriched eclogite veins. Since then, mantle flow has distributed this ‘metasomatically’ enriched MORB source to the oblique supersegment and to a lesser degree beneath the orthogonal supersegment. Subsequent passive upwelling of this two-lithology mantle



source causes decompression partial melting of the enriched eclogite veins much deeper (~100 km) than partial melting of depleted peridotite (~55-60 km), and as a result the source volume for enriched eclogite melt is substantially larger than that for the hydrous depleted peridotite. Based on the estimated difference in solidi, the eclogite lithology may be 60% molten by the time the peridotite solidus is reached.

The end-member melts mix to varying proportions and travel upwards via a combination of channelized dunite flow and reactive porous flow within the host peridotite. Major element signatures are dominated by depleted peridotite compositions, with the exception of  $K_2O$ . The decoupling of  $K_2O$  from the other major element oxides results from re-equilibration of enriched melts with a residual peridotite column that has little to no Cpx remaining and thus has no buffering capacity for major and trace elements that are incompatible in Oliv, Plag, and Opx. So while the eclogite dominated melts reactive with depleted harzburgite, thereby equilibrating  $SiO_2$ ,  $FeO^*$ ,  $MgO$ , and so on,  $K_2O$  remains elevated, resulting the high K/Ti values seen at the Narrowgate segment.

However, in order to account for highly elevated K/Ti at the Narrowgate segment and moderately elevated values at Joseph Mayes Seamount, we invoke 3-D melt focusing beneath these segments. This process aggregates significant volumes of enriched mafic melt over wavelengths greater than the respective segment lengths, thereby drawing melt away from accretionary segments with thickened lithosphere and focusing it towards volcanically active segments (Figure 15). This is consistent with our observations of spreading geometry, inferred upwelling rate, ridge segmentation, relative crustal thickness, and estimated lithospheric thickness, which are all correlated in terms of the distinct tectonomagmatic provinces.

In addition to enhanced melt focusing (presumably along the rheologic boundary layer), the topography created by variable lithospheric thickness has been demonstrated to have a significant impact on the total amount of peridotite melting, as increased conductive cooling at depth brought on by ultraslow-spreading rates, shuts off partial melting deeper than at faster spreading rates. The fact that the Narrowgate segment and Joseph Mayes Seamount have effective spreading rates similar to the orthogonal supersegment, and nearly double rates along some portions of the amagmatic accretionary segments, is consistent with a high rate of magma generation, melt focusing to these segments, and a mantle column proportionally more depleted than segments with slower effective spreading rates. Therefore, it is likely that the presence of elevated K/Ti alkali lavas at the Narrowgate segment is a function of both melt focusing and the diminished trace element buffering capacity of the underlying mantle column, that has been stripped of nearly all its clinopyroxene by continuous porous flow of large volumes of eclogite and peridotite melt percolating to the surface. This of course is relative to other segments, such as the Joseph Mayes Seamount volcano, which is only 1.3 Ma old with an underlying mantle column more fertile and thus capable of moderately buffering incompatible element concentrations of migrating melts, resulting in only moderately elevated K/Ti basalts. Melt-rock reaction or reactive-porous flow between enriched mafic melt and host peridotite is a process we have few constraints on, but one that



further investigation and modeling may determine to be the crucial mechanism for producing incompatible element enriched mid-ocean ridge basalt as well as normal mid-ocean ridge basalt. Regardless of the specific mechanism responsible for determining final melt composition, this study illustrates the importance of “process” and mantle source, especially at ultraslow-spreading rates, as the smallest changes in melting parameters can result in significant compositional differences for MORB.

## 8. Conclusions

Detailed bathymetry and closely spaced dredging from 9° and 25° E on the SW Indian Ridge has revealed many unique 1<sup>st</sup> order observations and correlations between ridge morphology, segmentation, lithology, and major element basalt chemistry. From these correlations we have constructed a melting model that accounts for the along-axis compositional variations and is consistent with the 1<sup>st</sup> order observations. Below we list the most important observations and conclusions.

- 1) Four individual tectonomagmatic provinces are defined using high-resolution bathymetry, gravity data, geologic information, and major element basalt chemistry: 1) the orthogonal supersegment, 2) the Narrowgate segment, 3) the amagmatic accretionary segments, and 4) Joseph Mayes Seamount. Distinct differences exist in spreading geometry, rift valley morphology, ridge segmentation, relative crustal thickness, and basalt chemistry.
- 2) Variable fractionation-corrected H<sub>2</sub>O contents between 0.18 – 0.60 wt% influence parental melt liquid lines of descent by suppressing crystallization of plagioclase and clinopyroxene to lower temperature (or lower MgO), thus allowing olivine to crystallize alone over a larger temperature range. The dominant effect is seen as decreased Fe<sub>8</sub> and increased Al<sub>8</sub>, with lesser effects on Na<sub>8</sub>, Si<sub>8</sub>, and Ca<sub>8</sub> for parental melts with elevated H<sub>2</sub>O contents (largely E-MORBs). This effect accounts for only a portion of the major element compositional heterogeneity.
- 3) Orthogonal supersegment basalts lie squarely on the global array, but reflect lower extents of melting compared with average Indian Ocean, East Pacific Rise, and Mid-Atlantic Ridge basalt. This is consistent with the predicted effect of increased conductive cooling of the mantle from above, as a function of ultraslow-spreading rates. The other tectonomagmatic provinces lie off the array to lower Fe<sub>8</sub>, which is partly explained by H<sub>2</sub>O-influenced fractional crystallization.
- 4) Along-axis chemical variability of Fe<sub>8</sub>, Na<sub>8</sub>, Mg#, and particularly (K/Ti)<sub>8</sub> cannot be explained by conventional passive upwelling models that rely on partial melting to varying degrees of a homogeneous peridotite source. Alternatively, we propose a tectonomagmatic melting model that requires a heterogeneous source.
- 5) The elevated K<sub>2</sub>O contents of the Narrowgate segment lavas require a high-K end-member melt component. Low to moderate degree partial melts of K-rich eclogite lithologies satisfy this constraint and are consistent with the bulk of the major element oxide constraints. Mixing of varying proportions of eclogite melt

with peridotite melt, followed by partial re-equilibration of the aggregate melt with depleted, Cpx-absent peridotite produces the range of MORB compositions we observe.

- 6) The correlation of ridge geometry, inferred upwelling rate, lithospheric thickness, relative crustal thickness, ridge segmentation, and major element chemistry illustrates the importance that ridge geometry, lithospheric thickness, and “process” in general have on 1) basalt chemistry, 2) lithospheric accretion, and even 3) MORB mantle depletion.

## Acknowledgements

The authors would like to thank Nancy Grindlay John Madsen, and T. Dulaney for access to their full data set for 16° to 25°E, which provided a basis for much of our fieldwork and later interpretation. Many thanks to Paula Smith and Paul Asimow for their patience and instruction during use of “Adiabat\_1ph” and MELTS. A sincere thanks goes out to the Crews and Scientific Party participants on the RV Knorr Cruise 162 Legs VII to IX in 2000-2001 and the RV Melville-Vancouver expedition in 2003. A special thanks from J. Standish and H. Dick is extended to “Mr. Butterscotch Pudding” himself Ron Comer, for his expertise at the winch, often under somewhat stressful conditions. Peter Kelemen has been an invaluable source of major element information and this manuscript has benefited from many discussions with him. Many valuable ‘oh yeah, I remember that’ discussions on phase diagrams also occurred with Glenn Gaetani. The members of my committee including, Stan Hart, Mark Kurz, Ken Sims, Jian Lin, Hans Schouten, Anton le Roex, and Fred Frey have provided useful critiques and comments throughout the process. The authors would also like to thank Mark Behn and Jenny Barry for their timely discussions on numerical modeling. The authors would also like to recognize and thank Paul E. Oberlander in WHOI’s Graphic Services for his assistance developing Figure 15. This work was funded in large part by NSF grant OCE 9907630.

## Appendix 1.

“Adiabat\_1ph” is a text-menu public front-end subroutine for running the thermodynamic models MELTS, pMELTS, and pHMELTS [Asimow et al., 2004; Ghiorso et al., 2002; Ghiorso and Sack, 1995]. MELTS is largely calibrated on experiments at atmospheric pressures, and thus is best equipped to model low pressure fractional crystallization. For all of the modeled liquid paths presented in Figures 5 + 13 a number of initial conditions were kept constant. The MELTS model was set to “fractionate solids” (i.e. crystal fractionation), the P/T path setting to “isobaric”, and a starting temperature between 1250° and 1300° C with a delta T of 1°. The bulk starting composition did not include Cr<sub>2</sub>O<sub>3</sub>, therefore spinel was not a stable fractionating phase and is severely under estimated (see *Asimow et al.*, [1995] for details), and the oxygen fugacity was kept constant at FMQ (–1 log unit). Sample KN162 48-21 was chosen as the starting bulk composition based on its high MgO content. All four LLDs shown in Figure 5 model the same major element starting composition, except red LLDs have H<sub>2</sub>O = 0.18 wt% (water content was actually measured in KN162 48-04) and blue LLDs have H<sub>2</sub>O = 0.6 wt%. The activity of water is set to zero for all fractional crystallization trends using MELTS.

## References

- Aharonov, E., J. A. Whitehead, P. B. Kelemen, and M. Spiegelman (1995), Channeling instability of upwelling melt in the mantle, *Journal of Geophysical Research*, 100, 20,433-420,450.
- Allègre, C. J., B. Hamelin, and B. Dupré (1984), Statistical analysis of isotopic ratios in MORB: the mantle blob cluster model and the convective regime of the mantle, *Earth and Planetary Science Letters*, 71, 71-84.
- Asimow, P. D., J. E. Dixon, and C. H. Langmuir (2004), A hydrous melting and fractionation model for mid-ocean ridge basalts: Applications to the Mid-Atlantic Ridge near the Azores, *Geochemistry, Geophysics, Geosystems*, 5, 24.
- Asimow, P. D., M. M. Hirschmann, M. S. Ghiorso, M. J. O'Hara, and E. M. Stolper (1995), The effect of pressure-induced solid-solid phase transitions on decompression melting of the mantle, *Geochimica Et Cosmochimica Acta*, 59, 4489-4506.
- Asimow, P. D., and C. Langmuir (2003), The importance of water to oceanic mantle melting regimes, *Nature*, 421, 815-820.
- Baker, M. B., and E. M. Stolper (1994), Determining the composition of high-pressure mantle melts using diamond aggregates, *Geochimica Cosmochimica Acta*, 59, 4489-4506.
- Barry, J. B., M.D. (2005), Melting and mantle flow beneath oblique ultraslow-spreading ridges, in prep.
- Batiza, R., and D. Vanko (1984), Petrology of young Pacific seamounts, *Journal of Geophysical Research*, 89, 11,235-211,260.
- Bender, J. F., F. N. Hodges, and A. E. Bence (1978), Petrogenesis of basalts from the Project FAMOUS Area: Experimental study from 0-15 kbars, *Earth and Planetary Science Letters*, 41, 277-302.
- Boudier, F., and R. G. Coleman (1981), Cross section through the peridotite in the Samail ophiolite, southeastern Oman Mountains, *Journal of Geophysical Research*, 86, 2573-2592.
- Bown, J. W., and R. S. White (1994), Variation with spreading rate of oceanic crustal thickness and geochemistry, *Earth and Planetary Science Letters*, 121, 435-439.
- Braun, M. G., J. G. Hirth, and E. M. Parmentier (2000), The effects of deep damp melting on mantle flow and melt generation beneath mid-ocean ridges, *Earth and Planetary Science Letters*, 176, 339-356.
- Bryan, W. B. (1979), Regional variation and petrogenesis of basalt glasses from the FAMOUS Area, Mid-Atlantic Ridge, *Journal of Petrology*, 20, 293-325.
- Bryan, W. B. (1983), Systematics of modal phenocryst assemblages in submarine basalts: Petrologic implications, *Contributions to Mineralogy and Petrology*, 83, 62-74.
- Bryan, W. B., and J. G. Moore (1977), Compositional variations of young basalts in the Mid-Atlantic Ridge rift valley near lat 36°49'N, *Geological Society of America Bulletin*, 88, 556-570.
- Buck, W. R., and W. Su (1989), Focused mantle upwelling below mid-ocean ridges due to feedback between viscosity and melting, *Geophysic. Res. Lett.*, 16, 641-644.

- Cannat, M. (1996), How thick is the magmatic crust at slow spreading oceanic ridges, *Journal of Geophysical Research*, 101, 2847-2857.
- Cannat, M., C. Rommevaux-Jestin, and H. Fujimoto (2003), Melt supply variations to a magma-poor ultra-slow spreading ridge (Southwest Indian Ridge 61° to 69° E), *Geochemistry, Geophysics, Geosystems*, 4, 21.
- Cannat, M., C. Rommevaux-Jestin, D. Sauter, C. Deplus, and V. Mendel (1999), Formation of the axial relief at the very slow spreading Southwest Indian Ridge (49° to 69°E), *Journal of Geophysical Research*, 104, 22,825-822,843.
- Castillo, P. R., E. Klein, J. Bender, C. Langmuir, S. Shirey, R. Batiza, and W. White (2000), Petrology and Sr, Nd, and Pb isotope geochemistry of mid-ocean ridge basalt glasses from the 11°45' N to 15°00' N segment of the East Pacific Rise, *Geochemistry, Geophysics, Geosystems*, 1, 40.
- Christie, D. M., R. Werner, F. Hauff, K. Hoernle, and B. B. Hanan (2005), Morphological and geochemical variations along the eastern Galapagos Spreading Center, *Geochemistry, Geophysics, Geosystems*, 6, 44.
- Cochran, J. R., G. J. Kurras, M. H. Edwards, and B. J. Coakley (2003), The Gakkel Ridge: Bathymetry, gravity anomalies and crustal accretion at extremely slow spreading rates, *Journal of Geophysical Research*, 108.
- Crane, K. (1985), The spacing of rift axis highs: dependence upon diapiric processes in the underlying asthenosphere? 72, 405-414.
- Cushman, B., J. Sinton, G. Ito, and J. E. Dixon (2004), Glass compositions, plume-ridge interaction, and hydrous melting along the Galapagos Spreading Center, 90.5° W to 98° W, *Geochemistry, Geophysics, Geosystems*, 5, 30.
- Danyushevsky, L. V. (2001), The effect of small amounts of H<sub>2</sub>O on crystallization of mid-ocean ridge and backarc basin magmas, *Journal of Volcanology and Geothermal Research*, 110, 265-280.
- DeMets, C., R. G. Gordon, D. F. Argus, and S. Stein (1990), Current plate motions, *Geophys. J. Int.*, 101, 425-478.
- Dick, H., J. Lin, and H. Schouten (2003), An ultraslow-spreading class of ocean ridge, *Nature*, 426, 405-412.
- Dick, H. J. B. (1989), Abyssal peridotites, very slow spreading ridges and ocean ridge magmatism, in *Magmatism in the Ocean Basins*, Geological Society Special Publication No. 42, edited by A. D. Saunders and M. J. Norry, pp. 71-105.
- Dick, H. J. B., and R. L. Fisher (1984), Mineralogic studies of the residues of mantle melting: Abyssal and alpine-type peridotites, in *Kimberlites II. The Mantle and Crust -- Mantle Relationships*, edited by J. Kornprobst, pp. 295-308, Elsevier Science Publishers B.V., Amsterdam, The Netherlands.
- Dick, H. J. B., R. L. Fisher, and W. B. Bryan (1984), Mineralogic variability of the uppermost mantle along mid-ocean ridges, *Earth and Planetary Science Letters*, 69, 88-106.
- Dixon, J. E., and E. Stolper (1995b), An experimental study of water and carbon dioxide solubilities in mid-ocean ridge basaltic liquids, Part II, Applications to degassing, *Journal of Petrology*, 36, 1633-1646.



- Dixon, J. E., E. Stolper, and J. R. Delaney (1988), Infrared spectroscopic measurements of CO<sub>2</sub> and H<sub>2</sub>O in Juan de Fuca Ridge basaltic glasses, *Earth & Planetary Science Letters*, 90, 87-104.
- Dixon, J. E., E. Stolper, and J. R. Holloway (1995a), An experimental study of water and carbon dioxide solubilities in mid-ocean ridge basaltic liquids, Part I, Calibrations and solubility models, *Journal of Petrology*, 36, 1607-1631.
- Dmitriev, L. (1998), Chemical variability of mid-ocean ridge basalts as a function of the geodynamic setting of their formation, *Petrology*, 6, 314-334.
- Donnelly, K. E., S. L. Goldstein, C. Langmuir, and M. Spiegelman (2004), Origin of enriched ocean ridge basalts and implications for mantle dynamics, *Earth & Planetary Science Letters*, 226, 20.
- Dulaney, T. (2002), Volcanic morphology of the ultraslow spreading Southwest Indian Ridge (15°-35° E): Implications for crustal construction, 203 pp, University of North Carolina, Wilmington, Wilmington.
- Elthon, D. (1989), Pressure of origin of primary mid-ocean ridge basalts, in *Magmatism in the Ocean Basins*, edited by A. D. Saunders and M. J. Norry, pp. 125-136, Geological Society Special Publication No. 42.
- Elthon, D. (1992), Chemical trends in abyssal peridotites: refertilization of depleted suboceanic mantle, *Journal of Geophysical Research*, 97, 9015.
- Elthon, D., R. D. Kent, and J. K. Meen (1995), Compositional variations of basaltic glasses from the Mid-Cayman Rise spreading center, *Journal of Geophysical Research*, 100, 12497-12512.
- Faul, U. H. (1997), Permeability of partially molten upper mantle rocks from experiments and percolation theory, *Journal Geophysical Research*, 102, 10299-10311.
- Frey, F. A., J. S. Dickey, Jr., G. Thompson, W. B. Bryan, and H. L. Davies (1980), Evidence for heterogeneous primary MORB and mantle sources, NW Indian Ocean, *Contributions to Mineralogy and Petrology*, 74, 387-402.
- Gaetani, G. A., and T. E. Grove (1998), The influence of water on melting of mantle peridotite, *Contr. Mineral. and Petrol.*, 131, 323-346.
- Galer, S. J. G., and R. K. O'Nions (1986), Magmagenesis and the mapping of chemical and isotopic variations in the mantle, *Chemical Geology*, 56, 45-61.
- Gauger, S., T. Kohls, S. Roeber, and J. Snow (2004), Hydrosweep measurements during the expedition ARK XX-2 to Lena Trough and western Gakkel Ridge, *EOS Transactions, AGU*, 85.
- Georgen, J. E., J. Lin, and H. J. B. Dick (1998), Evidence from gravity anomalies for interactions of the Marion and Bouvet hotspots with the Southwest Indian Ridge: effect of transform offsets, *Earth and Planetary Science Letters*, 187, 283-300.
- Georgen, J. E., J. Lin, and H. J. B. Dick (2001), Evidence from gravity anomalies for interactions of the Marion and Bouvet hotspots with the Southwest Indian Ridge: Effects of transform offsets, *Earth & Planetary Science Letters*, 187, 283-300.
- Ghiorso, M. S., M. M. Hirschmann, P. W. Reiners, and V. C. I. Kress (2002), The pMELTS: A revision of MELTS for improved calculation of phase relations and major element partitioning related to partial melting of the mantle to 3 GPa, *Geochemistry, Geophysics, Geosystems*, 3, 1030, doi:10.1029/2001GC000217.

- Ghiorso, M. S., and R. O. Sack (1995), Chemical mass-transfer in magmatic processes IV. A revised and internally consistent thermodynamic model for the interpolation and extrapolation of liquid-solid equilibria in magmatic systems at elevated temperatures and pressures, *Contrib Mineral Petrol*, 119, 197-212.
- Ghose, I., M. Cannat, and M. Seyler (1996), Transform fault effect on mantle melting in the MARK area (Mid-Atlantic Ridge south of the Kane Transform), *Geology*, 24, 1139-1142.
- Grindlay, N., F. J. Madsen, T. Dulaney, and D. Smith (2000), Variations in axial relief and gravity anomalies at the Southwest Indian Ridge 15°-35°E, paper presented at European Geophysical Society Meeting, *Geophysical Research Abstracts*.
- Grindlay, N. R., J. A. Madsen, C. Rommevaux-Jestin, and J. Sclater (1998), A different pattern of ridge segmentation and mantle Bouguer gravity anomalies along the ultra-slow spreading Southwest Indian Ridge (15°30'E to 25°E), *Earth and Planetary Science Letters*, 161, 243-253.
- Grove, T. L., R. J. Kinzler, and W. B. Bryan (Eds.) (1992), Fractionation of Mid-Ocean Ridge Basalt (MORB), 281-310 pp., American Geophysical Union.
- Hall, C. E., and E. M. Parmentier (2000), Spontaneous melt localization in a deforming solid with viscosity and variations due to water weakening, *Geophysic. Res. Lett.*, 27, 9-12.
- Hall, P. S., and C. Kincaid (2003), Melting, dehydration, and the dynamics of off-axis plume-ridge interaction, *Geochemistry, Geophysics, Geosystems*, 4, 19.
- Hamelin, B., and C. J. Allègre (1985), Large-scale regional units in the depleted upper mantle revealed by an isotope study of the South-West Indian Ridge, *Nature*, 315, 196-199.
- Hanson, G. N. (1977), Geochemical evolution of the suboceanic mantle, *Journal of the Geological Society of London*, 134, 1-19.
- Hart, S. R. (1988), Heterogeneous mantle domains: signatures, genesis and mixing chronologies, *Earth & Planetary Science Letters*, 90, 273-296.
- Hart, S. R., and A. Zindler (1986), In search of a bulk-earth composition, *Chemical Geology*, 57, 247-267.
- Hekinian, R., G. Thompson, and D. Bideau (1989), Axial and off-axial heterogeneity of basaltic rocks from the East Pacific Rise at 12°35'N-12°51'N and 11°26'N-11°30'N, *Journal Geophysical Research*, 94, 17437-17463.
- Herzberg, C. T. (2004), Partial crystallization of mid-ocean ridge basalts in the crust and mantle, *Journal of Petrology*, 45, 17.
- Herzberg, C. T., P. Raterron, and J. Zhang (2000), New experimental observations on the anhydrous solidus for peridotite KLB-1, *Geochemistry, Geophysics, Geosystems*, 1.
- Hirose, K., and I. Kushiro (1993), Partial melting of dry peridotites at high pressures: determination of compositions of melts segregated from peridotite using aggregates of diamond, *Earth & Planetary Science Letters*, 114, 477-489.
- Hirschmann, M. M. (2000), Mantle solidus: Experimental constraints and the effects of peridotite composition, *Geochemistry, Geophysics, Geosystems*, 1.
- Hirschmann, M. M., T. Kogiso, M. B. Baker, and E. M. Stolper (2002), Alkalic magmas generated by partial melting of garnet pyroxenite, *Geology*, in submission.

- Hirschmann, M. M., and E. M. Stolper (1996), A possible role for garnet pyroxenite in the origin of the "garnet signature" in MORB, *Contributions to Mineralogy and Petrology*, 124, 185-208.
- Hirth, G., and D. L. Kohlstedt (1996), Water in the oceanic upper mantle: implications for rheology, melt extraction and the evolution of the lithosphere, *Earth and Planetary Science Letters*, 144, 93-108.
- Irving, A. J. (1980), Petrology and geochemistry of composite ultramafic xenoliths in alkalic basalts and implications for magmatic processes within the mantle, *Am. Jour. Sci.*, 280A, 389-426.
- Ito, G., and J. J. Mahoney (2004), Flow and melting of a heterogeneous mantle: 1. Method and importance to the geochemistry of ocean island and mid-ocean ridge basalts, *Earth & Planetary Science Letters*, 230, 18.
- Ito, G., Y. Shen, G. Hirth, and C. J. Wolfe (1999), Mantle flow, melting, and dehydration of the Iceland mantle plume, *Earth & Planetary Science Letters*, 165, 81-96.
- Jackson, H. R., I. Reid, and R. K. H. Falconer (1982), Crustal structure near the Arctic mid-ocean ridge, *Journal of Geophysical Research*, 87, 1773-1783.
- Janney, P. E., A. P. le Roex, and R. W. Carlson (2005), Hafnium isotope and trace element constraints on the nature of mantle heterogeneity beneath the central Southwest Indian Ridge (13° E to 47° E), Submitted to *Journal of Petrology*.
- Jaques, A. L., and D. H. Green (1980), Anhydrous melting of peridotite at 0-15 Kb pressure and the genesis of tholeiitic basalts, *Contributions to Mineralogy and Petrology*, 73, 287-310.
- Jha, K., E. M. Parmentier, and J. Phipps Morgan (1994), The role of mantle depletion and melt-retention buoyancy in spreading-center segmentation, *Earth and Planetary Science Letters*, 125, 221-234.
- Johnson, K. T. M., H. J. B. Dick, and N. Shimizu (1990), Melting in the oceanic upper mantle: An ion microprobe study of diopsides in abyssal peridotites, *Journal of Geophysical Research*, 95, 2661-2678.
- Jokat, W., O. Ritzmann, M. C. Schmidt-Aursch, S. Drachev, S. Gauger, and J. E. Snow (2003), Geophysical evidence for reduced melt production on the Arctic ultraslow Gakkel mid-ocean ridge, *Nature*, 423, 962-965.
- Karsten, J. L., J. R. Delaney, J. M. Rhodes, and R. A. Lias (1990), Spatial and temporal evolution of magmatic systems beneath the Endeavour segment, Juan de Fuca Ridge: Tectonic and petrologic constraints, *Journal of Geophysical Research*, 95, 19,235-219,256.
- Kelemen, P., M. Braun, and G. Hirth (2000), Spatial distribution of melt conduits in the mantle beneath oceanic spreading ridges: Observations from the Ingalls and Oman ophiolites, *Geochemistry, Geophysics, Geosystems*, 1, 21 pp.
- Kelemen, P., G. Hirth, N. Shimizu, M. Spiegelman, and H. Dick (1997), A review of melt migration processes in the adiabatically upwelling mantle beneath oceanic spreading ridges, *Phil. Trans. R. Soc. Lond.*, 355, 283-318.
- Kelemen, P., E. Kikawa, D. J. Miller, and Shipboard Scientific Party (2004), Drilling Mantle Peridotite along the Mid-Atlantic Ridge from 14° to 16°N, in *Proceedings of*

- the Ocean Drilling Program, edited by L. L. Peters, p. 139 pp, Ocean Drilling Program, Texas A&M University.
- Kelemen, P. B., and H. J. B. Dick (1995), Focused melt flow and localized deformation in the upper mantle: Juxtaposition of replacive dunite and ductile shear zones in the Josephine peridotite, SW Oregon, *Journal of Geophysical Research*, 100, 423-438.
- Kincaid, C., J.-G. Schilling, and C. Gable (1996), The dynamics of off-axis plume-ridge interaction in the uppermost mantle, *Earth and Planetary Science Letters*, 137, 29-43.
- Kinzler, R. J. (1997), Melting of mantle peridotite at pressures approaching the spinel to garnet transition: application to mid-ocean ridge basalt petrogenesis, *Journal of Geophysical Research*, 102, 853-874.
- Kinzler, R. J., and T. Grove (1992b), Primary magmas of mid-ocean ridge basalts 2. Applications, *Journal of Geophysical Research*, 97, 6907-6926.
- Kinzler, R. J., and T. L. Grove (1992a), Primary magmas of mid-ocean ridge basalts 1. Experiments and methods, *Journal of Geophysical Research*, 97, 6885-.
- Klein, E. M., and C. H. Langmuir (1987), Global correlations of ocean ridge basalt chemistry with axial depth and crustal thickness, *Journal of Geophysical Research*, 92, 8089-8115.
- Kogiso, T., M.M. Hirschmann, and M. Pertermann (2004), High-pressure partial melting of mafic lithologies in the mantle, *Journal of Petrology*, 45, 2407-2422.
- Kogiso, T. M., M. M. Hirschmann, and P. W. Reiners (2000), Constraints from isotopic variations on the physical dimensions of chemical heterogeneities in oceanic basalt source regions, paper presented at EOS Trans. AGU Fall Meeting, San Francisco.
- Kuo, B.-Y., and D. W. Forsyth (1988), Gravity anomalies of the ridge-transform system in the South Atlantic between 31 and 34.5°S: Upwelling centers and variations in crustal thickness, *Marine Geophysical Researches*, 10, 205-232.
- Kushiro, I. (1964), The system diopside-forsterite-enstatite at 20 kilobars, *Carnegie Institution of Washington Yearbook*, 63, 101-108.
- Kushiro, I. (1972), Effect of water on the composition of magmas formed at high pressures, *Journal of Petrology*, 13, 311-334.
- Kushiro, I. (1973), Origin of some magmas in oceanic and circum-oceanic regions, *Tectonophysics*, 17, 211-222.
- Kushiro, I. (1975), Nature of silicate melt and its significance in magma genesis - Regularities in shift of liquidus boundaries involving olivine, pyroxene, and silica minerals, *American Journal of Science*, 275, 411-431.
- Langmuir, C. H., and J. F. Bender (1984), The geochemistry of oceanic basalts in the vicinity of transform faults; observations and implications., *Earth and Planetary Science Letters*, 69, 107-127.
- Langmuir, C. H., E. M. Klein, and T. Plank (1992), Petrological systematics of mid-ocean ridge basalts: constraints on melt generation beneath ocean ridges, in *Mantle Flow and Melt Generation at Mid-Ocean Ridges*, edited by J. Phipps Morgan, D. K. Blackman and J. M. Sinton, pp. 183-280, American Geophysical Union, Washington, D.C.
- le Roex, A. P. (1985), A geochemical correlation between source region signatures of southern African kimberlites and South Atlantic hotspots, abstract, 1-7.

- le Roex, A. P., H. J. B. Dick, A. J. Erlank, A. M. Reid, F. A. Frey, and S. R. Hart (1983), Geochemistry, mineralogy and petrogenesis of lavas erupted along the Southwest Indian Ridge between the Bouvet Triple Junction and 11 degrees east, *Journal of Petrology*, 24, 267-318.
- le Roex, A. P., H. J. B. Dick, and R. L. Fisher (1989), Petrology and geochemistry of MORB from 25°E to 46°E along the Southwest Indian Ridge: evidence for contrasting styles of mantle enrichment., *Journal of Petrology*, 30, 947-986.
- le Roex, A. P., H. J. B. Dick, A. M. Reid, F. A. Frey, and A. J. Erlank (1985), Petrology and geochemistry of basalts from the American-Antarctic Ridge, Southern Ocean: implications for the westward influence of the Bouvet mantle plume, *Contributions to Mineralogy and Petrology* 90, 90, 367-380.
- le Roex, A. P., H. J. B. Dick, and R. T. Watkins (1992), Petrogenesis of anomalous K-enriched MORB from the Southwest Indian Ridge: 11°53'E to 14°38'E, *Contributions to Mineralogy and Petrology*, 110, 253-268.
- le Roux, P. J., A. le Roex, and J.-G. Schilling (2002a), MORB melting processes beneath the southern Mid-Atlantic Ridge (40-55°S): a role for mantle plume-derived pyroxenite, *Contr. Mineral. and Petrol.*, 144, 206-229.
- le Roux, P. J., A. P. le Roex, and J.-G. Schilling (2002b), Crystallization processes beneath the southern Mid-Atlantic Ridge (40-55° S), evidence for high-pressure initiation of crystallization, *Contrib. Min. Petrol.*, 142, 582-602.
- Lin, J., H. Dick, and H. Schouten (2003), Evidence for highly focused magmatic accretion along the ultraslow Southwest Indian Ridge, *EOS Transactions, AGU*, 84, T11B-03.
- Lin, J., G. M. Purdy, H. Schouten, J.-C. Sempere, and C. Zervas (1990), Evidence from gravity data for focused magmatic accretion along the Mid-Atlantic Ridge, *Nature*, 344, 627-632.
- Macdonald, K. C., and T. L. Holcombe (1978), Inversion of magnetic anomalies and sea-floor spreading in the Cayman Trough, *Earth and Planetary Science Letters*, 40, 407-414.
- Magde, L. S., and D. W. Sparks (1997), Three-dimensional mantle upwelling, melt generation, and melt migration beneath segment slow spreading ridges, *Journal of Geophysical Research*, 102, 20571-20583.
- Mahoney, J., A. P. Le Roex, Z. Peng, R. L. Fisher, and J. H. Natland (1992), Southwestern limits of Indian Ocean ridge mantle and the origin of low  $^{206}\text{Pb}/^{204}\text{Pb}$  mid-ocean ridge basalt: isotope systematics of the Central Southwest Indian Ridge (17°-50°E), *Journal of Geophysical Research*, 97, 19,771-719,790.
- McKenzie, D. (1989), Some remarks on the movement of small melt fractions in the mantle, *Earth & Planetary Science Letters*, 95, 53-72.
- McKenzie, D., and M. J. Bickle (1988), The volume and composition of melt generated by extension of the lithosphere, *Journal of Petrology*, 29, 625-679.
- Melson, W. G., T. O'Hearn, and E. Jarosewich (2001), A data brief on the Smithsonian abyssal volcanic glass data file, *G-cubed*, 3.
- Melson, W. G., T. L. Vallier, T. L. Wright, G. Byerly, and J. Nelen (1976), Chemical diversity of abyssal volcanic glass erupted along Pacific, Atlantic, and Indian Ocean



- sea-floor spreading centers, *The Geophysics of the Pacific Ocean Basin and Its Margin*, Geophysical Monograph 19, 351-368.
- Mendel, V., and D. Sauter (1997), Seamount volcanism at the super slow-spreading Southwest Indian Ridge between 57° and 70°E, *Geology*, 25, 99-102.
- Mendel, V., D. Sauter, C. Rommevaux-Jestin, P. Patriat, F. Lefebvre, and L. M. Parson (2003), Magmato-tectonic cyclicity at the ultra-slow spreading Southwest Indian Ridge: Evidence from variations of axial volcanic ridge morphology and abyssal hills pattern, *G-cubed*, 4, 23.
- Menke, W. (2005), <http://www.ldeo.columbia.edu/users/menke/plates.html>, edited by R. S. R. Calculator.
- Meyzen, C. M., M. J. Toplis, E. Humler, J. N. Ludden, and C. Mevel (2003), A discontinuity in mantle composition beneath the southwest Indian ridge, *Nature*, 421, 731-733.
- Michael, P. (1999), Implications for magmatic processes at Ontong Java Plateau from volatile and major element contents of Cretaceous basalt glasses, *Geochemistry, Geophysics, Geosystems*, 1.
- Michael, P. J. (1995), Regionally distinctive sources of depleted MORB: Evidence from trace elements and H<sub>2</sub>O, *Earth and Planetary Science Letters*, 131, 301-320.
- Michael, P. J., and R. Chase (1987), The influence of primary magma composition, H<sub>2</sub>O and pressure on mid-ocean ridge basalt differentiation., *Contributions to Mineralogy and Petrology*, 96, 245-263.
- Michael, P. J., and W. C. Cornell (1998), Influence of spreading rate and magma supply on crystallization and assimilation beneath mid-ocean ridges: evidence from chlorine and major element chemistry of mid-ocean ridge basalts, *Journal of Geophysical Research*, 103, 18325-18356.
- Michael, P. J., C. H. Langmuir, H. J. B. Dick, J. E. Snow, S. L. Goldstein, D. W. Graham, K. Lehnert, G. Kurras, W. Jokar, R. Mühe, and H. N. Edmonds (2003), Magmatic and amagmatic seafloor generation at the ultraslow-spreading Gakkel Ridge, Arctic Ocean, *Nature*, 423, 956-961.
- Mével, C., P. Agrinier, M. Cannat, S. Decitre, A. Dappoigny, E. Humler, N. Jendzejewski, J. R. Kienast, J. Ludden, B. Murton, O. Oufi, A. Rabain, M. Seyler, and Y. Tamura (1997), Sampling the South West Indian Ridge: first results of the EDUL cruise (R/V Marion Dufresne II, August 1997), *InterRidge News*, 6, 25-26.
- Niu, Y., and R. Batiza (1991), An empirical method for calculating melt compositions produced beneath mid-ocean ridges: Application for axis and off-axis (seamounts) melting, *Journal of Geophysical Research*, 96, 21753-21777.
- O'Hara, M. J. (1968), Are any ocean floor basalts primary magma? *Nature*, 220, 683-686.
- O'Hara, M. J. (1985), Importance of the 'shape' of the melting regime during partial melting of the mantle, *Nature*, 314, 58-62.
- Okino, K., D. Curewitz, M. Asada, K. Tamaki, P. Vogt, and K. Crane (2002), Preliminary analysis of the Knipovich Ridge segmentation: influence of focused magmatism and ridge obliquity on an ultraslow spreading system, *Earth and Planetary Science Letters*, 202.

- Parmentier, E. M., and J. Phipps Morgan (1990), Spreading-rate dependence of three-dimensional structure in oceanic spreading centers, *Nature*, 348, 325-328.
- Pearson, D. G., G. R. Davies, and P. H. Nixon (1993), Geochemical constraints on the petrogenesis of diamond facies pyroxenites from the Beni Bousera Peridotite Massif, North Morocco, *Journal of Petrology*, 34, 125-172.
- Perfit, M. R., and J. Chadwick, W.M. (1998), Magmatism at mid-ocean ridges: constraints from volcanological and geochemical investigations, in *Faulting and Magmatism at Mid-Ocean Ridges*, edited by W. Buck, P. T. Delaney, J. A. Karson and Y. Lagabrielle, pp. 59-116, American Geophysical Union, Washington, DC.
- Pertermann, M., and M. M. Hirschmann (2003a), Partial melting experiments on a MORB-like pyroxenite between 2 and 3 GPa: Constraints on the presence of pyroxenite in basalt source regions from solidus location and melting rate, *Journal of Geophysical Research*, 108, 16.
- Pertermann, M., and M. M. Hirschmann (2003b), Anhydrous partial melting experiments on MORB-like Eclogite: Phase relations, phase compositions and mineral/melt partitioning of major elements at 2-3 GPa, *Journal of Petrology*, 44, 2173-2201.
- Phipps Morgan, J., and D. W. Forsyth (1988), Three-dimensional flow and temperature perturbations due to a transform offset; effects on oceanic crustal and upper mantle structure, *Journal of Geophysical Research*, 93, 2955-2966.
- Pickering-Witter, J., and A. D. Johnston (2000), The effects of variable bulk compositions on the melting systematics of fertile peridotitic assemblages, *Contr. Mineral. and Petrol.*, 140, 190-211.
- Plank, T., and C. H. Langmuir (1992), Effects of the melting regime on the composition of the oceanic crust, *Journal of Geophysical Research*, 97, 19,749-719,770.
- Prinzhofer, A., E. Lewin, and C. J. Allègre (1989), Stochastic melting of the marble cake mantle: Evidence from local study of the East Pacific Rise at 12°50'N, *Earth & Planetary Science Letters*, 150, 291-302.
- Quick, J. E. (1981), Petrology and petrogenesis of the Trinity Peridotite, an upper mantle diapir in the Eastern Klamath Mountains, Northern California, *Journal of Geophysical Research*, 86, 11,837-811,863.
- Rapp, R. P., and E. B. Watson (1995), Dehydration melting of metabasalt at 8-32 kbar: Implications for continental growth and crust-mantle recycling, *Journal of Petrology*, 36, 891-931.
- Reid, I., and H. R. Jackson (1981), Oceanic spreading rate and crustal thickness, *Marine Geophysical Researches*, 5, 165-172.
- Reynolds, J. R., and C. H. Langmuir (1997), Petrological systematics of the Mid-Atlantic Ridge south of Kane: Implications for ocean crust formation, *Journal of Geophysical Research*, 102, 14915-14946.
- Reynolds, J. R., C. H. Langmuir, J. F. Bender, K. A. Kastens, and W. B. F. Ryan (1992), Spatial and temporal variability in the geochemistry of basalts from the East Pacific Rise, *Nature*, 359, 493-499.
- Ross, K., and D. Elthon (1993), Cumulates from strongly depleted mid-ocean-ridge basalt, *Nature*, 365, 826-829.

- Salters, V. J. M., and H. J. B. Dick (2002), Mineralogy of the mid-ocean-ridge basalt source from neodymium isotopic composition of abyssal peridotites, *Nature*, 418, 68-72.
- Sauter, D., H. Carton, V. Mendel, M. Munsch, C. Rommevaux-Jestin, J.-J. Schott, and H. Whitechurch (2004a), Ridge segmentation and the magnetic structure of the Southwest Indian Ridge (at 50°30'E, 55°30'E and 66°20'E): Implications for magmatic processes at ultraslow-spreading centers, *Geochemistry, Geophysics, Geosystems*, 5, 25.
- Sauter, D., V. Mendel, C. Rommevaux-Jestin, L. Parson, H. Fujimoto, C. Mevel, M. Cannat, and K. Tamaki (2004b), Focused magmatism versus amagmatic spreading along the ultraslow-spreading Southwest Indian Ridge: Evidence from TOBI side scan imagery, *Geochemistry, Geophysics, Geosystems*, 5, 20.
- Sauter, D., P. Patriat, C. Rommevaux-Jestin, M. Cannat, A. Briais, and G. S. S. Party (2001), The Southwest Indian Ridge between 49°15'E and 57°E: focused accretion and magma redistribution, *Earth and Planetary Science Letters*, 192, 303-317.
- Schilling, J.-G. (1973), Iceland mantle plume: Geochemical evidence along Reykjanes Ridge, *Nature*, 242, 565-571.
- Schilling, J.-G., M. Zajac, R. Evans, T. Johnston, W. White, J. D. Devine, and R. Kingsley (1983), Petrologic and geochemical variations along the Mid-Atlantic Ridge from 29°N to 73°N, *American Journal of Science*, 283, 510-586.
- Scott, D. R., and D. J. Stevenson (1989), A self-consistent model of melting, magma migration, and buoyancy-driven circulation beneath mid-ocean ridges, *Journal Geophysical Research*, 94, 2973-2988.
- Seyler, M., M. Cannat, and C. Mevel (2003), Evidence for major-element heterogeneity in the mantle source of abyssal peridotites from the Southwest Indian Ridge (52° to 68° E), *Geochemistry, Geophysics, Geosystems*, 4, 33.
- Shen, Y., and D. W. Forsyth (1995), Geochemical constraints on initial and final depths of melting beneath mid-ocean ridges, *Journal of Geophysical Research*, 100, 2211-2237.
- Sinton, J. M., S. M. Smaglik, J. J. Mahoney, and K. C. Macdonald (1991), Magmatic processes at superfast spreading mid-ocean ridges: glass compositional variations along the East Pacific Rise 13°-23° S., *Journal of Geophysical Research*, 96, 6133-6155.
- Sleep, N. H. (1984), Tapping of magmas from ubiquitous mantle heterogeneities: An alternative to mantle plumes? *Journal Geophysical Research*, 89, 10029-10041.
- Small, C., and L. V. Danyushevsky (2003), Plate-kinematic explanation for mid-oceanic-ridge depth discontinuities, *Geology*, 31, 399-402.
- Smith, M. C., M. R. Perfit, and I. R. Jonasson (1994), Petrology and geochemistry of basalts from the southern Juan de Fuca Ridge: Controls on the spatial and temporal evolution of mid-ocean ridge basalt, *Journal of Geophysical Research*, 99, 4787-4812.
- Smith, P. M. a. P. D. A. (2005), *Adiabat\_1ph*: a new public front-end to the MELTS, pMELTS, and pHMELTS models, *Geochemistry, Geophysics, Geosystems*, 6, 1-8.

- Snow, J. E., E. Hellebrand, A. Handt, F. Nauret, Y. Gao, S. Feig, Z. Jovanovic, and S. Gauger (2004), Lena Trough (Arctic Ocean): An oblique 'amagmatic' rift, EOS Transactions, AGU, 85, T11G-01.
- Sparks, D. W., and E. M. Parmentier (1991), Melt extraction from the mantle beneath spreading centers, *Earth & Planetary Science Letters*, 105, 368-377.
- Sparks, D. W., and E. M. Parmentier (1993), The structure of three-dimensional convection beneath oceanic spreading centers, *Geophysical Journal International*, 112, 81-91.
- Spiegelman, M., and T. Elliot (1993), Consequences of melt transport for U-series disequilibrium in young lavas, *Earth and Planetary Science Letters*, 118, 1-20.
- Spiegelman, M., and J. R. Reynolds (1999), Combined dynamic and geochemical evidence for convergent melt flow beneath the East Pacific Rise, *Nature*, 402, 282-285.
- Standish, J., K. W. W. Sims, and H. Dick (2005a), Producing U-series disequilibria on an ultraslow-spreading mid-ocean ridge, paper presented at Goldschmidt Conference, Moscow, Idaho.
- Standish, J. J., and H. J. B. Dick (2004), The influence of ridge geometry at ultraslow spreading rates, EOS, Transactions American Geophysical Union, 85.
- Standish, J. J., S. R. Hart, and A. le Roex (2005b), Trace element and isotopic evidence of two-component melting beneath the ultraslow-spreading SW Indian Ridge (9-25°E), in prep.
- Su, Y., and C. Langmuir (2002), Global MORB chemistry compilation at the segment scale, in *Petrologic Database of the Ocean Floor*, edited by <http://www.petdb.org/documentation/morbcompilation/index.jsp>.
- Suen, C. J., and F. A. Frey (1987), Origins of the mafic and ultramafic rocks in the Ronda peridotite, *Earth and Planetary Science Letters*, 85, 183-202.
- Sun, S.-s., and W. F. McDonough (1989), Chemical and isotopic systematics of oceanic basalts: implications for mantle composition and processes, in *Magmatism in the Ocean Basins*, edited by A. D. Saunders and M. J. Norry, pp. 313-345, Geological Society Special Publication No. 42.
- Sun, S. S., and G. N. Hanson (1975), Origin of Ross Island basanitoids and limitations upon the heterogeneity of mantle sources for alkali basalts and nephelinites, *Contributions to Mineralogy and Petrology*, 52, 77-106.
- Takahashi, E., and K. Nakajima (2002), Melting process in the Hawaiian Plume: An experimental study, in *Hawaiian Volcanoes: Deep Underwater Perspectives*, Geophysical Monograph Series, edited by E. Takahashi, pp. 403-418, AGU, Washington, D.C.
- Thompson, G., W. B. Bryan, and W. G. Melson (1980), Geological and geophysical investigation of the Mid-Cayman Rise Spreading Center: Geochemical variation and petrogenesis of basalt glasses, *Journal of Geology*, 88, 41-55.
- Walter, M. J. (1998), Melting of garnet peridotite and the origin of komatiite and depleted lithosphere, *Journal of Petrology*, 39, 29-60.
- Warren, J. M., N. Shimizu, and H. Dick (2004), Ultraslow spreading ridges and mantle heterogeneities, in *Goldschmidt Conference*, edited, Copenhagen, Denmark.

- Wasylenki, L. E., M. B. Baker, A. J. R. Kent, and E. M. Stolper (2003), Near-solidus melting of shallow upper mantle: Partial melting experiments on depleted peridotite., *Journal of Petrology*, 44, 1163-1191.
- Weaver, B. L. (1991), The origin of ocean island basalt end-member compositions: Trace element and isotopic constraints, *Earth & Planetary Science Letters*, 104, 381-397.
- White, R. S., D. McKenzie, and R. K. O'Nions (1992), Oceanic crustal thickness from seismic measurements and rare earth element inversions, *Journal of Geophysical Research*, 97, 19683-19715.
- White, R. S., T. A. Minshull, M. J. Bickle, and C. J. Robinson (2001), Melt generation at very slow-spreading oceanic ridges: Constraints from geochemical and geophysical data, *Journal of Petrology*, 42, 1171-1196.
- Whitehead, J. A., Jr., H. J. B. Dick, and H. Schouten (1984), A mechanism for magmatic accretion under spreading centers, *Nature*, 312, 146-148.
- Yaxley, G. M. (2000), Experimental study of the phase and melting relations of homogeneous basalt + peridotite mixtures and implications for the petrogenesis of flood basalts, *Contr. Mineral. and Petrol.*, 139, 326-338.
- Yaxley, G. M., and D. H. Green (1998), Reactions between eclogite and peridotite: Mantle refertilization by subduction of oceanic crust, *Schweiz, Mineralogische und Petrographische Mitteilungen*, 78, 243-255.
- Yoder, H. S., and C. E. Tilley (1962), Origin of basaltic magmas: Experimental study of natural and synthetic rock systems, *Journal of Petrology*, 3, 342-532.
- Zhu, W., and G. Hirth (2003), A network model for permeability in partially molten rocks, *Earth & Planetary Science Letters*, 212, 407-416.
- Zindler, A., and S. Hart (1986), Chemical geodynamics, *Annual Review of Earth and Planetary Sciences*, 14.
- Zindler, A., H. Staudigel, and R. Batiza (1984), Isotope and trace element geochemistry of young Pacific seamounts: implications for the scale of upper mantle heterogeneity, *Earth and Planetary Science Letters*, 70, 175-195.



Table 1. Representative ridge characteristics for each tectonomagmatic province

Ridge characteristics*	Orthogonal Supersegment 15°45'-25°06'E	Amagmatic Accretionary Segments <sup>a</sup>	Joseph Mayes Seamount 11°-11°35'E	Narrowgate Segment 14°15'-14°54'E
Average axial depth (m)	3796±374	4151±425	2574±711	3532±295
Spreading Rate (mm/yr full-rate) <sup>b</sup>	14.4±0.1	14.1±0.1	14.1±0.1	14.2±0.1
Effective Spreading Rate (mm/yr) <sup>c</sup>	14.3±0.5	9.1±2.1 <sup>f</sup>	13.3±0.1	14.2±0.1
Rift Valley Width (km)	28.8±1.5	40.8±11.5	67.5 <sup>d</sup>	18.3
Inner Valley Floor Width (km)	13.7	10.6	n.a.	8.8
Cross-axis Relief (km)	2.5	2.4	2.6 <sup>e</sup>	1.7
Number of Segments	14	4	1	1
Segment Length (km)	42±15	~100	~50	35

\* data is compiled from profiles presented in Figure 2 & 3, and in the case of the orthogonal supersegment and amagmatic accretionary segments is averaged

<sup>a</sup> three segments comprise this tectonomagmatic province: 9°30'-11°E, 11°35'-14°15'E, and 14°54'-15°45'E

<sup>b</sup> Full spreading rate and FSR azimuth calculated at <http://www.ldeo.columbia.edu/users/menke/plates.html>

<sup>c</sup> ESR calculated following the method of *Abelson & Agnon [1997]*, with ESR azimuth measured by hand.

<sup>d</sup> measured from northern bounding peridotite block to southern bounding block

<sup>e</sup> this value reflects relief on profile, but total relief of JMS, measured from the floor of the adjacent amagmatic trough to its highest volcanic peak, is ~3.9 km

<sup>f</sup> value does not include the amagmatic segment west of JMS, due to unconstrained rift valley boundaries and morphology

Table 2. Dredge averaged statistics compiled from sample descriptions \*

General Dredge Information						Dredged Rock Lithologies <sup>1</sup>										Basalt Statistics <sup>2</sup>			
Dredge # <sup>3</sup>	Latitude (°S)	Longitude (°E)	Depth <sup>4</sup> (mbsl)	Full Effective Spreading Rate <sup>5</sup> (mm/yr)	Full Effective Spreading Rate <sup>6</sup> (mm/yr)	Total Wt. Described Samples (kg)	Pillow Basalt/ Basalt	Peridotite /Dunite	Gabbro	Diabase	Andesite	Hydthm. Rocks/ Volc-clst.	Sed. Rocks/ Erratics	% Plag Phenos	% Oliv Phenos	% Cpx Phenos	% Vesicles		
Oblique Supersegment (9°56' - 15°45' E)																			
Amagmatic Segments (9°56' - 11° E; 11°36' - 14°15' E; 14°54' - 15°45' E)																			
VAN7-95	52.880	9.940	4394	14.04	12.34	15.7	0.5	0.0	0.2	0.1	0.0	0.3	14.6	10.0	1.5	0.0	10.5		
VAN7-96	53.140	9.979	3143	14.06	12.36	70.6	0.0	25.6	2.9	6.8	0.0	35.4	0.0	0.0	0.0	0.0	0.0		
VAN7-94	52.990	10.130	4500	14.06	12.38	1.0	1.0	0.0	0.0	0.0	0.0	0.0	0.0	0.0	0.0	0.0	0.0		
VAN7-93	52.979	10.547	3260	14.07	12.43	20.1	20.1	0.0	0.0	0.0	0.0	0.0	0.0	10.5	0.5	0.0	0.0		
KN162-9-28	52.896	10.674	3803	14.07	12.45	212.5	211.6	0.0	0.4	0.0	0.0	0.5	0.0	1.1	2.4	0.0	5.2		
KN162-9-27*	52.403	10.696	2880	14.05	n.d.	180.6	120.9	0.0	5.0	4.7	0.0	50.0	0.0	4.4	0.0	0.0	6.0		
VAN7-92	52.860	10.888	3633	14.08	12.48	41.0	41.0	0.0	0.0	0.0	0.0	0.0	0.0	5.7	2.3	0.0	2.4		
KN162-9-29a	52.956	11.035	3516	14.09	13.28	2.0	0.0	0.0	0.0	0.0	0.0	0.0	2.0	0.0	0.0	0.0	0.0		
KN162-9-29b	52.962	11.097	3665	14.09	13.29	0.0	0.0	0.0	0.0	0.0	0.0	0.0	0.0	0.0	0.0	0.0	0.0		
KN162-9-30	52.994	11.157	3587	14.10	13.30	106.9	42.8	60.8	0.0	0.0	0.0	0.0	3.3	2.6	0.9	0.0	4.0		
KN162-9-36	52.749	11.711	4017	14.11	7.52	101.5	101.5	0.0	0.0	0.0	0.0	0.0	0.0	1.0	0.0	0.0	1.6		
KN162-9-37	52.679	11.812	3916	14.11	7.54	214.7	0.8	207.2	0.0	4.8	0.0	0.0	1.9	3.3	0.0	0.0	1.3		
KN162-9-38	52.777	11.854	4061	14.11	7.54	176.8	166.1	0.0	0.0	2.4	0.0	2.9	5.4	2.0	1.3	0.1	4.9		
KN162-9-39	52.672	12.045	4502	14.12	7.59	0.9	0.0	0.0	0.0	0.0	0.0	0.9	0.0	0.0	0.0	0.0	0.0		
KN162-9-40	52.670	12.070	4282	14.12	7.59	66.8	2.6	0.0	0.0	0.0	0.0	0.0	64.2	0.6	0.8	0.0	0.0		
KN162-9-41	52.589	12.132	4361	14.11	7.60	52.3	21.3	0.0	0.0	0.7	0.0	30.0	0.3	4.7	2.5	1.0	10.3		
KN162-7-01*	51.626	12.174	2320	14.07	n.d.	18.1	0.0	0.0	0.0	0.0	0.0	12.7	4.5	0.0	0.0	0.0	0.0		
KN162-9-42	52.720	12.230	3690	14.12	7.63	90.4	0.5	85.0	0.0	0.0	0.0	0.2	4.7	0.0	0.0	0.0	24.0		
KN162-9-44b	52.611	12.373	4278	14.13	7.65	0.0	0.0	0.0	0.0	0.0	0.0	0.0	0.0	0.0	0.0	0.0	0.0		
KN162-9-44a	52.590	12.403	4503	14.13	7.65	0.0	0.0	0.0	0.0	0.0	0.0	0.0	0.0	0.0	0.0	0.0	0.0		
KN162-9-46	52.631	12.491	4070	14.13	7.68	85.2	0.0	73.1	0.0	0.5	0.0	10.6	1.0	0.0	0.0	0.0	0.0		
KN162-9-45	52.490	12.496	4048	14.12	7.69	52.6	0.2	32.4	0.0	0.0	0.0	19.4	0.6	0.0	0.0	0.0	0.0		
KN162-9-43	52.645	12.526	3730	14.13	7.68	141.5	8.7	55.9	0.0	0.0	0.0	67.7	9.2	12.2	0.5	0.1	14.8		
KN162-9-47	52.562	12.662	4361	14.13	7.72	143.7	0.5	137.8	0.0	0.0	0.0	3.0	2.4	0.0	0.0	0.0	0.0		
KN162-9-50a	52.420	12.748	3930	14.13	7.74	0.0	0.0	0.0	0.0	0.0	0.0	0.0	0.0	0.0	0.0	0.0	0.0		
KN162-9-50b	52.420	12.748	3930	14.13	7.74	32.9	0.0	32.4	0.0	0.0	0.0	0.0	0.5	0.0	0.0	0.0	0.0		
KN162-9-48	52.560	12.799	4090	14.14	7.74	157.7	137.0	0.0	0.0	20.5	0.0	0.1	0.1	5.3	4.9	0.0	13.3		
KN162-9-49	52.479	12.861	4193	14.14	7.76	49.6	48.7	0.0	0.0	0.0	0.0	0.0	0.9	1.8	0.4	0.0	6.3		
KN162-9-51	52.296	13.062	7210	14.14	8.80	181.1	123.5	30.2	0.0	0.0	0.0	1.7	25.7	2.0	4.3	0.4	9.4		
KN162-9-53	52.475	13.144	4315	14.15	8.81	45.6	23.6	21.7	0.0	0.0	0.0	0.0	0.3	2.3	0.5	0.0	2.3		
KN162-9-52	52.392	13.197	4399	14.15	8.83	0.0	0.0	0.0	0.0	0.0	0.0	0.0	0.0	0.0	0.0	0.0	0.0		
VAN7-91	52.090	13.267	3100	14.14	8.84	109.7	60.0	0.0	21.1	0.0	0.0	16.3	12.4	5.3	0.2	0.1	4.5		
KN162-9-54	52.437	13.312	4291	14.15	8.85	1.6	0.0	0.0	0.0	0.0	0.0	0.0	1.6	0.0	0.0	0.0	0.0		
KN162-9-55	52.433	13.410	4094	14.16	8.87	66.3	3.2	57.7	2.9	0.0	0.0	0.0	2.5	4.2	9.5	0.0	0.0		
KN162-9-56	52.370	13.506	4050	14.16	8.89	59.0	0.4	57.4	0.0	0.0	0.0	0.1	1.1	0.0	0.0	0.0	1.5		
KN162-9-58	52.157	13.731	2575	14.16	10.20	204.9	25.7	136.2	0.0	25.0	0.0	0.0	18.0	3.3	3.3	0.0	8.7		
KN162-9-57	52.224	13.738	3526	14.16	10.20	3.4	0.0	0.0	0.0	0.0	0.0	0.0	3.4	0.0	0.0	0.0	0.0		
KN162-9-59	52.278	13.996	3553	14.17	10.26	35.5	0.0	35.3	0.0	0.0	0.0	0.0	0.2	0.0	0.0	0.0	0.0		
KN162-9-60	52.157	14.118	3249	14.17	10.28	0.0	0.0	0.0	0.0	0.0	0.0	0.0	0.0	0.0	0.0	0.0	0.0		
KN162-9-62	52.253	15.103	4005	14.21	11.96	53.0	0.0	52.7	0.0	0.0	0.0	0.0	0.3	0.0	0.0	0.0	0.0		
VAN7-86	52.140	15.166	3749	14.21	11.97	131.6	0.0	115.7	0.0	0.0	0.0	0.0	16.0	0.0	0.0	0.0	0.0		
VAN7-85	52.253	15.233	4181	14.22	11.99	89.6	0.0	75.5	0.0	1.9	0.0	11.7	0.6	0.0	0.0	0.0	0.0		
KN162-9-63	52.148	15.403	3857	14.22	12.01	0.5	0.5	0.0	0.0	0.0	0.0	0.0	0.0	15.0	9.0	0.0	20.0		
VAN7-84	52.157	15.428	4050	14.22	12.02	20.0	0.0	0.0	0.0	0.0	0.0	0.0	20.0	0.0	0.0	0.0	0.0		
GC-1*	52.205	15.512	4067	14.23	12.03	0.0	0.0	0.0	0.0	0.0	0.0	0.0	0.0	0.0	0.0	0.0	0.0		
VAN7-82	52.022	15.655	2344	14.23	12.04	0.0	0.0	0.0	0.0	0.0	0.0	0.0	0.0	0.0	0.0	0.0	0.0		
Amagmatic Segment Averages						2410.9	3.7%	80%	1%	2%	0%	2%	4%	2%	2%	0%	0%		
Joseph Mayes Seamount (11° - 11°36' E, excluding D29 & D30)																			
KN162-9-31	52.805	11.082	3074	14.08	13.28	2.2	2.2	0.0	0.0	0.0	0.0	0.0	0.0	33.8	0.0	0.0	0.0		
KN162-9-32	52.749	11.218	2720	14.09	13.30	83.9	74.7	0.0	0.0	6.4	0.0	0.8	2.0	11.2	0.8	0.0	6.6		
KN162-9-33	52.817	11.387	1462	14.10	13.32	50.3	49.1	0.0	0.0	0.0	0.0	0.1	1.1	1.9	0.2	0.0	22.8		
KN162-9-34	52.857	11.430	2126	14.10	13.32	79.6	79.6	0.0	0.0	0.0	0.0	0.0	0.0	10.7	0.8	0.0	5.4		
KN162-9-35	52.927	11.555	2606	14.11	13.34	100.1	100.1	0.0	0.0	0.0	0.0	0.0	0.0	6.6	2.2	0.0	19.0		
Joseph Mayes Seamount Averages						310.0	2.2%	0%	0%	2%	0%	0.2%	1%	12%	1%	0%	11%		
Narrowgate Segment (14°15' - 14°54' E)																			
VAN7-90	52.180	14.353	3800	14.18	14.14	222.3	222.3	0.0	0.0	0.0	0.0	0.0	0.0	0.5	1.3	0.0	3.6		
VAN7-89	52.250	14.597	2570	14.19	14.15	235.0	224.6	0.0	0.0	0.0	0.0	10.4	0.0	1.8	0.2	0.0	6.0		
KN162-9-61	52.104	14.601	2282	14.19	14.15	252.8	23.9	0.0	0.0	100.7	0.0	106.6	21.6	5.8	0.5	0.0	3.5		
VAN7-88	52.220	14.706	3032	14.20	14.17	211.7	211.7	0.0	0.0	0.0	0.0	0.0	0.0	4.3	0.5	0.0	18.8		
VAN7-87	52.240	14.789	3611	14.20	14.17	0.5	0.5	0.0	0.0	0.0	0.0	0.0	0.0	30.0	0.0	0.0	4.3		
Narrowgate Segment Averages						922.3	24%	0%	0%	11%	0%	15%	2%	8%	1%	0%	8%		
Oblique Supersegment Averages (All dredges)						4048.7	10%	72%	1%	4%	0%	8%	5%	6%	2%	0%	0%		

General Dredge Information						Dredged Rock Lithologies <sup>1</sup>										Basalt Statistics <sup>2</sup>			
Dredge # <sup>3</sup>	Latitude (°S)	Longitude (°E)	Depth <sup>4</sup> (mbsl)	Full Spreading	Full Effective Spreading	Total Wt. Described Samples (kg)	Pillow Basalt/ Basalt	Peridotite /Dunit	Gabbro	Diabase	Andesitic Volc-clst.	Hydthm. Rocks/ Volc-clst.	Sed. Rocks/ Erratics	% Plag Phenos	% Oliv Phenos	% Cpx Phenos	% Vesicles		
				Rate <sup>5</sup> (mm/yr)	Rate <sup>5</sup> (mm/yr)														
Orthogonal Supersegment (15°45' - 25° E)																			
KN162-9-64	52.293	15.644	2947	14.23	12.04	42.6	4.5	0.0	0.0	37.1	0.0	0.0	1.0	0.1	3.4	0.0	2.8		
VAN7-81	52.228	15.789	4231	14.24	12.08	0.0	0.0	0.0	0.0	0.0	0.0	0.0	0.0	0.0	0.0	0.0	0.0		
VAN7-83	52.170	15.837	3993	14.24	12.08	58.1	58.1	0.0	0.0	0.0	0.0	0.0	0.0	2.7	1.7	0.0	3.1		
VAN7-80	52.230	16.007	4134	14.25	14.24	56.4	56.4	0.0	0.0	0.0	0.0	0.0	0.0	1.3	2.0	0.0	7.8		
VAN7-79	52.300	16.125	4145	14.25	14.24	299.3	299.0	0.0	0.0	0.0	0.0	0.3	0.0	1.8	1.0	0.0	3.9		
KN162-7-02	52.330	16.233	3855	14.23	14.22	11.2	11.2	0.0	0.0	0.0	0.0	0.0	0.0	0.0	0.0	0.0	7.5		
KN162-7-03	52.299	16.507	3481	14.27	14.04	6.4	6.4	0.0	0.0	0.0	0.0	0.0	0.0	1.0	0.0	0.0	0.8		
VAN7-78	52.380	16.635	4025	14.27	14.04	173.8	7.2	129.5	36.7	0.0	0.0	0.0	0.5	0.4	0.6	0.0	0.3		
AG22-01	52.300	16.980	4000	14.28	14.23	11.7	11.7	0.0	0.0	0.0	0.0	0.0	0.0	0.0	0.0	0.0	0.0		
VAN7-77	52.422	17.065	3063	14.29	14.24	38.9	4.1	1.3	0.0	31.7	0.0	0.8	1.0	10.0	1.0	0.0	0.0		
KN162-7-04	52.358	17.113	3928	14.29	14.24	203.5	203.5	0.0	0.0	0.0	0.0	0.0	0.0	0.1	0.4	0.0	0.2		
KN162-7-05	52.423	17.428	3090	14.30	14.25	7.5	7.5	0.0	0.0	0.0	0.0	0.0	0.0	1.0	0.5	0.0	7.5		
KN162-7-06	52.520	17.702	3582	14.32	14.28	39.5	39.5	0.0	0.0	0.0	0.0	0.0	0.0	5.4	1.0	0.0	1.3		
AG22-03	52.294	17.914	4200	14.28	14.14	14.8	9.4	0.0	0.0	5.5	0.0	0.0	0.0	0.0	0.0	0.0	0.0		
VAN7-76	52.631	17.922	3442	14.33	14.21	163.8	92.5	15.7	0.0	54.4	0.0	1.3	4.6	4.4	0.0	0.0	2.9		
KN162-7-07	52.548	18.028	4001	14.33	14.22	38.6	38.6	0.0	0.0	0.0	0.0	0.0	0.0	0.5	0.0	0.0	6.3		
KN162-7-08	52.615	18.336	3702	14.34	14.24	96.2	96.2	0.0	0.0	0.0	0.0	0.0	0.0	0.4	0.4	0.0	3.8		
KN162-7-09b	52.700	18.826	4012	14.36	14.27	6.4	6.4	0.0	0.0	0.0	0.0	0.0	0.0	2.0	0.0	0.0	1.0		
KN162-7-09a	52.695	18.827	4060	14.36	14.27	0.0	0.0	0.0	0.0	0.0	0.0	0.0	0.0	0.0	0.0	0.0	0.0		
AG22-05	54.760	19.097	3700	14.37	14.28	56.7	52.7	0.0	0.0	4.0	0.0	0.0	0.0	0.0	0.0	0.0	0.0		
KN162-7-11	52.799	19.200	3886	14.37	14.29	115.5	115.5	0.0	0.0	0.0	0.0	0.0	0.0	0.3	0.1	0.0	5.0		
KN162-7-10	52.745	19.269	3165	14.37	14.29	49.0	49.0	0.0	0.0	0.0	0.0	0.0	0.0	0.4	0.0	0.0	2.9		
KN162-7-12b	52.842	19.767	4440	14.39	14.38	0.0	0.0	0.0	0.0	0.0	0.0	0.0	0.0	0.0	0.0	0.0	0.0		
KN162-7-12a	52.835	19.769	4397	14.39	14.38	0.0	0.0	0.0	0.0	0.0	0.0	0.0	0.0	0.0	0.0	0.0	0.0		
VAN7-75	53.000	19.775	1731	14.40	14.39	96.5	85.7	0.0	0.0	3.3	0.2	0.9	6.5	14.8	0.1	0.0	1.0		
VAN7-74	52.900	19.783	4111	14.40	14.39	74.9	73.0	0.0	0.0	0.0	0.0	1.9	0.0	0.5	0.2	0.0	2.6		
KN162-7-13	52.856	19.913	4071	14.40	14.39	35.4	34.9	0.0	0.0	0.0	0.0	0.0	0.5	1.0	0.0	0.0	0.0		
KN162-7-15	52.923	20.382	3489	14.41	14.39	16.6	16.6	0.0	0.0	0.0	0.0	0.0	0.0	2.2	0.0	0.0	3.8		
KN162-7-14a	52.873	20.398	3450	14.41	14.39	0.0	0.0	0.0	0.0	0.0	0.0	0.0	0.0	0.0	0.0	0.0	0.0		
KN162-7-14b	52.902	20.412	3420	14.41	14.39	33.3	33.3	0.0	0.0	0.0	0.0	0.0	0.0	4.5	0.0	0.0	2.5		
KN162-7-16	52.922	20.661	4283	14.42	14.40	11.5	11.5	0.0	0.0	0.0	0.0	0.0	0.0	13.6	0.0	0.0	0.0		
VAN7-73	52.980	20.693	3795	14.43	14.41	213.3	209.8	0.0	0.0	2.9	0.0	0.2	0.5	0.0	0.0	0.0	0.1		
KN162-7-17	52.949	20.925	3874	14.43	14.41	124.1	124.1	0.0	0.0	0.0	0.0	0.0	0.0	1.0	0.0	0.0	1.8		
VAN7-72	53.010	20.935	2953	14.43	14.41	149.7	0.0	0.0	93.7	51.2	0.7	4.3	0.0	0.0	0.0	0.0	0.0		
KN162-7-19	53.050	21.376	3992	14.45	14.44	81.2	45.8	22.0	0.6	9.4	0.0	0.1	3.3	1.0	0.0	0.0	0.4		
KN162-7-18	52.990	21.406	4507	14.45	14.44	76.7	76.7	0.0	0.0	0.0	0.0	0.0	0.0	0.9	0.0	0.0	0.5		
VAN7-71a	53.090	21.473	3289	14.45	14.44	0.0	0.0	0.0	0.0	0.0	0.0	0.0	0.0	0.0	0.0	0.0	0.0		
VAN7-71b	53.075	21.473	3331	14.45	14.44	62.3	9.3	0.0	0.0	0.0	0.0	53.0	0.0	0.0	0.0	0.0	0.0		
AG22-07	53.023	21.833	3300	14.46	14.46	1.0	1.0	0.0	0.0	0.0	0.0	0.0	0.0	0.0	0.0	0.0	0.0		
VAN7-70	53.040	21.978	3968	14.47	14.47	233.7	233.7	0.0	0.0	0.0	0.0	0.0	0.0	0.9	0.3	0.0	1.5		
KN162-7-20	53.039	22.177	4246	14.47	14.47	35.1	35.1	0.0	0.0	0.0	0.0	0.0	0.0	0.3	0.0	0.0	5.0		
AG22-08	53.105	22.197	3690	14.47	14.47	26.0	26.0	0.0	0.0	0.0	0.0	0.0	0.0	0.0	0.0	0.0	0.0		
VAN7-69	53.140	22.451	3890	14.48	14.48	150.5	150.5	0.0	0.0	0.0	0.0	0.0	0.0	3.0	1.1	0.0	2.1		
KN162-7-21	53.035	22.468	3787	14.48	14.48	138.6	138.6	0.0	0.0	0.0	0.0	0.0	0.0	3.3	0.0	0.0	0.4		
KN162-7-23	53.173	22.574	3658	14.49	14.49	136.4	135.8	0.0	0.0	0.0	0.0	0.0	0.6	0.9	0.0	0.0	0.7		
KN162-7-22	53.109	22.647	3875	14.49	14.49	175.1	175.1	0.0	0.0	0.0	0.0	0.0	0.0	1.6	0.0	0.0	2.4		
VAN7-68	53.230	22.791	3353	14.49	14.49	70.2	65.5	0.0	0.0	0.2	0.0	4.4	0.2	1.7	0.4	0.0	0.9		
KN162-7-24	53.158	22.852	3290	14.49	14.49	178.3	175.8	0.0	0.0	0.0	0.0	0.0	2.5	2.9	0.0	0.0	2.8		
AG22-09	53.130	22.880	3800	14.49	14.49	6.0	6.0	0.0	0.0	0.0	0.0	0.0	0.0	0.0	0.0	0.0	0.0		
VAN7-67	53.290	23.019	3775	14.50	14.50	27.7	26.9	0.0	0.0	0.2	0.0	0.6	0.0	0.0	0.4	0.0	1.1		
KN162-7-25	53.173	23.117	3995	14.50	14.50	53.3	53.3	0.0	0.0	0.0	0.0	0.0	0.0	0.1	0.0	0.0	0.2		
VAN7-66a	53.277	23.271	3896	14.51	14.51	0.0	0.0	0.0	0.0	0.0	0.0	0.0	0.0	0.0	0.0	0.0	0.0		
VAN7-66b	53.277	23.271	3905	14.51	14.51	228.2	228.2	0.0	0.0	0.0	0.0	0.0	0.0	2.6	2.7	0.0	1.3		
KN162-7-26	53.214	23.358	3325	14.51	14.51	56.8	56.8	0.0	0.0	0.0	0.0	0.0	0.0	2.6	0.0	0.0	2.3		
AG22-12	53.393	23.692	3650	14.52	14.52	36.95	33.75	0.0	0.0	3.0	0.0	0.2	0.0	0.0	0.0	0.0	0.0		
AG22-13	53.408	24.758	3850	14.55	14.55	25.9	25.9	0.0	0.0	0.0	0.0	0.0	0.0	0.0	0.0	0.0	0.0		

<sup>1</sup> dredged rock lithologies - mass of rock in kilograms which falls into each general lithologic classification

<sup>2</sup> basalt statistics - compiled sample specific descriptions averaged for each dredge and presented as percentages

<sup>3</sup> dredge labels represent expeditions Knorr 162-Legs 7&9 (KN162), Melville-Vancouver Leg 7 (VAN7), and Agulhas 22 (AG22); dredges are generally listed according to Longitude (°E) from east to west; PS4 samples are not included here due to lack of statistical data compilation, but are shown in Figure 1 and described in detail in Le Roex et al., 1992

<sup>4</sup> depth represent meters below sea level as determined when the dredge hit bottom

<sup>5</sup> full spreading rate calculated at <http://www.ldeo.columbia.edu/users/mckenzie/plates.html>

<sup>6</sup> ESR calculated following the method of Abelson & Agnon (1997), with ESR azimuth measured by hand.

<sup>7</sup> averages for dredged lithologies represent percent lithology of 'non-empty' dredges; averages for basalt statistics are averaged percentages of dredges recovering basalt

<sup>8</sup> dredge KN162-7-01 and KN162-7-27 are both located on the Shaka Ridge (transform trace), and thus are not included in statistics; GC-1 recovered < 1 kg of sand and rock and thus is not included in statistics

<sup>9</sup> descriptive information (i.e. phenocryst %, vesicle %) was reviewed at sea by the authors to ensure consistency and minimize error

n.d. = not determined, as both these dredges are off-axis

Table 3. Microprobe major element oxide weight percents and FTIR volatile concentrations for glass samples from 9°-25° E on SW Indian Ridge.

Sample no. *	Latitude	Longitude	Depth	SiO <sub>2</sub>	Al <sub>2</sub> O <sub>3</sub>	FeO*	MgO	CaO	Na <sub>2</sub> O	K <sub>2</sub> O	TiO <sub>2</sub>	P <sub>2</sub> O <sub>5</sub>	MnO	H <sub>2</sub> O	CO <sub>2</sub> *	Mg#*	CaO/ Al <sub>2</sub> O <sub>3</sub>	κ/τi
Oblique supersegment (9°56'-15°45' E)																		
Amagmatic Segments (9°56' - 11° E; 11°36' - 14°15' E; 14°54' - 15°45' E)																		
VAN7-96-28	53.140	9.979	3134	50.05	16.37	9.00	6.79	10.92	3.48	0.49	1.91	0.25	0.17			61.28	0.67	0.22
KN162-7 28-15	52.896	10.674	3635	50.11	16.03	9.26	6.33	10.05	3.77	0.48	2.17	0.34	0.12			58.91	0.63	0.19
KN162-7 28-16	52.896	10.674	3635	50.41	16.25	9.60	6.47	10.08	3.51	0.50	2.22	0.36	0.17			58.57	0.62	0.19
KN162-7 28-17	52.896	10.674	3635	50.21	16.17	9.48	6.46	9.98	3.75	0.50	2.18	0.36	0.20			58.84	0.62	0.19
KN162-9 28-24	52.896	10.674	3635	50.01	16.47	7.92	7.40	11.90	3.02	0.49	1.45	0.26	0.15			66.21	0.72	0.29
KN162-9 28-26	52.896	10.674	3635	50.21	16.99	8.01	6.62	10.42	3.43	0.86	1.79	0.43	0.18			63.42	0.61	0.41
KN162-9 28-32	52.896	10.674	3635	50.29	16.09	9.21	6.38	10.02	3.75	0.48	2.19	0.35	0.17			59.23	0.62	0.19
KN162-9 28-35	52.896	10.674	3635	50.27	16.92	7.82	6.53	10.49	3.47	0.87	1.79	0.42	0.13			63.66	0.62	0.41
KN162-9 28-40	52.896	10.674	3635	49.61	17.52	7.88	7.47	10.96	3.41	0.46	1.51	0.28	0.15			66.54	0.63	0.26
KN162-9 28-52	52.896	10.674	3635	49.61	17.55	7.70	7.55	10.90	3.38	0.45	1.52	0.29	0.15			67.28	0.62	0.25
KN162-9 28-58	52.896	10.674	3635	50.27	16.64	7.66	7.36	11.74	3.05	0.52	1.42	0.27	0.15			66.84	0.71	0.31
KN162-9 28-60	52.896	10.674	3635	49.99	17.56	7.90	7.47	10.96	3.40	0.46	1.55	0.28	0.15			66.48	0.62	0.25
KN162-9 28-63	52.896	10.674	3635	50.26	17.03	7.78	6.60	10.45	3.39	0.87	1.84	0.42	0.14			64.02	0.61	0.40
KN162-9 28-65	52.896	10.674	3635	49.88	17.49	7.79	7.49	10.99	3.36	0.46	1.50	0.28	0.13			66.85	0.63	0.26
KN162-9 28-66	52.896	10.674	3635	50.26	17.04	7.88	6.59	10.57	3.41	0.88	1.79	0.40	0.09			63.69	0.62	0.42
KN162-9 28-67	52.896	10.674	3635	49.72	17.40	7.87	7.58	10.78	3.39	0.48	1.60	0.29	0.14			66.89	0.62	0.25
VAN7-92-01	52.855	10.888	3700	50.48	15.07	10.46	5.70	10.52	3.71	0.54	2.16	0.37	0.20			53.34	0.70	0.21
VAN7-92-03	52.855	10.888	3700	50.12	15.28	10.08	5.87	11.00	3.58	0.61	2.02	0.21	0.19	0.64	192	54.98	0.72	0.26
KN162-9 30-06	52.994	11.157	3536	49.09	17.59	9.32	8.27	11.43	2.63	0.25	1.10	0.12	0.16			65.05	0.65	0.19
KN162-9 30-11	52.994	11.157	3536	50.27	16.32	8.83	7.44	11.68	2.75	0.42	1.50	0.21	0.16			63.86	0.72	0.24
KN162-9 30-12	52.994	11.157	3536	50.35	16.32	8.86	7.43	11.60	2.80	0.42	1.51	0.22	0.15	0.35	173	63.75	0.71	0.24
KN162-9 30-16	52.994	11.157	3536	49.05	17.49	9.38	8.17	11.30	2.59	0.25	1.09	0.14	0.18			64.63	0.65	0.19
KN162-9 30-18	52.994	11.157	3536	50.21	16.28	8.72	7.41	11.67	2.79	0.42	1.53	0.22	0.18			64.06	0.72	0.23
KN162-9 30-21	52.994	11.157	3536	50.34	16.30	8.85	7.47	11.58	2.77	0.42	1.49	0.20	0.17			63.90	0.71	0.24
KN162-9 30-23	52.994	11.157	3536	50.33	16.20	8.81	7.40	11.63	2.77	0.42	1.49	0.19	0.17			63.79	0.72	0.24
KN162-9 30-25	52.994	11.157	3536	49.05	17.70	9.37	8.31	11.35	2.58	0.26	1.05	0.14	0.17			65.04	0.64	0.21
KN162-9 30-34	52.994	11.157	3536	48.98	17.61	9.21	8.46	11.15	2.63	0.29	1.11	0.14	0.17			65.83	0.63	0.22
KN162-9 36-01	52.749	11.711	3981	50.90	16.77	8.24	7.31	10.59	3.85	0.16	1.56	0.18	0.18			65.04	0.63	0.09
KN162-9 36-05	52.749	11.711	3981	50.91	16.78	8.25	7.35	10.54	3.87	0.16	1.54	0.19	0.18			65.14	0.63	0.09
KN162-9 36-07	52.749	11.711	3981	50.92	16.69	8.52	7.17	10.49	3.89	0.20	1.68	0.21	0.17			63.84	0.63	0.10
KN162-9 36-11	52.749	11.711	3981	50.59	16.55	8.60	7.22	10.37	3.94	0.21	1.73	0.22	0.17			63.78	0.63	0.10
KN162-9 36-17	52.749	11.711	3981	50.93	16.61	8.33	7.08	10.55	3.91	0.16	1.64	0.20	0.19			64.06	0.64	0.08
KN162-9 36-18	52.749	11.711	3981	50.83	16.77	8.27	7.25	10.58	3.93	0.16	1.59	0.19	0.17			64.77	0.63	0.09
KN162-9 36-27	52.749	11.711	3981	50.78	16.48	8.57	7.19	10.37	3.91	0.21	1.76	0.21	0.18	0.34	165	63.76	0.63	0.10
KN162-9 36-28	52.749	11.711	3981	50.52	16.73	8.69	7.02	10.48	3.92	0.20	1.76	0.21	0.17			62.89	0.63	0.10
KN162-9 36-44	52.749	11.711	3981	50.86	16.68	8.48	7.18	10.58	3.87	0.22	1.65	0.21	0.17			63.98	0.63	0.11
KN162-9 38-02	52.777	11.854	3964	50.89	15.94	9.48	6.46	10.23	3.47	0.60	1.85	0.27	0.21			58.84	0.64	0.28
KN162-9 38-03	52.777	11.854	3964	50.66	15.89	9.57	6.52	10.17	3.45	0.60	1.84	0.28	0.21			58.83	0.64	0.28
KN162-9 38-04	52.777	11.854	3964	50.88	15.88	9.45	6.52	10.18	3.34	0.60	1.84	0.28	0.19			59.14	0.64	0.28
KN162-9 38-07	52.777	11.854	3964	50.65	16.03	9.36	6.55	10.12	3.35	0.58	1.79	0.30	0.17			59.48	0.63	0.27
KN162-9 38-15	52.777	11.854	3964	50.84	16.05	9.46	6.56	10.21	3.41	0.58	1.86	0.30	0.19			59.26	0.64	0.26
KN162-9 38-16	52.777	11.854	3964	50.81	16.07	9.38	6.56	10.16	3.44	0.57	1.80	0.30	0.17			59.46	0.63	0.27
KN162-9 38-17	52.777	11.854	3964	50.82	16.05	9.46	6.58	10.21	3.37	0.57	1.81	0.30	0.18			59.33	0.64	0.27
KN162-9 38-21	52.777	11.854	3964	50.93	16.04	9.61	6.57	10.12	3.40	0.57	1.81	0.29	0.19			58.92	0.63	0.27
KN162-9 41-05	52.589	12.132	4333	49.89	17.62	7.92	8.27	11.67	3.00	0.21	1.08	0.11	0.14			68.65	0.66	0.16
KN162-9 41-07	52.589	12.132	4333	50.69	15.42	9.65	6.08	10.65	3.70	0.54	2.19	0.34	0.18	0.61	230	56.93	0.69	0.21
KN162-9 41-12	52.589	12.132	4333	50.48	15.94	9.36	6.73	11.32	3.45	0.31	1.77	0.22	0.16			60.13	0.71	0.15
KN162-9 41-13	52.589	12.132	4333	50.69	15.90	8.57	6.95	11.44	3.26	0.46	1.75	0.28	0.16			62.98	0.72	0.22
KN162-9 48-04	52.560	12.799	3897	49.58	17.57	8.20	8.40	11.84	3.15	0.08	1.10	0.10	0.16	0.18	246	68.24	0.67	0.06
KN162-9 48-08	52.560	12.799	3897	49.25	16.98	9.71	7.64	10.57	3.56	0.13	1.70	0.19	0.19			62.27	0.62	0.06
KN162-9 48-18A	52.560	12.799	3897	49.69	17.55	8.33	8.43	11.83	3.12	0.07	1.10	0.09	0.15			67.98	0.67	0.05
KN162-9 48-18B	52.560	12.799	3897	49.78	17.66	8.34	8.46	11.79	3.14	0.08	1.07	0.10	0.14			68.03	0.67	0.06
KN162-9 48-21	52.560	12.799	3897	48.83	18.68	7.75	9.82	11.96	2.48	0.04	0.58	0.04	0.15			72.06	0.64	0.06
KN162-9 48-23	52.560	12.799	3897	49.20	16.86	9.78	7.63	10.62	3.62	0.12	1.69	0.19	0.18			62.67	0.63	0.06
KN162-9 49-01	52.479	12.861	4199	50.52	17.28	8.08	7.24	10.71	4.23	0.08	1.38	0.14	0.15			65.27	0.62	0.05
KN162-9 49-05	52.479	12.861	4199	50.50	17.12	8.25	7.18	10.66	4.26	0.09	1.35	0.14	0.17			64.61	0.62	0.06
KN162-9 49-11	52.479	12.861	4199	50.31	17.24	7.34	7.76	10.96	3.35	0.54	1.44	0.24	0.13			69.32	0.64	0.32
KN162-9 49-13	52.296	12.861	4199	50.34	17.20	7.18	7.76	10.92	3.40	0.53	1.47	0.23	0.14	0.49	192	68.99	0.63	0.31
KN162-9 49-16	52.475	12.861	4199	50.28	17.09	8.15	7.11	10.71	4.19	0.08	1.40	0.15	0.17			64.66	0.63	0.05
KN162-9 49-17	52.370	12.861	4199	50.44	17.22	8.16	7.23	10.6										

73



Sample no. *	Latitude	Longitude	Depth	SiO <sub>2</sub>	Al <sub>2</sub> O <sub>3</sub>	FeO*	MgO	CaO	Na <sub>2</sub> O	K <sub>2</sub> O	TiO <sub>2</sub>	P <sub>2</sub> O <sub>5</sub>	MnO	H <sub>2</sub> O	CO <sub>2</sub> *	Mg#*	CaO/ Al <sub>2</sub> O <sub>3</sub>	K/Ti
PS4-02-17	52.220	14.630	3200	51.22	15.80	7.73	6.39	11.36	3.30	1.19	1.79	0.39	0.13			63.42	0.72	0.56
PS4-02-18	52.220	14.630	3200	51.18	15.81	7.89	6.46	11.30	3.34	1.14	1.70	0.40	0.11			63.20	0.71	0.57
PS4-02-19	52.220	14.630	3200	51.29	15.61	8.33	6.25	10.87	3.48	1.22	1.92	0.43	0.00			61.15	0.70	0.54
PS4-02-20	52.220	14.630	3200	51.50	15.99	7.84	6.45	11.26	3.34	1.21	1.73	0.37	0.11			63.31	0.70	0.59
PS4-02-21	52.220	14.630	3200	51.36	15.88	7.79	6.45	11.01	3.41	1.29	1.82	0.35	0.17			63.46	0.69	0.60
PS4-02-24	52.220	14.630	3200	52.09	16.06	8.02	6.20	10.75	3.50	1.22	1.80	0.44	0.15			61.85	0.67	0.57
PS4-02-25	52.220	14.630	3200	51.15	15.71	7.68	6.41	11.40	3.38	1.21	1.80	0.43	0.16			63.64	0.73	0.57
PS4-02-27	52.220	14.630	3200	51.37	16.14	7.97	6.36	11.23	3.42	1.13	1.78	0.45	0.15			62.60	0.70	0.54
PS4-02-28	52.220	14.630	3200	51.48	16.10	7.83	6.59	11.23	3.41	1.17	1.76	0.41	0.00			63.84	0.70	0.56
PS4-02-29	52.220	14.630	3200	51.80	16.19	8.30	6.50	11.15	3.42	1.20	1.78	0.43	0.00			62.16	0.69	0.57
PS4-02-30	52.220	14.630	3200	50.96	15.63	7.91	6.55	11.23	3.52	1.12	1.72	0.38	0.16			63.46	0.72	0.55
PS4-02-31	52.220	14.630	3200	51.11	15.91	7.66	6.82	11.97	3.04	1.03	1.55	0.34	0.00			65.13	0.75	0.56
PS4-02-32	52.220	14.630	3200	51.72	15.84	7.75	6.10	10.72	3.47	1.18	1.77	0.49	0.00			62.28	0.68	0.57
PS4-02-33	52.220	14.630	3200	51.80	15.62	7.84	6.14	10.75	3.49	1.23	1.78	0.31	0.17			62.16	0.69	0.59
PS4-02-34	52.220	14.630	3200	51.72	15.81	8.09	6.14	10.67	3.59	1.28	1.77	0.36	0.16			61.42	0.67	0.61
VAN7-88-01	52.217	14.707	2984	50.57	16.41	7.60	6.34	11.31	3.21	1.05	1.78	0.30	0.16			63.63	0.69	0.50
VAN7-88-03	52.217	14.707	2984	50.38	16.33	7.68	6.40	11.25	3.32	1.07	1.77	0.25	0.15	0.63	141	63.61	0.69	0.51
VAN7-88-09	52.217	14.707	2984	50.57	16.38	7.73	6.34	11.20	3.11	1.05	1.80	0.38	0.14			63.24	0.68	0.49
VAN7-88-12	52.217	14.707	2984	50.61	16.32	7.79	6.42	11.31	3.36	1.06	1.75	0.36	0.12			63.35	0.69	0.51
VAN7-87-01	52.235	14.789	3546	50.44	16.54	7.21	6.56	11.63	2.97	1.16	1.69	0.24	0.15	0.75	165	65.62	0.70	0.58
VAN7-87-02	52.235	14.789	3546	50.21	16.46	7.27	6.58	11.74	2.96	1.15	1.64	0.29	0.17			65.50	0.71	0.59
VAN7-87-03	52.235	14.789	3546	50.28	16.46	7.30	6.46	11.77	2.99	1.18	1.65	0.26	0.13			64.99	0.72	0.61
VAN7-87-04	52.235	14.789	3546	50.45	16.55	7.37	6.54	11.77	3.00	1.16	1.63	0.26	0.15			65.05	0.71	0.60
Orthogonal supersegment (15°45'-25° E)																		
KN162-9 64-01	52.293	15.644	2950	50.32	15.79	10.18	7.23	10.68	3.10	1.14	1.99	0.18	0.17			65.89	0.68	0.06
KN162-9 64-05	52.293	15.644	2950	50.02	15.95	9.94	7.20	10.80	3.16	1.13	1.93	0.18	0.18			59.83	0.68	0.06
VAN7-83-01	52.173	15.837	3976	50.31	15.19	10.52	6.51	10.74	3.26	0.24	2.08	0.28	0.21	0.39	176	66.48	0.71	0.10
VAN7-83-02	52.173	15.837	3976	50.38	15.26	10.44	6.60	10.72	3.25	0.24	2.13	0.12	0.23			57.01	0.70	0.10
VAN7-80-01	52.232	16.007	4038	51.13	16.19	8.56	6.84	10.62	3.01	0.53	1.72	0.25	0.16			62.63	0.66	0.26
VAN7-80-02	52.232	16.007	4038	50.72	15.80	9.37	7.27	10.84	3.05	0.34	1.91	0.29	0.19			61.94	0.69	0.15
VAN7-80-03	52.232	16.007	4038	50.66	15.72	9.22	7.01	10.82	3.06	0.35	1.95	0.20	0.20			61.46	0.69	0.15
VAN7-80-04	52.232	16.007	4038	50.67	15.72	9.31	6.99	10.78	3.01	0.33	1.93	0.16	0.21	0.40	170	61.16	0.69	0.14
VAN7-79-03	52.296	16.125	4110	50.45	15.88	8.97	7.35	10.97	3.02	0.36	1.82	0.19	0.21			63.22	0.69	0.17
VAN7-79-08	52.296	16.125	4110	50.50	15.81	9.17	7.46	10.99	2.87	0.36	1.81	0.21	0.19			63.05	0.70	0.17
VAN7-79-11	52.296	16.125	4110	50.33	15.76	9.24	7.31	11.13	3.08	0.36	1.76	0.21	0.18			62.40	0.71	0.17
VAN7-79-13	52.296	16.125	4110	50.73	15.84	8.90	7.17	10.95	3.07	0.35	1.75	0.21	0.17			62.82	0.69	0.17
VAN7-79-25	52.296	16.125	4110	50.60	15.79	9.09	7.31	10.96	3.10	0.36	1.77	0.35	0.18			62.78	0.69	0.17
VAN7-79-34	52.296	16.125	4110	50.66	15.99	9.26	7.23	11.11	2.96	0.35	1.82	0.22	0.21			62.09	0.69	0.16
VAN7-79-38	52.296	16.125	4110	51.31	14.92	10.01	6.00	10.13	3.25	0.49	2.25	0.29	0.21			55.70	0.68	0.18
KN162-7 02-01	52.330	16.233	4000	50.42	14.82	11.11	7.12	10.28	3.30	0.22	2.12	0.20	0.25	0.36	192	57.34	0.69	0.09
KN162-7 03-01	52.299	16.507	3666	50.95	15.98	9.13	7.30	10.99	3.09	0.30	1.64	0.19	0.23			62.65	0.69	0.16
KN162-7 03-02	52.299	16.507	3666	50.60	16.04	9.01	7.22	11.12	3.07	0.29	1.66	0.19	0.23			62.70	0.69	0.15
VAN7-78-01	52.380	16.635	3901	49.35	16.07	10.77	6.99	10.59	3.11	0.16	1.76	0.24	0.22			57.65	0.66	0.08
AG22-01-01	52.300	16.980	4000	50.28	16.21	9.21	8.01	11.53	2.89	0.10	1.55	0.16	0.14	0.18	256	64.59	0.71	0.05
AG22-01-04	52.300	16.980	4000	50.19	16.14	9.39	8.06	11.64	2.87	0.10	1.54	0.16	0.14			64.29	0.72	0.06
AG22-01-05	52.300	16.980	4000	50.13	16.25	9.13	7.96	11.63	2.88	0.10	1.53	0.19	0.14			64.65	0.72	0.06
AG22-01-06	52.300	16.980	4000	50.29	15.93	9.37	7.64	11.52	2.91	0.11	1.63	0.19	0.15			63.10	0.72	0.06
AG22-01-08	52.300	16.980	4000	50.28	15.92	9.39	7.72	11.69	2.95	0.12	1.64	0.17	0.15			63.30	0.73	0.06
AG22-01-13	52.300	16.980	4000	50.20	15.86	9.24	7.67	11.62	2.95	0.11	1.63	0.17	0.14			63.52	0.73	0.06
AG22-01-16	52.300	16.980	4000	50.17	16.21	9.04	7.90	11.55	2.90	0.11	1.53	0.17	0.12			64.70	0.71	0.06
AG22-01-17	52.300	16.980	4000	49.94	16.27	9.01	7.91	11.46	2.88	0.10	1.54	0.12	0.14			64.81	0.70	0.06
AG22-01-30	52.300	16.980	4000	50.21	15.97	9.40	7.66	11.50	2.92	0.11	1.64	0.18	0.15			63.09	0.72	0.06
AG22-01-31	52.300	16.980	4000	49.99	15.97	9.30	7.68	11.55	2.90	0.11	1.64	0.19	0.16			63.40	0.72	0.06
KN162-7 04-03	52.358	17.113	3650	50.46	15.75	10.05	7.15	10.90	3.16	0.24	1.87	0.21	0.22			59.88	0.69	0.11
KN162-7 04-06	52.358	17.113	3650	50.34	15.62	10.06	7.33	10.84	3.18	0.24	1.88	0.20	0.24			60.45	0.69	0.11
KN162-7 04-07	52.358	17.113	3650	50.16	15.51	9.94	7.38	10.83	3.14	0.24	1.82	0.22	0.20			60.90	0.70	0.11
KN162-7 04-13	52.358	17.113	3650	50.28	15.66	9.71	7.41	10.86	3.16	0.23	1.81	0.21	0.20	0.35	201	61.55	0.69	0.11
KN162-7 04-15	52.358	17.113	3650	50.24	15.74	10.09	7.28	10.89	3.19	0.24	1.82	0.21	0.22			60.21	0.69	0.11
KN162-7 04-16	52.358	17.113	3650	50.35	15.62	10.02	7.35	10.78	3.15	0.24	1.82	0.20	0.16			60.61	0.69	0.11
KN162-7 04-22	52.358	17.113	3650	50.37	15.46	9.98	7.13	10.70	3.20	0.26	1.91	0.20	0.17			59.98	0.69	0.12
KN162-7 04-31	52.358	17.113	3650	50.45	15.75	9.85	7.38	10.88	3.18	0.26	1.85	0.20	0.22			61.11	0.69	0.12
KN162-7 04-33	52.358	17.113	3650	50.75	15.79	10.20	7.42	10.92	3.09	0.27	1.88	0.22	0.17			60.41	0.69	0.12
KN162-7 04-46	52.358	17.113	3650	50.29	15.77	9.96	7.48	10.82	3.11	0.26	1.77	0.18	0.20			61.17	0.69	0.12
KN162-7 04-52	52.358	17.113	3650	50.48	15.70	9.95	7.23	10.87	3.12	0.28	1.83	0.21	0.23			60.38	0.69	0.13
KN162-7 05-01	52.423	17.428	3030	50.96	14.80	11.06	6.12	10.42	3.38	0.41	2.20	0.26	0.23	0.46	178	53.72	0.70	0.16
KN162-7 05-05	52.423	17.428	3030	50.34	15.37	10.24	7.00	10.86	3.28	0.21	1.88	0.20	0.18			58.91	0.71	0.09
KN162-7 05-06	52.423	17.428	3030	50.48	15.44	10.39	6.91	10.87	3.30	0.21	1.91	0.20	0.21			58.25	0.70	0.09
KN162-7 06-01	52.520	17.702	3															

Sample no. *	Latitude	Longitude	Depth	SiO <sub>2</sub>	Al <sub>2</sub> O <sub>3</sub>	FeO*	MgO	CaO	Na <sub>2</sub> O	K <sub>2</sub> O	TiO <sub>2</sub>	P <sub>2</sub> O <sub>5</sub>	MnO	H <sub>2</sub> O	CO <sub>2</sub> *	Mg#*	CaO/ Al <sub>2</sub> O <sub>3</sub>	K/Ti
AG22-05-06	54.760	19.097	3700	49.73	16.76	9.06	7.92	11.03	3.11	0.13	1.48	0.15	0.15			64.71	0.66	0.07
AG22-05-07	54.760	19.097	3700	50.44	16.20	8.98	7.63	11.07	3.10	0.17	1.66	0.15	0.16			64.06	0.68	0.09
AG22-05-08	54.760	19.097	3700	49.73	16.80	9.04	7.85	11.09	3.17	0.13	1.49	0.17	0.13			64.56	0.66	0.07
AG22-05-10	54.760	19.097	3700	49.96	16.26	9.73	7.78	10.74	3.11	0.16	1.60	0.16	0.16			62.65	0.66	0.08
AG22-05-11	54.760	19.097	3700	50.32	16.12	8.97	7.63	11.15	3.08	0.16	1.63	0.15	0.16			64.08	0.69	0.08
AG22-05-14	54.760	19.097	3700	50.22	15.80	9.96	6.75	10.67	3.47	0.32	2.09	0.20	0.22			58.70	0.68	0.13
AG22-05-18	54.760	19.097	3700	50.46	16.17	9.08	7.69	11.12	3.11	0.16	1.67	0.18	0.17			63.98	0.69	0.08
AG22-05-19	54.760	19.097	3700	50.42	15.99	9.14	7.72	11.04	3.10	0.16	1.67	0.18	0.16			63.92	0.69	0.08
AG22-05-22	54.760	19.097	3700	50.14	16.07	8.99	7.64	11.03	3.09	0.16	1.66	0.13	0.16			64.06	0.69	0.08
AG22-05-27	54.760	19.097	3700	50.46	15.99	8.97	7.59	10.98	3.16	0.16	1.63	0.17	0.17			63.96	0.69	0.08
AG22-05-31	54.760	19.097	3700	50.17	15.95	9.51	7.63	10.78	3.24	0.16	1.76	0.18	0.18			62.73	0.68	0.08
AG22-05-35	54.760	19.097	3700	50.37	16.06	9.06	7.64	11.18	3.12	0.17	1.67	0.17	0.17			63.88	0.70	0.09
AG22-05-38	54.760	19.097	3700	50.06	15.90	9.20	7.82	10.82	3.19	0.27	1.74	0.14	0.20			64.07	0.68	0.13
AG22-05-75	54.760	19.097	3700	50.22	16.36	9.52	7.35	11.00	3.21	0.14	1.68	0.17	0.17			61.82	0.67	0.07
KN162-7 11-02	52.799	19.200	3913	49.69	15.77	10.23	8.24	10.50	3.17	0.13	1.70	0.14	0.19			62.82	0.67	0.06
KN162-7 11-08	52.799	19.200	3913	49.56	15.68	10.19	8.26	10.56	3.20	0.14	1.64	0.16	0.17			62.97	0.67	0.07
KN162-7 11-11	52.799	19.200	3913	50.58	15.73	9.60	7.49	10.95	3.26	0.13	1.74	0.16	0.20			62.07	0.70	0.06
KN162-7 11-13	52.799	19.200	3913	50.33	15.72	9.67	7.53	10.86	3.26	0.13	1.75	0.17	0.20			62.03	0.69	0.06
KN162-7 11-21	52.799	19.200	3913	50.44	15.77	9.40	7.51	10.99	3.21	0.13	1.77	0.17	0.17			62.63	0.70	0.06
KN162-7 11-23	52.799	19.200	3913	50.22	15.78	9.56	7.49	10.93	3.20	0.14	1.72	0.17	0.14			62.17	0.69	0.07
KN162-7 11-25	52.799	19.200	3913	49.53	15.62	10.18	8.23	10.50	3.15	0.14	1.65	0.14	0.14			62.90	0.67	0.07
KN162-7 11-28	52.799	19.200	3913	50.22	15.72	9.49	7.48	10.96	3.22	0.13	1.74	0.17	0.18			62.31	0.70	0.06
KN162-7 11-30	52.799	19.200	3913	50.21	15.71	9.48	7.43	10.94	3.25	0.13	1.76	0.16	0.17			62.18	0.70	0.06
KN162-7 11-34	52.799	19.200	3913	49.68	15.83	10.24	8.19	10.58	3.16	0.13	1.66	0.14	0.18			62.65	0.67	0.07
KN162-7 11-35	52.799	19.200	3913	50.13	15.71	10.03	7.72	10.71	3.18	0.15	1.65	0.17	0.18			61.75	0.68	0.08
KN162-7 10-01	52.745	19.269	3097	50.29	15.96	9.37	7.34	10.80	3.17	0.23	1.77	0.20	0.23			62.17	0.68	0.11
KN162-7 10-02	52.745	19.269	3097	50.17	16.03	9.42	7.27	10.90	3.24	0.24	1.79	0.21	0.17			61.81	0.68	0.11
KN162-7 10-07	52.745	19.269	3097	50.26	15.86	9.54	7.04	10.86	3.31	0.25	1.89	0.19	0.17			60.75	0.68	0.11
KN162-7 10-10	52.745	19.269	3097	50.36	15.50	9.86	6.88	10.66	3.20	0.24	2.00	0.23	0.18			59.41	0.69	0.10
KN162-7 10-16	52.745	19.269	3097	50.11	15.76	9.32	7.34	10.82	3.17	0.23	1.80	0.20	0.17			62.29	0.69	0.11
KN162-7 10-21	52.745	19.269	3097	50.05	15.97	9.32	7.44	10.83	3.17	0.23	1.80	0.20	0.20	0.33	189	62.61	0.68	0.11
KN162-7 10-23	52.745	19.269	3097	50.25	15.53	9.97	6.93	10.90	3.26	0.20	1.90	0.20	0.21			59.32	0.70	0.09
VAN7-75-28	52.995	19.775	1731	50.91	15.89	8.97	7.66	11.33	3.24	0.13	1.53	0.14	0.18			64.17	0.71	0.07
VAN7-75-29	52.995	19.775	1731	50.75	16.03	9.02	7.65	11.35	3.31	0.13	1.44	0.15	0.16			64.01	0.71	0.08
VAN7-75-32	52.995	19.775	1731	50.72	15.29	10.25	6.51	10.27	3.63	0.19	2.07	0.23	0.19			57.12	0.67	0.08
VAN7-75-33	52.995	19.775	1731	49.68	17.78	8.06	8.76	11.33	2.88	0.09	1.20	0.11	0.19			69.51	0.64	0.06
VAN7-74-01	52.904	19.783	4130	50.73	15.03	10.21	6.87	11.11	3.22	0.10	1.88	0.14	0.18			58.53	0.74	0.05
VAN7-74-02	52.904	19.783	4130	50.54	15.07	10.20	6.88	11.12	3.25	0.11	1.92	0.16	0.20			58.59	0.74	0.05
VAN7-74-08	52.904	19.783	4130	50.04	15.29	10.68	7.03	10.26	3.53	0.13	2.12	0.21	0.19			57.99	0.67	0.05
KN162-7 13-01	52.856	19.913	4067	50.74	15.53	9.60	7.20	10.98	3.24	0.18	1.77	0.17	0.20			61.14	0.71	0.09
KN162-7 13-02	52.856	19.913	4067	50.46	15.38	9.66	7.38	10.91	3.26	0.18	1.78	0.18	0.19			61.57	0.71	0.09
KN162-7 13-29	52.856	19.913	4067	50.53	15.42	9.71	7.37	10.87	3.27	0.18	1.79	0.17	0.19	0.29	213	61.42	0.70	0.09
KN162-7 13-31	52.856	19.913	4067	50.45	15.37	9.49	7.09	10.90	3.27	0.19	1.78	0.17	0.20			61.04	0.71	0.09
KN162-7 13-39	52.856	19.913	4067	50.56	15.43	9.51	7.34	10.89	3.27	0.18	1.76	0.17	0.17			61.82	0.71	0.09
KN162-7 13-41	52.856	19.913	4067	50.55	15.36	9.56	7.34	10.84	3.28	0.18	1.78	0.17	0.23			61.69	0.71	0.09
KN162-7 13-42	52.856	19.913	4067	50.53	15.33	9.44	7.00	11.14	3.25	0.17	1.78	0.17	0.20			60.87	0.73	0.08
KN162-7 13-43	52.856	19.913	4067	50.71	15.30	9.59	6.91	11.10	3.26	0.18	1.81	0.18	0.23			60.18	0.73	0.08
KN162-7 15-05	52.923	20.382	3403	50.29	16.15	8.90	7.59	11.19	3.11	0.20	1.51	0.18	0.19	0.30	170	64.14	0.69	0.11
KN162-7 14-01	52.873	20.398	3403	50.04	16.08	9.35	7.45	10.98	3.16	0.14	1.69	0.15	0.19			62.56	0.68	0.07
KN162-7 14-02	52.873	20.398	3403	49.94	15.95	9.34	7.50	10.95	3.13	0.14	1.67	0.16	0.24			62.75	0.69	0.07
KN162-7 14-03	52.873	20.398	3403	49.91	16.00	9.27	7.47	11.01	3.13	0.14	1.68	0.16	0.24			62.83	0.69	0.07
KN162-7 14-04	52.873	20.398	3403	50.03	15.98	9.30	7.53	10.94	3.11	0.14	1.63	0.15	0.24			62.94	0.68	0.07
KN162-7 14-06	52.873	20.398	3403	49.98	16.05	9.40	7.51	11.03	3.16	0.14	1.69	0.15	0.25			62.63	0.69	0.07
KN162-7 14-07	52.873	20.398	3403	49.91	15.80	9.33	7.46	11.00	3.12	0.14	1.70	0.17	0.21			62.65	0.70	0.07
KN162-7 14-08	52.873	20.398	3403	50.06	15.93	9.46	7.46	10.99	3.09	0.14	1.66	0.17	0.23			62.32	0.69	0.07
KN162-7 14-09	52.873	20.398	3403	50.06	15.91	9.46	7.54	11.02	3.11	0.14	1.70	0.18	0.25			62.57	0.69	0.07
KN162-7 14-10	52.873	20.398	3403	50.09	15.89	9.38	7.45	11.04	3.06	0.14	1.70	0.16	0.25			62.49	0.69	0.07
KN162-7 16-01	52.922	20.661	4235	50.60	15.48	9.31	7.48	11.61	3.00	0.10	1.65	0.17	0.22			62.76	0.75	0.05
KN162-7 16-02	52.922	20.661	4235	50.60	15.52	9.37	7.52	11.62	2.95	0.10	1.60	0.15	0.23			62.73	0.75	0.05
KN162-7 16-04	52.922	20.661	4235	50.50	15.20	9.54	7.31	11.68	2.99	0.10	1.80	0.17	0.17			61.64	0.77	0.05
KN162-7 16-07	52.922	20.661	4235	50.34	15.41	9.14	7.59	11.58	3.02	0.10	1.67	0.15	0.21			63.53	0.75	0.05
VAN7-73-01	52.976	20.693	3797	50.42	16.30	9.24	7.64	11.16	3.17	0.13	1.59	0.15	0.18			63.43	0.68	0.07
VAN7-73-02	52.976	20.693	3797	50.18	16.08	9.20	7.94	10.65	3.30	0.19	1.75	0.19	0.19			64.42	0.66	0.09
VAN7-73-03	52.976	20.693	3797	50.86	15.63	9.97	7.64	10.61	3.08	0.14	1.79	0.19	0.20			61.65	0.68	0.07
VAN7-73-06	52.976	20.693	3797	50.49	15.52	9.82	7.57	10.62	3.39	0.13	1.79	0.16	0.16			61.79	0.68	0.06
KN162-7 17-01	52.949	20.925	3850	49.99	15.63	9.53	7.36	10.88	3.35	0.12	1.83	0.17	0.20			61.83	0.70	0.06
KN162-7 17-02	52.949	20.925	3850	50.22	15.83	9.58	7.48	10.90	3.39	0.11	1.72	0.17	0.22			62.09	0.69	0.05

Sample no. *	Latitude	Longitude	Depth	SiO <sub>2</sub>	Al <sub>2</sub> O <sub>3</sub>	FeO*	MgO	CaO	Na <sub>2</sub> O	K <sub>2</sub> O	TiO <sub>2</sub>	P <sub>2</sub> O <sub>5</sub>	MnO	H <sub>2</sub> O	CO <sub>2</sub> *	Mg# <sup>†</sup>	CaO/ Al <sub>2</sub> O <sub>3</sub>	K/Ti
KN162-7 18-17	52.990	21.406	4525	50.49	15.84	9.05	7.41	11.10	3.39	0.12	1.73	0.15	0.23	0.25	216	63.20	0.70	0.06
KN162-7 18-19	52.990	21.406	4525	50.41	16.01	8.85	7.47	11.09	3.36	0.12	1.72	0.16	0.19			63.90	0.69	0.06
KN162-7 18-21	52.990	21.406	4525	50.69	15.97	9.13	7.46	11.16	3.40	0.13	1.72	0.16	0.19			63.15	0.70	0.06
AG22-07-01	53.023	21.833	3300	50.98	16.11	8.96	7.62	11.18	3.10	0.11	1.61	0.15	0.15			64.08	0.69	0.06
AG22-07-02	53.023	21.833	3300	50.88	16.12	8.84	7.57	11.06	3.07	0.11	1.65	0.16	0.15			64.24	0.69	0.06
VAN7-70-01	53.043	21.978	3869	50.96	14.96	9.58	6.87	11.45	3.23	0.14	1.84	0.16	0.19			60.07	0.77	0.06
VAN7-70-48	53.043	21.978	3869	50.47	16.14	9.09	7.79	10.89	3.23	0.13	1.65	0.16	0.18			64.25	0.67	0.07
VAN7-70-51	53.043	21.978	3869	50.45	16.01	9.06	7.75	10.91	3.27	0.12	1.63	0.17	0.17			64.21	0.68	0.06
VAN7-70-65	53.043	21.978	3869	50.41	16.09	9.06	7.69	10.95	3.22	0.11	1.61	0.16	0.17			64.03	0.68	0.06
VAN7-70-79	53.043	21.978	3869	50.46	16.03	9.05	7.80	10.93	3.23	0.12	1.66	0.15	0.15			64.38	0.68	0.06
VAN7-70-87	53.043	21.978	3869	50.53	16.04	9.08	7.79	10.94	3.23	0.12	1.64	0.14	0.18	0.23	196	64.28	0.68	0.06
KN162-7 20-01	53.039	22.177	4170	50.54	16.53	8.24	7.98	11.09	3.14	0.13	1.45	0.14	0.18			67.01	0.67	0.08
KN162-7 20-02	53.039	22.177	4170	50.44	16.45	8.30	8.03	11.19	3.11	0.12	1.43	0.12	0.16			66.99	0.68	0.07
KN162-7 20-03	53.039	22.177	4170	50.60	16.62	8.28	8.03	11.20	3.16	0.13	1.45	0.14	0.12			67.04	0.67	0.08
KN162-7 20-04	53.039	22.177	4170	50.53	16.57	8.29	8.06	11.21	3.17	0.12	1.40	0.14	0.16			67.10	0.68	0.07
KN162-7 20-06	53.039	22.177	4170	50.50	16.65	8.41	8.07	11.22	3.11	0.12	1.44	0.14	0.16			66.81	0.67	0.07
KN162-7 20-09	53.039	22.177	4170	50.65	16.54	8.38	8.06	11.08	3.17	0.12	1.39	0.14	0.16			66.86	0.67	0.07
KN162-7 20-10	53.039	22.177	4170	50.54	16.56	8.40	8.03	11.12	3.14	0.12	1.39	0.14	0.18			66.72	0.67	0.07
VAN7-69-35	53.135	22.451	3864	50.17	15.64	9.77	7.48	10.58	3.27	0.14	1.88	0.19	0.19			61.63	0.68	0.06
VAN7-69-39	53.135	22.451	3864	50.58	15.78	9.67	7.40	10.71	3.31	0.14	1.89	0.18	0.18			61.61	0.68	0.06
VAN7-69-50	53.135	22.451	3864	50.35	16.48	8.74	7.88	11.13	3.09	0.11	1.46	0.11	0.18			65.41	0.68	0.06
VAN7-69-57	53.135	22.451	3864	50.37	16.52	8.86	7.88	11.03	3.11	0.11	1.43	0.13	0.16			65.10	0.67	0.07
VAN7-69-71	53.135	22.451	3864	50.30	16.60	8.80	7.87	11.06	3.12	0.10	1.47	0.14	0.17			65.23	0.67	0.06
VAN7-69-79	53.135	22.451	3864	50.49	15.82	9.60	7.42	10.73	3.36	0.13	1.86	0.16	0.17			61.85	0.68	0.06
KN162-7 21-01	53.035	22.468	3722	50.90	16.51	8.40	8.00	11.41	2.98	0.12	1.39	0.12	0.17			66.64	0.69	0.07
KN162-7 21-02	53.035	22.468	3722	50.84	16.45	8.13	8.04	11.43	3.00	0.11	1.36	0.12	0.18			67.47	0.69	0.07
KN162-7 21-05	53.035	22.468	3722	50.87	16.44	8.29	7.95	11.43	2.95	0.11	1.39	0.12	0.16			66.79	0.70	0.07
KN162-7 21-06	53.035	22.468	3722	50.88	16.60	8.34	8.06	11.49	3.02	0.11	1.37	0.13	0.17			66.96	0.69	0.07
KN162-7 21-08	53.035	22.468	3722	51.04	16.41	8.53	8.01	11.38	3.02	0.12	1.37	0.13	0.17			66.33	0.69	0.07
KN162-7 21-13	53.035	22.468	3722	51.00	16.54	8.30	8.09	11.30	2.95	0.11	1.39	0.12	0.17			67.15	0.68	0.07
KN162-7 21-21	53.035	22.468	3722	50.72	16.22	8.74	7.72	11.38	3.11	0.17	1.50	0.14	0.17			64.95	0.70	0.10
KN162-7 21-23	53.035	22.468	3722	50.72	16.36	8.35	7.90	11.36	2.98	0.11	1.43	0.13	0.17			66.49	0.69	0.07
KN162-7 21-25	53.035	22.468	3722	50.79	16.66	8.25	8.07	11.40	2.97	0.11	1.37	0.12	0.18			67.23	0.68	0.07
KN162-7 21-30	53.035	22.468	3722	50.79	16.36	8.63	7.70	11.32	3.04	0.17	1.51	0.15	0.17			65.17	0.69	0.10
KN162-7 23-107	53.173	22.547	3609	50.34	15.43	9.79	7.37	10.11	3.42	0.18	2.02	0.24	0.17			61.23	0.66	0.08
KN162-7 23-31	53.173	22.547	3609	50.33	16.44	8.81	7.61	10.93	3.15	0.10	1.57	0.15	0.15			64.44	0.66	0.05
KN162-7 23-32	53.173	22.547	3609	50.26	16.52	8.99	7.67	10.98	3.14	0.10	1.58	0.16	0.13			64.15	0.66	0.05
KN162-7 23-36	53.173	22.547	3609	50.36	16.52	8.91	7.68	10.94	3.25	0.10	1.57	0.15	0.16			64.39	0.66	0.05
KN162-7 23-38	53.173	22.547	3609	50.41	16.48	8.88	7.71	10.98	3.22	0.10	1.59	0.16	0.16			64.55	0.67	0.05
KN162-7 23-42	53.173	22.547	3609	50.38	16.62	8.97	7.72	10.98	3.29	0.11	1.56	0.15	0.17			64.35	0.66	0.06
KN162-7 23-44	53.173	22.547	3609	50.30	16.48	9.05	7.70	10.97	3.15	0.11	1.62	0.16	0.18			64.09	0.67	0.06
KN162-7 23-64	53.173	22.547	3609	50.42	15.42	10.29	7.53	10.12	3.42	0.17	2.07	0.22	0.14			60.55	0.66	0.07
KN162-7 22-02	53.109	22.647	3852	50.75	16.60	8.43	7.95	11.30	3.02	0.12	1.45	0.16	0.21			66.42	0.68	0.07
KN162-7 22-05	53.109	22.647	3852	50.93	16.59	8.41	8.02	11.22	3.13	0.13	1.41	0.15	0.21			66.67	0.68	0.08
KN162-7 22-13	53.109	22.647	3852	50.70	16.59	8.41	8.00	11.16	3.02	0.13	1.43	0.15	0.20			66.61	0.67	0.08
KN162-7 22-14	53.109	22.647	3852	50.89	16.72	8.49	7.97	11.23	3.09	0.13	1.43	0.15	0.17	0.23	189	66.32	0.67	0.08
KN162-7 22-16	53.109	22.647	3852	50.65	16.74	8.32	8.00	11.23	3.07	0.13	1.45	0.13	0.17			66.83	0.67	0.08
KN162-7 22-27	53.109	22.647	3852	50.92	16.60	8.46	7.96	11.35	3.10	0.12	1.44	0.15	0.18			66.37	0.68	0.07
KN162-7 22-34	53.109	22.647	3852	51.13	16.60	8.47	8.02	11.19	3.03	0.12	1.48	0.15	0.19			66.51	0.67	0.07
KN162-7 22-35	53.109	22.647	3852	50.62	16.26	8.47	7.73	11.38	3.11	0.14	1.50	0.16	0.13			65.69	0.70	0.08
KN162-7 22-38	53.109	22.647	3852	50.70	16.63	8.37	7.87	11.32	3.10	0.13	1.44	0.15	0.15			66.35	0.68	0.08
VAN7-68-01	53.227	22.791	3323	50.92	14.65	10.26	6.80	11.26	3.20	0.14	1.81	0.15	0.20			58.16	0.77	0.07
VAN7-68-02	53.227	22.791	3323	50.06	16.36	8.79	7.68	11.12	3.18	0.16	1.64	0.15	0.16			64.70	0.68	0.08
VAN7-68-21	53.227	22.791	3323	50.02	16.40	8.71	7.63	11.09	3.09	0.16	1.64	0.14	0.17			64.76	0.68	0.08
KN162-7 24-03	53.158	22.852	3202	50.82	16.49	8.52	8.07	11.42	3.01	0.10	1.43	0.14	0.18			66.52	0.69	0.06
KN162-7 24-04	53.158	22.852	3202	50.97	16.41	8.38	8.03	11.44	3.00	0.10	1.44	0.13	0.14			66.78	0.70	0.06
KN162-7 24-07	53.158	22.852	3202	50.71	16.44	8.55	8.06	11.37	3.04	0.09	1.44	0.13	0.16			66.41	0.69	0.05
KN162-7 24-08	53.158	22.852	3202	50.81	16.27	8.60	8.05	11.32	2.95	0.10	1.41	0.13	0.14			66.25	0.70	0.06
KN162-7 24-25	53.158	22.852	3202	51.05	15.72	9.11	7.42	11.61	3.09	0.10	1.59	0.14	0.18			63.08	0.74	0.05
KN162-7 24-30	53.158	22.852	3202	50.69	16.51	8.32	8.03	11.52	3.03	0.09	1.43	0.13	0.15			66.94	0.70	0.05
KN162-7 24-31	53.158	22.852	3202	50.82	16.45	8.57	8.07	11.48	3.07	0.10	1.41	0.13	0.17			66.39	0.70	0.06
KN162-7 24-33	53.158	22.852	3202	50.91	16.10	8.77	7.64	11.52	3.10	0.10	1.52	0.14	0.16			64.63	0.72	0.06
KN162-7 24-34	53.158	22.852	3202	51.06	15.86	8.70	7.48	11.47	3.09	0.10	1.57	0.14	0.20			64.33	0.72	0.05
KN162-7 24-37	53.158	22.852	3202	50.87	16.24	8.63	7.69	11.44	3.08	0.10	1.43	0.13	0.15			65.15	0.70	0.06
KN162-7 24-47	53.158	22.852	3202	50.83	16.48	8.47	7.98	11.43	2.99	0.09	1.42	0.13	0.18			66.40	0.69	0.05
AG22-09-01	53.130	22.880	3800	50.73	16.45	8.28	7.97	11.72	2.94	0.06	1.34	0.14	0.11	0.18	182	66.88	0.71	0.04
AG22-09-02	53.130	22.880	3800	50.78	16.21	8.28	7.93	11.72	2.90	0.06	1.33	0.15	0.11			66.76		

Sample no. *	Latitude	Longitude	Depth	SiO <sub>2</sub>	Al <sub>2</sub> O <sub>3</sub>	FeO*	MgO	CaO	Na <sub>2</sub> O	K <sub>2</sub> O	TiO <sub>2</sub>	P <sub>2</sub> O <sub>5</sub>	MnO	H <sub>2</sub> O	CO <sub>2</sub> *	Mg#*	CaO/ Al <sub>2</sub> O <sub>3</sub>	K/Ti
KN162-7 26-21	53.214	23.358	3329	50.48	16.99	7.93	8.44	11.91	2.88	0.07	1.16	0.10	0.16			69.06	0.70	0.05
KN162-7 26-23	53.214	23.358	3329	50.34	16.90	8.09	8.41	11.91	2.86	0.07	1.15	0.10	0.19	0.15	213	68.56	0.70	0.05
KN162-7 26-27	53.214	23.358	3329	50.70	16.83	8.20	8.36	11.76	2.86	0.07	1.14	0.08	0.20			68.14	0.70	0.05
KN162-7 26-29	53.214	23.358	3329	50.51	17.00	8.02	8.40	11.91	2.85	0.07	1.15	0.09	0.18			68.72	0.70	0.05
AG22 12-01	53.393	23.692	3650	50.71	16.54	8.69	7.73	11.54	3.41	0.13	1.57		0.17			65.11	0.70	0.07
AG22 12-04	53.393	23.692	3650	50.48	15.18	10.22	6.77	10.98	3.64	0.10	2.19		0.20			58.15	0.72	0.04
AG22 12-20	53.393	23.692	3650	50.23	16.86	9.05	7.91	11.24	3.26	0.13	1.63		0.17			64.71	0.67	0.07
AG22 12-26	53.393	23.692	3650	50.30	16.91	9.05	7.91	11.27	3.17	0.13	1.62		1.17			64.71	0.67	0.07
AG22 12-32	53.393	23.692	3650	50.14	16.68	9.09	7.88	11.18	3.18	0.08	1.60		0.18			64.52	0.67	0.04
AG22 12-33	53.393	23.692	3650	49.91	16.84	9.09	7.89	11.09	3.21	0.12	1.61		0.16			64.55	0.66	0.06
AG22 12-35	53.393	23.692	3650	50.24	16.19	9.56	7.73	11.01	3.45	0.16	1.96		0.17			62.91	0.68	0.07
AG22 13-01	53.408	24.758	3850	50.38	17.07	8.36	8.46	11.06	3.17	0.14	1.43		0.17	0.19	197	67.98	0.65	0.08
AG22 13-05	53.408	24.758	3850	50.18	17.07	8.35	8.40	11.33	3.17	0.09	1.49		0.17			67.85	0.66	0.05
AG22 13-06	53.408	24.758	3850	50.22	17.22	8.42	8.50	11.26	3.24	0.14	1.54		0.16			67.92	0.65	0.08
AG22 13-08	53.408	24.758	3850	50.91	16.33	9.16	7.76	11.68	3.23	0.10	1.39		0.18			63.99	0.72	0.06
AG22 13-09	53.408	24.758	3850	50.42	17.32	8.39	8.42	11.22	3.07	0.13	1.52		0.17			67.79	0.65	0.07
AG22 13-11	53.408	24.758	3850	50.51	16.21	9.05	7.55	11.88	3.44	0.10	1.30		0.20			63.63	0.73	0.07
AG22 13-14	53.408	24.758	3850	50.51	16.07	9.03	7.78	11.34	3.32	0.09	1.36		0.16			64.38	0.71	0.06
AG22 13-16	53.408	24.758	3850	49.98	16.86	8.25	8.52	10.95	3.09	0.12	1.43		0.17			68.42	0.65	0.07
AG22 13-19	53.408	24.758	3850	50.09	16.20	9.16	7.61	11.46	3.28	0.10	1.36		0.16			63.54	0.71	0.06
AG22 13-24	53.408	24.758	3850	49.99	17.13	8.48	8.64	10.97	3.22	0.10	1.41		0.17			68.12	0.64	0.06
AG22 13-25	53.408	24.758	3850	50.22	17.19	8.49	8.81	10.70	3.37	0.15	1.40		0.18			68.52	0.62	0.09
AG22 13-28	53.408	24.758	3850	50.03	16.99	8.30	8.57	10.76	3.08	0.12	1.36		0.14			68.41	0.63	0.07
AG22 13-30	53.408	24.758	3850	50.44	16.25	9.01	7.78	11.39	3.35	0.10	1.35		0.17			64.43	0.70	0.06
AG22 13-31	53.408	24.758	3850	50.39	17.28	8.17	8.65	10.81	3.17	0.11	1.41		0.17			68.95	0.63	0.07
AG22 13-32	53.408	24.758	3850	50.25	17.38	8.14	8.64	10.77	3.15	0.11	1.43		0.15			69.01	0.62	0.07

\* Sample names refer to the following cruises. KN162-7 & KN162-9 are from Knorr 162 - Legs 7 & 9; VAN7 is from the Vancouver 7 cruise aboard the RV Melville; PS4 samples are from F.S. Polanstern - Leg IV (unpublished data); AG22 samples are from the Agulhas 22 expedition (unpublished data).

\* CO<sub>2</sub> abundance reported in ppm.

\* Mg# = 100\*(Mg<sup>2+</sup>)/(Mg<sup>2+</sup> + Fe<sup>2+</sup>); Fe<sub>2</sub>O<sub>3</sub>/FeO = 0.15



Table 4. Average basalt composition for each tectonomagmatic province, compared with average ocean compositions<sup>a</sup>.

	Orthogonal Supersegment	st. dev.	Amagmatic Accretionary Segment	st. dev.	Joseph Mayes Segment	st. dev.	Narrowgate Segment	st. dev.	9°-25°E Normal MORB	st. dev.	Global Normal MORB	st. dev.	MAP Normal MORB	st. dev.	EPR Normal MORB	st. dev.	Indian Ridges Normal MORB	st. dev.	Mid- Cayman Rise MORB	st. dev.
SiO <sub>2</sub>	50.42	0.33	50.94	0.90	50.66	0.22	50.74	1.07	50.39	0.42	50.48	0.54	50.42	0.46	50.46	0.49	50.74	0.52	52.31	0.34
Al <sub>2</sub> O <sub>3</sub>	16.05	0.52	16.63	0.56	15.07	0.33	16.12	0.42	16.23	0.60	15.43	0.69	15.50	0.54	15.05	0.60	15.93	0.77	15.69	0.5
FeO*	9.21	0.66	8.33	0.68	10.44	0.91	8.17	0.81	9.03	0.62	9.98	0.95	10.03	0.85	10.61	0.70	9.18	0.93	9.55	0.69
MgO	7.63	0.45	7.16	0.60	5.95	0.79	6.08	0.75	7.75	0.43	8.05	0.60	8.24	0.51	7.73	0.56	8.22	0.59	6.53	0.64
CaO	11.07	0.36	10.60	0.48	10.26	1.06	10.94	1.00	11.14	0.37	11.55	0.58	11.44	0.54	11.62	0.40	11.37	0.66	9.8	0.46
Na <sub>2</sub> O	3.16	0.17	3.62	0.41	3.79	0.36	3.47	0.41	3.17	0.24	2.77	0.35	2.71	0.34	2.77	0.20	2.91	0.45	3.78	0.21
K <sub>2</sub> O	0.15	0.10	0.40	0.18	0.67	0.19	1.28	0.33	0.12	0.03	0.12	0.07	0.10	0.04	0.12	0.06	0.13	0.06	0.3	0.06
TiO <sub>2</sub>	1.65	0.22	1.62	0.25	1.20	0.37	1.87	0.25	1.57	0.22	1.49	0.27	1.42	0.21	1.64	0.27	1.42	0.3	1.98	0.28
P <sub>2</sub> O <sub>5</sub>	0.16	0.04	0.24	0.07	0.36	0.09	0.39	0.09	0.15	0.03	0.15	0.05	0.14	0.04	0.16	0.06	0.14	0.05	0.3	0.07
CO <sub>2</sub> <sup>b</sup>	197	24.5	194	32.7	178	23.8	175	28.0	205.7	27.3										
H <sub>2</sub> O	6.28	0.09	6.48	0.17	6.63	0.10	6.74	0.20	6.21	0.04										
Mg# <sup>c</sup>	59.5	3.0	60.4	3.0	48.5	5.7	56.9	5.6	64.3	2.5	59.0		59.8		56.7		61.5		54.9	
Fractionation Corrected <sup>d</sup>																				
H <sub>2</sub> O <sub>1</sub>	0.22	0.04	0.37	0.12	0.32	0.08	0.45	0.16	0.20	0.04										
K <sub>2</sub> /Ti <sub>1</sub> <sup>e</sup>	0.07	0.03	0.17	0.09	0.20	0.05	0.49	0.10	0.06	0.02	0.07		0.06		0.06		0.08		0.13	
Na <sub>2</sub>	3.13	0.13	3.34	0.35	2.94	0.11	2.95	0.30	3.16	0.21	2.74	0.34	2.74	0.32	2.63	0.19	2.96	0.43	3.04	0.05
Ca <sub>2</sub> /Al <sub>1</sub>	0.69	0.02	0.64	0.03	0.84	0.02	0.80	0.03	0.69	0.03										
Fe <sub>2</sub>	8.84	0.44	7.42	0.74	7.75	0.28	6.36	0.39	8.72	0.50	9.78	0.83	10.04	0.73	9.91	0.59	9.22	0.86	7.13	0.17
Si <sub>2</sub> /Fe <sub>1</sub>	3.72	0.29	6.90	0.70	6.46	0.23	7.93	0.49	5.80	0.36										

<sup>a</sup> averages of 'Normal' MORB are taken from Su [2002].

<sup>b</sup> CO<sub>2</sub> values are in ppm

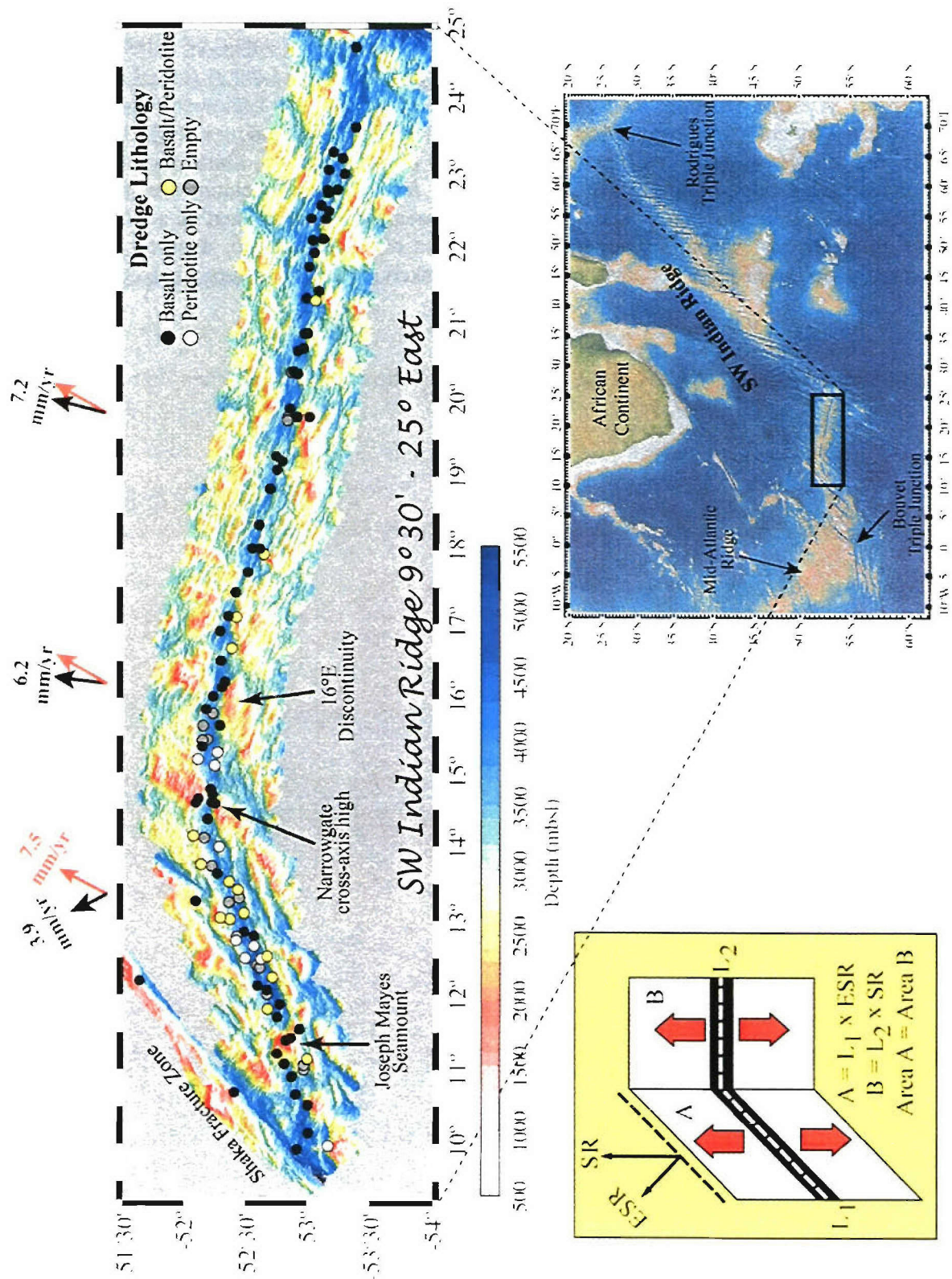
<sup>c</sup> Mg# = 100\*(Mg<sup>2+</sup>/(Mg<sup>2+</sup>+Fe<sup>3+</sup>)), where Fe<sup>3+</sup> is FeO\*

<sup>d</sup> see text for details of element-8 corrections

<sup>e</sup> values for global oceans are not fractionation corrected

<sup>f</sup> 9°-25°E N-MORB is derived by averaging all lavas from this study with K/Ti < 0.09





(previous page)

**Figure 1.** Southwest Indian Ridge bathymetry and lithologic distribution. 9-16° E swath sonar data [this manuscript] combined with bathymetry from 16-25° E [Grindlay et al., 1998]. Dredge locations and information given in Table 1. Lithologic distribution indicated by color (see legend and discussion in text). Half spreading rate (SR) marked by red arrows and effective spreading rate (ESR) by black arrows, illustrating the effect of increasing ridge obliquity from east to west. *Inset* Cartoon depicting calculation of ESR. Lithospheric sections A and B have equal area, but segment length  $L_1 > L_2$ . ESR is component of spreading perpendicular to trend of ridge axis (i.e. mantle upwelling rate). *Map inset* Regional bathymetric site map [taken from [www.geomapapp.org](http://www.geomapapp.org)].



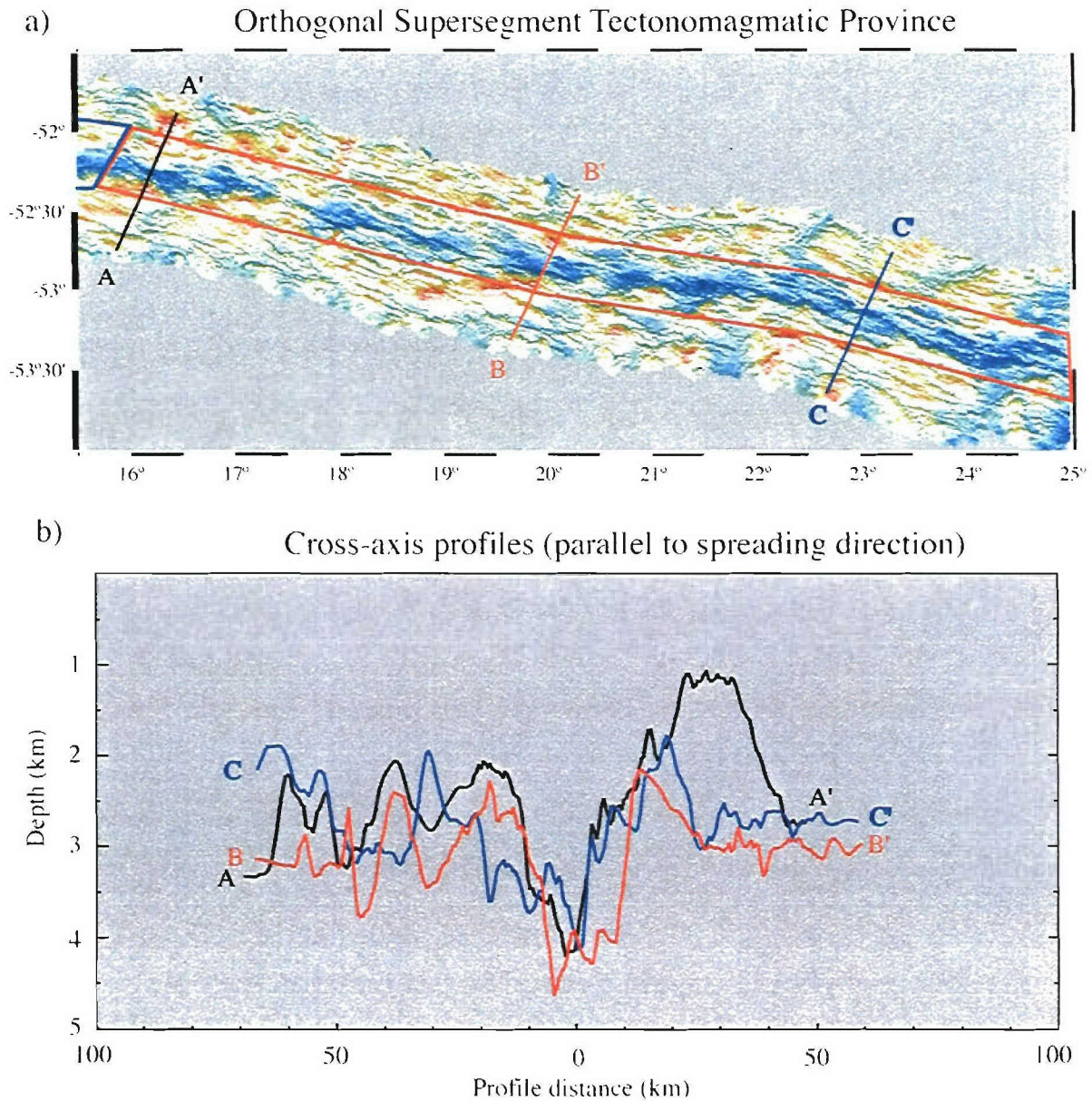
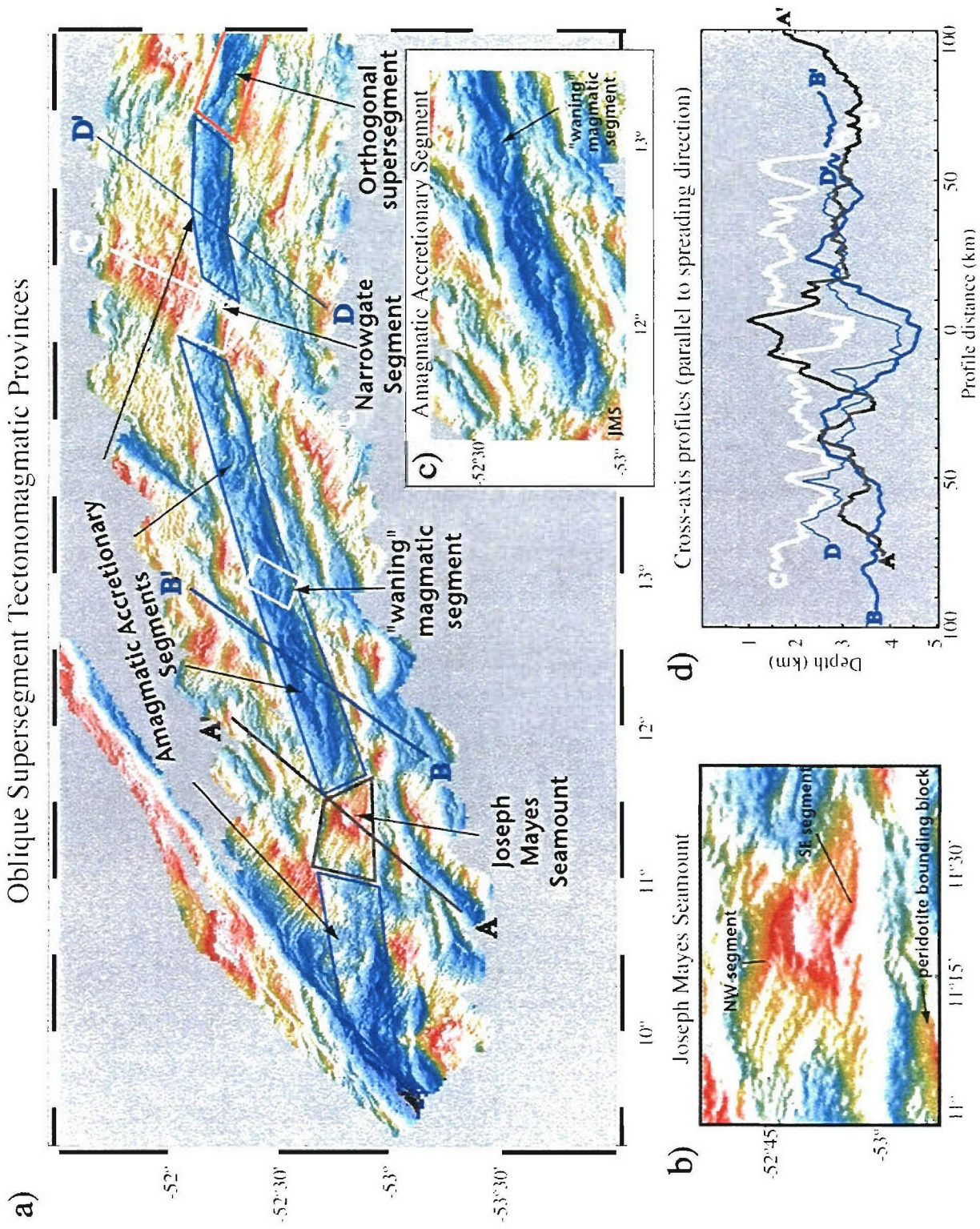


**Figure 2.** Tectonomagmatic province for the orthogonal supersegment. a) Entire orthogonal supersegment is a single tectonomagmatic area (outlined in red) from  $\sim 15^{\circ}45'$  to  $25^{\circ}$ E. b) Cross-axis profiles (A-A', B-B', and C-C') taken parallel to spreading direction, show similar along-axis rift mountain symmetry, but variable rift valley morphology. Vertical exaggeration is 40:1.



# Oblique Supersegment Tectonomagmatic Provinces



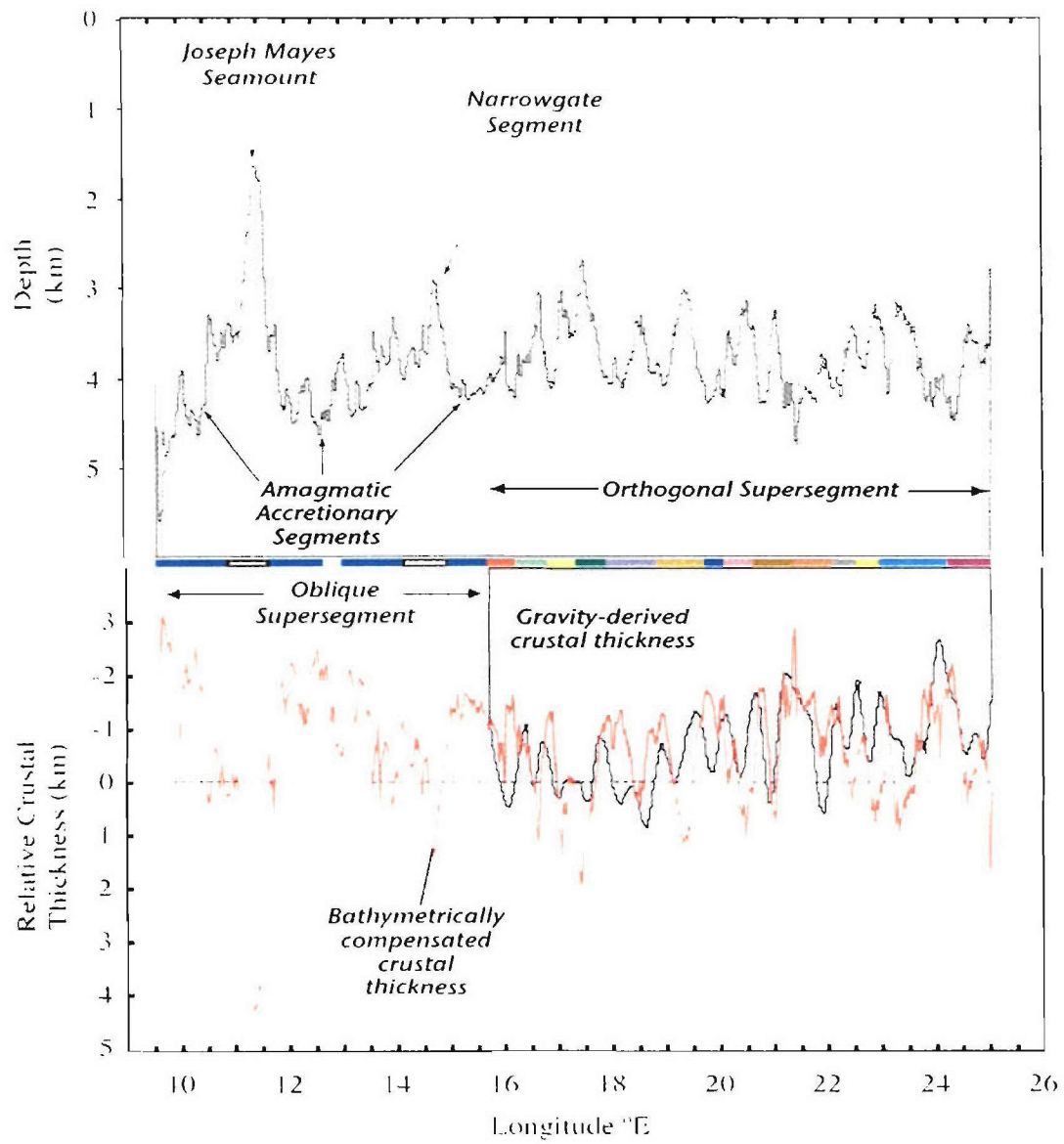
(opposite page)

**Figure 3.** Bathymetry and cross-axis topographic profiles of the oblique supersegment (9°-16°E). a) Bathymetry of the oblique supersegment, which consists of three tectonomagmatic areas; 1) Joseph Mayes Seamount at 11°20' E is outlined in grey, 2) the amagmatic accretionary segments (west of JMS, between JMS and Narrowgate segments, and east of Narrowgate segment) are outlined in blue; the “waning” magmatic segment (outlined in white) at ~ 12°50'E is considered part of this tectonomagmatic province, and 3) the Narrowgate segment at 14°41' E is outlined in white. b) Enlarged picture of Joseph Mayes Seamount illustrating dual peaks, with associated segments extending to the SE and NW. c) Enlarged view of the central amagmatic accretionary segment between JMS and 13°E. The oblique rift valley contains many large fault blocks and little evidence of volcanic lineations. d) Cross-axis profiles representing each of the tectonomagmatic settings. Profiles are parallel to spreading direction (for profiles B & D that is ~ 52° oblique to axis). Narrowgate profile (C-C') follows bathymetric high on south side of ridge. Vertical exaggeration for each profile is 40:1.

(following page)

**Figure 4.** Along-axis bathymetry and relative crustal thickness profiles for Southwest Indian Ridge (9°-25°E). Bathymetry (kilometers below sea level) is taken along the rift axis. Gravity-derived crustal thicknesses [Dulaney 2002; Grindlay *et al.*, 2000] are not unique and are model dependent, calculated relative to a 6 km thick oceanic crust, and shown with y-axis reversed to mimic depth to the Moho. Airy crustal thickness or isostatically compensated crustal thickness is calculated assuming crustal, mantle, and seawater densities of 2750, 3300, and 1030 kg m<sup>-3</sup>, respectively. Airy crustal thickness generally agrees with gravity-derived crustal thickness on orthogonal supersegment, indicating full isostatic compensation. Variations in Airy crustal thickness along oblique supersegment can be compared to orthogonal supersegment, suggesting large variations among the three tectonomagmatic provinces west of 16°E. Colored bars connecting the upper and lower panels indicate individual magmatic and amagmatic accretionary segments. Segments on the orthogonal supersegment are from Dulaney [2002] and Grindlay *et al.*, [2000]. Segments on the oblique supersegment are colored-coded as follows; Narrowgate segment is white, Joseph Mayes Seamount is grey, and the amagmatic accretionary segments are blue (with the main amagmatic segment between JMS and Narrowgate segment separated by a “waning” magmatic segment).





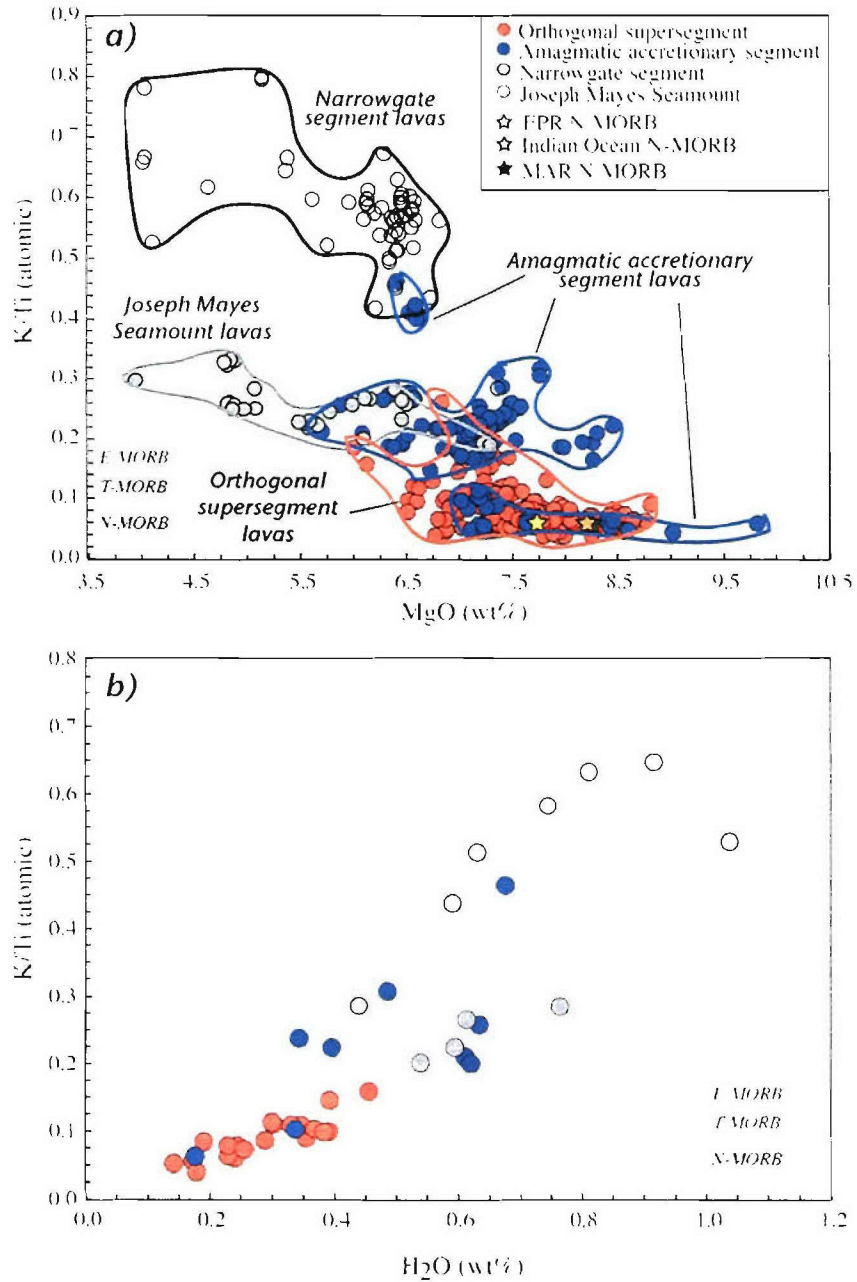
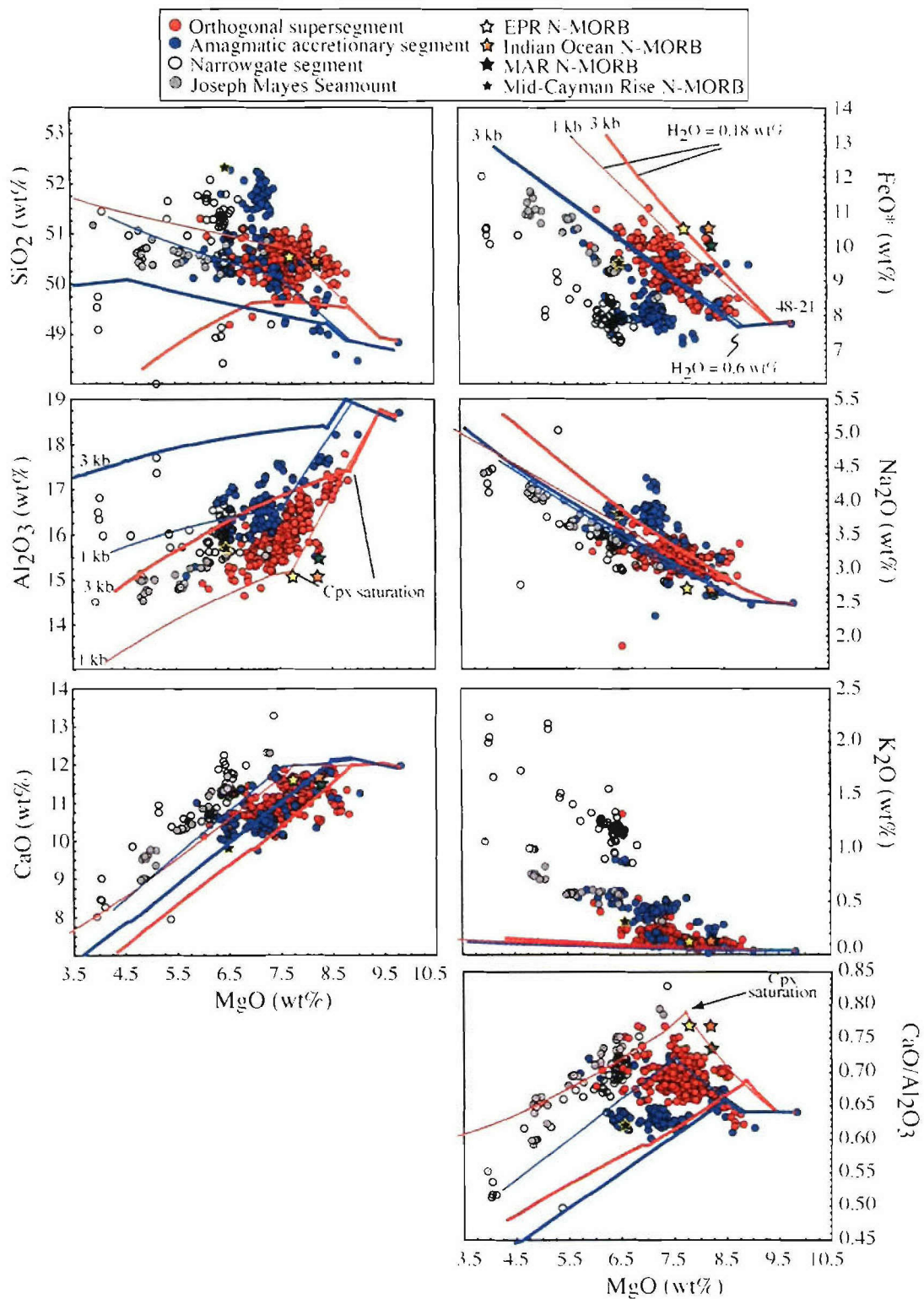
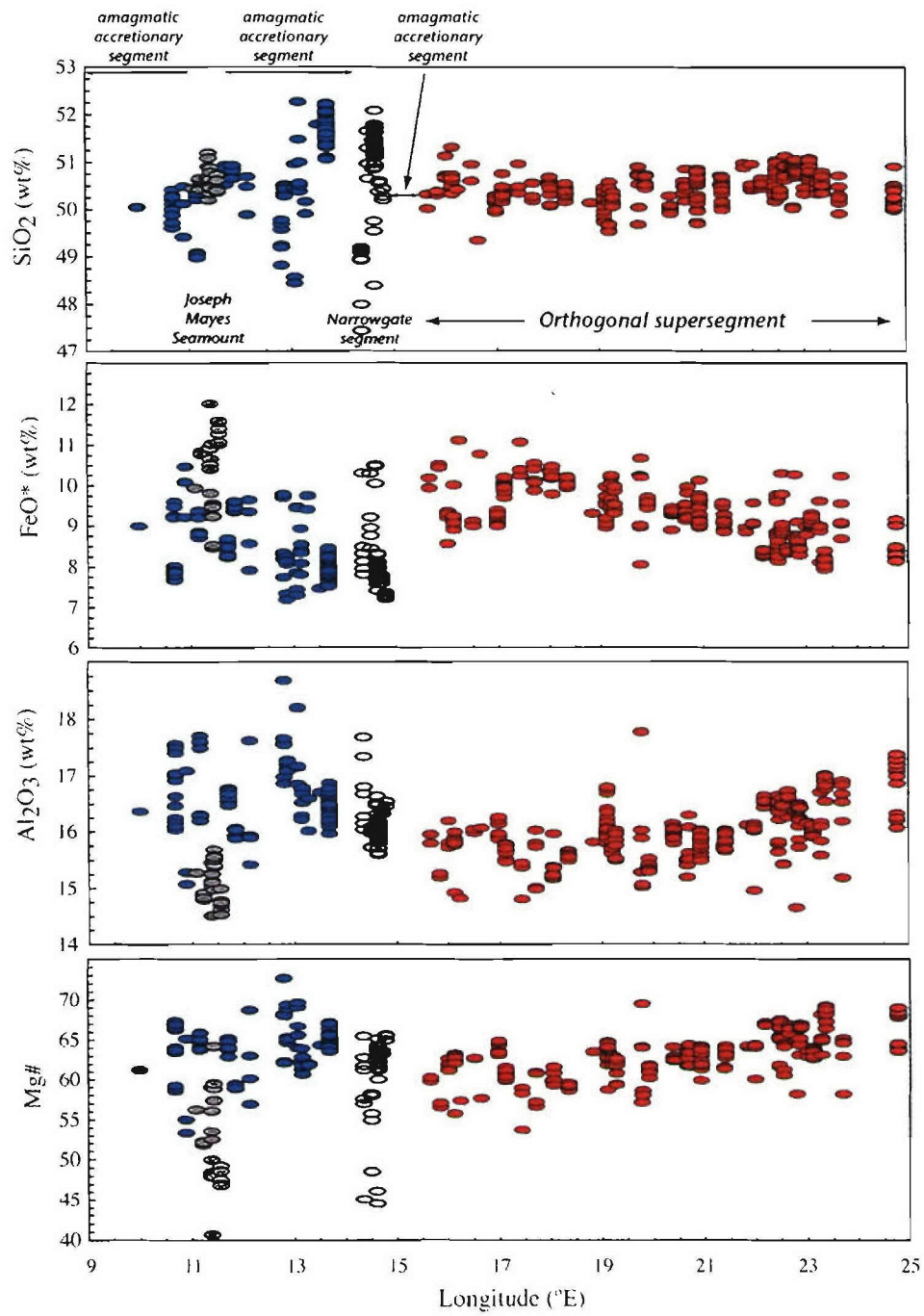


**Figure 5.** K/Ti versus MgO wt% and H<sub>2</sub>O wt% for Southwest Indian Ridge basalts (9°-25°E) divided by tectonomagmatic province; orthogonal supersegment, amagmatic accretionary segment, Joseph Mayes Seamount, and the Narrowgate segment. Average “normal”-MORB compositions plotted for MAR, EPR, and Indian Ocean [Su & Langmuir, 2002]. The positive trend in K/Ti versus H<sub>2</sub>O illustrates the variable enrichment of lava compositions within each province and among them.

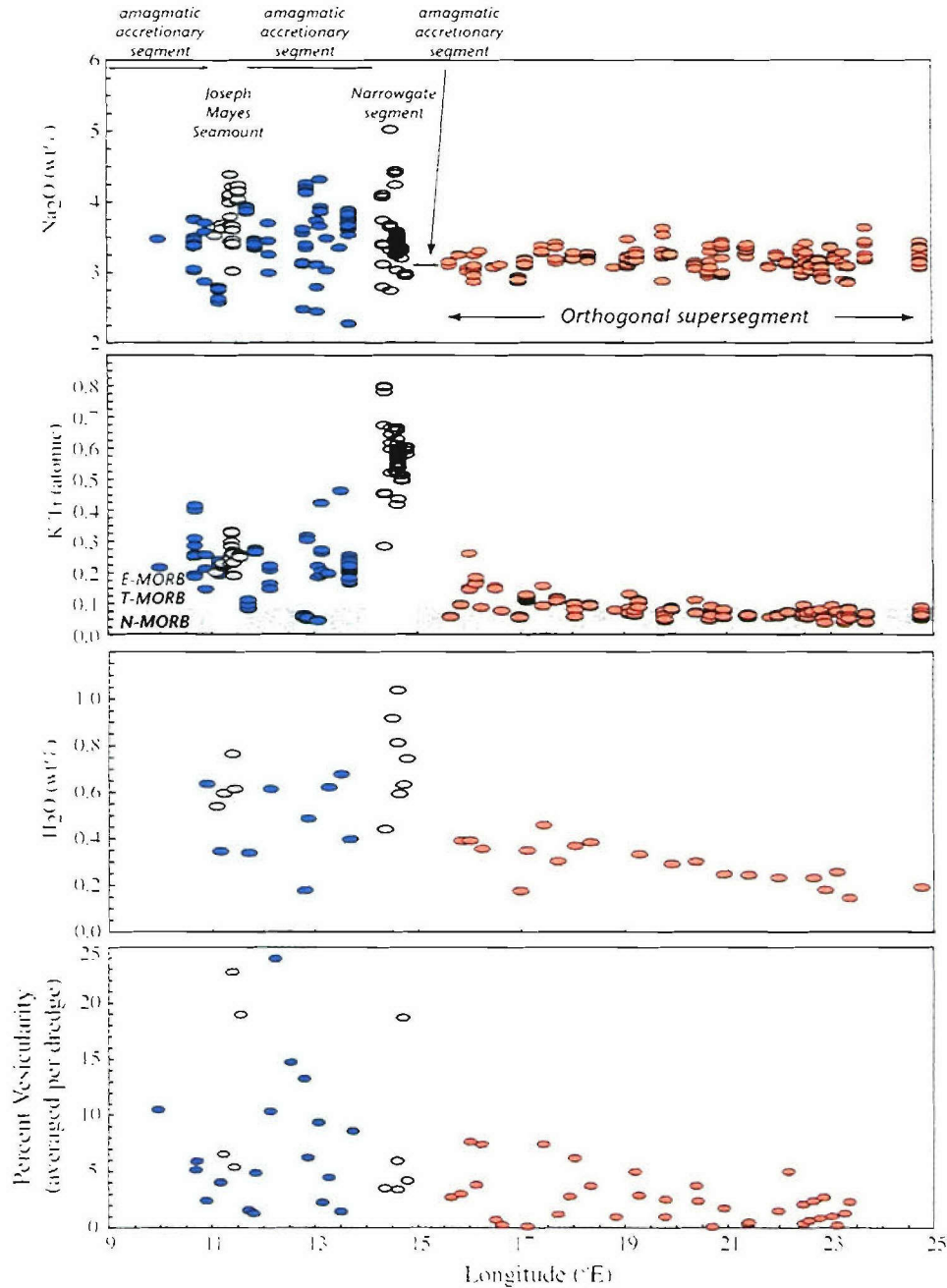


(opposite page)

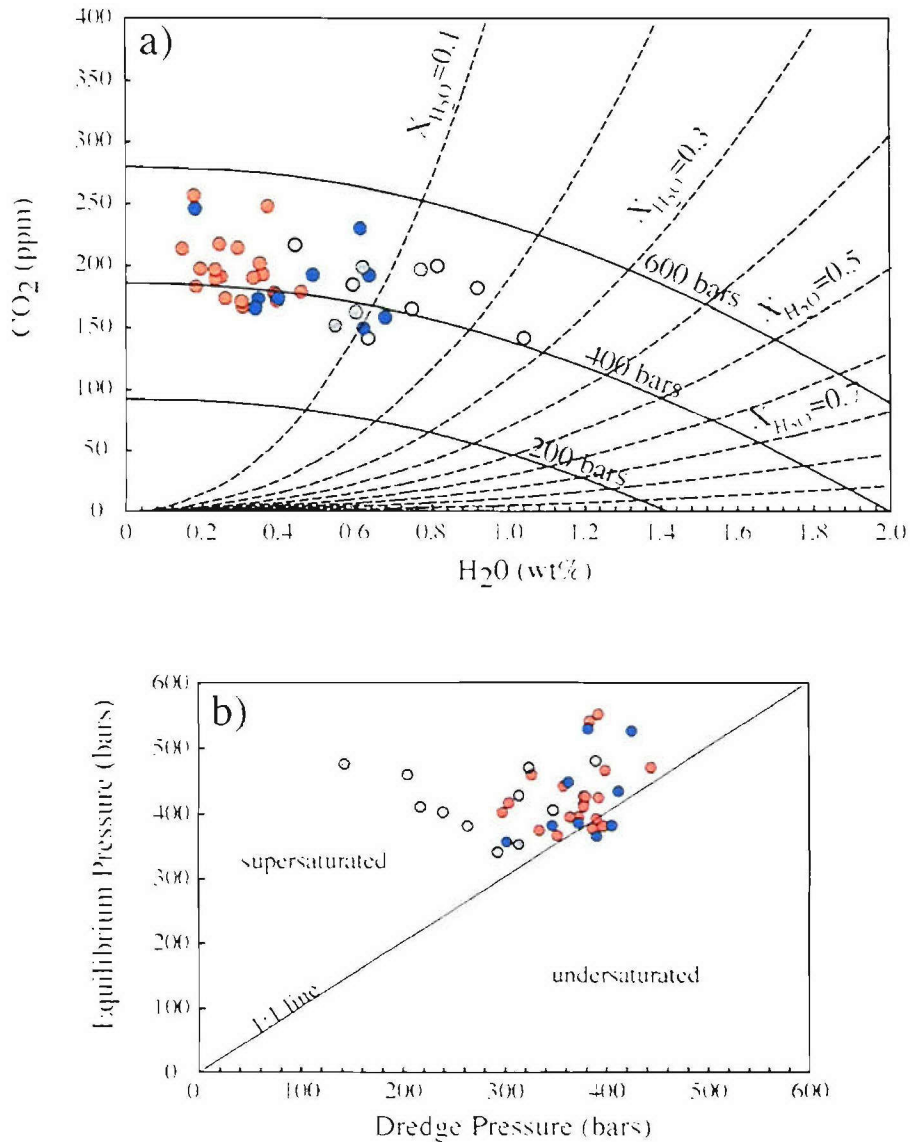
**Figure 6.** Major element oxides plotted against MgO wt% for orthogonal supersegment glasses (15°45'–25° E; filled red circles), amagmatic accretionary segment glasses (9°30'–15°45' E; filled blue circles), Joseph Mayes Seamount glasses (11°–11°35' E; filled grey circles), and Narrowgate segment glasses (14°15'–14°54' E; open black circles). Liquid lines of descent (LLD) modeled using MELTS (details in text). All LLDs start at same initial composition (KN162-9-48-21) with red lines indicating a dissolved H<sub>2</sub>O content in the melt of 0.18 wt% and blue lines indicating an H<sub>2</sub>O content of 0.6 wt%. Thin LLDs are modeled at 1 kb and thick LLDs at 3 kb. Stars represent averaged 'normal'-MORB compositions for MAR (green), EPR (yellow), Indian Ocean (orange) [Su, 2002], and Mid-Cayman Rise (black) [Elthon *et al.*, 1995].



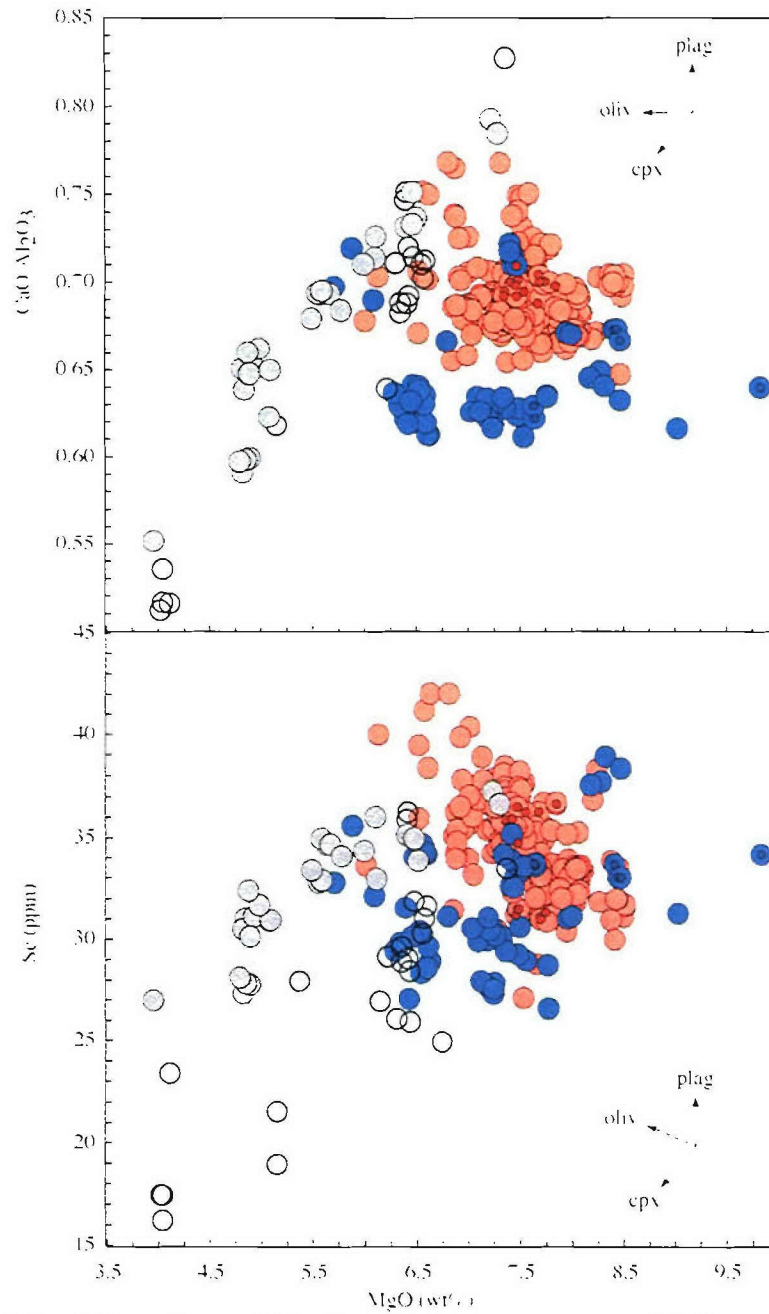




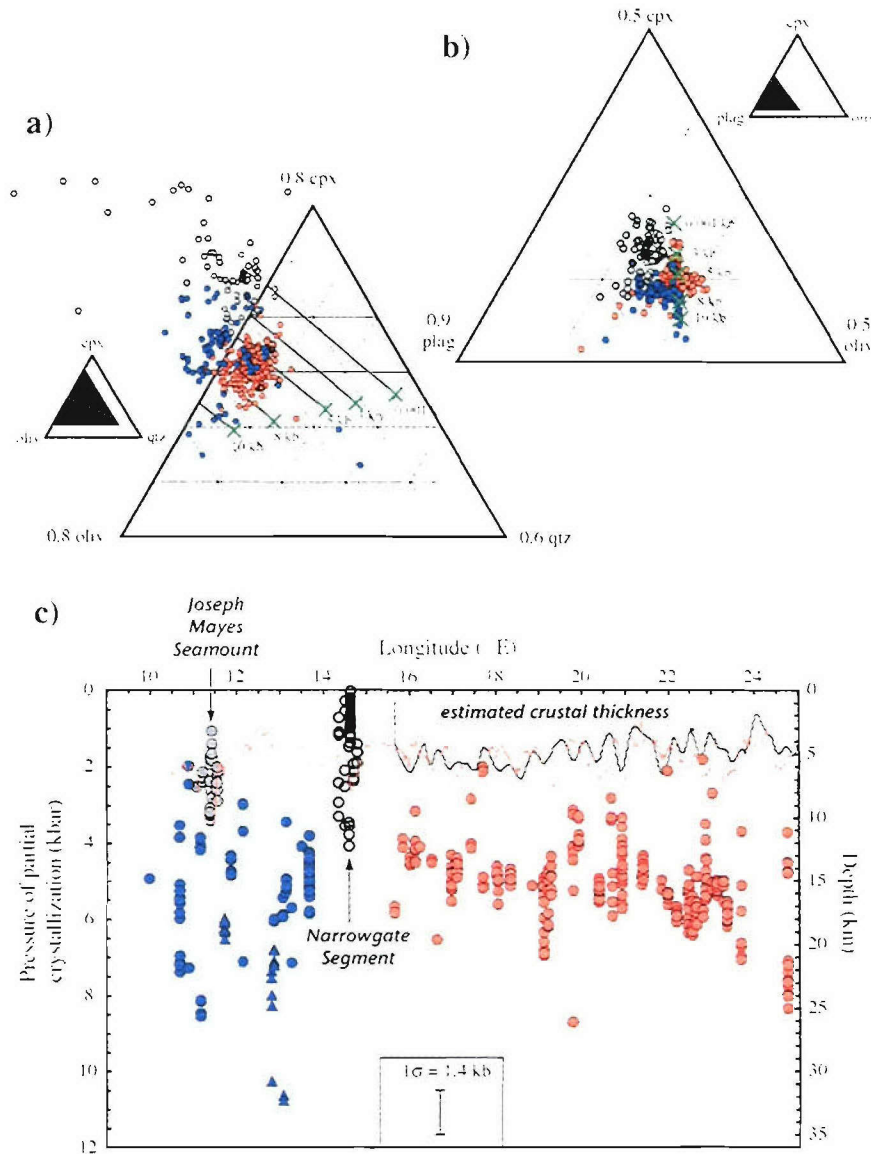
**Figure 7.** Along-axis major element compositional variation for Southwest Indian Ridge (9°-25°E). Symbols for each tectonomagmatic province the same as in Figure 6. Light grey vertical fields designate Joseph Mayes Seamount and Narrowgate segment provinces. Fields for K/Ti profile are same as in Figure 6.  $Mg\# = 100 \cdot Mg^{2+} / (Mg^{2+} + Fe^{2+})$ , where  $Fe_2O_3/FeO = 0.15$ .



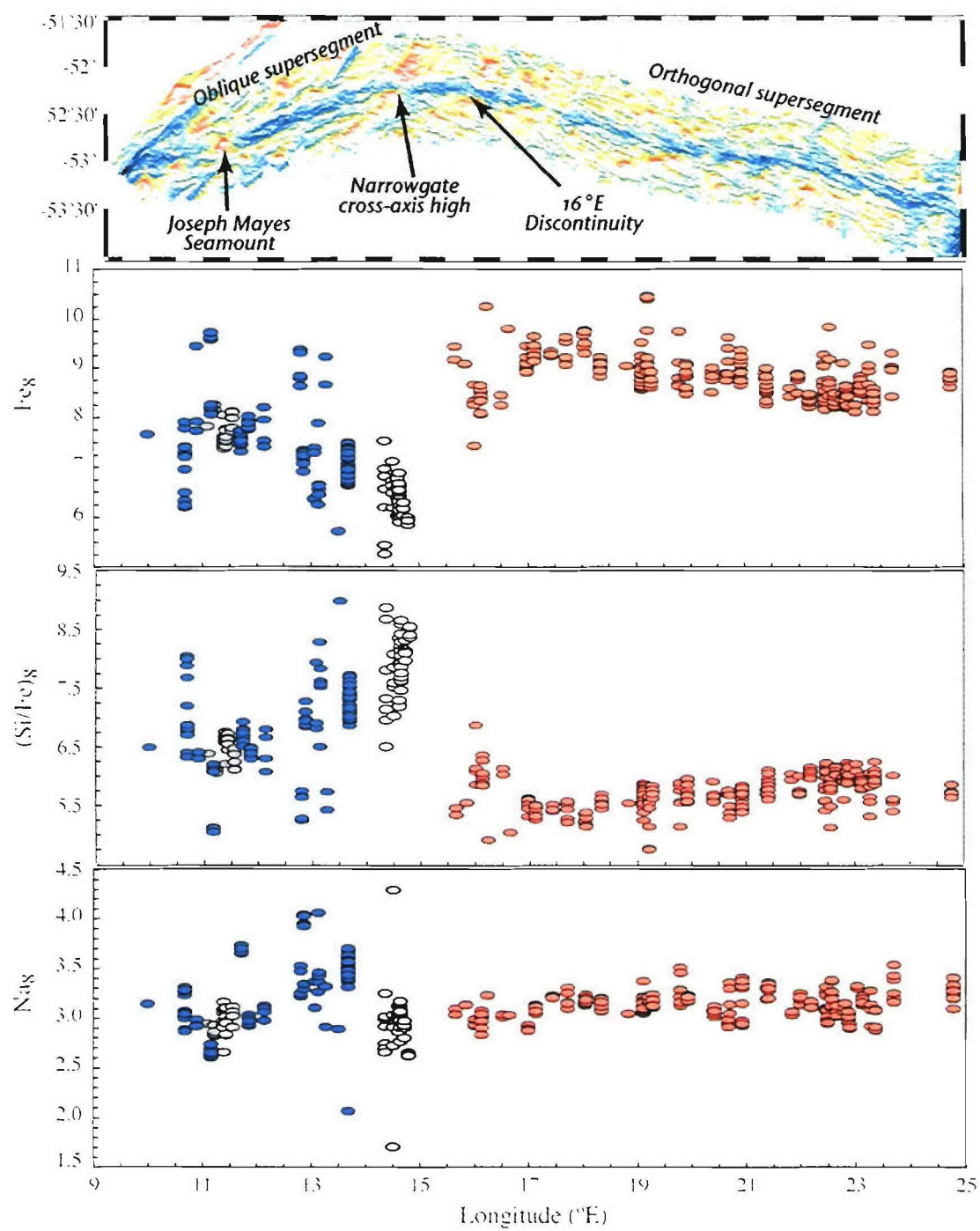
**Figure 8.** Dissolved water and carbon dioxide contents measured in SW Indian Ridge glasses. a) Vapor saturation diagram for tholeiite at 1200° C. Isobars (constant pressure) are shown as solid curves. Dashed curves are isopleths (constant vapor composition), marked with values of mole percent H<sub>2</sub>O. b) Equilibrium vapor saturation pressures plotted against dredge pressure. Dredge pressures are calculated from the depth at start of dredge and thus represent pressure maximums. The position of nearly all glasses above the 1:1 line indicates that they were supersaturated with a CO<sub>2</sub>-rich vapor upon eruption, likely a result of rapid ascent rates that limit the amount of degassing before eruption.



**Figure 9.** CaO/Al<sub>2</sub>O<sub>3</sub> ratios and Sc abundances (ppm) versus MgO content (wt%) of Southwest Indian Ridge basalts. Vectors qualitatively indicate the effects of phase crystallization on the liquid composition. Small dark red and dark blue dots indicate lavas from single dredges of the orthogonal supersegment and amagmatic accretionary segment, respectively. They illustrate differentiation trends that require the involvement of cpx as a crystallizing phase.



**Figure 10.** a) & b) Pseudoternary projections of major element lava compositions recalculated into mineral norms following the method of *Grove et al., [1992]*. Symbols the same as in Figure 6, except for N-MORB from amagmatic accretionary segment with low K/Ti ( $< 0.1$ ), shown as blue triangles. Predicted saturation boundaries for olivine + plagioclase + augite + low-Ca pyroxene + melt (OPALM) at pressures ranging from 1 bar to 10 kbar (green X's), with saturation boundaries for olivine + plagioclase + augite + melt (OPAM) extending toward oliv-cpx tie line (thick black lines). OPAM boundaries extend out of page in b). c) Pressures of partial crystallization calculated assuming 3-phase saturation, using the method of *Herzberg [2004]*. Estimated crustal thickness field (grey) and bathymetrically compensated crustal thickness (thin red curve) profiles are taken from Figure 4.





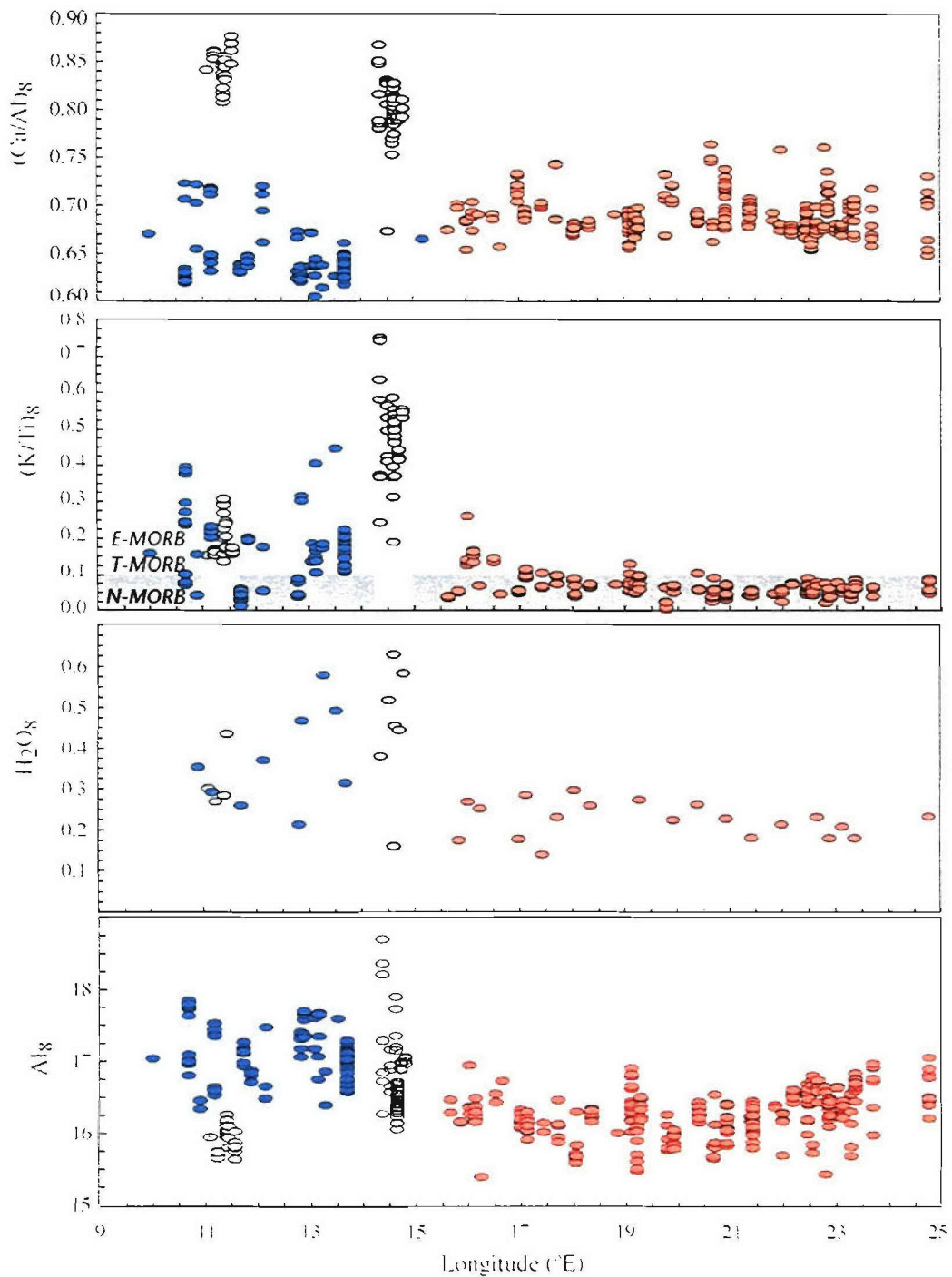


**Figure 11.** Along-axis variations of fractionation-corrected major element abundances for glasses from the Southwest Indian Ridge (9°-25°E). Symbols and fields are the same as in Figure 7.

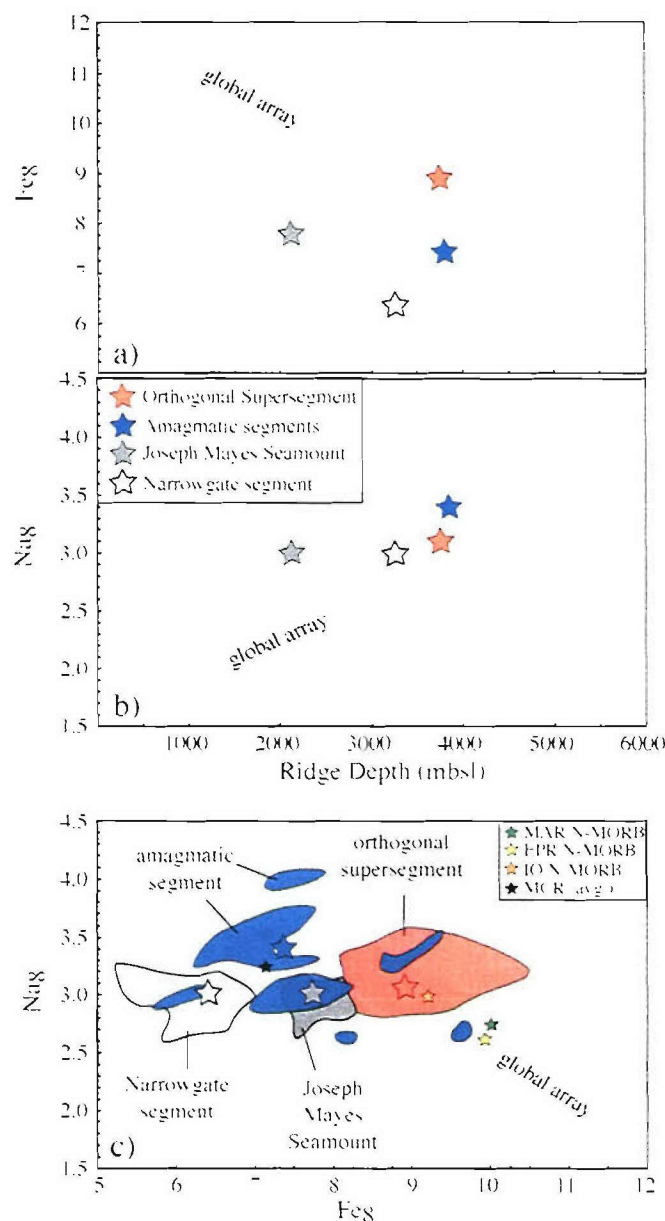
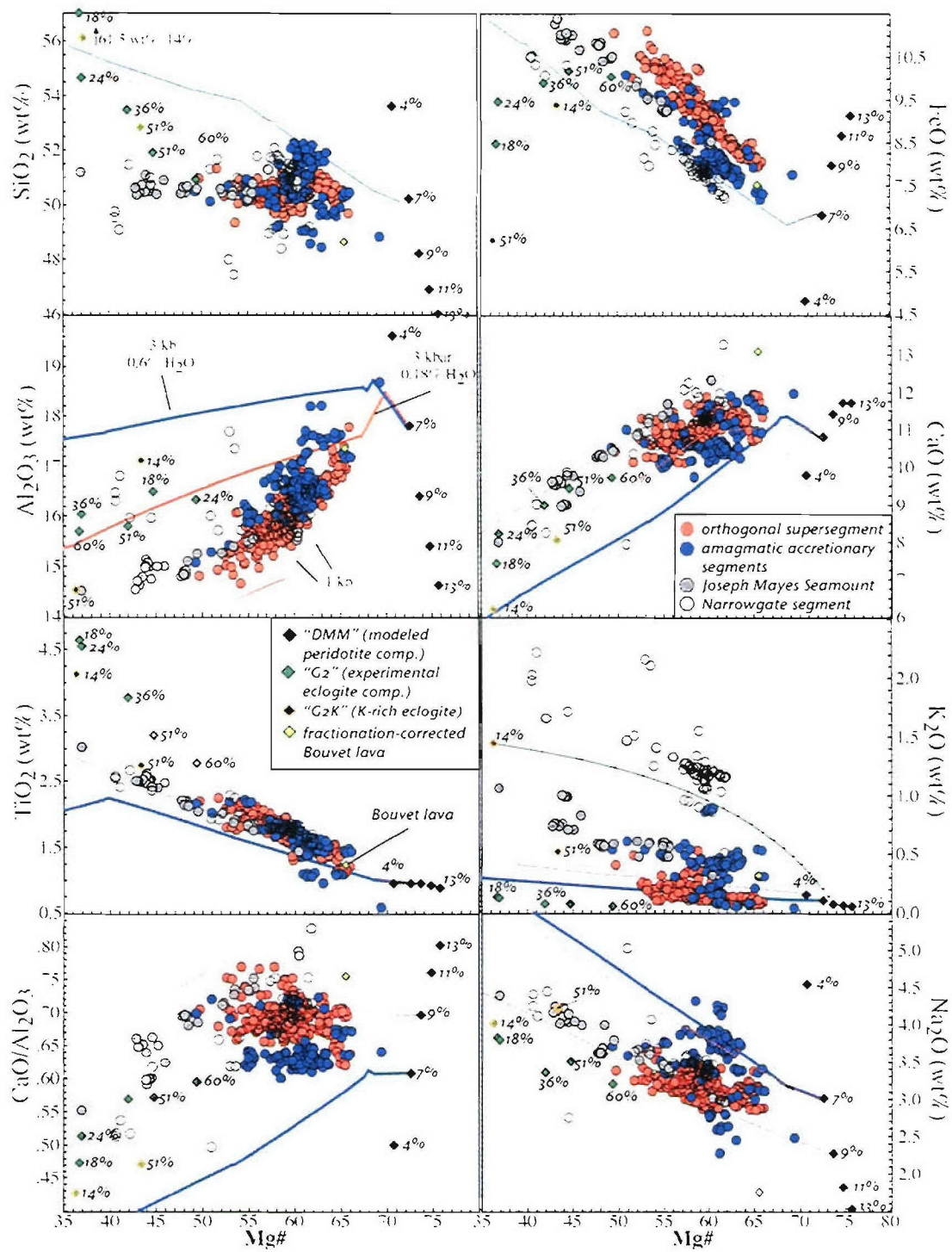


**Figure 12.**  $Na_8$ ,  $Fe_8$ , and depth correlations for averages from each of the tectonomagmatic provinces. Orthogonal supersegment (red star), amagmatic accretionary segments (blue star), Joseph Mayes Seamount (grey star), and the Narrowgate segment (white star) plotted relative to the 'global array' [Klein and Langmuir, 1987], which represents regional averages from the global ridge system. a)  $Fe_8$  vs. depth. b)  $Na_8$  vs. depth. c)  $Na_8$  vs.  $Fe_8$ , with colored fields corresponding to glass data from each tectonomagmatic group. N-MORB data for MAR, EPR, and Indian Ocean (IO) are taken from Su & Langmuir, [2003], and MCR = Mid-Cayman Rise [Meyzen *et al.*, 2003].



(opposite page)

**Figure 13.** Major element abundance variations plotted with near-fractional aggregate melts of a depleted spinel lherzolite from *Kinzler*, [1997], and partial melts of “G2” and “G2K” (K-rich) eclogite compositions from *Pertermann & Hirschmann*, [2003a]. Green curve represents a continuum of parental liquids produced by mixing of peridotite melts with eclogite melts, at 5% increments. Modeled liquid lines of descent follow the same descriptive key as in Figure 6, and illustrate the abundance variation constrained by fractional crystallization of variable composition peridotite melts. The thick grey arrow represents the estimated linear regression for fractionation-correction for the Narrowgate segment lavas. Reaction of eclogite melt with depleted peridotite would have similar effects. The yellow diamond represents a fractionation-corrected (MgO=8 wt%) parental composition for Bouvet Island.  $Mg\# = 100 * Mg / (Mg + Fe)$ , where all Fe is FeO\*. Data symbols for lavas are same as Figure 6.

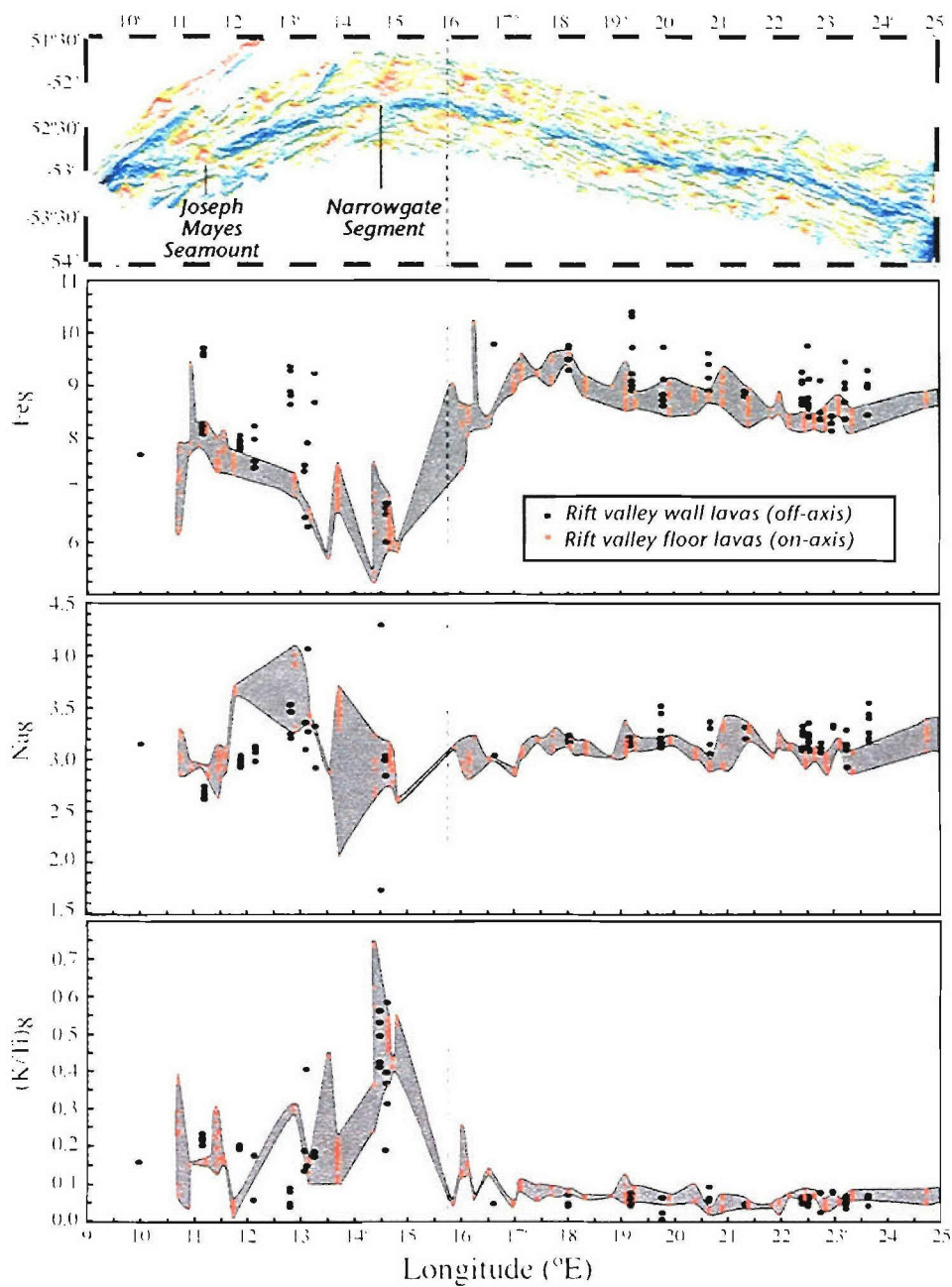
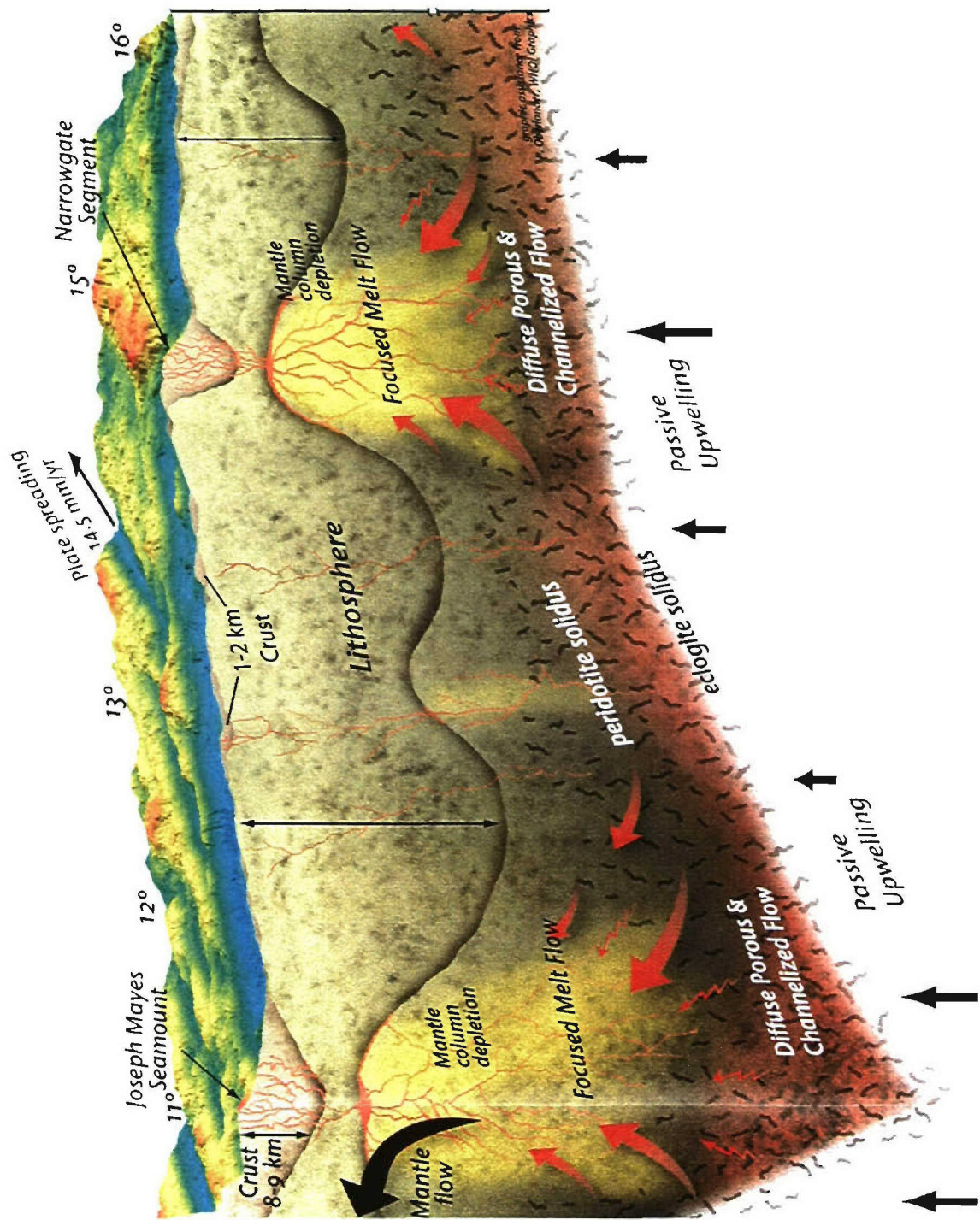


**Figure 14.** Fractionation-corrected major element compositions for on-axis versus off-axis glasses from 9-25°E. Grey fields represent the range for on-axis compositional variation with the red dots indicating the actual data. Black dots represent the off-axis glasses. The dotted line marks the morphologic and geochemical discontinuity between the orthogonal supersegment and the oblique supersegment. Light grey vertical fields highlight Joseph Mayes Seamount and Narrowgate segment.





(previous page)

**Figure 15.** Schematic 3-D along-axis cross-section illustrating the preferred tectonomagmatic melting model for the oblique supersegment on the Southwest Indian Ridge (9°-16°E). Top surface is seabeam bathymetry (map view in Figure 1) covering a ~300 km long portion of the study area between ~11° to 16°E. At the base of the image, depleted mantle containing ~3% mafic veins (black pattern) passively upwells at various inferred rates ranging from 14 mm/yr (large arrows) to 7 mm/yr (small arrows). The veins begin to partially melt (red shading) near 120 km at the pyroxenite/eclogite solidus, and by the time the peridotite solidus is reached (~50-60 km) the vein component has likely melted ~50%. Extraction and focusing of the mafic melts at depth and mixed vein/peridotite melts shallower occurs via both diffuse porous flow (small irregular red arrows) and channelized flow via dunite conduits (large solid red arrows), but presumably involves some chemical interaction or re-equilibration with the host peridotite. Melt focusing is enhanced by the topography of the lithosphere and the potential feedback mechanism of more highly depleted peridotite (i.e. less cpx) creating greater permeability [Zhu and Hirth, 2003], which in turn creates higher melt flow, and so on. Lithospheric thickness varies along-axis as a function of spreading geometry or inferred upwelling rate, thus with slower upwelling comes increased conductive cooling from above and thicker lithosphere. Focusing of melt away from the amagmatic accretionary segments and towards the volcanic segments (Narrowgate segment and Joseph Mayes Seamount) occurs over length-scales about twice the volcanic segment length, thus large volumes of enriched mafic melt flow up through the mantle columns of Narrowgate segment and Joseph Mayes Seamount. This focusing likely removes much or all of the clinopyroxene within the residual mantle, thereby reducing the trace element buffering capacity of the local mantle column. The absence of cpx allows initially enriched melts to migrate vertically to the surface without losing their trace element signature, and likely explains the compositional difference between Joseph Mayes Seamount, a younger less depleted mantle, and the highly depleted mantle column of the Narrowgate segment. The focused melt flow also results in thicker than average crust at the Narrowgate segment (~7 km) and Joseph Mayes Seamount (~9 km), and thinner than average to non-existent crust along the amagmatic accretionary segments, where average crust is 6 km (gravity inferred) as seen at the westernmost volcanic segment on the orthogonal supersegment. Spreading direction and full rate are indicated by the black arrow parallel to and extending from the extinct transform trace at 14°E, and by the curved arrow labeled “mantle flow” on the left-hand face.

***Chapter 3. Trace element modeling and isotopic constraints on the importance of melting processes versus source at the ultraslow-spreading Southwest Indian Ridge (9°-25°E)***

### Chapter 3. Trace element modeling and isotopic constraints on the importance of melting processes versus source at the ultraslow-spreading Southwest Indian Ridge (9°-25°E)

#### 1. Introduction

Mid-ocean ridge basalts are compositionally homogeneous relative to ocean island and arc related lavas, yet comparison of basalts from various ridges finds significant diversity, with the Southwest Indian Ridge debatably the most chemically heterogeneous [Hamelin and Allègre, 1985; Mahoney *et al.*, 1992]. Variation in basalt composition is not isolated to the SWIR [Melson *et al.*, 1976], and although MORB is dominated by incompatible element depleted tholeiite, the occurrence of incompatible element enriched basalt (E-MORB) reflects a key component of ocean crust generation. In some cases E-MORB is attributed to nearby plume-influence, for example the Iceland plume on the northern Mid-Atlantic Ridge [Bougault *et al.*, 1988; Schilling *et al.*, 1983; Sun *et al.*, 1975] or Galapagos plume on the Galapagos Spreading Center [Christie and Sinton, 1981; Christie *et al.*, 2005; Fisk *et al.*, 1982; Schilling *et al.*, 1976; Schilling *et al.*, 1982]. However, for non-plume influenced ridge sections, most notably along the East Pacific Rise (EPR) [Batiza and Niu, 1992; Langmuir *et al.*, 1986; Mahoney *et al.*, 1994; Perfit *et al.*, 1994; Sinton *et al.*, 1991], the occurrence is not well understood. This has prompted recent investigations into the factors controlling MORB generation [Asimow *et al.*, 2004; Niu *et al.*, 2001; Niu *et al.*, 2002] and specifically models for E-MORB generation [Donnelly *et al.*, 2004; Ito and Mahoney, 2004; Meyzen *et al.*, 2005].

Equally diverse as basalt chemistry are the tectonic and segmentation characteristics of the SWIR [Cannat *et al.*, 2003; Cannat *et al.*, 1999; Mahoney *et al.*, 1992; Mendel *et al.*, 1997; Mendel *et al.*, 2003; Sauter *et al.*, 2004a], suggesting the possibility that basalt chemical variation is directly or indirectly controlled by tectonic environment (Chapter 2). Others have proposed links between sub-ridge melting processes and tectonic setting [Langmuir and Bender, 1984] or spreading rate [Niu *et al.*, 2001; Niu and Hekinian, 1997], but many of the studies assessing the importance of mantle source versus melting process have focused on fast-spreading ridge environments [Niu *et al.*, 2002; Niu *et al.*, 1996] where melt volume is high and homogenization is efficient. In contrast, the entire Southwest Indian Ridge maintains a constant full-spreading rate of ~14.5 mm/yr, classifying it as an ultraslow-spreading ridge (< 20 mm/yr). The entire western portion of the Southwest Indian Ridge, from 25°E to the Bouvet triple junction, exemplifies this chemical and tectonic diversity, but the area between 9°-25°E (see Fig. 1 *inset*) containing two contrasting accretionary supersegments displays the most significant variability. This 1050 km section of the Southwest Indian Ridge provides a unique opportunity to evaluate the influence of tectonics and spreading rate on melting processes and thus ultimately on MORB chemistry.

Basalts dredged from the rift valley between 9°-25°E on the Southwest Indian Ridge display significant isotopic and trace element variation. One 630 km long supersegment



(16°-25°E) erupts N-MORB that is progressively enriched from east to west towards the Bouvet Hotspot, despite being over 1000 km from the current plume location. The second 400 km long supersegment (9°-16°E) consists of three separate volcanic centers erupting moderately to highly enriched E-MORB and connected by long amagmatic accretionary segments, themselves erupting scattered N-MORB and E-MORB. Fractionation-corrected incompatible element abundances and ratios are compared along-axis showing systematic trends between 16°-25°E and locally variable behavior to the west. We model non-modal aggregate fractional melting of variously enriched incompatible element compositions for single and multi-lithology mantle sources in an attempt to constrain the local MORB source. Correlations between isotope and incompatible element compositions and tectonics and ridge characteristics suggest the importance of “process” rather than “source” during MORB generation. Furthermore, the use of  $^3\text{He}/^4\text{He}$  isotopic compositions in conjunction with heavy isotopic signatures provides some insight into regional mantle heterogeneity and the influence of the Bouvet plume. Overall, this manuscript serves to illustrate the important role melting process can have on MORB chemistry at ultraslow-spreading ridges where the total volume of melt generated is small relative to faster spreading ridges, thereby increasing basalt composition sensitivity to small perturbations in melting parameters.

## 2. Tectonic Setting

Situated between the African and Antarctic plates, the Southwest Indian Ridge (SWIR) is one of the slowest spreading mid-ocean ridges in the global ridge system, with an average full rate of 14-15 mm/yr [DeMets *et al.*, 1990; Menke, 2005]. The SW Indian Ridge measures ~7700 km in length from the Bouvet Triple Junction (55° S, 0° E) to the Rodrigues Triple Junction (25° S, 70° E) and maintains a highly oblique (~60°) SW-NE overall orientation relative to the plate spreading direction. Numerous studies have observed variations in segmentation pattern and geochemistry along axis, leading to the division of the SWIR into three regional sections. The eastern SW Indian Ridge from 46° E to 70° E [Cannat *et al.*, 1999; Mendel and Sauter, 1997; Meyzen *et al.*, 2003; Sauter *et al.*, 2004a; Sauter *et al.*, 2004b; Seyler *et al.*, 2003] is characterized by sections having a segmentation pattern typical of slow spreading ridges contrasted with highly oblique sections devoid of transform offsets [Sauter *et al.*, 2004a]. The central SW Indian ridge from 25° E to 46° E [Hamelin and Allègre, 1985; le Roex *et al.*, 1989; Mahoney *et al.*, 1992] is strongly influenced by the Marion Hotspot and contains many large transform offsets. The western SW Indian Ridge [le Roex *et al.*, 1985; le Roex *et al.*, 1992] between the Bouvet Triple Junction (~ 0°) and 25° E has an overall E-W trend, thereby lacking the extreme 1<sup>st</sup> order obliquity of the rest of the SW Indian Ridge along most of its length. From 0° to 9° E it consists of a series of orthogonal ridge segments separated by transform faults, but for 1050 km from 9°-25° E (see Fig. 1 *inset*) it entirely lacks transforms, consisting of two supersegments of strikingly different character.

The eastern supersegment, from here on referred to as the “orthogonal supersegment” maintains an overall axial orientation perpendicular to sub-perpendicular to the spreading direction from 25°E to ~16°E, at which point the rift valley floor drops nearly 500 m, and



the morphology, physiography, lithology, and segmentation pattern of the ridge changes. From 16° E for nearly 400 km the western supersegment rift valley, from here on referred to as the “oblique” supersegment, maintains a general southwesterly trend, reaching an maximum obliquity relative to the spreading direction of ~57°, and intersecting the Shaka Fracture Zone at about 9°50' E. In Chapter 2 we delineate four separate tectonomagmatic provinces from 9°-25°E based on morphology, segmentation, crustal thickness, and major element chemistry. The three provinces that lie within the oblique supersegment (the Narrowgate segment, Joseph Mayes Seamount, and amagmatic accretionary segments) are quite diverse among themselves, and they all differ from the orthogonal supersegment. For a detailed discussion of the characteristics of each province refer to section 2 of Chapter 2.

### **3. Analytical Methods**

#### **3.1. Trace Element Measurements**

Glasses were hand picked at sea and detailed rock classification, description and statistics can be found in Chapter 2. Sample preparation, including glass dissolution was conducted at University of Cape Town according to techniques described in [le Roex *et al.*, 2001]. Trace element abundance measurements were collected using a Perkin-Elmer ELAN 6000 inductively coupled plasma mass spectrometer in the Department of Geological Sciences, at the University of Cape Town. Replicate analyses of international rock standards BHVO-1 and JB-2 by ICP-MS at Cape Town are reported in [le Roex *et al.*, 2001]. Procedural error generally runs ~ 3% and relative standard deviations (RSD in %) for each element, averaged for all samples in this study, are reported in Table 1. Using Ba/Rb values as an indicator of potential alteration, where MORB is generally ~11, we observed a few N-MORB samples with anomalously high Ba/Rb (>25). Four samples were rerun at WHOI using isotope dilution techniques and new measurements were significantly different than UCT measurements. Ba/Rb values for those samples are now near 11, but investigation of further alteration issues will need to be addressed before publication.

#### **3.2. Isotope Measurements**

##### ***Sample Preparation***

Basalt glasses were sampled while at sea and upon return to the lab. Overall, glasses were high quality, with little discoloration or visible evidence of hydrothermal alteration. To ensure removal of possible alteration surfaces, large phenocrysts, and general poor quality fractions, glass fractions were hand picked under a binocular microscope before powdering in a tungsten/carbide shaker using agate beads. The shaker was cleaned with SiO<sub>2</sub> between each sample powdering. Minor alteration surfaces were visible in some fractions, thus a light to moderate leaching step was used on all samples. Powders were leached for 1 hour at room temperature in 6 N HCl, then centrifuged, decanted, and rinsed (twice) in de-ionized H<sub>2</sub>O. Most of the samples showed little evidence of heavy alteration, however a couple samples, especially VAN7 90-77 lost noticeable mass

fractions, presumably from dissolution and leaching of alteration phases; although chemical signatures of alteration (i.e. Ba/Rb,  $^{87}\text{Sr}/^{86}\text{Sr}$ ) are absent.

Following leaching, glass fractions were digested according to conventional dissolution methods for Sr, Nd, Hf, and Pb chemical separation [Hart and Brooks, 1977; Münker *et al.*, 2001; Salters, 1994; Zindler *et al.*, 1979], as generally outlined in Appendix A. Due to a fire at Woods Hole Oceanographic Institution, clean lab facilities were not operational for over a year and thus the vast majority of the sample dissolution, column chemistry, and Hf isotopic measurement was completed in Vincent Salter's clean lab at the National High Magnetic Field Laboratory, on the campus of Florida State University. Mainly as a time-saving efficiency we conducted bulk dissolutions for 20 of 27 samples, meaning we digested between 3 – 4 grams of glass, which upon dissolution was split into concentration calibrated aliquots at various stages during the column separation process for each of the isotopic systems. Further details are presented in Appendix A.

### **Measurement Techniques**

Isotope measurements were conducted on the basalt glasses collected during two separate research cruises, Knorr162-Legs 7,8,9 and Melville-Vancouver 07, as well as a few samples collected by the RV Agulhas cruise 22 between 16° and 26°E in 1981 [le Roex, unpublished], and the PFS Polarstern between 11° and 16°E in 1986 [le Roex *et al.*, 1992]. Sr, Nd, Pb, and Hf isotopic compositions were measured on 27 basalt glasses and are reported in Table 2. Sr, Nd, and Pb measurements were conducted at Woods Hole Oceanographic Institution, using the ThermoFinnigan Neptune multi-collector ICP-MS. Detailed sample introduction methods and operating conditions for the Neptune are presented in Appendix A.2. He compositions were measured on 19 glasses, combined with existing  $^3\text{He}/^4\text{He}$  values [Georgen *et al.*, 2003], and presented in Table 3.

In run external reproducibility for Sr standard measurements of *NIST SRM 987* yielded an average  $^{87}\text{Sr}/^{86}\text{Sr}$  of  $0.710266 \pm 13$  ( $2\sigma$ ,  $n=15$ ). Day to day replication of separate sample aliquots from the same dissolution yielded a reproducibility of 16 ppm. Similar in run measurements of Nd standard *NIST LaJolla* gives an average value of  $0.511825 \pm 8$  ( $2\sigma$ ,  $n=10$ ). Pb isotopic values were measured on the Neptune, using a Tl-spiked internal standard. Any daily 'drift' due to Tl mass bias is corrected using linear interpolation. External precision from repeat analysis of NBS-981 is represented by average 'daily' values of  $^{206}\text{Pb}/^{204}\text{Pb} = 16.933 \pm 2$  ( $2\sigma$ ,  $n=34$ ),  $^{207}\text{Pb}/^{204}\text{Pb} = 15.485 \pm 3$  ( $2\sigma$ ,  $n=34$ ),  $^{208}\text{Pb}/^{204}\text{Pb} = 36.678 \pm 9$  ( $2\sigma$ ,  $n=34$ ). External long-term reproducibility on the Neptune for NBS-981 is reported in Hart *et al.*, [Hart *et al.*, 2003], and is generally ~ 100 ppm. All data is normalized to NBS-981 values of Todt *et al.*, [1996].

Hafnium isotopic measurements for 20 of 27 samples reported in Table 2 were carried out at NHMFL by HOT-SIMS techniques [Bizimis *et al.*, 2003; Salters, 1994; Salters and Zindler, 1995] on the Lamont ISOLAB [England *et al.*, 1992]. External reproducibility over a 2-year period was measured by repeat runs on JMC-475, with  $^{176}\text{Hf}/^{177}\text{Hf} = 0.282200 \pm 31$  ( $2\sigma$ ,  $n=44$ ) [Bizimis *et al.*, 2003]. Measurement of JMC-475 in an immediate window around the time when these samples were run gives external

reproducibility less than 1 epsilon unit, with  $^{176}\text{Hf}/^{177}\text{Hf} = 0.282185 \pm 18$  ( $2\sigma$ ,  $n=16$ ). All Hf isotopic compositions are reported relative to the accepted value of 0.282160 for the JMC-475 standard.

Additional Hf isotope measurements on 7 additional samples were conducted at WHOI on the Neptune multicollector ICP-MS. Hf column separation chemistry was done at WHOI as well and generally follows previously described methods (Appendix A) [Münker *et al.*, 2001; Salters, 1994]. External reproducibility from repeat runs of JMC-475 was  $^{176}\text{Hf}/^{177}\text{Hf} = 0.282149 \pm 3$  ( $2\sigma$ ,  $n=5$ ), which is much less than 1 epsilon unit. We also re-measured 3 samples that had originally been run at NHMFL via HOT-SIMS, and reproducibility for all 3 samples was  $< 32$  ppm ( $\sim 1$  epsilon unit). The 7 new samples measured at WHOI are noted in Table 2, and many of them have anomalously radiogenic  $^{176}\text{Hf}/^{177}\text{Hf}$ , relative to geographically surrounding samples. Therefore, some concern exists that the newly developed Hf column separation chemistry at WHOI may need further fine-tuning, with specific concern of Hf yield. In light of this, these samples are not included in plots of Hf data and are not considered during interpretation and discussion. These seven values will need to be reproduced before being considered valid.

$^3\text{He}/^4\text{He}$  compositions and  $^4\text{He}$  concentrations are reported in Table 3 for samples measured for this study together with previously measured glasses [Georgen *et al.*, 2003]. Fresh, vitreous glass fractions (0.5-2mm size) were handpicked using binocular microscope and cleaned in an ethanol/acetone solution, in an ultrasonic bath. Handpicking to remove altered or oxidized glass chips generally assured high-quality fractions. Samples were carefully described to document dominant vesicle size (relative to chip size), crystal percentage, and glass quality. Helium measurements were performed by crushing in vacuo [Georgen *et al.*, 2003] on the  $90^\circ$  sector mass spectrometer at Woods Hole Oceanographic Institution. Extraction lines for crushing, mass spectrometry, and blank values are described elsewhere [Kurz *et al.*, 1987; Kurz *et al.*, 1996].  $^4\text{He}$  blanks calculated during the course of these measurements were generally  $\sim 6 \times 10^{-11}$  ccSTP. Specific samples (noted in Table 3) were corrected for size/ratio dependence, but correction values were similar to or less than the internal measurement error. Average internal precision for all measurements is 0.04 ( $2\sigma$ ).

## 4. Results & Observations

### 4.1. Trace Element Composition

325 basalt glasses collected between  $9^\circ$ - $25^\circ\text{E}$  on the Southwest Indian Ridge were measured for trace element content and are displayed in Table 1. Select trace elements representing a range of incompatibility are plotted against MgO (Figure 2). The suite shows a wide range in concentrations, with La ranging from 1.3-51.1 (ppm), Ni from 13.3-211.5 (ppm), Sm from 1.3-8.2 (ppm), and Yb from 1.5-4.9 (ppm). Ni, which is compatible in olivine, displays a positive linear correlation between Ni and MgO, with individual trends within each tectonomagmatic province (Figure 2b). Rare earth elements are incompatible in the low-pressure fractionation assemblage of olivine, plagioclase, and clinopyroxene. Consequently the general increase in La, Sm, and Yb abundance with



decreasing MgO content is consistent with low-pressure fractionation (Figure 2a, c-d). Despite the general negative correlations between REEs and MgO, there are noticeable complexities to the trends; for example at a given MgO content the Narrowgate segment lavas have relatively high La and Sm and low Yb concentrations.

Plots of these same elements versus longitude (Figure 3) illustrate the along-axis variation in trace element abundance. Systematic trace element behavior for the orthogonal supersegment lavas shows increasing abundances from east to west for Sm, La, and Yb, and decreasing abundance for Ni. The Narrowgate segment lavas have significantly elevated La, slightly elevated Sm, highly variable Ni, and dominantly lower Yb, relative to the orthogonal supersegment lavas. Joseph Mayes Seamount lavas have abundances that generally follow the trends of the Narrowgate segment lavas, with similar Sm, moderately elevated La, dominantly low Ni, and Yb concentrations that span the range of the orthogonal supersegment lavas. Ni and La concentrations for the amagmatic accretionary segment lavas are similar, while Sm and Yb range to slightly lower values relative to the orthogonal supersegment lavas.

Trace element compositions extend from depleted N-MORB to highly elevated E-MORB type lavas. The orthogonal supersegment lavas are dominantly N-MORB, as characterized by global N-MORB values of  $(\text{La}/\text{Sm})_n < 1$ ,  $\text{Zr}/\text{Y} < 3.3$ ,  $\text{Ba}/\text{Nb} < 6.7$ ,  $\text{Zr}/\text{Nb} > 12$ ,  $\text{Lu}/\text{Hf} > 0.17$ ,  $\text{La}/\text{Yb} < 3.5$ , and  $\text{Th}/\text{U} < 3.3$  [le Roux *et al.*, 2002b (and references within); Sun and McDonough, 1989]. Trace element ratios vary systematically on the orthogonal supersegment, becoming more enriched in incompatible elements from east to west (i.e. increasing  $(\text{La}/\text{Sm})_n$ ,  $\text{Ba}/\text{Nb}$ ,  $\text{La}/\text{Yb}$ ,  $\text{Th}/\text{U}$  and decreasing  $\text{Lu}/\text{Hf}$  and  $\text{Zr}/\text{Nb}$ ), as seen in Figure 4. Orthogonal supersegment lavas from the western most volcanic segment (~16-17°E) have enriched trace element ratios classified as either transitional-MORB or E-MORB. Joseph Mayes Seamount lavas are dominantly E-MORB with moderately enriched trace element ratios, for example  $(\text{La}/\text{Sm})_n = 1.47\text{-}2.19$  and  $\text{Zr}/\text{Nb} = 6.75\text{-}10.15$ . The level of LREE and MREE enrichment is greatest in the Narrowgate segment lavas, where  $(\text{La}/\text{Sm})_n$  ranges from 2.3-4.6,  $\text{La}/\text{Yb}$  from 6.5-21.8, and  $\text{Zr}/\text{Y}$  from 5-9.6. The Narrowgate segment incompatible element ratios extend to much higher extremes and are on average elevated relative to the orthogonal supersegment lavas, whereas, Joseph Mayes Seamount lavas often range from transitional-MORB compositions, similar to lavas from the western end of the orthogonal supersegment, to moderately enriched-MORB. The compositional range of the amagmatic segment lavas nearly covers the range observed in the other provinces, with a few lavas having depleted compositions similar to depleted N-MORB from the eastern end of the orthogonal supersegment, but with the majority of the lavas falling in the transitional-MORB to moderate E-MORB compositions.

Southwest Indian Ridge trace element abundances are compared to global N-MORB compositions for the Mid-Atlantic Ridge, East Pacific Rise, and Indian Ocean [Su and Langmuir, 2002] in Figure 5. The average N-MORB compositions for each of the three ocean basins plot within the range of the orthogonal supersegment lavas. Trace element abundances for Joseph Mayes Seamount and the Narrowgate segment lavas extend too much higher values, with the highly incompatible elements Ce and Nb showing excellent

linear correlations with La. HREE elements such as Yb and Lu along with Sc are correlated for the majority of the orthogonal supersegment lavas, but closer inspection reveals that basalts from the 16°E segment (westernmost segment on the orthogonal supersegment) fall off the general trend to higher La (Figure 5c-e), and thus lie with T-MORBs and E-MORBs from the amagmatic accretionary segments and Joseph Mayes Seamount. Yb and Lu contents for the three oblique supersegment provinces show little correlation with La. On the other hand, Sc concentrations display a well-defined negative linear trend for the Joseph Mayes Seamount and the Narrowgate segment lavas. Concentrations of Sm and La show distinct trends for the Narrowgate segment and Joseph Mayes Seamount, and largely for the orthogonal supersegment, while the amagmatic accretionary segment lavas are generally split into two (maybe 3) linear trends and the lavas from the 16°E segment again fall off the main N-MORB trend to higher La. Separation among trends for each province is not seen for Ce and Nb versus La where the entire suite shows a positive linear trend intersecting the origin, implying similar compatibilities for Ce, Nb, and La. However, overall Figure 5 illustrates a significant difference in behavior between LREE and HREE that is reflected by variable compositions and trends both within the orthogonal supersegment lavas and among the four tectonomagmatic provinces. This suggests variable source compositions or varying extents of melting, or both.

Primitive upper mantle 'PUM' [McDonough and Sun, 1995] normalized trace element abundance patterns are plotted in Figure 6 (a-d) displaying "spidergrams" of each lava from the four tectonomagmatic provinces, with the most compatible elements on the right with increasing incompatibility to the left. Typical depleted N-MORBs with low LREE/HREE relative to PUM, but abundances generally higher than PUM have flat or slightly concave downward patterns characterizing most of the lavas from the orthogonal supersegment and numerous lavas from the amagmatic accretionary segments (Figure 6c,d). E-MORBs have different patterns, characterized by elevated highly incompatible LREE and LILE abundances, relative to HREE. The Narrowgate segment lavas have the most incompatible element enriched patterns, with LILE and LREE abundances up to 100 times primitive upper mantle. Joseph Mayes Seamount lavas are also incompatible element enriched, having 10 to 50 times PUM. More than half of the amagmatic accretionary segment lavas have trace element patterns with LILE and LREE concentrations greater than 10 times PUM, while the rest of the lavas, along with nearly all of the orthogonal supersegment lavas, with the exception of most 16°E segment lavas, have N-MORB trace element patterns. The range in absolute abundance of the orthogonal supersegment basalts is bound by Dredge 26 and Dredge 2, the most LREE depleted and LREE enriched, respectively, and not coincidentally dredged from the easternmost and westernmost volcanic segments on the orthogonal supersegment. This is consistent with a systematic gradient in source composition beneath the orthogonal supersegment, as suggested by major element measurements in Chapter 2.

Overall differences in pattern shape are even more apparent in Figure 6e despite the number of patterns plotted. A couple specific areas of interest are highlighted by the rectangles in all the panels of Figure 6, showing the variation in PUM-normalized Sr



abundance and the differences in Nb/Ta ratios both within and among the individual provinces. Another very subtle but potentially important difference is Hf/Sm, which for the Narrowgate segment lavas is  $< 1$  and for the majority of the other lavas is  $> 1$ .

#### 4.2. Isotopic Composition

The Southwest Indian Ridge lavas from 9°-25°E span a substantial range in isotopic compositional space. The heterogeneity is prevalent throughout all the isotopic systems presented and discussed here, including Sr, Nd, Pb, Hf, and He, with the data listed in Table 2.

Nd-Sr isotopic variation forms a negative linear trend of decreasing  $^{143}\text{Nd}/^{144}\text{Nd}$  with increasing  $^{87}\text{Sr}/^{86}\text{Sr}$ , typical of the mantle array (Figure 7a).  $^{143}\text{Nd}/^{144}\text{Nd}$  varies from  $0.513101 \pm 12$  –  $0.512786 \pm 46$  ( $2\sigma$  in last decimal place of reported value) and  $^{87}\text{Sr}/^{86}\text{Sr}$  from  $0.70248 \pm 22$  –  $.703631 \pm 12$  ( $2\sigma$ ), reflecting a continuous variation from depleted N-MORB to radiogenic E-MORB compositions. The suite is shifted to slightly lower  $^{143}\text{Nd}/^{144}\text{Nd}$  for a given  $^{87}\text{Sr}/^{86}\text{Sr}$ , relative to Indian Ocean MORB, placing it at the lower edge of the global MORB data field. The depleted end of our basalt array, represented by the orthogonal supersegment lavas, have lower  $^{143}\text{Nd}/^{144}\text{Nd}$  than most Pacific N-MORB (at a given  $^{87}\text{Sr}/^{86}\text{Sr}$ ), and noticeably lower  $^{87}\text{Sr}/^{86}\text{Sr}$  than Indian Ocean N-MORB. Modestly radiogenic  $^{87}\text{Sr}/^{86}\text{Sr}$  values at lower  $^{143}\text{Nd}/^{144}\text{Nd}$  are present in the amagmatic accretionary segment and Joseph Mayes Seamount lavas, but the Narrowgate segment lavas have the most radiogenic  $^{87}\text{Sr}/^{86}\text{Sr}$  and unradiogenic  $^{143}\text{Nd}/^{144}\text{Nd}$  of the suite, extending to enriched compositions similar to Bouvet Island. In fact, these values are some of the most radiogenic Sr compositions on the SWIR (along with anomalously high values between 39°-41°E [Mahoney *et al.*, 1992]). The Sr-Nd isotopic array defined by this suite covers significant isotopic space, extending from DMM-like compositions towards EM1 or EM2 mantle components.

The variation in Pb isotopic ratios also covers a significant range from relatively unradiogenic  $^{206}\text{Pb}/^{204}\text{Pb}$  of  $18.418 \pm 12$  to radiogenic  $^{206}\text{Pb}/^{204}\text{Pb}$  of  $19.508 \pm 2$  ( $2\sigma$ ). The depleted N-MORB have more radiogenic  $^{206}\text{Pb}/^{204}\text{Pb}$  than average Indian Ocean N-MORB or Pacific N-MORB. E-NORB from the Narrowgate segment corroborate previous measurements by *le Roex et al.*, [1992] that recorded the most radiogenic  $^{206}\text{Pb}/^{204}\text{Pb}$  along the Southwest Indian Ridge, up to  $19.042 \pm 9$ .  $^{207}\text{Pb}/^{204}\text{Pb}$  and  $^{208}\text{Pb}/^{204}\text{Pb}$  ratios range from  $15.492 \pm 12$  to  $15.642 \pm 6$  and  $37.965 \pm 38$  to  $39.454 \pm 4$ , respectively, spanning much of the range covered by global N-MORB (Figure 7g & h). The suite in general falls along a loose linear trend parallel, but offset to higher  $^{207}\text{Pb}/^{204}\text{Pb}$  for a given  $^{206}\text{Pb}/^{204}\text{Pb}$ , relative to the northern hemisphere reference line “NHRL” (Figure 7h). In the plot of  $^{208}\text{Pb}/^{204}\text{Pb}$  vs.  $^{206}\text{Pb}/^{204}\text{Pb}$  the lavas from the orthogonal supersegment fall along the NHRL, while the amagmatic accretionary segment, Joseph Mayes Seamount, and the Narrowgate segment lavas form a separate linear trend showing increasing divergence from the NHRL at higher  $^{206}\text{Pb}/^{204}\text{Pb}$ . Pb isotopic compositions in the Narrowgate segment lavas plot near the compositions of Bouvet Island lavas.

The most depleted N-MORBs from the orthogonal supersegment and the amagmatic accretionary segments have higher  $^{206}\text{Pb}/^{204}\text{Pb}$  at a given  $^{87}\text{Sr}/^{86}\text{Sr}$  and  $^{143}\text{Nd}/^{144}\text{Nd}$  than the vast majority of Indian Ocean MORB (Figure 7 e & f). Atlantic Ocean MORB does span the compositional space of the orthogonal supersegment lavas, stretching between DMM and HIMU. In both  $^{87}\text{Sr}/^{86}\text{Sr}$   $^{206}\text{Pb}/^{204}\text{Pb}$  and less so for  $^{143}\text{Nd}/^{144}\text{Nd}$  versus  $^{206}\text{Pb}/^{204}\text{Pb}$  the orthogonal supersegment lavas define a separate trend from the other provinces. The orthogonal supersegment basalts have nearly constant  $^{87}\text{Sr}/^{86}\text{Sr}$  and only slightly decreasing  $^{143}\text{Nd}/^{144}\text{Nd}$  with increasing  $^{206}\text{Pb}/^{204}\text{Pb}$ , defining linear trends that lie between DMM and HIMU. The lavas from the amagmatic accretionary segment, Joseph Mayes Seamount, and the Narrowgate segment define a strong linear trend of increasing  $^{87}\text{Sr}/^{86}\text{Sr}$  with increasing  $^{206}\text{Pb}/^{204}\text{Pb}$ , and a less well-defined trend of decreasing  $^{143}\text{Nd}/^{144}\text{Nd}$  with more radiogenic  $^{206}\text{Pb}/^{204}\text{Pb}$ . Both trends however, terminate in close proximity to Bouvet Island compositions, which lies between the HIMU and EM2 mantle components.

Relative to most MORB from the global database, lavas from this study sit at lower  $^{176}\text{Hf}/^{177}\text{Hf}$  for a given  $^{143}\text{Nd}/^{144}\text{Nd}$  and  $^{87}\text{Sr}/^{86}\text{Sr}$ , although a few Indian Ocean basalts do extend to lower  $^{176}\text{Hf}/^{177}\text{Hf}$  with decreasing  $^{143}\text{Nd}/^{144}\text{Nd}$  and increasing  $^{87}\text{Sr}/^{86}\text{Sr}$  (Figure 7c & d).  $^{176}\text{Hf}/^{177}\text{Hf}$  values range from  $0.282963 \pm 12$  ( $2\sigma$ ) to  $0.283235 \pm 18$  ( $2\sigma$ ), equivalent to a range in  $\epsilon\text{Hf}$  of 6.75-16.37 (using  $^{176}\text{Hf}/^{177}\text{Hf}_{\text{CHUR}} = 0.282772$  [Blichert-Toft and Albarede, 1997]). Although there is only a weak positive correlation of decreasing  $^{176}\text{Hf}/^{177}\text{Hf}$  with decreasing  $^{143}\text{Nd}/^{144}\text{Nd}$ , and negative correlation between  $^{176}\text{Hf}/^{177}\text{Hf}$  and  $^{87}\text{Sr}/^{86}\text{Sr}$ , the lavas are distinctly lower than average MORB from any of the three ocean basins. Hf-Nd and Hf-Sr compositions for the enriched lavas are more similar to OIBs (especially Indian Ocean hotspots) than to N-MORB, but at least for Hf-Nd systematics do not diverge significantly from the general trend of the “mantle array” (as defined by over 1500 Hf and Nd data points both published and unpublished from J. Blichert-Toft and others; [Blichert-Toft and Albarede, 1997; Patchett et al., 1984; Vervoort et al., 1999]). N-MORBs from the orthogonal supersegment and amagmatic accretionary segments also have generally lower  $^{176}\text{Hf}/^{177}\text{Hf}$  for a given  $^{206}\text{Pb}/^{204}\text{Pb}$ . The suite defines a negative trend of decreasing  $^{176}\text{Hf}/^{177}\text{Hf}$  with increasing  $^{206}\text{Pb}/^{204}\text{Pb}$ , which is opposite the poorly constrained trend seen for the Indian Ocean MORB. However, Hf-Sr, Hf-Nd, and Hf- $^{206}\text{Pb}/^{204}\text{Pb}$  systematics show linear enrichment trends from depleted N-MORB to more radiogenic compositions similar to Bouvet Island.

The large range in Sr, Nd, Hf, and Pb isotopic heterogeneity visible in isotope-isotope space is also clearly illustrated along-axis. Systematic east to west trends to more radiogenic  $^{87}\text{Sr}/^{86}\text{Sr}$  and Pb isotopic values, and less radiogenic  $^{143}\text{Nd}/^{144}\text{Nd}$  are well defined by the orthogonal supersegment lavas (Figure 9).  $^{176}\text{Hf}/^{177}\text{Hf}$  shows a slight decreasing trend from east to west, but is more or less constant. Lavas from the Narrowgate segment are markedly enriched relative to the orthogonal supersegment, with distinctly more radiogenic  $^{87}\text{Sr}/^{86}\text{Sr}$ ,  $^{206}\text{Pb}/^{204}\text{Pb}$ , and  $^{208}\text{Pb}/^{204}\text{Pb}$ , and only slightly elevated  $^{207}\text{Pb}/^{204}\text{Pb}$ .  $^{143}\text{Nd}/^{144}\text{Nd}$  is significantly less radiogenic than the most unradiogenic  $^{143}\text{Nd}/^{144}\text{Nd}$  from the orthogonal supersegment, and  $^{176}\text{Hf}/^{177}\text{Hf}$  is only moderately less radiogenic. The amagmatic accretionary segment and Joseph Mayes Seamount lavas are intermediate between the depleted N-MORB from the eastern end of

the orthogonal supersegment and the highly elevated E-MORB from the Narrowgate segment, with no longitudinal trends visible. The amagmatic accretionary segment and Joseph Mayes Seamount lavas have Pb isotopic compositions very similar to the western end of the orthogonal supersegment, Nd and Sr isotopic compositions between the Narrowgate segment and western end of the orthogonal supersegment, and highly variable Hf isotopic compositions. It is clear from the along-axis isotopic heterogeneity that the MORB source composition is quite variable throughout the entire study area, but that the simple systematic variation observed along the orthogonal supersegment is not present between 9°-16°E.

As reported in *Georgen et al.*, [2003], measured  $^3\text{He}/^4\text{He}$  in basalt glasses from 9°-25°E along the SW Indian Ridge are dominantly lower than observed at many normal mid-ocean ridges.  $^3\text{He}/^4\text{He}$  values measured for this study (Table 3), with  $^4\text{He}$  concentrations at or above the 0.4 uccSTP/g cutoff used by *Georgen et al.*, [2003] and adopted here, vary from  $5.64 \pm 0.04$  ( $2\sigma$ ) -  $7.27 \pm 0.04$  ( $2\sigma$ ), which is nearly identical to the range of the combined data set ( $5.64 \pm 0.04$  ( $2\sigma$ ) -  $7.29 \pm 0.04$  ( $2\sigma$ )). Helium, despite being volatile and thus easily degassed, behaves fairly systematically along this ultraslow-spreading ridge, especially the orthogonal supersegment.  $^3\text{He}/^4\text{He}$  ratios are highest in N-MORB lavas to the east ( $\sim 7.3$ ) and gradually decrease to the west, where lavas from the westernmost volcanic segment of the orthogonal supersegment have  $^3\text{He}/^4\text{He}$  equal  $\sim 6.5$  (Figure 9d). Lavas from the Narrowgate segment and Joseph Mayes Seamount have on average lower  $^3\text{He}/^4\text{He}$  than the orthogonal supersegment lavas, but are relatively quite variable, with  $^3\text{He}/^4\text{He}$  of  $5.93 \pm 0.04$  -  $6.63 \pm 0.06$  and  $5.64 \pm 0.04$  -  $6.61 \pm 0.05$ , respectively (compared to MORBs in general this range is very tight). Amagmatic accretionary segment lavas have  $^3\text{He}/^4\text{He}$  compositions that generally overlap the orthogonal supersegment, with values between  $6.2 \pm 0.07$  and  $6.94 \pm 0.05$ . It should be noted, and will be discussed in greater detail later, that the overall lower  $^3\text{He}/^4\text{He}$ , and the gradually decreasing  $^3\text{He}/^4\text{He}$  trend, between 25° and 9°E, does not continue to the west of Shaka Fracture Zone. In fact,  $^3\text{He}/^4\text{He}$  ranges widely from typical N-MORB values of 8 to elevated “Bouvet-like”  $^3\text{He}/^4\text{He}$  of  $\sim 15$  between the Shaka FZ and the Bouvet triple junction, suggesting that the large-offset Shaka FZ may provide some sort of petrologic or geochemical boundary.

## 5. Petrogenesis

### 5.1. Effects of Fractional Crystallization on Trace Elements

The majority of trace elements have mineral/melt partition coefficients much less than one with regard to the common crystallizing phases (i.e. olivine, plagioclase, and clinopyroxene) involved in MORB differentiation. Thus, during fractional crystallization they behave incompatibly and are accumulated in the decreasing melt volume. Strontium is an exception, as it is compatible in plagioclase, with a  $K_{\text{id}} \approx 1.5$ -2.5 [*Bindeman et al.*, 1998]. Therefore, fractional crystallization of plagioclase from basaltic magma commonly results in depleted Sr contents in the evolving and eventually erupted lava. Evidence of this process is illustrated by trace element abundance patterns (Figure

6), where negative Sr anomalies (lower Sr relative to the expected Sr content interpolated between Nd and Zr) dominate the patterns for the orthogonal supersegment, amagmatic accretionary segment, and Joseph Mayes Seamount lavas (Figure 6a, c-d). However positive Sr anomalies characterize the Narrowgate segment trace element patterns (Figure 6b), providing chemical evidence that is consistent with plagioclase modal abundances (Table 2 of Chapter 2) and petrographic information suggesting plagioclase accumulation and resorption. For example, although sample 61-71 does not have an extreme modal abundance of plagioclase (5.8%) and actually is one of only a couple Narrowgate segment lavas that have a negative Sr anomaly, petrographic investigation finds nearly half of the phenocrysts examined show signs of resorption (i.e. cusped crystal edges). The same is true for a few lavas from both the amagmatic accretionary segment and orthogonal supersegment, where positive Sr anomalies are correlated with elevated plagioclase modes and petrographic features of plagioclase resorption.

Furthermore, although Eu has a  $K_d \approx 0.44$  [Fujimaki *et al.*, 1984] and is incompatible in plagioclase, Sm and Gd flank Eu and have  $K_d$ 's an order of magnitude lower, and thus are highly incompatible. As a result, the ratio Eu/Eu\* (where Eu\* is the interpolated value between primitive mantle-normalized values of Sm and Gd, calculated using  $\text{Eu}/\text{Eu}^* = \text{Eu}_n / (\text{Sm}_n \times \text{Gd}_n)^{1/2}$ ) is useful in distinguishing plagioclase accumulation ( $\text{Eu}/\text{Eu}^* > 1$ ) from plagioclase crystal fractionation ( $\text{Eu}/\text{Eu}^* < 1$ ) (Figure 4d). Indeed, detailed inspection of individual lava chemistry finds that lavas with  $\text{Eu}/\text{Eu}^* > 1$  also have positive Sr anomalies, as well as elevated  $\text{Al}_2\text{O}_3$  abundances (Figure 5 – Chapter 2), thus providing additional evidence of plagioclase accumulation and resorption.

Much of the major element variation documented in Chapter 2 is the result of low-pressure fractional crystallization. Similarly, crystallization of common basaltic phases influences the trace element concentrations. A linear negative correlation between Sm and MgO and positive correlation between Ni and MgO (Figure 2) are examples of trace element abundance variation related to low-pressure differentiation. La and Yb versus MgO show less correlation, with a greater range in La and Yb for a given MgO content, suggesting significant heterogeneity among parental melt compositions. That La (with a lower D) is more variable than Sm is not altogether surprising, as elevated  $(\text{La}/\text{Sm})_n$  is indicative of low degrees of melting and/or an incompatible element enriched source. However, greater variability in Yb (with a higher D) relative to Sm suggests the involvement of a residual phase in which Yb and other HREE are more compatible than Sm.

In an attempt to remove the effects of low-pressure crystal fractionation from the trace element compositional variation, trace element abundances are corrected to 8 wt% MgO, similar to the corrections applied to major element oxides. Trace element concentrations are projected to 8 wt% MgO by initially correcting Ce, using the equation

$\text{Ce}_8 = 10^{[\log \text{Ce} - 0.11(8 - \text{MgO})]}$  [Plank and Langmuir, 1992]. The rest of the trace element

concentrations are then adjusted accordingly, based on the following equation

$\text{La}_8 = 10^{[\log \text{La} - \log(\text{Ce}/\text{Ce}_8)]}$  [Meyzen *et al.*, 2003].

To assess the influence of fractional crystallization on trace element content, Figure 8 compares  $(\text{La}/\text{Sm})_n$  versus  $\text{La}_n$  for the raw unadjusted data with  $(\text{La}_8/\text{Sm}_8)_n$  versus  $(\text{La}_8)_n$  for fractionation corrected data. Both plots show strong positive correlations, as  $\text{La}_n$  abundance varies 5-fold in the raw data and 4-fold in the corrected data, and  $(\text{La}/\text{Sm})_n$  shows very similar ranges in both a) and b). As *Hofmann* [2003] points out, the coherent relationship and strong positive correlation between  $(\text{La}/\text{Sm})_n$  and  $\text{La}_n$ , for global MORB data, suggests fractional crystallization has little control on REE abundances, as varying degrees of crystallization would effect La and Sm similarly. The Southwest Indian Ridge data show the same robust positive correlation as the global data for both raw data and corrected data, with a substantial range in  $(\text{La}/\text{Sm})_n$ . Additionally, the fact that the range in  $\text{La}_n$  abundance changes very little when corrected for low-pressure fractional crystallization, indicates that the abundance variation is not significantly influenced by crystallization. Therefore, the range in  $(\text{La}/\text{Sm})_n$  reflects a greater variability of lanthanum abundance versus samarium abundance, and is interpreted to be a function of source variation or varying degrees of partial melting rather than low-pressure differentiation.

## 5.2. Along-Axis Variations

Small-scale isotopic equilibrium between mantle and melt underpins the longstanding tenant of isotope geochemistry that the isotopic composition of the liquid produced by mantle melting can be inferred from the isotopic composition of the mantle residue, and vice versa [*Hofmann and Hart*, 1978]. In this way a homogeneous mantle source with  $^{87}\text{Sr}/^{86}\text{Sr} = 0.7025$  will produce a melt with the same  $^{87}\text{Sr}/^{86}\text{Sr}$  regardless of whether it is melted 1%, 25%, or completely. However, the length-scale at which isotopic equilibrium in the mantle is maintained has long been debated [*Zindler and Hart*, 1986]. Diffusive equilibrium is a function of temperature, age, and chemistry, but the actual scale of chemical or physical heterogeneities in the mantle is poorly constrained. Thus, if a chemical heterogeneity in the mantle is large enough to remain out of diffusive equilibrium with the host mantle it can, when melted, impart a trace element and isotopic signature on that melt, different from that of the host. Chemical heterogeneity within the upper mantle can be introduced by a physically distinct lithology (i.e. veining), thereby creating a multi-lithology mantle, or by a chemical process such as metasomatism, which adds trace element and/or isotopic variation, but maintains a single lithology mantle peridotite. Distinguishing between a heterogeneous single lithology upper mantle and a multi-lithology heterogeneous upper mantle is difficult, but as we attempt to show in the following sections some geologic, geophysical, and chemical constraints can be used to address this issue.

### *Isotopic Compositions – Local Mantle Heterogeneity?*

Large variations observed in long-lived Sr, Nd, Pb, and Hf isotope compositions indicate the presence of an isotopically heterogeneous MORB source beneath 9°-25°E.  $^{87}\text{Sr}/^{86}\text{Sr}$ ,  $^{143}\text{Nd}/^{144}\text{Nd}$ ,  $^{176}\text{Hf}/^{177}\text{Hf}$ ,  $^{206}\text{Pb}/^{204}\text{Pb}$ ,  $^{207}\text{Pb}/^{204}\text{Pb}$ ,  $^{208}\text{Pb}/^{204}\text{Pb}$ , and  $^3\text{He}/^4\text{He}$ , all mark an anomalous spike at the 35 km long Narrowgate segment, which diverges from a systematic along-axis trend of increasing  $^{87}\text{Sr}/^{86}\text{Sr}$ ,  $^{206}\text{Pb}/^{204}\text{Pb}$ ,  $^{207}\text{Pb}/^{204}\text{Pb}$ , and



$^{208}\text{Pb}/^{204}\text{Pb}$ , and decreasing  $^{143}\text{Nd}/^{144}\text{Nd}$ ,  $^{176}\text{Hf}/^{177}\text{Hf}$ , and  $^3\text{He}/^4\text{He}$  extending east to west from 25°E on the orthogonal supersegment to 10°E on the oblique supersegment (Figure 9). At first glance the anomalous enrichment at the Narrowgate segment would appear to suggest the presence of local mantle heterogeneity. However lava compositions at Joseph Mayes Seamount and some scattered within the amagmatic accretionary segments, while not as highly enriched as the Narrowgate segment lavas, on average have higher Sr and Pb and lower Nd and He than orthogonal supersegment lavas (Figure 9 and Table 4).  $^{176}\text{Hf}/^{177}\text{Hf}$  is highly variable in the amagmatic accretionary segment lavas and a single Joseph Mayes Seamount lava is similar in composition to the orthogonal supersegment. The range in isotopic compositions among the three provinces of the oblique supersegment clearly indicates that whatever source lithology is contributing the long-lived isotopic signature to the Narrowgate segment lavas is not isolated to that segment, but is in fact present to a lesser degree at Joseph Mayes Seamount and in scattered lavas on the amagmatic accretionary segment. Furthermore, the systematic isotopic variation on the orthogonal supersegment suggests that this isotopic source signature is progressively increasing from east to west with the largest contribution observed at the 16°E segment. The observed source heterogeneity thus redefines the orthogonal supersegment mantle source from previous observations [Janney *et al.*, 2005; Mahoney *et al.*, 1992] based on a much broader sample spacing that characterized the 17°-25°E section as typical Atlantic N-MORB.

Additional arguments against the Narrowgate segment lavas being generated by a local “point source” mantle heterogeneity cite the presence of non-symmetrical eastward pointing v-shaped ridges that extend off-axis from the Narrowgate segment and at least two moderately robust volcanic segments farther to the east on the orthogonal supersegment (Figure 1). The orientation of these features indicates eastward plate-driven segment migration consistent with the continued growth of the oblique supersegment since its inception ~22-30 Ma [Dick *et al.*, 2003]. That these geologically recent trends give an opposite sense of movement relative to the westward pointing v-shaped trace left by the passage of the plate over the Bouvet plume, indicates shallow plate-driven processes are involved in the stability of this region. The contribution of a source lithology responsible for the enriched isotopic signature in lava throughout the oblique supersegment, but focused at the Narrowgate segment, together with the relative motions indicated by the Narrowgate segment and Bouvet hotspot, are consistent with an enriched source lithology that is dispersed beneath the oblique supersegment and to a lesser extent beneath the western portion of the orthogonal supersegment.

### ***Trace Element Concentrations and Ratios***

In addition to the along-axis variation in isotopic compositions, the trace element concentrations and ratios display remarkable along-axis systematic behavior. This is illustrated by representative trace element abundances (Figure 3) and abundance ratios (Figure 4) plotted against longitude, where particular attention is drawn to the orthogonal supersegment lavas (16°-25°E) by the robust systematic east to west variations. Further to the west, the lavas comprise three very different tectonomagmatic environments (i.e. ridge segments) that show less systematic behavior, albeit distinct chemistry from one

another, and from the orthogonal supersegment basalts. Below we will discuss in detail the variations in content and composition along-axis.

Although the highly incompatible trace elements (i.e. LREEs and LILEs) display smooth systematic enrichment trends along the orthogonal supersegment this type of behavior is not matched by the middle rare-earth and heavy rare-earth elements (Figure 10).  $\text{La}_8$  steadily increases from east to west between 17° and 25°E, but at the 16°E segment displays a slightly larger range to both higher and lower  $\text{La}_8$  than predicted by the systematic trend. A less well-defined trend for  $\text{Sm}_8$  increases smoothly from 25° to 17°E, with the 16°E segment lavas largely below the dominant orthogonal supersegment trend.  $\text{Yb}_8$  contents are constant with only the slightest increase in content east to west along the orthogonal supersegment and a small jog to lower values at the 16°E segment. The systematic trends of increasing  $\text{La}_8$ ,  $\text{Sm}_8$ , and less so for  $\text{Yb}_8$  content to the west on the orthogonal supersegment are well correlated with isotopic variations indicating trace element variations largely attributed to source heterogeneity. The systematic nature of the variation suggests a progressively increasing influence of an incompatible element and radiogenic isotope enriched source composition. The differences in the  $\text{La}_8$ ,  $\text{Sm}_8$ , and  $\text{Yb}_8$  trends reflects the changing source composition and suggests the involvement of a phase in which Sm and Yb are more compatible than La. This is highlighted by the inverse correlation between  $\text{La}_8$  and  $\text{Sm}_8$  or  $\text{Yb}_8$  at the 16°E segment, where  $\text{La}_8$  continues to increase and  $\text{Sm}_8$  and  $\text{Yb}_8$  decrease, relative to their respective trends. It is also telling to note that both  $\text{Sm}_8$  and  $\text{Yb}_8$  for the orthogonal supersegment lavas display a larger standard deviation, relative to  $\text{La}_8$ , another indication of differing trace element behavior related to source variation.

On the oblique supersegment the fractionation-corrected contents of  $\text{La}_8$ ,  $\text{Sm}_8$ , and  $\text{Yb}_8$  show very different behavior for each of the tectonomagmatic provinces. At the Narrowgate segment the differences are quite distinct, as  $\text{La}_8$  is highly enriched,  $\text{Yb}_8$  is highly depleted, and  $\text{Sm}_8$  is moderately lower, relative to the orthogonal supersegment lavas. The Joseph Mayes Seamount lavas have  $\text{La}_8$  equivalent to the 16°E segment,  $\text{Sm}_8$  level with the Narrowgate segment, and  $\text{Yb}_8$  intermediate between the orthogonal supersegment and the Narrowgate segment concentrations. As has been observed for major element and isotopic compositions, the amagmatic accretionary segment lavas cover a large range of trace element space, with  $\text{La}_8$  ranging from moderate Narrowgate segment to depleted orthogonal supersegment contents,  $\text{Sm}_8$  covering the range exhibited by the other provinces, and  $\text{Yb}_8$  ranging from the most elevated Narrowgate contents to the most elevated orthogonal supersegment contents. The large overall range in trace element abundances in association with heterogeneous isotopic compositions throughout the region suggests the influence of a LREE enriched/HREE depleted melt component that is focused beneath the Narrowgate segment and to a lesser extent beneath Joseph Mayes Seamount. The heterogeneity of the trace element contents for the amagmatic accretionary segment lavas suggests the presence of melt dominated by both depleted peridotite melt and LREE enriched/HREE depleted melt components in varying proportions. That both melt components are erupted on the seafloor indicates poor

homogenization of melts, which may be related to the diminished volume of melt produced along segments with ultraslow upwelling rates.

The extreme separation of  $\text{Yb}_8$  to lower values (with little overlap) and the small range in content indicates that melts produced beneath the Narrowgate segment are tapping a strikingly different source composition than beneath the orthogonal supersegment. The decoupling of LREE from HREE is not generally seen due to melting of spinel lherzolite consisting of spinel, olivine, orthopyroxene and clinopyroxene, as illustrated by the similar trends for  $\text{La}_8$ ,  $\text{Sm}_8$ , and less so for  $\text{Yb}_8$  along the orthogonal supersegment, where depleted peridotite is likely the dominant source lithology. The decoupling of La from Sm and La from Yb is more visible at the 16°E segment, and by inference indicates the growing influence of a melt component that was produced in the presence of a phase in which Sm and Yb are more compatible than La. The most likely phase common to MORB petrogenesis is garnet, as it is stable at higher pressures in the melting regime. Garnet will effectively withhold Sm and Yb during melting as  $D^{\text{Yb}}$  and  $D^{\text{Sm}} \gg D^{\text{La}}$  [Johnson, 1998; Salters and Longhi, 1999]. Therefore, elevated  $\text{La}_8$  and depressed  $\text{Yb}_8$  at the Narrowgate segment is consistent with melt generation involving residual garnet, however lavas farther to the west along the amagmatic accretionary segment reflect melts produce both with and without garnet present.

Further evidence of melting in the presence of garnet is illustrated by along axis variations in Lu/Hf (Figure 4). The orthogonal supersegment lavas actually show a slight decreasing trend from east to west, as Lu is more compatible in garnet than Hf, thereby decreasing Lu/Hf in the melt when residual garnet is present. It is therefore inferred that the Narrowgate segment lavas with the lowest Lu/Hf and minimal standard deviation are dominated by garnet melting. Higher Lu/Hf in the Joseph Mayes Seamount lavas and a large range in Lu/Hf for the amagmatic accretionary segment lavas reflect variable but lesser amounts of garnet produced melts mixing with depleted peridotite melts.

The along-axis variation trends for incompatible trace element concentrations and ratios, as well as isotopic compositions do indicate a highly heterogeneous mantle source beneath this portion of the SW Indian Ridge. Well-defined statistically robust linear correlations between incompatible element ratios and isotopic ratios supply further support for a heterogeneous mantle. Although linear trends like those in Figure 11 are not required to represent mixing of end-member melts that lie on opposite ends of the trend, the range in isotopic composition on the x-axis must be the result of mantle heterogeneity. Variation along the y-axis for  $(\text{La}/\text{Sm})_n$  and  $(\text{Nd}/\text{Sm})_n$  may be attributable to either varying degrees of melting or source heterogeneity. Simple melting calculations are applied to a plot of  $(\text{La}/\text{Sm})_n$  vs.  $^{87}\text{Sr}/^{87}\text{Sr}$  (Figure 12) in an attempt to begin to constrain how much of the trace element variation is due to source vs. process. Since isotopic ratios are not affected by melting it is not possible to derive Narrowgate segment lava with an elevated  $^{87}\text{Sr}/^{87}\text{Sr}$  composition by melting depleted MORB mantle (black X). Instead, constraining the Rb/Sr and  $^{87}\text{Sr}/^{87}\text{Sr}$  composition of DMM with the present-day  $^{87}\text{Sr}/^{87}\text{Sr}$  composition of the most radiogenic Narrowgate segment lava derives an enriched single lithology peridotite source. Since the Rb/Sr of DMM is determined by



the measured basalt compositions, the entire trace element composition of DMM is altered and thus  $(\text{La}/\text{Sm})_n$  for the “enriched SWIR-DMM source” (green X) is elevated. Aggregate fractional melting of this incompatible element and isotope enriched source composition to varying degrees is marked by green dashes ranging from 0.1 to 10 percent melting. Although melting this composition to 0.1% will generate  $(\text{La}/\text{Sm})_n$  similar to the Narrowgate segment lavas, there are a number of reasons why this small of a melt fraction should not be realistically considered for generating the Narrowgate segment lavas. Some of those reasons include extraction of such small melt fractions and generation of enough ocean crust. From these quick melting calculations it seems unlikely that a single lithology peridotite source would be capable of generating the incompatible element enriched lavas of the Narrowgate segment, and that a second source lithology may be necessary to generate the high  $(\text{La}/\text{Sm})_n$  and  $^{87}\text{Sr}/^{87}\text{Sr}$  that characterizes the melt component prevalent at Narrowgate.

### 5.3. Trace element modeling

It was observed through major element studies that the accumulation of various melt fractions from throughout the melting column [Klein and Langmuir, 1987; Langmuir *et al.*, 1992; McKenzie, 1985; McKenzie and Bickle, 1988] suggested the polybaric nature of mantle melting, and the possibility that partial melting was occurring as a fractional melting process. In a seminal study that analyzed the trace element composition of multiple clinopyroxenes from residual abyssal peridotites [Johnson *et al.*, 1990], it was documented that highly incompatible elements with similar distribution coefficients were highly fractionated, thereby indicating decompression mantle melting was occurring in a fractional manner rather than a batch equilibrium style. Numerous melting algorithms exist with batch melting and fractional melting serving as the end-member models, and each one has its own advantages and disadvantages. Despite the fact that liquids created by batch melting versus aggregated fractional melting have nearly indistinguishable compositions, we use the following expression for non-modal aggregate fractional melting,

$$\frac{\bar{C}_L}{C_0} = \left[ \frac{1}{F} \right] * \left[ 1 - \left( 1 - \frac{PF}{D_0} \right)^{(1/P)} \right]$$

taken from [Shaw, 1970], where  $\bar{C}_L$  is the elemental concentration in an aggregated melt,  $C_0$  is the concentration in the un-melted source,  $F$  is the extent of melting by weight,  $D_0$  is the bulk distribution coefficient in the initial solid, and  $P$  is the bulk distribution coefficient of the minerals in the proportion in which they enter the melt.  $D_0$  and  $P$  are derived from mineral/melt partition coefficients together with respective modes for the initial source and the phases entering the melt (i.e. melting equation). Bulk solid  $D$ s and bulk melt  $D$ s are specifically chosen from the literature for the appropriate lithologies and mineral compositions and will be specifically described when needed. Since  $F$  is assigned, the only other variable is  $C_0$ , the initial source composition, and it is described below.

### ***Generation of N-MORB from depleted MORB mantle (DMM)***

The vast majority of basalts collected from the orthogonal supersegment and a large portion of those from the amagmatic accretionary segment have major element, trace element, and isotopic compositions that characterize them as “normal”-MORB. N-MORBs from this study are most similar isotopically to Atlantic/Pacific Ocean N-MORB with distinctively more radiogenic  $^{206}\text{Pb}/^{204}\text{Pb}$  than Indian Ocean N-MORB (Figure 7). This was previously documented [Janney *et al.*, 2005; le Roex *et al.*, 1989; le Roex *et al.*, 1992; Mahoney *et al.*, 1992; Mahoney *et al.*, 1989] to suggest that the 17°-25°E region was the easternmost extent of Atlantic/Pacific-type mantle, as much less radiogenic  $^{206}\text{Pb}/^{204}\text{Pb}$  exists to the east [Mahoney *et al.*, 1989]. A great deal of compositional variation exists from N-MORB to E-MORB, thus a logical first step toward determining a MORB source consistent with the chemical variation across the entire basalt suite, is modeling the source and degree of melting responsible for generation of Southwest Indian Ridge (9°-25°E) N-MORB.

To do this we chose the recently published trace element composition for depleted MORB mantle (DMM) (Table 5) [Workman and Hart, 2005] as our starting mantle composition. As the source region to mid-ocean ridge basalts, this estimated composition combines 1) trace element contents of clinopyroxene from abyssal peridotites, 2) heavy-element isotopic evolution from primitive upper mantle (PUM), and 3) canonical trace element ratios in MORBs, producing a generally smooth, average trace element pattern reflecting DMM. The first part of the trace element pattern is derived using the global database of abyssal peridotite cpx trace element depletion trends and modal abundances [Dick and Fisher, 1984; Dick and Natland, 1996; Hellebrand *et al.*, 2002; Johnson and Dick, 1992; Johnson *et al.*, 1990; Salters and Dick, 2002; Tartarotti *et al.*, 2002]. Average long-lived isotopic compositions (Sr, Nd, Pb) for normal-MORB are taken from Su and Langmuir, [2002] and incorporated into the trace element pattern by calculating present day parent-daughter ratios using a 3 Ga gradual depletion model (please see [Workman and Hart, 2005] for details). The final pieces of the trace element pattern are derived from canonical trace element ratios including, Ce/Pb, Nb/Ta, Nb/U, and Ba/Rb.

Trace element compositions for aggregate liquids are generated from this depleted MORB mantle (DMM) using a model for non-modal aggregate fractional melting within the spinel stability field. Source D's are taken from Workman & Hart, [2005] and the melt D's are a combination of mineral/melt partition coefficients from Kelemen *et al.*, [2003] and spinel lherzolite melting coefficients from Wasylenki *et al.*, [2003]. Figure 13 shows a series of trace element patterns that are normalized to primitive upper mantle (PUM) with the most incompatible elements on the left and increasing in compatibility to the right. As a representative composition of N-MORB from between 9°-25°E on the Southwest Indian Ridge, the red trace element pattern is an average of Dredge 25 and 26 lava compositions. Although these lavas may not be the most depleted from the suite, they lie at the eastern end of the orthogonal supersegment well removed from any E-MORBs. The DMM trace element composition is shown as a black line and by definition lies at concentrations below PUM, which is equal to 1. Aggregate fractional melting of DMM produces modeled melt compositions that we attempt to match with the measured



N-MORB pattern. The best match to the average N-MORB composition is 6% aggregate fractional melting of DMM in the spinel lherzolite stability field (green line).

This 6% modeled melt provides a very tight match across nearly all REEs, and only Pb and Rb show any significant discrepancies, with minor misfits for other highly incompatible elements including Ba and Nb. The 2-fold difference for Rb and Ba, and the general misfit in pattern shape for elements Rb thru U is largely a function of Rb/Sr, which is derived from the gradual depletion model. Rb/Sr is dependent on and very sensitive to the age at which depletion begins (much less so for Sm/Nd) [Workman and Hart, 2005], which for this modeling is 3 Ga. Small variations in depletion age cause significant changes in Rb/Sr, therefore the extreme left side of the trace element pattern is the least constrained portion of the derived composition, and since the age of depletion is poorly constrained to begin with, a factor of two misfit is not worrisome. An added factor may be the variable Ba concentrations observed in a handful of N-MORBs from the eastern end of the orthogonal ridge, in close proximity to anomalously elevated Ba and Ba/Nb in lavas to the east Du Toit Fracture Zone [le Roex *et al.*, 1989].

The large contrast seen for Pb abundance is not easily explained here, but it is apparent that the DMM source composition has a large negative Pb anomaly. While some of the individual samples from which the average N-MORB composition is derived display negative Pb anomalies they are not of similar amplitude. There is a great deal of uncertainty regarding the phases that control the Pb budget during MORB generation, with some suggestions that residual sulfide may play a key role in sequestering Pb from the melt [Hart *et al.*, 2005], leading to the often seen negative Pb anomalies in MORB. Small misfits in Sr and Zr are not entirely understood either, but uncertainties regarding bulk D's for Zr are likely responsible for a portion of the offset. Unfortunately, inclusion of garnet in the melting assemblage would only increase the observed difference, based on experimental Ds.

A final observation regarding the trace element patterns is the slight depletion of Hf and to a lesser extent Zr, relative to Sm and Eu. The Narrowgate segment lavas dominantly have  $Hf/Sm < 1$ , while the rest of the basalts, with the exception of a few from the amagmatic accretionary segment, have  $Hf/Sm > 1$ . This subtle difference is consistent with the presence of residual garnet in a peridotite source where  $D_{Hf}/D_{Sm}$  for garnet is commonly 2-3 and significantly larger than  $D_{Hf}/D_{Sm}$  for clinopyroxene of about 0.5 - 1 [Salters and Longhi, 1999].

The same melting calculations are also presented on a series of incompatible element x-y plots, where a better understanding of the relationships between the melting trends and basalt data can be attained. A range of incompatibilities from highly incompatible to moderately incompatible are represented by Ce, Sm, Yb, and Lu, and plotted against La, a highly incompatible element itself. The lavas have been fractionation-corrected and thus theoretically reflect parental compositions comparable to aggregate melts produced during mantle melting. Non-modal aggregate fractional melting of DMM in the spinel lherzolite stability field produces a curved melting array (black line) for  $Sm_8$ ,  $Yb_8$ , and  $Lu_8$  versus  $La_8$ , and a nearly linear array for  $Ce_8$  versus  $La_8$  (Figure 14). The melting

trend for each panel is marked with X's indicating 1, 2, 3, 5, 8, 10, and 15% melting. In Ce vs. La the N-MORBs from the orthogonal supersegment (red circles) span a large range from the lowest Ce and La concentrations to La contents just below 10 ppm, with N-MORBs from the amagmatic accretionary segment (blue circles) covering a similar range. The tight linear nature of the N-MORB lavas and the entire suite in general indicates similar compatibility for Ce and La, and this is verified by the nearly linear melting array for DMM. In Figure 14b a bit more information is available as the MREE Sm behaves independently from La. The spinel lherzolite melting trend has a distinct curvature to it with low degrees of melting showing more change in La than Sm. The N-MORBs from the orthogonal supersegment and amagmatic accretionary segment lie in positive linear arrays that span a range of melting on the spinel lherzolite melting trend between ~10% and 4%. The fit to N-MORB is not quite as exact for Lu and Yb vs. La, but the curvature of the spinel lherzolite array is similar to the most depleted lavas with La < 5 and a range of Lu and Yb. Certainly mixing of high and low degree spinel lherzolite melts will generate trends extending directly through the orthogonal supersegment lavas.

Overall, the average N-MORB composition (Figure 13) as well as other N-MORBs from the orthogonal supersegment and the amagmatic accretionary segments (Figure 14) are well modeled by a 6% non-modal aggregate fractional melt of a spinel lherzolite having an initial trace element composition of DMM. While 6% partial melting of DMM is on the low side of previous melting studies (6%-20%) [Kinzler and Grove, 1992b; Langmuir *et al.*, 1992] recent hydrous melting models indicate that MORB can be produced by 7% near-fractional melting while generating 6.3 km of ocean crust (P. Asimow, pers. comm., 2004, as cited in [Workman and Hart, 2005]). 6% melting also coincides with the value arrived at by Workman and Hart [2005]. This value is consistent with estimated crustal thicknesses for the eastern end of the orthogonal supersegment of < 5 km [Dulaney, 2002; Grindlay *et al.*, 2000] as opposed to 6.3 km for ridges spreading > 20 mm/yr [Bown and White, 1994; White *et al.*, 1992].

### ***Melting modified-DMM to produce E-MORB***

Localized or even along-axis isotopic variation in MORB suites has often been attributed to isotopic heterogeneity within a single lithology mantle peridotite [Hart, 1988]. To simulate this, we derive an isotopic and incompatible element enriched version of DMM using the gradual depletion model presented in Workman and Hart, [2005]. The DMM trace element composition is partially derived from present-day parent/daughter ratios that are constrained by the measured isotopic compositions of average N-MORB from [Su and Langmuir, 2002] and arrived at using a 3 Ga gradual depletion curve. If instead of constraining the gradual depletion model with the isotopic composition of average N-MORB we use the most radiogenic Sr and Pb and unradiogenic Nd compositions of E-MORB from the Narrowgate segment, the new trace element source composition will then reflect the long-lived isotopic ratios measured in the basalts. The Sm/Nd ratio of present day depleted mantle, or in this case “enriched SWIR-DMM”, then constrains the other parent daughter ratios and trace element

abundances through the abyssal peridotite depletion trend (see *Workman and Hart, [2005]*).

Figure 13b depicts calculated melting curves for two different melting regimes in an attempt to satisfactorily model the average E-MORB trace element pattern, which is an average of Dredge 89 lavas. A 2% non-modal aggregate fractional melt produced in the spinel stability field (green curve) is overlain, illustrating the difficulty of fitting a melt produced shallow (no garnet) with a highly LREE enriched composition. Ta, La, and Ce are fit, but that leaves the LILEs to low and the MREE and HREE significantly elevated, relative to the average E-MORB. Bulk source D's used to calculate this modeled trace element pattern are from *Workman and Hart, [2005]*, and melting mode D's are from *Wasylenki et al., [2003]* and *Kelemen et al., [2003]*. The inability of spinel peridotite melting to generate the necessary HREE to LREE slope as seen for the average E-MORB, indicates that melting should incorporate garnet. Garnet in the residue will retain HREE elements from the melt, thereby creating the slope from La to Yb.

Melting in the garnet and spinel stability fields use bulk Ds taken from *Kelemen et al., [2003]* for garnet lherzolite and spinel lherzolite, respectively. The initial starting composition is melted within the garnet stability field and continued melting of the residue proceeds within the spinel stability field, therefore representing continuous polybaric melting (even if the calculations are done in two steps). The modeled trace element pattern produced by this methodology that best fits the average E-MORB has a HREE to LREE slope that is very similar to E-MORB, although it is elevated. Furthermore, by deriving a melt that has a similar pattern slope for HREE to LREE, the left side of the pattern is sacrificed and shows a worse fit than the shallow melt pattern. This trace element pattern is generated by 3% melting in the garnet stability field, followed by 5% melting of the residue within the spinel stability field. In this case the problem once again is trying to produce 30-fold enrichment in the most incompatible elements, while maintaining the steady shallow slope of the right hand side of the pattern. In order to achieve this level of enrichment for Rb, Ba, Th, U, and La from an initial source composition like DMM or even "enriched SWIR-DMM" requires low extents of melting. Yet to get the correct shape and REE slope as seen for average E-MORB, requires higher degrees of melting, which is opposite that needed for the LREE and LILEs. This illustrates that even an isotopically enriched and LREE elevated "DMM-like" source beneath the Southwest Indian Ridge cannot easily generate LREE enriched trace element patterns similar to lavas measured at the Narrowgate segment.

#### ***Necessity of garnet in the mantle source***

E-MORB compositions from the Southwest Indian Ridge (9°-25°E) extend to elevated abundances of highly incompatible elements and much lower abundances of less incompatible HREE. As previously noted, the differences in incompatible element abundance relationships (Figure 5), the decoupling of LREE from HREE in along-axis concentration profiles (Figure 10), and the along axis variations of incompatible element ratios, for example Lu/Hf (Figure 4) strongly suggest the involvement of garnet in the mantle source beneath the oblique supersegment and also the western end of the

orthogonal supersegment. Illustration of the entire suite of basalts in Figure 14 clearly shows that the highly incompatible element enrichment to higher La that is characteristic of E-MORBs produces little variation in Sm and inverse correlations with Lu and Yb contents. This is suggestive of a garnet-bearing source lithology.

Using four incompatible elements with differing compatibilities (Ce, Sm, Lu, and Yb) it is quickly apparent that melting of a garnet-free source cannot produce the E-MORB compositions. Non-modal aggregate fractional melting using bulk D's for garnet lherzolite [Kelemen *et al.*, 2003] (with garnet partition coefficients for Sr, Zr, and Hf from [Donnelly *et al.*, 2004] and Ti from [Cushman *et al.*, 2004]) shows a much different melting trajectory than for spinel lherzolite (Figure 14). With the exception of Ce vs. La where the addition of garnet to the source makes little difference in abundance concentrations for either element, Sm, Yb, and Lu are all more compatible than La in garnet and thus display flat to negative trends reflecting melting of a garnet-bearing lithology. The separation between the spinel lherzolite and garnet lherzolite melting arrays is greatest for Lu and Yb, as they are the most compatible rare earth elements in garnet. It is obvious that the Narrowgate segment lavas have the largest garnet signature, with a linear trend extending toward unrealistically low degree melts of garnet lherzolite. Partial melting of depleted peridotite within the garnet stability field likely will continue to melt within the spinel stability field, and thus mixing of proportions may explain a large portion of the chemical variation. This is exemplified by the orange curve in b), c), and d), reflecting mixing of a 1% garnet lherzolite melt with increasing proportions of spinel lherzolite melt.

However, upon closer inspection both melting arrays fall short of encompassing the entire range of La. As a result, the mixing trend or either melting array can account for the elevated La within the Narrowgate segment lavas unless calling upon melt fractions < 1, which was already mentioned to be inconsistent with creating 7 km of crust. This suggests that garnet lherzolite may not have a high enough incompatible element budget to account for the extreme enrichment at the Narrowgate segment, and thus investigation of other garnet-bearing mantle lithologies with elevated incompatible element contents is warranted.

### ***Multi-lithology mantle compositions***

The observed isotopic and trace element variations measured in basalts along the entire length of the SW Indian Ridge have been attributed to a number of multi-lithology, chemically heterogeneous sources including, but not limited to, recycled oceanic crust and/or pelagic sediment [Dupré and Allègre, 1983; Rehkämper and Hofmann, 1997], continental lithospheric mantle [Mahoney *et al.*, 1992] or subduction-modified mantle [Kempton *et al.*, 2002], delaminated continental crust [Escrige *et al.*, 2005], or addition of plume material [Storey *et al.*, 1989]. We do not address all of these potential variations in mantle source, but do briefly investigate the possibility that the MORB source beneath the 9°-25°E portion of the SW Indian Ridge is contaminated by materials that have enriched large ion lithophile element and light rare earth element compositions, 1) continental crust material or 2) an 'EM2' mantle source. Our interest in looking at these



two theoretical mantle lithologies stems from the observation that Southwest Indian Ridge lavas have isotopic enrichment trends from N-MORB to E-MORB generally oriented toward EM2 and/or HIMU locations for Sr-<sup>64</sup>Pb, Pb-Pb, and Sr-Nd isotopic space. Trace element compositions for EM2 and HIMU are also similar to E-MORB at the Narrowgate segment.

### ***DMM mixed with continental crust***

Mixing of continental crust into the depleted upper mantle, through the subduction of sedimentary material, has often been suggested as an explanation for incompatible element enriched basalts, as terrigenous sediments have high LILE and LREE relative to high field strength elements (HFSE; e.g. Nb, Ta, Zr, Hf), but are not generally enriched in Ba relative to other LILE, as seen for pelagic sediment [Ben Othman *et al.*, 1989; Weaver, 1991]. The mechanism for introducing terrestrial sediment into the mantle is usually subduction of oceanic crust containing terrestrial sediments, and thus the combination of these two lithologies has come to be known as the EM2 mantle reservoir [Hart, 1988]. Mixing continental crust material (composition taken from [Taylor and McLennan, 1985]) into DMM creates a hybridized source that should generate a LILE and LREE enriched basalt. Initial modeling suggests that mixing varying proportions of continental crust into the depleted upper mantle is largely successful in producing a trace element pattern that has a HREE to LREE slope similar to average E-MORB, however other discrepancies exist. The best-fit modeled melt is shown in Figure 15 (orange curve with diamonds) and is produced by 14% total melting of a source that has 5% continental crust mixed into DMM (solid brown curve; Table 5). A number of trace element anomalies exist in the source composition, which are reflected in the modeled liquid. One of the most important discrepancies is the large negative Nb anomaly and Nb/Ta < 1 that is common for continental crust, but is opposite the slight positive anomaly and Nb/Ta > 1 observed for average E-MORB. Pb also shows an opposite anomaly to E-MORB, but as discussed earlier, the budget of Pb is poorly constrained and therefore in depth investigation outside the scope of this study is warranted. Despite the general agreement in shape the modeled liquid has low La and high Sm, relative to average E-MORB, resulting in depressed La/Sm. In general, melting of a DMM source contaminated by a small proportion (5%) of continental crust material (terrigenous sediment) cannot adequately account for the trace element abundances and ratios seen for E-MORB.

### ***Enriched mantle II composition***

We further investigate the possibility of our enrichment signal being the result of recycled oceanic material ± sediment input by modeling a newly derived trace element composition for EM2 source (Table 5) [Workman *et al.*, 2004]. The source composition for EM2 used here is listed in Table 5. Using bulk D's taken from Kelemen *et al.*, [2003], we melt this trace element composition to varying degrees to generate the best model fit to the measured E-MORB composition. Figure 15 shows the best fit liquid, which was generated by 10% total melting (6% garnet melting plus 4% spinel melting). We are able to most closely reproduce the HREE abundances, but the modeled liquid

diverges to higher normalized abundances in the MREE, again not able to account for the sharp increase in LREE relative to MREE. The biggest difference between the trace element pattern for the 10% melt of EM2 and that of average E-MORB is between Ce and Rb. The EM2 melt maintains a steady enrichment trend of constant slope along nearly its entire length, but most importantly between Ce and Rb. This is contrast with E-MORB which has a steep slope from Ce to Ta, the greatest normalized abundance at Nb, and then fall back down to a nearly flat pattern from U to Rb (with some scatter in Rb values). Additionally, the Nb/Ta of EM2 is  $< 1$ , while that of average E-MORB is  $> 1$ .

Nb/Ta  $< 1$  is typical for continental crust [Barth *et al.*, 2000; Plank and Langmuir, 1998] and for MORB [Niu and Batiza, 1997], although Nb/Ta for MORB is greater than for continental crust. In any regard, with both continental crust and MORB, and by inference DMM, having subchondritic Nb/Ta, an additional reservoir is required with superchondritic Nb/Ta to correct the mass imbalance [Rudnick *et al.*, 2000]. One reservoir that may satisfy the requirement of elevated Nb, Ta, and Ti is a refractory, rutile-bearing eclogite, as sampled in xenoliths from cratonic kimberlites. The idea of rutile-bearing eclogite as a significant reservoir for these elements was initially proposed by [McDonough, 1991]. The fact that the Narrowgate segment lavas dominantly have Nb/Ta  $> 1$  and the Joseph Mayes Seamount lavas have Nb/Ta  $\approx 1$ , certainly suggests inclusion of an eclogitic melt component.

#### 5.4. Garnet-bearing mantle lithology

The anomalous incompatible trace element and isotopic enrichment in lavas from the oblique supersegment 10°-16°E was first measured by *le Roex et al.*, [1992], and more recently discussed by *Janney et al.*, [2005]. As we mentioned earlier, *le Roex et al.*, [1992] attribute the chemical enrichment to unusually low ( $< 5\%$ ) degrees of melting of a vein-impregnated mantle formed by partial melting of upwelling Bouvet plume (page 266 in [le Roex *et al.*, 1992]). On the other hand, based on Nd-Hf isotopic and trace element values of 4 orthogonal supersegment lavas and 4 lavas from between 13°-15°E, *Janney et al.*, [2005] conclude that west of 26°E, basalt compositions are derived from an Atlantic/Pacific-type N-MORB [Andres *et al.*, 2002] source composition, and those west of 16°E, appear to be variably overprinted by contamination from the Bouvet plume [Janney *et al.*, 2005]. While both studies agree that the Bouvet plume has in some way contaminated the present day upwelling mantle beneath the western Southwest Indian Ridge, they also indicate that the eastern extent of Bouvet plume influence on the source composition is the transition from the oblique supersegment to the orthogonal supersegment ( $\sim 16^\circ\text{E}$ ). This statement reflects the lack of geographical coverage, as *Le Roex et al.*, [1992] does not deal with lavas east of 15°E, and *Janney et al.*, [2005] only has data from 4 orthogonal supersegment lavas. In contrast to this conclusion, the chemical data presented in this manuscript illustrates clearly that systematic isotopic and incompatible trace element enrichment exists from 25° to 16°E and in more pronounced fashion along the oblique supersegment. The previous sections have attempted to explain this enrichment through melting of various depleted and enriched source compositions, but with little success. Based on trace

element observations suggesting the involvement of a garnet-bearing residue during mantle melting, the following section will assess the importance of eclogite melting.

### ***Can eclogite explain the Narrowgate segment lavas?***

Many chemical indicators discussed above and within Chapters 2 and 4 have suggested the involvement of residual garnet. The next question to address is whether the garnet is present in the mantle as garnet lherzolite or as a separate lithology (i.e. pyroxenite, eclogite, etc.). Distinguishing garnet peridotite from garnet pyroxenite or eclogite is not a simple task, and many recent studies have tackled this general dilemma in both the OIB and MORB setting [Donnelly *et al.*, 2004; Gaffney *et al.*, 2005; Hirschmann *et al.*, 2002; Hirschmann and Stolper, 1996; Ito and Mahoney, 2004; Stracke *et al.*, 1999].

Figure 16 shows multiple melting curves overlying the 9°-25°E basalts from the Southwest Indian Ridge, which show variation for Sm in a) and more so for Sc in b), but more importantly show separation for Sm/Yb among tectonomagmatic provinces in both panels. The range in Sm/Yb for these fractionation-corrected lavas is substantial relative to regionally averaged MORB, which is typically 1.3-1.5 [Hofmann, 1988; Shen and Forsyth, 1995; White *et al.*, 1992]. It has been well established that elevated Sm/Yb is commonly associated with residual garnet in the mantle source [Bender *et al.*, 1984; Frey *et al.*, 1993], however some studies [Blundy *et al.*, 1998] based on variation in partition coefficients have suggested that garnet may not be required to create this fractionation and the related REE patterns. It can be clearly seen in Figure 16a that garnet lherzolite melting will create variation in Sm/Yb rather than spinel lherzolite melting. The Narrowgate segment lavas have Sm/Yb roughly between 2 -3 and this requires garnet in the source. According to the melting parameters specified in Figure 16 caption, between 1% and 3% partial melting of depleted garnet lherzolite can account for the elevated Sm/Yb of the Narrowgate segment. The other tectonomagmatic provinces lie at lower Sm/Yb and thus most likely have a lower proportion of garnet lherzolite melt relative to spinel lherzolite melt. Mixing of variable proportions of garnet and spinel lherzolite could roughly account for the majority of the lavas.

The remarkable agreement between the garnet lherzolite melting curve and the Narrowgate segment lavas does however suggest that little if any spinel peridotite melt is mixed in. This is troublesome as 1-3% melting is not sufficient to generate the estimated 7 km of crust at Narrowgate segment. An alternative way of generating the high Sm/Yb is by mixing depleted peridotite melt with eclogite melts of varying degrees. Bulk eclogite has Sm/Yb of ~3.1 and thus melting of eclogite provides a huge lever for elevated Sm/Yb. Although it may seem unrealistic to be mixing an 80% eclogite melt with a 6% depleted peridotite melt, recall from discussions in Chapter 2 that based on the abundance of volatiles in many of the E-MORBs the solidus for volatile-rich eclogite is likely significantly deeper (lower temp) relative to anhydrous peridotite. Therefore, > 60% melting of the eclogite lithology even before the peridotite solidus is reached is a distinct possibility [Pertermann and Hirschmann, 2003a].

The other part of Figure 16 plots Sm/Yb versus Sc and once again illustrates the futility of attempting to use spinel lherzolite melting to explain the negative correlation to



increasing Sm/Yb and decreasing Sc. And once again, small extents of garnet lherzolite melting can produce some of the variation within the Joseph Mayes Seamount and Narrowgate segment lavas, but not all of it. While the melting array for garnet lherzolite between 1 and 10% melting has constant Sc and variable Sm/Yb, the trend in the data extends to significantly lower Sc contents than attributable to garnet lherzolite. In fact many of the Narrowgate segment and Joseph Mayes Seamount lavas extend to Sc and Sm/Yb values similar to, but even higher in Sm/Yb and lower in Sc, than MORB from the South Atlantic characterized to be generated by preferential melting of pyroxenite veins, which as a result of tectonically affected melting processes, was 20–40% of the final melt volume [le Roux *et al.*, 2002a]. This strongly suggests that a low Sc/high Sm/Yb lithology is involved in melting beneath parts of the oblique supersegment, and as shown in Figure 16b, eclogite melting is located in the right area to provide this melt component.

As noted in Figure 14 the elevation of La displayed by the Narrowgate segment lavas is noticeably greater than a 1% melt of either a spinel lherzolite or garnet lherzolite. Other potential mantle source compositions have been explored, and even EM2 only has a La abundance of ~16, while the Narrowgate segment extends to ~22. Figure 17a) and b) plot Lu and Yb versus La (as in Figure 14), but in this case eclogite melting trends are added. Produced by modal fractional melting of “bulk eclogite”, the Narrowgate segment lavas extend in a curved trend that appears to intersect the eclogite melting curve near 30%. The bulk of the data lie in a rather narrow band that implies mixing of varying degree depleted peridotite melts with varying degree eclogite melts.

Based on earlier discussion and from the spider diagrams in Figure 6,  $(\text{Nb/Ta})_n$  is observed to be  $> 1$  for the Narrowgate segment lavas and  $< 1$  for the remaining lavas, which suggests eclogite in the source, possibly with trace amounts of rutile. Another characteristic of eclogites containing trace rutile is depletion of Zr and Hf, relative to Sm and Eu. To test whether these characteristics were actually present in any of the lavas from the study area, Figure 17c plots  $(\text{Hf/Sm})_n$  versus  $(\text{Nb/Ta})_n$ , along with respective melting curves for spinel lherzolite, garnet lherzolite, and rutile-bearing eclogite. The primitive mantle normalized ratios and chondritic lines = 1 allow straightforward assessment of subchondritic vs. superchondritic values. The vast majority of the lavas have superchondritic  $(\text{Hf/Sm})_n$  and subchondritic  $(\text{Nb/Ta})_n$ , but nearly every Narrowgate segment lava has superchondritic  $(\text{Nb/Ta})_n$  and subchondritic  $(\text{Hf/Sm})_n$ . This is consistent with eclogite lithologies that have  $\text{Nb/Ta} > 1$  and depleted Hf/Sm, relative to N-MORB. In addition, the spinel and garnet lherzolite melting trajectories are of little help in explaining the variation with the basalt suite and especially the enrichment of  $(\text{Nb/Ta})_n$ . Partial melting of refractory, rutile-bearing eclogite can easily explain the superchondritic  $(\text{Nb/Ta})_n$ , and as seen in 17a and 17b will also explain the highly elevated La contents and negative correlations between LREE and HREE.

#### ***Idealized melt modeling of eclogite/peridotite multi-lithology source***

Because of the potential connection between the Bouvet plume and this study area, a proxy for the low-degree partial melts of upwelling Bouvet plume material that infiltrated



the local asthenosphere is derived. We average the available trace element measurements for Bouvet Island lavas, including a suite of whole rock data from the literature consisting of four hawaiites [*le Roex and Erlank, 1982*] and four alkali basalts [*Weaver et al., 1986*], all of which are highly evolved and thus are corrected for low-pressure fractionation to  $\text{MgO}_8$  using the same algorithms reported in Chapter 2. The chosen two-lithology source consists of 5% enriched basaltic eclogite/pyroxenite veins and 95% depleted peridotite, which is partially constrained by arguments made in Chapter 2 and 4. To calculate non-modal aggregate fractional melting we use eclogitic bulk D's [*Pertermann and Hirschmann, 2002; Pertermann and Hirschmann, 2003b*] for melting of the enriched lithology and bulk Ds as in Figure 13 for melting of DMM. We show the results from this modeling effort in Figure 18, where our best fit model liquid (purple curve) represents 11% total melting of the two-lithology source. To match the trace element pattern of average E-MORB requires generation and aggregation of three distinct melt fractions from different regions of the melting zone. Below we outline each of these melt generation steps and why they are necessary for the final trace element abundance pattern. Similar to *Plank and Langmuir, [1992]*, we assume passive upwelling and adiabatic melting, perfect fractional melting, and near-perfect melt focusing.

Based on experimental studies of eclogite/pyroxenite melting [*Kogiso, 2004; Pertermann and Hirschmann, 2003a, 2003b*], passively upwelling mantle with 5% eclogite/pyroxenite veins distributed throughout a harzburgite host, will initiate partial melting of the vein lithology at depths 35-50 km deeper than peridotite, thus allowing substantial melting of the vein lithology prior to crossing the peridotite solidus. Our model takes advantage of this relationship between solidi and subsequent melt productivity [*Pertermann and Hirschmann, 2003a*], as ubiquitous partial melting of the enriched vein lithology occurs beneath all segments along the ridge. As a result of the separation in solidi between the two lithologies, the enriched vein lithology will likely melt at least 50% before reaching the peridotite solidus, thus the liquid will have a similar composition to that of the initial source lithology. It is expected that the vein lithology will continue to melt above the peridotite solidus, and thus 50% may be a minimum estimate, but the melting productivity of our eclogitic lithology will significantly decrease upon crossing the peridotite solidus [*Hirschmann and Stolper, 1996; Phipps Morgan, 2001*], and thus add little additional melt, especially if conductive cooling shuts off mantle melting deeper than on most slow spreading ridges. Taking into account the potential shape of the melting regime, we limit this extent of melting of the 5% vein lithology to a moderate across-axis width, and along-axis length equivalent to the length of the Narrowgate segment (35 km). This 50% melt of the vein lithology is the first of three melt fractions that aggregate to derive an enriched "Narrowgate segment-like" trace element pattern. This melt fraction, stemming from the initially enriched source composition, provides much of the LREE enrichment, and also the general LREE-HREE slope in the final pattern.

Simultaneously, in the off-axis regions of the melting zone, often referred to as the "wings" of the melting triangle [*Galer and O'Nions, 1986*], low-degree melts of the same vein lithology are produced. Obviously, these low-degree vein melts are produced at the

base of the main melting region, but because the veins continue melting to high extents in this region, the enriched low-degree melt signatures are diluted (and thus depleted) by aggregation of increasingly higher degree melts throughout the column. It is within the off-axis “wings” of the melting regime that conductive cooling of the lithosphere from above combined with orthogonal mantle flow lines, prevent upwelling mantle from reaching the DMM solidus, thus producing only vein melts within these local mantle columns. In essence, mass conservation for adiabatic melting requires that the horizontal mantle velocity exiting the melting regime equal the vertical upwelling velocity entering the bottom [Ahern and Turcotte, 1979], which in the case of passive flow suggests the upwelling rate is of the order of the spreading rate [Phipps Morgan *et al.*, 1987], and thereby defines the boundary of the melting regime at 45°, theoretically the point at which mantle upwelling ceases. Because melting on the periphery of the regime is limited the trace element signatures of these melts are enriched. Hence, this melting mechanism has been called upon as a source of increased incompatible element enrichment in MORB [Plank and Langmuir, 1992]. Physical limits such as, the amount of “extra” source volumes present beneath ridges, the ability to extract low-degree melt fractions, and the efficiency of melt focusing from the “wings” to the ridge axis, may limit the importance of this process. These physical parameters and thus the importance of this mechanism of enrichment, may be a function of the spacing of volcanic segments, where the along-axis upwelling rate and related segmentation at ultraslow-spreading rates (as seen on the oblique supersegment), control the effective source volume and the efficiency of melt focusing.

However, a number of factors may alleviate many of these constraints, providing us with a viable mechanism for producing an incompatible trace element enriched melt fraction to account for the lavas of the Narrowgate segment. Since the initial composition of our vein lithology is LREE and LILE enriched,  $F = 2\%$  (rather than  $< 1\%$ ) will produce enriched melt sufficient for our needs. This increase in melt fraction could be critical for both extraction of the melt from the host peridotite, and efficiency of melt focusing, where larger  $F$  makes both processes more likely. It has been suggested that small degree melts out of equilibrium with the surrounding mantle will react and solidify before extraction [Yaxley, 2000; Yaxley and Green, 1998], but this effect can be diminished if reactive porous flow quickly becomes high permeability focused flow through melt conduits [Hart, 1993; Kelemen *et al.*, 1997]. This transition in melt segregation process would be enhanced by the lower viscosities associated with volatile-rich, alkali melts [Standish *et al.*, 2005] and the resulting increase in mantle buoyancy and thus melt focusing [Buck and Su, 1989; Scott, 1993; Scott and Stevenson, 1989]. Focusing may also be aided by variable along-axis upwelling rates creating lithospheric topography. The source composition of the vein lithology also means that fewer “extra” source volumes are necessary to gain the same enrichment factor as a more depleted source.

Therefore, we model this low-degree vein melt fraction as a 2% melt with a source volume multiplier of 6, which is similar to the upper limit derived by Plank and Langmuir, [1992] of 5. Preliminary numerical modeling of the effects of spreading

geometry on the thermal regime and melt flow pathways beneath a mid-ocean ridge [Barry, 2005], suggest that the for passive upwelling at ultraslow-spreading rates (1 cm/yr) the melting regime may in fact be shaped more like an upside down martini glass, with a narrow, steeply sided region of melting immediately beneath the ridge (perhaps in 3-D), gradually splaying out deeper in the mantle and then quickly becoming a very shallowly sloped thermal boundary layer. Considering the depth to the solidus of the vein lithology, relative to that of peridotite, the “wings” of this regime may be more extensive, thus increasing the limit on available “extra” source volumes and further legitimizing our use of 6 “extra” source volumes.

The last melt fraction produced is produced in the main melt column by melting of DMM, which melts a total of 11%, significantly more than expected. The resulting liquid is important for the aggregate model liquid, as this depleted melt provides much of the shape for the MREE and HREE, due to the relatively large proportion of garnet melting. You may recall that we successfully fit a model liquid to our representative N-MORB dredge average, by melting DMM 6% (Section 5.3). The discrepancy between the extents of melting at the eastern end of the orthogonal supersegment versus beneath the Narrowgate segment may be a function of the enhanced melt focusing or possibly a component of buoyant upwelling. The absence of a significant vein lithology beneath the eastern end of the orthogonal supersegment indicates that partial melting will initiate shallower, even with typical N-MORB H<sub>2</sub>O contents of 0.2 wt%, than beneath the oblique supersegment. In conjunction with the ultraslow-spreading rates (i.e. upwelling rates), conductive cooling will cease mantle melting at fairly deep levels, thereby shortening the height of the melting column [Bown and White, 1994; Reid and Jackson, 1981; White *et al.*, 2001]. The inferred upwelling rate at the Narrowgate segment is similar to that at the eastern end of the orthogonal supersegment, however as alluded to above, the added melt production from fusion of the vein lithology and resulting from the higher overall volatile content of the mantle (i.e. deeper solidus), is consistent with a taller melting column and thus higher degrees of total melting beneath the Narrowgate segment. When all three melt fractions described above are aggregated within the melt column, the total extent of melting necessary to produce a model liquid similar to measured trace element composition of Narrowgate segment basalt is ~12%. This heightened total degree of melting, relative to N-MORB production, may be qualitatively consistent with the differences in estimated crustal thickness, but the reader should be reminded that these values are model produced and thus assumptions inherent within the modeling exercise may not be completely explainable.

### **5.5. Regional isotopic variations – Is this Bouvet material?**

In general all of the models proposed to explain isotopic and trace element compositions of MORB from 9°-16°E, which we extend to 25°E, involve melting of a vein lithology impregnated within DMM during partial melting in and around the ascending Bouvet mantle plume. Previous studies were correct in placing an isotopic boundary at the Du Toit Fracture Zone (~25°E), separating SW Indian Ridge depleted mantle to the east from Atlantic/Pacific depleted mantle to the west. Comparison of the

orthogonal supersegment and amagmatic accretionary segment N-MORB isotopic compositions with Indian Ocean N-MORB finds our lavas higher in  $^{206}\text{Pb}/^{204}\text{Pb}$  for both a given  $^{87}\text{Sr}/^{86}\text{Sr}$  and  $^{143}\text{Nd}/^{144}\text{Nd}$ , as well as lower in  $^{176}\text{Hf}/^{177}\text{Hf}$  and  $^{143}\text{Nd}/^{144}\text{Nd}$  for a given  $^{87}\text{Sr}/^{86}\text{Sr}$ . Semi-linear trends from N-MORB to E-MORB (Figure 5 and 7) extend to and in some cases past Bouvet Island signatures and toward an EM2/HIMU type reservoir, indicating the enriched source may not be Bouvet categorically.

Is it a coincidence that the Bouvet plume was located at the Shaka Fracture Zone approximately the same time that the oblique supersegment was initiated?

### **$^3\text{He}/^4\text{He}$ variation**

We observe a striking discontinuity in  $^3\text{He}/^4\text{He}$  at the Shaka Fracture Zone, with extremely systematic behavior to the east within our study area compared to highly variable  $^3\text{He}/^4\text{He}$  to the west (Figure 19). This contrasts with  $^{87}\text{Sr}/^{86}\text{Sr}$ ,  $^{143}\text{Nd}/^{144}\text{Nd}$ , and  $^{206}\text{Pb}/^{204}\text{Pb}$  over the same section, showing similar, albeit less systematic, variation to both sides of the fracture zone. This abrupt compositional change in  $^3\text{He}/^4\text{He}$  without corresponding changes in long-lived heavy isotopes, suggests a  $^3\text{He}/^4\text{He}$  signature to the west reflecting variable influence from primary, previously un-melted Bouvet plume material; whereas to the east, lower overall and decreasing to the west  $^3\text{He}/^4\text{He}$  reflects an increasing contribution of previously melted, Bouvet plume material. Georgen *et al.*, [2003] noted the light and heavy isotope differences between the  $0^\circ$ - $9^\circ\text{E}$  and  $9^\circ$ - $25^\circ\text{E}$  regions (see Figure 9 in [Georgen *et al.*, 2003]), but largely due to the lack of supporting heavy isotopic data in the  $10^\circ$ - $25^\circ\text{E}$  region (presented here), concluded  $^3\text{He}/^4\text{He}$  values on both the oblique and orthogonal did not reflect influence from the Bouvet plume. Instead, they attributed the low  $^3\text{He}/^4\text{He}$ , relative to putative N-MORB ( $\sim 8 \pm 1 R_a$ ), to generation by a SWIR mantle source that incorporated recycled crustal or lithospheric material having elevated U+Th.

The mechanism we invoke to explain the low  $^3\text{He}/^4\text{He}$  to the east of the Shaka Fracture Zone is ingrowth of  $^4\text{He}$  in our vein lithology, resulting from a previous melting and presumed enrichment of U+Th/He. Our recent mapping shows that from Ma to 30 Ma the Bouvet hotspot was situated on the SW Indian Ridge at the Shaka Fracture Zone, then migrated rapidly to the west along the ridge due to a spreading direction change. We suggest that the change in spreading direction simultaneously caused the Bouvet plume to leave the Shaka Fracture Zone and nucleate formation and growth, by eastward ridge propagation, of the oblique supersegment  $9^\circ$ - $16^\circ\text{E}$ . The continued propagation of the oblique supersegment has tapped upwelling mantle previously infiltrated with Bouvet plume melts. The highly enriched trace element character of Bouvet lavas indicates enrichment of U+Th/He could occur, assuming even a slight difference in the bulk Ds where  $D_U$  and  $D_{Th} < D_{He}$ .

Using the composition of a Bouvet lava ( $U$  (ppm) = 0.25,  $Th/U = 3.48$ ) and a conservative estimate of  $[^4\text{He}] = 1.25 \text{ uccstp/g}$  (taken from Bouvet influenced lavas west of the Shaka FZ), we can calculate the amount of time required for ingrowth of enough  $^4\text{He}$  to change the un-melted Bouvet plume  $^3\text{He}/^4\text{He} = 14 (R_a)$  [Kurz *et al.*, 1998] to reported values for the Narrowgate segment lavas  $^3\text{He}/^4\text{He} \approx 6 (R_a)$  (Table 4). Even



though this calculation is somewhat unconstrained as the free parameter is [ $^4\text{He}$ ], we calculate that in 12.4 Ma  $^4\text{He}$  ingrowth can produce the range in  $^3\text{He}/^4\text{He}$  that we observe on both the orthogonal and oblique supersegments. The decreasing  $^3\text{He}/^4\text{He}$  from east to west can then be explained by an increasing proportion of vein melt ( $^3\text{He}/^4\text{He} < 6$ ) mixing with DMM melt, presumably with  $^3\text{He}/^4\text{He} = 8$  [Graham *et al.*, 1992; Kurz *et al.*, 1982].

In contrast, the ridge to the west of the Shaka Fracture Zone is tapping mantle that contains un-melted plume material. Lavas from ridge segments proximal to Bouvet Island and a single lava from Bouvet Island itself, are documented to have primary  $^3\text{He}/^4\text{He}$  of  $\sim 14$  (Figure 19), indicating MORB upwelling and melting is tapping a high  $^3\text{He}/^4\text{He}$  lithology [Georgen *et al.*, 2003]. It is important to note that while the  $^3\text{He}/^4\text{He}$  isotopic signature is being controlled by modern and ancient melting events associated with Bouvet plume, the long-lived heavy isotope compositions of the basalts on both the east and west sides of the Shaka Fracture Zone display a similar range, as the signatures reflect the time-integrated evolution of the Bouvet plume material. The melting event associated with U+Th/He enrichment also fractionates parent/daughter ratios (i.e. Rb/Sr), but 12 Ma is not nearly enough time for ingrowth to occur, thus the  $^{87}\text{Sr}/^{86}\text{Sr}$ ,  $^{143}\text{Nd}/^{144}\text{Nd}$ ,  $^{176}\text{Hf}/^{177}\text{Hf}$ , and Pb isotopic ratios are presumably inherited from the primary Bouvet source.

Thus, the discontinuity in  $^3\text{He}/^4\text{He}$  at Shaka Fracture Zone, 1) indicates a subtle but extremely important difference in the upwelling mantle source beneath  $0^\circ$ - $9^\circ\text{E}$  versus  $9^\circ$ - $25^\circ\text{E}$ , 2) provides robust evidence supporting our previously proposed tectonomagmatic model for the generation of along-axis chemical variation, and 3) implicates the Shaka Fracture Zone as a significant impediment to along-axis mantle flow on the SW Indian Ridge [Georgen *et al.*, 1998].

## 6. Conclusions

In coordination with geologic, geophysical, and major element data presented in Chapter 2, we report a full trace element suite of data along with Sr, Nd, Pb, Hf, and He isotopic compositions, to better define the MORB mantle source and the melting processes controlling basalt chemistry. The following observations and conclusions are of importance:

1. Sr, Nd, Pb, and Hf isotope and trace element measurements on glasses from  $9^\circ$ - $25^\circ\text{E}$  are highly variable, indicating a MORB source that is isotopically heterogeneous. Along-axis systematic variation in basalt isotopic compositions along the orthogonal supersegment and local variability on the oblique supersegment further indicates progressive enrichment to higher  $^{87}\text{Sr}/^{86}\text{Sr}$ ,  $^{206}\text{Pb}/^{204}\text{Pb}$ ,  $^{207}\text{Pb}/^{204}\text{Pb}$ , and  $^{208}\text{Pb}/^{204}\text{Pb}$ , and lower  $^{143}\text{Nd}/^{144}\text{Nd}$ ,  $^{176}\text{Hf}/^{177}\text{Hf}$ ,  $^3\text{He}/^4\text{He}$ .
2. Incompatible trace element concentrations and ratios (i.e.  $(\text{La}/\text{Sm})_n$ ,  $(\text{Sm}/\text{Yb})_n$ ,  $\text{Ba}/\text{Zr}$ ) also show a substantial compositional range, but in general mimic the source enrichment displayed by isotope compositions, with striking systematic incompatible element enrichment trends from east to west along the orthogonal supersegment. Greater enrichment of the most incompatible over less incompatible element ratios is observed at

the Narrowgate segment with moderate enrichment at Joseph Mayes Seamount and also along much of the amagmatic accretionary segment. Tight linear trends in plots of  $(\text{La/Sm})_n$  and  $(\text{Sm/Yb})_n$  vs.  $^{87}\text{Sr}/^{86}\text{Sr}$  and  $^{143}\text{Nd}/^{144}\text{Nd}$  indicate strong coupling with long-lived isotopic indicators of source enrichment.

3. N-MORB trace element compositions typical of lavas from the eastern end of the orthogonal supersegment can be closely modeled as produced by at least 6% non-modal aggregate fractional melting of a DMM trace element composition, within the spinel lherzolite stability field.

4. Modeling shows that melting of depleted spinel lherzolite cannot explain the chemical variation observed for the E-MORB. Trace element contents and ratios indicate the necessity of a garnet-bearing lithology within the source. Garnet lherzolite melting is able to explain much of the variation within the E-MORBs, with the exception of the Narrowgate segment lavas.

5. Many incompatible trace element signatures of eclogite melting are observed in the Narrowgate segment lavas, including  $(\text{Nb/Ta})_n > 1$ ,  $(\text{Hf/Sm})_n < 1$ , inverse correlations between HREE and LREE, and extreme depletion of Sc correlated with elevated  $(\text{Sm/Yb})_n$ . These observations along with other chemical, geologic, and geophysical constraints strongly suggest that E-MORB compositions in the study area are generated by preferential vein melting, which provides a large proportion of the final melt volume erupted, especially on the oblique supersegment where melt focusing and conductive cooling indirectly control crustal accretion.

6. A discontinuity in  $^3\text{He}/^4\text{He}$  and absence of a discontinuity in heavy isotope compositions at Shaka Fracture Zone, suggests a  $^3\text{He}/^4\text{He}$  signature to the west reflecting variable influence from primary, previously un-melted Bouvet plume material; whereas to the east, lower overall and decreasing to the west  $^3\text{He}/^4\text{He}$  reflects an increasing contribution of ingrown  $^4\text{He}$  from previously melted Bouvet plume material. This observation is critical as it, 1) indicates a subtle but extremely important difference in the upwelling source mantle beneath  $0^\circ$ - $9^\circ\text{E}$  versus  $9^\circ$ - $25^\circ\text{E}$ , 2) provides robust evidence supporting our previously proposed tectonomagmatic model for the generation of along-axis chemical variation, and 3) implicates the Shaka Fracture Zone as a significant impediment to along-axis mantle flow on the Southwest Indian Ridge.

7. Through trace element melt modeling we are able to generate a PUM-normalized abundance pattern similar to those from Narrowgate segment by melting a source consisting of 96% DMM + 4% enriched “basaltic eclogite” lithology (represented by Bouvet lavas). The aggregate primary 12% melt is derived from 1) 50% melting of the enriched vein lithology, 2) 11% melting of DMM, with 6% garnet melting and 5% spinel melting, and 3) 2% melting of the enriched vein lithology in the “wings” of the melting regime, multiplied by 6, which represents the number of “extra” mantle source volumes from which these low-degree melts can be segregated and focused toward the main melting column.

## Acknowledgements

Foremost, I would like to extend a great deal of thanks to Jurek Blusztajn for his unending assistance, support, and advice on everything from isotope column chemistry to vacationing in New England, and most of all his friendship during long hours in the WHOI cleanroom or sitting in front of the Neptune ICP-MS. Thanks is also extended to Tracy Abbruzzese in the chemistry department at WHOI, who has endlessly been unselfish in assisting myself and others in cleanroom techniques, supplies, and goings on; not too mention the contagious smile she regularly brings to the lab. And speaking of mass spectrometers, I am greatly indebted to Lary Ball and Dave Schneider, long-standing professional mass spectrometists who, with a bit of my help (at least moral encouragement), produced a large portion of the isotopic data from each of their respective babies, the Neptune multicollector and the Element II single collector. Lary is also to thank for wonderful espresso, which luckily had an opposing effect on the Neptune relative to me – a stable Neptune signal despite jittery hands from the caffeine overload! Much of the initial isotope chemistry and Hf analytical work could not have occurred without the gracious access to Vincent Salters lab at FSU, and special thanks is due Michael Bizimis, who took me under his wing during two separate trips to FSU and showed me the subtleties of HOT-TIMS analytics...thanks Michael! Much of this manuscript revolves around trace element modeling and I owe Peter Kelemen a huge amount of gratitude for access to spreadsheets and his time, both of which were invaluable. And I need to thank my committee for their patience, comments, and guidance during the many stages of this work.

## Appendix A: Sample Digestion & Column Chemistry

### *Sample Digestion*

Acid digestion of basalt glasses used ultra-pure Seastar HF, HNO<sub>3</sub>, HCl, and HBr. Rather than digest separate glass fractions for Sr-Nd and Pb-Hf separation, we dissolved a single glass fraction, which was then split for respective column separation. For each sample approximately 500 mg of glass was digested in ~ 7 ml of a 3:1 HF-HNO<sub>3</sub> mixture, within Savillex vials. Vials were heated to 125°C for 12 hours, sealed, then uncovered at 110°C and dried down for 18-24 hours. If un-dissolved glass remained, additional 3:1 HF:HNO<sub>3</sub> was added and the same process repeated. Once the glass was completely dissolved, samples were picked up in 5-7 ml 6 N HCl and dried down slowly at ~100° C (6-8 hours), in order to 1) further attack and destroy any fluorides that may have formed during the HF dissolution step, and 2) to assess the completeness of dissolution. The 6 N HCl sample solutions should be relatively clear in color, if fully dissolved. The presence of glass requires further HF:HNO<sub>3</sub> digestion and the presence of grey, cloudy residues likely indicates fluorides precipitated from HF, and this requires additional 6 N HCl at ~110° C. Solutions were eventually dried down and put back into solution using 1-1.5 ml of 0.5N HBr. The sample solutions were ready for Pb ion exchange column separation.

### *Pb Column Chemistry*

Each 40 *ul* column was filled with new AG1-X8 (100-200 mesh) anion resin and cleaned prior to loading dissolved sample. Resin cleaning was a four-step process (each step requiring complete elution before continuing). The cleaning steps are the following, 1) 1 *ml* of 0.25N HNO<sub>3</sub>, 2) 0.5 *ml* of 0.25N HNO<sub>3</sub>, 3) repeat step 2, and 4) 0.5 *ml* of 6N HCl. Each column is then conditioned by loading 0.2 *ml* of 0.5N HBr three times.

Completely digested samples were brought into solution using 1-1.5 *ml* of 0.5N HBr. Teflon beakers were placed back on hotplates and taken to dryness slowly. 1 *ml* of 0.5N HBr was again added, this time carefully washing the sides of each beaker to ensure no sample is left on lid or beaker walls. After letting sample digest for ~30 minutes, solution was transferred carefully into centrifuge tubes. Additional HBr was used to rinse the residue from the beaker into the centrifuge tube. Each sample was spun for 2-3 minutes or until solution is clear. The sample solution was then ready to be loaded onto a cleaned and conditioned 40 *ul* anion column (see Appendix A for details). The residue-free portion of the sample solution was pipetted out of the centrifuge tube and slowly loaded onto the Pb column, careful not to stir the resin. (Note: The amount of sample solution loaded onto the column should not be much greater than 0.5 *ml* of 0.5N HBr. Sample volumes greater than this run the risk of washing through the columns during intermediate wash steps.) Two wash steps then followed, 1) 0.5 *ml* of 0.5N HBr and 2) 0.2 *ml* of 2N HCl were loaded onto each column. The eluted solution from all three steps was collected in the original dissolution beaker. The Pb fraction was then collected in a clean 7 ml Teflon Savillex beaker by loading 0.7 *ml* of 6N HCl.



At this point we have separated the Pb from the dissolved glass, but this Pb fraction must still go through some additional processing. For further purification of the Pb fraction (removal of Zr) it is passed through a second anion column. The Pb fraction is loaded onto the column in 0.5 ml of 0.5N HBr. Incidentally, the Pb fraction was collected from the first column in 6N HCl, thus that solution must be dried down and picked up in 0.5N HBr a couple of times prior to loading it on the second column. After Pb fraction is loaded it is washed down the column using 0.5 ml of 0.5N HBr and then 0.2 ml of 2N HCl. This second wash step involving 2N HCl brings the Pb to the bottom of the column, thus the final step, adding 1.5 ml of 0.4N HCl, strips all the Pb from the column. The Pb solutions are dried down and picked up with a few drops of conc. HNO<sub>3</sub>. Repeat 2-3 times and seal beaker dry until analysis at WHOI.

### ***Sr Column Chemistry***

Based on previously published elemental concentrations for basalts from nearby sections of the SWIR, the 1<sup>st</sup> eluted fraction from the Pb column was split into an Sr/Nd fraction and an Hf fraction. Assuming 100% elution of the sample solution loaded onto the column, with the equivalent of 400 mg of sample remaining in 2 ml of 2.5N HCl (Pb washout), we pipetted off 250  $\mu$ l ( $\approx$ 50 mg of glass) of solution to be the Sr/Nd fraction. This amount of sample was taken based on the calibrated limit for the cation columns, any more than this would run the risk of overloading the column. This new 50 mg Sr/Nd fraction was centrifuged and the residue-free portion loaded onto the cation columns. Please refer to Appendix A for description of cation column preparation and cleaning. The Sr/Nd fraction was loaded onto the calibrated AG50W-X8 (200-400 mesh) cation column in 0.25 ml of 2.5N HCl. Once each sample was loaded, three consecutive wash steps of 0.25 ml of 2.5N HCl were used to move the sample sufficiently into the resin to prevent disturbance of the sample by forthcoming loading steps. Since the elution curve for Sr and Nd is a function of the total volume of acid through the column, we report total volume through column rather than individual steps. 17 ml of 2.5N HCl was loaded onto each column and discarded. Sr was then collected in a clean 7 ml Teflon Savillex beaker and put aside. HREEs are removed from the column by loading 4-5 ml of 6N HCl and discarding. Collection of the REE fraction (Nd) was done in clean 7 ml Teflon Savillex beakers after loading 4 ml of 6N HCl to each column. 2-3 drops of HClO<sub>4</sub> is added to Sr fraction and then placed on hotplate at  $\sim$ 180° C until dry. The addition of HClO<sub>4</sub> enhances the breakdown of any organics that may have been stripped off the resin. Once dry, 2-3 drops of conc. HNO<sub>3</sub> is added and hotplate is turned down to  $\sim$ 105° C. Samples are dried down and HNO<sub>3</sub> step is repeated two more times at same temperature. Samples are then sealed dry until analysis at WHOI.

### ***Nd Column Chemistry***

Nd fractions collected from last step on the cation columns are picked up in 0.25 ml of 0.25N HCl and sonicated for 5-10 minutes to assure complete dissolution. Using a 125  $\mu$ l pipette and small tips load the 0.25 ml of sample through the hole located just above the resin. After loading sample use 3 rinse steps of 0.25 ml volumes of 0.25N HCl to move any drops of sample from hole into resin. Once rinse steps are complete, re-tape the

holes with Teflon tape. Then load 30 *ml* of 0.25N HCl and monitor until volume remaining in reservoir reaches 10 *ml*. At this point start timing, and refer to lab-calibrated worksheet. Each column has a time calibration for 1) amount of time (i.e. volume of acid eluting) before collecting Nd fraction, and 2) amount of time for Nd collection. Once you have collected Nd from each column for the specified amount of time, you can continue with the lab-calibrated worksheet if collecting Sm, or drain the column if Sm is of no interest. Columns are then cleaned before using again in 4 step as follows: 1) 20 *ml* of 6.2N HCl, 2) 10 *ml* of 6.2N HCl, 3) 5 *ml* of 0.25N HCl, and 4) 5 *ml* of 0.25 N HCl. Nd fractions are then dried and brought up in 1N HNO<sub>3</sub> for analysis via ICPMS.

## References

- Ahern, J. L., and D. L. Turcotte (1979), Magma migration beneath an ocean ridge, *Earth and Planetary Science Letters*, **45**, 115-122.
- Andres, M., J. Blichert-Toft, and J.-G. Schilling (2002), Hafnium isotopes in basalts from the southern Mid-Atlantic Ridge from 40° S to 55° S: Discovery and Shona plume-ridge interactions and the role of recycled sediments, *Geochemistry, Geophysics, Geosystems*, **3**, 25.
- Asimow, P. D., J. E. Dixon, and C. H. Langmuir (2004), A hydrous melting and fractionation model for mid-ocean ridge basalts: Applications to the Mid-Atlantic Ridge near the Azores, *Geochemistry, Geophysics, Geosystems*, **5**, 24.
- Barry, J. B., M.D. (2005), Melting and mantle flow beneath oblique ultraslow-spreading ridges, *in prep.*
- Barth, G. M., W. F. McDonough, and R. L. Rudnick (2000), Tracking the budget of Nb and Ta in the continental crust, *Chemical Geology*, **165**, 197-213.
- Batiza, R., and Y. Niu (1992), Petrology and magma chamber processes at the East Pacific Rise ~ 9°30'N, *Journal of Geophysical Research*, **97**, 6779-6797.
- Ben Othman, D., W. M. White, and J. Patchett (1989), The geochemistry of marine sediments, island arc magma genesis, and crust-mantle recycling, *Earth & Planetary Science Letters*, **94**, 1-21.
- Bender, J. F., C. H. Langmuir, and G. N. Hanson (1984), Petrogenesis of basalt glasses from the Tamayo Region, East Pacific Rise, *Journal of Petrology*, **25**, 213-254.
- Bindeman, I. N., A. M. Davis, and M. J. Drake (1998), Ion microprobe study of plagioclase-basalt partition experiments at natural concentration levels of trace elements, *Geochimica Cosmochimica Acta*, **64**, 1175-1193.
- Bizimis, M., V. J. M. Salters, and J. B. Dawson (2003), The brevity of carbonotite sources in the mantle: evidence from Hf isotopes, *Contr. Mineral. and Petrol.*, **145**, 281-300.
- Blichert-Toft, J., and F. Albarede (1997), The Lu-Hf isotope geochemistry of chondrites and the evolution of the mantle-crust system, *Earth & Planetary Science Letters*, **148**, 243-258.
- Blundy, J. D., J. A. C. Robinson, and B. J. Woods (1998), Heavy REE are compatible in clinopyroxene on the spinel lherzolite solidus, *Earth & Planetary Science Letters*, **160**, 493-504.
- Bougault, H., L. Dmitriev, J. G. Schilling, A. Sobolev, J. L. Joron, and H. D. Needham (1988), Mantle heterogeneity from trace elements: MAR triple junction near 14 °N, *Earth and Planetary Science Letters*, **88**, 27-36.
- Bown, J. W., and R. S. White (1994), Variation with spreading rate of oceanic crustal thickness and geochemistry, *Earth and Planetary Science Letters*, **121**, 435-439.
- Buck, W. R., and W. Su (1989), Focused mantle upwelling below mid-ocean ridges due to feedback between viscosity and melting, *Geophysic. Res. Lett.*, **16**, 641-644.

- Cannat, M., C. Rommevaux-Jestin, and H. Fujimoto (2003), Melt supply variations to a magma-poor ultra-slow spreading ridge (Southwest Indian Ridge 61° to 69° E), *Geochemistry, Geophysics, Geosystems*, 4, 21.
- Cannat, M., C. Rommevaux-Jestin, D. Sauter, C. Deplus, and V. Mendel (1999), Formation of the axial relief at the very slow spreading Southwest Indian Ridge (49° to 69°E), *Journal of Geophysical Research*, 104, 825-822,843.
- Christie, D. M., and J. M. Sinton (1981), Evolution of abyssal lavas along propagating segments of the Galapagos spreading center, *Earth and Planetary Science Letters*, 56, 321-335.
- Christie, D. M., R. Werner, F. Hauff, K. Hoernle, and B. B. Hanan (2005), Morphological and geochemical variations along the eastern Galapagos Spreading Center, *Geochemistry, Geophysics, Geosystems*, 6, 44.
- Cushman, B., J. Sinton, G. Ito, and J. E. Dixon (2004), Glass compositions, plume-ridge interaction, and hydrous melting along the Galapagos Spreading Center, 90.5° W to 98° W, *Geochemistry, Geophysics, Geosystems*, 5, 30.
- DeMets, C., R. G. Gordon, D. F. Argus, and S. Stein (1990), Current plate motions, *Geophys. J. Int.*, 101, 425-478.
- Dick, H., J. Lin, and H. Schouten (2003), An ultraslow-spreading class of ocean ridge, *Nature*, 426, 405-412.
- Dick, H. J. B., and R. L. Fisher (1984), Mineralogic studies of the residues of mantle melting: Abyssal and alpine-type peridotites, in *Kimberlites II. The Mantle and Crust -- Mantle Relationships*, edited by J. Kornprobst, pp. 295-308, Elsevier Science Publishers B.V., Amsterdam, The Netherlands.
- Dick, H. J. B., and J. H. Natland (1996), Late stage melt evolution and transport in the shallow mantle beneath the East Pacific Rise, in *Scientific Results*, edited by K. Gillis, C. Mevel, J. Allan and e. al., pp. 103-134, Ocean Drilling Program, Texas A&M University, College Station, TX.
- Donnelly, K. E., S. L. Goldstein, C. Langmuir, and M. Spiegelman (2004), Origin of enriched ocean ridge basalts and implications for mantle dynamics, *Earth & Planetary Science Letters*, 226, 20.
- Dulaney, T. (2002), Volcanic morphology of the ultraslow spreading Southwest Indian Ridge (15°-35° E): Implications for crustal construction, 203 pp, University of North Carolina, Wilmington, Wilmington.
- Dupré, B., and C. J. Allègre (1983), Pb-Sr isotope variation in Indian Ocean basalts and mixing phenomena, *Nature*, 303, 142-146.
- England, J. G., A. Zindler, L. Reisberg, J. L. Rubenstone, V. J. M. Salters, F. Marcantonio, B. Bourdon, H. K. Brueckner, P. J. Turner, S. D. Weaver, and P. Read (1992), The Lamont Doherty Geological Observatory ISOLAB 54 isotope ratio mass spectrometer, *International Journal of Mass Spectrometry and Ion Processes*, 121, 210-240.
- Escrig, S., F. Capmas, B. Dupré, and C. Allègre (2005), Osmium isotopic constraints on the nature of the DUPAL anomaly from Indian mid-ocean ridge basalts, *Nature*, 431, 59-63.



- Fisk, M. R., A. E. Bence, and J.-G. Schilling (1982), Major element chemistry of Galapagos Rift Zone magmas and their phenocrysts, *Earth and Planetary Science Letters*, *61*, 171-189.
- Frey, F. A., D. Stakes, N. Walker, S. R. Hart, and R. Nielsen (1993), Geochemical characteristics of basaltic glasses from the AMAR and FAMOUS axial valleys, Mid-Atlantic Ridge (36°-37°N): petrogenetic implications, *Earth and Planetary Science Letters*, *115*, 117-136.
- Fujimaki, H., M. Tatsumoto, and K. Aoki (1984), Partition coefficients of Hf, Zr, and REE between phenocrysts and groundmass, *Journal Geophysical Research*, *89*, B662-B672.
- Gaffney, A. M., B. K. Nelson, and J. Blichert-Toft (2005), Melting in the Hawaiian plume at 1-2 Ma as recorded at Maui Niu: The role of eclogite, peridotite, and source mixing, *Geochemistry, Geophysics, Geosystems*, *6*, 1-30.
- Galer, S. J. G., and R. K. O'Nions (1986), Magmagenesis and the mapping of chemical and isotopic variations in the mantle, *Chemical Geology*, *56*, 45-61.
- Georgen, J. E., M. Kurz, H. Dick, and J. Lin (2003), Low  $^3\text{He}/^4\text{He}$  ratios in basalt glasses from the western Southwest Indian Ridge (10°-24°E), *Earth & Planetary Science Letters*, *206*, 509-528.
- Georgen, J. E., J. Lin, and H. J. B. Dick (1998), Models of mantle upwelling beneath the Southwest Indian Ridge: the effects of ridge-transform geometry on magma supply at an ultra-slow spreading ridge, *EOS, Transactions of the American Geophysical Union*, *79*, 854.
- Graham, D. W., M. Kurz, W. J. Jenkins, J.-G. Schilling, G. Thompson, and S. Humphris (1992), Helium isotope geochemistry of mid-ocean ridge basalts from the South Atlantic, *Earth & Planetary Science Letters*, *110*, 133-147.
- Grindlay, N., F. J. Madsen, T. Dulaney, and D. Smith (2000), Variations in axial relief and gravity anomalies at the Southwest Indian Ridge 15°-35°E, paper presented at European Geophysical Society Meeting, Geophysical Research Abstracts.
- Hamelin, B., and C. J. Allègre (1985), Large-scale regional units in the depleted upper mantle revealed by an isotope study of the South-West Indian Ridge, *Nature*, *315*, 196-199.
- Hart, S. R. (1988), Heterogeneous mantle domains: signatures, genesis and mixing chronologies, *Earth & Planetary Science Letters*, *90*, 273-296.
- Hart, S. R. (1993), Equilibration during mantle melting: A fractal tree model, *Geology*, *90*, 11914-11918.
- Hart, S. R., and C. Brooks (1977), The geochemistry and evolution of the early Precambrian mantle, *Contr. Mineral. and Petrol.*, *61*, 109-128.
- Hart, S. R., G. A. Gaetani, and P. Kelemen (2005), Mantle Pb paradoxes: The sulfide solution, *Earth & Planetary Science Letters*, *submitted*.
- Hart, S. R., R. Workman, L. Ball, and J. Blusztajn (2003), High Precision Pb Isotope Techniques from the WHOI Neptune PIMMS, 7 pp, Woods Hole Oceanographic Institution, Woods Hole, MA.

- Hellebrand, E., J. E. Snow, P. Hoppe, and A. W. Hofmann (2002), Garnet-field melting and late-stage refertilization in 'residual' abyssal peridotites from the Central Indian Ridge, *Journal of Petrology*, **43**, 2305-2338.
- Hirschmann, M. M., T. Kogiso, M. B. Baker, and E. M. Stolper (2002), Alkalic magmas generated by partial melting of garnet pyroxenite, *Geology*, *in submission*.
- Hirschmann, M. M., and E. M. Stolper (1996), A possible role for garnet pyroxenite in the origin of the "garnet signature" in MORB, *Contributions to Mineralogy and Petrology*, **124**, 185-208.
- Hofmann, A. W. (1988), Chemical differentiation of the Earth: the relationship between mantle, continental crust, and oceanic crust, *Earth and Planetary Science Letters*, **90**, 297-314.
- Hofmann, A. W. (2003), Sampling Mantle Heterogeneity Through Oceanic Basalts: Isotopes and Trace Elements, in *Treatise on Geochemistry*, edited by R. W. Carlson, Elsevier.
- Hofmann, A. W., and S. R. Hart (1978), An assessment of local and regional isotopic equilibrium in the mantle, *Earth and Planetary Science Letters*, **38**, 44-62.
- Ito, G., and J. J. Mahoney (2004), Flow and melting of a heterogeneous mantle: 1. Method and importance to the geochemistry of ocean island and mid-ocean ridge basalts, *Earth & Planetary Science Letters*, **230**, 18.
- Janney, P. E., A. P. le Roex, and R. W. Carlson (2005), Hafnium isotope and trace element constraints on the nature of mantle heterogeneity beneath the central Southwest Indian Ridge (13° E to 47° E), *Submitted to Journal of Petrology*.
- Johnson, K. T. M. (1998), Experimental determination of partition coefficients for rare earth and high-field strength elements between clinopyroxene, garnet, and basaltic melt at high pressures, *Contr. Mineral. and Petrol.*, **133**, 60-68.
- Johnson, K. T. M., and H. J. B. Dick (1992), Open system melting and the temporal and spatial variation of peridotite and basalt compositions at the Atlantis II Fracture Zone, *Journal of Geophysical Research*, **97**, 9219-9241.
- Johnson, K. T. M., H. J. B. Dick, and N. Shimizu (1990), Melting in the oceanic upper mantle: An ion microprobe study of diopsides in abyssal peridotites, *Journal of Geophysical Research*, **95**, 2661-2678.
- Kelemen, P., G. Hirth, N. Shimizu, M. Spiegelman, and H. Dick (1997), A review of melt migration processes in the adiabatically upwelling mantle beneath oceanic spreading ridges, *Phil. Trans. R. Soc. Lond.*, **355**, 283-318.
- Kelemen, P. B., G. M. Yogodzinski, and D. W. Scholl (2003), Along-strike variation in lavas of the Aleutian island arc: implications for the genesis of high Mg# andesite and the continental crust, in *Inside the Subduction Factory*, edited by J. Eiler, AGU Monograph, Washington, DC.
- Kempton, P. D., J. A. Pearce, T. L. Barry, J. Godfrey-Fitton, C. Langmuir, and D. M. Christie (2002), Sr-Nd-Hf-Pb isotope results from ODP leg 187: Evidence for mantle dynamics and origin of the Indian MORB source, *Geochemistry, Geophysics, Geosystems*, **3**, 1074.
- Kinzler, R. J., and T. Grove (1992b), Primary magmas of mid-ocean ridge basalts 2. Applications, *Journal of Geophysical Research*, **97**, 6907-6926.

- Klein, E. M., and C. H. Langmuir (1987), Global correlations of ocean ridge basalt chemistry with axial depth and crustal thickness, *Journal of Geophysical Research*, **92**, 8089-8115.
- Kogiso, T., M.M. Hirschmann, and M. Pertermann (2004), High-pressure partial melting of mafic lithologies in the mantle, *Journal of Petrology*, **45**, 2407-2422.
- Kurz, M. D., J. J. Gurney, W. J. Jenkins, and D. E. Lott III (1987), Helium isotopic variability within single diamonds from the Orapa kimberlite pipe, **86**, 57-68.
- Kurz, M. D., W. J. Jenkins, J. G. Schilling, and S. R. Hart (1982), Helium isotopic variations in the mantle beneath the central North Atlantic Ocean, **58**, 1-14.
- Kurz, M. D., T. C. Kenna, J. C. Lassiter, and D. J. DePaolo (1996), Helium isotopic evolution of Mauna Kea Volcano: first results from the 1-km drill core, *Journal of Geophysical Research*, **101**, 11781-11791.
- Kurz, M. D., A. P. le Roex, and H. J. B. Dick (1998), Isotope geochemistry of the oceanic mantle near the Bouvet Triple Junction, *Geochim. Cosmochim. Acta*, **62**, 841-852.
- Langmuir, C. H., and J. F. Bender (1984), The geochemistry of oceanic basalts in the vicinity of transform faults; observations and implications., *Earth and Planetary Science Letters*, **69**, 107-127.
- Langmuir, C. H., J. F. Bender, and R. Batiza (1986), Petrological and tectonic segmentation of the East Pacific Rise, 5 degrees 30'-14 degrees 30' N, *Natures*, **322**, 422-429.
- Langmuir, C. H., E. M. Klein, and T. Plank (1992), Petrological systematics of mid-ocean ridge basalts: constraints on melt generation beneath ocean ridges, in *Mantle Flow and Melt Generation at Mid-Ocean Ridges*, edited by J. Phipps Morgan, D. K. Blackman and J. M. Sinton, pp. 183-280, American Geophysical Union, Washington, D.C.
- le Roex, A., A. Späth, and R. E. Zartman (2001), Lithospheric thickness beneath the southern Kenya Rift: implications from basalt geochemistry, *Contr. Mineral. and Petrol.*, **142**, 89-106.
- le Roex, A. P., H. J. B. Dick, and R. L. Fisher (1989), Petrology and geochemistry of MORB from 25°E to 46°E along the Southwest Indian Ridge: evidence for contrasting styles of mantle enrichment., *Journal of Petrology*, **30**, 947-986.
- le Roex, A. P., H. J. B. Dick, A. M. Reid, F. A. Frey, and A. J. Erlank (1985), Petrology and geochemistry of basalts from the American-Antarctic Ridge, Southern Ocean: implications for the westward influence of the Bouvet mantle plume, *Contributions to Mineralogy and Petrology*, **90**, 367-380.
- le Roex, A. P., H. J. B. Dick, and R. T. Watkins (1992), Petrogenesis of anomalous K-enriched MORB from the Southwest Indian Ridge: 11°53'E to 14°38'E, *Contributions to Mineralogy and Petrology*, **110**, 253-268.
- le Roex, A. P., and A. J. Erlank (1982), Quantitative evaluation of fractional crystallization in Bouvet Island lavas, *Journal of Volcanology and Geothermal Research*, **13**, 309-338.
- le Roux, P. J., A. le Roex, and J.-G. Schilling (2002a), MORB melting processes beneath the southern Mid-Atlantic Ridge (40-55°S): a role for mantle plume-derived pyroxenite, *Contr. Mineral. and Petrol.*, **144**, 206-229.

- le Roux, P. J., A. le Roex, J.-G. Schilling, N. Shimizu, W. W. Perkins, and N. J. G. Pearce (2002b), Mantle heterogeneity beneath the southern Mid-Atlantic Ridge: trace element evidence for contamination of ambient asthenospheric mantle, *Earth & Planetary Science Letters*, 203, 479-498.
- Mahoney, J., A. P. Le Roex, Z. Peng, R. L. Fisher, and J. H. Natland (1992), Southwestern limits of Indian Ocean ridge mantle and the origin of low  $^{206}\text{Pb}/^{204}\text{Pb}$  mid-ocean ridge basalt: isotope systematics of the Central Southwest Indian Ridge (17°-50°E), *Journal of Geophysical Research*, 97, 19,771-719,790.
- Mahoney, J. J., J. H. Natland, W. M. White, R. Poreda, S. H. Bloomer, R. L. Fisher, and A. N. Baxter (1989), Isotopic and geochemical provinces of the western Indian Ocean spreading centers, *Journal of Geophysical Research*, 94, 4033-4052.
- Mahoney, J. J., J. M. Sinton, M. D. Kurz, J. D. Macdougall, K. J. Spencer, and G. W. Lugmair (1994), Isotope and trace element characteristics of a super-fast spreading ridge: East Pacific rise, 13-23°S., *Earth and Planetary Science Letters*, 121, 173-193.
- McDonough, W. (1991), Partial melting of subducted oceanic crust and isolation of its residual eclogitic lithology, *Phil. Trans. R. Soc. Lond., A* 335, 407-418.
- McDonough, W. F., and S.-s. Sun (1995), The composition of the Earth, *Chemical Geology*, 120, 223-253.
- McKenzie, D. (1985), The extraction of magma from the crust and mantle, 74, 81-91.
- McKenzie, D., and M. J. Bickle (1988), The volume and composition of melt generated by extension of the lithosphere, *Journal of Petrology*, 29, 625-679.
- Melson, W. G., T. L. Vallier, T. L. Wright, G. Byerly, and J. Nelen (1976), Chemical diversity of abyssal volcanic glass erupted along Pacific, Atlantic, and Indian Ocean sea-floor spreading centers, *The Geophysics of the Pacific Ocean Basin and Its Margin*, *Geophysical Monograph* 19, 351-368.
- Mendel, V., and D. Sauter (1997), Seamount volcanism at the super slow-spreading Southwest Indian Ridge between 57° and 70°E, *Geology*, 25, 99-102.
- Mendel, V., D. Sauter, L. M. Parson, and J. R. Vanney (1997), Segmentation and morphotectonic variations along a super slow-spreading centre: the Southwest Indian Ridge (57°E-70°E), *Marine Geophysical Research*, 19, 503-531.
- Mendel, V., D. Sauter, C. Rommevaux-Jestin, P. Patriat, F. Lefebvre, and L. M. Parson (2003), Magmato-tectonic cyclicity at the ultra-slow spreading Southwest Indian Ridge: Evidence from variations of axial volcanic ridge morphology and abyssal hills pattern, *G-cubed*, 4, 23.
- Menke, W. (2005), <http://www.ldeo.columbia.edu/users/menke/plates.html>, edited by R. S. R. Calculator.
- Meyzen, C. M., J. N. Ludden, E. Humler, B. Luais, M. J. Toplis, and C. Mével (2005), Isotopic systematics from hot and cold mantle along the Southwest Indian Ridge, *submitted*.
- Meyzen, C. M., M. J. Toplis, E. Humler, J. N. Ludden, and C. Mevel (2003), A discontinuity in mantle composition beneath the southwest Indian ridge, *Nature*, 421, 731-733.

- Münker, C., S. Weyer, E. Scherer, and K. Mezger (2001), Separation of high field strength elements (Nb, Ta, Zr, Hf) and Lu from rock samples for MC-ICPMS measurements, *Geochemistry, Geophysics, Geosystems*, 2, 19.
- Niu, Y., and R. Batiza (1997), Trace element evidence from seamounts for recycled oceanic crust in the Eastern Pacific mantle, *Earth and Planetary Science Letters*, 148, 471-483.
- Niu, Y., D. Bideau, R. Hekinian, and R. Batiza (2001), Mantle compositional control on the extent of mantle melting, crust production, gravity anomaly, ridge morphology, and ridge segmentation: a case study at the Mid-Atlantic Ridge 33-35°N, *Earth & Planetary Science Letters*, 186, 383-399.
- Niu, Y., and R. Hekinian (1997), Spreading-rate dependence of the extent of mantle melting beneath ocean ridges, *Nature*, 385, 326-329.
- Niu, Y., M. Regelous, I. J. Wendt, R. Batiza, and M. J. O'Hara (2002), Geochemistry of near-EPR seamounts: importance of source vs. process and the origin of enriched mantle component, *Earth & Planetary Science Letters*, 199, 327-345.
- Niu, Y., D. G. Waggoner, J. M. Sinton, and J. J. Mahoney (1996), Mantle source heterogeneity and melting processes beneath seafloor spreading centers: The East Pacific Rise, 18 degrees-19 degrees S, *Journal of Geophysical Research*, 101, 27,711-727,733.
- Patchett, J., W. M. White, H. Feldmann, S. Kielinczuk, and A. W. Hofmann (1984), Hafnium/rare earth element fractionation in the sedimentary system and crustal recycling into the Earth's mantle, *Earth & Planetary Science Letters*, 69, 365-378.
- Perfit, M. R., D. J. Fornari, M. C. Smith, J. F. Bender, G. H. Langmuir, and R. M. Haymon (1994), Small-scale spatial and temporal variations in mid-ocean ridge crest magmatic processes, *Geology*, 22, 375-379.
- Pertermann, M., and M. M. Hirschmann (2002), Trace-element partitioning between vacancy-rich eclogitic clinopyroxene and silicate melt, *American Mineralogist*, 87, 1365-1376.
- Pertermann, M., and M. M. Hirschmann (2003a), Partial melting experiments on a MORB-like pyroxenite between 2 and 3 GPa: Constraints on the presence of pyroxenite in basalt source regions from solidus location and melting rate, *Journal of Geophysical Research*, 108, 16.
- Pertermann, M., and M. M. Hirschmann (2003b), Anhydrous partial melting experiments on MORB-like Eclogite: Phase relations, phase compositions and mineral/melt partitioning of major elements at 2-3 GPa, *Journal of Petrology*, 44, 2173-2201.
- Phipps Morgan, J. (2001), Thermodynamics of pressure release melting in a veined plum pudding mantle, *Geochemistry, Geophysics, Geosystems*, 2, 2000GC000049.
- Phipps Morgan, J., E. M. Parmentier, and J. Lin (1987), Mechanisms for the origin of mid-ocean ridge axial topography; implications for the thermal and mechanical structure of accreting plate boundaries, *Journal of Geophysical Research*, 92, 12823-12836.
- Plank, T., and C. Langmuir (1998), The chemical composition of subducting sediment and its consequences for the crust and mantle, *Chemical Geology*, 145, 325-394.



- Plank, T., and C. H. Langmuir (1992), Effects of the melting regime on the composition of the oceanic crust, *Journal of Geophysical Research*, 97, 19,749-719,770.
- Rehkämper, M., and A. W. Hofmann (1997), Recycled ocean crust and sediment in Indian Ocean MORB, *Earth and Planetary Science Letters*, 147, 93-106.
- Reid, I., and H. R. Jackson (1981), Oceanic spreading rate and crustal thickness, *Marine Geophysical Researches*, 5, 165-172.
- Rudnick, R. L., M. G. Barth, I. Horn, and W. McDonough (2000), Rutile-bearing refractory eclogites: Missing link between continents and depleted mantle, *Science*, 287, 278-281.
- Salters, V. J. M. (1994),  $^{176}\text{Hf}/^{177}\text{Hf}$  determination in small samples by a high temperature SIMS technique, *Analytical Chemistry*, 66, 4186-4189.
- Salters, V. J. M., and H. J. B. Dick (2002), Mineralogy of the mid-ocean-ridge basalt source from neodymium isotopic composition of abyssal peridotites, *Nature*, 418, 68-72.
- Salters, V. J. M., and J. Longhi (1999), Trace element partitioning during the initial stages of melting beneath mid-ocean ridges, *Earth & Planetary Science Letters*, 166, 15-30.
- Salters, V. J. M., and A. Zindler (1995), Extreme  $^{176}\text{Hf}/^{177}\text{Hf}$  in the sub-oceanic mantle, *Earth and Planetary Science Letters*, 129, 13-30.
- Sauter, D., H. Carton, V. Mendel, M. Munsch, C. Rommevaux-Jestin, J.-J. Schott, and H. Whitechurch (2004a), Ridge segmentation and the magnetic structure of the Southwest Indian Ridge (at 50°30'E, 55°30'E and 66°20'E): Implications for magmatic processes at ultraslow-spreading centers, *Geochemistry, Geophysics, Geosystems*, 5, 25.
- Sauter, D., V. Mendel, C. Rommevaux-Jestin, L. Parson, H. Fujimoto, C. Mevel, M. Cannat, and K. Tamaki (2004b), Focused magmatism versus amagmatic spreading along the ultraslow-spreading Southwest Indian Ridge: Evidence from TOBI side scan imagery, *Geochemistry, Geophysics, Geosystems*, 5, 20.
- Schilling, J.-G., R. N. Anderson, and P. Vogt (1976), Rare earth, Fe and Ti variations along the Galapagos spreading centre, and their relationship to the Galapagos mantle plume, *Nature*, 261, 108-113.
- Schilling, J.-G., R. H. Kingsley, and J. D. Devine (1982), Galapagos hot spot-spreading center system I. Spatial petrological and geochemical variations (83°W-101°W), *Journal of Geophysical Research*, 87, 5593-5610.
- Schilling, J.-G., M. Zajac, R. Evans, T. Johnston, W. White, J. D. Devine, and R. Kingsley (1983), Petrologic and geochemical variations along the Mid-Atlantic Ridge from 29°N to 73°N, *American Journal of Science*, 283, 510-586.
- Scott, D. R. (1993), Small-scale convection and mantle melting beneath mid-ocean ridges, in *Mantle Flow and Melt Generation at Mid-Ocean Ridges*, edited by J. Phipps Morgan, D. K. Blackman and J. M. Sinton, pp. 327-352, American Geophysical Union, Washington, D.C.
- Scott, D. R., and D. J. Stevenson (1989), A self-consistent model of melting, magma migration, and buoyancy-driven circulation beneath mid-ocean ridges, *Journal of Geophysical Research*, 94, 2973-2988.

- Seyler, M., M. Cannat, and C. Mevel (2003), Evidence for major-element heterogeneity in the mantle source of abyssal peridotites from the Southwest Indian Ridge (52° to 68° E), *Geochemistry, Geophysics, Geosystems*, **4**, 33.
- Shaw, D. M. (1970), Trace element fractionation during anatexis, *Geochim. Cosmochim. Acta*, **34**, 237-243.
- Shen, Y., and D. W. Forsyth (1995), Geochemical constraints on initial and final depths of melting beneath mid-ocean ridges, *Journal of Geophysical Research*, **100**, 2211-2237.
- Sinton, J. M., S. M. Smaglik, J. J. Mahoney, and K. C. Macdonald (1991), Magmatic processes at superfast spreading mid-ocean ridges: glass compositional variations along the East Pacific Rise 13°-23° S., *Journal of Geophysical Research*, **96**, 6133-6155.
- Standish, J. J., H. J. B. Dick, W. Melson, T. O'Hearn, and P. J. Michael (2005), The Influence of ridge geometry on magma chemistry at ultraslow-spreading rates (SW Indian Ridge from 9-25°E: A tectonomagmatic model for the origin of non-hotspot E-MORB, *Geochemistry, Geophysics, Geosystems*, *in prep.*
- Storey, M., A. D. Saunders, J. Tarney, I. L. Gibson, M. J. Norry, M. F. Thirwall, R. N. Thompson, and M. A. Menzies (1989), Contamination of Indian ocean asthenosphere by the Kerguelen Heard mantle plume, *Nature*, **338**, 574-576.
- Stracke, A., V. J. M. Salters, and K. W. W. Sims (1999), Assessing the presence of Garnet-Pyroxenite in the mantle source of basalts through combined Hafnium-Neodymium-Thorium Isotope systematics, *Geochemistry, Geophysics, Geosystems*, **1**, 14.
- Su, Y., and C. Langmuir (2002), Global MORB chemistry compilation at the segment scale, in *Petrologic Database of the Ocean Floor*, edited by <http://www.petdb.org/documentation/morbcompilation/index.jsp>.
- Sun, S.-s., and W. F. McDonough (1989), Chemical and isotopic systematics of oceanic basalts: implications for mantle composition and processes, in *Magmatism in the Ocean Basins*, edited by A. D. Saunders and M. J. Norry, pp. 313-345, Geological Society Special Publication No. 42.
- Sun, S.-S., M. Tatsumoto, and J.-G. Schilling (1975), Mantle plume mixing along the Reykjanes Ridge Axis: Lead isotopic evidence, *Science*, **190**, 143-147.
- Tartarotti, P., S. Susini, P. Nimis, and L. Ottolini (2002), Melt migration in the upper mantle along the Romanche Fracture Zone (Equatorial Atlantic), *Lithos*, **63**, 125-149.
- Taylor, S. R., and S. M. McLennan (1985), *The Continental Crust: Its Composition and Evolution*, Blackwell Scientific, Oxford.
- Todt, W., R. A. Cliff, A. Hanser, and A. W. Hofmann (1996), Evaluation of a <sup>202</sup>Pb-<sup>205</sup>Pb double spike for high-precision lead isotope analysis, in *Earth Processes: Reading the Isotopic Code*, edited by A. Basu and S. R. Hart, AGU - Geophysical Monograph Series 95, Washington, DC.
- Vervoort, J. D., J. Patchett, J. Blichert-Toft, and F. Albarede (1999), Relationships between Lu-Hf and Sm-Nd isotopic systems in the global sedimentary system, *Earth & Planetary Science Letters*, **168**, 79-99.

- Wasylenki, L. E., M. B. Baker, A. J. R. Kent, and E. M. Stolper (2003), Near-solidus melting of shallow upper mantle: Partial melting experiments on depleted peridotite., *Journal of Petrology*, 44, 1163-1191.
- Weaver, B. L. (1991), The origin of ocean island basalt end-member compositions: Trace element and isotopic constraints, *Earth & Planetary Science Letters*, 104, 381-397.
- Weaver, B. L., D. A. Wood, J. Tarney, and J. L. Joron (1986), Role of subducted sediment in the genesis of ocean island basalts: geochemical evidence from South Atlantic Ocean Islands, *Geology*, 14, 275-278.
- White, R. S., D. McKenzie, and R. K. O'Nions (1992), Oceanic crustal thickness from seismic measurements and rare earth element inversions, *Journal of Geophysical Research*, 97, 19683-19715.
- White, R. S., T. A. Minshull, M. J. Bickle, and C. J. Robinson (2001), Melt generation at very slow-spreading oceanic ridges: Constraints from geochemical and geophysical data, *Journal of Petrology*, 42, 1171-1196.
- Workman, R. K., and S. R. Hart (2005), Major and trace element composition of the depleted MORB mantle (DMM), *Earth & Planetary Science Letters*, 231, 53-72.
- Workman, R. K., S. R. Hart, M. Jackson, M. Regelous, K. A. Farley, J. Blusztajn, M. Kurz, and H. Staudigel (2004), Recycled metasomatised lithosphere as the origin of the Enriched Mantle II (EM2) end-member: Evidence from the Samoan Volcanic Chain, *Geochemistry, Geophysics, Geosystems*, 5, 44 pp.
- Yaxley, G. M. (2000), Experimental study of the phase and melting relations of homogeneous basalt + peridotite mixtures and implications for the petrogenesis of flood basalts, *Contr. Mineral. and Petrol.*, 139, 326-338.
- Yaxley, G. M., and D. H. Green (1998), Reactions between eclogite and peridotite: Mantle refertilization by subduction of oceanic crust, *Schweiz, Mineralogische und Petrographische Mitteilungen*, 78, 243-255.
- Zindler, A., F. A. Frey, and S. P. Jakobsson (1979), Nd and Sr isotope ratios and rare earth element abundances in Reykjanes Peninsula basalts: Evidence for mantle heterogeneity beneath Iceland, *Earth and Planetary Science Letters*, 45, 249-262.
- Zindler, A., and S. Hart (1986), Chemical geodynamics, *Annual Review of Earth and Planetary Sciences*, 14.

Table 1. Trace element concentrations (ppm) in glasses from 9°-25°E along the SW Indian Ridge, measured by inductively coupled plasma mass spectrometry (ICP-MS)\*.

Sample <sup>†</sup>	Latitude (°S)	Longitude (°E)	Depth (mbs)	Se	V	Cr	Ni	Cu	Tm	Rb	Ba	Th	U	Nb	Ta	K <sup>+</sup>	La	Ce	Pb	Pr	Nd	Sr	Zr	Hf	Sm	Eu	Ti <sup>†</sup>	Gd	Tb	Dy	Ho	Y	Er	Yb	Lu		
Oblique subsegment (9°56' - 11° E; 11°36' - 14°54' - 15°45' E)																																					
AN7-96-28	53.14	9.98	3134	31.2	245.9	190.7	36.7	77.0	67.6	0.43	9.28	106.7	1.29	0.39	16.15	0.92	4068	11.89	28.0	1.51	3.59	17.3	261.5	158.1	3.37	4.23	1.50	11449	516	0.81	5.27	1.06	37.3	3.03	2.80	0.41	
KN162-9-28-24	52.90	10.67	3635	32.7	243.0	283.4	37.0	102.7	76.5	0.36	10.82	120.6	1.48	0.41	19.09	1.45	4068	11.30	25.2	1.53	3.20	14.4	234.9	159.1	2.53	3.48	1.24	8691	417	0.67	4.37	0.88	22.9	2.47	2.28	0.34	
KN162-9-28-26	52.90	10.67	3635	29.0	247.3	337.3	35.0	109.6	60.2	0.41	9.66	94.9	1.45	0.41	18.70	2.64	717	10.13	32.1	1.59	3.11	22.0	262.2	168.5	3.56	4.70	1.55	10729	524	0.81	5.03	1.02	36.6	3.88	3.63	0.39	
KN162-9-28-32	52.90	10.67	3635	31.6	279.8	180.5	34.8	90.7	59.1	0.54	9.96	94.9	1.45	0.41	18.70	2.64	717	10.13	32.1	1.59	3.11	22.0	262.2	168.5	3.56	4.70	1.55	10729	524	0.81	5.03	1.02	36.6	3.88	3.63	0.39	
KN162-9-28-35	52.90	10.67	3635	28.4	243.5	232.0	34.7	112.9	59.2	0.40	10.32	112.0	2.96	0.80	34.53	1.26	723	20.45	42.9	1.73	3.34	50.9	21.6	263.1	168.1	3.56	4.69	1.51	10729	518	0.79	4.94	1.02	36.6	3.88	3.63	0.39
KN162-9-28-52	52.90	10.67	3635	29.0	217.7	220.0	40.9	73.4	59.0	0.36	8.38	95.3	1.25	0.35	15.25	1.26	372	11.01	25.8	1.23	3.33	15.1	279.1	131.1	2.74	3.62	1.28	9111	424	0.67	4.37	0.89	33.2	3.49	3.21	0.34	
KN162-9-28-63	52.90	10.67	3635	29.7	257.6	282.1	37.7	129.1	60.6	0.42	20.15	216.8	3.95	0.80	33.02	1.89	3719	11.25	45.4	1.68	3.32	22.7	261.0	170.3	3.61	4.66	1.29	9291	431	0.68	4.42	0.91	33.5	3.52	3.15	0.35	
KN162-9-28-65	52.90	10.67	3635	30.6	233.6	285.7	38.6	137.9	61.6	0.39	8.81	95.3	1.25	0.35	15.25	1.26	372	11.01	25.8	1.23	3.33	15.1	279.1	131.1	2.74	3.62	1.28	9111	424	0.67	4.37	0.89	33.2	3.49	3.21	0.34	
KN162-9-28-66	52.90	10.67	3635	28.6	249.0	288.2	35.5	125.0	59.0	0.42	19.86	212.0	2.92	0.80	32.87	1.89	3705	12.00	27.9	1.39	3.56	14.0	288.8	137.2	3.60	4.71	1.60	10779	549	0.88	5.14	1.05	36.6	3.90	3.69	0.39	
AN7-92-01	52.86	10.89	3700	32.6	272.0	110.2	45.2	107.2	67.8	0.41	10.12	121.3	1.17	0.39	16.22	0.87	4068	11.46	26.6	1.59	3.34	17.6	265.5	154.3	3.31	4.19	1.50	12108	528	0.78	5.13	1.03	27.0	2.86	2.61	0.36	
KN162-9-30-03	52.86	10.89	3700	32.6	272.0	110.2	45.2	107.2	67.8	0.41	10.12	121.3	1.17	0.39	16.22	0.87	4068	11.46	26.6	1.59	3.34	17.6	265.5	154.3	3.31	4.19	1.50	12108	528	0.78	5.13	1.03	27.0	2.86	2.61	0.36	
KN162-9-30-06	52.90	11.16	3536	31.8	192.1	105.3	49.0	186.8	90.8	0.39	4.70	56.6	0.64	0.19	7.80	0.44	2075	5.43	12.7	0.84	1.69	8.4	131.5	69.2	1.67	2.48	0.94	6593	331	0.81	4.07	0.89	23.1	2.61	2.59	0.39	
KN162-9-30-11	52.90	11.16	3536	33.1	257.2	248.5	43.4	171.6	68.9	0.42	6.92	82.3	1.06	0.39	12.31	0.70	3497	8.88	19.6	1.08	2.53	12.1	169.5	98.2	2.36	3.35	1.22	8991	451	0.77	4.88	1.02	26.3	2.90	2.67	0.40	
KN162-9-30-12	52.90	11.16	3536	32.6	254.4	244.7	44.6	194.7	67.8	0.41	6.77	83.6	1.05	0.39	12.15	0.69	3497	8.78	19.4	0.99	2.49	12.0	168.4	98.4	2.37	3.30	1.22	8951	459	0.77	4.88	1.02	26.3	2.90	2.67	0.40	
KN162-9-30-18	52.90	11.16	3536	37.6	199.6	93.6	48.6	175.6	89.5	0.40	4.95	57.6	0.88	0.19	8.19	0.45	2075	5.64	13.0	0.73	1.74	8.6	134.1	70.5	1.72	2.52	0.96	6534	338	0.61	4.06	0.90	23.4	2.67	2.62	0.40	
KN162-9-30-21	52.90	11.16	3536	35.2	261.6	239.8	45.6	132.6	71.9	0.43	7.07	83.9	1.13	0.31	12.81	0.78	3497	9.10	20.2	1.13	2.63	12.7	121.6	101.5	2.44	3.47	1.23	9171	469	0.79	4.91	1.04	26.8	2.97	2.71	0.42	
KN162-9-30-23	52.90	11.16	3536	33.7	255.1	233.1	45.1	170.7	69.0	0.41	6.92	82.6	1.09	0.30	12.24	0.75	3497	8.81	19.6	1.22	2.52	12.3	122.6	99.5	2.39	3.49	1.20	8931	446	0.75	4.79	1.00	26.3	2.84	2.63	0.40	
KN162-9-30-25	52.90	11.16	3536	33.9	257.4	267.7	42.9	163.9	70.0	0.42	7.01	84.5	1.11	0.30	12.45	0.75	3497	8.81	19.6	1.22	2.52	12.3	122.6	99.5	2.39	3.49	1.20	8931	446	0.75	4.79	1.00	26.3	2.84	2.63	0.40	
KN162-9-30-34	52.90	11.16	3536	39.0	200.2	327.3	48.5	175.3	92.9	0.40	5.14	58.5	0.74	0.20	8.41	0.48	2159	5.76	13.4	0.88	1.80	8.9	137.3	71.7	1.73	2.57	0.95	6294	351	0.67	4.08	0.89	23.4	2.62	2.58	0.39	
KN162-9-36-01	52.75	11.71	3981	30.2	225.8	295.3	37.4	142.7	66.1	0.47	3.11	35.7	0.41	0.12	4.59	0.31	1328	5.10	15.7	1.47	2.48	13.0	149.9	130.9	2.99	3.78	1.33	9231	496	0.82	5.27	1.12	29.1	3.16	2.90	0.45	
KN162-9-36-05	52.75	11.71	3981	29.5	218.5	364.9	38.7	160.8	63.8	0.46	2.95	34.8	0.41	0.12	4.55	0.30	1328	5.10	15.7	1.47	2.48	13.0	149.9	130.9	2.99	3.78	1.33	9231	496	0.82	5.27	1.12	29.1	3.16	2.90	0.45	
KN162-9-36-07	52.75	11.71	3981	30.0	233.2	317.4	37.2	134.7	61.2	0.48	3.94	49.0	0.52	0.15	6.12	0.40	1660	6.11	18.0	2.03	2.77	14.3	158.2	144.0	3.18	4.12	1.41	10070	524	0.88	5.58	1.17	31.2	3.34	3.11	0.46	
KN162-9-36-11	52.75	11.71	3981	30.6	241.6	318.7	38.3	142.6	63.9	0.49	4.36	46.4	0.57	0.17	6.57	0.41	1743	6.42	18.8	2.03	2.77	14.3	158.2	144.0	3.18	4.12	1.41	10070	524	0.88	5.58	1.17	31.2	3.34	3.11	0.47	
KN162-9-36-17	52.75	11.71	3981	30.0	228.3	342.4	39.2	178.7	72.4	0.48	3.02	34.0	0.41	0.11	4.79	0.31	1328	5.10	15.7	1.47	2.48	13.0	149.9	130.9	2.99	3.78	1.33	9231	496	0.82	5.27	1.12	29.1	3.16	2.90	0.45	
KN162-9-36-18	52.75	11.71	3981	30.2	230.6	279.3	37.1	134.7	63.9	0.47	3.04	35.6	0.42	0.11	4.79	0.31	1328	5.10	15.7	1.47	2.48	13.0	149.9	130.9	2.99	3.78	1.33	9231	496	0.82	5.27	1.12	29.1	3.16	2.90	0.45	
KN162-9-36-27	52.75	11.71	3981	30.5	240.7	343.0	39.9	163.1	62.7	0.49	4.34	46.3	0.57	0.17	6.54	0.41	1743	6.47	18.8	2.03	2.77	14.3	158.2	144.0	3.18	4.12	1.41	10070	524	0.88	5.58	1.17	31.2	3.34	3.11	0.47	
KN162-9-36-44	52.75	11.71	3981	30.6	242.3	355.3	40.1	159.8	64.7	0.50	4.29	46.7	0.56	0.16	6.48	0.41	1660	6.45	18.8	2.03	2.77	14.3	158.2	144.0	3.18	4.12	1.41	10070	524	0.88	5.58	1.17	31.2	3.34	3.11	0.47	
KN162-9-38-02	52.78	11.85	3964	34.1	244.2	322.5	38.5	128.3	61.6	0.51	4.54	52.2	0.64	0.19	7.32	0.44	1826	6.85	19.4	0.94	2.94	15.4	160.6	146.3	3.36	4.32	1.45	9890	545	0.90	5.84	1.22	31.7	3.50	3.25	0.48	
KN162-9-38-03	52.78	11.85	3964	34.1	276.9	260.8	38.7	112.6	59.6	0.36	11.04	119.7	1.75	0.30	19.10	1.10	4981	14.42	32.3	1.55	4.10	19.0	220.4	169.1	3.70	4.86	1.61	11029	592	0.97	6.32	1.33	33.9	3.80	3.55	0.54	
KN162-9-38-04	52.78	11.85	3964	34.4	277.1	259.7	38.9	118.0	59.3	0.55	11.04	119.9	1.75	0.49	18.82	1.08	4981	14.40	32.1	1.46	4.10	18.9	220.4	169.1	3.70	4.86	1.61	11029	592	0.97	6.32	1.33	34.0	3.77	3.57	0.53	
KN162-9-38-18B	52.78	11.85	3964	34.7	283.7	264.0	38.4	105.3	60.6	0																											

Sample <sup>1</sup>	Latitude (°S)	Longitude (°E)	Depth (mbs)	Se	V	Cr	Co	Ni	Cu	Tm	Rb	Ba	Th	U	Nb	Ta	K	La	Ce	Pb	Pr	Nd	Sr	Zr	Hf	Sm	Eu	Ti	Gd	Tb	Dy	Ho	Y	Er	Yb	Lu	
KN162-9-31-01	52.81	11.08	3184	36.0	275.1	204.3	39.2	69.7	79.0	0.50	9.70	106.7	1.43	0.40	16.09	0.93	3985	12.20	29.1	107	3.84	18.4	23.31	158.8	3.54	4.71	1.62	121.68	6.12	0.98	5.94	122	31.7	34.2	31.9	0.47	
KN162-9-32-03	52.75	11.22	2664	34.7	307.5	139.1	41.7	51.8	74.6	0.52	11.81	136.7	1.67	0.47	19.71	1.09	4732	13.97	33.0	179	4.30	20.2	23.52	169.0	3.78	5.20	1.77	13747	6.53	1.04	6.28	139	33.7	3.65	3.25	0.49	
KN162-9-32-04	52.75	11.22	2664	34.7	307.1	148.6	40.8	47.4	74.6	0.51	11.66	134.0	1.68	0.45	19.07	1.08	4732	13.96	32.5	171	4.28	20.2	23.52	167.4	3.77	5.16	1.76	13747	6.53	1.04	6.31	139	33.4	3.56	3.22	0.49	
KN162-9-32-09	52.75	11.22	2664	34.8	292.8	138.8	40.8	50.0	72.6	0.50	11.45	133.8	1.61	0.46	18.81	1.10	4698	13.66	32.4	173	4.25	20.2	23.58	164.9	3.74	5.12	1.72	12747	6.37	1.00	6.18	139	33.1	3.47	3.20	0.48	
KN162-9-32-16	52.75	11.22	2664	34.0	297.2	139.5	40.2	47.8	73.9	0.51	11.53	134.1	1.61	0.46	19.07	1.11	4815	13.85	32.8	173	4.27	20.2	23.59	165.8	3.77	5.15	1.71	12827	6.33	1.00	6.11	139	33.1	3.47	3.20	0.48	
KN162-9-33-18	52.82	11.39	1436	31.0	300.2	135.1	34.3	17.5	50.1	0.76	24.56	236.6	3.67	0.99	18.867	2.22	8800	26.63	40.5	259	7.67	36.2	240.2	223.5	6.59	8.22	2.44	18102	9.82	1.55	9.20	189	48.5	53.2	48.7	0.72	
KN162-9-33-41	52.82	11.39	1436	31.0	301.1	142.8	36.1	32.9	64.4	0.59	18.78	190.1	2.60	0.73	29.62	1.72	8801	20.19	45.6	177	5.76	26.2	240.2	223.5	6.59	8.22	2.44	18102	9.82	1.55	9.20	189	48.5	53.2	48.7	0.72	
KN162-9-33-49	52.82	11.39	1436	31.0	294.8	12.5	35.9	27.3	61.9	0.60	22.79	246.6	3.17	0.89	35.51	2.04	8802	23.99	45.6	177	5.76	26.2	240.2	223.5	6.59	8.22	2.44	18102	9.82	1.55	9.20	189	48.5	53.2	48.7	0.72	
KN162-9-33-56	52.82	11.39	1436	31.0	296.9	11.7	36.7	28.9	61.2	0.57	22.15	246.6	3.17	0.89	35.51	2.04	8802	23.99	45.6	177	5.76	26.2	240.2	223.5	6.59	8.22	2.44	18102	9.82	1.55	9.20	189	48.5	53.2	48.7	0.72	
KN162-9-33-59	52.82	11.39	1436	31.0	295.1	15.1	36.6	29.6	59.7	0.58	22.27	244.4	3.06	0.85	34.48	1.90	8719	23.10	51.7	171.8	6.38	28.3	230.2	234.2	6.89	6.67	2.04	15105	7.70	1.20	7.12	140	37.4	3.97	3.69	0.54	
KN162-9-33-60	52.82	11.39	1436	34.4	276.9	77.5	37.7	48.3	85.5	0.45	13.05	188.5	1.86	0.51	20.97	1.36	5984	14.38	31.1	152	4.27	19.7	253.8	159.5	3.54	4.76	1.64	12048	5.94	0.92	5.65	115	29.2	3.16	2.85	0.43	
KN162-9-33-66	52.83	11.39	1436	38.2	300.1	121	36.4	27.9	60.3	0.61	23.57	251.8	3.20	0.89	35.52	2.07	8302	24.03	52.7	173.5	6.42	29.2	280.9	147.1	5.13	6.92	2.14	14645	6.18	0.99	6.11	125	36.8	34.7	32.0	0.47	
KN162-9-34-01	52.83	11.39	1436	31.2	297.7	129.9	37.8	62.0	84.0	0.45	13.66	156.9	1.79	0.48	19.79	1.16	4732	14.14	31.2	156	3.98	18.3	248.2	175.8	3.83	5.16	1.74	12707	6.36	1.03	6.28	139	33.1	3.58	3.30	0.46	
KN162-9-34-07	52.86	11.43	2070	36.7	228.0	309.2	37.4	81.6	92.1	0.34	6.16	72.8	0.87	0.25	10.09	0.59	2657	7.70	18.6	108	24.7	12.0	215.5	102.3	2.35	3.27	1.17	8691	4.23	0.70	4.30	0.89	23.0	24.8	22.2	0.33	
KN162-9-34-06	52.86	11.43	2070	35.0	246.6	218.3	36.8	66.2	83.1	0.40	11.35	131.6	1.62	0.45	18.95	1.09	4698	13.92	29.6	149	3.77	17.4	253.9	144.9	3.10	4.20	1.42	11209	5.06	0.81	4.78	100	25.6	2.78	2.52	0.38	
KN162-9-34-19	52.86	11.43	2070	35.9	262.6	99.6	37.7	53.6	85.3	0.40	12.00	144.0	1.69	0.48	19.32	1.15	4698	13.92	29.6	149	3.77	17.4	253.9	144.9	3.10	4.20	1.42	11209	5.06	0.81	4.78	100	25.6	2.78	2.52	0.38	
KN162-9-34-23	52.86	11.43	2070	35.0	267.2	101.8	38.8	54.3	84.4	0.42	11.80	145.2	1.65	0.47	19.20	1.15	4732	13.42	30.6	199	3.88	18.0	257.6	145.5	3.21	4.41	1.45	10969	5.33	0.84	5.16	104	26.7	2.91	2.66	0.39	
KN162-9-34-42	52.86	11.43	2070	31.1	308.9	31.8	36.6	31.0	65.2	0.63	16.57	173.6	2.51	0.68	27.48	1.64	6309	18.80	43.0	170	5.53	25.6	229.5	223.6	4.94	6.32	2.01	14805	7.85	1.24	7.42	135	35.5	4.36	4.07	0.60	
KN162-9-35-02	52.93	11.36	2555	30.5	296.6	58.7	40.3	53.0	68.6	0.55	14.77	166.7	2.08	0.59	23.59	1.39	6309	16.70	38.5	178	4.91	22.7	240.9	192.3	4.24	5.65	1.88	14925	6.86	1.10	6.71	136	35.1	3.81	3.51	0.52	
KN162-9-35-04	52.93	11.36	2555	31.2	297.7	64.2	39.1	45.9	84.4	0.54	14.62	163.3	2.06	0.59	23.18	1.34	6143	16.33	38.0	176	4.84	22.6	241.2	190.9	4.16	5.55	1.84	15165	6.82	1.10	6.58	137	34.8	3.77	3.52	0.52	
KN162-9-35-05	52.93	11.36	2555	30.2	295.4	61.1	39.6	54.2	85.3	0.54	14.18	166.2	2.02	0.58	22.83	1.31	6309	16.33	38.2	198	4.83	22.4	239.2	191.8	4.19	5.58	1.85	15045	6.79	1.09	6.58	135	34.2	3.79	3.44	0.52	
KN162-9-35-09	52.93	11.36	2555	31.0	294.6	60.7	40.0	51.5	70.8	0.54	14.61	163.5	2.07	0.58	22.75	1.27	5894	16.50	37.9	174	4.83	22.6	241.3	191.9	4.15	5.51	1.87	14386	6.77	1.11	6.58	137	34.9	3.72	3.46	0.51	
KN162-9-35-10	52.93	11.36	2555	31.7	291.8	55.6	39.6	46.2	69.1	0.54	14.60	165.1	2.09	0.58	23.25	1.37	5894	16.50	37.9	174	4.83	22.6	241.3	190.4	4.11	5.58	1.85	14446	6.74	1.08	6.61	135	35.2	3.72	3.45	0.51	
KN162-9-35-14	52.93	11.36	2555	32.4	302.6	57.6	38.1	34.8	71.6	0.54	14.89	167.3	2.11	0.59	23.89	1.41	6143	16.68	38.4	281	4.93	22.8	247.7	191.7	4.16	5.65	1.83	15045	6.77	1.06	6.65	136	35.5	3.78	3.47	0.52	
Narrowgate Segment (14°15' - 14°54' E)																																					
VAN7-90-03	52.18	14.35	3973	16.3	319.1	15.0	33.7	16.8	35.8	0.43	54.10	731.6	7.09	1.81	82.82	4.25	18430	47.43	88.3	3.25	9.17	36.6	55.2	213.2	4.10	6.74	2.21	14446	6.80	0.96	5.80	1.11	28.2	31.3	28.0	0.40	
VAN7-90-06	52.18	14.35	3973	19.0	258.9	118.1	33.9	90.4	58.6	0.32	49.24	643.2	6.19	1.81	78.02	4.00	17932	44.72	83.3	3.25	9.17	36.6	55.2	213.2	4.10	6.74	2.21	14446	6.80	0.96	5.80	1.11	28.2	31.3	28.0	0.40	
VAN7-90-35	52.18	14.35	3973	26.2	246.2	198.5	40.2	189.1	74.3	0.28	31.07	387.2	3.53	0.98	45.22	3.27	12868	26.65	51.5	205	5.59	23.1	452.5	148.5	3.02	4.54	1.54	11688	4.73	0.66	3.99	0.76	18.9	21.0	1.82	0.26	
VAN7-90-52	52.18	14.35	3973	21.6	270.8	123.4	34.5	89.9	56.6	0.30	49.91	627.0	3.12	0.97	46.11	4.04	17517	42.43	81.3	30.8	74.3	33.6	74.3	23.4	3.89	5.85	1.96	13487	5.84	0.79	4.68	0.86	22.5	23.1	1.98	0.26	
VAN7-90-77	52.18	14.35	3973	33.5	291.1	177.9	37.5	110.9	94.1	0.30	9.80	133.0	1.47	0.43	17.78	1.08	4234	12.69	27.4	156	3.31	15.0	314.9	105.3	2.40	3.45	1.24	9111	4.03	0.61	3.84	0.77	19.6	22.0	1.95	0.28	
VAN7-90-82a	52.18	14.35	3973	35.9	246.8	195.7	38.0	110.8	92.4	0.28	16.78	210.6	2.55	0.72	31.45	1.68	7970	19.95	40.7	210	4.58	19.6	418.8	135.6	2.79	3.96											





Sample#	Latitude (°N)	Longitude (°E)	Depth (m)	Sc	V	Cr	Co	Ni	Cu	Tm	Rb	Ba	Th	U	Nb	Ta	K	La	Ce	Pb	Pr	Nd	Si	Zr	Hf	Sm	Eu	Tb	Gd	Tb	Dy	Ho	Y	Er	Yb	Lu
KN162-7-13-31	52.86	19.91	4067	36.9	289.1	275.2	41.2	113.7	66.0	0.50	2.55	27.2	0.41	0.13	5.75	0.51	1577	562	16.4	0.75	2.54	13.6	158.7	135.2	13.8	410.14	10669	536	0.91	5.90	1.73	32.1	33.8	3.70	0.49	
KN162-7-13-39	52.86	19.91	4067	37.5	296.2	278.5	42.7	119.1	66.2	0.51	2.60	28.7	0.42	0.13	5.97	0.59	1494	538	16.5	0.78	2.53	13.7	160.3	135.8	13.7	409.14	10550	540	0.91	5.91	1.74	32.4	35.7	3.30	0.49	
KN162-7-13-41	52.86	19.91	4067	37.1	296.2	284.5	42.4	122.1	69.6	0.51	2.56	26.9	0.43	0.13	5.95	0.55	1494	538	16.5	0.78	2.53	13.6	161.1	136.1	13.9	410.14	10669	555	0.93	5.94	1.74	32.4	35.8	3.35	0.49	
KN162-7-13-42	52.86	19.91	4067	36.6	283.9	280.4	41.5	120.7	66.1	0.46	2.35	24.6	0.38	0.12	5.30	0.50	1494	538	15.7	0.69	2.44	13.0	158.4	129.4	13.9	409.14	10669	527	0.87	5.72	1.19	31.1	34.3	3.19	0.46	
KN162-7-15-05	52.86	20.38	3403	35.3	247.5	304.2	42.7	129.8	66.1	0.48	2.32	21.0	0.32	0.12	6.89	0.60	1494	538	15.7	0.69	2.44	12.9	158.4	129.4	13.9	409.14	10669	527	0.87	5.72	1.19	31.1	34.3	3.19	0.46	
KN162-7-15-08	52.87	20.38	3403	35.3	247.5	304.2	42.7	129.8	66.1	0.48	2.32	21.0	0.32	0.12	6.89	0.60	1494	538	15.7	0.69	2.44	12.9	158.4	129.4	13.9	409.14	10669	527	0.87	5.72	1.19	31.1	34.3	3.19	0.46	
KN162-7-14-02	52.87	20.40	3403	34.6	272.6	254.2	41.4	115.8	64.4	0.50	1.31	16.7	0.28	0.09	4.21	0.41	1162	477	14.6	0.71	2.32	12.7	158.5	127.7	13.7	409.14	10669	527	0.87	5.72	1.19	31.1	34.3	3.19	0.46	
KN162-7-14-03	52.87	20.40	3403	34.6	272.6	254.2	41.4	115.8	64.4	0.50	1.31	16.7	0.28	0.09	4.21	0.41	1162	477	14.6	0.71	2.32	12.7	158.5	127.7	13.7	409.14	10669	527	0.87	5.72	1.19	31.1	34.3	3.19	0.46	
KN162-7-14-04	52.87	20.40	3403	34.7	273.7	254.1	41.4	116.0	64.4	0.50	1.46	16.9	0.28	0.10	4.23	0.41	1162	485	14.3	0.69	2.29	12.4	154.5	125.2	13.7	409.14	10669	527	0.87	5.72	1.19	31.1	34.3	3.19	0.46	
KN162-7-14-06	52.87	20.40	3403	34.4	274.3	259.9	41.6	116.3	65.8	0.50	1.53	17.4	0.28	0.10	4.21	0.41	1162	470	14.3	0.56	2.27	12.5	154.2	125.2	13.7	409.14	10669	527	0.87	5.72	1.19	31.1	34.3	3.19	0.46	
KN162-7-14-08	52.87	20.40	3403	35.5	275.0	261.1	41.6	119.5	66.1	0.50	1.59	17.5	0.28	0.10	4.41	0.48	1162	470	14.3	0.56	2.27	12.5	154.2	125.2	13.7	409.14	10669	527	0.87	5.72	1.19	31.1	34.3	3.19	0.46	
KN162-7-14-09	52.87	20.40	3403	35.6	276.4	268.9	41.5	118.2	67.1	0.50	1.58	17.9	0.29	0.10	4.39	0.41	1162	472	14.4	1.19	2.32	12.5	156.2	125.6	13.7	409.14	10669	527	0.87	5.72	1.19	31.1	34.3	3.19	0.46	
KN162-7-14-10	52.87	20.40	3403	35.4	276.2	265.2	41.7	120.5	67.4	0.49	1.57	16.9	0.28	0.10	4.29	0.41	1162	473	14.6	1.19	2.32	12.5	156.2	125.6	13.7	409.14	10669	527	0.87	5.72	1.19	31.1	34.3	3.19	0.46	
KN162-7-16-01	52.92	20.66	4235	35.5	276.3	265.7	41.6	119.3	67.2	0.50	1.58	17.4	0.28	0.10	4.32	0.41	1162	472	14.4	1.19	2.32	12.5	156.2	125.6	13.7	409.14	10669	527	0.87	5.72	1.19	31.1	34.3	3.19	0.46	
KN162-7-16-02	52.92	20.66	4235	35.6	265.3	352.6	43.0	123.7	74.1	0.45	0.69	8.1	0.15	0.06	2.34	0.33	830	33.2	11.3	0.66	1.91	10.9	137.1	109.4	2.65	3.46	1.22	10789	474	0.79	5.16	1.09	29.0	31.1	2.92	0.44
KN162-7-16-04	52.92	20.66	4235	34.7	261.2	356.6	42.3	118.2	72.9	0.45	0.70	8.4	0.14	0.05	2.27	0.38	830	33.5	11.3	0.73	1.90	10.8	136.7	109.6	2.65	3.46	1.22	10789	474	0.79	5.16	1.09	29.0	31.1	2.92	0.44
KN162-7-16-05	52.92	20.66	4235	35.3	265.1	343.9	42.2	118.8	72.9	0.45	0.70	7.6	0.14	0.05	2.30	0.30	830	33.3	11.4	0.66	1.92	11.0	136.8	109.5	2.67	3.50	1.23	10010	476	0.80	5.19	1.09	29.0	31.1	2.92	0.43
KN162-7-16-07	52.98	20.69	3797	33.3	250.7	304.7	42.2	152.4	66.5	0.46	0.80	9.5	0.18	0.07	2.85	0.31	1079	375	12.0	1.12	1.98	11.1	144.4	113.2	2.68	3.51	1.29	9531	472	0.79	5.35	1.13	28.6	3.26	0.30	0.44
KN162-7-17-01	52.98	20.69	3797	30.4	240.4	262.5	39.6	147.5	59.3	0.47	1.31	15.5	0.23	0.10	3.88	0.24	1577	522	15.9	1.17	2.46	13.4	180.2	137.6	3.10	3.94	1.41	10490	521	0.85	5.68	1.16	30.1	33.8	3.13	0.46
KN162-7-17-02	52.98	20.69	3797	33.1	264.6	283.6	40.3	132.5	65.6	0.53	0.74	8.9	0.17	0.07	2.81	0.36	1162	446	14.7	1.67	2.39	13.4	154.1	136.0	3.19	4.18	1.48	10729	562	0.91	6.23	1.28	32.7	37.3	3.49	0.51
KN162-7-17-03	52.98	20.69	3797	33.0	274.4	294.5	42.3	145.0	66.0	0.52	0.71	9.0	0.17	0.07	2.80	0.32	1096	444	14.6	1.21	2.37	13.3	155.3	137.9	3.24	4.15	1.45	10729	549	0.89	6.06	1.25	32.2	36.4	3.43	0.50
KN162-7-17-04	52.95	20.93	3850	37.5	273.0	302.3	41.5	125.6	70.1	0.53	0.72	6.9	0.18	0.07	2.86	0.33	913	416	13.9	0.85	2.28	12.6	157.3	130.9	3.09	3.96	1.41	10310	540	0.91	5.92	1.26	32.9	36.4	3.41	0.50
KN162-7-17-05	52.95	20.93	3850	37.1	199.0	259.1	37.2	104.0	55.2	0.34	0.76	9.8	0.15	0.06	2.31	0.28	1162	305	9.7	0.76	1.55	8.5	123.4	86.4	2.01	2.57	0.93	9351	333	0.61	3.85	0.81	21.5	23.3	2.18	0.33
KN162-7-17-06	52.95	20.93	3850	34.3	252.4	330.2	40.9	139.6	71.6	0.42	0.97	10.9	0.19	0.07	3.16	0.35	1245	385	12.2	0.72	1.94	10.7	156.5	109.4	2.46	3.29	1.18	9791	446	0.75	4.91	1.04	27.1	29.6	2.78	0.41
KN162-7-17-07	52.95	20.93	3850	37.4	279.4	288.4	42.4	127.9	68.2	0.53	0.78	8.1	0.19	0.07	3.03	0.36	996	432	13.7	0.82	2.33	13.2	154.4	134.0	3.14	4.11	1.46	10729	549	0.94	6.07	1.28	34.1	37.1	3.49	0.52
KN162-7-17-08	52.95	20.93	3850	33.3	248.9	324.9	41.6	135.0	68.5	0.44	0.94	12.7	0.19	0.07	3.44	0.30	1162	385	12.2	0.72	1.94	10.4	154.4	134.0	3.14	4.11	1.46	10729	549	0.94	6.07	1.28	34.1	37.1	3.49	0.52
KN162-7-17-09	52.95	20.93	3850	33.8	251.0	330.7	40.7	128.7	69.7	0.44	0.95	12.7	0.20	0.08	3.35	0.51	1162	390	12.3	0.71	1.96	10.6	154.7	134.0	3.14	4.11	1.46	10729	549	0.94	6.07	1.28	34.1	37.1	3.49	0.52
KN162-7-17-10	52.95	20.93	3850	33.3	251.0	330.7	40.7	128.7	69.7	0.44	0.95	12.7	0.20	0.08	3.35	0.51	1162	390	12.3	0.71	1.96	10.6	154.7	134.0	3.14	4.11	1.46	10729	549	0.94	6.07	1.28	34.1	37.1	3.49	0.52
KN162-7-17-11	52.95	20.93	3850	33.8	251.0	330.7	40.7	128.7	69.7	0.44	0.95	12.7	0.20	0.08	3.35	0.51	1162	390	12.3	0.71	1.96	10.6	154.7	134.0	3.14	4.11	1.46	10729	549	0.94	6.07	1.28	34.1	37.1	3.49	0.52
KN162-7-17-12	52.95	20.93	3850	35.6	245.5	409.9	43.7	171.6	67.2	0.42	0.95	11.9	0.20	0.07	3.40	0.69	1162	395	12.4	1.10	1.96	10.6	155.3	134.0	3.14	4.11	1.46	10729	549	0.94	6.07	1.28	34.1	37.1	3.49	0.52
KN162-7-17-13	52.95	20.93	3850	33.8	253.2	351.5	41.8	138.8	69.1	0.42	0.97	13.2	0.19	0.07	3.48	0.49	1162	395	12.4	1.10	1.96	10.6	155.3	134.0	3.14	4.11	1.46	10729	549	0.94	6.07	1.28	34.1	37.1	3.49	0.52
KN162-7-17-14	52.95	20.93	3850	36.8	272.8	302.3	42.9	126.7	68.9	0.53	0.72	7.6	0.18	0.07	3.12	0.49	996	418	13.9	0.60	2.31	12.5	155.1	129.2	3.07	3.89	1.47	10669	555	0.93	6.08	1.27	33.2	36.2	3.38	0.51
KN162-7-17-21	52.95	20.93	3850	35.4	244.9	302.8	43.4	166.1	67.0	0.42	0.94	12.9	0.19	0.07	3.39	0.51	1162	382	12.1	0.71	1.92	10.5	155.6	130.9	3.03	4.00	1.48	10610	560	0.95	6.08	1.30	33.1	36.7	3.42	0.51
KN162-7-17-29	52.95	20.93	3850	32.9	272.9	307.9	41.9	118.4	69.8	0.53	0.68	8.1	0.18	0.07	3.19	0.42	1245	379	12.1	0.52	2.31	12.8	155.8	130.9	3.03	4.00	1.48	10610	560	0.95	6.08	1.30	33.1	36.7	3.42	0.51
KN162-7-17-32	52.95	20.93	3850	28.8	248.2	323.1	41.1	134.1	68.3	0.43	0.91	12.5	0.19	0.07	3.42	0.43	1245	379	12.1	0.52	2.31	12.8	155.8	130.9	3.03	4.00	1.48									

Sample	Latitude (°S)	Longitude (°E)	Depth (mbsl)	V	Cr	Co	Ni	Cu	Tm	Rb	Ba	Th	U	Nb	Ta	K'	La	Ce	Pb	Pr	Nd	Sr	Zr	Hf	Sm	Eu	Ti	Gd	Tb	Dy	Ho	Y	Er	Yb	Lu	
KN162-72-04	53.04	22.18	4170	33.4	243.1	338.4	40.9	143.5	66.1	0.42	0.70	9.7	0.15	0.06	2.80	0.42	996	377	12.2	0.61	1.98	10.6	171.2	109.0	2.53	3.25	1.23	8392	4.49	0.75	4.76	1.01	25.9	2.87	2.64	0.40
KN162-72-06	53.04	22.18	4170	33.5	243.2	342.3	41.9	149.3	65.5	0.41	0.68	10.3	0.15	0.06	2.86	0.42	996	3.81	12.3	0.56	1.99	10.7	173.0	108.9	2.47	3.33	1.22	8631	4.40	0.75	4.74	1.00	25.9	2.84	2.63	0.40
KN162-72-10	53.04	22.18	4170	33.9	243.6	339.1	41.6	151.5	65.2	0.41	0.66	9.6	0.15	0.06	2.84	0.42	996	3.79	12.2	0.46	1.96	10.7	167.5	108.5	2.48	3.31	1.22	8332	4.41	0.74	4.76	1.00	25.9	2.84	2.62	0.39
KN162-72-10	53.04	22.18	4170	33.5	243.6	340.4	41.3	142.2	65.4	0.41	0.69	9.9	0.15	0.06	2.85	0.41	996	3.77	12.3	0.51	1.97	10.6	172.8	108.8	2.53	3.28	1.24	8332	4.41	0.75	4.76	1.01	26.0	2.86	2.68	0.39
VAN7-69-35	53.14	22.45	3864	35.2	296.4	272.8	42.7	129.0	66.6	0.57	0.71	9.3	0.16	0.07	2.73	0.16	1162	4.43	15.4	1.20	2.58	14.4	159.8	150.7	3.50	4.51	1.56	11269	6.14	0.99	6.60	1.35	35.3	3.96	3.62	0.54
VAN7-69-39	53.14	22.45	3864	35.2	293.2	279.3	42.3	129.9	65.5	0.55	0.42	6.5	0.13	0.06	2.34	0.15	1162	4.43	14.5	1.16	2.39	13.5	160.6	145.5	3.39	4.24	1.52	11329	5.78	0.96	6.47	1.33	34.2	3.86	3.55	0.52
VAN7-69-50	53.14	22.45	3864	32.8	256.5	318.5	41.2	132.6	64.5	0.44	0.46	6.4	0.11	0.05	1.94	0.12	913	3.43	14.3	1.17	1.87	10.7	155.1	111.6	2.61	3.39	1.28	8751	4.69	0.78	5.31	1.09	27.8	3.14	2.86	0.42
VAN7-69-57	53.14	22.45	3864	33.2	258.1	319.2	41.1	135.1	64.8	0.42	0.47	7.0	0.11	0.05	1.86	0.10	913	3.36	11.1	1.10	1.84	10.7	153.6	109.5	2.53	3.34	1.25	8811	4.52	0.75	5.06	1.07	27.7	3.08	2.86	0.42
VAN7-69-71	53.14	22.45	3864	33.0	255.8	318.0	41.0	133.1	65.0	0.43	0.47	7.0	0.11	0.05	1.88	0.10	909	3.40	11.4	1.09	1.88	10.8	155.7	111.3	2.59	3.34	1.25	8811	4.52	0.75	5.06	1.07	27.7	3.08	2.86	0.42
VAN7-69-79	53.14	22.45	3864	32.4	278.8	257.2	40.2	125.9	65.0	0.54	0.48	6.7	0.14	0.06	2.87	0.34	1099	4.41	14.8	1.20	2.44	13.9	152.9	144.2	3.35	4.28	1.53	11149	5.79	0.96	6.40	1.33	33.4	3.88	3.52	0.51
KN162-72-01-01	53.04	22.47	3722	33.1	240.7	344.8	41.1	158.9	66.2	0.40	0.80	12.1	0.16	0.06	2.58	0.24	996	3.51	11.5	0.66	1.84	9.9	161.2	100.7	2.32	3.01	1.16	8332	4.27	0.72	4.59	0.96	24.8	2.76	2.58	0.38
KN162-72-01-02	53.04	22.47	3722	33.0	237.4	423.6	40.2	141.5	65.1	0.38	0.77	10.8	0.17	0.06	2.66	0.24	913	3.50	11.0	0.61	1.79	9.8	157.2	96.9	2.32	3.01	1.16	8332	4.12	0.67	4.42	0.94	24.4	2.68	2.50	0.37
KN162-72-01-05	53.04	22.47	3722	33.4	247.5	374.9	40.2	141.5	65.1	0.38	0.77	10.8	0.17	0.06	2.66	0.24	913	3.50	11.0	0.61	1.79	9.8	157.2	96.9	2.32	3.01	1.16	8332	4.12	0.67	4.42	0.94	24.4	2.68	2.50	0.37
KN162-72-01-06	53.04	22.47	3722	33.5	243.5	413.9	41.7	162.7	66.4	0.40	0.81	12.9	0.17	0.07	2.97	0.21	996	3.52	11.2	0.68	1.83	10.1	163.1	100.3	2.42	3.14	1.17	8332	4.12	0.70	4.58	0.97	24.9	2.77	2.52	0.39
KN162-72-01-06*	53.04	22.47	3722	33.86	236.2	325.9	41.56	153.4	66.3	0.39	0.58	10.6	0.15	0.06	2.31	0.25	996	3.52	11.1	0.87	1.81	9.77	143.4	100.2	2.34	3.14	1.17	8332	4.12	0.69	4.65	0.94	25.2	2.75	2.47	0.35
KN162-72-11-03	53.04	22.47	3722	33.4	242.9	380.7	40.7	154.7	67.6	0.39	0.80	11.7	0.15	0.06	2.58	0.21	913	3.46	11.1	0.74	1.83	10.0	164.2	99.6	2.39	3.15	1.14	8332	4.06	0.68	4.55	0.96	24.9	2.74	2.58	0.39
KN162-72-11-21	53.04	22.47	3722	33.3	234.4	330.2	39.6	144.9	62.5	0.39	0.80	12.3	0.18	0.07	2.98	0.23	1411	3.68	11.7	0.71	1.88	10.3	179.3	104.1	2.44	3.18	1.15	8891	4.09	0.85	5.60	1.18	30.5	3.35	3.14	0.47
KN162-72-21-05	53.04	22.47	3722	33.5	245.8	366.7	39.5	130.4	66.8	0.41	0.81	13.2	0.17	0.06	2.64	0.21	913	3.58	11.6	0.80	1.90	10.5	165.6	101.9	2.50	3.29	1.16	8572	4.17	0.71	4.73	0.99	25.6	2.79	2.64	0.40
KN162-72-21-25	53.04	22.47	3722	33.5	244.3	342.2	40.2	142.6	66.2	0.39	0.81	13.4	0.16	0.06	2.64	0.21	913	3.49	11.3	0.62	1.87	10.3	165.1	100.0	2.37	3.17	1.14	8212	4.04	0.69	4.63	0.97	25.0	2.75	2.53	0.38
KN162-72-21-30	53.04	22.47	3722	33.3	228.7	333.9	40.2	154.2	63.5	0.40	0.81	12.9	0.17	0.07	2.97	0.21	1411	3.73	11.7	0.59	1.88	10.0	176.7	102.3	2.38	3.09	1.17	9051	4.13	0.69	4.59	0.97	24.7	2.75	2.56	0.38
KN162-72-31-07	53.17	22.55	3699	34.4	292.0	252.0	41.9	134.6	59.1	0.59	1.24	15.7	0.26	0.11	4.25	0.39	1404	5.57	17.8	1.42	2.87	15.7	169.1	164.2	3.28	4.03	1.65	12108	6.23	1.04	6.87	1.43	37.4	4.07	3.84	0.57
KN162-72-31-31	53.17	22.55	3699	32.9	256.4	302.7	40.3	126.2	61.9	0.48	0.43	6.6	0.12	0.05	2.05	0.20	830	3.69	12.6	0.68	2.14	11.9	153.6	121.2	2.87	3.71	1.36	9411	4.95	0.84	5.53	1.18	30.4	3.35	3.11	0.46
KN162-72-31-36	53.17	22.55	3699	33.1	257.3	304.4	40.3	127.0	61.8	0.48	0.43	7.2	0.12	0.05	2.06	0.19	830	3.70	12.6	0.75	2.12	11.8	154.5	121.5	2.89	3.71	1.38	9411	4.99	0.85	5.60	1.18	30.5	3.35	3.14	0.47
KN162-72-31-38	53.17	22.55	3699	32.6	254.7	306.1	40.3	127.0	61.8	0.48	0.43	6.6	0.12	0.05	2.05	0.19	830	3.69	12.7	0.70	2.12	11.8	154.5	121.3	2.89	3.75	1.36	9531	4.91	0.84	5.57	1.17	30.3	3.36	3.12	0.47
KN162-72-31-42	53.17	22.55	3699	32.4	254.3	306.9	40.0	125.3	61.6	0.49	0.43	8.3	0.12	0.05	2.07	0.19	913	3.69	12.5	0.64	2.11	11.8	153.6	121.2	2.90	3.75	1.36	9351	4.99	0.85	5.57	1.17	30.3	3.35	3.11	0.47
KN162-72-31-64	53.17	22.55	3699	32.8	256.0	303.3	40.3	126.8	61.7	0.48	0.45	6.2	0.12	0.05	2.05	0.19	913	3.70	12.7	0.70	2.13	11.8	154.7	122.3	2.88	3.70	1.36	9351	4.99	0.85	5.57	1.17	30.3	3.35	3.11	0.47
KN162-72-31-66	53.17	22.55	3699	34.9	297.1	242.9	41.8	127.4	58.8	0.61	1.01	12.1	0.23	0.10	3.73	0.32	1411	5.35	17.5	0.94	2.85	15.4	162.9	161.5	3.77	4.78	1.68	12408	6.18	1.07	6.97	1.48	37.5	4.21	3.93	0.59
KN162-72-31-02	53.17	22.55	3852	32.9	241.0	344.7	39.7	141.1	64.9	0.41	0.63	12.6	0.16	0.07	2.58	0.24	996	3.65	12.5	0.74	1.99	10.6	168.3	109.6	2.55	3.28	1.21	8691	4.34	0.72	4.78	1.01	25.8	2.85	2.63	0.40
KN162-72-22-05	53.11	22.65	3852	33.3	246.1	336.5	39.7	140.9	65.7	0.42	0.63	12.0	0.15	0.07	2.61	0.23	1079	3.88	12.5	0.76	2.00	10.8	170.0	111.7	2.59	3.33	1.22	8572	4.39	0.74	4.88	1.02	26.3	2.88	2.66	0.41
KN162-72-22-14	53.11	22.65	3852	32.8	241.6	355.3	40.7	151.0	63.7	0.41	0.62	9.0	0.16	0.07	2.59	0.23	1079	3.82	12.3	0.58	2.01	10.7	170.8	111.4	2.56	3.34	1.22	8691	4.28	0.72	4.76	1.00	26.2	2.84	2.65	0.40
KN162-72-22-16	53.11	22.65	3852	32.9	241.1	345.6	40.1	152.7	66.4	0.41	0.63	14.0	0.15	0.07	2.58	0.23	1079	3.84	12.5	0.76	1.99	10.6	169.6	111.0	2.56	3.34	1.22	8691	4.31	0.73	4.78	1.01	26.2	2.86	2.65	0.40
KN162-72-22-27	53.11	22.65	3852	33.1	242.2	362.4	41.2	162.7	65.5	0.41	0.63	10.4	0.15	0.07	2.55	0.23	996	3.86	12.4	0.54	2.00	10.8	169.1	108.8	2.53	3.29	1.22	8871	4.28	0.72	4.81	1.01	26.0	2.85	2.65	0.41
KN162-72-22-34	53.11	22.65	3852	31.9	240.2	363.1	40.7	155.0	65.3	0.42	0.63	10.8	0.15	0.07	2.56	0.23	996	3.82	12.5	0.58	1.98	10.7	170.8	111.9	2.54	3.27	1.22	8891	4.36	0.73	4.80	1.01	26.2	2.90	2.66	0.40
KN162-72-22-38	53.11	22.65	3852	32.3	243.4	348.7	40.3	147.2	66.1	0.42	0.60	11.9	0.16	0.07	2.67	0.21	1079	3.79	12.2	0.62	1.96	10.6	164.6	107.8	2.50	3.24	1.20	8631	4.23	0.73	4.66	1.01	25.5	2.84	2.61	0.40
KN162-72-22-38	53.11	22.65	3852	32.5	241.6	376.2	40.5	164.6	64.5	0.41	0.60	9.0	0.16	0.07	2.67	0.21																				

Sample <sup>1</sup>	Latitude (°S)	Longitude (°E)	Depth (mbsl)	Sc	V	Cr	Co	Ni	Cu	Tm	Rb	Ba	Th	U	Nb	Ta	K <sup>2</sup>	La	Ce	Pb	Pr	Nd	Sr	Zr	Hf	Sm	Eu	Ti <sup>2</sup>	Gd	Tb	Dy	Ho	Y	Er	Yb	Lu
KN162-7 26-03	53.21	23.36	3329	312	236.3	343.2	40.3	145.1	66.1	0.39	0.64	9.3	0.15	0.06	2.53	0.23	1162	1.58	11.7	1.03	1.86	10.2	171.2	101.9	233	331	136	8631	4.07	0.68	4.52	0.95	24.5	2.70	2.49	0.37
KN162-7 26-06	53.21	23.36	3329	312	197.6	377.4	40.9	141.9	72.7	0.31	0.24	6.3	0.06	0.02	0.99	0.10	664	1.83	6.5	0.79	1.11	6.5	144.5	62.6	138	231	092	6534	3.12	0.53	1.60	0.76	19.6	2.32	2.05	0.31
KN162-7 26-08	53.21	23.36	3329	311	237.8	340.3	39.5	132.7	64.1	0.40	0.62	9.2	0.14	0.06	2.55	0.23	1162	1.64	11.8	0.52	1.91	10.2	172.4	103.8	240	317	119	8831	4.14	0.70	4.62	0.97	24.8	2.75	2.54	0.38
KN162-7 26-13	53.21	23.36	3329	317	208.8	365.2	40.8	133.2	74.2	0.35	0.27	4.8	0.07	0.03	1.11	0.11	664	2.11	7.5	0.35	1.29	7.4	130.4	71.2	178	252	097	6753	3.44	0.59	3.99	0.87	21.7	2.46	2.38	0.34
KN162-7 26-13	53.21	23.36	3329	318	208.4	364.4	40.8	142.0	74.1	0.35	0.26	4.9	0.07	0.03	1.11	0.11	581	2.07	7.1	1.23	1.26	7.4	131.1	71.7	179	246	097	6953	3.48	0.60	3.99	0.86	21.8	2.45	2.29	0.34
KN162-7 26-16	53.21	23.36	3329	320	210.4	351.4	41.5	142.3	74.6	0.35	0.26	4.9	0.06	0.03	1.08	0.11	581	2.03	7.1	0.42	1.25	7.3	131.1	70.9	178	245	096	7013	3.40	0.59	3.97	0.83	21.7	2.39	2.24	0.34
KN162-7 26-19 <sup>4</sup>	53.21	23.36	3329	320.1	211.4	357.1	41.59	148.1	74.9	0.34	0.22	3.04	0.06	0.03	0.94	0.07	581	2.02	4.9	0.58	1.2	6.92	129.5	71.5	188	246	097	7073	3.44	0.58	3.9	0.83	22.6	2.42	2.25	0.33
KN162-7 26-21 <sup>4</sup>	53.21	23.36	3329	315.6	210.2	355.4	41.52	148.8	74.7	0.35	0.215	3.37	0.06	0.02	0.92	0.07	581	2	6.92	0.52	1.23	7	127.1	70.2	189	249	099	6953	3.46	0.6	3.99	0.82	22.4	2.45	2.28	0.33
KN162-7 26-23	53.21	23.36	3329	32.0	212.5	378.4	40.5	140.4	73.4	0.32	0.24	4.8	0.06	0.03	1.05	0.11	581	2.03	7.2	0.35	1.25	7.3	131.3	72.1	183	249	098	6893	3.50	0.59	3.99	0.85	22.2	2.47	2.27	0.34
KN162-7 26-27	53.21	23.36	3329	310	199.0	376.3	40.2	140.7	73.4	0.32	0.24	6.0	0.06	0.02	0.96	0.10	581	1.81	6.4	0.41	1.12	6.6	145.1	63.1	161	224	092	6833	3.18	0.53	3.67	0.79	20.0	2.25	2.06	0.31
KN162-7 26-29 <sup>4</sup>	53.21	23.36	3329	30.03	204.4	343.9	41.28	148.8	73.8	0.34	0.149	3.09	0.06	0.02	0.94	0.06	581	1.99	6.94	0.46	1.21	6.88	105.2	70.1	168	244	096	6893	3.43	0.58	3.9	0.8	21.1	2.35	2.11	0.31

Trace element abundances (ppm) where measured via ICP-MS at University of Cape Town, South Africa  
<sup>1</sup> Sample are order by longitude from west to east within each of the four tectonomagmatic provinces defined in Chapter 2  
<sup>2</sup> K and Ti abundances (converted from wt% to ppm) were measured by microprobe at Smithsonian Institution of Washington, DC  
<sup>4</sup> Sample were re-measured at University of Cape Town (via same technique) due to anomalous Ba contents.

Table 2. Sr, Nd, Hf, and Pb isotopic compositions for basalt glasses from 9°-25°E on the SW Indian Ridge.

Sample	Latitude	Longitude	Depth	<sup>87</sup> Sr/ <sup>86</sup> Sr	2σ	<sup>187</sup> Hf/ <sup>181</sup> Hf	2σ	<sup>143</sup> Nd/ <sup>142</sup> Nd	2σ	<sup>206</sup> Pb/ <sup>204</sup> Pb	2σ	<sup>207</sup> Pb/ <sup>204</sup> Pb	2σ	<sup>208</sup> Pb/ <sup>204</sup> Pb	2σ	
Oblique supersegment (9°56'-15°45' E)																
Anmagmatic Segments (9°56' - 11° E; 11°56' - 15°45' E)																
VAN7-92-03	52.86	10.89	3700	0.702960	8	0.283032		5	0.512940	6	19.065	0.002	15.601	0.001	38.893	0.004
KNI62-9-36-27	52.75	11.71	3981	0.702726	10	0.283235	18	0.513096	12	18.472	0.001	15.513	0.001	38.256	0.002	
KNI62-9-41-07	52.59	12.13	4333	0.702878	10	0.283101	6	0.512996	36	18.879	<0.001	15.565	<0.001	38.759	0.002	
KNI62-9-48-04	52.56	12.80	3897	0.702812	10	0.283101	15	0.512982	28	18.431	0.002	15.494	0.002	38.016	0.005	
						0.283121	11									
KNI62-9-49-13	52.30	12.86	4199	0.702969	6	0.283114	11	0.512914	24	19.134	<0.001	15.591	<0.001	38.984	<0.001	
PS4-06-01 <sup>1</sup>	52.35	13.13	4000	0.703090	22			0.512950	12	18.867	0.010	15.572	0.008	38.822	0.024	
PS4-06-02 <sup>1</sup>	52.35	13.13	4000	0.702900	22	0.283100	12	0.513004	12	18.741	0.006	15.551	0.004	38.541	0.012	
KNI62-9-56-88	52.37	13.51	4132	0.703212	10	0.283128	13	0.512903	8	18.958	0.002	15.582	0.001	39.063	0.004	
PS4-05-36 <sup>2</sup>	52.28	13.68	3800	0.702920	22			0.513020	12	18.769	0.014	15.560	0.012	38.623	0.038	
Joseph Mayes Seamount (11° - 11°56' E)																
KNI62-9-32-09	52.75	11.22	2664	0.702968	10	0.283175	10	0.512978	36	19.021	0.001	15.580	<0.001	38.819	0.001	
KNI62-9-33-49	52.82	11.39	1436	0.702984	10	0.283067	6	0.512952	8	19.118	0.000	15.603	0.000	38.951	0.001	
						0.283076	4									
KNI62-9-34-23	52.86	11.43	2070	0.703093	12	0.283392	11	0.512971	20	19.109	<0.001	15.589	<0.001	38.939	0.001	
Narrowgate Segment (14°15' - 14°54' E)																
VAN7-90-77	52.18	14.35	3973	0.703446	6	0.282982	18	0.512870	102	19.402	0.009	15.629	0.008	39.338	0.019	
						0.283011	12									
PS4-03-14 <sup>2</sup>	53.12	14.50	3300	0.703520	22	0.282963	12	0.512837	12	19.254	0.008	15.642	0.006	39.305	0.018	
VAN7-89-02	52.25	14.60	2439	0.703631	12	0.282965	6	0.512786	46	19.350	0.002	15.620	0.002	39.454	0.004	
KNI62-9-61-71	52.10	14.60	2211	0.703424	12	0.283024	10	0.512857	10	19.288	<0.001	15.642	<0.001	39.368	0.002	
PS4-02-01 <sup>1</sup>	52.22	14.63	3200	0.703380	22	0.283002	12	0.512876	12	19.243	0.010	15.632	0.008	39.315	0.024	
VAN7-88-03	52.22	14.71	2984	0.703390	16	0.283267	12	0.512880	16	19.211	<0.001	15.601	<0.001	39.195	0.001	
VAN7-87-01	52.24	14.79	3546	0.703379	6	0.283068	8	0.512877	22	19.335	<0.001	15.616	<0.001	39.313	0.001	
Orthogonal supersegment (15°45' - 25° E)																
VAN7-83-01	52.17	15.84	3976	0.702644	14	0.283059	5	0.513020	18	19.003	0.002	15.570	0.001	38.702	0.002	
VAN7-80-04	52.23	16.01	4038	0.702900	10	0.283065	5	0.512992	16	19.106	0.002	15.589	0.002	38.911	0.003	
KNI62-7-02-01	52.33	16.23	4000	0.702584	6	0.283045	6	0.513039	12	18.986	0.002	15.574	0.002	38.639	0.004	
AG22-01-01 <sup>3</sup>	52.30	16.98	4000	0.702480	22	0.283078	12	0.513056	12	19.045	0.012	15.557	0.012	38.554	0.038	
KNI62-7-04-13	52.36	17.11	3650	0.702639	6	0.283041	7	0.513003	16	19.072	0.003	15.610	0.003	38.819	0.008	
						0.283046	6									
KNI62-7-06-02	52.32	17.70	3586	0.702599	18	0.283240	9	0.512974	48	19.080	0.001	15.563	0.001	38.678	0.003	
KNI62-7-08-05	52.62	18.34	3713	0.702630	8	0.283032	6	0.513043	12	19.014	0.002	15.577	0.002	38.651	0.004	
KNI62-7-10-21	52.75	19.27	3097	0.702597	6	0.283049	12	0.513018	26	19.070	0.002	15.597	0.002	38.696	0.006	
VAN7-75-29	53.00	19.78	1731	0.702534	8	0.283077	7	0.513072	30	18.790	0.003	15.570	0.003	38.322	0.004	
KNI62-7-15-05	52.92	20.38	3403	0.702490	74	0.283019	6	0.513047	38	19.038	0.002	15.617	0.002	38.713	0.006	
KNI62-7-18-17	52.99	21.41	4525	0.702505	8	0.283304	12	0.513057	22	18.649	0.001	15.513	0.001	38.218	0.002	
VAN7-70-87	53.04	21.98	3869	0.702519	10	0.283090	7	0.513070	42	18.828	0.002	15.551	0.000	38.548	0.002	
						0.283101	8									
AG22-09-02 <sup>3</sup>	53.13	22.88	3800	0.702560	22	0.283120	12	0.513101	12	18.418	0.012	15.492	0.012	37.965	0.038	
KNI62-7-25-03	53.17	23.12	3940	0.702522	12	0.283069	5	0.513070	18	18.572	0.001	15.548	0.001	38.230	0.002	
AG22-13-01	53.41	24.76	3850	0.702533	6	0.283074	7	0.513061	20	18.831	0.001	15.554	0.001	38.553	0.005	

<sup>1</sup> values undiluted represent averaged measurements of multiple aliquots of the same dissolution, with reproducibility similar to the quoted 2σ; *italicized* values represent measurements made on the Neptune ICPMS at WHOI - these values are reported, but are not included in plots or interpretation due to significant uncertainty introduced during separation chemistry carried out at WHOI; **bold italicized** values are duplicates run on the Neptune ICPMS at WHOI - illustrating the Neptune's high precision and reproducibility relative to HOT-TIMS data collected at FSU (value immediately above).

<sup>2</sup> Sr, Nd, and Pb data from [de Roer *et al.*, 1992] and Hf data from [Janney *et al.*, 2005]

<sup>3</sup> Sr, Nd, and Pb data from [Mahoney *et al.*, 1992] and Hf data from [Janney *et al.*, 2005]



**Table 3.** Helium isotopic compositions for glasses from SW Indian Ridge (9°-25°E).

Sample	Latitude (°S)	Longitude (°E)	Depth	<sup>4</sup> He conc. (uccSTP/g)	<sup>3</sup> He/ <sup>4</sup> He (R/R <sub>e</sub> ) *	(+/-)
<b>Oblique supersegment (9°56'-15°45' E)</b>						
<b>Amagmatic Accretionary Segments (9°56' - 11° E; 11°36' - 14°15' E; 14°54' - 15°45' E)</b>						
VAN7-92-03	52.86	10.89	3700	0.001	6.64	0.56
VAN7-92-03	52.86	10.89	3700	3E-04	5.73	0.65
KN162-9-30-12 *	52.99	11.16	3587	2.970	6.49	0.04
KN162-9-36-27 *	52.75	11.71	4017	13.800	6.94	0.05
KN162-9-41-07	52.59	12.13	4333	0.026	2.57	0.02
KN162-9-41-07	52.59	12.13	4333	0.023	1.16	0.03
KN162-9-41-07	52.59	12.13	4333	0.016	1.60	0.28
KN162-9-48-04	52.56	12.80	4090	0.508	6.76	0.04
KN162-9-49-13	52.48	12.86	4193	1.550	6.80	0.04
KN162-9-56-88 *	52.37	13.51	4132	0.018	6.20	0.07
KN162-9-56-88	52.37	13.51	4132	0.014	5.82	0.12
PS4-05-36	52.28	13.68	3800	0.944	6.84	0.03
<b>Joseph Mayes Seamount (11° - 11°36' E)</b>						
KN162-9-31-01	52.81	11.08	3074	2.020	6.61	0.05
KN162-9-32-09 *	52.75	11.22	2664	0.041	6.26	0.10
KN162-9-33-49	52.82	11.39	1462	0.531	6.02	0.06
KN162-9-33-49 *	52.82	11.39	1462	0.523	5.99	0.03
KN162-9-33-64 *	52.82	11.39	1462	0.608	5.64	0.04
KN162-9-33-64	52.82	11.39	1462	0.106	1.90	0.07
KN162-9-34-23	52.86	11.43	2070	0.029	1.20	0.02
KN162-9-34-39	52.86	11.43	2126	2.050	6.52	0.04
<b>Narrowgate Segment (14°15' - 14°54' E)</b>						
VAN7-90-77	52.18	14.35	3973	0.727	6.00	0.06
PS4-03-14	53.12	14.50	3300	0.005	n.d.	
VAN7-89-02	52.25	14.60	2439	1.009	6.00	0.05
KN162-9-61-71	52.10	14.60	2211	0.023	1.10	0.02
PS4-02-01	52.22	14.63	3200	22.588	5.93	0.04
PS4-02-14	52.22	14.63	3200	15.920	6.26	0.03
VAN7-88-03 *	52.22	14.71	2984	8.776	6.12	0.07
VAN7-87-01 *	52.24	14.79	3546	0.608	6.00	0.08

**Table 3.** Helium isotopic compositions for glasses from SW Indian Ridge (9°-25°E).

Sample	Latitude (°S)	Longitude (°E)	Depth	<sup>4</sup> He conc. (uccSTP/g)	<sup>3</sup> He/ <sup>4</sup> He (R/R <sub>a</sub> ) <sup>*</sup>	(+/-)
<b>Orthogonal supersegment (15°45'-25° E)</b>						
<b>VAN7-83-01</b>	<b>52.17</b>	<b>15.84</b>	<b>3976</b>	<b>0.215</b>	<b>6.60</b>	<b>0.03</b>
<b>VAN7-80-04</b>	<b>52.23</b>	<b>16.01</b>	<b>4038</b>	<b>2.184</b>	<b>6.63</b>	<b>0.06</b>
<i>KN162-7-02-01</i>	<i>52.33</i>	<i>16.23</i>	<i>3855</i>	<i>0.484</i>	<i>6.58</i>	<i>0.03</i>
<b>KN162-7-03-27</b>	<b>52.30</b>	<b>16.51</b>	<b>3481</b>	<b>0.548</b>	<b>6.57</b>	<b>0.03</b>
<b>AG22 01-01</b>	<b>52.30</b>	<b>16.98</b>	<b>4000</b>	<b>12.800</b>	<b>6.21</b>	<b>0.08</b>
<b>AG22 01-04<sup>†</sup></b>	<b>52.30</b>	<b>16.98</b>	<b>4000</b>	<b>10.730</b>	<b>6.76</b>	<b>0.04</b>
<b>KN162-7-04-13</b>	<b>52.36</b>	<b>17.11</b>	<b>3928</b>	<b>3.760</b>	<b>6.56</b>	<b>0.04</b>
<b>KN162-7-04-13<sup>†</sup></b>	<b>52.36</b>	<b>17.11</b>	<b>3928</b>	<b>2.878</b>	<b>6.64</b>	<b>0.03</b>
<b>KN162-7-04-13</b>	<b>52.36</b>	<b>17.11</b>	<b>3928</b>	<b>2.570</b>	<b>6.59</b>	<b>0.05</b>
<i>KN162-7-04-31</i>	<i>52.36</i>	<i>17.11</i>	<i>3928</i>	<i>2.972</i>	<i>6.67</i>	<i>0.03</i>
<i>KN162-7-05-01</i>	<i>52.42</i>	<i>17.43</i>	<i>3090</i>	<i>1.106</i>	<i>6.64</i>	<i>0.04</i>
<i>KN162-7-06-02</i>	<i>52.52</i>	<i>17.70</i>	<i>3582</i>	<i>15.100</i>	<i>6.80</i>	<i>0.04</i>
<i>KN162-7-07-02</i>	<i>52.55</i>	<i>18.03</i>	<i>4001</i>	<i>11.450</i>	<i>6.91</i>	<i>0.05</i>
<i>KN162-7-08-05</i>	<i>52.61</i>	<i>18.34</i>	<i>3702</i>	<i>2.882</i>	<i>6.88</i>	<i>0.03</i>
<i>AG22 05-07</i>	<i>52.76</i>	<i>19.10</i>	<i>3700</i>	<i>3.541</i>	<i>7.03</i>	<i>0.06</i>
<i>AG22 05-02</i>	<i>52.76</i>	<i>19.10</i>	<i>3700</i>	<i>0.727</i>	<i>6.97</i>	<i>0.03</i>
<i>AG22 05-18</i>	<i>52.76</i>	<i>19.10</i>	<i>3700</i>	<i>0.717</i>	<i>6.87</i>	<i>0.03</i>
<i>KN162-7-11-25</i>	<i>52.80</i>	<i>19.20</i>	<i>3886</i>	<i>38.060</i>	<i>6.89</i>	<i>0.03</i>
<i>KN162-7-10-21</i>	<i>52.75</i>	<i>19.27</i>	<i>3165</i>	<i>3.309</i>	<i>6.90</i>	<i>0.04</i>
<i>KN162-7-13-29</i>	<i>52.86</i>	<i>19.91</i>	<i>4071</i>	<i>22.490</i>	<i>6.91</i>	<i>0.04</i>
<i>KN162-7-14-07</i>	<i>52.92</i>	<i>20.38</i>	<i>3450</i>	<i>18.330</i>	<i>6.94</i>	<i>0.04</i>
<b>KN162-7-15-05<sup>†</sup></b>	<b>52.92</b>	<b>20.38</b>	<b>3489</b>	<b>4.666</b>	<b>6.57</b>	<b>0.05</b>
<b>KN162-7-15-05</b>	<b>52.92</b>	<b>20.38</b>	<b>3489</b>	<b>3.788</b>	<b>6.82</b>	<b>0.06</b>
<i>KN162-7-17-16</i>	<i>52.95</i>	<i>20.93</i>	<i>3874</i>	<i>6.040</i>	<i>7.21</i>	<i>0.04</i>
<i>KN162-7-18-17</i>	<i>52.99</i>	<i>21.41</i>	<i>4507</i>	<i>2.822</i>	<i>7.03</i>	<i>0.02</i>
<b>VAN7-70-87</b>	<b>53.04</b>	<b>21.98</b>	<b>3869</b>	<b>35.170</b>	<b>6.91</b>	<b>0.03</b>
<i>KN162-7-20-06</i>	<i>53.04</i>	<i>22.18</i>	<i>4246</i>	<i>27.000</i>	<i>7.29</i>	<i>0.04</i>
<i>KN162-7-21-02</i>	<i>53.03</i>	<i>22.47</i>	<i>3787</i>	<i>33.300</i>	<i>7.10</i>	<i>0.03</i>
<i>KN162-7-23-107</i>	<i>53.17</i>	<i>22.57</i>	<i>3658</i>	<i>20.470</i>	<i>7.28</i>	<i>0.04</i>
<i>KN162-7-22-14</i>	<i>53.11</i>	<i>22.65</i>	<i>3875</i>	<i>30.530</i>	<i>7.03</i>	<i>0.04</i>
<i>KN162-7-24-04</i>	<i>53.16</i>	<i>22.85</i>	<i>3290</i>	<i>9.472</i>	<i>7.01</i>	<i>0.03</i>
<i>AG22 09-02</i>	<i>53.13</i>	<i>22.88</i>	<i>3800</i>	<i>25.530</i>	<i>7.23</i>	<i>0.04</i>
<i>KN162-7-25-03</i>	<i>53.17</i>	<i>23.12</i>	<i>3995</i>	<i>1.478</i>	<i>7.09</i>	<i>0.03</i>
<i>KN162-7-26-23</i>	<i>53.21</i>	<i>23.36</i>	<i>3325</i>	<i>2.351</i>	<i>7.25</i>	<i>0.06</i>
<b>AG22 13-01</b>	<b>53.41</b>	<b>24.76</b>	<b>3850</b>	<b>28.280</b>	<b>7.27</b>	<b>0.04</b>

<sup>†</sup> <sup>3</sup>He/<sup>4</sup>He ratios are presented relative to the atmospheric ratio (R<sub>a</sub>) equal to 1.38 x 10<sup>-6</sup><sup>\*</sup> italicized entries are measurements (crushing in vacuo) from Georgen et al., [2003], with <sup>4</sup>He concentrations above 0.4 uccSTP/g<sup>\*</sup> bold entries are measurements (crushing in vacuo) from this study with <sup>4</sup>He concentrations above 0.4 uccSTP/g<sup>†</sup> measured raw data has been corrected for a pressure dependence using monitored air standards

**Table 4.** Averaged trace element and isotopic compositions for each of the four tectonomagmatic provinces.

	Orthogonal Supersegment	1 $\sigma$	Amagmatic Segments	1 $\sigma$	Joseph Mayes Seamount	1 $\sigma$	Narrowgate Segment	1 $\sigma$
Sc	34.7	2.3	31.7	2.9	32.5	2.9	27.1	5.7
V	270.6	27.6	232.1	34.2	285.8	24.1	256.9	43.4
Cr	297.2	54.4	291.3	62.7	100.4	81.7	141.8	85.5
Co	41.5	1.8	39.9	3.8	38.4	1.9	35.1	2.1
Ni	129.6	23.7	137.3	28.9	47.7	15.8	80.1	39.6
Cu	67.9	5.3	67.5	9.7	74.4	10.2	64.5	18.5
Tm	0.48	0.06	0.43	0.07	0.51	0.09	0.34	0.09
Rb	1.83	2.16	7.54	5.29	14.31	4.84	31.64	15.48
Ba	21.3	22.4	84.0	57.3	160.3	47.5	390.7	174.2
Th	0.32	0.30	1.10	0.77	2.02	0.68	4.19	1.84
U	0.11	0.08	0.31	0.21	0.57	0.20	1.14	0.47
Nb	4.6	3.6	12.7	8.7	22.8	7.3	48.8	20.2
Ta	0.44	0.26	0.79	0.57	1.32	0.42	2.64	1.07
K	1354	620	3170	1956	5622	1602	11135	3938
La	5.0	2.0	9.4	5.1	16.0	4.6	28.2	11.6
Ce	14.7	4.0	22.6	9.7	36.7	10.0	54.6	20.8
Pb	0.93	0.60	1.35	0.74	1.87	0.43	2.33	0.63
Pr	2.31	0.49	3.02	1.05	4.69	1.18	5.99	2.06
Nd	12.4	2.2	14.5	4.2	21.7	5.0	24.7	7.8
Sr	159	15	198	51	246	18	430	101
Zr	124	21	130	35	181	44	163	44
Hf	2.9	0.5	2.9	0.7	4.0	0.9	3.4	0.8
Sm	3.8	0.6	3.8	0.8	5.4	1.1	4.9	1.3
Eu	1.4	0.3	1.3	0.2	1.8	0.3	1.6	0.4
Ti	10079	1369	9459	1887	13257	2214	11600	2041
Gd	5.1	0.7	4.7	0.9	6.5	1.2	5.1	1.2
Tb	0.84	0.12	0.77	0.14	1.04	0.19	0.75	0.17
Dy	5.6	0.8	5.0	0.9	6.3	1.1	4.6	1.0
Ho	1.2	0.2	1.0	0.2	1.3	0.2	0.9	0.2
Y	30.2	4.0	27.2	4.6	33.0	5.6	23.0	5.1
Er	3.4	0.5	3.0	0.5	3.6	0.6	2.5	0.6
Yb	3.1	0.4	2.8	0.5	3.3	0.6	2.2	0.5
Lu	0.46	0.06	0.41	0.07	0.48	0.08	0.32	0.08
(La/Sm) <sub>n</sub>	0.80	0.24	1.49	0.61	1.84	0.19	3.49	0.62
(Sm/Yb) <sub>n</sub>	1.33	0.07	1.49	0.24	1.78	0.10	2.44	0.34
Ba/Nb	4.6	1.1	6.6	0.8	7.0	0.3	8.0	0.7
Zr/Nb	37.0	15.9	17.5	14.0	8.2	0.9	3.6	0.8
Zr/Y	4.1	0.3	4.7	0.9	5.4	0.5	7.1	1.0
Lu/Hf	0.16	0.01	0.14	0.03	0.12	0.01	0.09	0.01
La/Yb	1.6	0.6	3.4	1.9	4.9	0.8	12.9	3.9
Th/U	3.0	0.5	3.6	0.2	3.6	0.1	3.7	0.1
<sup>87</sup> Sr/ <sup>86</sup> Sr	0.702583	105	0.702941	144	0.703015	68	0.703453	93
<sup>143</sup> Nd/ <sup>144</sup> Nd	0.513042	34	0.512977	56	0.512967	14	0.512855	34
<sup>206</sup> Pb/ <sup>204</sup> Pb	18.898	0.228	18.827	0.160	19.083	0.052	19.320	0.156
<sup>207</sup> Pb/ <sup>204</sup> Pb	15.578	0.083	15.570	0.064	15.591	0.009	15.645	0.101
<sup>208</sup> Pb/ <sup>204</sup> Pb	38.554	0.274	38.689	0.175	38.903	0.064	39.372	0.302
<sup>176</sup> Hf/ <sup>177</sup> Hf <sup>2</sup>	0.283063	27	0.283116	66	0.283067	3	0.282987	26
<sup>3</sup> He/ <sup>4</sup> He (R/R <sub>a</sub> )	6.87	0.26	6.55	0.27	6.17	0.36	6.05	0.28

<sup>1</sup> 1 $\sigma$  represents standard deviation about the averages; values for Sr, Nd, Hf are in the last decimal place

<sup>2</sup> values only uses 20 of 27 measurements; excludes those that may have Hf yield problems

Table 5. Primitive upper mantle - normalized trace element abundances for melt modeling

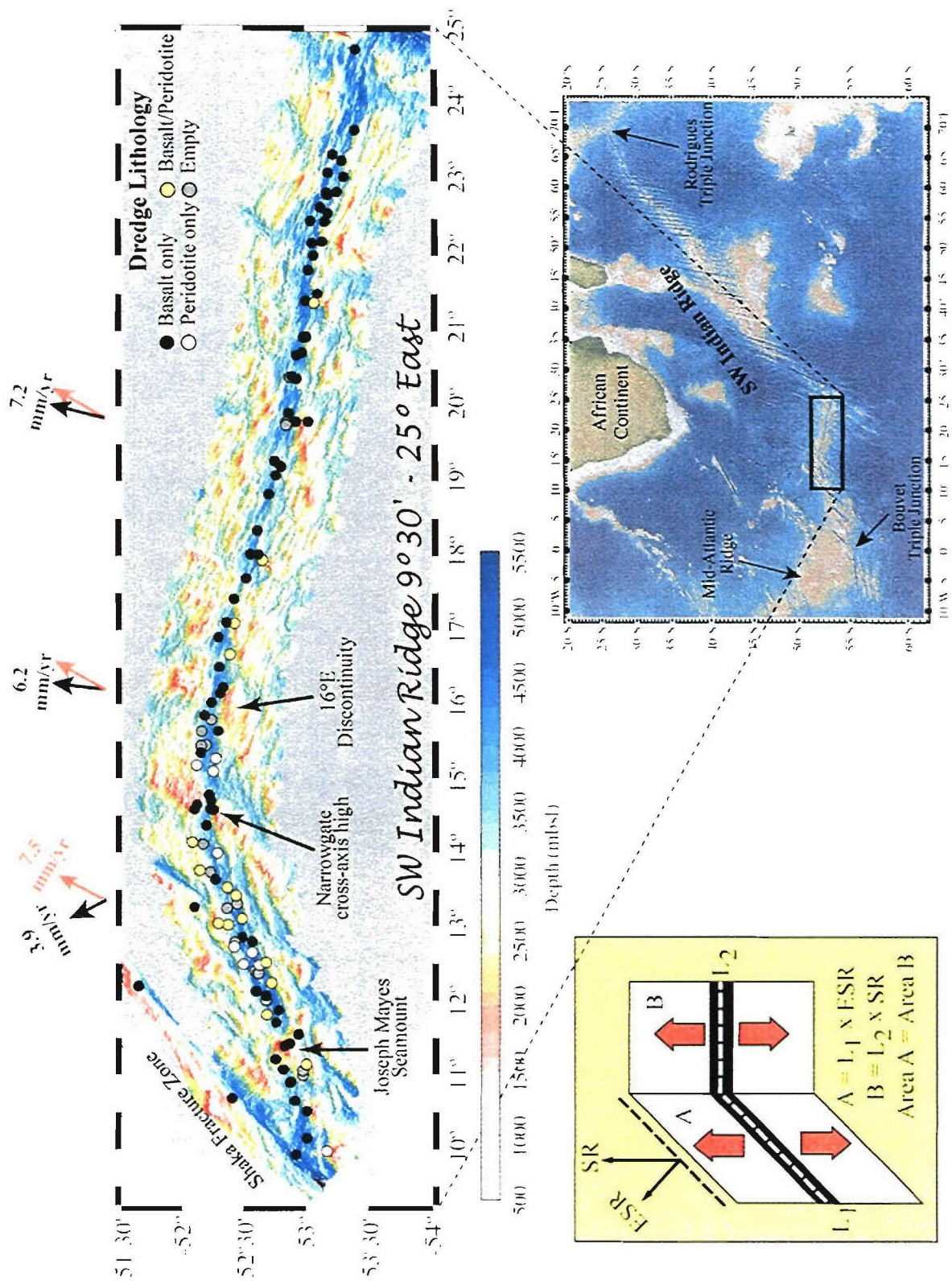
Measured basalts			Source compositions				Best fit model liquid <sup>a</sup>
N-MORB (average of dredge 25 lavas)	E-MORB (average of dredge 89 lavas)		DMM <sup>1</sup>	"enriched SWIR-DMM" <sup>2</sup>	enriched vein component <sup>1</sup>	DMM with 5% CC <sup>4</sup>	13% melt of 2-component source (DMM + enriched veins)
Rb	0.670	28.671	0.083	0.445	9.88	2.75	23.14
Ba	1.062	36.616	0.085	0.457	11.24	1.98	26.19
Th	1.402	31.946	0.099	0.290	12.12	2.32	28.34
U	2.355	33.367	0.156	0.494	12.34	2.44	29.68
Nb	2.902	44.795	0.226	0.717	20.30	1.13	43.14
Ta	4.612	40.881	0.259	0.822	26.72	1.69	62.99
La	4.782	27.155	0.296	0.692	14.92	1.55	27.38
Ce	6.202	20.084	0.329	0.769	10.08	1.34	15.71
Pb	5.312	8.638	0.122	0.286	9.86	2.80	14.53
Pr	6.747	14.249	0.420	0.813	9.64	1.21	13.38
Nd	7.629	11.872	0.465	0.835	9.43	1.12	12.22
Sr	7.474	10.551	0.385	0.799	8.22	1.06	12.18
Zr	9.192	9.025	0.484	0.843	8.50	0.98	9.58
Hf	8.038	6.757	0.555	0.844	7.60	1.16	9.90
Sm	7.530	7.158	0.588	0.883	7.65	1.02	9.58
Eu	7.487	6.221	0.624	0.895	6.51	0.98	8.06
Ti	6.917	7.165	0.594	0.809	5.63	0.73	7.49
Gd	7.541	5.647	0.658	0.906	5.09	0.96	6.34
Tb	6.982	4.489	0.704	0.920	4.55	1.00	5.18
Dy	6.845	4.053	0.749	0.934	3.97	1.01	4.55
Ho	6.547	3.536	0.772	0.941	3.40	1.02	3.94
Y	5.871	3.104	0.774	0.941	2.84	0.99	3.33
Er	6.391	3.402	0.795	0.947	2.51	1.03	3.10
Yb	5.881	3.019	0.827	0.956	2.19	1.05	2.86
Lu	5.734	2.833	0.859	0.965	1.84	1.05	2.73

<sup>1</sup> DMM is taken from *Workman and Hart*, [2005]<sup>2</sup> "enriched SWIR-DMM" is derived using the gradual depletion model of *Workman and Hart*, [2005], with E-MORB isotopic values constraining parent/daughter ratios<sup>3</sup> enriched vein component is derived from the average of Bouvet Island lavas [Le Roex and Erlank, 1982; Weaver et al., 1986]; values underlined are interpolated from neighboring elements<sup>4</sup> continental crust material "CC" added to DMM is taken from *Taylor and McClellan*, [1985]<sup>5</sup> EM2 composition is taken from *Workman et al.*, [2004]<sup>6</sup> values underlined are interpolated from neighboring elements

Table A-1. Sample introduction and mass spectrometer operating conditions for isotopic measurements on the Neptune.

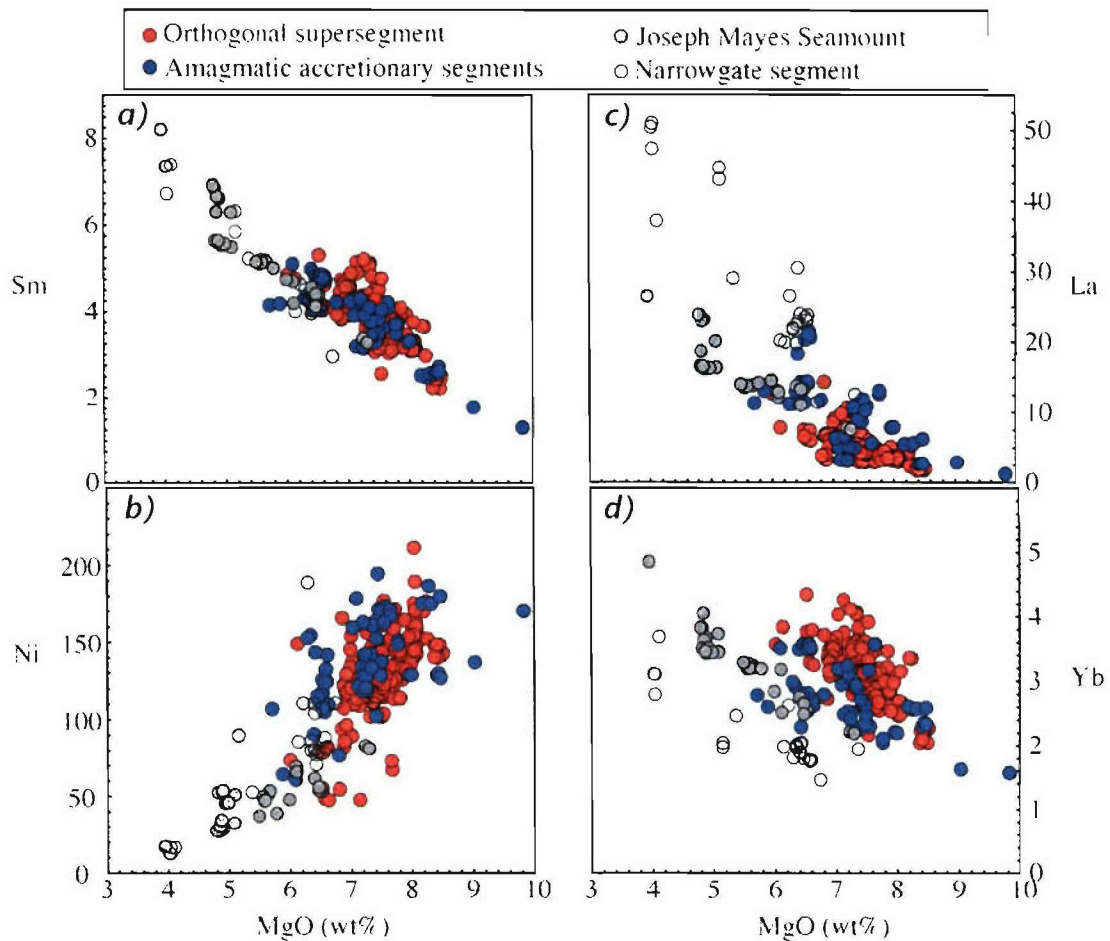
Sample Introduction Hardware and specifications	Sr	Nd	Pb (w/TL spiking)	Hf
Elemental Scientific, Inc. (ESI) Stable Sample Introduction System	X	X	X	X
50 $\mu$ l/min uptake PFA Neb	X	X	X	X
quartz 'high-precision' dual spray chamber	X	X	X	X
high-sensitivity skimmer cones	X	X	X	X
Coolant gas = 16 l/min	X	X	X	X
Auxiliary gas flow = 0.8 l/min	X	X	X	X
Sample gas flow $\approx$ 1 l/min (optimized)	X	X	X	X
ThermoFinnigan Neptune operating conditions				
RF Power - 1250 Watts	X	X	X	X
Lenses tuned daily for optimum sensitivity, peakshape, and stability	X	X	X	X
Faraday Amplifiers calibrated weekly	X	X	X	X
Mass Bias determined simultaneously on Faraday cups	X	X	X	X
ESI Apex sample introduction system (w/o membrane desolvator)				
ESI quartz 100dC spray chamber; -5dC desolvator chamber			X	
50 $\mu$ l/min uptake PFA Neb			X	
N <sub>2</sub> flow $\sim$ 5 ml/min (optimized)			X	
Ar sweep gas $\sim$ 6 l/min (optimized)			X	



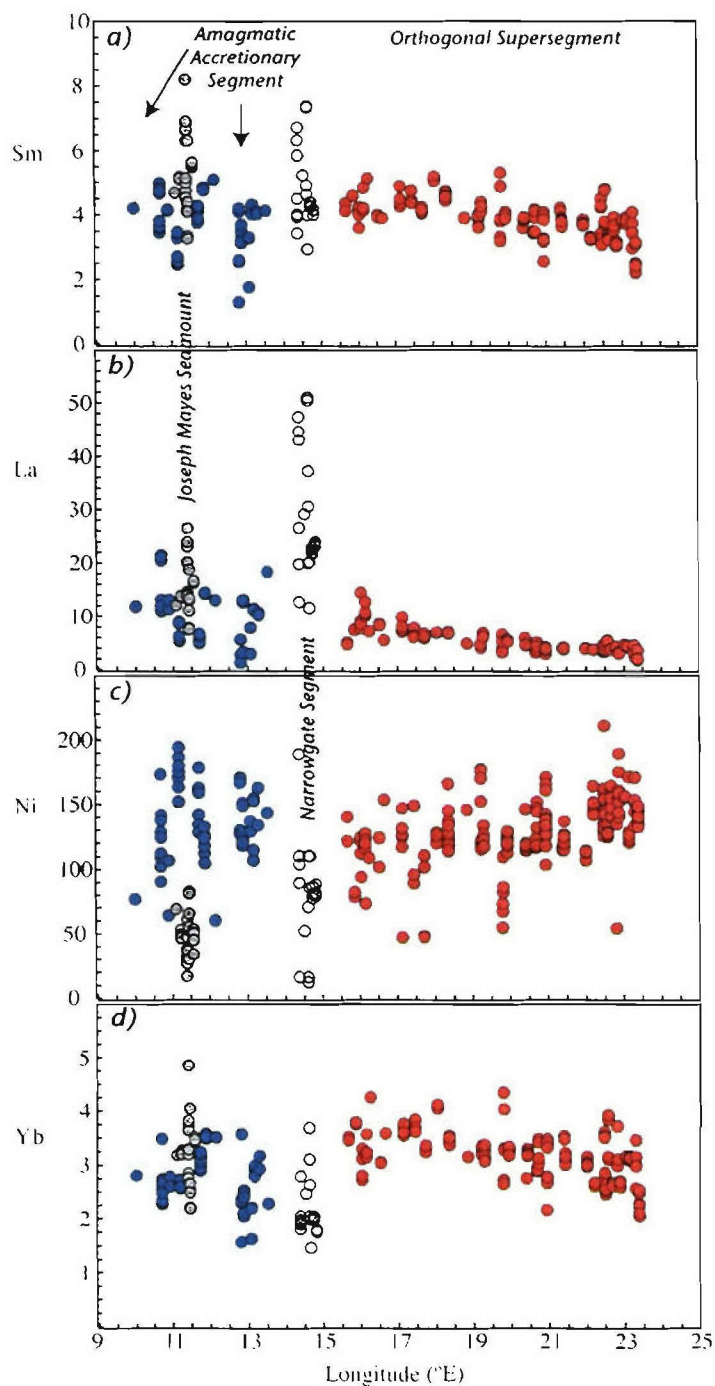


(opposite page)

**Figure 1.** Southwest Indian Ridge bathymetry and lithologic distribution. 9–16° E swath sonar data [this manuscript] combined with bathymetry from 16–25° E [Grindlay et al., 1998]. Dredge locations for trace element data and a subset for isotopic data given in Table 1 & 2. Lithologic distribution indicated by color (see legend and discussion in text). Half spreading rate (SR) marked by red arrows and effective spreading rate (ESR) by black arrows, illustrating the effect of increasing ridge obliquity from east to west. *Inset* Cartoon depicting calculation of ESR. Lithospheric sections A and B have equal area, but segment length  $L_1 > L_2$ . ESR is component of spreading perpendicular to trend of ridge axis (i.e. mantle upwelling rate). *Map inset* Regional bathymetric site map [taken from [www.geomapapp.org](http://www.geomapapp.org)].

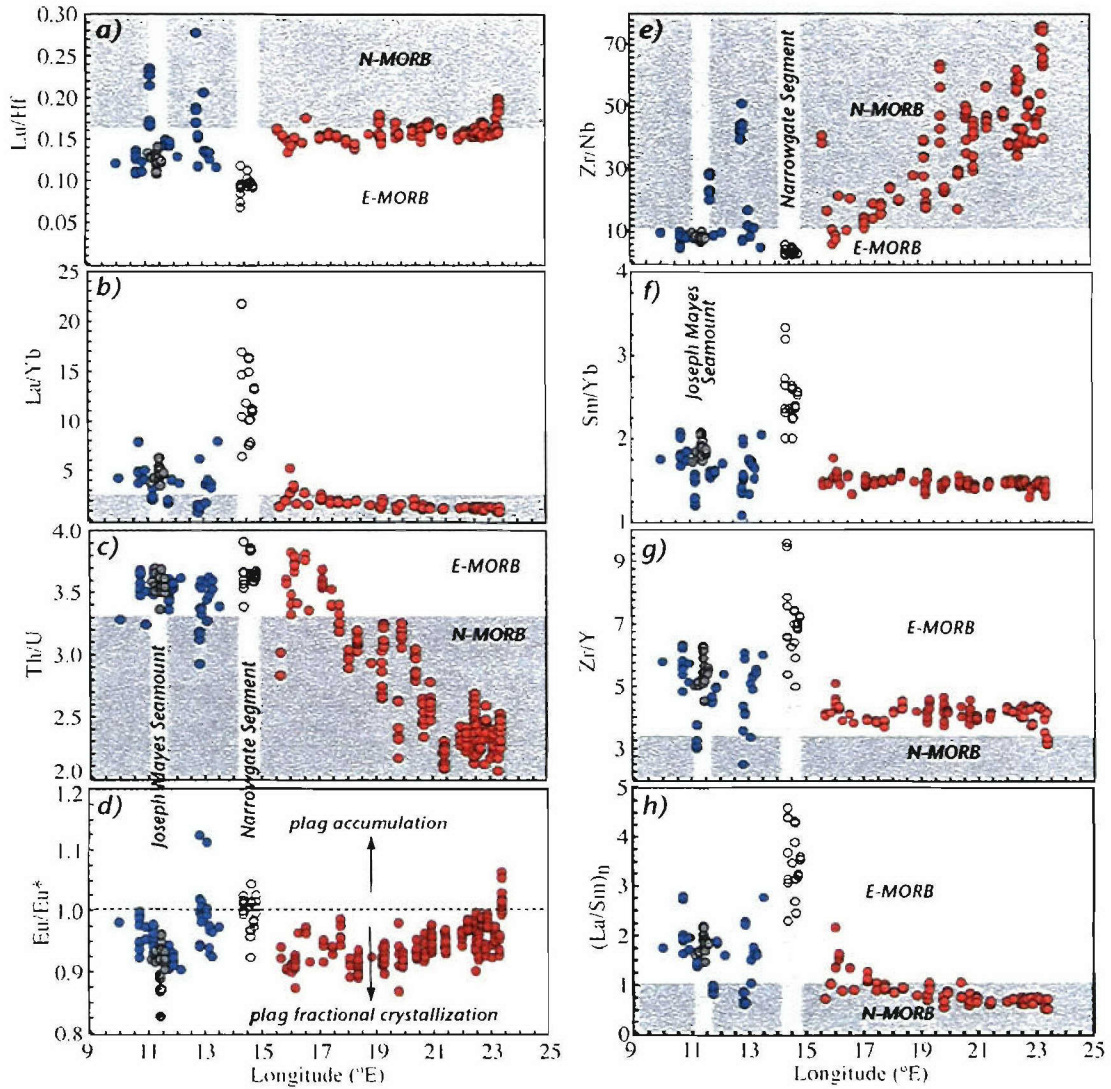


**Figure 2.** (a-d) Trace element abundances (ppm) plotted against MgO (wt%) for basalt glasses from 9°-25°E on the Southwest Indian Ridge. Lavas are grouped into four tectonomagmatic provinces: orthogonal supersegment (red circles), amagmatic accretionary segments (blue circles), the Narrowgate segment (open circles), and Joseph Mayes Seamount (grey circles).



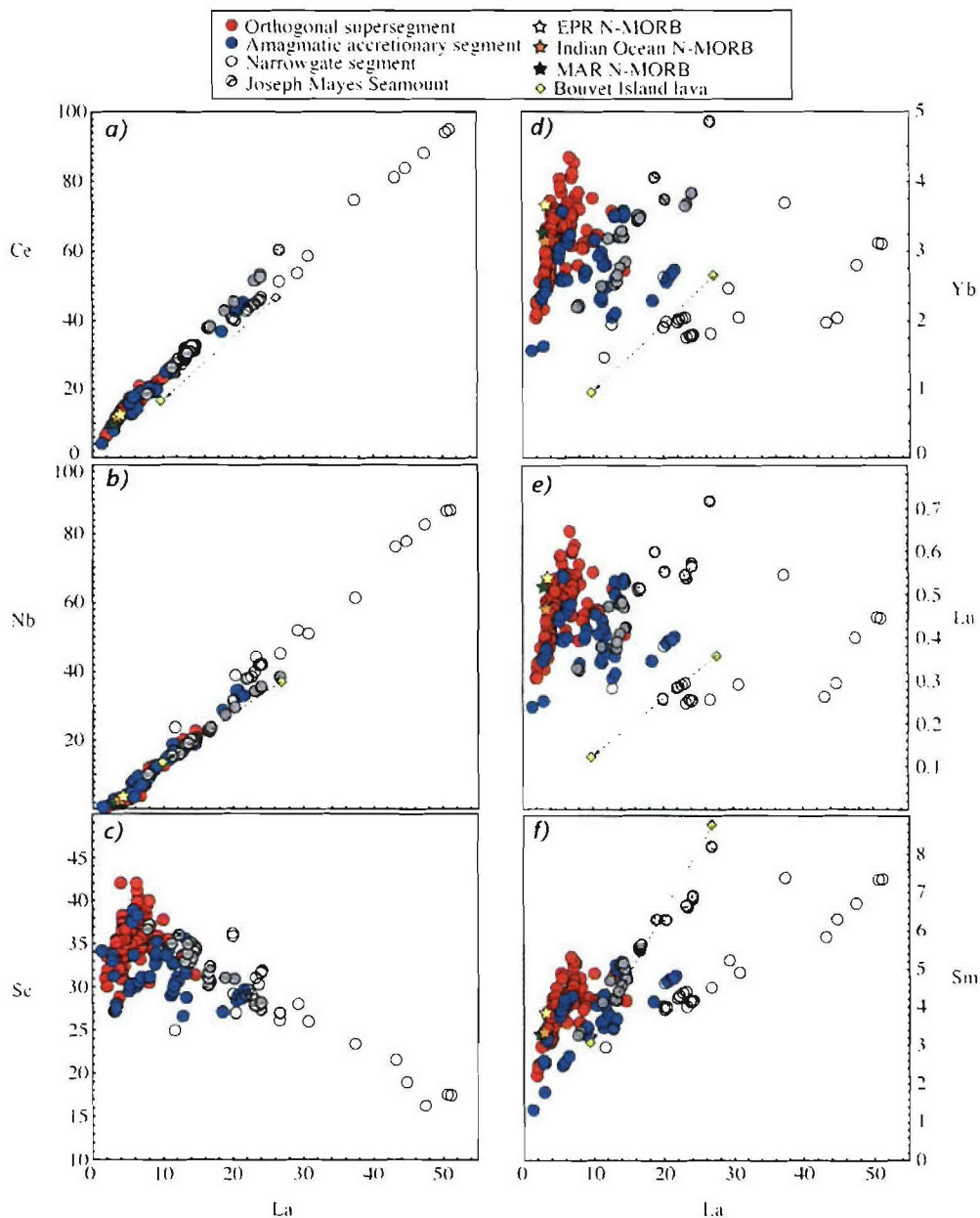
**Figure 3.** (a-d) Along-axis variation of select trace element abundances for Southwest Indian Ridge glasses between 9°-25°E. Symbols same as Figure 2. Vertical grey fields represent Joseph Mayes Seamount lavas (11°-11°36'E) and the Narrowgate segment lavas (14°15'-14°54'E).



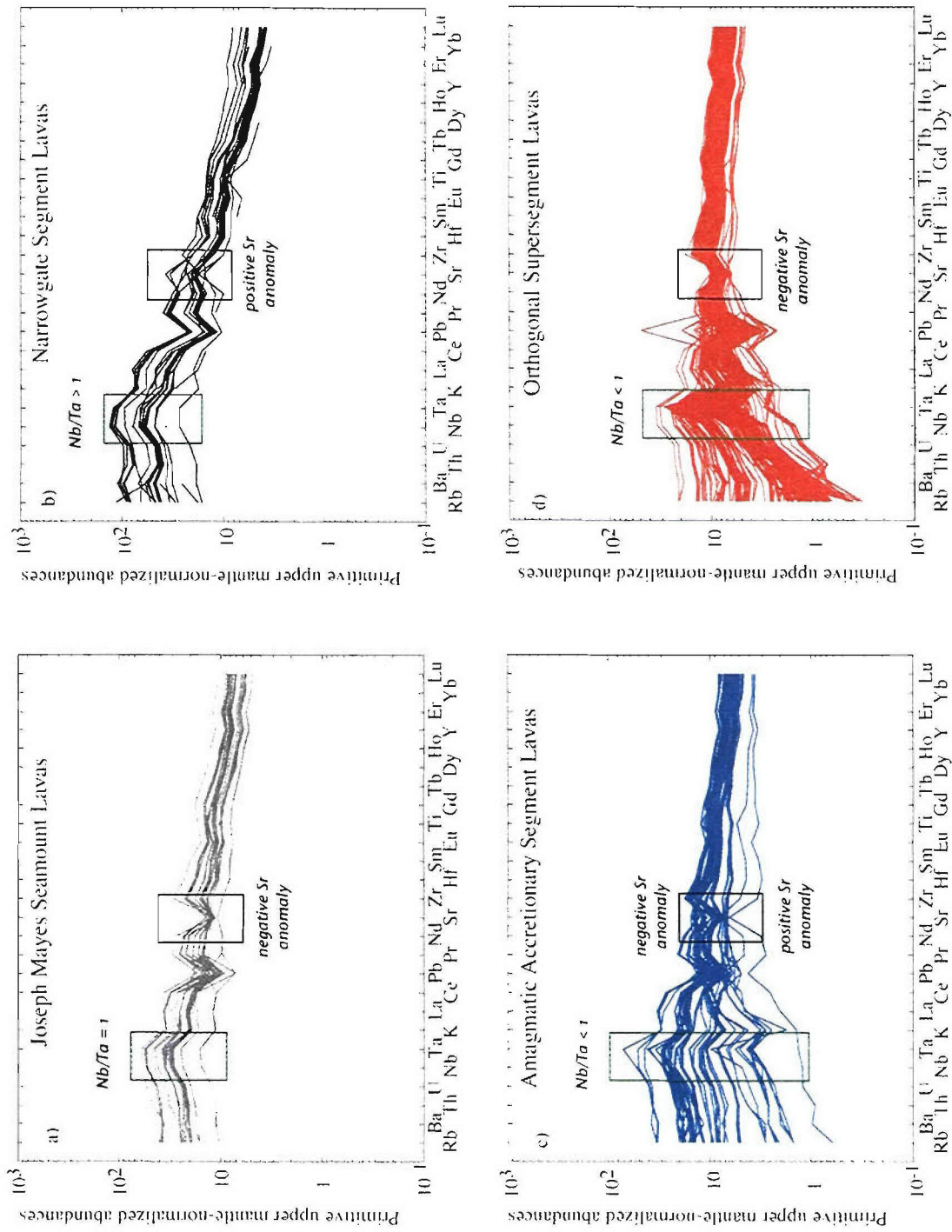


**Figure 4.** Along-axis variation in selected incompatible trace element ratios for Southwest Indian Ridge basalts between 9°-25°E. Symbols the same as in Figure 2. “n” (for La/Sm) indicates chondritic normalization [McDonough and Sun, 1995]. Grey shaded fields indicate global N-MORB and T-MORB compositions [Sun and McDonough, 1989, Le Roux et al., 2002]. Light grey vertical fields denote lavas from Joseph Mayes Seamount and the Narrowgate segment. d) Eu/Eu\* (where Eu\* is estimated by extrapolation between Sm and Gd on a primitive mantle-normalized plot of REE) distinguishes plagioclase accumulation (Eu/Eu\* > 1) from plagioclase fractionation (Eu/Eu\* < 1).





**Figure 5.** (a-f) Incompatible trace element abundances for Southwest Indian Ridge basalts (9°-25°E); symbols same as Figure 2. Also plotted are average N-MORB compositions for the Mid-Atlantic Ridge (green star), East Pacific Rise (yellow star), and Indian Ocean (orange star) [Su, 2002]. Average Bouvet Island lava composition (yellow/green diamond; [Weaver *et al.*, 1986; le Roex & Erlank, 1982]) is plotted with arrow pointing to fractionation corrected composition (MgO 8.0 wt%). Scandium data was not reported in Su [2002].



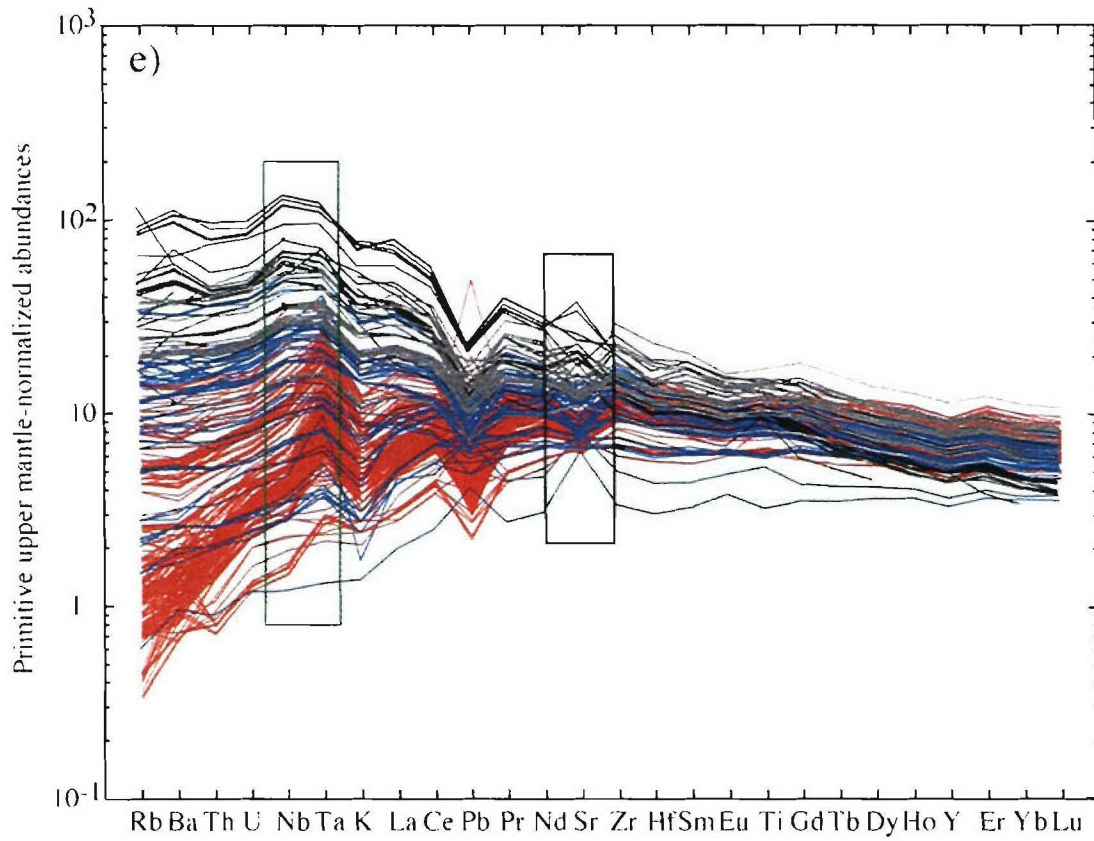
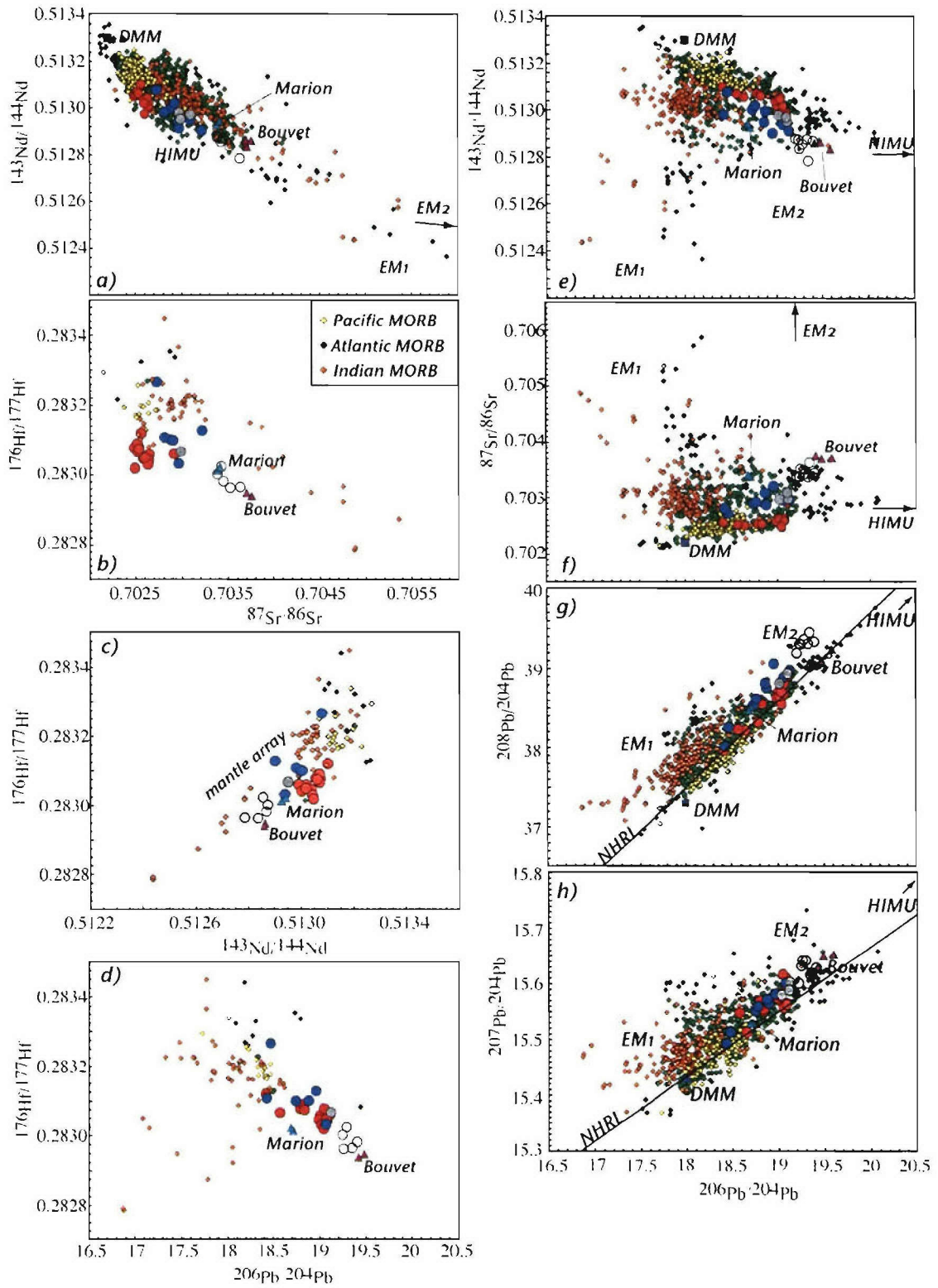


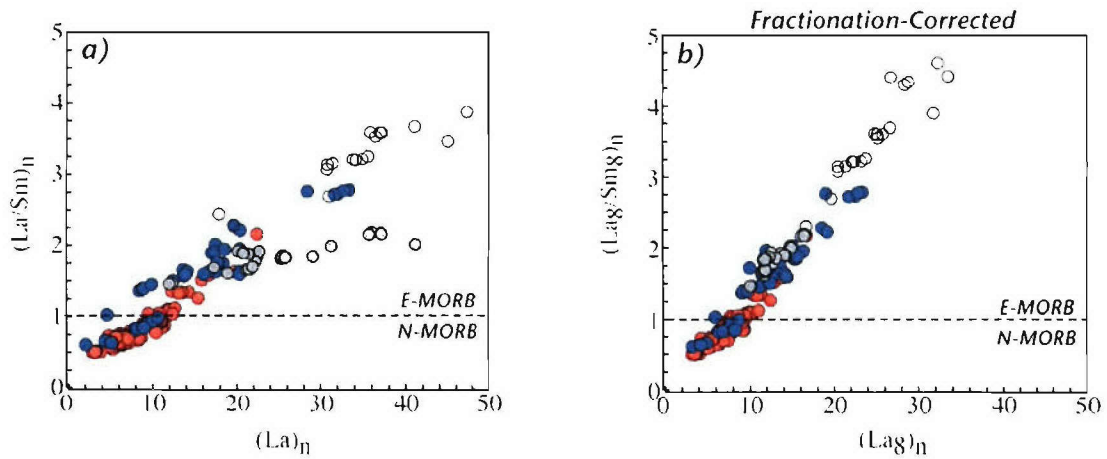
**Figure 6.** Trace element abundance patterns for Southwest Indian Ridge lavas (9°-25°E), grouped by tectonomagmatic province (panels a-d) and as a cumulative basalt suite (panel e). All concentrations are normalized to primitive upper mantle 'PUM' [McDonough & Sun, 1995]. Black boxes highlight the variable Sr anomalies among and within provinces, and green boxes highlight variable Nb/Ta.



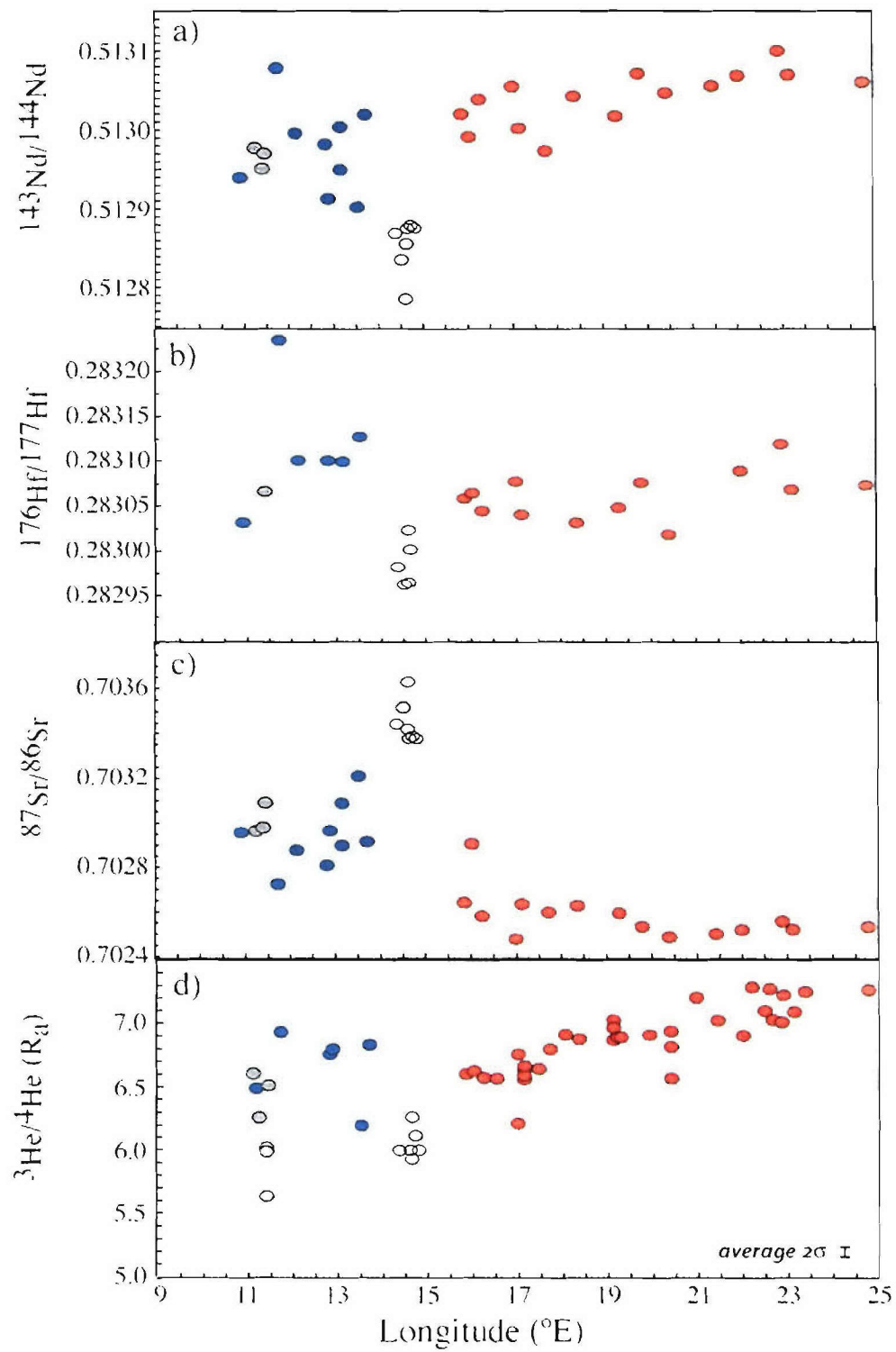
(opposite page)

**Figure 7.** Heavy isotope compositional variations for Southwest Indian Ridge lavas. a)  $^{143}\text{Nd}/^{144}\text{Nd}$  vs.  $^{87}\text{Sr}/^{88}\text{Sr}$ , b)  $^{176}\text{Hf}/^{177}\text{Hf}$  vs.  $^{87}\text{Sr}/^{88}\text{Sr}$ , c)  $^{176}\text{Hf}/^{177}\text{Hf}$  vs.  $^{143}\text{Nd}/^{144}\text{Nd}$ , d)  $^{176}\text{Hf}/^{177}\text{Hf}$  vs.  $^{206}\text{Pb}/^{204}\text{Pb}$ , e)  $^{143}\text{Nd}/^{144}\text{Nd}$  vs.  $^{206}\text{Pb}/^{204}\text{Pb}$ , f)  $^{87}\text{Sr}/^{88}\text{Sr}$  vs.  $^{206}\text{Pb}/^{204}\text{Pb}$ , g)  $^{208}\text{Pb}/^{204}\text{Pb}$  vs.  $^{206}\text{Pb}/^{204}\text{Pb}$ , and h)  $^{207}\text{Pb}/^{204}\text{Pb}$  vs.  $^{206}\text{Pb}/^{204}\text{Pb}$ . Southwest Indian Ridge suite is plotted with global MORB data for Pacific ridges (yellow diamonds), Atlantic ridges (green diamonds), and Indian ridges (orange diamonds) from the compilation of *Stracke et al.*, [2003] (and references within). Mantle reservoir end-members DMM (purple square), EM1, EM2, and HIMU from Zindler and Hart, [1986]. Additional Hf isotopic data for central Indian Ocean MORB (13°-47°E), Marion Island (light blue triangles), and Bouvet Island (maroon triangles) from *Janney et al.*, [2005]. Large grey arrow represents general trend of “mantle array” based on published and unpublished Hf and Nd data from J. Blichert-Toft. “NHRL” refers to northern hemisphere reference line. Southwest Indian Ridge sample symbols same as Figure 2.





**Figure 8.** a)  $(La/Sm)_n$  versus  $(La)_n$  using uncorrected trace element abundances, and b)  $(La_8/Sm_8)_n$  versus  $(La_8)_n$  for fractionation corrected (8 wt% Mg) trace element abundances for Southwest Indian Ridge basalts between 9°-25°E. Correction of trace element abundances is explained in text. The strong positive correlation in both a) and b) illustrate that trace element abundance variations are not strongly controlled by fractional crystallization, but instead reflect source or partial melting effects. Sample symbols same as Figure 2. Dashed line represents commonly used division between depleted N-MORB and E-MORB.



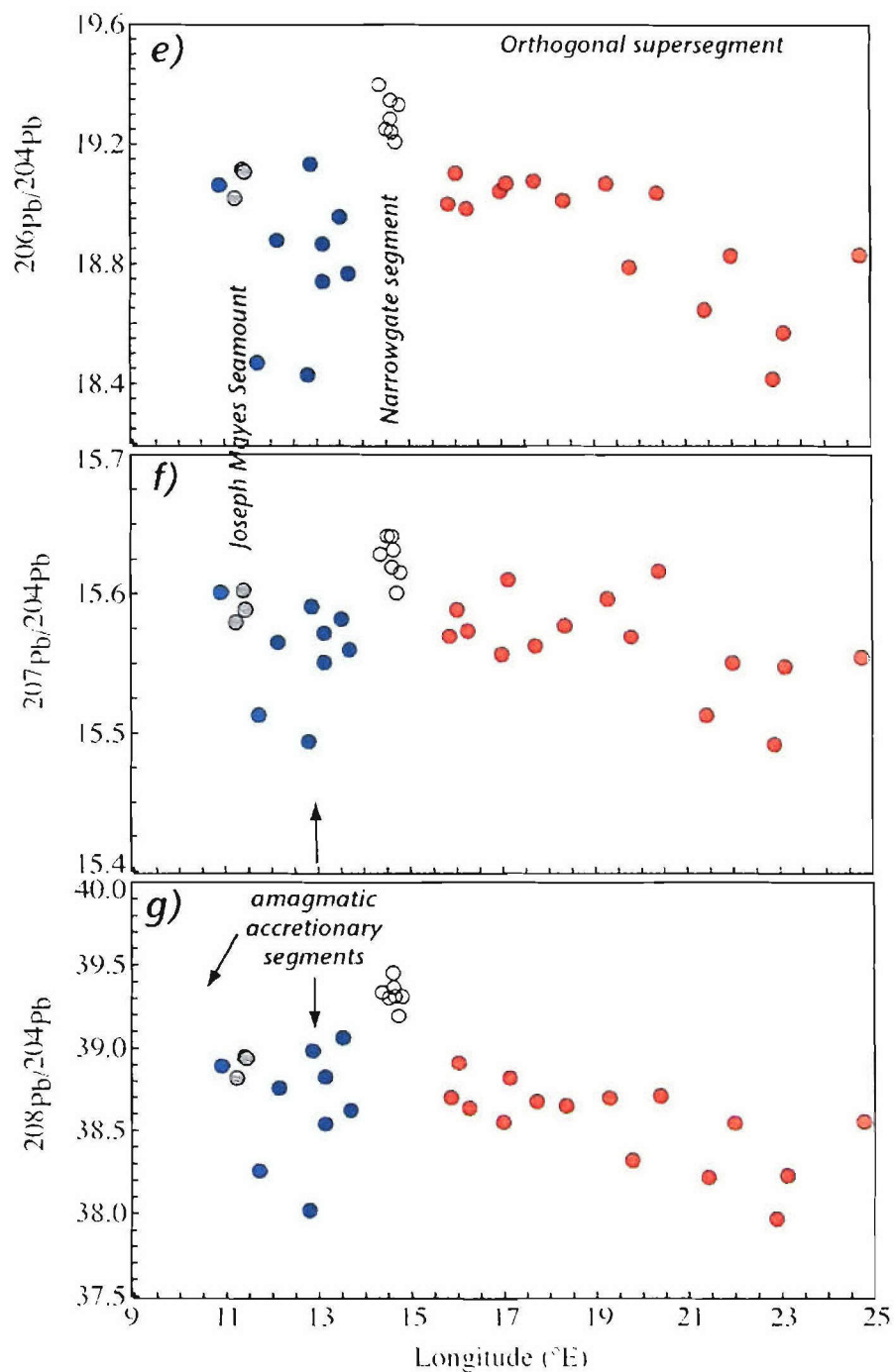


**Figure 9.** Along-axis isotopic compositional variations for Southwest Indian Ridge lavas between 9°-25°E. Symbols are the same as Figure 2. External precision for all ratios is smaller than symbol size, with the exception of  $^3\text{He}/^4\text{He}$  (noted above). Please see Table 2 for notes regarding exclusion of specific  $^{176}\text{Hf}/^{177}\text{Hf}$  measurements.

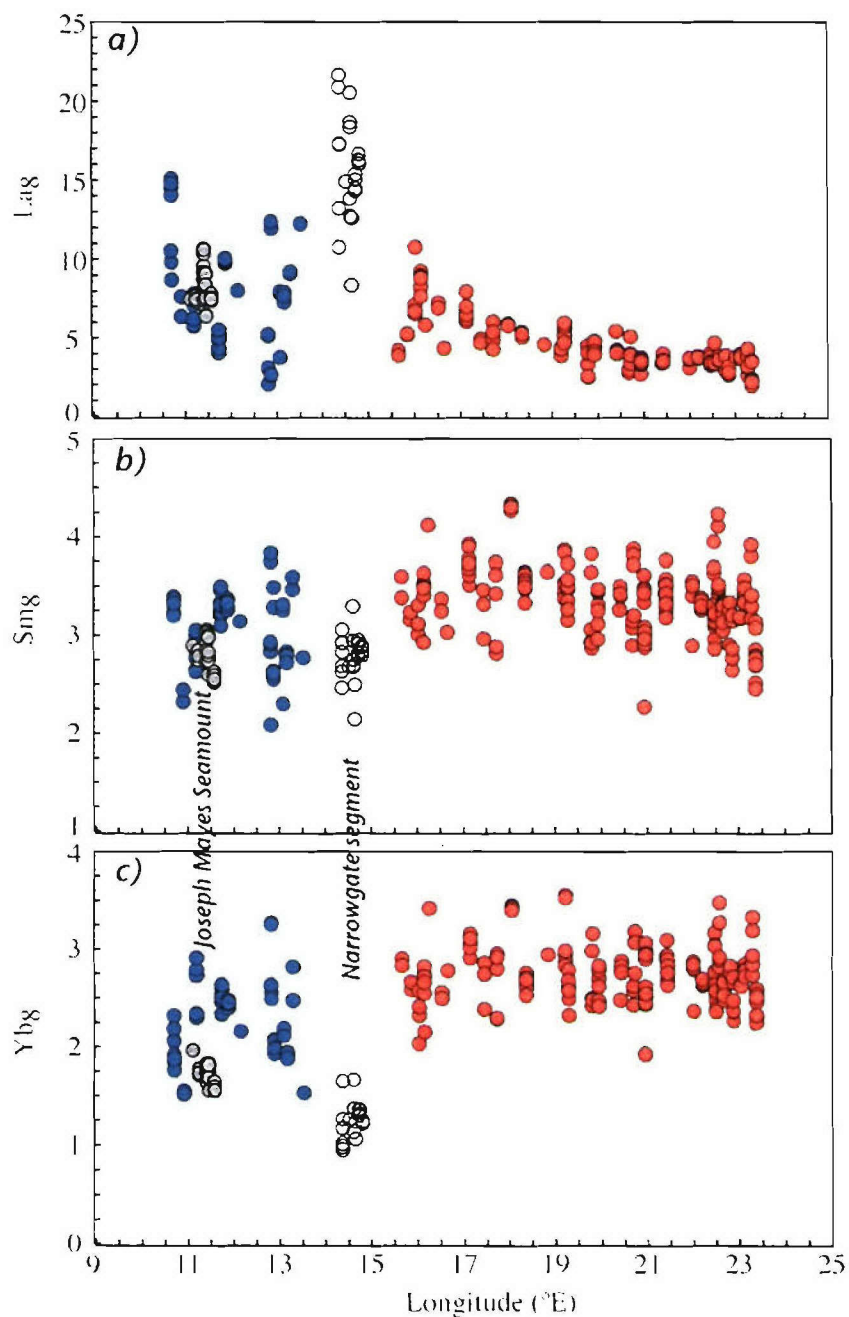


**Figure 10.** (a-c) Along-axis variation of fractionation corrected trace element abundances for Southwest Indian Ridge glasses between 9°-25°E. Symbols same as Figure 2. Vertical grey fields represent Joseph Mayes Seamount lavas (11°-11°36'E) and the Narrowgate segment lavas (14°15'-14°54'E). The Narrowgate segment lavas are enriched in La<sub>8</sub> and depleted in Yb<sub>8</sub>, suggesting the involvement of residual garnet during melting.

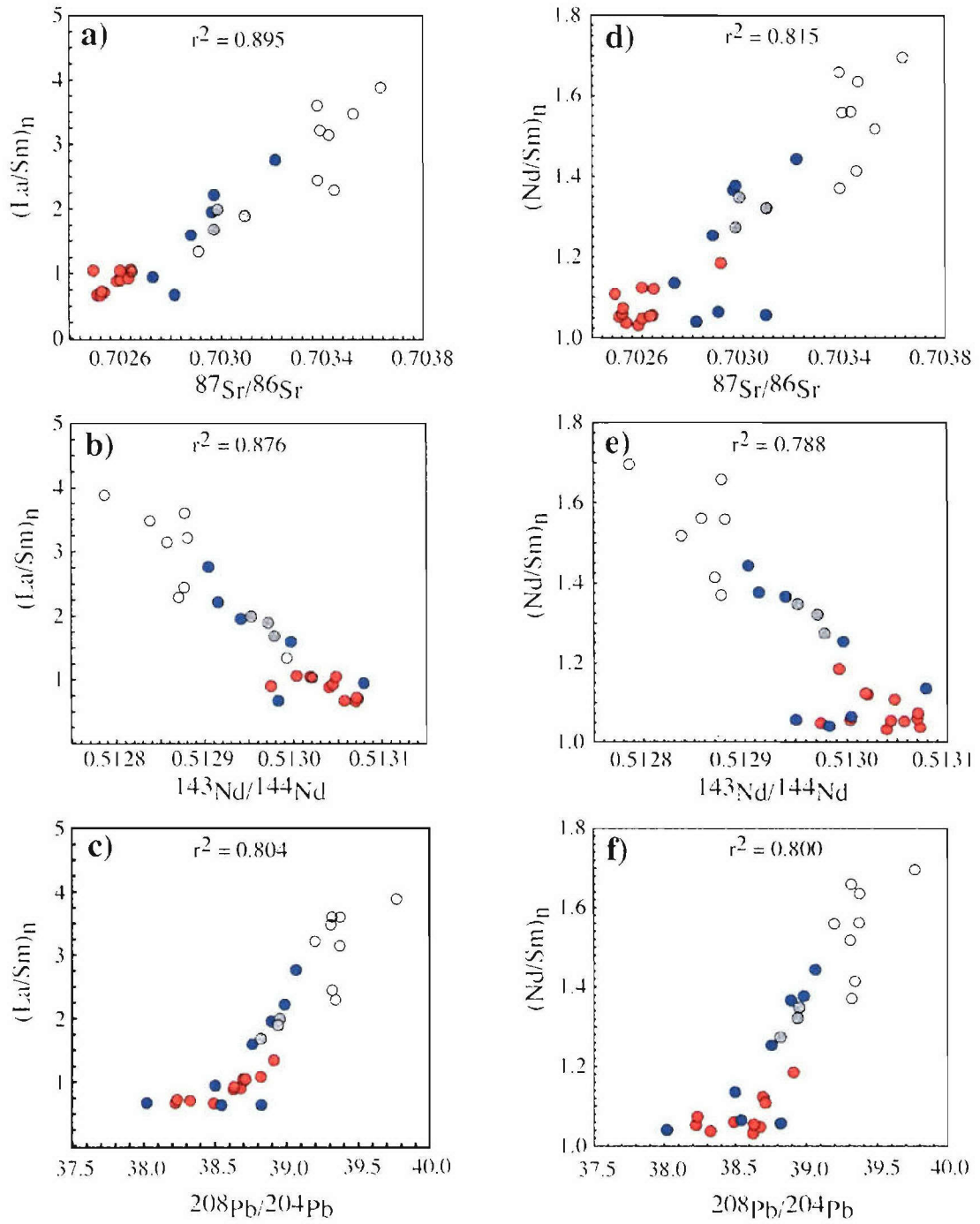


**Figure 11.** Incompatible trace element ratios  $(\text{La}/\text{Sm})_n$  and  $(\text{Nd}/\text{Sm})_n$  versus  $^{87}\text{Sr}/^{86}\text{Sr}$  in a & d,  $^{143}\text{Nd}/^{144}\text{Nd}$  in b & e, and  $^{208}\text{Pb}/^{204}\text{Pb}$  in c & f, for basalts from 9°-25°E on Southwest Indian Ridge. Symbols as in Figure 2.



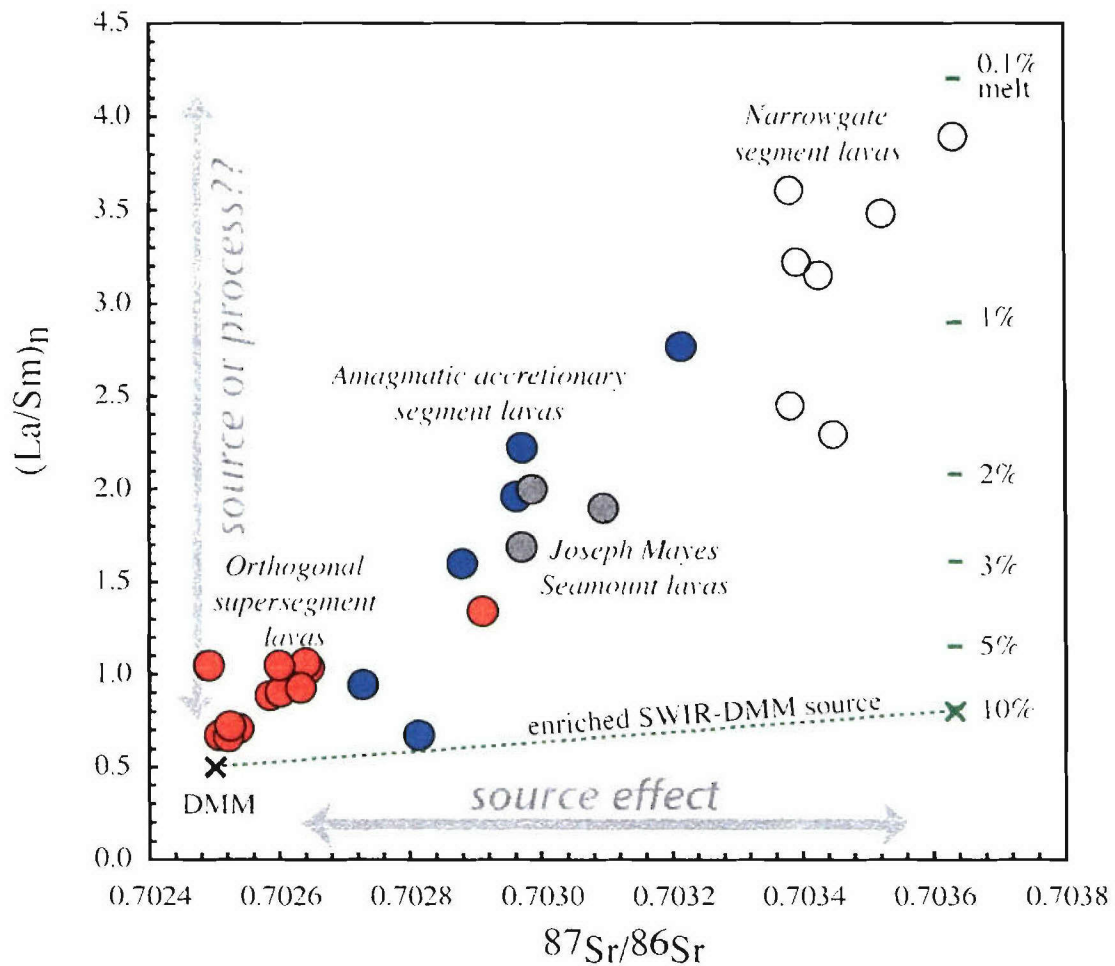
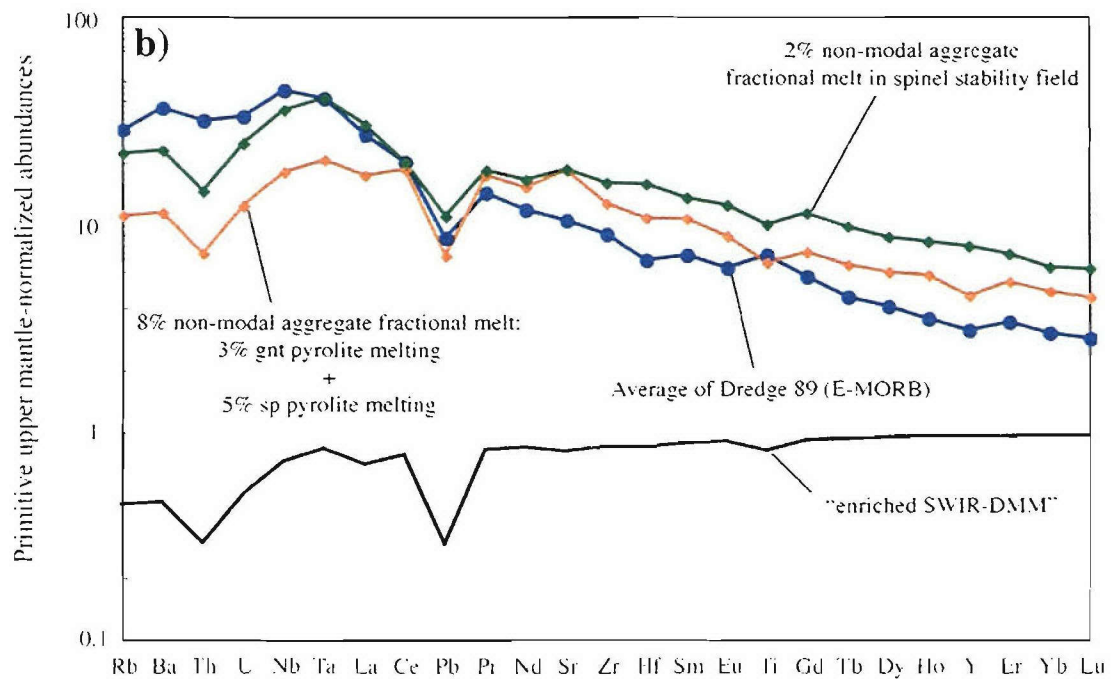
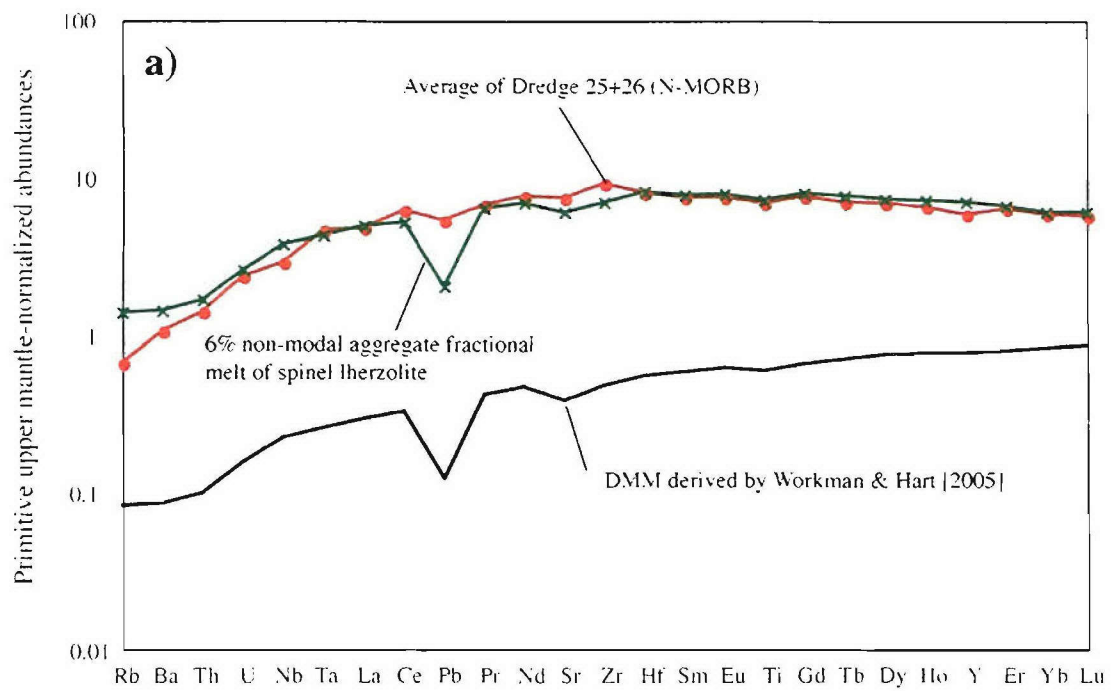


**Figure 12.**  $(\text{La}/\text{Sm})_n$  versus  $^{87}\text{Sr}/^{86}\text{Sr}$  for SW Indian Ridge lavas, where “n” indicates PUM normalized [McDonough and Sun, 1995]. Lava symbols are the same as Fig. 2. Black X represents DMM source composition from Workman & Hart [2005]. Green X represents “enriched SWIR-DMM” source composition (see text for details), with dashed line indicating that if desired, an individual source composition could be calculated for the specific isotopic composition of each lava, but here we use the enriched end-member. In association with Figure 10b, we calculate  $(\text{La}/\text{Sm})_n$  for varying extents of melting (green labeled tick marks) for the “enriched SWIR-DMM” source. See Figure 10b for melting parameters. Even with a trace element enriched source, constrained by isotopic enrichment specific to the lava, we still require  $F < 1\%$  to account for the highly enriched  $(\text{La}/\text{Sm})_n$  of the Narrowgate lavas.



(opposite page)

**Figure 13.** Trace element abundance patterns normalized to PUM [McDonough & Sun, 1995] for a) LREE depleted end-member composition (N-MORB) represented by an average for Dredge 25+26 and b) LREE enriched end-member composition (E-MORB) represented by Dredge 89 average. The average N-MORB composition (red curve) is best fit by a 6% non-modal aggregate fractional melt (green curve) of average DMM (black curve) [Workman & Hart, 2005], using bulk source D's also from Workman & Hart, [2005] (and references within) and melt modes derived by Kd's from Kelemen *et al.*, [2003] and melting coefficients for the spinel stability field from Wasylenki *et al.*, [2003]. The average E-MORB pattern (blue curve) has an incompatible element enriched pattern and is difficult to fit by melting "enriched SWIR-DMM" (black curve). The green curve represents a 2% non-modal aggregate fractional melt of the "enriched SWIR-DMM" source composition (see text for explanation), using spinel peridotite bulk D's for shallow melting. Alternatively, melting of the same source composition beginning within in the garnet stability field (3%) and continuing into the spinel stability field (5%) provides a better overall shape along the REEs, but lacks the abundance levels for LILEs (orange curve). Bulk D's for garnet and spinel pyrolite taken from Kelemen *et al.*, [2003] (Kd's for Sr, Zr, and Hf taken from Donnelly *et al.*, [2004], and Ti from Cushman *et al.*, [2004], and references within). Estimated  $2\sigma \sim 20\%$  for bulk D's.

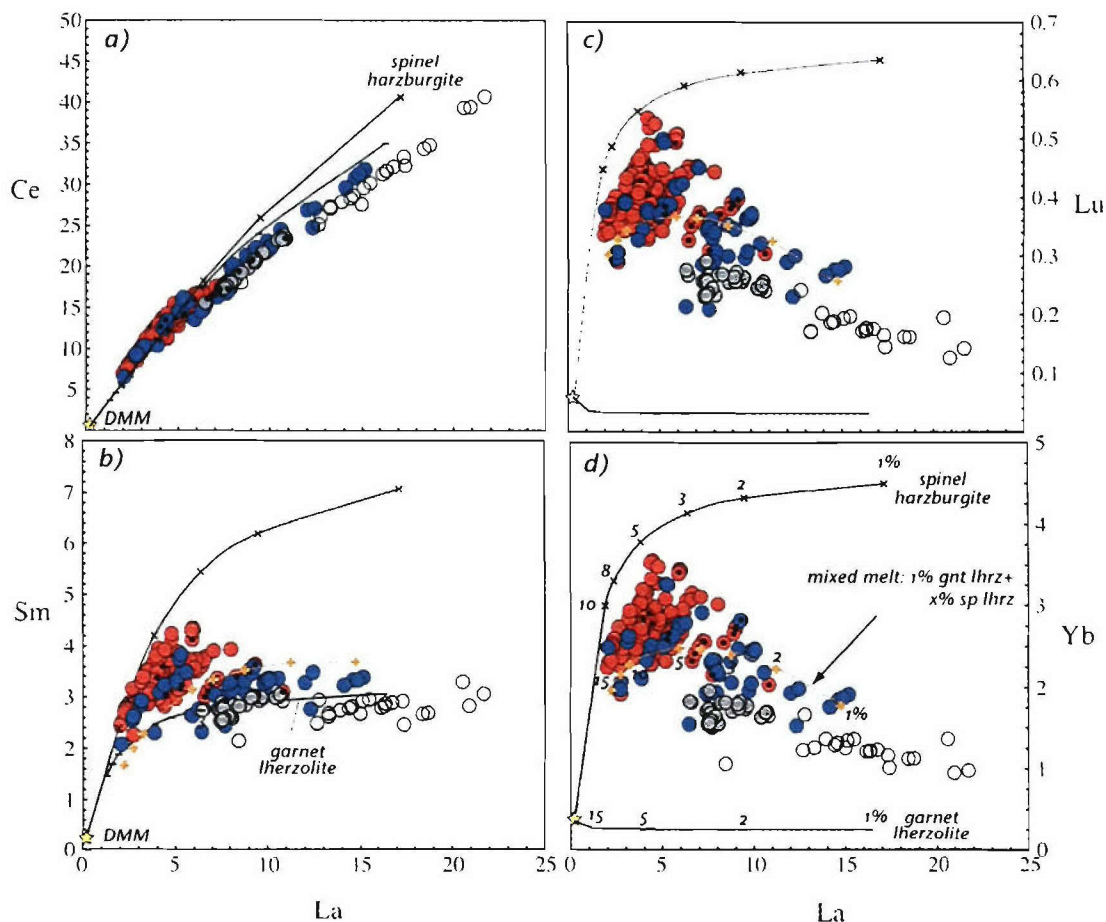


**Figure 14.** Fractionation corrected trace element abundances with modeled melt trajectories. Sample symbols the same as in Figure 2. Black circles represent orthogonal supersegment lavas erupted from the westernmost volcanic segment (15.5°-16.5°E), and illustrate the correlation between trace element systematics and along-axis location. DMM [Workman & Hart, 2005] is represented as a yellow star and serves as the source composition for the modeled “aggregate fractional melting” trajectories. Shallow-melting of DMM in the spinel stability field is reflected by the black solid line with X’s. Deep-melting in the garnet stability field (only) is shown by the black lines with tick-marks. Partition coefficients and modes are from Wasylenki et al., [2003] and the compilation of Kelemen et al., [2003]. The orange line with pluses reflects a mixed melt that has constant contribution of melt produced in the garnet stability field at 1%, mixed with increasing percent melts from the spinel stability field (as labeled on the line). Thus the first tick mark (end of the line) is actually a mixture of 1% garnet melt with 1% spinel melt.

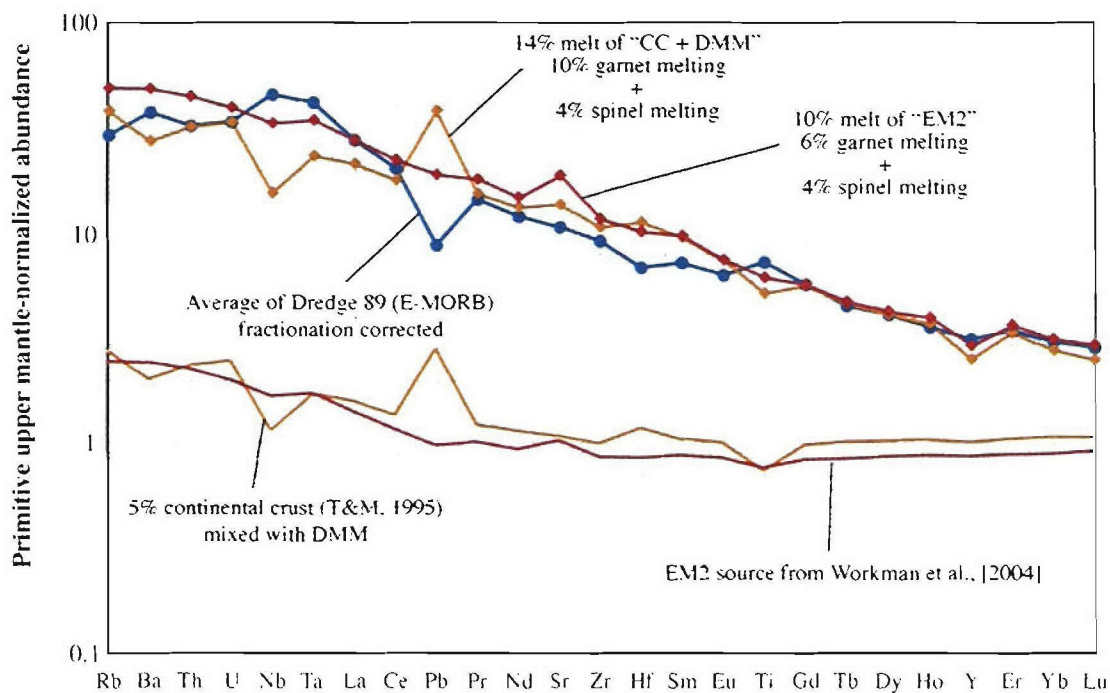


**Figure 15.** Trace element abundance patterns for mantle reservoir source compositions (solid lines), modeled liquids (lines with symbols), and average E-MORB from dredge 89 (blue line) of the Southwest Indian Ridge. The solid maroon curve represents the derived “EM2” source composition [Workman *et al.*, 2004] and the solid orange curve represents a source composition of 5% continental crust [Taylor and McLennan, 1985] mixed into DMM [Workman and Hart, 2005]. All abundance patterns are normalized to PUM [McDonough & Sun, 1995]. Non-modal aggregate fractional melting for both source compositions, used bulk *D*’s from Kelemen *et al.*, [2003] for garnet and spinel peridotite.



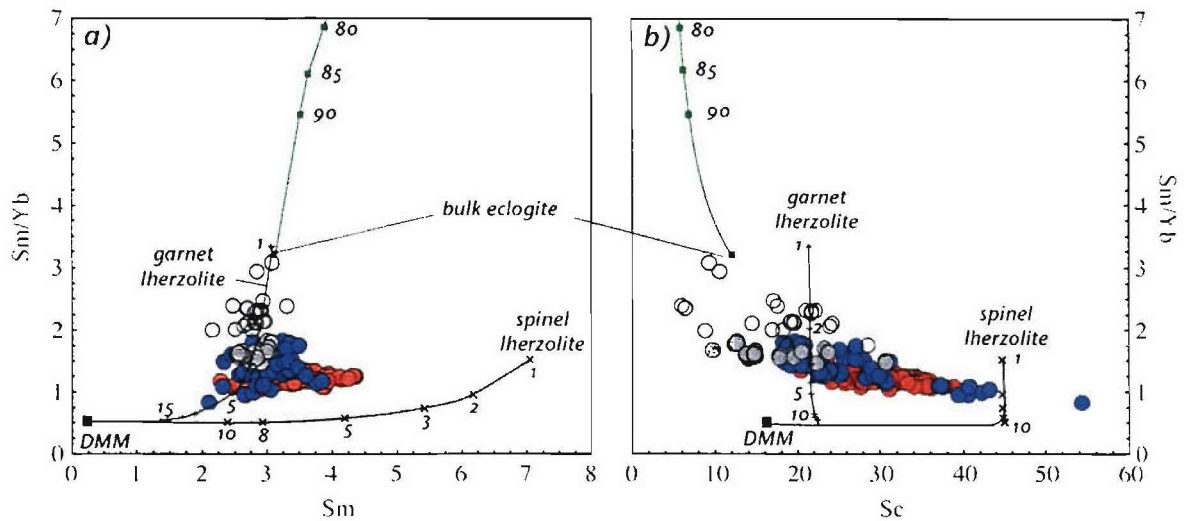


**Figure 16.** Modeling of various melting trajectories for a) Sm/Yb vs. Sm (ppm) and b) Sm/Yb vs. Sc (ppm). Elemental concentrations and ratios use fractionation-corrected data. Basalt symbols are the same as previous figures. The source composition for peridotite melting is DMM [Workman and Hart, 2005] with non-modal near-fractional aggregate melting in the spinel stability field (black curve with X's) modeled using mineral/melt partition coefficients from [Kelemen *et al.*, 2003, and references within] and melting modes from [Wasylenki *et al.*, 2003]. Peridotite partial melting in the garnet stability field only (black curve with pluses) is calculated using “garnet lherzolite” bulk D's from [Kelemen *et al.*, 2003]. The eclogite source composition is an average fractionation-corrected Bouvet Island lava calculated from measurements of *le Roex and Erlank*, [1982] and *Weaver et al.*, [1986]. Eclogite partition coefficients are from *Pertermann et al.*, [2004] for cpx and garnet, and melting calculations assume modal melting, based on the stability of garnet during eclogite melting. All curves are annotated with melting fractions (%).

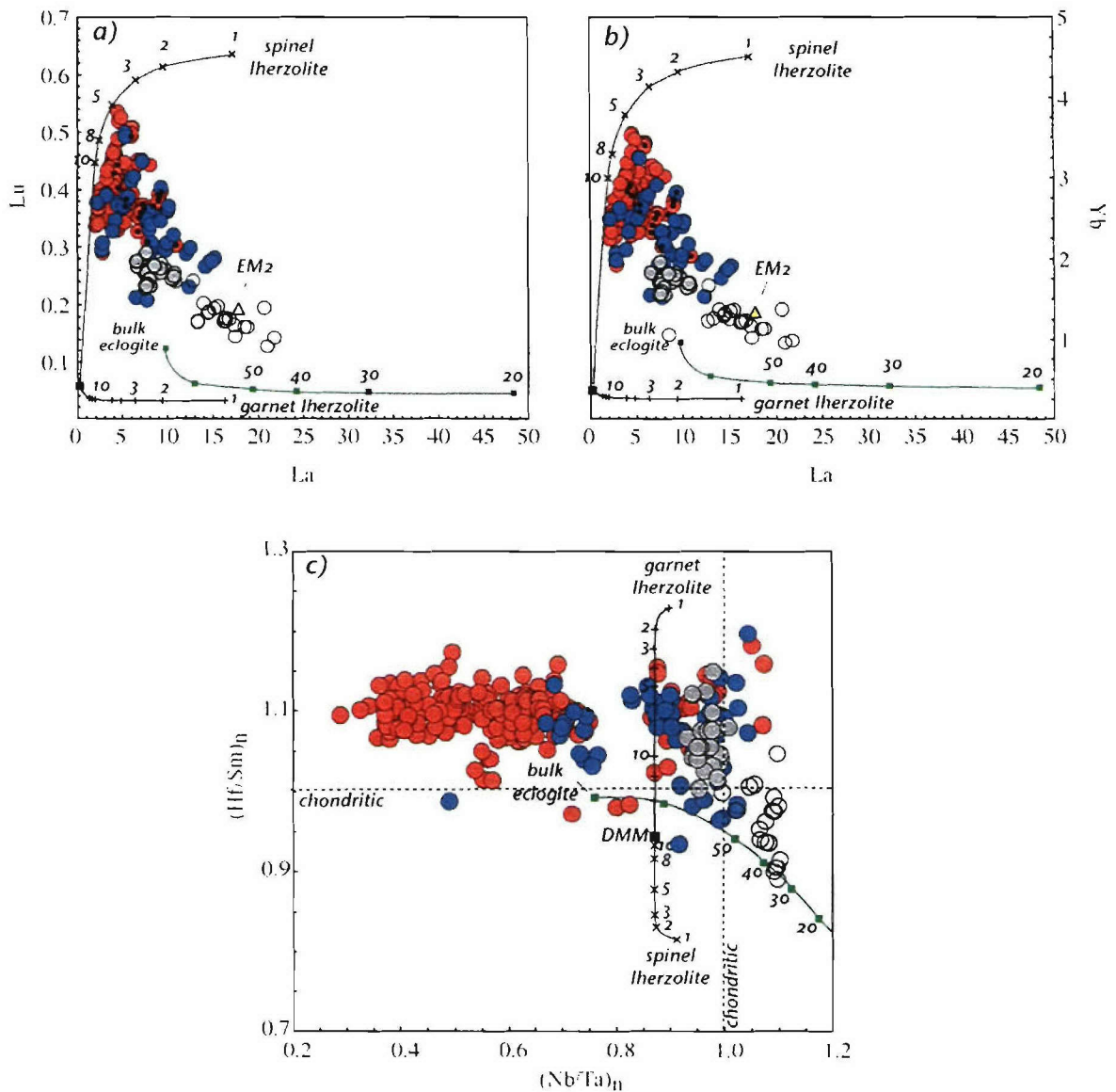
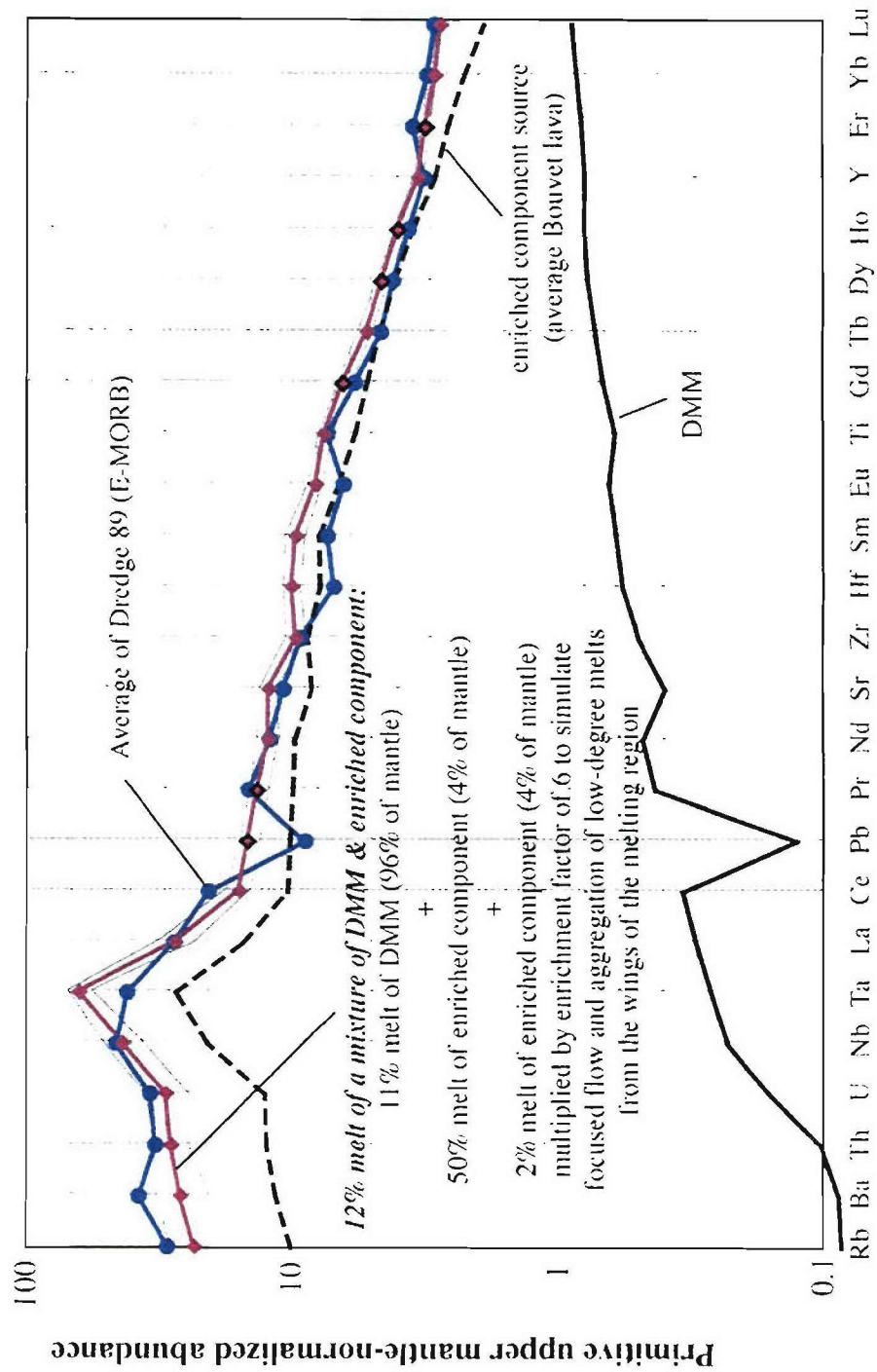
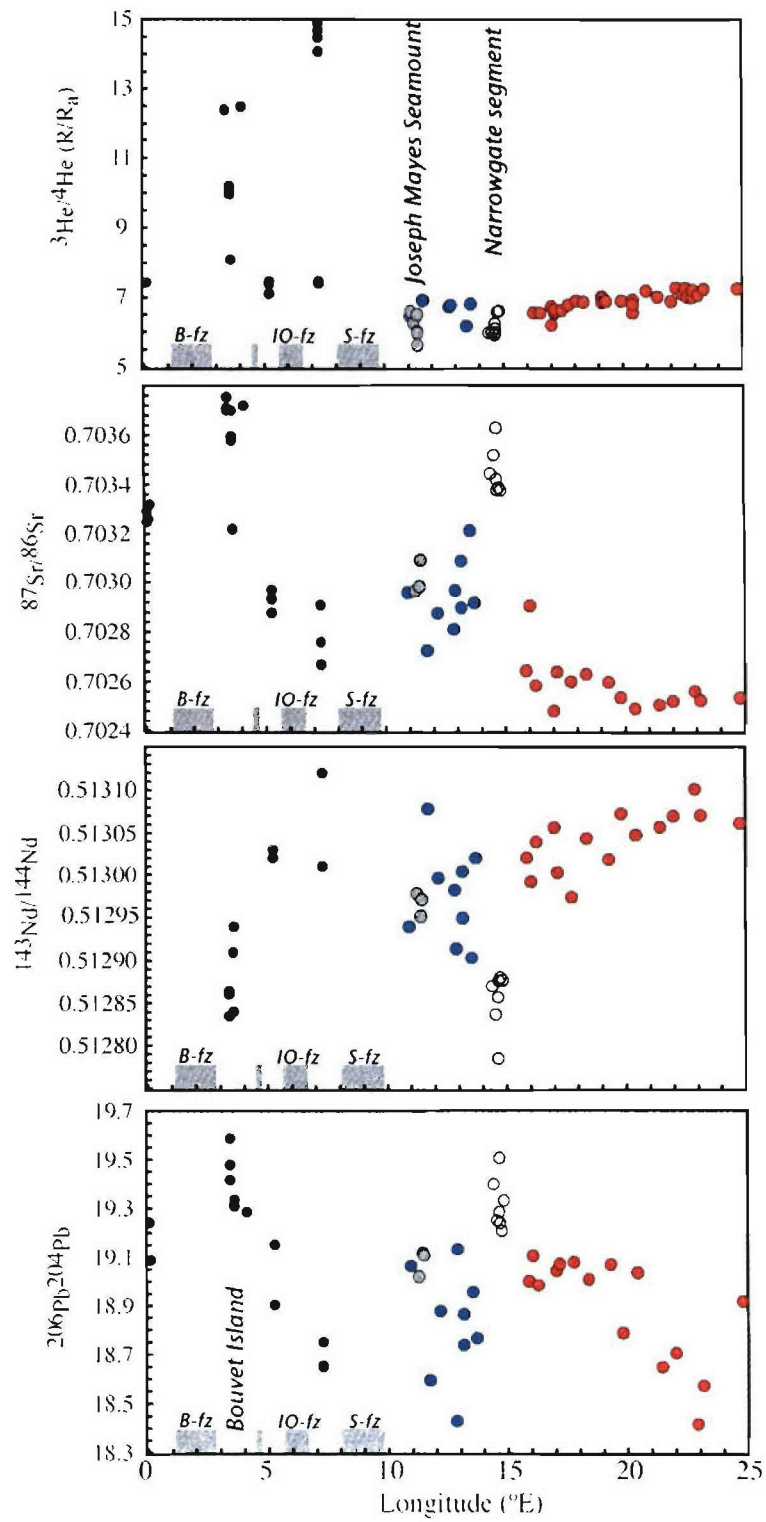


**Figure 17.** Additional modeling of peridotite and eclogite melting for a) Lu vs. La, b) Yb vs. La, and c)  $(\text{Hf}/\text{Sm})_n$  vs.  $(\text{Nb}/\text{Ta})_n$ , where “n” indicates primitive upper mantle normalized [Sun and McDonough, 1995]. Dashed lines in c) mark the chondritic values of 1. Elemental concentrations and ratios use fractionation-corrected data. Basalt symbols are the same as previous figure. Melting curves are derived using the same methodology described in Figure 18. Only additional data point from Figure 18 is “EM2” (yellow triangle in a) and b)) which represents a 10% melt of the newly derived EM2 trace element composition [Workman et al., 2004].



(opposite page)

**Figure 18.** Trace element abundance patterns two-lithology source components, modeled best-fit liquid, and dredge 89 average (E-MORB) from the SW Indian Ridge. The solid black curve represents DMM source composition [Workman and Hart, 2005] and the dashed black curve represents the enriched end-member component, which is taken to be the average lava composition of Bouvet hotspot (all lava compositions are whole rock XRF analyses from *le Roex and Erlank*, [1982] and *Weaver et al.*, [1986]). The blue curve is an average of “fractionation-corrected” lavas from dredge 89 from the Narrowgate segment. The purple curve is the best-fit modeled liquid generated by non-modal aggregate fractional melting of a two-component (distinct lithology) source (4% enriched component with 96% DMM, by mass). The model liquid represents ~12% total melting of the two-component source and is broken down in the following melt fractions: 1) low-degree melts (2%) of the enriched vein component form at depth, aggregate on the fringe of the melting region, and are focused toward the ridge (represented by an enrichment factor of 6), thereby adding significant leverage in LREE and LIL enriched melts, 2) high-degree melts (50%) of the enriched vein component form in the main portion of the melting region at depth and continue to melt up to and beyond the peridotite solidus, hence the large extent of melting, and 3) DMM melts 11%, beginning in the garnet stability field (6%) and finishing in the spinel stability field (5%). All abundance patterns are normalized to PUM [McDonough & Sun, 1995]. Non-modal aggregate fractional melting model used bulk D’s for DMM melting taken from *Kelemen et al.*, [2003] and *Wasylenki et al.*, [2003] for garnet and spinel peridotite, respectively. Bulk D’s for enriched component melting were taken from *Pertermann and Hirschmann*, [2003], including cpx/melt partition coefficients (Th, U, Nb, La, Ce, Nd, Sr, Zr, Sm, Eu, Ti, Dy, Y, Yb, Lu) and source and melt modes from *Pertermann and Hirschmann*, [2002], and all other partition coefficients from *Kelemen et al.*, [2003]. Light grey curves are model liquids reflecting the range in composition of Bouvet lavas used to derive the source composition.





(opposite page)

**Figure 19.** Along-axis isotopic variations in  $^3\text{He}/^4\text{He}$ ,  $^{87}\text{Sr}/^{86}\text{Sr}$ ,  $^{143}\text{Nd}/^{144}\text{Nd}$ , and  $^{206}\text{Pb}/^{204}\text{Pb}$  for glasses between  $0^\circ$ - $25^\circ\text{E}$  on the SW Indian Ridge. Black dots represent glass measurements from *Kurz et al.*, [1998] and *le Roex et al.*, [1983], otherwise sample symbols as in Figure 2. Light grey vertical fields mark the Narrowgate segment and Joseph Mayes Seamount lavas. Dark grey bars note the positions of B-fz (Bouvet Fracture Zone), IO-fz (Islas Orcadas Fracture Zone), and S-fz (Shaka Fracture Zone). Bouvet Island is located at  $3.4^\circ\text{E}$ .

***Chapter 4. The generation of  $^{238}\text{U}$ - $^{230}\text{Th}$ - $^{226}\text{Ra}$  disequilibria on the ultraslow-spreading Southwest Indian Ridge (9°-25°E): Spatially and temporally variable volcanism***

## Chapter 4. The generation of $^{238}\text{U}$ - $^{230}\text{Th}$ - $^{226}\text{Ra}$ disequilibria on the ultraslow-spreading Southwest Indian Ridge (9°-25°E): Spatially and temporally variable volcanism

Jared J. Standish - MIT/WHOI Joint Program in Oceanography

Kenneth W. W. Sims - Woods Hole Oceanographic Institution, Woods Hole, MA. 02543

Henry J. B. Dick - Woods Hole Oceanographic Institution, Woods Hole, MA. 02543

### Abstract

Measured U-Th and Th-Ra disequilibria in mid-ocean ridge basalts from 9°-25°E on the ultraslow-spreading Southwest Indian Ridge reveal abnormally young lavas sampled significant distances from the axis of accretionary rifting. ( $^{230}\text{Th}/^{238}\text{U}$ ) > 1 in 10 of 12 basalt glasses limits their eruption ages to < 300 ka, which for 6 lavas is significantly younger than the predicted spreading rate age of the crust they sit on. Further age limits are obtained from Th-Ra disequilibrium measurements, where excess  $^{226}\text{Ra}$  indicates eruption ages < 8 ka. The U-Th and Th-Ra disequilibrium measured in these basalts documents spatially and temporally variable volcanism distributed throughout an ultraslow-spreading rift valley, which in places reaches 25-30 km wide. These observations provide valuable insight into the complexities of lithospheric accretion. Constraints from the U-series systematics in concert with additional geochemical, geophysical, and geologic constraints enable a more complete understanding of ultraslow-spreading accretionary ridge environments.

5 of 12 basalts are characterized as E-MORBs as constrained by their major element, trace element, and isotopic compositions. With the exception of a single 'rift-axis' sample from the orthogonal supersegment with ( $^{230}\text{Th}/^{238}\text{U}$ ) =  $1.266 \pm 0.02$  ( $2\sigma$ )), the E-MORBs have disequilibria ranging from 5% excess  $^{230}\text{Th}$  to 4% excess  $^{238}\text{U}$ . The other 7 samples are N-MORBs with excess  $^{230}\text{Th}$  ranging from secular equilibrium or 0% to 15%. ( $^{238}\text{U}/^{232}\text{Th}$ ) and ( $^{230}\text{Th}/^{232}\text{Th}$ ) are well correlated with  $^{87}\text{Sr}/^{86}\text{Sr}$  and ( $\text{La}/\text{Sm}$ )<sub>n</sub> for N-MORBs and E-MORBs, with more radiogenic  $^{87}\text{Sr}/^{86}\text{Sr}$  having lower ( $^{238}\text{U}/^{232}\text{Th}$ ) and ( $^{230}\text{Th}/^{232}\text{Th}$ ). However ( $^{230}\text{Th}/^{238}\text{U}$ ) is not well correlated with  $^{87}\text{Sr}/^{86}\text{Sr}$  in N-MORBs and shows a trend of decreasing ( $^{230}\text{Th}/^{238}\text{U}$ ) with increasing  $^{87}\text{Sr}/^{86}\text{Sr}$  for E-MORBs. This is opposite the conventional model for generation of U-Th disequilibrium, which predicts increasing ( $^{230}\text{Th}/^{238}\text{U}$ ) and long-lived isotopic source enrichment due to increased proportions of garnet-bearing mafic lithology melts, mixed with depleted peridotite melts.

Comparison of ( $\text{La}/\text{Sm}$ )<sub>n</sub>,  $^{87}\text{Sr}/^{86}\text{Sr}$  and ( $^{230}\text{Th}/^{238}\text{U}$ ) along-axis shows systematic enrichment from east to west on the orthogonal supersegment, strongly suggesting that isotopic and trace element indicators of source variation are coupled with U-Th disequilibrium, and thus the variation in excess  $^{230}\text{Th}$  is controlled by the source composition. On the other hand, the oblique supersegment lavas have ( $^{230}\text{Th}/^{238}\text{U}$ ) that is inversely correlated with ( $\text{La}/\text{Sm}$ )<sub>n</sub> and  $^{87}\text{Sr}/^{86}\text{Sr}$ , and thus is not directly controlled by source heterogeneity. Rather, the oblique supersegment U-Th disequilibrium

measurements reflect melts suggestive of an eclogites signature, but that have incorporated U-Th disequilibrium signatures typical of shallow equilibration with or melting of a depleted spinel harzburgite. This model provides an alternative explanation for the lack of correlation between ( $^{230}\text{Th}/^{238}\text{U}$ ) and long-lived isotopic heterogeneity often seen in MORB suites.

## 1. Introduction

Melt generation within the mantle, extraction and transport from the mantle to the oceanic crust, and eruption at the seafloor all occur over highly variable time scales, making them difficult to constrain. However, the Uranium-series decay scheme  $^{238}\text{U}$ - $^{230}\text{Th}$ - $^{226}\text{Ra}$ , with its short-lived nuclides, is ideal for investigating petrogenetic processes during mid-ocean ridge crustal accretion. The similarity in time scales between mid-ocean ridge magmatic processes and the half-lives of  $^{230}\text{Th}$  ( $t_{1/2} \approx 75,400$  years) and  $^{226}\text{Ra}$  ( $t_{1/2} \approx 1,600$  years) enables parent/daughter disequilibria data to provide temporal constraints on melt generation, melt transport, and eruption ages. Over the past 15 years workers have applied U-series disequilibria measurements to the investigation of crustal accretion mechanisms on the East Pacific Rise [Goldstein et al., 1991; Goldstein et al., 1994; Sims et al., 2003; Sims et al., 2002] and the Mid-Atlantic Ridge [Bourdon et al., 1996a; Lundstrom et al., 1998a; Peate et al., 2001] with interesting results. Groundbreaking work on the fast- and intermediate-spreading Juan de Fuca and Gorda Ridges [Goldstein et al., 1991; Sims et al., 1995] used U-series age constraints to illustrate a lack of temporal progression with distance from the neo-volcanic zone, thereby indicating young volcanism over a relatively wide zone (up to 4 km off-axis). To date, no studies on the U-series systematics of basalts from ultraslow-spreading ridges have been published, leaving a gap in our understanding of how U-series disequilibrium is influenced by the tectonic and geochemical complexity recently documented in these end-member spreading environments [Cannat et al., 2003; Dick et al., 2003; Gauger et al., 2004; Jokat et al., 2003; Meyzen et al., 2003; Michael et al., 2003; Sauter et al., 2004a; Snow et al., 2004; Standish and Dick, 2004].

The Southwest Indian Ridge spreads at a full-rate varying between 14 – 16 mm/yr, classifying it as an ultraslow-spreading ridge (< 20 mm/yr). Between 9°-25°E along the Southwest Indian Ridge, a straight, orthogonally spreading supersegment gives way (without a transform offset) to an obliquely oriented amagmatic accretionary supersegment, where the orthogonal full-rate of 14 mm/yr drops to an effective spreading rate of 7 mm/yr (see Section 2). This 1050 km long section of the ridge is characterized by dramatic changes in ridge segmentation, morphology, basalt chemistry, and estimated crustal thickness, all potentially related to the variable effective spreading rate (i.e. upwelling rate). By investigating the U-series systematics along this portion of the Southwest Indian Ridge, we hope to gain valuable insight into the factors that influence crustal accretion on an ultraslow-spreading ridge. In this light, we present U and Th concentration data and  $^{230}\text{Th}/^{232}\text{Th}$ ,  $^{234}\text{U}/^{238}\text{U}$ ,  $^{238}\text{U}/^{230}\text{Th}$ , and  $^{226}\text{Ra}/^{228}\text{Ra}$  isotope measurements on 12 glasses from 9°-25°E, representing the initial systematic study of U-series disequilibria on an ultraslow-spreading ridge.

We use existing major element chemistry, geologic, bathymetric, and geophysical data and observations (Chapter 2), trace element and isotopic chemistry (Chapter 3), and these new U-series disequilibrium data to 1) assess the spatial and temporal variability of volcanism across the rift valley, and 2) constrain the petrogenetic processes involved in creating U-series disequilibrium in this complex tectonic and magmatic environment.

## **2. Tectonic setting, spreading rates, and sample locations**

Situated between the African and Antarctic plates, the ultraslow spreading Southwest Indian Ridge (SWIR) is one of the slowest mid-ocean spreading ridges in the global ridge system, with an average full rate of 14–15 mm/yr [DeMets et al., 1990; Menke, 2005]. The Southwest Indian Ridge measures 7700 km in length from the Bouvet Triple Junction (55° S, 0° E) to the Rodrigues Triple Junction (25° S, 70° E) and maintains a highly oblique (~60°) SW-NE orientation to the plate spreading direction. As a consequence of the ultraslow spreading rates and the unique segmentation observed, the Southwest Indian Ridge has garnered considerable attention over the past decade. The Southwest Indian Ridge has been divided along its length into three general regions of interest: 1) the eastern Southwest Indian Ridge from 46° E to 70° E [Cannat et al., 1999; Mendel and Sauter, 1997; Meyzen et al., 2003; Sauter et al., 2004a; Sauter et al., 2004b; Seyler et al., 2003] is characterized by sections with a segmentation pattern identical to that at slow spreading ridges contrasted with highly oblique sections devoid of transform offsets [Sauter et al., 2004a], 2) the central Southwest Indian ridge from 25° E to 46° E [Hamelin and Allègre, 1985; le Roex et al., 1989; Mahoney et al., 1992], strongly influenced by the Marion Hotspot, contains many large transform offsets, and 3) the western Southwest Indian Ridge between the Bouvet Triple Junction (~0°) and 25° E [le Roex et al., 1983; le Roex et al., 1992] contains numerous transform offsets linking orthogonal magmatic segments from 0° to 10° E and then no transform offsets between 9–25° E (see fig. 1 inset).

Much of the Southwest Indian Ridge shows typical slow-spreading ridge segmentation, characterized by second-order magmatic segmentation [Macdonald et al., 1991] linked by transform offsets. Yet other sections, notably portions of the eastern SWIR [Sauter et al., 2004a] and our study area between 9–25° E, lack transforms and instead have sub-orthogonal magmatic accretionary segments linked by oblique spreading amagmatic accretionary segments (also referred to as amagmatic troughs owing to their physiography). This transition in style of segmentation has also been observed on the Knipovich Ridge [Okino et al., 2002], the Lena Trough [Snow et al., 2004], and Gakkel Ridge [Cochran et al., 2003; Jokat et al., 2003; Michael et al., 2003] where it is also linked to decreasing spreading rate [Dick et al., 2003]. While it might appear that segmentation and general crustal architecture are directly related to spreading rate, the mechanism(s) responsible for stability on the segment-length scale remain poorly understood. One likely influence on ridge segmentation, especially at ultraslow-spreading rates, is the geometry of spreading. This work attempts to determine the effect of spreading geometry on crustal accretion and basalt chemistry. Geometrically as the obliquity of a ridge axis increases so does its length, and thus mantle upwelling must



decrease proportionately (Fig. 1, *inset*). The amount that mantle upwelling slows is calculated as the effective spreading rate (ESR), and is simply the spreading component perpendicular to the ridge axis.

Along the 1050 km long ridge section between the Shaka Fracture Zone at  $\sim 9^\circ$  E and the Du Toit Fracture Zone at  $25^\circ$  E (Fig. 1) there are two distinctly different supersegments. The 630 km long 'orthogonal' supersegment ( $15^\circ 45'$ – $25^\circ$  E) mapped by [Grindlay et al., 1998] is dominantly linear with typical slow-spreading morphology. Two 290 and 220 km orthogonal spreading subsections linked by a 120 km long slightly oblique ( $\sim 10^\circ$ ) subsection comprise the supersegment. All three subsections are composed of orthogonally spreading magmatic accretionary segments linked by short ( $< 10$  km) non-transform offsets. At approximately  $16^\circ$  E the orthogonal supersegment abruptly ends, the rift valley floor drops nearly 500 m, and the morphology, physiography, lithology, and segmentation patterns of the ridge change. From  $16^\circ$  E for nearly 400 km the ridge maintains a southwesterly trend, reaching an obliquity of  $\sim 57^\circ$ , intersecting the Shaka Fracture Zone at about  $9^\circ 50'$  E. The oblique supersegment is quite diverse along its length containing two highly robust orthogonal magmatic accretionary segments, Narrowgate segment and Joseph Mayes Seamount, which are connected along-axis by a spectacular oblique amagmatic trough. Detailed tectonic descriptions along with ridge characteristics for different regions along axis within our study area can be found in (Chapter 2).

Samples were collected during two separate dredging expeditions: 1) RV Knorr162, legs 7-9 in 2001 and 2) RV Melville–Vancouver 7 expedition in 2003. Nearly 100 dredges were conducted both within the rift valley and on the rift valley walls. For this study we selected 12 basalts with fresh and abundant glass based on a number of criteria: 1) representative of the along-axis variation in major and trace element variations (i.e. each of the tectonomagmatic zones), 2) representative of the along-axis isotopic heterogeneity (e.g., Sr, Nd, He), and 3) samples were fresh, phenocryst-free lavas, if possible, from the rift valley floor (suggesting young ages). The sample locations are presented in Table 1, along with effective spreading rates and descriptions of the dredge locations. Samples are geologically distinguished as 'rift valley floor lavas', 'rift valley wall lavas', or 'axial rift lavas'. It should be noted that although this distinction gives a general sense of expected age, the complex tectonic environment renders many observational or geologic age constraints meaningless. Abundant evidence from bathymetric and tectonic observations, along with basalt chemistry (Chapter 2) indicate that magmatic activity within our study area is highly dispersed and may largely be controlled by tectonic forces. We use the U-series disequilibrium measurements in these glasses to place limits on their ages in order to verify whether temporally variable off-axis eruptions are occurring throughout the rift valley.

### 3. Methods

#### 3.1. Leaching

The glasses were picked while at sea and then picked again in the lab to assure a high-quality starting fraction. Glass fractions were handpicked to remove contaminated glass with altered or weathered rinds and phenocrysts or glass fractions dominated by phenocrysts. In most cases upwards of 4 grams of glass was picked. Picked fractions were then leached according to the following sequence: 1) in a Teflon beaker cover glass with a 0.1 M oxalic + 2%  $\text{H}_2\text{O}_2$  solution for 15 minutes in sonic bath, 2) rinse thoroughly (3 times) in Millipore DI water while sonicating for 15 minutes, 3) cover glass with 0.1 M HCl + 2%  $\text{H}_2\text{O}_2$  solution for 30 minutes in sonic bath, 4) rinse as above and dry slowly, but thoroughly.

#### 3.2. Dissolution and fuming

Enough glass is weighed out to insure sufficient concentrations of U, Th, and Ra for analysis. Begin dissolution by adding enough concentrated HCl (Seastar <sup>TM</sup>) to cover the basalt glass (~2-3 ml), then seal the Teflon beaker tightly. Let sit in concentrated HCl for 24-48 hours, then add 2-5 ml concentrated HF to each beaker, reseal, and let sit for 24 hours at room temperature. Place beakers on hotplate and heat without boiling for 24-48 hours. Remove lids and dry samples slowly. Bring samples back into solution with appropriate amount of concentrated HCl, to assess completeness of dissolution. If glass remains, repeat above sequence until glass is no longer visible. When undissolved glass (black specks) is no longer visible add 5 ml concentrated HCl, plus 3 ml concentrated  $\text{HClO}_4$ , and 20 drops (~0.5 ml)  $\text{H}_3\text{BO}_3$ . Transfer Teflon beakers to the closed-system fuming oven and fume as explained below.

The closed Teflon fuming oven is a solid graphite block with Teflon coating, along with openings into which pairs of sealed 30 ml Teflon beakers are inserted. Each pair consists of a beaker holding the sample solution that is connected via a previously cleaned, threaded Teflon elbow, to a second 30 ml Teflon beaker (empty). The beaker holding the sample solution is inserted into the internally heated Teflon oven, with the 2nd beaker sitting outside the oven at room temperature. The internal temperature of the heating element (oven) can be precisely controlled ( $\pm 1^\circ \text{C}$ ). Preset stepwise heating programs can be used to heat the sample in stages at varying temperature gradients and for varying durations. The fine-scale temperature control prevents the sample solution from boiling, while maximize fuming. The sharp temperature contrast between each pair of sealed beakers (across the elbow) allows efficient fuming of  $\text{HClO}_4$ , and minimal splatter (if boiling is avoided). Once fuming has completed the initial sample solution should be dry and dark burnt-red in color. Once again assess for complete dissolution by adding 2-5 ml 3 N HCl. If sample contains black material, repeat above HF dissolution sequence. If white or grey gelatinous material exists repeat  $\text{HClO}_4$  fuming sequence – gelatinous material likely represents silica-fluorides that form during HF dissolution. It is imperative, especially for Th column chemistry and analysis, that all fluorides go into

solution, as Th is highly fractionated by fluorides. Numerous dissolution and fuming steps may be required, especially when dealing with large sample sizes (> 2 grams).

It is necessary to make sure glass is completely dissolved. If no visible residue exists, transfer solution into a centrifuge tube and spin at moderately high revolutions per second for 20 minutes. Solution in centrifuge tube should pour out easily into a cleaned, tarred LDPE bottle to be diluted with 3 M HCl until a concentration of 10 mg rock/gm solution exists. If upon pouring solution from centrifuge tube there is evidence of undissolved material, or clear or white viscous material that phase-separated from the liquid, further digestion is required. (Note: Following extensive digestion and centrifuging, a few of our samples had tiny black Cr-spinels remaining in the centrifuge tube that were undigestable and thus discarded.)

### 3.3. Spiking

From each LDPE sample stock solution (diluted to 10 mg rock/gm solution) remove enough solution to provide ~10 ng U and transfer to a clean Teflon beaker. Samples are then spiked with  $^{233}\text{U}$  and  $^{229}\text{Th}$  at spike:sample concentration ratios of 1:8 ( $^{233}\text{U}/^{238}\text{U}$ ) and 1:30 ( $^{229}\text{Th}/^{232}\text{Th}$ ), respectively. Rock standards ATHO and TML are also spiked according to their predetermined concentrations. Spike concentrations are explicitly predetermined through analysis of a series of standard/spike calibrations. To achieve complete sample/spike equilibration we added 0.5 ml conc.  $\text{HClO}_4$  to each sample, covered tightly, and left on low heat for at least 48 hours. All solution was carefully removed from caps and beaker sides, and then fumed and taken to dryness. Samples were brought back into solution with 1 ml DI  $\text{H}_2\text{O}$ , 0.25 ml conc.  $\text{HClO}_4$ , and 2 ml 2 M  $\text{HNO}_3$ . Resume  $\text{HClO}_4$  fuming (at high temperature) before adding 2-3 ml conc.  $\text{HNO}_3$ , thereby converting the sample to a  $\text{HNO}_3$  matrix for column chemistry. The remaining stock solutions were re-weighed and spiked with  $^{228}\text{Ra}$ . With a  $^{226}\text{Ra}/^{228}\text{Ra}$  ratio of ~0.25 in the spike, we used a spike/sample ratio of 1:10-15. A few of the most depleted lavas were spiked closer to a 1:5 spike/sample ratio. Sample solutions were spiked in the LDPE bottles and left on low heat for 48 hours to completely equilibrate. Solutions were then transferred to 100 ml beakers and taken to dryness iteratively, until all remaining solutions were dry, and had a dark red color. 5 ml of 3 M HCl and 1 ml conc.  $\text{HClO}_4$  is added and then taken to dryness or until fuming ceases. Repeat previous step, then bring into solution with 10-40 ml 3 M HCl and 2 ml saturated boric acid before transferring into centrifuge tubes.

### 3.4. Column chemistry

From the previous section we end up with two separate solution fractions for each sample, the first is spiked with  $^{233}\text{U}$  and  $^{229}\text{Th}$  and the second (larger volume) fraction is spiked with  $^{228}\text{Ra}$ . The separation of U, Th, and Ra into concentrated aliquots is conducted using established column chemistry procedures [Goldstein et al., 1989; Layne and Sims, 2000; Pickett et al., 1996; Volpe et al., 1993], which are outlined in Appendix A. For an overview of the sequential procedure please refer to Figure A-1.

### 3.5. Mass spectrometry methods

U, Th, and Ra concentrations were measured on the ThermoFinnigan Element 2 high-resolution single collector ICP-MS, while ( $^{234}\text{U}/^{238}\text{U}$ ), ( $^{230}\text{Th}/^{232}\text{Th}$ ), and ( $^{226}\text{Ra}/^{228}\text{Ra}$ ) activity ratios were measured via plasma ionization multicollector mass spectrometry (PIMMS) techniques on the ThermoFinnigan Neptune high-resolution multi collector ICP-MS [Ball et al., 2002]. Please refer to Appendix B and Table B1 for details on mass spectrometer setup for PIMMS.

## 4. Results

Below we present brief summaries of the major element, trace element, and isotopic compositional variation within the twelve basalts selected for U-series investigation. The detailed major element chemistry and tectonic setting are discussed in Chapter 2, while the trace element and isotopic data is contained within Chapter 3.

### 4.1. Major and Trace Elements

The 12 basalt glasses picked for U-series disequilibria measurements span a major element compositional range from tholeiitic basalt to alkali-olivine basalt. 7 of the basalts are tholeiitic and are dredged from the orthogonal supersegment and amagmatic accretionary segment. The alkali basalts are from the 16°E segment of the orthogonal supersegment, the amagmatic accretionary segment, and 3 nepheline-normative basalts from the Narrowgate segment (2) and Joseph Mayes Seamount (1). Basalt compositions vary from "normal-type" mid-ocean ridge basalt (N-MORB) with  $\text{K}/\text{Ti} < 0.09$ , to "enriched-type" mid-ocean ridge basalt with  $\text{K}/\text{Ti} > 0.15$ , and some highly enriched lavas with  $\text{K}/\text{Ti}$  as high as 0.69. Figure 2 illustrates the large range in  $\text{Fe}_8$  seen in the lavas; with E-MORB compositions extending toward much lower  $\text{Fe}_8$  and slightly lower  $\text{Na}_8$ . Negative trends exist in Figure 2a & 2b, where N-MORBs at low  $(\text{K}/\text{Ti})_8$  have higher  $\text{Na}_8$  and  $\text{Fe}_8$  than E-MORBs with high  $(\text{K}/\text{Ti})_8$  and low  $\text{Na}_8$  and  $\text{Fe}_8$ . The E-MORB compositions tend to be more highly evolved (lower  $\text{MgO}$ ) than the N-MORB, but there are exceptions within this subset and in the larger dataset. The negative correlation in Figure 2b can be largely explained by the low  $\text{Fe}_8$  of the E-MORB, which was shown in Chapter 2 to be a function of the  $\text{H}_2\text{O}$  content of the parental melt. E-MORB parental melts also have elevated  $\text{H}_2\text{O}$  contents, which affects the liquid line of descent by suppressing plagioclase and clinopyroxene saturation to lower temperatures (lower  $\text{MgO}$ ). Olivine crystallizes alone to lower temperatures lowering the  $\text{FeO}^*$  more quickly than a parental melt with less  $\text{H}_2\text{O}$ . The influence of  $\text{H}_2\text{O}$  during fractional crystallization does not greatly affect  $\text{Na}_2\text{O}$  in the melt, thus the negative correlation in 2a suggests that N-MORB have higher amounts of sodium and low source enrichment, whereas E-MORB has lower sodium, but strong source enrichment signatures.

Trace element abundances are highly variable between N-MORBs and E-MORBs. Incompatible element ratios typical for N-MORB are  $(\text{La}/\text{Sm})_n < 1$  and  $\text{Zr}/\text{Nb} > 25$  and E-MORB  $(\text{La}/\text{Sm})_n > 1$  and  $\text{Zr}/\text{Nb} < 15$ . In comparison  $(\text{La}/\text{Sm})_n$  is 0.7 – 1.1 and  $\text{Zr}/\text{Nb}$  14.8 – 45.1 for the N-MORBs, while  $(\text{La}/\text{Sm})_n$  is 1.4 – 4.0 and  $\text{Zr}/\text{Nb}$  3.0 – 10.7 for the E-MORBs from this study. REE patterns (Figure 3) are also quite distinctive for N-MORB



versus E-MORB with E-MORB LREE enrichment by as much as an order of magnitude higher than the most depleted sample. HREE concentrations are much less variable, but show crossing patterns due to the variable MREE to HREE slopes between E-MORB and N-MORB.

#### 4.2. Sr, Nd, Pb, Hf, and He Isotopic Compositions

In Table 3 we report Sr, Nd, Hf, Pb, and He isotopic compositions for 12 glasses and for comparison list average N-MORB isotopic compositions of the East Pacific Rise, Mid-Atlantic Ridge, and Indian Ocean [Su and Langmuir, 2002], along with two basalts from Bouvet Island [Janney et al., 2005]. Lavas from our suite display a large range in isotopic composition, from N-MORB to E-MORB (Figure 4 & 5). The N-MORB glasses show some isotopic variation ( $^{87}\text{Sr}/^{86}\text{Sr}$  from 0.702490 – 0.702812;  $^{143}\text{Nd}/^{144}\text{Nd}$  from 0.513079 – 0.512982;  $^{176}\text{Hf}/^{177}\text{Hf}$  from 0.283266 – 0.283019) and have an average  $^{87}\text{Sr}/^{86}\text{Sr}$  value ( $0.702624 \pm 113$ ;  $1\sigma$  standard deviation) closer to MAR than Indian Ocean, but average  $^{143}\text{Nd}/^{144}\text{Nd}$  ( $0.513034 \pm 35$ ;  $1\sigma$  represents standard deviation) nearly identical to Indian Ocean N-MORB. Pb isotopes for the N-MORB lavas are variable and have average  $^{206}\text{Pb}/^{204}\text{Pb}$  of 18.810,  $^{207}\text{Pb}/^{204}\text{Pb}$  of 15.568, and  $^{208}\text{Pb}/^{204}\text{Pb}$  of 38.498 (Figure 5) that are significantly higher than Indian Ocean, MAR, or EPR N-MORB. E-MORB lavas also show a good deal of isotopic variation ( $^{87}\text{Sr}/^{86}\text{Sr}$  from 0.702909 – 0.703631;  $^{143}\text{Nd}/^{144}\text{Nd}$  from 0.512992 – 0.512786;  $^{176}\text{Hf}/^{177}\text{Hf}$  from 0.283128 – 0.282965) and in some cases (especially  $^{176}\text{Hf}/^{177}\text{Hf}$  values) overlap with the N-MORB compositional range above.

Sr and Nd isotopic compositions are negatively correlated (Figure 4a), illustrating significant mantle heterogeneity from elevated  $^{143}\text{Nd}/^{144}\text{Nd}$  and low  $^{87}\text{Sr}/^{86}\text{Sr}$  at the depleted end-member to low  $^{143}\text{Nd}/^{144}\text{Nd}$  and high  $^{87}\text{Sr}/^{86}\text{Sr}$ . This isotopic heterogeneity along with the major and trace element systematics indicate source composition variability, that may be represented by a heterogeneous peridotite or a two-lithology mantle source, comprised of depleted peridotite and enriched mafic veins. This is discussed in detail in Chapter 2 & 3. Bouvet Island lavas, also plotted in Figure 4, have isotopic compositions similar to the most enriched basalts from our suite, suggesting the possible influence of Bouvet plume material during generation of Southwest Indian Ridge MORB.

#### 4.3. U-Series Disequilibria Measurements

U and Th concentrations and  $^{234}\text{U}/^{238}\text{U}$ ,  $^{230}\text{Th}/^{232}\text{Th}$ , and ( $^{226}\text{Ra}/^{228}\text{Ra}$ ) measured on 12 glasses from 9°-25°E on the Southwest Indian Ridge are reported in Table 4. Instrumental mass bias for all measurements was monitored via frequent intra-session runs of NBS 960 ( $^{238}\text{U}/^{235}\text{U}_{\text{cert.}} = 137.88$ ) or U010 ( $^{238}\text{U}/^{236}\text{U}_{\text{cert.}} = 14,535.10$ ), and averaged  $\sim 1.5\%$ . Procedural blanks for  $^{232}\text{Th}$ ,  $^{238}\text{U}$ , and  $^{226}\text{Ra}$  were 0.0052 picomols ( $< 0.07\%$ ), 0.0109 picomols ( $< 0.05\%$ ), and below detection limit for Ra ( $< 5$  fg), respectively.  $^{234}\text{U}/^{238}\text{U}$  and  $^{230}\text{Th}/^{232}\text{Th}$  measurements on the Neptune were conducted using the faraday cup configuration and thus were corrected for detector yield ( $\leq 1\%$ ). External standards (reported in Table 4) were measured during the course of each session and [U], [Th],



( $^{234}\text{U}/^{238}\text{U}$ ), and ( $^{230}\text{Th}/^{232}\text{Th}$ ) values for TML and ATHO are consistent, within error, with values reported in the literature [Pietruszka et al., 2002; Sims et al., 2002]. Duplicate sample runs (separate aliquots of same dissolution) are reported in Table 4 and show internal reproducibility for ( $^{234}\text{U}/^{238}\text{U}$ ) of < 1% and for ( $^{230}\text{Th}/^{232}\text{Th}$ ) averaging < 1%. Further confidence in our measurements comes from our ability to measure two external rock standards TML and A-THO to within 5‰ of accepted ( $^{234}\text{U}/^{238}\text{U}$ ) values in equilibrium.

#### $^{238}\text{U}$ - $^{234}\text{U}$

Due to the tectonic setting and ultraslow-spreading rates, and because many of our samples have very low U and Th concentrations, relative to the high concentrations in seawater, contamination by seawater must be considered. To verify that the U-series systematics have not been significantly affected by seawater alteration we measured  $^{234}\text{U}/^{238}\text{U}$ , and calculate the ( $^{234}\text{U}/^{238}\text{U}$ ) activity ratio. Since seawater is enriched in  $^{234}\text{U}$  over  $^{238}\text{U}$ , with a ( $^{234}\text{U}/^{238}\text{U}$ ) =  $1.14 \pm 0.03$  [Ku et al., 1977; Thurber, 1967], any seawater induced contamination should result in elevated ( $^{234}\text{U}/^{238}\text{U}$ ) in the glass, relative to equilibrium (( $^{234}\text{U}/^{238}\text{U}$ ) = 1). All Southwest Indian Ridge glasses have ( $^{234}\text{U}/^{238}\text{U}$ ) values within 5‰ (2 $\sigma$ ) of equilibrium (Table 4). Relative to the global MORB dataset, which is scattered largely to higher ( $^{234}\text{U}/^{238}\text{U}$ ), the SWIR lavas plot in a well behaved cluster around ( $^{234}\text{U}/^{238}\text{U}$ ) = 1 (Figure 6). That ( $^{234}\text{U}/^{238}\text{U}$ ) is within error of unity is a necessary but not sufficient constraint indicating these basalts to be unaffected by seawater contamination. That the Southwest Indian Ridge lavas plot so tightly within the error envelope provides confidence that seawater contamination has not affected the ( $^{234}\text{U}/^{238}\text{U}$ ) of these glasses, which thereby allows direct interpretation of U-series disequilibria. Major element, trace element, and isotopic compositions of a larger suite of glasses similarly indicate little to no glass alteration, with only 3 of ~320 glasses showing any compositional sign of alteration (those 3 have been removed from the dataset).

#### $^{238}\text{U}$ - $^{230}\text{Th}$ - $^{226}\text{Ra}$

12 glasses from 9°-25°E show a large range in ( $^{238}\text{U}/^{232}\text{Th}$ ) and ( $^{230}\text{Th}/^{232}\text{Th}$ ) (Figure 7). The majority of the samples are clustered at the enriched end of the MORB array, with sample 25-03 plotting at the depleted end of the array, in the vicinity of EPR lavas. The E-MORBs within our suite extend to compositions similar to many OIB suites, including Samoan and Hawaiian lavas. Calculated ( $^{230}\text{Th}/^{238}\text{U}$ ) activity ratios range from excess  $^{230}\text{Th}$  of 26.6% to excess  $^{238}\text{U}$  of 4.0% (hereafter, ( $^{230}\text{Th}/^{238}\text{U}$ ) > 1.0 will be referred to as excess  $^{230}\text{Th}$ , and ( $^{230}\text{Th}/^{238}\text{U}$ ) < 1.0 will be referred to as excess  $^{238}\text{U}$ ). With the exception of one sample, the rest of the E-MORBs have excess  $^{230}\text{Th}$  < 5% or excess  $^{238}\text{U}$  < 4%, while the N-MORBs range from secular equilibrium to 15% excess  $^{230}\text{Th}$ .

( $^{226}\text{Ra}/^{230}\text{Th}$ ) has been measured by mass spectrometric methods in two samples: KN162-9 33-49 and KN162-9 61-71, and both samples were found to have excess  $^{226}\text{Ra}$ , meaning excess daughter nuclide  $^{226}\text{Ra}$  relative to its parent  $^{230}\text{Th}$ . Excess  $^{226}\text{Ra}$  measurements were 32% and 41%, respectively and are reported in Table 4. ( $^{226}\text{Ra}/^{230}\text{Th}$ ) has also been estimated using traditional  $^{214}\text{Pb}$  alpha counting techniques, for those samples with at least 10 grams of material. By counting the decays per second of  $^{214}\text{Pb}$

( $t_{1/2} = 26.9$  minutes) we can use this value as a proxy for the activity of  $^{226}\text{Ra}$ , assuming the U-series decay chain is in equilibrium below  $^{226}\text{Ra}$ . Alpha counting showed sample KN162-9 10-21 to have 12% excess  $^{226}\text{Ra}$ .

## **5. U-Th-Ra disequilibrium discussion**

### **5.1. Age constraints: coeval lavas beyond the axis of rifting**

Experimentally determined mineral-melt partition coefficients, show that petrologic processes of melt generation and melt transport can fractionate U from Th and/or Th from Ra producing disequilibria in the U-Th-Ra decay series. To return to secular equilibrium the excess nuclide decays at a rate proportional to its half-life, which in the case of  $^{230}\text{Th}$  and  $^{226}\text{Ra}$  are 75 and 1.6 ka, respectively. Based on these half-lives, age constraints within the time-interval of  $10^2 - 10^6$  years can be placed on MORB petrologic processes using U-series disequilibria. In the discussion to follow we use U-Th-Ra disequilibria as a chronometer to provide limits on eruption age for glasses collected throughout the rift valley and on the rift valley walls of the ultraslow-spreading Southwest Indian Ridge.

In order to use U-Th and Th-Ra disequilibria measurements to constrain eruption ages for each lava, we presume that fractionation of the parent and daughter nuclide occurred prior to eruption and that upon eruption the system became closed, so in a sense the U-series system can be used as a “stop-watch”. In this way, measured disequilibria within each lava provides an estimate of the amount of time since eruption, so that the mere presence of excess  $^{230}\text{Th}$  or  $^{238}\text{U}$  indicates that a sample is out of secular (radioactive) equilibrium and is younger than 300 ka - the amount of time it would take for either parent or daughter excess to decay away (5 half-lives). Similarly, measured  $^{226}\text{Ra}$  excess signifies an eruption age younger than 8 ka, based on the much shorter half-life of  $^{226}\text{Ra}$ .

Previous studies on the  $9^\circ$ - $10^\circ\text{N}$  section of the EPR have used this method to provide age limits for lavas from a wide range of on-axis and off-axis locations [Goldstein et al., 1994; Sims et al., 2003; Sims et al., 2002; Zou et al., 2002]. Because the EPR is a fast-spreading ridge, with a well-defined axial summit trough (AST), designation of on-axis versus off-axis, and as a result estimation of eruption ages based on spreading rate is relatively straightforward. Therefore, as pictured in Figure 11 of Sims et al., [2003], age limits by U-Th-Ra disequilibrium can be compared to time-integrated spreading rate ages, illustrating that near axis lavas ( $< 4$  km from AST) have excess  $^{230}\text{Th}$  consistent with spreading rate ages (i.e.  $< 300$  ka). However, the presence of excess  $^{226}\text{Ra}$  in many of these lavas indicates younger ages ( $< 8$  ka) than is predicted by a spreading rate of 55 mm/yr, and thus the possibility of temporal variation in eruption of off-axis lavas [Sims et al., 2003]. Lava from even farther off-axis (up to 28 km) were also shown, using U-Th disequilibrium measurements, relative to spreading rate ages, to be younger than predicted [Zou et al., 2002], suggesting eruptions are occurring far off-axis.

On the ultraslow-spreading Southwest Indian Ridge, where the spreading rate is  $< 15$  mm/yr (full-rate), designation of on-axis versus off-axis becomes significantly more difficult, mostly due to the general absence of a well-defined lineated volcanic ridge. The

morphology of the SWIR is also much different than that of the EPR, as the volcanic crestal plateau is replaced by a wider and significantly more topographically complex rift valley (see Section 2 and also Chapter 2). The diminished volcanic output at ultraslow-spreading ridges in general [Jokat et al., 2003], and the increased tectonic complexity within the Southwest Indian Ridge rift valley make it difficult to distinguish the current location of a volcanic axis, especially on the oblique spreading supersegment. Thus, along segments with ill- or undefined lineated volcanic spreading ridges, we use high-resolution topography and our understanding of ultraslow-spreading accretion to designate the axis of rifting. In most cases, the location of the rift axis is fairly well defined, but if not, we infer the axis to be the symmetric center of the rift valley. In light of this, we use the terms “axis of rifting” and “rift-axis” interchangeably with on- and off-axis to indicate similar meanings. It should also be noted that because of the ultraslow-spreading rates on the Southwest Indian Ridge, comparison of  $^{226}\text{Ra}$  disequilibrium versus spreading rate age for dredged samples is fruitless, as the age limit of  $< 8$  ka is much less than the uncertainty inherent in sample locations. This is a function of the ultraslow-spreading rate and the fact that the amount of time required for excess  $^{226}\text{Ra}$  to completely decay away (8 ka) is equivalent to 56 meters of movement at the Southwest Indian Ridge, which is much less than 500 to 1000 m long dredges.

We have measured ( $^{230}\text{Th}/^{238}\text{U}$ ) in 12 lavas from various tectonic regimes within our study area and 9 show measurable excess  $^{230}\text{Th}$ , 1 has excess  $^{238}\text{U}$ , and 2 are within  $2\sigma$  of secular equilibrium ( $1.0 \pm 0.02$ ). Thus, based on the presence or absence of U-Th disequilibria, 10 of 12 samples are out of equilibrium and are younger than 300 ka. This finding is somewhat surprising considering the ultraslow-spreading environment and their distance from the axis of rifting (Table 1). We present this data in Figure 8a, which plots individual ( $^{230}\text{Th}/^{238}\text{U}$ ) versus the lava's distance from the axis of rifting, here taken to be the symmetric center of the rift valley (parallel to spreading direction). Since distance from the center of the rift valley equates to time, assuming a constant half-spreading rate of 7 mm/yr, a curve representing the decay of excess  $^{230}\text{Th}$  with time is plotted. The rate of decay along this curve is proportional to the half-life of  $^{230}\text{Th}$ , and assumes the initial ( $^{230}\text{Th}/^{238}\text{U}$ ) was measured in a basalt erupted at the axis of rifting. Thus, by using sample VAN7 80-04 with a 26% excess  $^{230}\text{Th}$  we calculate a decay curve that delineates the maximum excess  $^{230}\text{Th}$  predicted for a lava at a given distance from the axis of rifting, provided it was erupted on-axis and moved off-axis by asymmetric seafloor spreading at 7 mm/yr.

Four of twelve samples plot at the center of the rift valley representing two N-MORBs (red squares) and two E-MORBs (blue squares) and have highly variable excess  $^{230}\text{Th}$  from 2.8% to 26%. The two N-MORBs, KN162-7 04-13 and KN162-7 10-21 (from here on samples will be referenced by dredge and sample # only, for example 04-13 or 10-21), were dredged from separate magmatic segments within the orthogonal supersegment, and using high resolution bathymetry, magnetics, and gravity data are constrained to be closely associated with linear ‘axial’ volcanic features (Chapter 2). Sample 04-13 has a moderate excess  $^{230}\text{Th}$  of 13% and 10-21 has excess  $^{230}\text{Th}$  of 15% and excess  $^{226}\text{Ra}$  of 12%. Sample 33-49 and 80-04 are the two ‘axial’ E-MORBs and again both are fairly

well constrained to be associated with neo-volcanic features. 33-49 is from Joseph Mayes Seamount and was collected near the saddle between the two volcanic peaks (Figure 9). Although 33-49 has only small excess  $^{230}\text{Th}$  of 2.8%, it has a measured excess  $^{226}\text{Ra}$  of 32% constraining it to be < 8 ka. On the other hand, 80-04 has the highest excess  $^{230}\text{Th}$  of 26%.

Five of the six rift valley floor lavas are N-MORB, with ( $^{230}\text{Th}/^{238}\text{U}$ ) ranging from 1.02 to 1.09 ( $\pm 2\%$ ), while the E-MORB (56-88) has an intermediate excess of 4.8%. The remaining two lavas were sampled from the rift valley walls of Narrowgate segment on the oblique supersegment (Figure 9, Inset 2), and are two of the most enriched basalts in the full geochemical suite. Sample 89-02 has a measured ( $^{230}\text{Th}/^{238}\text{U}$ ) of  $0.99 \pm 2\%$ , which is within error of secular equilibrium, indicating that either it erupted with U and Th in equilibrium, or that it is older and any excess it had upon eruption decayed away. We favor the latter, and thus constrain it to be > 300 ka old, which is not surprising since 89-02 lies 5.8 km away from the estimated axial volcanic ridge (which at a half-rate of 7 mm/yr means a predicted crustal age of  $\sim 800$  ka) and just below the crest of the southern rift valley wall,  $\sim 1000$  m shallower than the current volcanic ridge. We are not able however, to determine whether 89-02 was erupted on the rift valley floor and was tectonically emplaced in the rift valley wall, or it erupted from the rift valley wall.

The other rift valley wall dredge, we interpret to have had quite a different recent petrologic history. 61-71 was sampled nearly 2/3 up the 1500 m northern rift valley wall, and is currently just over 9 km removed from the axial volcanic ridge (as seen in Figure 9, Inset 2). This evolved E-MORB has a 4%  $^{238}\text{U}$  excess and at 41%  $^{226}\text{Ra}$  excess, constraining its eruption age to be < 8 ka. Two explanations exist, either this eruption age of < 8 ka is legitimate, thereby 61-71 was erupted in place via tectonically controlled volcanism, or the U-Th and Th-Ra disequilibria was produced by secondary elemental fractionation during alteration. Considering the complex tectonic environment, observations made above that young volcanism is occurring throughout this ultraslow-spreading rift valley, and documented examples of similarly young off-axis lavas on faster-spreading [Sims et al., 2003; Sturm et al., 2000; Zou et al., 2002], we favor the former option, that 61-71 was erupted in situ and the  $^{226}\text{Ra}$  excess indicates an age < 8 ka.

#### ***U-Th & Th-Ra model ages?***

It is possible using this same decay relationship, to calculate U-Th and Th-Ra model ages for lavas away from the axis of rifting [Goldstein et al., 1991; Goldstein et al., 1993, 1994; Rubin and MacDougall, 1990], by assuming 'off-axis' lavas had initial activity ratios similar to measured activities in 'axial' lavas. As discussed in detail by Sims et al., [2003], two criteria must be satisfied for this method to be valid; 1) that both axial and off-axis lavas have homogeneous Sr, Nd, Hf, and Pb isotopic compositions, in other words they were generated from the same time-averaged source, and 2) that they were produced by the same petrogenetic melting regimes or styles of melting (i.e. similar extents of melting, pressures of melting, extents of melt/rock interaction, crustal processing, and melt transport and storage times). Unlike the isotopically homogeneous 9°-10°N section of the EPR [Sims et al., 2002], the time-averaged Rb/Sr, Sm/Nd, Lu/Hf,



and U/Th ratios of the 12 basalts in this study, are highly variable along-axis and between N-MORB and E-MORB, as illustrated by Sr, Nd, Hf, Pb, and He isotopic compositions [Standish et al., 2004] and the extremely large range of  $^{230}\text{Th}/^{232}\text{Th}$  and  $^{238}\text{U}/^{232}\text{Th}$  observed in Figure 7. Because of the isotopic heterogeneity we are unable to say that lavas erupted along the ridge (or even throughout the rift valley) were generated from the same source or process, thus assumptions about initial excess  $^{230}\text{Th}$  would have significant uncertainty. As a result, we resort to using U-series to establish age limits only.

The Southwest Indian Ridge has a half spreading rate of 7 mm/yr and assuming lavas erupt from the rift axis and spread symmetrically, the age of the ocean crust is known at any distance off-axis. With the age of the ocean crust as a function of “distance from the axis of rifting”, Figure 8b compares this age curve (actually a v-shaped line about the axis) to the limits on eruption age interpreted from the U-Th and Th-Ra disequilibrium. Since the presence of U-Th disequilibrium provides an upper age limit of ~300,000 years, and the absence of disequilibrium a lower limit of the same age, all the lavas are plotted on the 300 Ka isochron, unless Th-Ra disequilibrium data has been measured. Those basalts with measured U-Th disequilibrium have eruption ages younger than 300,000 years old, and thus have dotted arrows extending downward from 300,000 indicating a younger age. Sample 89-02 is the only basalt with U and Th measured to be in equilibrium, and thus it has a dotted arrow pointing upward indicating that it is older than 300,000 years (and younger than the age of the ocean crust). Three basalts have excess  $^{226}\text{Ra}$  indicating eruption ages 8,000 years or less, which because of the scale for Figure 8b, is indistinguishable from zero age (x-axis). So, with the exception of basalt 89-02 the other 11 lavas possess eruption ages anomalously young relative to the predicted age of the ocean crust they sit. This demonstrates that younger than expected lavas are distributed and erupting throughout the rift valley and into the rift valley walls, suggesting highly variable spatial and temporal volcanism and crustal accretion.

### ***Mechanisms for ‘off-axis’ volcanism***

Similar to observations on the EPR between 9°-10°N, the lavas erupted along the Southwest Indian Ridge from 9°-25°E exhibit significant temporal and spatial variability that cannot be explained by eruption at the axis of rifting and subsequent movement off-axis due to plate spreading. Therefore, the eruption of anomalously young lavas, at varying distances from the rift-axis, both on the EPR and here on the Southwest Indian Ridge (Table 5), requires explanation. Below we discuss and evaluate three different potential mechanisms for off-axis volcanism at fast- and ultraslow-spreading ridges; 1) shallow crustal magma bodies, 2) lateral surficial and/or shallow sub-surface flow, and 3) locally heterogeneous off-axis mantle source material.

#### ***1) Shallow subsurface magma bodies***

The occurrence of young, ‘off-axis’ eruptions on the fast-spreading East Pacific Rise, as documented by U-series disequilibria, spatial and temporal geochemical variability, and various geologic features, has been explained by a number of crustal accretion processes. Anomalously young near-axis volcanism (< 4 km from axis), as constrained



by U-series disequilibrium [Goldstein et al., 1993, 1994; Sims et al., 2003], and consistent with temporal and spatial variability observed in axial and off-axis lavas along the 9°-10°N section of the EPR, was originally attributed to the presence of spatially restricted small magma bodies feeding eruptions outside the width of the axial-summit caldera (ASC) [Perfit et al., 1994]. On the Southwest Indian Ridge we lack seismic data to confirm or deny the presence of subsurface magma bodies. In lieu of seismic measurements, estimated crustal thickness measurements for the amagmatic accretionary segments [Dick et al., 2003; Chapter 2] and seismic crustal thickness measurements along the ultraslow-spreading Gakkel Ridge [Jokat et al., 2003] both support theoretical studies suggesting diminished melt production on ridges spreading at rates < 20 mm/yr [Bown and White, 1994; White et al., 2001], which means significantly thinned crust, too thin to effectively host magma bodies. In addition, the thermal effects of slower upwelling rates have been modeled showing greater conductive cooling of the lithosphere [Barry, 2005], which would also tend to prohibit establishment of crustal magma bodies. This intuitively implies that the existence of laterally continuous or even isolated steady-state magma bodies beneath segments with thickened lithosphere is unlikely, especially at shallow depths. This is contrary to Joseph Mayes Seamount or the Narrowgate segment, where thicker than normal crust combined with melt focusing inhibits conductive cooling and may create favorable conditions for a crustal magma chamber. However, this does not explain the variable off-axis compositions that span the entire study area.

## 2) *Surficial and shallow subsurface lava flow*

More recent studies of the (9°-10°N) EPR area have measured U-series disequilibrium in lavas up to 4 km [Sims et al., 2003] and between 5 -20 km [Zou et al., 2002] from the ASC, further confirming that young volcanism is not restricted to the ASC and its associated volcanic crestal plateau. In *Sims et al., [2003]*, detailed side scan imagery, observational data, and precise sample locations collected by DSRV Alvin depict numerous large volume lobate and sheet flows from the ASC eruptive vents, supplying young lavas at least 1 km off-axis and possibly as far as 2 km off-axis [Sims et al., 2003], consistent with the observed 1991 BBQ flow [Gregg et al., 1996; Haymon et al., 1993]. While this may adequately explain near-axis volcanism, surficial transport of ASC erupted lavas cannot realistically account for young lavas up to 20 km off-axis. Alternatively, *Zou et al., [2002]* attribute the occurrence of these eruptions to either, lateral subsurface transport of magma via sill propagation [Fialko, 2001], hence tapping the same axial system responsible for ASC eruptions, or independent off-axis magma systems, possibly tapping a metasomatised spinel peridotite source (containing Ca-clinopyroxene and amphibole) to account for the enriched signature of these off-axis lavas relative to the N-MORB axial lavas.

Within this study area, abnormally young lavas are found throughout the rift valley at distances from the estimated rift axis ranging from < 4 km, or “near-axis” in terms of a fast-spreading ridge ASC, up to 12 km. Unlike the fast-spreading EPR, the ultraslow-spreading Southwest Indian Ridge is characterized by a morphologically and tectonically complex rift valley. Whereas lavas erupt from the summit of the EPR axial summit trough and flow off-axis across the crestal plateau, the roughness and undulatory

topography of ultraslow-spreading rift valley floor makes it unlikely that surficial or near-surface flows would travel very far. A 3D bathymetric image of a portion of the oblique supersegment (Figure 9) well illustrates the extreme roughness of the rift valley floor (especially semi-normal to the rift valley), reinforcing that lateral transport of erupting axial lavas throughout the rift valley is not likely. The rift valley floor of both the orthogonal supersegment and oblique supersegment reflects significant tectonic activity, creating difficulty discerning a morphologic volcanic ridge or lineation. The exceptions are Joseph Mayes Seamount and the Narrowgate segment. The volcanic segments at Narrowgate and for the most part on the orthogonal supersegment have defined axial volcanic ridges, but chaotic topography would likely prohibit surficial or shallow subsurface flow of lava farther than a couple kilometers. The potential for subsurface transport of lava off-axis via sill emplacement is likely limited by faulting. Furthermore, the documentation of thinned crust associated with the ultraslow-spreading Gakkel Ridge [Jokat et al., 2003] in conjunction with estimated crustal thickness measurements along the oblique supersegment (Chapter 2) make it hard to envision sill emplacement in an environment of reduced melt production. This is certainly different from Joseph Mayes Seamount, which sits directly on the ridge and erupts lavas from its peaks, thus making it possible that flows could extend significant distances (~10 km) down the seamount's basal slopes.

Although highly tectonized and faulted rift valley floors and walls are not generally conducive to shallow subsurface or surficial lateral flow of lava, they may act as possible pathways for vertically migrating magmas. As previously mentioned, sample 61-71 has a 41%  $^{226}\text{Ra}$  excess, and was dredged from high up the rift valley wall (1000 m above the rift valley floor) and 9.5 km from the Narrowgate segment linear volcanic ridge (as shown in Figure 9, Inset 2). The detailed bathymetry and the cross-axis morphology of the Narrowgate segment, particularly the steep, faulted rift valley bounding walls, which, at their base are only ~10 km apart, distinguish it from other portions of the amagmatic segments or orthogonal supersegment. Pervasive tectonic fabric normal to the spreading direction is visible within the rift valley and rift mountains, indicating strong localized tectonic activity and the importance of tectonics during crustal accretion. Assuming igneous processes caused the excess  $^{238}\text{U}$  and  $^{226}\text{Ra}$ , the position of sample 61-71 can be explained two ways. Either the lava was erupted on the rift valley floor and emplaced 1000 meters up the rift valley wall by tectonic forces, or it was erupted near its current location. In order for the prior explanation to be valid, faulting would have to move this lava over 1000 vertical feet in less than 8 ka - highly unrealistic. Therefore, the fact that sample 61-71 must have erupted in the vicinity of its current location, provides strong evidence that young lavas are erupting on and within the rift valley walls. By inference this suggests that volcanism associated with the rift valley walls, and throughout the rift valley, is largely controlled by faulting, and thus the depths to which these faults penetrate the lithosphere is of critical importance.

### 3) *Discrete enriched off-axis source*

Similar to the E-MORB compositions of the young off-axis EPR lavas [Zou et al., 2002], the young off-axis lavas from the study area have enriched LREE and isotopic

compositions and occasionally depleted N-MORB compositions. Interestingly, the majority of these E-MORB compositions both axial and off-axis have low  $^{230}\text{Th}$  excesses or even  $^{238}\text{U}$  excesses, much like the way off-axis E-MORBs from 9°-10°N EPR. However, rather than resulting from an independent off-axis enriched mantle source [Zou et al., 2002], the enriched signature in axial and off-axis basalts on the Southwest Indian Ridge is generated from a continuous two-lithology mantle source that varies along-axis but not across-axis in the proportion of vein component. The occurrence of such disparate compositions in close proximity, both along the ridge and normal to the axis of rifting is a function of the melting style and not the mantle source *per se* (Chapter 3), as the thermal regime beneath each segment is highly variable both along- and across-axis.

In order for these young lavas to erupt away from the axis of rifting, there must be a physical mechanism that allows mantle melts to penetrate the lithosphere at presumably cooler and thicker locations relative to the rift axis. The thickening of lithosphere away from the center of the rift valley is reflected by a sloping thermal boundary layer, often designated to be 1100°C isotherm, and has been suggested to act as a permeability barrier, focusing melt towards the axis of rifting [Sparks and Parmentier, 1991]. Observations that eruptions are occurring at varying distances off-axis imply that not all the lava is efficiently focused toward the ridge axis. How though, if the lithosphere is thickening off-axis, do melts find their way across the permeability layer and thru the conductively cooled lithosphere, eventually erupting on the seafloor? We do not have an answer to this question, yet, considering the diminished melt generation and thus the dominance of tectonic accretion, it would not be surprising if off-axis eruptions were controlled near the lithospheric boundary layer by a “leaky lithosphere” model [Sohn and Sims, 2005].

While *Sohn and Sims* [2005] recently published model is specific to fast-spreading ridges, the general idea that tensile stresses in bending lithosphere may enable seepage of melt through the permeability boundary via hydrofracture could be applicable to a tectonically active ultraslow-spreading environment. Hydrofracture was previously proposed as a mechanism for melt transport to the surface at mid-ocean ridges [Nicolas, 1986; Sleep, 1988], although *Kelemen et al.*, [1997] suggested that if hydrofractures exist they are transient features. Additionally, with little constraint on the depth to which faults at ultraslow-spreading ridges penetrate, rift valley bounding faults may penetrate deep enough into the lithosphere to act as conduits for magma. Clearly, further theoretical and modeling work is needed to more closely address ultraslow-spreading accretionary tectonics and specifically the mechanisms for off-axis eruptions.

## 5.2. Effects of melting processes on U-series disequilibria

In addition to eruption age constraints, U-series disequilibria measurements provide significant insight into melt generation and transport processes, by indicating the extent of U-Th-Ra fractionation as a function of the modal mineralogy of the source. One of the key advantages of U-series disequilibrium measurements over other compositional tracers, is the *a priori* knowledge that all source materials, enriched or depleted, begin melting in secular equilibrium, and thus disequilibrium measurements reflect

fractionation during melting or transport, and not initial source differences. Having said that, the fractionation of U from Th and Th from Ra, and thus the generation of disequilibrium during mantle melting and transport of magma are dominantly controlled by mineral/melt partitioning within two phases - garnet and clinopyroxene. Therefore, the modal mineralogy of the source is important, specifically the proportion of clinopyroxene versus garnet. Partition coefficients determined experimentally generally agree that U is preferentially incorporated into garnet over Th [Beattie, 1993b; LaTourrette et al., 1993], and Th is preferred over U in clinopyroxene [Beattie, 1993a], except in the case of aluminous pyroxene, which at high pressures is documented to have  $D_{\text{U}}^{\text{solid/melt}}/D_{\text{Th}}^{\text{solid/melt}} > 1$  [Wood et al., 1999]. Since most MORB measured have  $(^{230}\text{Th}/^{238}\text{U}) > 1$ , it is believed that U-Th fractionation occurs during mantle melting involving residual garnet [Landwehr et al., 2001] or possibly high-pressure (> 1.5 GPa) aluminous pyroxene [Beattie, 1993a; Landwehr et al., 2001; LaTourrette and Burnett, 1992; Wood et al., 1999].

Additional chemical information including, Lu/Hf isotopic systematics in MORB [Salters, 1994; Salters and Hart, 1989], HREE depletion and general REE systematics in MORB [Beattie, 1993b; Bender et al., 1984; Frey et al., 1993; Kay and Gast, 1973], and LREE depletion of abyssal peridotite clinopyroxene grains [Johnson et al., 1990], suggest a garnet-bearing source for MORB generation. As a result of these and other constraints, two end-member models for the generation and transport of melt beneath mid-ocean ridges have been proposed. The first, “dynamic melting”, creates U-Th-Ra disequilibrium at the base of the melting column through near fractional melting, and in order to maintain the short-lived  $^{226}\text{Ra}$  excess, moves the melt rapidly to the surface in high-porosity conduits or channels, keeping it chemically isolated and disallowing re-equilibration with the surrounding mantle [Langmuir, 1977; McKenzie, 1984, 1985; Williams and Gill, 1989]. Thus, the presence of Th-Ra disequilibria in MORB, and the presumption that it was produced near the garnet peridotite solidus (> 80 km), requires rapid melt ascent, and places a strong constraint on magma transport times. The second model, “porous reactive flow” or “equilibrium flow”, considers melting and melt transport a reactive process between liquid and solid host material, where equilibrium is maintained and chromatographic exchange fractionates parent from daughter [Navon and Stolper, 1987; Spiegelman and Elliot, 1993] during melt migration. The main difference from dynamic melting being, that due to continued chromatographic exchange during transport (i.e. polybaric) and  $D_{\text{Ra}} < D_{\text{Th}}$  for both garnet and spinel lherzolite [Beattie, 1993a, 1993b; Blundy and Wood, 1994; Cooper et al., 2000; Sims et al., 1999],  $^{226}\text{Ra}$  excesses are not required to be produced near the solidus. Even though the transport time is much slower during reactive porous flow, excess  $^{226}\text{Ra}$  is produced and maintained to shallow levels, thereby dismissing the previous constraint of rapid melt transport. Yet, reactive porous flow cannot be the only mechanism generating U-series disequilibrium, as U-Th partitioning constrain excess  $^{230}\text{Th}$  to deep melt extraction in the presence of garnet [Landwehr et al., 2001] and not shallow re-equilibration.



### *U-Th systematics versus long-term source enrichment*

Over the past 5 years there has been a substantial increase in the size of the global MORB U-series database, however, very few of these MORB studies contain a full complement of major element, trace element, and most importantly long-lived radiogenic isotope data. The absence of independent tracers and determinants of source enrichment and melting process parameters limits geochemical interpretation. This suite of 12 glasses from the Southwest Indian Ridge is one of two MORB suites, along with 20 basalts from the EPR (9°-10°N)[Sims et al., 2003; Sims et al., 2002], for which  $^{238}\text{U}$ - $^{230}\text{Th}$ - $^{226}\text{Ra}$  disequilibria; Sr, Nd, Pb, and Hf isotopes; and major and trace element data have been collected on the same samples. Similar to the EPR suite, the advantage of having a full quiver of geochemical tools, is the ability to place independent constraints on source heterogeneity, as related to U-series disequilibrium. Sims et al., [2002] showed convincingly, that U-Th-Ra disequilibria and U-series systematics were not a function of source composition, but rather melting style and melt transport “processes”. In the rest of this section we will explore the relationships between the U-series systematics and independent geochemical indicators of source enrichment, in order to evaluate the importance of source composition on generation of disequilibrium.

Unlike the relatively homogeneous isotopic compositions of the EPR (9°-10°N) basalts, Southwest Indian Ridge glasses have incompatible trace element ratios and Sr, Nd, Pb, Hf, and He isotopic compositions that are quite variable, indicating systematic source enrichment along-axis (Chapter 3). Major element and geodynamic constraints together with trace element modeling and isotopic compositions illustrate that the chemical heterogeneity observed within the study area cannot be explained by melting of a single lithology depleted peridotite. Even though major element compositions largely reflect a signature of peridotite melting, elevated  $\text{K}_2\text{O}$  in the Narrowgate segment lavas requires a second source lithology capable of generating K-rich melts. Eclogite is proposed as the enriched lithology and although few constraints exist within the major element chemistry, trace element ratios and melt modeling provide significant evidence for mixing of enriched melts of an eclogite lithology with depleted melts from a spinel harzburgite (Chapter 3). Ridge characteristics such as volcanic segmentation, estimated crustal and lithospheric thickness, and upwelling rate correlate well with major element, trace element, and isotopic indicators of enrichment, suggesting that the range in MORB chemistry is influenced by not only source variation, but also “process” related parameters (i.e. degree melting, source volume, melt focusing). These parameters appear to have a more significant effect on the basalt chemistry along portions of the ridge where spreading geometry results in sharp variations in upwelling rate. This is summarized in Chapter 2 where we present a tectonomagmatic melting model to explain the range from N-MORB to E-MORB that consistently accounts for the correlations between chemistry and tectonics/geophysics.

The foundation of the model is the MORB source. The favored source is a depleted spinel harzburgite impregnated with an enriched eclogitic lithology – estimated to be present as ~5% veins by mass. Radiogenic isotope compositions indicate along-axis source heterogeneity and various incompatible element ratios (i.e.  $(\text{La}/\text{Sm})_n$ ,  $\text{Sm}/\text{Yb}$  – not



shown) suggest that the heterogeneity is a result of varying proportions of enriched versus depleted melts. Indeed, the variation in lithology (i.e. garnet/cpx ratio), volatile content, or fertility/productivity of the mixed source composition may largely affect the bulk partitioning behavior of U versus Th, and thus potentially the U-Th systematics of the melts [Prinzhofer et al., 1989; Williams and Gill, 1989]. Based on the previously proposed model, the following sections will assess the consistency of the model in terms of the measured U-series disequilibrium. Unlike many previous studies of MORB U-series disequilibrium that were limited to interpreting only U-series data, the full complement of long-lived isotopic and major and trace element data provide additional constraints on the source lithology and melting process.

### ***N-MORB versus E-MORB***

Considering the strong correlations among trace element ratios, it is not surprising that ( $^{238}\text{U}/^{232}\text{Th}$ ) for both N-MORB and E-MORB correlates nicely with  $^{87}\text{Sr}/^{86}\text{Sr}$  (Figure 11a&b), showing a negative trend from low Th/U and unradiogenic  $^{87}\text{Sr}/^{86}\text{Sr}$  to high Th/U and radiogenic  $^{87}\text{Sr}/^{86}\text{Sr}$ . A similar negative correlation exists for ( $^{230}\text{Th}/^{232}\text{Th}$ ) versus  $^{87}\text{Sr}/^{86}\text{Sr}$ , and based on strong positive correlations between  $^{87}\text{Sr}/^{86}\text{Sr}$  and ( $\text{La}/\text{Sm}$ )<sub>n</sub> (Figure 10) or K/Ti, similar negative trends also exist between ( $^{238}\text{U}/^{232}\text{Th}$ ) and ( $^{230}\text{Th}/^{232}\text{Th}$ ) versus K/Ti or ( $\text{La}/\text{Sm}$ )<sub>n</sub> (not shown). These trends in separate MORB suites have previously been interpreted to suggest binary mixing of enriched and depleted mantle melts [Bourdon et al., 1996b; Lundstrom et al., 2000; Lundstrom et al., 1999]. *Sims and Hart* [2005] illustrate that a linear trend requires the Th/Sr of the enriched and depleted sources to be the same. On the other hand, curvature in the trend (i.e. hyperbolic trend) is interpreted to indicate variable Th/Sr ratios for the two end-members. The main portion of each trend (Figure 11) is linear, suggesting that both the depleted peridotite and enriched vein lithology have similar Th/Sr ratios. However, well off the trend at elevated ( $^{238}\text{U}/^{232}\text{Th}$ ) and ( $^{230}\text{Th}/^{232}\text{Th}$ ) for a given  $^{87}\text{Sr}/^{86}\text{Sr}$  sits sample 25-03, ensuring that the trend curves steeply up at unradiogenic  $^{87}\text{Sr}/^{86}\text{Sr}$ . In general these correlations imply that ( $^{238}\text{U}/^{232}\text{Th}$ ) and ( $^{230}\text{Th}/^{232}\text{Th}$ ) are coupled with trace element ratios and isotopic compositions, and thus intuition might then suggest that disequilibrium measurements would reflect similar, predictable behavior between N-MORB and E-MORB.

However, ( $^{230}\text{Th}/^{238}\text{U}$ ) versus  $^{87}\text{Sr}/^{86}\text{Sr}$  (or K/Ti, ( $\text{La}/\text{Sm}$ )<sub>n</sub>) does not illustrate these types of trends or even a defined correlation, as would be predicted by mixing of enriched and depleted melts [Lundstrom et al., 2000]. The enriched lavas exhibit a huge range in ( $^{230}\text{Th}/^{238}\text{U}$ ), but generally have decreasing excess  $^{230}\text{Th}$  as  $^{87}\text{Sr}/^{86}\text{Sr}$  increases, with one sample having excess  $^{238}\text{U}$  (Figure 11c). Sample 80-04 does exhibit excess  $^{230}\text{Th}$ , consistent with binary mixing of DMM and eclogite melts, with the eclogite veins controlling the excess  $^{230}\text{Th}$  budget [Bourdon et al., 1996b; Lundstrom et al., 1998b], but the remaining E-MORBs, having more radiogenic  $^{87}\text{Sr}/^{86}\text{Sr}$  do not have excess  $^{230}\text{Th}$  above 5%. An eclogite lithology composed of 20% garnet and 80% clinopyroxene (similar to “G2” from [Pertermann and Hirschmann, 2003a]) is expected to produce larger excesses than partial melting of spinel peridotite, assuming a constant upwelling rate and productivity. Using aluminous vacancy-rich cpx partition coefficients [Pertermann and Hirschmann, 2002] the mafic lithology generates excess  $^{230}\text{Th}$  of 1.22,

while partial melting of spinel peridotite, using cpx partition coefficients of Wood et al., [Wood et al., 1999], produces excess  $^{230}\text{Th}$  of 1.03-1.06. Therefore, E-MORBs with radiogenic isotopic compositions and enriched incompatible trace element ratios produced by mixing significant proportions of enriched eclogite melt with DMM melts, should also have moderate to high ( $^{230}\text{Th}/^{238}\text{U}$ ) disequilibrium. Yet, rather than a positive ( $^{230}\text{Th}/^{238}\text{U}$ ) vs.  $^{87}\text{Sr}/^{86}\text{Sr}$  trend, they display a negative correlation (among the 5 data points). Furthermore, E-MORB samples with elevated  $^{87}\text{Sr}/^{86}\text{Sr}$  showing similar amounts of enrichment have vastly different ( $^{230}\text{Th}/^{238}\text{U}$ ). Rift-axis samples 33-49 from Joseph Mayes Seamount and 80-04 from the western end of the orthogonal supersegment have similar  $^{87}\text{Sr}/^{86}\text{Sr}$  (Figure 11),  $^{143}\text{Nd}/^{144}\text{Nd}$ ,  $^{176}\text{Hf}/^{177}\text{Hf}$ , Pb isotopic compositions and incompatible trace element ratios, yet their primary excess  $^{230}\text{Th}$  (as determined by ( $^{226}\text{Ra}/^{230}\text{Th}$ ) disequilibria for 33-49) is 2.8% and ~ 26%, respectively.

The correlation between isotopic enrichment and ( $^{230}\text{Th}/^{238}\text{U}$ ) is not much better for the N-MORBs. The largest  $^{230}\text{Th}$  excesses do not coincide with the most radiogenic  $^{87}\text{Sr}/^{86}\text{Sr}$  compositions. The lack of correlation between U-Th disequilibrium and long-lived isotopic source heterogeneity within either the N-MORB or E-MORB populations and the dominantly low U-Th disequilibrium measurements for the E-MORB relative to N-MORB are not consistent with binary mixing of enriched and depleted partial melts. Although the Southwest Indian Ridge is thus inconsistent with global and local MORB data, which show ( $^{230}\text{Th}/^{238}\text{U}$ ) positively correlated with K/Ti and Th/U [Bourdon et al., 1996b; Lundstrom et al., 2000; Lundstrom et al., 1999], a study at the regional scale of the EPR also found no correlation between ( $^{230}\text{Th}/^{238}\text{U}$ ) and Sr or Pb isotopes [Sims et al., 2002].

### ***Orthogonal Supersegment versus Oblique Supersegment***

If instead of grouping the lavas by chemistry as N-MORB and E-MORB, which provides an assessment of the source heterogeneity with respect to U-Th disequilibrium, let us widen the view to consider the variation in disequilibrium along-axis. In the earlier chapters numerous correlations were observed between geochemical tracers and geophysical parameters, suggesting that together with the along-axis variation in source composition, “process” related parameters were influencing the final basalt compositions. Therefore comparison of along-axis profiles for trace element ratios, isotopic compositions, and ( $^{230}\text{Th}/^{238}\text{U}$ ) may provide important insight regarding the influence of processes that affect melt composition and elemental fractionation during melting and throughout melt transport within the mantle and crust. What differences exist between the orthogonal and oblique supersegments that may influence the composition of lavas erupted on each, and in particular will these differences affect U-Th disequilibrium measurements?

The systematic enrichment trend observed for trace element and isotope ratios for the orthogonal supersegment is also exhibited by U-Th disequilibrium. Figure 12 plots  $(\text{La}/\text{Sm})_n$ ,  $^{87}\text{Sr}/^{86}\text{Sr}$ , and ( $^{230}\text{Th}/^{238}\text{U}$ ) versus longitude, with the lavas located between 16° and 25°E (with the exception of sample 02-01 at 16°E) showing an increasing east to west trend for all three geochemical parameters. Major element compositions indicate

relatively little variation in extent of partial melting along the orthogonal supersegment, consistent with a constant upwelling rate, similar segmentation style, and little variation in estimated crustal thickness (Chapter 2). With a constant extent of partial melting from similar sized source volumes and an increasing proportion of eclogite veining from east to west, the robust agreement among  $(\text{La}/\text{Sm})_n$ ,  $^{87}\text{Sr}/^{86}\text{Sr}$ , and  $(^{230}\text{Th}/^{238}\text{U})$  is interpreted as indicating that U-Th disequilibrium of the orthogonal supersegment lavas is dominantly and directly a function of source heterogeneity, as exemplified by coupling between U-Th systematics and long-lived isotopic heterogeneity.

Farther to the west, the oblique supersegment lavas (9°-16°E) represent three different tectonomagmatic provinces with variable basalt chemistry. Four of the six oblique supersegment lavas are E-MORB. The Narrowgate segment lavas (~ 14.5°E) have the highest  $(\text{La}/\text{Sm})_n$  and  $^{87}\text{Sr}/^{86}\text{Sr}$  in the suite, the Joseph Mayes Seamount lava (11.5°E) is moderately enriched, and the lava from the amagmatic accretionary segment (~ 13.5°E) lies between the two, with compositions attributed to variable proportions of vein melts. Despite the range in incompatible element and isotopic ratios along-axis, the variation in  $(^{230}\text{Th}/^{238}\text{U})$  mirrors that seen in  $(\text{La}/\text{Sm})_n$  and  $^{87}\text{Sr}/^{86}\text{Sr}$ , but with slightly smaller amplitude.  $^{230}\text{Th}$  excess is inversely correlated with  $(\text{La}/\text{Sm})_n$  and  $^{87}\text{Sr}/^{86}\text{Sr}$ . The Narrowgate lavas with the highest  $(\text{La}/\text{Sm})_n$  and  $^{87}\text{Sr}/^{86}\text{Sr}$  have the lowest  $(^{230}\text{Th}/^{238}\text{U})$ , and the N-MORBs with the lowest  $(\text{La}/\text{Sm})_n$  and  $^{87}\text{Sr}/^{86}\text{Sr}$  have the highest  $(^{230}\text{Th}/^{238}\text{U})$ , again bringing into question the conventional model for U-series generation. How is it that  $(^{230}\text{Th}/^{238}\text{U})$  and long-lived isotopes like  $^{87}\text{Sr}/^{86}\text{Sr}$  can be so strongly correlated on the orthogonal supersegment and inversely correlated on the oblique supersegment?

#### ***“Source” versus “process” during ultraslow-spreading accretionary tectonics***

A fundamental difference exists between the orthogonal supersegment and the oblique supersegment. Even though both supersegments are classified as ultraslow-spreading ridges, the orthogonal supersegment is generated by slow-spreading accretionary tectonics, characterized by active volcanic segments offset by non-transform discontinuities. On the other hand the oblique supersegment is generated by ultraslow-spreading accretionary tectonics, which replaces non-transform offsets with amagmatic accretionary segments (Chapter 2) that reflect the drop in upwelling rate along the ridge. This difference is important because the variable upwelling rate along the oblique supersegment is the underlying explanation for subsequent variations in segmentation, conductive cooling of the lithosphere and thus lithospheric topography, melting column height, melt focusing, and ultimately the relative depletion of the mantle column beneath each segment. This differs from the orthogonal supersegment where the melting process beneath each segment is similar, thus the mantle column of each segment is equally depleted.

One of the basic assumptions inherent in the conventional model of U-series disequilibrium generation is that eclogite partial melts are extracted rapidly from the host without equilibrating with the surrounding peridotite [Kelemen et al., 1995; Takahashi and Nakajima, 2002]. The U-Th disequilibrium from the orthogonal supersegment lavas is consistent with this assumption, as the melts with the largest eclogite influence have

the highest ( $^{230}\text{Th}/^{238}\text{U}$ ),  $(\text{La}/\text{Sm})_n$ , and  $^{87}\text{Sr}/^{86}\text{Sr}$ . This is not the case on the oblique supersegment, where ( $^{230}\text{Th}/^{238}\text{U}$ ) is inversely correlated with  $(\text{La}/\text{Sm})_n$  and  $^{87}\text{Sr}/^{86}\text{Sr}$ , and thus implies that this assumption is not valid for this supersegment. Major element compositions similarly seem to invalidate this assumption. Lavas with the largest trace element and isotope signature of eclogite melting have oxide contents more similar to partial melting of peridotite than eclogite (i.e. MgO and  $\text{Al}_2\text{O}_3$  systematics). This suggests that beneath the Narrowgate segment and Joseph Mayes Seamount, melts containing large proportions of eclogite melt are being focused and then reacting with depleted spinel peridotite compositions, thereby wiping out much of the major element signature of eclogite partial melting.

The fate of eclogite melt when it infiltrates and reacts with the host peridotite is an area of ongoing debate. Because natural eclogite partial melts span a large range in major element composition, it is believed that substantial disequilibrium between melt and host peridotite (i.e. olivine) will result in reaction and subsequent freezing of eclogite melt [Yaxley, 2000; Yaxley and Green, 1998], producing a trace element fertilized peridotite. Re-melting of this fertilized peridotite could generate melts with trace element and isotopic compositions reflecting eclogite contributions, but with lower  $\text{SiO}_2$  and higher MgO indicative of peridotite contributions [Hirschmann et al., 2002; Yaxley and Green, 1998], although this single lithology source is not consistent with other chemical, petrologic, and geologic constraints. Therefore, realizing that the above scenario is an end-member model, we propose that the U-Th disequilibrium measured in the oblique supersegment lavas was generated reflecting ( $^{230}\text{Th}/^{238}\text{U}$ ) governed by source heterogeneity, but was erupted with ( $^{230}\text{Th}/^{238}\text{U}$ ) subsequently altered by variable amounts of eclogite melt interaction and equilibration with depleted spinel harzburgite.

Along with the inverse correlation between ( $^{230}\text{Th}/^{238}\text{U}$ ) and  $(\text{La}/\text{Sm})_n$  and  $^{87}\text{Sr}/^{86}\text{Sr}$  for the oblique supersegment lavas, they also have ( $^{230}\text{Th}/^{238}\text{U}$ ) ranging from 0.96 to  $\sim 1.08$ . In order to generate E-MORB with ( $^{230}\text{Th}/^{238}\text{U}$ ) much lower than predicted by incompatible element ratios and isotopic compositions, requires  $D_m > D_U$ . This sense of fractionation is produced by residual cpx at pressures below 1.5 GPa [Beattie, 1993a; Landwehr et al., 2001; LaTourrette and Burnett, 1992; Wood et al., 1999]. The involvement of cpx could occur in one of two ways, either partial melting of depleted spinel harzburgite at low pressures or partial equilibration of eclogite melt with depleted spinel harzburgite. Either mechanism requires that cpx is present as a residual phase in the depleted peridotite host, as the other phases (olivine, orthopyroxene, spinel) have very low U and Th partition coefficients, and thus will not influence the budget of either element. Elevated incompatible trace element concentrations and ratios in the E-MORBs from both supersegments indicate that eclogite melts largely retained their enriched signatures during migration, which precludes significant equilibration, at least with a cpx-rich peridotite, and provides a qualitative constraint on the amount of cpx within the host peridotite. Enhanced melt focusing leading to increased depletion of the mantle columns beneath the Narrowgate segment and Joseph Mayes Seamount also limits the modal abundance of cpx in the ambient peridotite.



Two lavas on the orthogonal supersegment were measured from the 16°E volcanic segment, which is the westernmost segment. These two lavas are discussed here separately because they display strikingly different  $(\text{La}/\text{Sm})_n$ ,  $^{87}\text{Sr}/^{86}\text{Sr}$ , and excess  $^{230}\text{Th}$  (Figure 12c). Sample 02-01 sits at lower  $(\text{La}/\text{Sm})_n$ ,  $^{87}\text{Sr}/^{86}\text{Sr}$ , and excess  $^{230}\text{Th}$  and thus well off the trend exhibited by the other orthogonal supersegment lavas. In fact 02-01 is more similar to N-MORBs from the oblique supersegment or the eastern end of the orthogonal supersegment. Why is an N-MORB on the western end of the orthogonal supersegment, where other lavas characterize the source to be enriched? In light of the above discussion highlighting the difference between the "source" dominated orthogonal supersegment and the "process" dominated oblique supersegment, the 16°E segment is termed a "transition zone". The segment has characteristics of both the orthogonal and oblique supersegments, for example the upwelling rate is similar to the rest of the orthogonal supersegment, but the source volume on the western side of the segment is much larger than the eastern side (Figure 13) due to the significant difference in segment spacing. It makes intuitive sense then that the basalts erupted on this segment would reflect the chemical traits of both an eclogite influenced melt (80-04) and a depleted peridotite melt (02-01).

### 5.3. Global & local U-Th systematics

#### *Tectonically influenced ridge settings - excess $^{238}\text{U}$ ?*

The global MORB U-series dataset spans a wide range of U-Th disequilibrium, from excess  $^{238}\text{U}$  of ~23% [Tepley et al., 2004] to excess  $^{230}\text{Th}$  as high as 48% [Peate et al., 2001], with a similarly large range for Th-Ra disequilibrium, although very few samples with  $^{226}\text{Ra}$  deficits exist. Within this spread, there seems to be little correlation between the amount of disequilibrium and the trace element or isotopic enrichment signature of the lavas. This is evident from Figure 14, where the global MORB data plotted as  $(^{230}\text{Th}/^{238}\text{U})$  versus K/Ti show the full extent of excess  $^{230}\text{Th}$  over a range of K/Ti enrichment. Even when broken out into N-MORB ( $\text{K}/\text{Ti} < 0.125$ ) and E-MORB ( $\text{K}/\text{Ti} > 0.125$ ), there is only slight evidence of a positive correlation for the former group and less so for the latter. Despite this, there are a couple of interesting global observations that are highlighted by the addition of the SWIR data presented here: 1) there is a strong tendency for lavas with low excess  $^{230}\text{Th}$  or  $^{238}\text{U}$  ( $< 5\%$ ) to be from ridge settings associated with cold mantle temperatures or thermal regimes (inferred from relative volume output comparisons) and possibly tectonically influenced melt generation, and 2) E-MORBs show small excess  $^{230}\text{Th}$  or  $^{238}\text{U}$ , calling into question the idea that enriched mantle lithologies always produce large excess  $^{230}\text{Th}$ .

An interesting observation is the number of MORB with low excess  $^{230}\text{Th}$  or  $^{238}\text{U}$  ( $< 5\%$ ) (Figure 14) that are sampled from fracture zone environments (Garrett FZ, [Tepley et al., 2004]; Siqueros FZ, [Lundstrom et al., 1999; Sims et al., 2002]), erupted off-axis (EPR - 9°-10°N, [Zou et al., 2002]; EPR – Lamont Seamounts, [Lundstrom et al., 1999]; N-MORBs and E-MORBs from this study), or erupted on other slow-spreading ridges (MAR-MARK area, [Sturm et al., 2000]). The common feature that these ridge environments presumably have is a colder thermal regime, especially relative to fast- and



intermediate-spreading ridges, and even most slow-spreading ridges. There don't appear to be any local correlations between excess  $^{238}\text{U}$  and K/Ti either, as the "depleted-MORB" (D-MORB) from the Siqueros Fracture Zone [Lundstrom et al., 1999; Sims et al., 2002] or Garrett Fracture Zone [Tepley et al., 2004] hover around the equiline (Figure 14b), similar to the N-MORBs from the EPR [Zou et al., 2002] and the E-MORBs from this study (Figure 14c). This suggests to us the important role that the thermal regime may play during generation of U-series disequilibrium. It has been demonstrated in Chapters 2 & 3 that the style of melting, as controlled by the source composition and lithospheric thickness, where "source" governs the relative locations of various solidi, and lithospheric thickness largely determines not only the top of the melting column, but also may influence melt focusing at depth. The influence of melting style on U-series disequilibrium is highlighted in Figures 14b and 14c, where a few of the MORB suites have been labeled with information regarding sample setting. A general correlation between distance off-axis and disequilibrium exists for N-MORBs and E-MORBs, where lavas specifically from the EPR (9°-10°N) and SWIR have smaller excess  $^{230}\text{Th}$  or  $^{238}\text{U}$  the farther off-axis they are erupted. This may not be too surprising, considering the potential similarities in melting regime and style between far off-axis fast-spreading ridges and ultraslow-spreading rift valleys.

#### 5.4. Amount of pyroxenite in MORB source

Pyroxenite abundances in alpine massif outcrops and mantle xenoliths have been observed to range between 2-5% [Mukasa et al., 1991; Nixon, 1987; Pearson et al., 1993; Suen and Frey, 1987; Wilshire et al., 1988]. Owing to a dearth of direct observations of mafic lithologies in the asthenosphere, this range is often used as a proxy for the proportion of pyroxenite in the convecting mantle, but it may not be representative of DMM or OIB sources. Pertermann and Hirschmann [Pertermann and Hirschmann, 2003a] present calculations that use the relative positions of the peridotite and pyroxenite solidi together with melt productivities to constrain the percent pyroxenite contained in the mantle source. Using this methodology in Chapter 2 the proportion of pyroxenite in the mantle source is 5%, based on an estimated crustal thickness at the Narrowgate segment of 7 km, and an assumed peridotite solidus depth of 50 km (taken from [Hirschmann, 2000]).

Once the percent pyroxenite in the source is known, Pertermann and Hirschmann [Pertermann and Hirschmann, 2003a] then use a set of mass balance equations to constrain the U content of the source peridotite, and determine how much of the U originated in the peridotite versus pyroxenite source lithology. However, from trace element modeling conducted in Chapter 3, it was determined that orthogonal supersegment N-MORB could be generated from 6-8% near-fractional partial melting of "DMM", a depleted peridotite composition derived by Workman & Hart [Workman and Hart, 2005]. The uranium concentration of "DMM", itself constrained by U-series measurements on global MORB, is 0.0032 ppm. Therefore, knowing the U content in the source peridotite, an independent estimate of the pyroxenite percentage in the source is available. Assuming generation of 7 km of ocean crust (e.g. Narrowgate segment) with

an average U content of 0.08 ppm (depleted MORB [Jochum et al., 1983]), from a mantle source containing a variable amount of pyroxenite with a U concentration of 0.136 ppm (proposed concentration for “SOC” from [Hirschmann and Stolper, 1996]), the amount of pyroxenite in the source is constrained to be ~2.5%. If the crust is assigned a U content of 0.11 ppm (MORB with > 8 wt% MgO; PETDB, <http://petdb.ldeo.columbia.edu/petdb/>), and the pyroxenite has a lower U concentration of 0.08 (proposed concentration for “AVG” from [Hirschmann and Stolper, 1996]), then the U abundance of the peridotite constrains the percent pyroxenite to be ~7.5%. These two mass balance scenarios also allow the percent of U in the aggregated crust supplied by the pyroxenite to be constrained. A mantle source that contains 2.5% pyroxenite will produce 30-70% of the U supplied to the aggregate crust, whereas a source with 7.5% pyroxenite will contribute 80-100%. While it is not likely that the pyroxenite would contribute 100% of the U, and therefore the amount of pyroxenite is < 7.5%, previous estimates from Chapter 2 suggest 5% pyroxenite in the source, which implies at least half if not more of the U in the crust is generated by the pyroxenite lithology.

## 5.5. Global Observations

With continued growth in size of the MORB U-series database, there have been a couple previous observations that have generally held up and have been able to explain perceived systematics within the global dataset. The first was recognized by Bourdon et al., [Bourdon et al., 1996b] showing a fairly linear negative correlation between ( $^{230}\text{Th}/^{238}\text{U}$ ) and axial depth (Figure 14a), where the excess  $^{230}\text{Th}$  increased as the ridge got shallower. The idea being similar to that discussed for the “global array” correlation between major element indicators of pressure ( $\text{Fe}_8$ ) and extent of melting ( $\text{Na}_8$ ) with axial depth [Klein and Langmuir, 1987]. In both models the shallowing of ridge depth is thought to reflect higher mantle temperatures, causing intersection of the solidus at greater depths, and thus deeper melting. Bourdon et al., [Bourdon et al., 1996b] attempted to distinguish between the proposed thermal effects and the influence of source heterogeneity on disequilibrium, and found it difficult to separate one from the other, concluding both were likely associated.

We plot our data from the Southwest Indian Ridge in Figure 14a and see that for the most part they fall well off the global trend. The oblique supersegment lavas (blue) fall dominantly below the trend at lower ( $^{230}\text{Th}/^{238}\text{U}$ ) for a given axial depth, while some of the orthogonal supersegment lavas have higher ( $^{230}\text{Th}/^{238}\text{U}$ ) than predicted by the global trend. Obviously our data are not consistent with the model inherent in the global trend, suggesting that either 1) locally large thermal variations beneath the SWIR cause melting regimes different than beneath faster spreading ridges, or 2) source heterogeneity, which we observe beneath the SWIR, but the effect of which we do not yet understand, is influencing the disequilibrium.

The other global observation was made by Lundstrom et al., [Lundstrom et al., 1998b], who interpreted trends of ( $^{230}\text{Th}/^{238}\text{U}$ ) from different ridges to be positively correlated with half-spreading rate. Ridge segment averages are plotted in Figure 14b illustrating this trend of decreasing slope of disequilibria with decreasing half spreading rate. The

( $^{230}\text{Th}/^{238}\text{U}$ ) trends on equiline diagrams were thought to represent mixing of enriched and depleted end-member melts, with each end-member melt producing disequilibrium. Thus, the variation in ( $^{230}\text{Th}/^{238}\text{U}$ ) slope was modeled to be a function of end-member mineralogy and upwelling rate [Lundstrom et al., 1998b]. As noted by Lundstrom [Lundstrom, 2003], MORB data added to the database over the last 5 or so years since this observational model was initially suggested, seem consistent with the global trend.

This is not true for our data, which when plotted in Figure 14b lie at much higher disequilibria slopes relative to ridges with similar half spreading rates. The SWIR data plot near “FAZAR” data [Bourdon et al., 1996a] which are explained to be heavily influenced by hotspot melting associated with the Azores, and thus the inherent correlation between upwelling rate and half-spreading rate does not hold up. This may also be important for explaining the position of the SWIR data relative to the global trend, as the unique spreading geometry of our area results in solid upwelling rates that are equal to “effective spreading rates” rather than actual spreading rates. This means upwelling rates are slower than the spreading rates, which should have the opposite affect on the slope of disequilibria. It should be quite interesting to see where soon to be measured disequilibria from Gakkel Ridge basalts plot, as the half spreading rate along this ridge is also ultraslow.

## 6. Conclusions

Our investigation of U-series systematics in 12 glasses from the Southwest Indian Ridge (9°-25°E) is the initial foray into MORB disequilibrium at an ultraslow-spreading ridge. The ultraslow-spreading environment is quite complex tectonically, and difficult to model petrologically. However, the data we present here has provided new insight into the processes involved in lithospheric accretion, particularly at the poorly understood ultraslow-spreading end-member environment. Petrologically, our modeling efforts and subsequent interpretation are in their infancy, yet many basic observations regarding this data have added to the local and global interpretations. With additional Ra data and continued exploration of the relationships between U-series disequilibrium and other geochemical tracers, we are hopeful that more systematic explanations will present themselves. Below we summarize the most important conclusions and observations thus far gleaned from the data in hand:

1. The presence of U-Th and Th-Ra disequilibrium in lavas erupted from the ultraslow-spreading Southwest Indian Ridge between 9°-25°E, illustrates that relatively young lavas are resurfacing much of the rift valley, even along amagmatic accretionary segments that are generally deprived of melt and have large areas of mantle peridotite emplaced at the seafloor.
2. The measurement of U-Th disequilibrium in 10 or 12 basalts places an age limit of < 300 ka on those lavas. When considering the dredge location of each sample, the age limits emplaced by U-Th disequilibrium shows these lavas to be younger than is predicted assuming eruption at the rift-axis with a half-spreading rate of 7 mm/yr. Therefore, U-Th disequilibrium documents anomalously young lavas erupted across the

rift valley floor and upon the rift valley walls. Th-Ra disequilibrium measured in 3 samples lowers the age limits on each to < 8 ka, indicating remarkably young glass within an ultraslow-spreading rift valley. One sample in particular, highlights the tectonic and petrologic complexity present in this dynamic ultraslow-spreading environment. 61-71 was dredged from near the crest of the northern rift valley wall at the Narrowgate segment, where it sits 9.5 km from the rift-axis and > 1000 m above the rift valley floor, and was measured to have excess  $^{238}\text{U}$  of 4% and excess  $^{226}\text{Ra}$  of 41%. This means it is younger than 8 ka and thus must have been erupted via tectonic controls near the top of the rift valley wall.

3. The observation that volcanism on the ultraslow-spreading Southwest Indian Ridge is temporally and spatially variable indicates the possibility that crustal accretion occurs over a broad region, and is not isolated to the axis of rifting. That young, off-axis volcanism is occurring on both fast and ultraslow-spreading ridges suggests, 1) that crustal accretion at any rate occurs farther from the axis of rifting and volcanism than previously recognized and 2) that investigation of viable mechanisms for off-axis volcanism need to be further explored.

4. Measurement of U-Th disequilibrium in 12 glasses from between 9°-25°E on the Southwest Indian Ridge reveals a significant range in ( $^{238}\text{U}/^{232}\text{Th}$ ) and ( $^{230}\text{Th}/^{232}\text{Th}$ ), extending from highly depleted N-MORB compositions to highly enriched, “OIB-like” E-MORB compositions. Both ( $^{238}\text{U}/^{232}\text{Th}$ ) and ( $^{230}\text{Th}/^{232}\text{Th}$ ) are generally correlated with other independent trace element and isotopic indicators of source heterogeneity.

5. ( $^{230}\text{Th}/^{238}\text{U}$ ) activity ratios for the 12 glasses also display a large range, from  $^{230}\text{Th}$  excess of 26% to  $^{238}\text{U}$  excess of 4%. N-MORBs show a range of ( $^{230}\text{Th}/^{238}\text{U}$ ) from 1.02 – 1.15, while E-MORBs range between 0.96 – 1.05, with a single lava at 1.26. The inverse correlation between ( $^{230}\text{Th}/^{238}\text{U}$ ) and  $^{87}\text{Sr}/^{86}\text{Sr}$  and ( $\text{La}/\text{Sm}$ )<sub>n</sub> for the oblique supersegment lavas is attributed to “process”, specifically the shallow equilibration of eclogite melt with cpx bearing depleted spinel peridotite, or even shallow melting of the latter. This contrasts with the orthogonal supersegment lavas, which are dominantly controlled by source heterogeneity, as exhibited by the systematic correlation between ( $^{230}\text{Th}/^{238}\text{U}$ ) and  $^{87}\text{Sr}/^{86}\text{Sr}$  and ( $\text{La}/\text{Sm}$ )<sub>n</sub>.

6. We observe the majority of MORBs with excess  $^{230}\text{Th}$  or  $^{238}\text{U}$  < 5% are sampled from fracture zones, off-axis environments, and ultraslow-spreading ridges. All these areas presumably have thermal regimes much different from fast-spreading or even robust slow-spreading near-axis ridge settings, where melting is suppressed so that crustal thickness decreases. The suppression of melting also enables enriched vein melts to contribute a greater proportion of the total melt volume.

7. The addition of the Southwest Indian Ridge U-series data to the global MORB dataset shows the SWIR does not fall on the global trends for ( $^{230}\text{Th}/^{238}\text{U}$ ) vs. axial depth or slope of disequilibria trend vs. half spreading rate. That our data is not consistent with either

observational model, indicates how different and unique a section of ridge 9°-25°E is, and suggests, as we have already proposed in Chapters 2 & 3, that the upwelling rate and style of melting are critical in determining the basalt chemistry.

## **Acknowledgements**

This study has benefited in many ways and is the result of a team effort from various people. From picking glass to editing this manuscript, none of it came easy. I would like to thank following people in no particular order. Brian Schroeder provided a great deal of help picking and re-picking glass fractions at various stages throughout the study. Thanks need to be extended to Jurek Blusztajn for general moral support and clean lab assistance, and Tracy Abbruzzese for providing a smiling and helpful face in the cleanroom. Fellow JP student, fellow U-series guru, Christian Miller has been a great sounding board in the clean lab. The ICP boys - Dave Schneider (Element) has shown a great deal of patience (especially with Ra measurements) and humor while dealing with tense situations, and Lary Ball (Neptune) who has been so helpful in the teachings of mass spectrometry, both during measurement days and beyond, but more importantly makes a mean espresso! Various visiting scientist in the clean lab have also contributed to procedure modifications and discussion and those that come to mind are Peter Kelley, and Carrie Cooper. Fruitful discussions with Henry Dick during writing have helped shape the manuscript. The authors would also like to thank Paul E. Oberlander in WHOI's Graphic Services for his assistance with Figure 9. Funding for this work was supported by two grants from the National Science Foundation-OCE 0137325 & OCE 9907630.



## Appendix A.

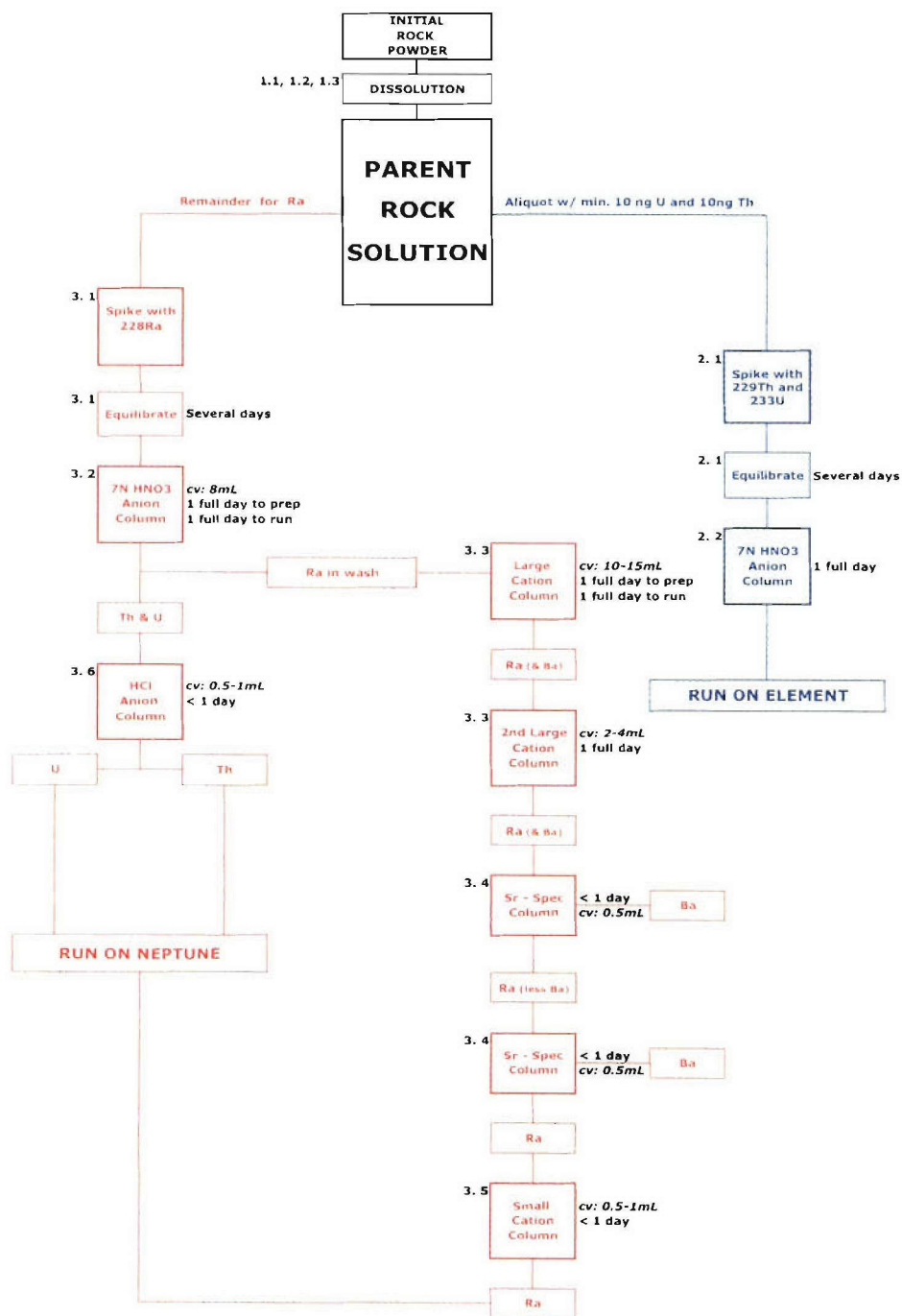


**Figure A1.** Flow chart of sample chemistry and column separation steps for U, Th, and Ra separation prior to analytical measurement via ICPMS. Boxed text indicates each step or procedure and additional text outside boxes refer to subsections in the *WHOI U-Series Cookbook* or length of time to complete each step.

The elemental separation methodology for this study described below varies slightly from the generic flow chart present above in that a separate U-Th fraction was produced just above step 3.1. The remaining U & Th from initial separation for concentration measurement is separated from Ra and taken through the U-Th separation methodology. Although all fractions are from the same parent rock dissolution, it does allow for replicate analysis, as reflected in Table 4 of the manuscript.

#### **A-1: U & Th separation**

##### **a) 1<sup>st</sup> Anion column – removal of major elements**

*Sample preparation:* Take sample aliquot with the equivalent of ~150 ng Th (in 3 M HCl) to dryness. Bring sample into solution in conc. HNO<sub>3</sub> and slowly take to dryness. Add 1 column volume (column volume “cv” is dependent on sample size and in this case is 10 ml) conc. HNO<sub>3</sub> and a few drops of H<sub>2</sub>O<sub>2</sub> and digest for 15 minutes (lid on tight). Dilute with 1 cv DI H<sub>2</sub>O, transfer to centrifuge tubes and spin. Separate solution from any residue left in centrifuge tube and take to dryness. Brought into solution with 2 cv 7 M HNO<sub>3</sub>.

*Column procedure:* Eichrom AG1-X8 (200-400 mesh) anion resin was loaded onto a Kontes™ column and the following steps were used.

	Volume (1 cv = 10 ml)	Reagent
Condition column	2 cv	10 M HCl
Condition column	1 cv	1 M HCl
Condition column	2 cv	DI H <sub>2</sub> O
Condition column	1 cv	10 M HNO <sub>3</sub>
Condition column	1 cv	DI H <sub>2</sub> O
Condition column	4 cv	7 M HNO <sub>3</sub>
Load sample	2 cv	7 M HNO <sub>3</sub>
Wash column	1.5 cv	7 M HNO <sub>3</sub>
<b>Collect Th &amp; U</b>	2 cv	DI H <sub>2</sub> O
<b>Collect Th &amp; U</b>	3 cv	1 M HCl
<b>Collect Th &amp; U</b>	3 cv	1 M HBr

Collected Th & U fractions were then taken to dryness and brought into solution with 1-2 ml conc. HNO<sub>3</sub>.

##### **b) 2<sup>nd</sup> Anion column – Th separation from U**

*Sample preparation:* Take sample aliquot from above to dryness, bring into solution with a few drops conc. HCl, and gently take to dryness again. Dissolve sample in 1 cv

conc. HCl/H<sub>2</sub>O<sub>2</sub> (HCl/H<sub>2</sub>O<sub>2</sub> solution is conc. HCl with 2 drops of H<sub>2</sub>O<sub>2</sub> for every 10 ml of HCl).

*Column procedure:* Eichrom AG1-X8 (100-200 mesh) anion resin was loaded onto an Eichrom™ column and the following steps were used.

	Volume (1 cv = 1 ml)	Reagent
Condition column	3 cv	DI H <sub>2</sub> O
Condition column	4 cv	8 M HCl
Condition column	1 cv	conc. HCl/H <sub>2</sub> O <sub>2</sub>
Load sample	1 cv	conc. HCl/H <sub>2</sub> O <sub>2</sub>
<b>Collect Th fraction</b>	2 cv	8 M HCl/H <sub>2</sub> O <sub>2</sub>
<b>Collect U fraction</b>	2 cv	DI H <sub>2</sub> O
<b>Collect U fraction</b>	3 cv	1 M HBr

U and Th fractions were each taken to dryness and then brought up in 5% HNO<sub>3</sub> for analysis.

#### A-2: Ra separation

##### a) **1<sup>st</sup> Anion column – separation of Ra from Th & U**

*Sample preparation:* Take Ra aliquot (in 3 M HCl) to dryness. Bring into solution in conc. HNO<sub>3</sub> and slowly take to dryness. Add 1 column volume (column volume “cv” is dependent on sample size and in this case is 10 ml) conc. HNO<sub>3</sub> and a few drops of H<sub>2</sub>O<sub>2</sub> and digest for 15 minutes (lid on tight). Dilute with 1 cv DI H<sub>2</sub>O, transfer to centrifuge tube and spin. Separate solution from any residue left in centrifuge tube and take to dryness. Bring into solution with 2 cv 7 M HNO<sub>3</sub>.

*Column procedure:* Eichrom AG1-X8 (100-200 mesh) anion resin was loaded onto a Kontes™ column and the following steps were used.

	Volume (1 cv = 10 ml)	Reagent
Condition column	2 cv	10 M HCl
Condition column	1 cv	1 M HCl
Condition column	2 cv	DI H <sub>2</sub> O
Condition column	1 cv	10 M HNO <sub>3</sub>
Condition column	1 cv	DI H <sub>2</sub> O
Condition column	4 cv	7 M HNO <sub>3</sub>
Load sample/	2 cv	7 M HNO <sub>3</sub>
<b>Collect Ra</b>		
Wash column/	1.5 cv	7 M HNO <sub>3</sub>
<b>Collect Ra</b>		
<b>Collect Th &amp; U</b>	2 cv	DI H <sub>2</sub> O

Collect <b>Th &amp; U</b>	3 cv	1 M HCl
Collect <b>Th &amp; U</b>	3 cv	1 M HBr

Since this column is identical to the 1<sup>st</sup> anion column during Th & U separation, we collected Th and U here to provide duplicate Th & U fractions for measurement. Collected Ra fractions are taken to dryness, brought into solution in conc. HCl, and taken to dryness again. Prior step is repeated to assure conversion to HCl. Once converted, Ra fraction is ready for the major element cation column.

**b) Major element cation column (initial Ba-Ra separation)**

*Sample preparation:* Take sample aliquot from above and bring up in 5 ml 1 M HCl and dry down. Bring sample back up in 1 cv 1 M HCl for loading.

*Column procedure:* Eichrom AG50W-X8 (200-400 mesh) cation resin was loaded onto an Eichrom™ column and the following steps were used.

	Volume (1 cv = 15 ml)	Reagent
Condition column	1 cv	8 M HCl
Condition column	4-6 cv	6 M HCl
Condition column	2 cv	2 M HCl
Condition column	<b>1 ml*</b>	1 M HCl
Load sample	1 cv – (wash beaker with 1 ml of 1 M HCl)	1 M HCl
Wash Column	5 cv	2 M HCl
Wash Column	1.5 cv	2.5 M HCl
Wash Column	1.5 cv	3 M HCl
Wash Column <sup>#</sup>	3 cv	4 M HCl
<b>Collect Ra fraction</b>	4.5 cv	6 M HCl
<b>Collect Ra fraction</b>	2 cv	8 M HCl (only for safety)

\* note volume of conditioning step

<sup>#</sup> this step (4 M HCl) removes ~ 30% of the Ba

Take Ra fraction to dryness.

**c) Sr-spec column – Ra separation from Ba**

*Sample preparation:* Take Ra fraction from above to dryness and bring up in 1 ml conc. HNO<sub>3</sub> and a few drops of H<sub>2</sub>O<sub>2</sub>. Take to dryness and bring into solution in 0.5 cv (0.25 ml) 3 M HNO<sub>3</sub> for loading on column.

*Column procedure:* Fill the bottom of an Eichrom column with 0.2 ml inert Eichrom resin and let settle. Carefully add 0.5 ml Sr-spec resin on top of inert resin (this latter resin volume is equal to cv).

	Volume (1 cv = 0.5 ml)	Reagent
Condition column	2 cv	3 M HNO <sub>3</sub>
Condition column	10 cv	DI H <sub>2</sub> O
Condition column	10 cv	3 M HNO <sub>3</sub>
Load sample	0.5 cv	3 M HNO <sub>3</sub>
Wash Column	1 cv	3 M HNO <sub>3</sub>
<b>Collect Ra fraction</b>	5 cv	3 M HNO <sub>3</sub>

This column separation in theory removes ~ 95% of the Ba in the sample fraction, but since these MORBs are Ba-rich we repeat this column to further purify the Ra fraction. After the 2<sup>nd</sup> Sr-spec column, Ra fractions are taken to dryness.

**d) Final cation clean-up column – removal of ingrown Th from Ra**

*Sample preparation:* Take Ra fraction from above to dryness and bring up in 1 ml conc. HNO<sub>3</sub> and a few drops of H<sub>2</sub>O<sub>2</sub>. Take to dryness and bring into solution in 1 cv 1 M HCl. Repeat previous step and load on column.

*Column procedure:* Fill Eichrom column with 0.5 ml AG50W-X8 (200-400 mesh) cation resin and follow steps below.

	Volume (1 cv = 0.5 ml)	Reagent
Condition column	4-6 cv	6 M HCl
Condition column	2 cv	2 M HCl
Condition column	0.5 cv	1 M HCl
Load sample	1 cv (wash beaker with 0.25 ml 1 M HCl)	1 M HCl
Wash Column	1 cv	2 M HCl
Wash Column	1.5 cv	2.5 M HCl
Wash Column	1.5 cv	3 M HCl
Wash Column	3 cv	4 M HCl
<b>Collect Ra fraction</b>	4.5 cv	6 M HCl

Take Ra fraction to dryness and bring up in conc. HNO<sub>3</sub>. Take to dryness again and bring up in 5% HNO<sub>3</sub> for analysis.



## Appendix B.

Analysis of  $^{232}\text{Th}/^{230}\text{Th}$  on the ThermoFinnigan Neptune used the recently developed techniques of *Ball et al.*, [2002], as they are presented below, and in Table B-1:

A technique is presented for the determination of  $^{232}\text{Th}/^{230}\text{Th}$  in volcanic rocks by plasma ionization multicollector mass spectrometry (PIMMS) utilizing the ThermoFinnigan Neptune. These analyses were made statically, measuring  $^{232}\text{Th}$  on a Faraday cup and  $^{230}\text{Th}$  on the RPQ channel using the SEM. Because of the large dynamic range in the  $^{232}\text{Th}/^{230}\text{Th}$  of volcanic rocks ( $> 10^5$ ), accurate and precise measurement of  $^{232}\text{Th}/^{230}\text{Th}$  using PIMMS requires: 1) high abundance sensitivity to minimize tailing of  $^{232}\text{Th}$  onto  $^{230}\text{Th}$ , and 2) explicit knowledge of the instrumental mass bias and the gain calibration of the two detectors used for the measurement. Using the RPQ on the ThermoFinnigan Neptune, the abundance sensitivity at 95% transmission was  $\sim 25$ ppb over 2 amu, resulting in a tail correction of  $^{232}\text{Th}$  on  $^{230}\text{Th}$  of 0.7% for a ratios of  $3 \times 10^5$  and 0.3% for ratios of  $1.5 \times 10^5$ . To correct for both instrumental mass fractionation between masses 230 and 232 and the relative difference in the efficiency of the Faraday and SEM detectors, Th isotopic measurements were corrected based upon a linear interpolation of the  $^{238}\text{U}/^{236}\text{U}$  measured in the NBS U010 interspersed between each sample, and normalized to its certified value ( $14,535 \pm 149$ ). Over three days of analyses (ca. 10 hrs each), the reproducibility in the measured  $^{238}\text{U}/^{236}\text{U}$  of the NBS U010 ( $n = 40$ ) was 0.6% (2s). Replicate measurements of  $^{232}\text{Th}/^{230}\text{Th}$  in synthetic and rock Th isotopic standards provide an overall reproducibility on the  $^{232}\text{Th}/^{230}\text{Th}$  of 0.1-0.5% ( $2\sigma$ ) and show excellent agreement with their “known” values established by other techniques, supporting the reliability and accuracy of this method. This level of precision indicates that the Th isotopic measurements on the Neptune are being limited by counting statistics on  $^{230}\text{Th}$  rather than system stability. This PIMMS technique has considerable advantages over existing TIMS and SIMS techniques in terms of ionization efficiency and total sample consumption (and hence sample size requirement), as well as the rapidity of analysis.

## References

- Ball, L., K. W. W. Sims, S. Weyer, and J. Schwieters (2002), Measurement of  $^{232}\text{Th}/^{230}\text{Th}$  in volcanic rocks by PIMMS, using the ThermoFinnigan Neptune, *Geochemica Cosmochemica Acta*, 66, A47.
- Barry, J. B., M.D. (2005), Melting and mantle flow beneath oblique ultraslow-spreading ridges, *in prep.*
- Beattie, P. (1993a), The generation of uranium series disequilibria by partial melting of spinel peridotite: constraints from partitioning studies, *Earth and Planetary Science Letters*, 117, 379-391.
- Beattie, P. (1993b), Uranium-thorium disequilibria and partitioning on melting of garnet peridotite, *Nature*, 363, 63-65.
- Bender, J. F., C. H. Langmuir, and G. N. Hanson (1984), Petrogenesis of basalt glasses from the Tamayo Region, East Pacific Rise, *Journal of Petrology*, 25, 213-254.
- Blundy, J. D., and B. J. Wood (1994), Prediction of crystal-melt partition coefficients from elastic moduli, *Nature*, 373, 452-454.
- Bourdon, B., C. Langmuir, and A. Zindler (1996a), Ridge-hotspot interaction along the Mid-Atlantic Ridge between 37°30' and 40°30'N; the U-Th disequilibrium evidence, *Earth & Planetary Science Letters*, 142, 175-189.
- Bourdon, B., A. Zindler, T. Elliott, and C. H. Langmuir (1996b), Constraints on mantle melting at mid-ocean ridges from global  $^{238}\text{U}$ - $^{230}\text{Th}$  disequilibrium, *Nature*, 384, 231-235.
- Bown, J. W., and R. S. White (1994), Variation with spreading rate of oceanic crustal thickness and geochemistry, *Earth and Planetary Science Letters*, 121, 435-439.
- Cannat, M., C. Rommevaux-Jestin, and H. Fujimoto (2003), Melt supply variations to a magma-poor ultra-slow spreading ridge (Southwest Indian Ridge 61° to 69° E), *Geochemistry, Geophysics, Geosystems*, 4, 21.
- Cannat, M., C. Rommevaux-Jestin, D. Sauter, C. Deplus, and V. Mendel (1999), Formation of the axial relief at the very slow spreading Southwest Indian Ridge (49° to 69°E), *Journal of Geophysical Research*, 104, 22,825-822,843.
- Cochran, J. R., G. J. Kurras, M. H. Edwards, and B. J. Coakley (2003), The Gakkel Ridge: Bathymetry, gravity anomalies and crustal accretion at extremely slow spreading rates, *Journal of Geophysical Research*, 108.
- Cooper, K. M., M. R. Reid, M. T. Murrell, and D. Clague (2000), Crystal and magma residence at Kilauea volcano, Hawaii:  $^{230}\text{Th}$ - $^{226}\text{Ra}$  dating of the 1955 east rift eruption, *Earth & Planetary Science Letters*, 184, 703-718.
- DeMets, C., R. G. Gordon, D. F. Argus, and S. Stein (1990), Current plate motions, *Geophys. J. Int.*, 101, 425-478.
- Dick, H., J. Lin, and H. Schouten (2003), An ultraslow-spreading class of ocean ridge, *Nature*, 426, 405-412.
- Fialko, Y. (2001), On the origin of near-axis volcanism and faulting at fast spreading mid-ocean ridges, *Earth & Planetary Science Letters*, 190, 31-39.
- Frey, F. A., D. Stakes, N. Walker, S. R. Hart, and R. Nielsen (1993), Geochemical characteristics of basaltic glasses from the AMAR and FAMOUS axial valleys, Mid-

- Atlantic Ridge (36°-37°N): petrogenetic implications, *Earth and Planetary Science Letters*, **115**, 117-136.
- Gauger, S., T. Kohls, S. Roeber, and J. Snow (2004), Hydrosweep measurements during the expedition ARK XX-2 to Lena Trough and western Gakkel Ridge, *EOS Transactions, AGU*, **85**.
- Goldstein, S. J., M. T. Murrell, and D. R. Janecky (1989), Th and U isotopic systematics of basalts from the Juan de Fuca and Gorda Ridges by mass spectrometry, *Earth & Planetary Science Letters*, **96**, 134-146.
- Goldstein, S. J., M. T. Murrell, D. R. Janecky, J. R. Delaney, and D. A. Clague (1991), Geochronology and petrogenesis of MORB from the Juan de Fuca and Gorda Ridges by  $^{238}\text{U}$ - $^{230}\text{Th}$  disequilibrium, *Earth and Planetary Science Letters*, **107**, 25-41. (Erratum, *Earth Planet. Sci. Lett.*, **109**, 255-272, 1992).
- Goldstein, S. J., M. R. Perfit, R. Batiza, D. J. Fornari, and M. T. Murrell (1993), Temporal variations in East Pacific Rise volcanism based on uranium-series dating of basalts, *Manuscript submitted to Nature*, **5/93**, 1-19.
- Goldstein, S. J., M. R. Perfit, R. Batiza, D. J. Fornari, and M. T. Murrell (1994), Off-axis volcanism at the East Pacific Rise detected by uranium-series dating of basalts, *Nature*, **367**, 157-159.
- Gregg, T. K. P., D. J. Fornari, M. R. Perfit, R. M. Haymon, and J. H. Fink (1996), Rapid emplacement of a mid-ocean ridge lava flow on the East Pacific Rise at 9° 46'-51'N, *Earth and Planetary Science Letters*, **144**, E1-E7.
- Grindlay, N. R., J. A. Madsen, C. Rommevaux-Jestin, and J. Sclater (1998), A different pattern of ridge segmentation and mantle Bouguer gravity anomalies along the ultra-slow spreading Southwest Indian Ridge (15°30'E to 25°E), *Earth and Planetary Science Letters*, **161**, 243-253.
- Hamelin, B., and C. J. Allègre (1985), Large-scale regional units in the depleted upper mantle revealed by an isotope study of the South-West Indian Ridge, *Nature*, **315**, 196-199.
- Haymon, R. M., D. J. Fornari, K. L. Von Damm, M. D. Lilley, M. R. Perfit, J. M. Edmond, W. C. Shanks, III, R. A. Lutz, J. M. Grebmeier, S. Carbotte, D. Wright, E. McLaughlin, M. Smith, N. Beedle, and E. Olson (1993), Volcanic eruption of the mid-ocean ridge along the East Pacific Rise crest at 9°45-52'N: Direct submersible observations of seafloor phenomena associated with an eruption event in April, 1991, *Earth and Planetary Science Letters*, **119**, 85-101.
- Hirschmann, M. M. (2000), Mantle solidus: Experimental constraints and the effects of peridotite composition, *Geochemistry, Geophysics, Geosystems*, **1**.
- Hirschmann, M. M., T. Kogiso, M. B. Baker, and E. M. Stolper (2002), Alkalic magmas generated by partial melting of garnet pyroxenite, *Geology*, *in submission*.
- Hirschmann, M. M., and E. M. Stolper (1996), A possible role for garnet pyroxenite in the origin of the "garnet signature" in MORB, *Contributions to Mineralogy and Petrology*, **124**, 185-208.
- Janney, P. E., A. P. le Roex, and R. W. Carlson (2005), Hafnium isotope and trace element constraints on the nature of mantle heterogeneity beneath the central Southwest Indian Ridge (13° E to 47° E), *Submitted to Journal of Petrology*.

- Jochum, K. P., A. W. Hofmann, E. Ito, H. M. Seufert, and W. M. White (1983), K, U, and Th in mid-ocean ridge basalt glasses and heat production, K/U and K/Rb in the mantle, *Nature*, 306, 431-436.
- Johnson, K. T. M., H. J. B. Dick, and N. Shimizu (1990), Melting in the oceanic upper mantle: An ion microprobe study of diopsides in abyssal peridotites, *Journal of Geophysical Research*, 95, 2661-2678.
- Jokat, W., O. Ritzmann, M. C. Schmidt-Aursch, S. Drachev, S. Gauger, and J. E. Snow (2003), Geophysical evidence for reduced melt production on the Arctic ultraslow Gakkel mid-ocean ridge, *Nature*, 423, 962-965.
- Kay, R. W., and P. W. Gast (1973), The rare earth content and origin of alkali-rich basalts, *Journal of Geology*, 81, 653-682.
- Kelemen, P., G. Hirth, N. Shimizu, M. Spiegelman, and H. Dick (1997), A review of melt migration processes in the adiabatically upwelling mantle beneath oceanic spreading ridges, *Phil. Trans. R. Soc. Lond.*, 355, 283-318.
- Kelemen, P. B., N. Shimizu, and V. J. M. Salters (1995), Extraction of mid-ocean-ridge basalt from the upwelling mantle by focused flow of melt in dunite channels, *Nature*, 375, 747-753.
- Klein, E. M., and C. H. Langmuir (1987), Global correlations of ocean ridge basalt chemistry with axial depth and crustal thickness, *Journal of Geophysical Research*, 92, 8089-8115.
- Ku, T.-L., K. G. Knauss, and G. G. Mathieu (1977), Uranium in open ocean: Concentration and isotopic composition, *Deep-Sea Research*, 24, 1005-1017.
- Landwehr, D., J. D. Blundy, E. M. Chamorro-Perez, E. Hill, and B. Woods (2001), U-series disequilibria generated by partial melting of spinel lherzolite, *Earth & Planetary Science Letters*, 188, 329-348.
- Langmuir, C. H. (1977), Modeling Dynamic Melting.
- LaTourrette, T. Z., and D. S. Burnett (1992), Experimental determination of U and Th during partitioning between clinopyroxene and natural and synthetic basalt liquid, *Earth & Planetary Science Letters*, 110, 227-244.
- LaTourrette, T. Z., A. K. Kennedy, and G. J. Wasserburg (1993), U-Th fractionation by garnet - Evidence for a deep source and rapid rise by oceanic basalts, *Science*, 261, 739-742.
- Layne, G., and K. W. W. Sims (2000), Secondary ion mass spectrometry for the measurement of  $^{232}\text{Th}/^{230}\text{Th}$  in volcanic rocks, *International Journal of Mass Spectrometry*, 203, 187-198.
- le Roex, A. P., H. J. B. Dick, A. J. Erlank, A. M. Reid, F. A. Frey, and S. R. Hart (1983), Geochemistry, mineralogy and petrogenesis of lavas erupted along the Southwest Indian Ridge between the Bouvet Triple Junction and 11 degrees east, *Journal of Petrology*, 24, 267-318.
- le Roex, A. P., H. J. B. Dick, and R. L. Fisher (1989), Petrology and geochemistry of MORB from 25°E to 46°E along the Southwest Indian Ridge: evidence for contrasting styles of mantle enrichment., *Journal of Petrology*, 30, 947-986.

- le Roex, A. P., H. J. B. Dick, and R. T. Watkins (1992), Petrogenesis of anomalous K-enriched MORB from the Southwest Indian Ridge: 11°53'E to 14°38'E, *Contributions to Mineralogy and Petrology*, 110, 253-268.
- Lundstrom, C. C. (2003), *Uranium-series disequilibria in mid-ocean ridge basalts: Observations and models of basalt genesis*, Mineralogical Society of America, Washington, DC.
- Lundstrom, C. C., J. Gill, and Q. Williams (2000), A geochemically consistent hypothesis for MORB generation, *Chemical Geology*, 162, 105-126.
- Lundstrom, C. C., J. B. Gill, and Q. Williams (1998a), Investigating solid mantle upwelling rates beneath mid-ocean ridges using U-series disequilibria: II. A local study at 33°S Mid-Atlantic Ridge, *Earth & Planetary Science Letters*, 157, 167-181.
- Lundstrom, C. C., D. E. Sampson, M. R. Perfit, J. Gill, and Q. Williams (1999), Insights into mid-ocean ridge basalt petrogenesis: U-series disequilibria from the Siqueiros Transform, Lamont Seamounts, and East Pacific Rise, *Journal Geophysical Research*, 104.
- Lundstrom, C. C., Q. Williams, and J. B. Gill (1998b), Investigating solid mantle upwelling rates beneath mid-ocean ridges using U-series disequilibria: I. A global approach, *Earth & Planetary Science Letters*, 157, 151-165.
- Macdonald, K. C., D. S. Scherer, and S. M. Carbotte (1991), Mid-ocean ridges: discontinuities, segments and giant cracks, *Science*, 253, 986-994.
- Mahoney, J., A. P. Le Roex, Z. Peng, R. L. Fisher, and J. H. Natland (1992), Southwestern limits of Indian Ocean ridge mantle and the origin of low <sup>206</sup>Pb/<sup>204</sup>Pb mid-ocean ridge basalt: isotope systematics of the Central Southwest Indian Ridge (17°-50°E), *Journal of Geophysical Research*, 97, 19,771-719,790.
- McKenzie, D. (1984), The generation and compaction of partially molten rock., *Journal of Petrology*, 25, 713-765.
- McKenzie, D. (1985), <sup>230</sup>U-<sup>238</sup>Th disequilibrium and the melting processes beneath ridge axes, *Earth and Planetary Science Letters*, 72, 149-157.
- Mendel, V., and D. Sauter (1997), Seamount volcanism at the super slow-spreading Southwest Indian Ridge between 57° and 70°E, *Geology*, 25, 99-102.
- Menke, W. (2005), <http://www.ldeo.columbia.edu/users/menke/plates.html>, edited by R. S. R. Calculator.
- Meyzen, C. M., M. J. Toplis, E. Humler, J. N. Ludden, and C. Mevel (2003), A discontinuity in mantle composition beneath the southwest Indian ridge, *Nature*, 421, 731-733.
- Michael, P. J., C. H. Langmuir, H. J. B. Dick, J. E. Snow, S. L. Goldstein, D. W. Graham, K. Lehnert, G. Kurras, W. Jokat, R. Mühe, and H. N. Edmonds (2003), Magmatic and amagmatic seafloor generation at the ultraslow-spreading Gakkel Ridge, Arctic Ocean, *Nature*, 423, 956-961.
- Mukasa, S. B., J. W. Shervais, H. G. Wilshire, and J. E. Nielsen (1991), Intrinsic Nd, Pb, and Sr isotopic heterogeneities exhibited by the Lherz alpine peridotite massif, French Pyrenees, *J. Petrol, Special Lherzolite Issue*, 117-134.
- Navon, O., and E. Stolper (1987), Geochemical consequences of melt percolation: the upper mantle as a chromatographic column, *Journal of Geology*, 95, 285-307.



- Nicolas, A. (1986), A melt extraction model based on structural studies in mantle peridotites, *Journal of Petrology*, 27, 999-1022.
- Nixon, P. H. (1987), *Mantle xenoliths*, Wiley, New York.
- Okino, K., D. Curewitz, M. Asada, K. Tamaki, P. Vogt, and K. Crane (2002), Preliminary analysis of the Knipovich Ridge segmentation: influence of focused magmatism and ridge obliquity on an ultraslow spreading system, *Earth and Planetary Science Letters*, 202.
- Pearson, D. G., G. R. Davies, and P. H. Nixon (1993), Geochemical constraints on the petrogenesis of diamond facies pyroxenites from the Beni Bousera Peridotite Massif, North Morocco, *Journal of Petrology*, 34, 125-172.
- Peate, D. W., C. J. Hawkesworth, P. W. van Calsteren, R. N. Taylor, and B. J. Murton (2001),  $^{238}\text{U}$ - $^{230}\text{Th}$  constraints on mantle upwelling and plume-ridge interaction along the Reykjanes Ridge, *Earth & Planetary Science Letters*, 187, 259-272.
- Perfit, M. R., D. J. Fornari, M. C. Smith, J. F. Bender, G. H. Langmuir, and R. M. Haymon (1994), Small-scale spatial and temporal variations in mid-ocean ridge crest magmatic processes, *Geology*, 22, 375-379.
- Pertermann, M., and M. M. Hirschmann (2002), Trace-element partitioning between vacancy-rich eclogitic clinopyroxene and silicate melt, *American Mineralogist*, 87, 1365-1376.
- Pertermann, M., and M. M. Hirschmann (2003a), Partial melting experiments on a MORB-like pyroxenite between 2 and 3 GPa: Constraints on the presence of pyroxenite in basalt source regions from solidus location and melting rate, *Journal of Geophysical Research*, 108, 16.
- Pickett, D. A., M. T. Murrell, and R. W. Williams (1996), Determination of femptogram quantities of protactinium in geological samples by thermal ionization mass spectrometry, *Analytical Chemistry*, 66, 91-108.
- Pietruszka, A. J., R. W. Carlson, and E. H. Hauri (2002), Precise and accurate measurement of  $^{226}\text{Ra}$ - $^{230}\text{Th}$ - $^{238}\text{U}$  disequilibria in volcanic rocks using plasma ionization multicollector mass spectrometry, *Chemical Geology*, 188, 171-191.
- Prinzhofer, A., E. Lewin, and C. J. Allègre (1989), Stochastic melting of the marble cake mantle: Evidence from local study of the East Pacific Rise at 12°50'N, *Earth & Planetary Science Letters*, 150, 291-302.
- Rubin, K. H., and J. D. MacDougall (1990), Dating of neovolcanic MORB using ( $^{226}\text{Ra}/^{230}\text{Th}$ ) disequilibrium, *Earth and Planetary Science Letters*, 101, 313-321.
- Salters, V. J. M. (1994),  $^{176}\text{Hf}/^{177}\text{Hf}$  determination in small samples by a high temperature SIMS technique, *Analytical Chemistry*, 66, 4186-4189.
- Salters, V. J. M., and S. R. Hart (1989), The hafnium paradox and the role of garnet in the source of mid-ocean-ridge basalts, 342, 420-422.
- Sauter, D., H. Carton, V. Mendel, M. Munschy, C. Rommevaux-Jestin, J.-J. Schott, and H. Whitechurch (2004a), Ridge segmentation and the magnetic structure of the Southwest Indian Ridge (at 50°30'E, 55°30'E and 66°20'E): Implications for magmatic processes at ultraslow-spreading centers, *Geochemistry, Geophysics, Geosystems*, 5, 25.

- Sauter, D., V. Mendel, C. Rommevaux-Jestin, L. Parson, H. Fujimoto, C. Mevel, M. Cannat, and K. Tamaki (2004b), Focused magmatism versus amagmatic spreading along the ultraslow-spreading Southwest Indian Ridge: Evidence from TOBI side scan imagery, *Geochemistry, Geophysics, Geosystems*, 5, 20.
- Seyler, M., M. Cannat, and C. Mevel (2003), Evidence for major-element heterogeneity in the mantle source of abyssal peridotites from the Southwest Indian Ridge (52° to 68° E), *Geochemistry, Geophysics, Geosystems*, 4, 33.
- Sims, K. W. W., J. Blichert-Toft, D. J. Fornari, M. R. Perfit, S. Goldstein, P. Johnson, D. J. DePaolo, S. R. Hart, M. T. Murrell, P. Michael, and G. Layne (2003), Aberrant youth: chemical and isotopic constraints on the young off-axis lavas of the East Pacific Rise, *Geochemistry, Geophysics, Geosystems*, 4.
- Sims, K. W. W., D. J. DePaolo, M. T. Murrell, W. S. Baldrige, S. Goldstein, D. Clague, and M. Jull (1999), Porosity of the melting zone and variations in the solid mantle upwelling rate beneath Hawaii: Inferences from  $^{238}\text{U}$ - $^{230}\text{Th}$ - $^{226}\text{Ra}$  and  $^{235}\text{U}$ - $^{231}\text{Pa}$  disequilibria, *Geochimica Et Cosmochimica Acta*, 63, 4119-4138.
- Sims, K. W. W., D. J. DePaolo, M. T. Murrell, W. S. Baldrige, S. J. Goldstein, and D. A. Clague (1995), Mechanisms of magma generation beneath Hawaii and mid-ocean ridges: uranium/thorium and samarium/neodymium isotopic evidence, *Science*, 267, 508-512.
- Sims, K. W. W., S. J. Goldstein, J. Blichert-Toft, M. R. Perfit, P. Kelemen, D. J. Fornari, P. Michael, M. T. Murrell, S. R. Hart, D. J. DePaolo, G. Layne, L. Ball, M. Jull, and J. F. Bender (2002), Chemical and isotopic constraints on the generation and transport of magma beneath the East Pacific Rise, *Geochimica Et Cosmochimica Acta*, 66, 3481-3504.
- Sims, K. W. W., and S. R. Hart (2005), Comparison of Th, Sr, Nd and Pb Isotopes in Oceanic Basalts: Implications for Mantle Heterogeneity and Magma Genesis, *Earth & Planetary Science Letters* (submitted).
- Sleep, N. H. (1988), Tapping of melt by veins and dikes, *Journal Geophysical Research*, 93, 10255-10272.
- Snow, J. E., E. Hellebrand, A. Handt, F. Nauret, Y. Gao, S. Feig, Z. Jovanovic, and S. Gauger (2004), Lena Trough (Arctic Ocean): An oblique 'amagmatic' rift, *EOS Transactions, AGU*, 85, T11G-01.
- Sohn, R. A., and K. W. W. Sims (2005), Bending as a mechanism for triggering off-axis volcanism on the East Pacific Rise, *Geology*, 33, 93-96.
- Sparks, D. W., and E. M. Parmentier (1991), Melt extraction from the mantle beneath spreading centers, *Earth & Planetary Science Letters*, 105, 368-377.
- Spiegelman, M., and T. Elliot (1993), Consequences of melt transport for U-series disequilibrium in young lavas, *Earth and Planetary Science Letters*, 118, 1-20.
- Standish, J. J., H. Dick, S. R. Hart, R. Workman, and A. le Roex (2004), Source enrichment versus degree of melting beneath the SWIR (9°-25°E), paper presented at Goldschmidt Conference, Copenhagen, Denmark.
- Standish, J. J., and H. J. B. Dick (2004), The influence of ridge geometry at ultraslow spreading rates, *EOS, Transactions American Geophysical Union*, 85.

- Sturm, M. E., S. J. Goldstein, E. M. Klein, J. A. Karson, and M. T. Murrell (2000), Uranium-series age constraints on lavas from the axial valley of the Mid-Atlantic Ridge, MARK area, *Earth & Planetary Science Letters*, 181, 61-70.
- Su, Y., and C. Langmuir (2002), Global MORB chemistry compilation at the segment scale, in *Petrologic Database of the Ocean Floor*, edited by <http://www.petdb.org/documentation/morbcompilation/index.jsp>.
- Suen, C. J., and F. A. Frey (1987), Origins of the mafic and ultramafic rocks in the Ronda peridotite, *Earth and Planetary Science Letters*, 85, 183-202.
- Takahashi, E., and K. Nakajima (2002), Melting process in the Hawaiian Plume: An experimental study, in *Hawaiian Volcanoes: Deep Underwater Perspectives, Geophysical Monograph Series*, edited by E. Takahashi, pp. 403-418, AGU, Washington, D.C.
- Tepley, F. J. I., C. C. Lundstrom, K. W. W. Sims, and R. Hekinian (2004), U-series disequilibria in MORB from the Garrett Transform and implications for mantle melting, *Earth & Planetary Science Letters*, 223, 79-97.
- Thurber, D. (1967), Anomalous  $^{234}\text{U}/^{238}\text{U}$  in nature, *Journal Geophysical Research*, 67, 4518.
- Volpe, A. M., J. A. Olivares, and M. T. Murrell (1993),  $^{226}\text{Ra}$ - $^{230}\text{Th}$  disequilibrium in axial and off-axis mid-ocean ridge basalts, *Geochimica Et Cosmochemica Acta*, 57, 1233-1242.
- White, R. S., T. A. Minshull, M. J. Bickle, and C. J. Robinson (2001), Melt generation at very slow-spreading oceanic ridges: Constraints from geochemical and geophysical data, *Journal of Petrology*, 42, 1171-1196.
- Williams, R. W., and J. B. Gill (1989), Effects of partial melting on the uranium decay series, *Geochim. Cosmochim. Acta*, 53, 1607-1619.
- Wilshire, H. G., C. E. Meyer, J. K. Nakata, L. C. Calk, J. W. Shervais, J. E. Nielson, and E. C. Schwartzman (1988), Mafic and ultramafic xenoliths from volcanic rocks of the western United States, *U.S. Geological Survey Professional Paper 1443*, 1-179.
- Wood, B. J., J. D. Blundy, and J. A. C. Robinson (1999), The role of clinopyroxene in generating U-series disequilibrium during mantle melting, *Geochimica Cosmochemica Acta*, 63, 1613-1620.
- Workman, R. K., and S. R. Hart (2005), Major and trace element composition of the depleted MORB mantle (DMM), *Earth & Planetary Science Letters*, 231, 53-72.
- Yaxley, G. M. (2000), Experimental study of the phase and melting relations of homogeneous basalt + peridotite mixtures and implications for the petrogenesis of flood basalts, *Contr. Mineral. and Petrol.*, 139, 326-338.
- Yaxley, G. M., and D. H. Green (1998), Reactions between eclogite and peridotite: Mantle refertilization by subduction of oceanic crust, *Schweiz, Mineralogische und Petrographische Mitteilungen*, 78, 243-255.
- Zou, H., A. Zindler, and Y. Niu (2002), Constraints on melt movement beneath the East Pacific Rise from  $^{230}\text{Th}$ - $^{238}\text{U}$  disequilibrium, *Science*, 295, 107-110.

**Table 1.** Sample locations, spreading rates, and dredge descriptions for samples from 9°-25°E

	Latitude (°S)	Longitude (°E)	Depth (mbsl)	Full		Effective		Dredge Description
				Spreading Rate <sup>1</sup> (mm/yr)	Spreading Rate <sup>2</sup> (mm/yr)			
Rift valley floor lavas								
KN162-9 33-49 <sup>3</sup>	52.82	11.39	1462	14.1	13.3			South side of northern peak of Joseph Mayes Seamount within saddle between two peaks, near midpoint of segment and
KN162-9 36-27	52.75	11.71	4017	14.1	7.5			Base to crest of the steep (~23°) NE wall serving as far western terminus of main amagmatic trough; wall may even be buttressing Joseph Mayes Seamount
KN162-9 48-04	52.56	12.80	4090	14.1	7.7			Base of southern steep sub-orthogonal (~102°) rift valley wall dipping ~25.1° to the NNE, associated with kink in rift valley walls signifying a vestigial magmatic segment
KN162-9 56-88	52.37	13.51	4050	14.2	8.9			Midpoint of an orthogonal ridge striking 120° and running across the rift valley, SW of segment T8.
VAN7 80-04 <sup>3</sup>	52.23	16.01	4134	14.3	14.2			North slope of central axial volcanic ridge on westernmost segment of the orthogonal supersegment (G&M 1), associated with mantle Bouguer anomaly low and magnetization high
KN162-7 02-01	52.33	16.23	3855	14.2	14.2			Southern inner rift valley wall on an extension of the axial oblique ridge that comprises the westernmost magmatic segment of the orthogonal supersegment (G&M segment 1)
KN162-7 04-13 <sup>3</sup>	52.36	17.11	3928	14.3	14.2			3
KN162-7 10-21 <sup>3</sup>	52.75	19.27	3165	14.4	14.3			Located at small rift in axial volcanic high at center of G&M segment 6
KN162-7 15-05	52.92	20.38	3489	14.4	14.4			Base of southern inner rift valley wall at center of G&M segment 8, where rift valley narrows
KN162-7 25-03	53.17	23.12	3995	14.5	14.5			NE side of 300m high, 3km diameter, flat topped volcano (breached caldera) in center of overlap basin just south of axial volcanic ridge, and between G&M segments 12 & 13
Rift valley wall lavas								
KN162-9 61-71	52.10	14.60	2282	14.2	14.2			Local high on crest of northern rift valley wall at Narrowgate segment, associated with local crustal magnetization high and mantle Bouguer anomaly low
VAN7 89-02	52.25	14.60	2570	14.2	14.2			Below crest of southern rift valley wall on Narrowgate segment

<sup>1</sup> full spreading rates calculated from NUVEL-1 parameters and plate spreading calculator at <http://www.ideo.columbia.edu/users/menke/plates.html>

<sup>2</sup> effective spreading rates use the method of Abelson & Agnon [1997] and azimuths measured by hand

<sup>3</sup> considered "axial" lavas, based on dredge locations near the geometric center of the rift valley and association with linear volcanic highs

**Table 2.** Major and trace element concentrations for 12 glasses measured for U-series disequilibria from 9°-25°E on the Southwest Indian Ridge.

Cruise #	KN162-9	KN162-9	KN162-9	KN162-9	VAN7-	KN162-9	VAN7-	KN162-7	KN162-7	KN162-7	KN162-7	KN162-7
Dredge-Sample	33-49	36-27	48-04	56-88	89-02	61-71	80-04	02-01	04-13	10-21	15-05	25-03
Latitude (°S)	52.817	52.749	52.560	52.370	52.246	52.104	52.232	52.330	52.358	52.745	52.923	53.173
Longitude (°E)	11.387	11.711	12.799	13.506	14.598	14.601	16.007	16.233	17.113	19.269	20.382	23.117
Depth (mbsl)	1436	3981	3897	4132	2439	2211	4038	4000	3650	3097	3403	3940
SiO <sub>2</sub> (wt%)	50.90	50.78	49.58	51.80	48.40	51.46	50.67	50.42	50.28	50.05	50.29	50.62
Al <sub>2</sub> O <sub>3</sub>	15.00	16.48	17.57	16.71	16.64	15.97	15.72	14.82	15.66	15.97	16.15	15.92
FeO	10.66	8.57	8.20	7.47	8.07	10.05	9.31	11.11	9.71	9.32	8.90	9.02
MgO	5.07	7.19	8.40	6.41	6.42	4.10	6.99	7.12	7.41	7.44	7.59	7.51
CaO	9.35	10.37	11.84	10.35	11.99	8.25	10.78	10.28	10.86	10.83	11.19	10.80
Na <sub>2</sub> O	3.99	3.91	3.15	3.35	3.25	4.45	3.01	3.30	3.16	3.17	3.11	3.17
K <sub>2</sub> O	0.83	0.21	0.08	0.89	1.34	1.66	0.33	0.22	0.23	0.23	0.20	0.14
TiO <sub>2</sub>	2.48	1.76	1.10	1.63	1.80	2.67	1.93	2.12	1.81	1.80	1.51	1.65
P <sub>2</sub> O <sub>5</sub>	0.44	0.21	0.10	0.29	0.31	0.62	0.16	0.20	0.21	0.20	0.18	0.17
MnO	0.22	0.18	0.16	0.12	0.15	0.20	0.21	0.25	0.20	0.20	0.19	0.17
H <sub>2</sub> O	0.77	0.34	0.18	0.68	0.81	1.04	0.40	0.36	0.35	0.33	0.30	0.26
CO <sub>2</sub> (ppm)	197	165	246	158	199	142	170	192	201	189	170	172
K/Ti (molar)	0.28	0.10	0.06	0.46	0.63	0.53	0.14	0.09	0.11	0.11	0.11	0.07
Sc (ppm)	31.0	30.5	33.7	27.1	26.0	23.5	34.0	39.0	37.1	35.7	35.3	35.3
V	301.1	240.7	197.4	213.5	264.4	314.9	304.7	342.9	304.0	279.5	247.5	276.6
Cr	42.8	343.0	320.8	244.6	55.0	1.1	277.7	206.4	314.7	268.0	364.3	265.1
Co	36.1	39.9	42.5	35.6	36.4	32.1	40.5	45.0	44.4	41.1	42.2	40.6
Ni	32.9	163.1	129.0	143.7	71.1	16.7	124.9	109.4	126.7	123.0	146.8	121.2
Cu	64.4	62.7	80.5	58.1	93.6	42.1	67.3	66.3	73.8	65.4	70.8	62.6
Rb	18.78	4.34	0.90	20.12	27.62	38.91	6.74	3.72	4.77	3.35	2.90	0.55
Sr	260.5	163.1	146.2	309.0	450.2	343.8	171.9	157.0	151.8	198.4	187.6	162.3
Y	37.9	31.8	22.1	24.1	20.7	38.1	30.5	40.9	34.2	30.7	27.4	30.7
Zr	223.5	148.6	79.0	144.4	153.0	266.9	137.4	159.4	134.2	140.9	119.3	132.0
Nb	29.62	6.54	1.88	28.71	51.10	61.56	12.83	7.39	9.07	7.87	6.89	2.93
Ba	199.1	46.3	11.2	249.7	459.9	424.7	76.1	38.7	49.1	37.7	31.0	8.0
La	20.19	6.47	2.77	18.40	30.68	37.29	8.68	7.33	7.29	6.92	6.10	4.48
Ce	45.64	18.65	9.37	36.98	58.71	74.75	21.17	19.94	18.50	19.03	16.57	14.57
Pr	5.76	2.86	1.50	4.36	6.28	8.62	2.87	3.16	2.75	2.77	2.40	2.32
Nd	26.19	14.88	8.22	18.45	25.73	35.56	14.71	16.40	14.14	14.26	12.37	12.78
Sm	6.31	4.25	2.56	4.15	4.92	7.40	4.03	5.16	4.28	4.12	3.62	3.86
Eu	2.04	1.41	1.01	1.41	1.68	2.28	1.38	1.92	1.54	1.46	1.26	1.40
Gd	7.76	5.32	3.55	4.67	5.15	7.66	5.29	7.11	5.76	5.46	4.70	5.10
Tb	1.21	0.89	0.59	0.74	0.73	1.18	0.83	1.18	0.97	0.90	0.78	0.84
Dy	7.24	5.62	3.99	4.50	4.41	7.19	5.66	7.82	6.35	5.61	4.96	5.55
Ho	1.47	1.18	0.86	0.92	0.84	1.46	1.14	1.63	1.33	1.16	1.06	1.18
Er	4.15	3.34	2.47	2.56	2.36	4.06	3.38	4.77	3.92	3.37	2.98	3.38
Tm	0.59	0.49	0.36	0.37	0.32	0.58	0.46	0.67	0.55	0.46	0.43	0.49
Yb	3.74	3.11	2.32	2.30	2.06	3.70	3.12	4.27	3.56	3.09	2.76	3.15
Lu	0.55	0.47	0.35	0.35	0.29	0.55	0.45	0.62	0.51	0.45	0.42	0.47
Hf	4.95	3.27	1.87	2.98	3.15	5.35	3.09	4.04	3.30	3.13	2.70	3.01
Ta	1.72	0.41	0.14	1.63	2.61	3.50	0.81	0.74	0.75	0.69	0.60	0.25
Pb	1.77	1.33	0.84	2.03	2.28	3.18	1.91	1.01	0.81	0.89	0.94	0.48
Th	2.60	0.57	0.16	2.88	4.22	5.86	0.96	0.54	0.71	0.58	0.52	0.17
U	0.73	0.17	0.05	0.76	1.16	1.60	0.28	0.16	0.20	0.18	0.17	0.07



**Table 3.** Sr, Nd, Pb, Hf, and He isotopic compositions measured by TIMS and ICPMS

	Latitude (°S)	Longitude (°E)	Depth (mbsl)	$^{87}\text{Sr}/^{86}\text{Sr}$	$^{143}\text{Nd}/^{144}\text{Nd}$	$^{206}\text{Pb}/^{204}\text{Pb}$	$^{207}\text{Pb}/^{204}\text{Pb}$	$^{208}\text{Pb}/^{204}\text{Pb}$	$^{176}\text{Hf}/^{177}\text{Hf}$	$2\sigma$	$^3\text{He}/^4\text{He}$	$1\sigma$			
Rift valley floor lavas															
KN162-9 33-49 *	52.82	11.39	1462	0.702984	10	0.512952	8	19.118	1	15.603	1	38.951	6	5.99	0.03
KN162-9 36-27	52.75	11.71	4017	0.702726	10	0.513079	12	18.472	1	15.513	1	38.256	1	0.283235	12
KN162-9 48-04	52.56	12.80	4090	0.702812	10	0.512982	28	18.431	2	15.494	2	38.016	5	0.283101	15
KN162-9 56-88	52.37	13.51	4050	0.703212	10	0.512903	8	18.958	2	15.582	2	39.063	4	0.283128	13
VAN7 80-04 *	52.23	16.01	4134	0.702909	10	0.512992	16	19.106	2	15.589	2	38.911	2	0.283065	5
KN162-7 02-01	52.33	16.23	3855	0.702584	6	0.513039	12	18.986	2	15.574	2	38.639	4	0.283045	6
KN162-7 04-13 *	52.36	17.11	3928	0.702639	6	0.513003	16	19.072	3	15.610	3	38.819	8	0.283041	7
KN162-7 10-21 *	52.75	19.27	3165	0.702597	7	0.513018	26	19.070	2	15.597	2	38.696	6	0.283049	12
KN162-7 15-05	52.92	20.38	3489	0.702490	74	0.513047	38	19.038	2	15.617	2	38.713	6	0.283019	6
KN162-7 25-03	53.17	23.12	3995	0.702522	12	0.513070	18	18.572	1	15.548	1	38.230	2	0.283069	5
Rift valley wall lavas															
KN162-9 61-71	52.10	14.60	2282	0.703424	12	0.512857	10	19.288	1	15.642	1	39.368	1	0.283024	10
VAN7 89-02	52.25	14.60	2570	0.703631	12	0.512786	46	19.350	2	15.620	2	39.454	4	0.282965	6
Average Global N-MORB *															
Mid-Atlantic Ridge				0.702593	203	0.513154	60	18.341	363	15.497	50	37.867	387	0.283227	9
East Pacific Rise				0.702535	128	0.513154	58	18.340	273	15.486	40	37.784	290	0.283196	8
Indian Ocean				0.702860	210	0.513069	49	18.056	402	15.472	40	37.839	298	0.283211	8
Bouvet Island															
WJM-2B				0.703700		0.512865		19.479		15.650		39.086		0.282948	12.4 ^
WJM-16B				0.703760		0.512861		19.418		15.631		39.050		0.282939	1

\* Considered to be located at geometric center of rift valley and associated with linear volcanic high

\* Sr, Nd, and Pb data taken from *Su & Langmuir*, [2003]

^  $^3\text{He}/^4\text{He}$  value is taken from *Kurz* [1982] and is from sample WJ8B (plagioclase mineral separate)

all  $2\sigma$  values are reported in last decimal place

**Table 4.** [U], [Th], [Ra], ( $^{235}\text{U}/^{232}\text{Th}$ ), ( $^{230}\text{Th}/^{232}\text{Th}$ ), ( $^{230}\text{Th}/^{234}\text{U}$ ), ( $^{226}\text{Ra}/^{230}\text{Th}$ ), and ( $^{234}\text{U}/^{238}\text{U}$ ) measured by ICPMS on glasses from 9°-25°E on the SW Indian Ridge.

	Latitude (°S)	Longitude (°E)	Depth (mbsl)	[Th] (ppm) <sup>1</sup>	[U] (ppm)	Th/U ( $^{235}\text{U}/^{232}\text{Th}$ )	( $^{230}\text{Th}/^{232}\text{Th}$ )	( $^{230}\text{Th}/^{234}\text{U}$ ) <sup>2</sup>	[ $^{226}\text{Ra}$ ] fg/g	( $^{226}\text{Ra}/^{230}\text{Th}$ ) <sup>4</sup>	( $^{234}\text{U}/^{238}\text{U}$ )
<b>Rift valley floor lavas</b>											
KN162-9 33-49	52.82	11.39	1462	2.5510	0.7149	3.568	0.850	0.874	1.028	327.9 327.3	1.001 0.998
KN162-9 36-27	52.75	11.71	4017	0.5650	0.1636	3.453	0.879	0.948	1.079		
KN162-9 48-04	52.56	12.80	4090	0.1589	0.0471	3.374	0.899	0.956	1.088		
								0.954	1.061		0.995
KN162-9 56-88	52.37	13.51	4050	2.7066	0.6799	3.981	0.762	0.962	1.070		
VAN7 80-04	52.23	16.01	4134	1.0534	0.3063	3.439	0.882	0.799	1.048		1.002
								1.131	1.282		1.000
KN162-7 02-01	52.33	16.23	3855	0.5470	0.1656	3.303	0.918	1.102	1.250		
								0.934	1.017		1.002
								0.934	1.017		1.001
KN162-7 04-13	52.36	17.11	3928	0.7102	0.2003	3.545	0.856	0.938	1.022		1.001
KN162-7 10-21	52.75	19.27	3165	0.5414	0.1707	3.171	0.957	0.964	1.126		1.003
								1.096	1.146	73.9	1.005
KN162-7 15-05	52.92	20.38	3489	0.5152	0.1669	3.087	0.983	1.111	1.161	1.12 (12)*	1.002
KN162-7 25-03	53.17	23.12	3995	0.1635	0.0747	2.190	1.385	1.069	1.088		1.000
								1.425	1.029		0.994
											0.999
<b>Rift valley wall lavas</b>											
KN162-9 61-71	52.10	14.60	2282	5.3561	1.5376	3.483	0.871	0.838	0.962	704.4	1.001
								0.834	0.958	706.6	
VAN7 89-02	52.25	14.60	2570	4.7238	1.2262	3.852	0.788	0.781	0.992		1.000
								0.784	0.995		
<b>Standards</b>											
ATHO				7.4559	2.2345	3.337	0.909	1.010	1.110		1.005
								1.018	1.119		1.002
TML 1				29.8217	10.5504	2.827	1.073	1.058	0.994 <sup>3</sup>	3604.4	0.999
TML 2											
TML 3											1.003
TML B											0.998
								1.081	0.994 <sup>3</sup>	3749.9	1.001

<sup>1</sup> concentrations measured by isotope dilution ICP-MS at WHOI; analytical errors (2 $\sigma$ ) for [Th] < 0.6% and [U] < 1.4%. Errors include 2 $\sigma$  for  $^{235}\text{U}$  spike (0.07%) and  $^{230}\text{Th}$  spike (0.30%). [Th] for KN162-9 33-49 & 48-04 use only two of three scans, due to analytical problems.

<sup>2</sup> average 2 $\sigma$  for ( $^{230}\text{Th}/^{232}\text{Th}$ ) is 2% and includes uncertainty in spike

<sup>3</sup> ( $^{230}\text{Th}/^{234}\text{U}$ ) measured separately by K. Cooper

<sup>4</sup> 2 $\sigma$  for ( $^{226}\text{Ra}/^{230}\text{Th}$ ) is ~ 3% and includes uncertainty in spike.

\* measured by  $^{214}\text{Pb}$  alpha-counting methods with 2 $\sigma$  % in O

**Table 5.** Sample ages based on spreading rate, U-Th limits, and Th-Ra limits for glasses from 9°-25°E on the SW Indian Ridge

Latitude (°S)	Longitude (°E)	Depth (mbsl)	Half Spreading Rate (mm/yr) <sup>1</sup>	Distance from rift-axis (km) <sup>2</sup>	Age based on	
					spreading rate (ka) <sup>3</sup>	Age constraints from U-Th-Ra disequilibria (ka) <sup>4</sup>
Rift valley floor lavas						
KN162-7 02-01	52.33	16.23	3855	7.1	-2.5	352 > 300
KN162-7 04-13 <sup>5</sup>	52.36	17.11	3928	7.2	0.0	0 < 300
KN162-7 10-21 <sup>5</sup>	52.75	19.27	3165	7.2	0.0	0 < 8
KN162-7 15-05	52.92	20.38	3489	7.2	-4.1	569 < 300
KN162-7 25-03	53.17	23.12	3995	7.3	-2.0	274 ≤ 300
KN162-9 33-49 <sup>5</sup>	52.82	11.39	1462	7.0	0.0	0 < 8
KN162-9 36-27	52.75	11.71	4017	7.0	3.8	541 < 300
KN162-9 48-04	52.56	12.80	4090	7.0	-12.0	1714 < 300
KN162-9 56-88	52.37	13.51	4050	7.1	-4.1	577 < 300
VAN7 80-04 <sup>5</sup>	52.23	16.01	4134	7.2	0.0	0 < 300
Rift valley wall lavas						
KN162-9 61-71	52.10	14.60	2282	7.1	9.5	1337 < 8
VAN7 89-02	52.25	14.60	2570	7.1	-5.8	820 > 300

<sup>1</sup> half spreading rates calculated using NUVEL-1 parameters and the plate spreading calculator available at

<http://www.ideo.columbia.edu/users/menke/plates.html>

<sup>2</sup> distance is measured from the amagmatic axis of rifting or by default from the center of the rift valley, where negative numbers indicate south

<sup>3</sup> age calculated assuming eruption at center of rift valley and subsequent symmetric spreading at 7.5 mm/yr half-rate

<sup>4</sup> age constraints based on U-Th and Th-Ra disequilibria reported in Table 4

<sup>5</sup> considered zero age lavas based on dredge locations in center of rift valley and association with linear volcanic highs

**Table 6.** Compilation of E-MORBs illustrating the variation in U-Th disequilibrium within lavas from various ridge settings, and N-MORBs that display low excess  $^{230}\text{Th}$  or excess  $^{234}\text{U}$ .

Tectonic/Petrologic						
Suite/Sample <sup>1</sup>	Setting <sup>2</sup>	( <sup>230</sup> Th/ <sup>238</sup> U)	( <sup>226</sup> Ra/ <sup>230</sup> Th)	K/Ti	<sup>87</sup> Sr/ <sup>86</sup> Sr	Reference
<b>E-MORB</b>						
<b>SW Indian Ridge (9°-25°E)</b>						Standish et al., 2005
KN162 33-49	rift-axis seamount	1.028	1.322	0.28	0.70298	
KN162 56-88	4.1 km from rift axis	1.048		0.46	0.70321	
<u>KN162 61-71</u>	9.5 km from rift axis <sup>3</sup>	0.960	1.411	0.53	0.70342	
VAN7 80-04	on-axis	1.266		0.14	0.70291	
<u>VAN7 89-02</u>	5.8 km from rift axis	0.994		0.63	0.70363	
<b>EPR (9°30'N)</b>						Zou et al., 2002
P2-3	5.7 km off-axis	1.070		0.15		
<u>P10-2</u>	17.7 km off-axis	0.894		0.18		
		0.898		0.18		
<u>P34-1</u>	22 km off-axis	0.849		0.19		
<u>P37-1</u>	28.4 km off-axis	0.982		0.18		
<b>EPR (9°-10°N)</b>						Goldstein et al., 1989, 1992, 1993
ARC-48	2 km off-axis	1.149		0.20		
R54-2	on-axis	1.233		0.19		
<b>EPR-Siqueiros Transform</b>						Lundstrom et al., 1999; Sims et al., 2002
A2390-1	RTI	1.196	1.03	0.25		
2390-5	RTI	1.195	1.03	0.27	0.70286	
SD8-6L	RTI	1.174	1.09	0.28		
SD8-5L	RTI	1.107	1.09	0.43		
<b>Juan de Fuca Ridge</b>						Goldstein et al., 1989, 1992, 1993
TT175-21, J3	on-axis	1.153		0.28		
TT175-21-13	on-axis	1.251		0.26		
TT175-59-1	on-axis	1.249		0.28		
<b>Gorda Ridge</b>						Goldstein et al., 1989; Sims et al., 1995
API 118-37	on-axis	1.374		0.16	0.70240	
<b>N-MORB</b>						
<b>EPR (9°30'N)</b>						Zou et al., 2002
<u>P31-9</u>	17.7 km off-axis	0.984		0.06		
<u>P35-1</u>	24.7 km off-axis	0.923		0.07		
<u>P36-7</u>	26.7 km off-axis	0.916		0.06		
<b>Garrett Transform</b>						Tepley et al., 2004
<u>GN 02-02</u>	intra-transform ridges	0.945	3.80	0.02	0.70236	
<u>GN 02-04</u>	intra-transform ridges	0.991	3.40	0.04	0.70236	
<u>GN 02-08</u>	intra-transform ridges	0.96	3.59	0.03		
<u>GN 05-05</u>	intra-transform ridges	0.986		0.01		
<u>GN 07-01</u>	intra-transform ridges	0.929	2.99	0.03	0.70222	
<u>GN 07-02/03</u>	intra-transform ridges	0.956	2.97	0.03		
<u>GN 09-02</u>	intra-transform ridges	0.773	1.30	0.02	0.70226	
<b>MAR - Kolbeinsey Ridge</b>						
<u>K21847</u>	on-axis	0.955			0.70290	
<u>K21854</u>	on-axis	0.951			0.70274	
<u>22DS2</u>	on-axis	0.96			0.70292	
<b>Lamont Seamount</b>						Lundstrom et al., 1999
<u>1558-2014</u>	off-axis seamount	0.975	1.05	0.03	0.70222	

<sup>1</sup> underlined sample entries indicate samples with ( $^{230}\text{Th}/^{234}\text{U}$ ) < 1

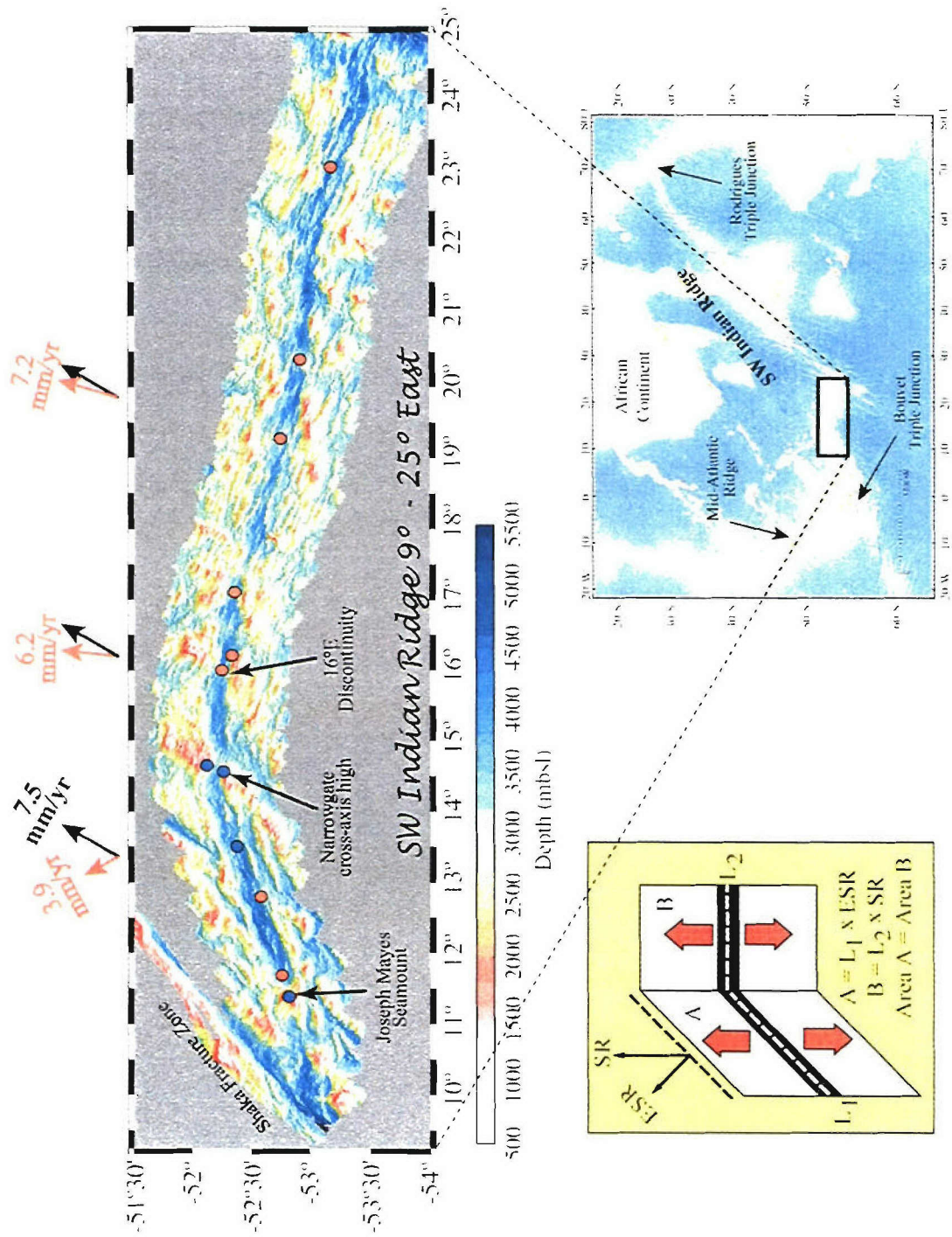
<sup>2</sup> rift-axis indicates either axial volcanic lineation or symmetric center of rift valley; RTI stands for ridge-transform intersection

<sup>3</sup> sample 61-71 is 9.5 km from rift axis, and also sits near the peak of the rift valley wall (> 1000 m above the rift valley floor)

**Table B-1.** Sample introduction and mass spectrometer operating conditions for U-series measurements on the ThermoFinnigan Neptune

<b>Sample Introduction Hardware and specifications</b>				
	U	Th	Ra	
Elemental Scientific, Inc. (ESI) Stable Sample Introduction System	X	X	X	
50 u/min uptake PFA Neb	X	X	X	
quartz dual spray chamber	X	X	X	
Coolant gas = 16 l/min	X	X	X	
Auxiliary gas flow = 0.8 l/min	X	X	X	
Sample gas flow ≈ 1 l/min (optimized)	X	X	X	
<b>ThermoFinnigan Neptune operating conditions</b>				
RF Power - 1250 Watts	X	X	X	
Lenses tuned daily for optimum sensitivity, peakshape, and stability	X	X	X	
Faraday Amplifiers calibrated weekly	X	X	X	
Mass Bias determined simultaneously on Faraday cups	X			
SEM Ion Counter	X	X		
High voltage bias determined weekly	X	X		
Dark noise verified < 10 cpm weekly	X	X		
Standard-Sample-Standard Bracketing for SEM Yield Calibration	X	X		
Mass Bias determined by Std-Sample-Std bracketing		X		
Channeltron "Multi-ion Counting System"			X	
High voltage bias determined weekly			X	
Dark noise verified < 10 cpm weekly			X	
Mass bias and detector yield determined with uranium standard at beginning and end of day			X	





(previous page)

**Figure 1.** Southwest Indian Ridge bathymetry from 9°-25°E. Data from 16-25° E is from *Grindlay et al.*, [1998]. Sample locations (red = N-MORB and blue = E-MORB) and descriptions in Table 1. Half-spreading rate (SR) marked by black arrows and effective spreading rate (ESR) by red arrows, illustrating the effect of increasing ridge obliquity from east to west. *Inset* Cartoon of calculated ESR. Lithospheric sections A and B have equal area, but segment length  $L_1 > L_2$ . ESR is component of spreading perpendicular to trend of ridge axis (i.e. mantle upwelling rate). *Map inset* Regional bathymetric site map [taken from [www.geomapapp.org](http://www.geomapapp.org)].

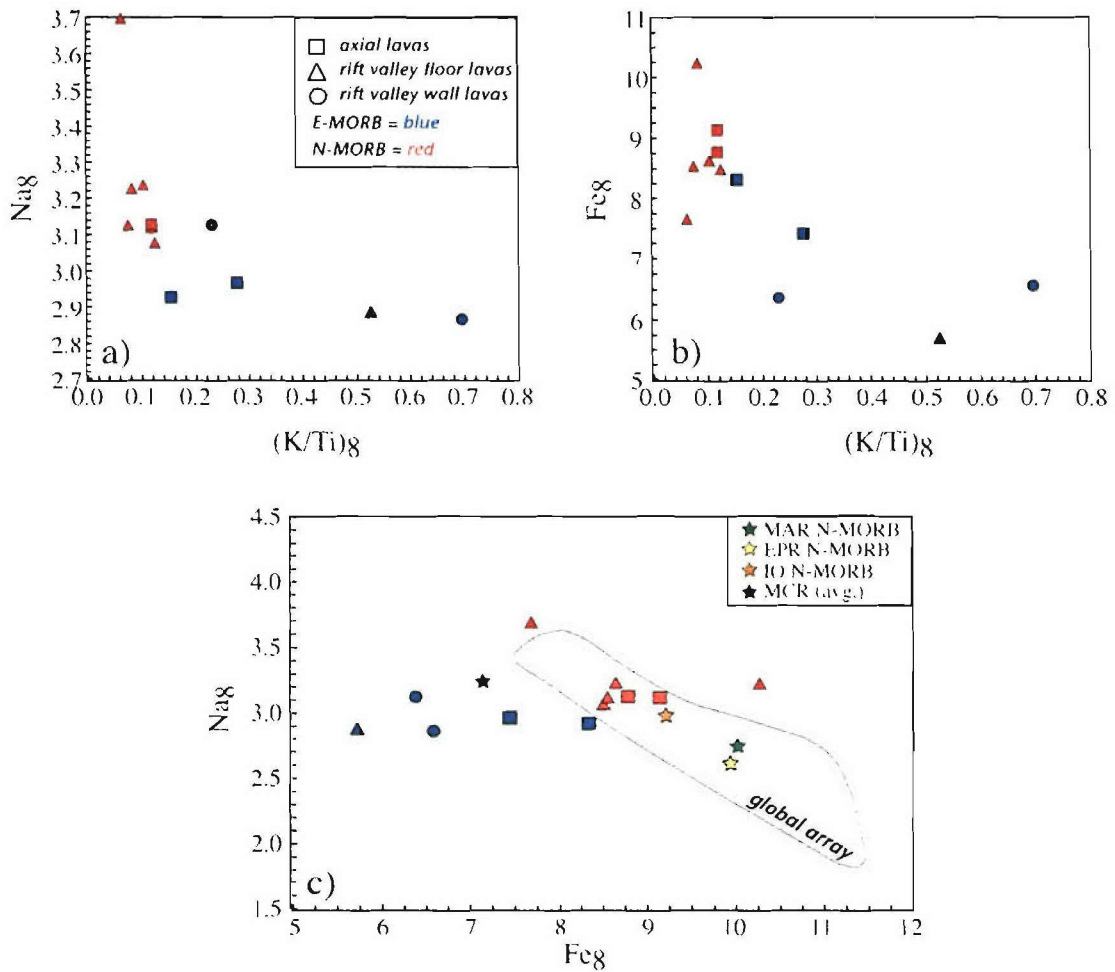


**Figure 2.** Major element compositional variation of Southwest Indian Ridge glasses. N-MORBs are red and E-MORBs are blue, with squares indicating lavas from the center of the rift valley (axial), triangles indicating lavas from the rift valley floor, and circles indicating lavas from the rift valley wall. N-MORB averages from EPR, MAR, and Indian Ocean (IO) are from Su, [2003], and Mid-Caymen Rise (MCR) is from Meyzen et al., [2003]. Global array field taken from Klein and Langmuir [1987].

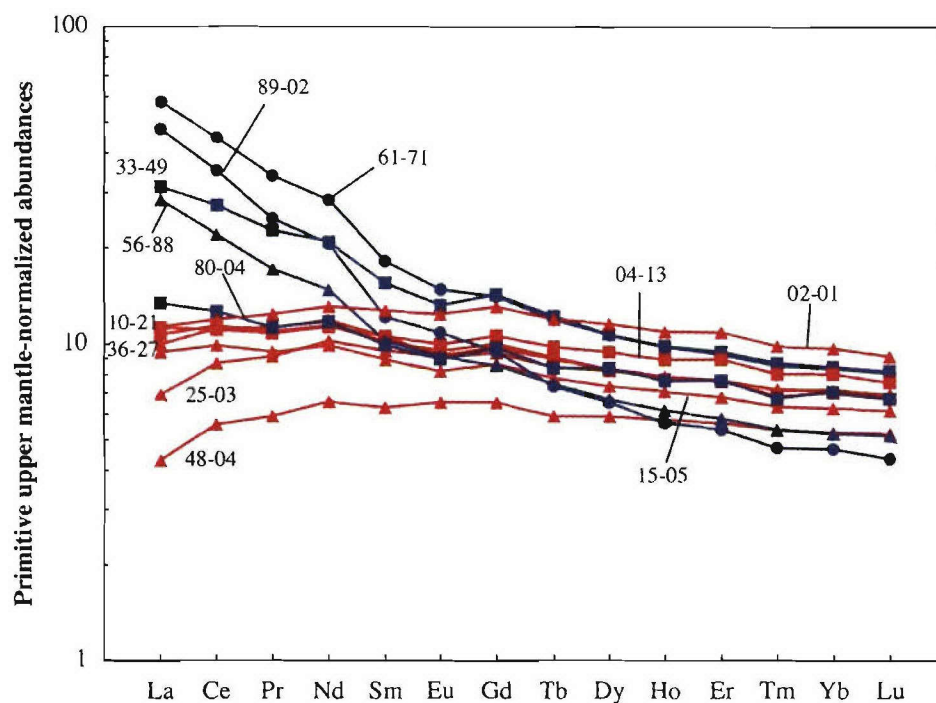


**Figure 3.** REE patterns for Southwest Indian Ridge basalts between 9°-25°E. Samples are colored red for N-MORB compositions and blue for E-MORB, with square patterns indicating lavas from the center of the rift valley (axial), triangles indicating rift valley floor lavas, and circles indicating rift valley wall lavas. Basalts are normalized to primitive upper mantle composition [McDonough & Sun, 1995].

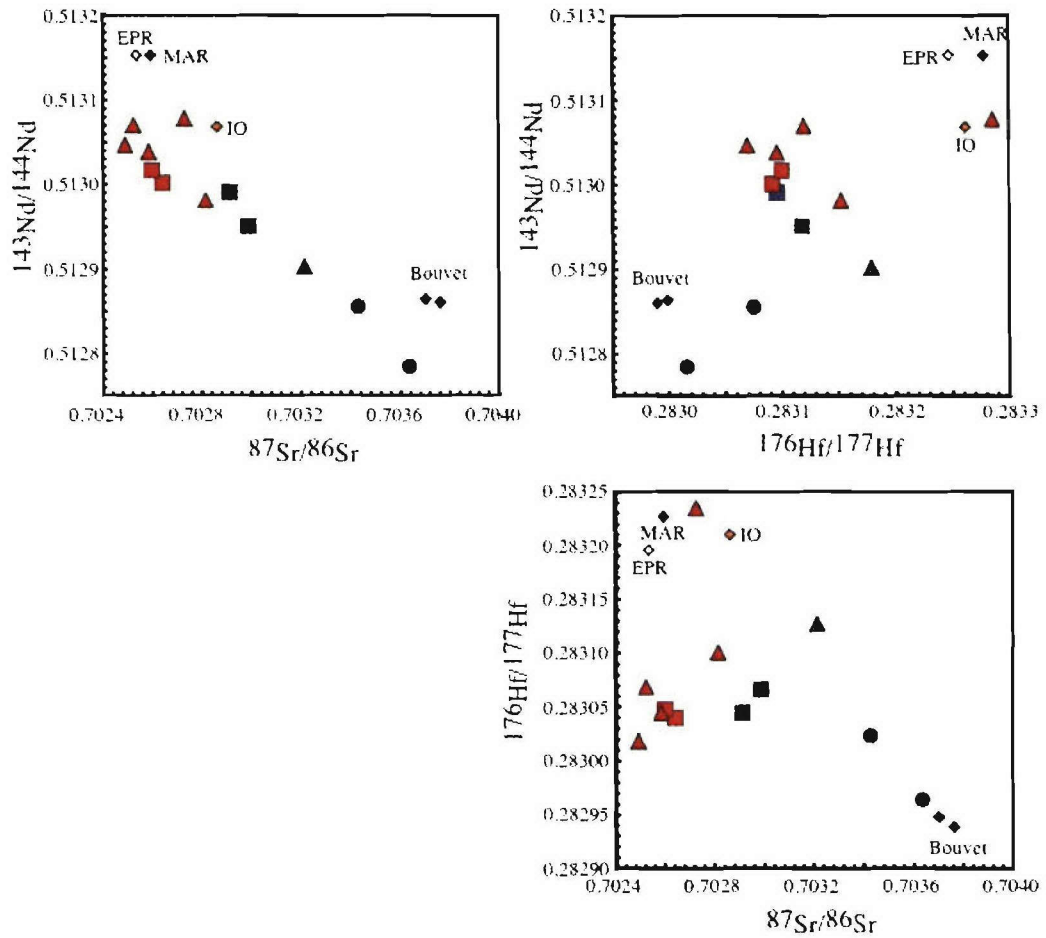


**Figure 4.** Sr, Nd, and Hf isotopic compositions for SW Indian Ridge basalts (9°-25°E). Sample symbols as in Figure 2. Average Sr and Nd compositions for EPR, MAR, and Indian Ocean (IO) are from *Su & Langmuir*, [2003] and Hf compositions from *Chauvel & Blichert-Toft*, [2001]. Bouvet Island values from *Janney* [2005]. All sample error bars are smaller than symbol size.



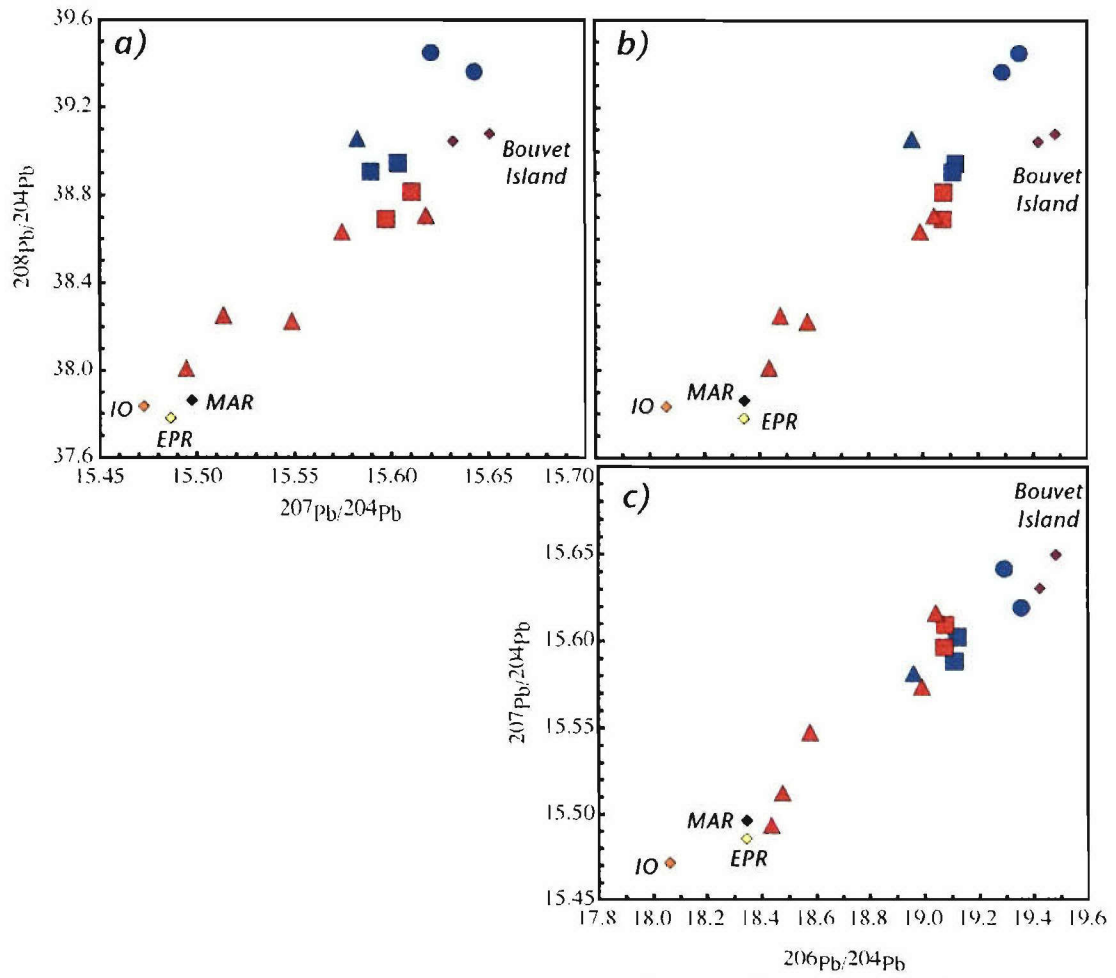


**Figure 5.** a)  $^{208}\text{Pb}/^{204}\text{Pb}$  vs.  $^{207}\text{Pb}/^{204}\text{Pb}$ , b)  $^{208}\text{Pb}/^{204}\text{Pb}$  vs.  $^{206}\text{Pb}/^{204}\text{Pb}$ , c)  $^{207}\text{Pb}/^{204}\text{Pb}$  vs.  $^{206}\text{Pb}/^{204}\text{Pb}$  for Southwest Indian Ridge lavas and average N-MORB values for MAR, EPR, IO (Indian Ocean) from Su and Langmuir [2003], and two Bouvet Island lavas from Janney [2005]. Symbols are the same as in Figure 2.

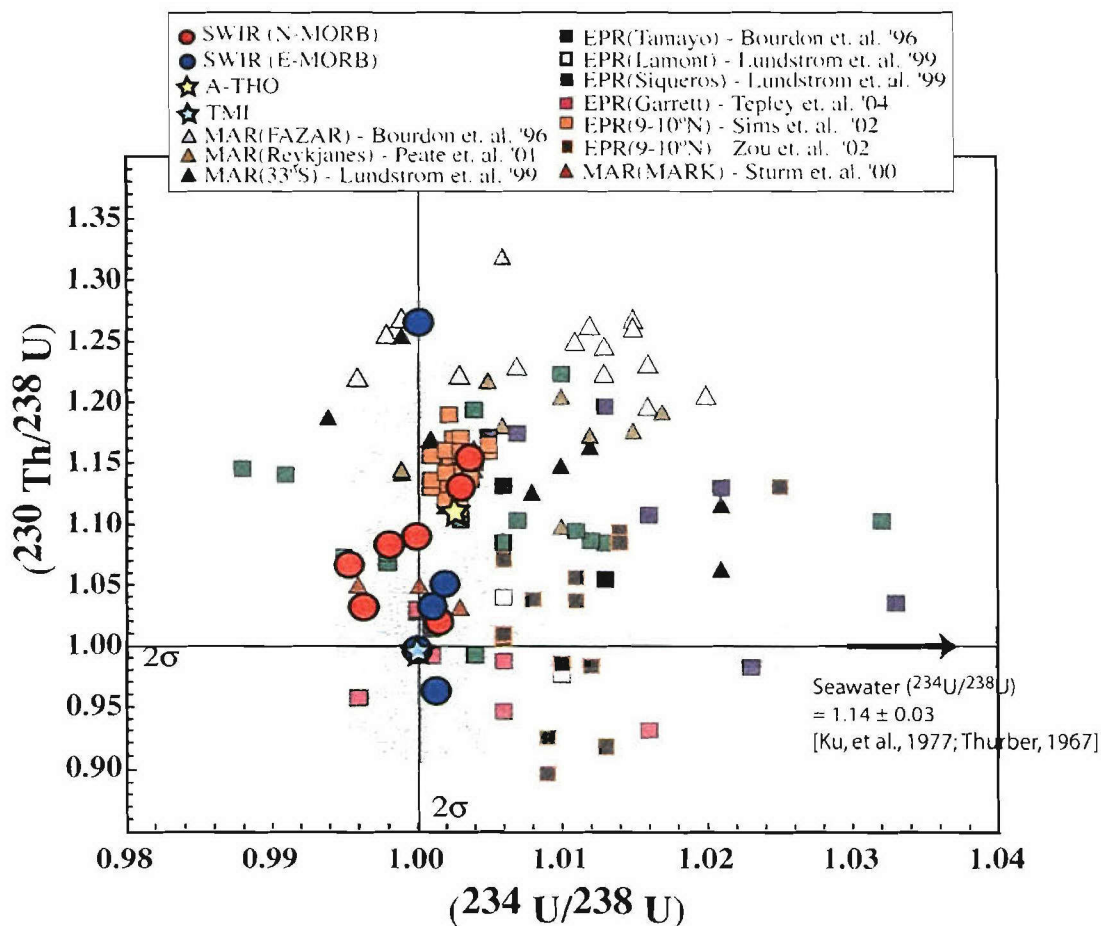
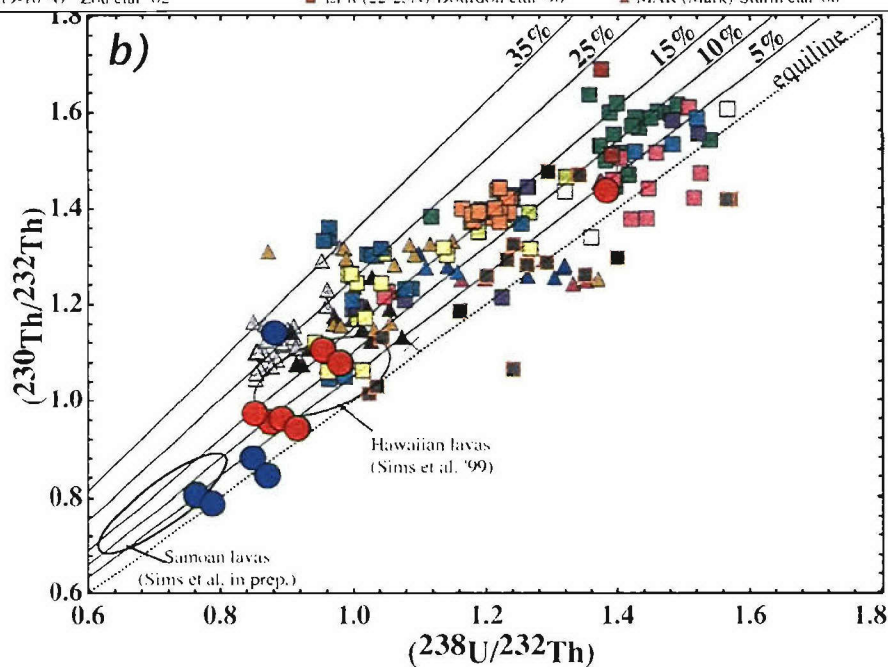
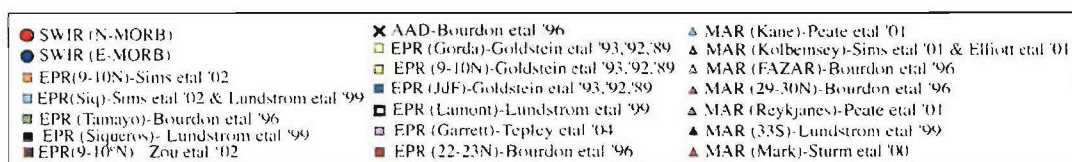
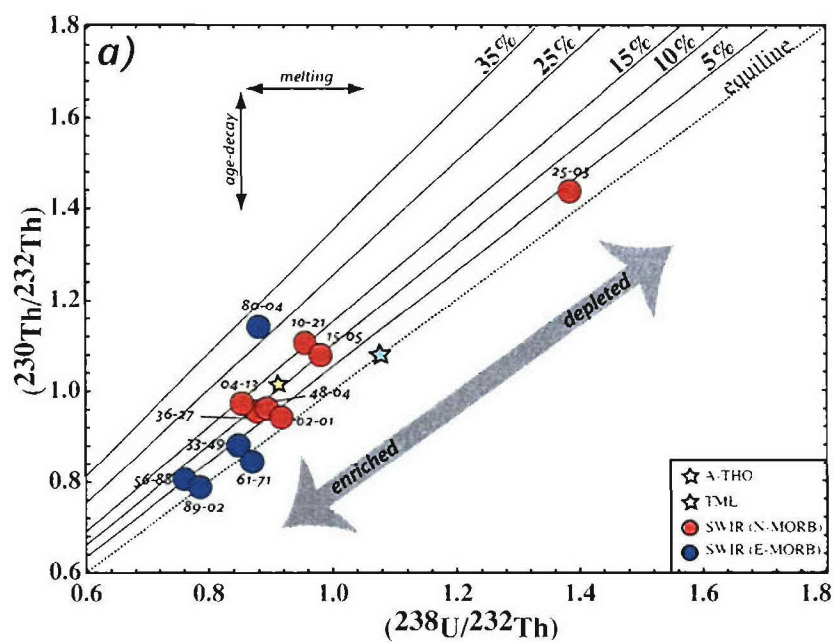
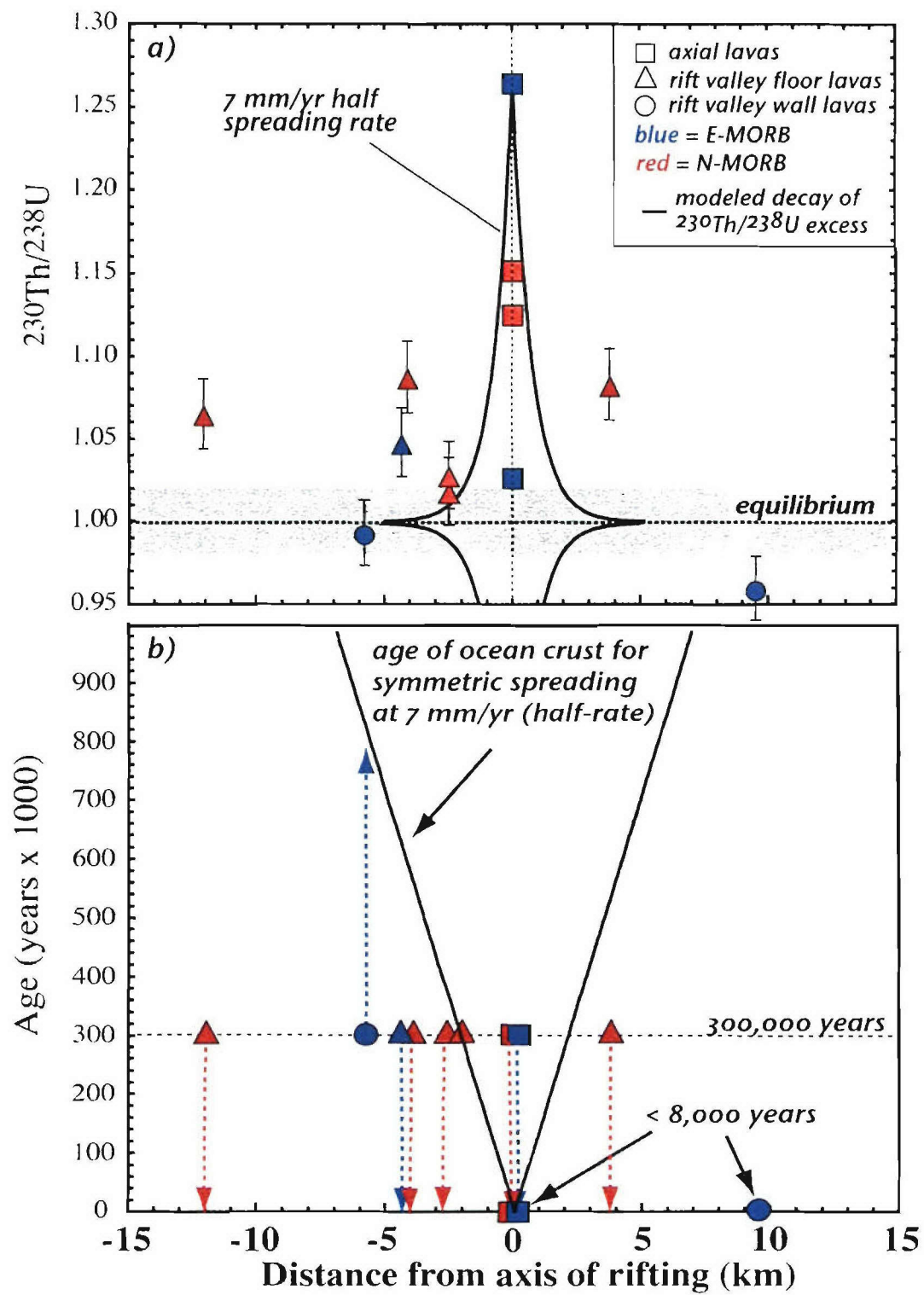


**Figure 6.** ( $^{230}\text{Th}/^{238}\text{U}$ ) vs. ( $^{234}\text{U}/^{238}\text{U}$ ) for twelve Southwest Indian Ridge basalts (N-MORBs = red, E-MORBs = blue), and each data point represents the average value of 2 or 3 duplicate measurements, with ( $^{234}\text{U}/^{238}\text{U}$ ) reproducibility < 5‰. Yellow star represents rock standard A-THO with accepted ( $^{230}\text{Th}/^{238}\text{U}$ ) = 1.12 and ( $^{234}\text{U}/^{238}\text{U}$ ) = 1.0, and blue star represents rock standard TML with accepted ( $^{230}\text{Th}/^{238}\text{U}$ ) = 1.0 and ( $^{234}\text{U}/^{238}\text{U}$ ) = 1.0. Grey fields reflect 2 $\sigma$  error for our measurements. All Southwest Indian Ridge basalts are within 2 $\sigma$  of ( $^{234}\text{U}/^{238}\text{U}$ ) = 1, and therefore show no indication of seawater contamination.



(opposite page)

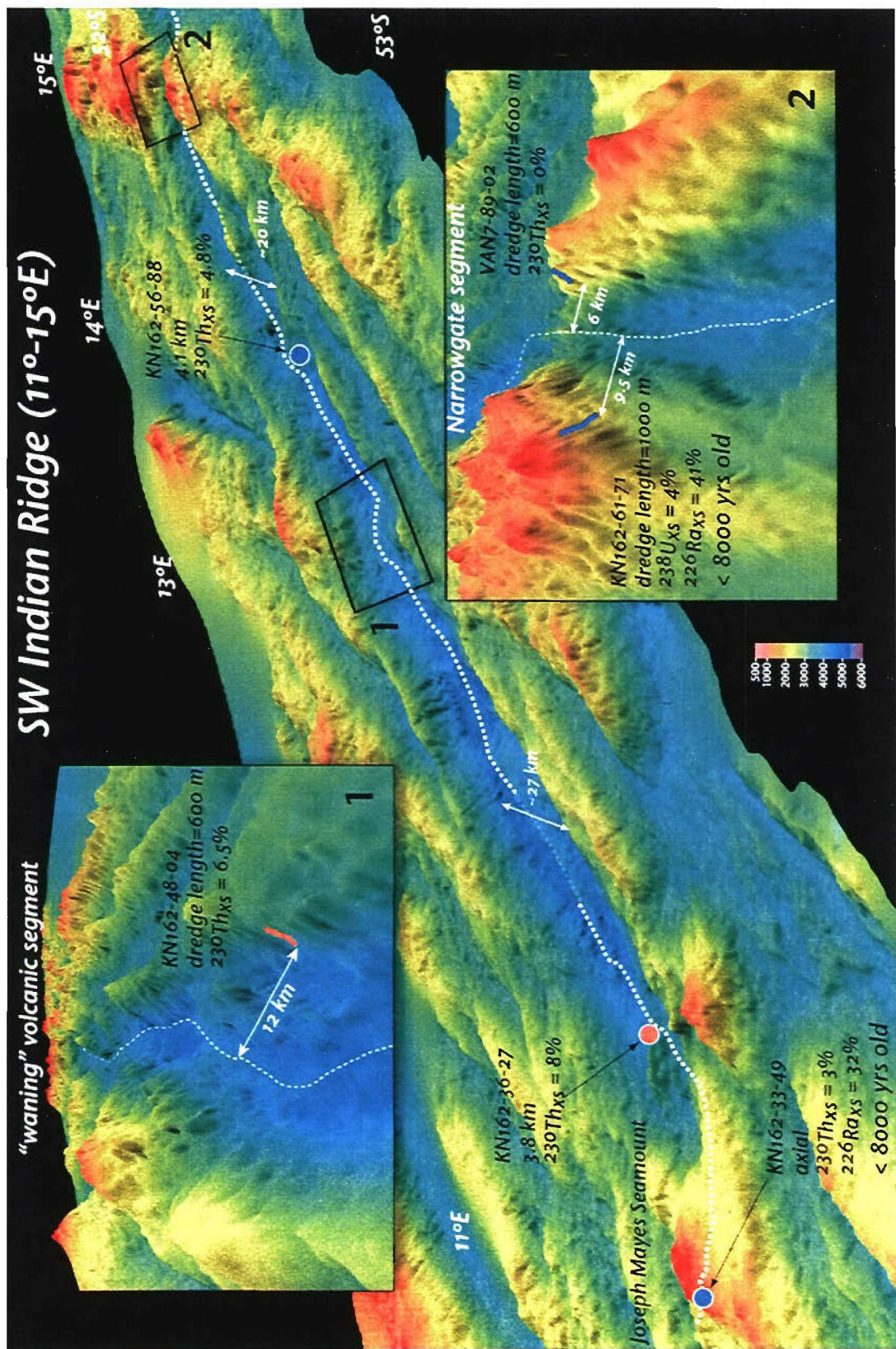
**Figure 7.** a)  $(^{238}\text{U}/^{232}\text{Th})$  vs.  $(^{230}\text{Th}/^{232}\text{Th})$  “equiline diagram” for Southwest Indian Ridge basalts, and b)  $(^{238}\text{U}/^{232}\text{Th})$  vs.  $(^{230}\text{Th}/^{232}\text{Th})$  “equiline diagram” for global MORB dataset. Data symbols the same as in Figure 5, with additional MORB datasets listed in key above. 1:1 equiline showing secular equilibrium, with contours of  $^{230}\text{Th}$  excess included. SW Indian Ridge basalts range from depleted N-MORB (high  $(^{238}\text{U}/^{232}\text{Th})$ ) to highly enriched MORB, in the vicinity of Samoan OIBs.





(opposite page)

**Figure 8.** **a)** ( $^{230}\text{Th}/^{238}\text{U}$ ) disequilibria in Southwest Indian Ridge basalts versus the distance from the axis of rifting. Sample symbols same as Fig. 2. Solid black curves represent modeled maximum excess  $^{230}\text{Th}$  and excess  $^{238}\text{U}$  decay curves, assuming maximum initial excess  $^{230}\text{Th}$  measured in 'axial' basalt of  $(^{230}\text{Th}/^{238}\text{U}) = 1.26 \pm 2\%$  and symmetric spreading at 7 mm/yr half-rate. **b)** Th and Ra disequilibria age constraints. Solid black curve represents the calculated age relative to distance from rift-axis, assuming a 7 mm/yr half-rate. Lavas that sit on 300 ka isochron and have dotted arrows extending down to younger ages have  $^{230}\text{Th}$  excesses, with lines reflecting absolute ages < 300 ka. A single basalt (89-02) lies 6 km 'off-axis' and has no  $^{230}\text{Th}$  excess, thus its arrow points up reflecting an absolute age between 300ka and ~800 ka. Two 'axial' lavas and one rift valley wall lava have  $^{226}\text{Ra}$  excesses and thus ages < 8 ka.



(opposite page)

**Figure 9.** 3D bathymetric image of the Southwest Indian Ridge from 11°-15°E. Assumed axis of rifting is marked by dashed white line (faded white line where axis is hidden by topography). White arrows on the main image note the rift valley width in the direction of plate spreading. Blue dots represent E-MORB sample locations measured for U-Th disequilibria, with associated text listing sample name, distance from the rift axis, and  $^{230}\text{Th}_{\text{xs}}$ . *Inset 1* - Detailed bathymetry of “waning” volcanic segment from ~13°E. Dashed white line designates volcanic/rift axis and white arrow indicates distance from axis for the designated dredges (similar notations for inset 2). Dredge track is red to indicate N-MORB and the position is based on recorded depths from the start and end of the dredge. Associated text for both insets lists sample name, dredge track length, and U-Th-Ra disequilibria measurements. *Inset 2* – Detailed bathymetry of the Narrowgate segment viewed from the west. Dredge tracks are blue to indicate E-MORB and their positions are once again based on recorded depths from the start and end of each dredge.

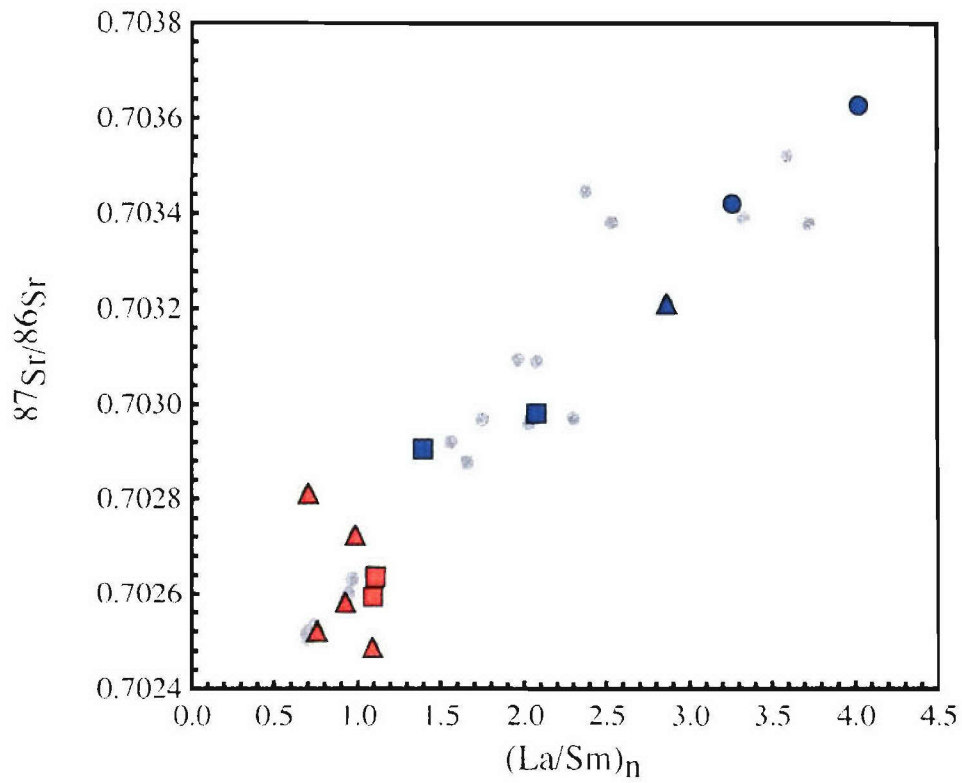
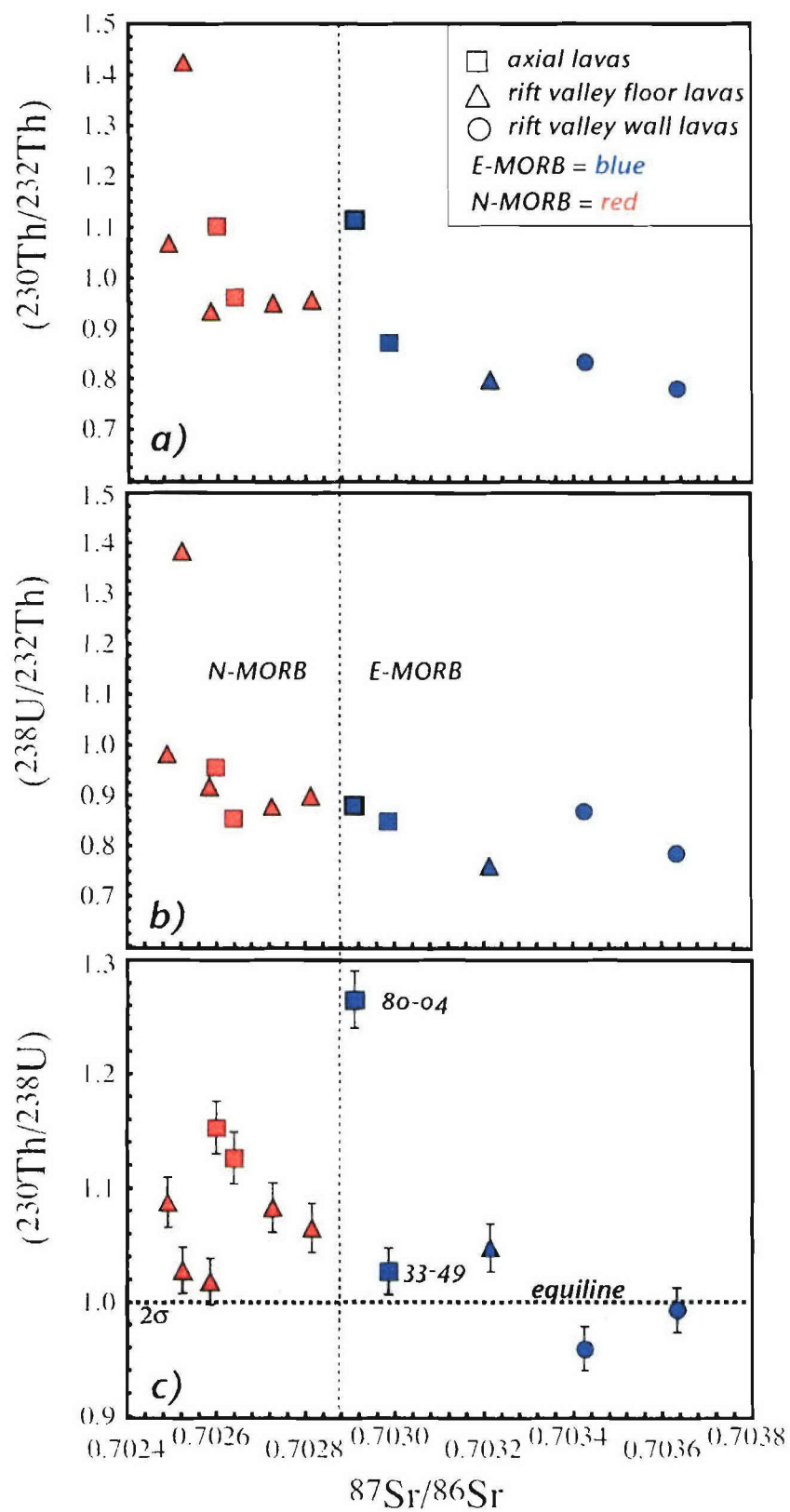


**Figure 9.**  $^{87}\text{Sr}/^{86}\text{Sr}$  vs.  $(\text{La}/\text{Sm})_n$  for Southwest Indian Ridge basalts. Symbols same as previous figure; grey dots represent other lavas from this suite that have not been measured for U-Th-Ra disequilibria.  $(\text{La}/\text{Sm})_n$  has been normalized by C1-chondrite [Sun & McDonough, 1989].



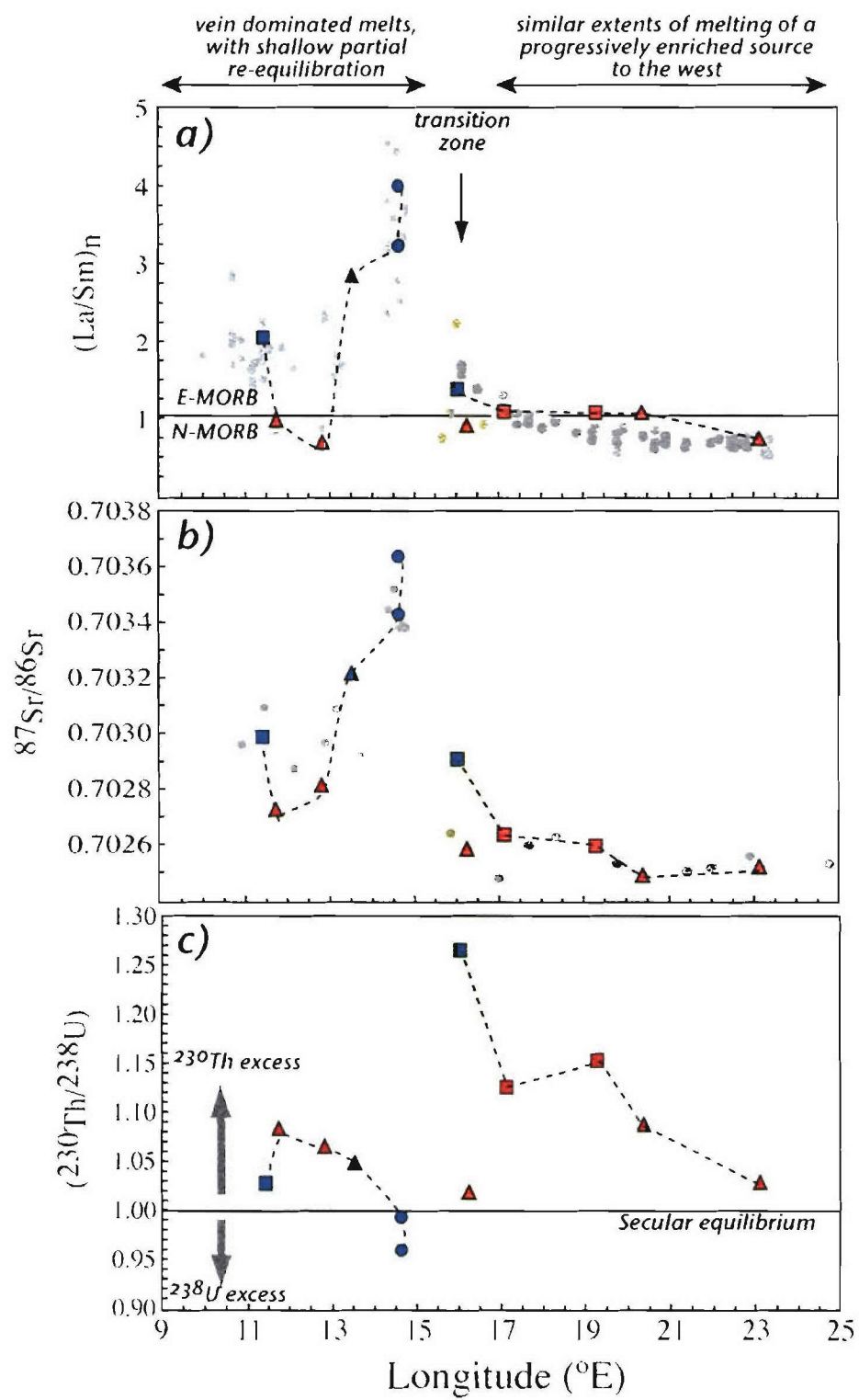


(previous page)

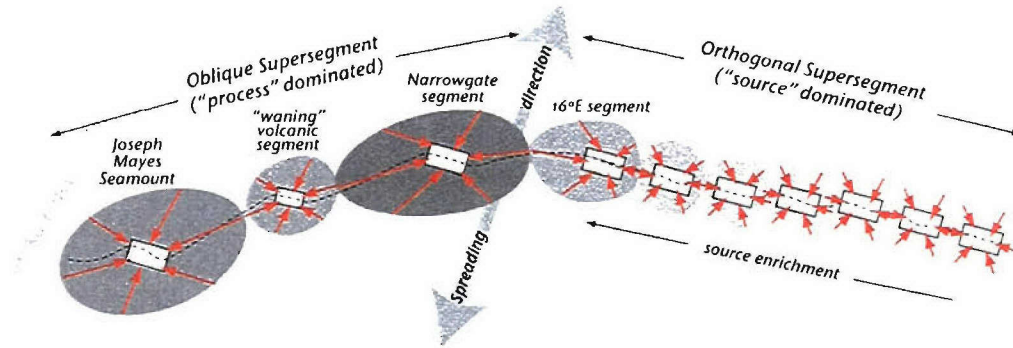
**Figure 11.** a) ( $^{230}\text{Th}/^{232}\text{Th}$ ) vs.  $^{87}\text{Sr}/^{86}\text{Sr}$ , b) ( $^{238}\text{U}/^{232}\text{Th}$ ) vs.  $^{87}\text{Sr}/^{86}\text{Sr}$ , c) ( $^{230}\text{Th}/^{238}\text{U}$ ) vs.  $^{87}\text{Sr}/^{86}\text{Sr}$  for Southwest Indian Ridge basalts. Symbols same as Figure 2. Error bars for a) & b) are similar to symbol size. Dotted line indicates local division between N-MORB and E-MORB.

(opposite page)

**Figure 12.** Along-axis variation of a)  $(\text{La}/\text{Sm})_n$ , b)  $^{87}\text{Sr}/^{86}\text{Sr}$ , and c) excess  $^{230}\text{Th}$  for lavas between 9°-25°E. Sample symbols same as Figure 2, with light grey dots in a) & b) representing the full suite of basalts from Chapter 3. Light grey arrows indicate general enrichment trend along orthogonal supersegment. Yellow vertical field marks the 16°E volcanic segment, termed the “transition zone”, as lavas from this segment reflect the influence of both “source” and “process”.



### Segmentation and Melt Generation Regions



### Relative Length-Scales for Melt Generation Regions

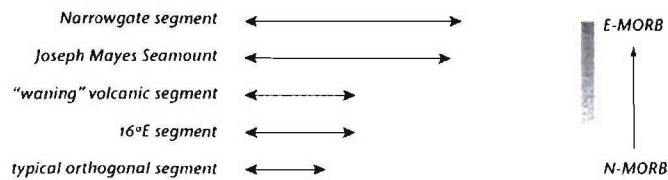


**Figure 13.** Schematic depiction of the volcanic segmentation and resulting along-axis length-scales of melt generation regions between 9°-25°E on the Southwest Indian Ridge. Volcanic segments are represented by white rectangles, which are linked by non-transform offsets (orthogonal supersegment) or oblique amagmatic accretionary segments (oblique supersegment). A dashed black line marks the axis of rifting with spreading direction indicated by the large grey arrow. Each volcanic segment is supplied with melt by a generation region (similar in concept to “source volume” [Plank and Langmuir, 1992]), shown by grey fields, which is a function of the segment spacing and along-axis lithospheric topography. Each generation region is colored a varying shade of grey to reflect the incompatible element and radiogenic isotopic enrichment, with light colors signifying depleted N-MORB compositions and dark grey E-MORB. Red arrows suggest general pathways of melt focusing both along- and across-axis. The relative length-scales of the variable melt generation regions are compared, with their associated basalt chemistry indicated, suggesting a mechanism for producing the range from N-MORB to E-MORB. With similar segmentation on the orthogonal supersegment it is inferred that the variable source composition controls the basalt chemistry. However on the oblique supersegment, the variation in source composition (altogether more enriched) is accompanied by the effects of “process”, which includes but is not limited to, segment spacing, lithospheric topography, melt focusing, and degree of melting.

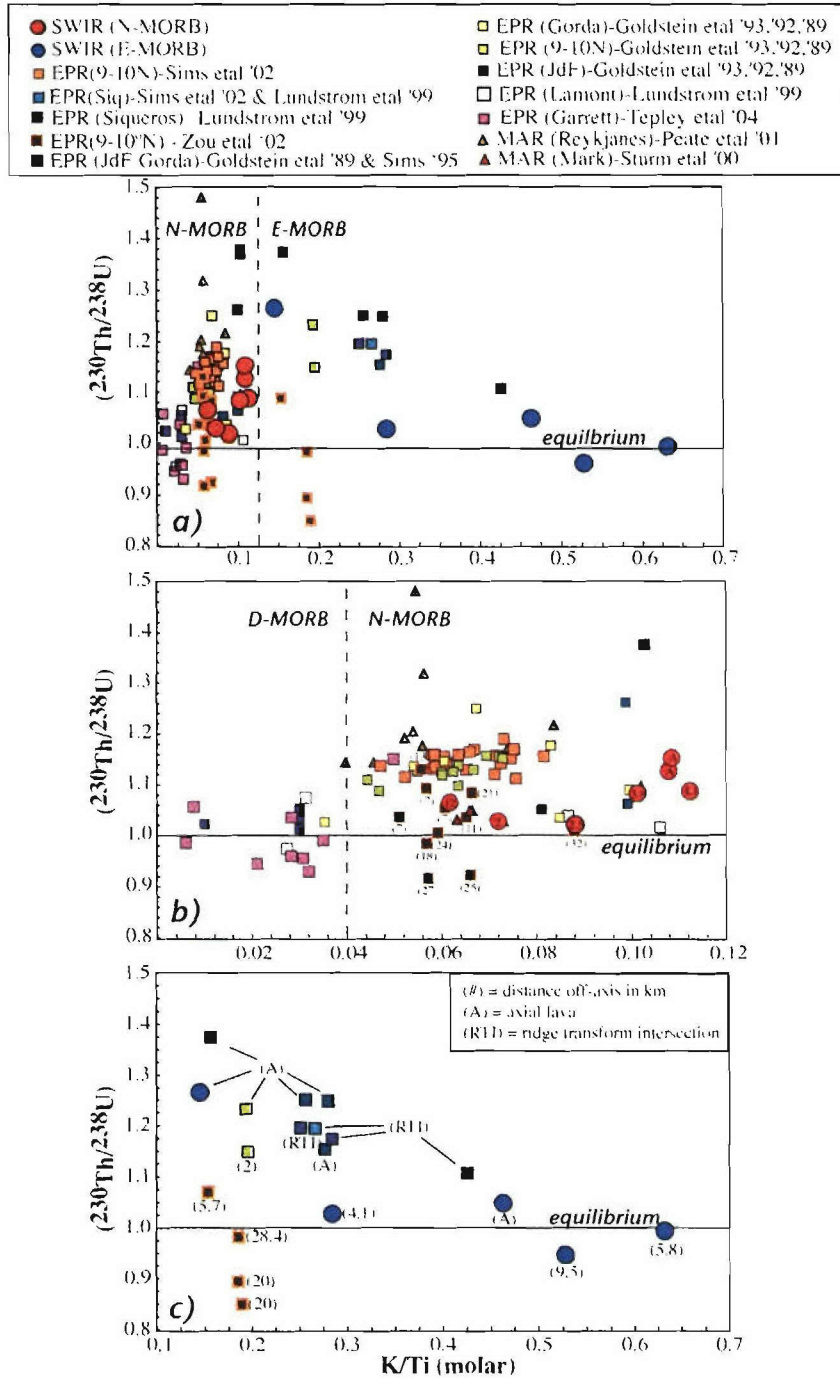


**Figure 14.**  $^{230}\text{Th}/^{238}\text{U}$  versus  $\text{K}/\text{Ti}$  for a) global dataset, b) global N-MORBs, and c) global E-MORBs. References for data are listed in legend, with samples from Southwest Indian Ridge as in Figure 6. Please note that the x-axis range for  $\text{K}/\text{Ti}$  is different for a), b), and c).

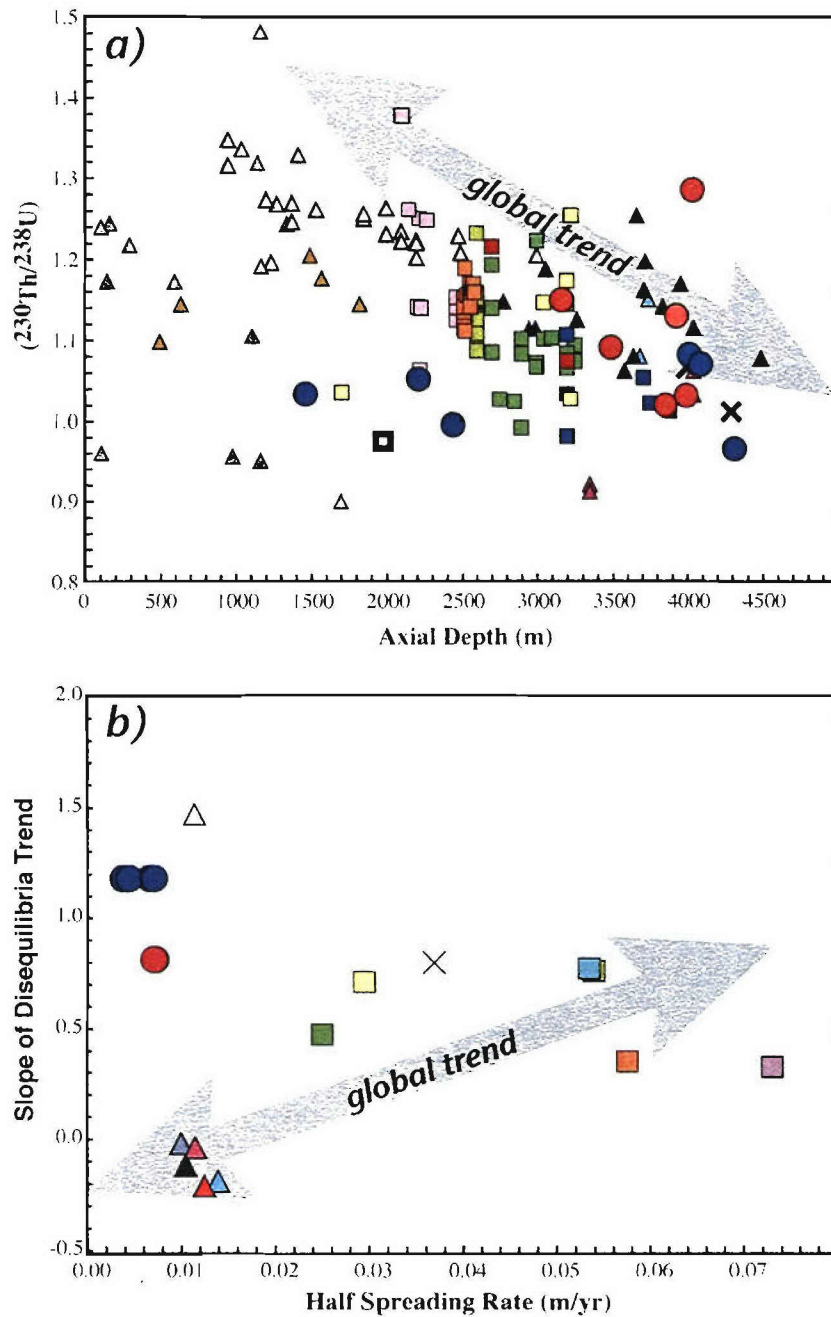
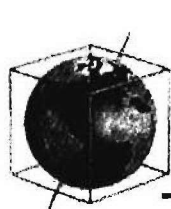


**Figure 15.** Global MORB trends of a)  $(^{230}\text{Th}/^{238}\text{U})$  versus depth from *Bourdon et al.*, [1996b] and b) slope of disequilibria trend versus half spreading rate from *Lundstrom* [2003] for segment averages. MORB sample symbols are same as in Figure 7, sample symbols for Southwest Indian Ridge reflect orthogonal supersegment lavas (red) and oblique supersegment lavas (blue). Grey arrows indicate general global trends suggested by respective authors.



***Chapter 5. Abyssal peridotite osmium isotopic compositions from Cr-spinel***

(appeared in *Geochemistry, Geophysics, Geosystems*, 3, 24 p., 2002.)



## Abyssal peridotite osmium isotopic compositions from Cr-spinel

J. J. Standish

*Massachusetts Institute of Technology Joint Program/Woods Hole Oceanographic Institution, Woods Hole, Massachusetts 02543, USA (jstandish@whoi.edu)*

S. R. Hart, J. Blusztajn, and H. J. B. Dick

*Woods Hole Oceanographic Institution, Woods Hole, Massachusetts 02543, USA (shart@whoi.edu; jblusztajn@whoi.edu; hdick@whoi.edu)*

K. L. Lee

*100 Foster-Sheldon Road, Wakefield, Rhode Island 02879, USA*

[1] Abyssal peridotites, fragments of residual upper oceanic mantle, are believed to have less radiogenic Os compositions and higher Os concentrations than primitive upper mantle (PUM,  $^{187}\text{Os}/^{188}\text{Os} = 0.129$  [Meisel *et al.*, 1996]). We have measured  $^{187}\text{Os}/^{188}\text{Os}$  in 10 whole rock abyssal peridotites representing non-plume-influenced mid-ocean ridge segments. The  $^{187}\text{Os}/^{188}\text{Os}$  ratios range from 0.1183–0.1582. This large range in Os composition, to both less radiogenic and more radiogenic values than primitive upper mantle, can be attributed to ancient melting and subsequent sequestering of isotopic signatures, melt-rock reaction, or secondary alteration, or a combination of any of the three. Petrographic, electron microprobe, and hand-sample inspection show the peridotites to have experienced varying amounts of serpentinization and weathering, accompanied by heterogeneity in  $^{187}\text{Os}/^{188}\text{Os}$  values. In addition, a majority of the peridotites studied here are spatially associated with gabbros having equally, if not more highly, heterogeneous Os isotopic compositions and N-MORBs with homogeneous Sr, Nd, and Pb isotopic signatures. This suggests secondary seawater alteration as the dominant influence on present-day Os signatures. We show that careful separation, leaching, and analysis of Cr-spinel from abyssal peridotite largely removes the radiogenic seawater Os isotopic signature, allowing a more accurate assessment of the Os signature of depleted mid-ocean ridge basalt mantle (DMM). Cr-spinel is a highly refractory mantle mineral and commonly host to tiny sulfide inclusions, which are carrier phases for Os. These sulfides are well protected by the Cr-spinel from high-temperature serpentinization and low-temperature seafloor weathering, thereby preserving nonradiogenic DMM-like Os isotopic signatures. Our analyses of treated Cr-spinel fractions finds  $^{187}\text{Os}/^{188}\text{Os}$  ratios that are dominantly less radiogenic (0.1238–0.1482) than corresponding whole rock compositions. Nonmagnetic Cr-spinels show more highly variable Os compositions and concentrations than magnetic Cr-spinels, overlapping with the more radiogenic whole rock values. Magnetic Cr-spinels are dominantly less radiogenic than PUM, with high but variable Os concentrations, possibly resulting from a sulfide “nugget” effect. The systematically lower  $^{187}\text{Os}/^{188}\text{Os}$  in Cr-spinels compared to whole rocks shows that whole rock abyssal peridotites are largely compromised by radiogenic seawater interaction, often obscuring the mantle signature. Measurements of treated abyssal peridotite Cr-spinels in some cases can circumvent this seawater alteration problem allowing more straightforward interpretation of isotopic values and thus further constraining the Os

isotopic signature for the depleted upper mantle. Our results suggest that the  $^{187}\text{Os}/^{188}\text{Os}$  for the upper mantle lies in the range 0.120–0.125.

**Components:** 11,935 words, 7 figures, 3 tables.

**Keywords:** Isotopes; osmium; mantle; heterogeneity; Cr-spinel; serpentinization.

**Index Terms:** 1040 Geochemistry: Isotopic composition/chemistry; 1025 Geochemistry: Composition of the mantle; 3035 Marine Geology and Geophysics: Mid-ocean ridge processes; 3620 Mineralogy and Petrology: Crystal chemistry.

**Received** 19 March 2001; **Revised** 27 August 2001; **Accepted** 17 September 2001; Published 17 January 2002.

Standish, J. J., S. R. Hart, J. Blusztajn, H. J. B. Dick, and K. L. Lee, 2001. Abyssal peridotite osmium isotopic compositions from cr-spinel, *Geochem. Geophys. Geosyst.*, 3(1), 10.1029/2001GC000161, 2002.

**Theme:** Plume-Ridge Interaction

**Guest Editor:** David Graham

## 1. Introduction

[2] A cornerstone assumption of chemical geodynamic theory is that mid-ocean ridge basalt is derived from, and is isotopically representative of, the depleted upper MORB mantle (DMM). This presumption has been difficult to test, owing, on the one hand, to the low concentrations of Sr, Nd, Hf, and Pb in abyssal peridotites [Johnson *et al.*, 1990; Snow *et al.*, 1994], and, on the other hand, to the low Os concentrations in MORB [Roy-Barman and Allègre, 1994; Schiano *et al.*, 1997; Roy-Barman *et al.*, 1998]. The most successful test to date showed that Nd isotopes in carefully leached Cpx from abyssal peridotites are similar to those in nearby MORB [Snow *et al.*, 1994].

[3] When comparing the  $^{187}\text{Os}/^{188}\text{Os}$  values for abyssal peridotites and zero-age MORB, the test for a cogenetic relationship is obscured by the extreme isotopic heterogeneity seen in abyssal peridotites [Roy-Barman and Allègre, 1994; Snow and Reisberg, 1995] and in MORBs [Schiano *et al.*, 1997; Roy-Barman *et al.*, 1998]. This presents the possibility that abyssal peridotites are not direct petrogenetically related residues of recent mid-ocean ridge basalt (MORB) melting [Esperanca *et al.*, 1999; Brandon *et al.*, 2000], thereby adding uncertainty to the use of MORB for isotopic fingerprinting of the upper mantle. Inherent mantle heterogeneity has been suggested to explain the wide range of osmium compositions on large scales but

may be difficult to justify on small scales, especially considering the recent work by Brenan *et al.* [2000] on closure temperatures for Os diffusion in sulfide. Alternatively, we argue that most abyssal peridotite Os compositions have been compromised by exposure to radiogenic Os during interaction with seawater. This is not surprising, since abyssal peridotites are arguably the most altered mantle rocks routinely studied and are nearly completely serpentinized (50–90%) and frequently weathered [Snow and Dick, 1995]. This study provides evidence that abyssal peridotite whole rock Os compositions are elevated owing to a radiogenic seawater component but that this alteration problem can be circumvented by analyzing Os from carefully treated Cr-spinels separated from abyssal peridotites. Cr-spinels have been utilized successfully in several previous Os isotope studies of peridotitic massifs, layered intrusions, and ophiolites [Marcantonio *et al.*, 1993; Meisel *et al.*, 1997; Walker *et al.*, 1996].

[4] Cr-spinel is a ubiquitous, accessory phase in mantle lithologies [Dick and Bullen, 1984] and is, furthermore, the most resistant mantle phase during low-temperature metamorphism and alteration. Recent work has shown Cr-spinel to be a common host of sulfide inclusions, which have been shown to be one of the principal Os carrier-phases in the mantle [Morgan, 1986; Hart and Ravizza, 1996; Burton *et al.*, 1999]. Utilizing the Os isotopic composition of spinel, we address two questions:

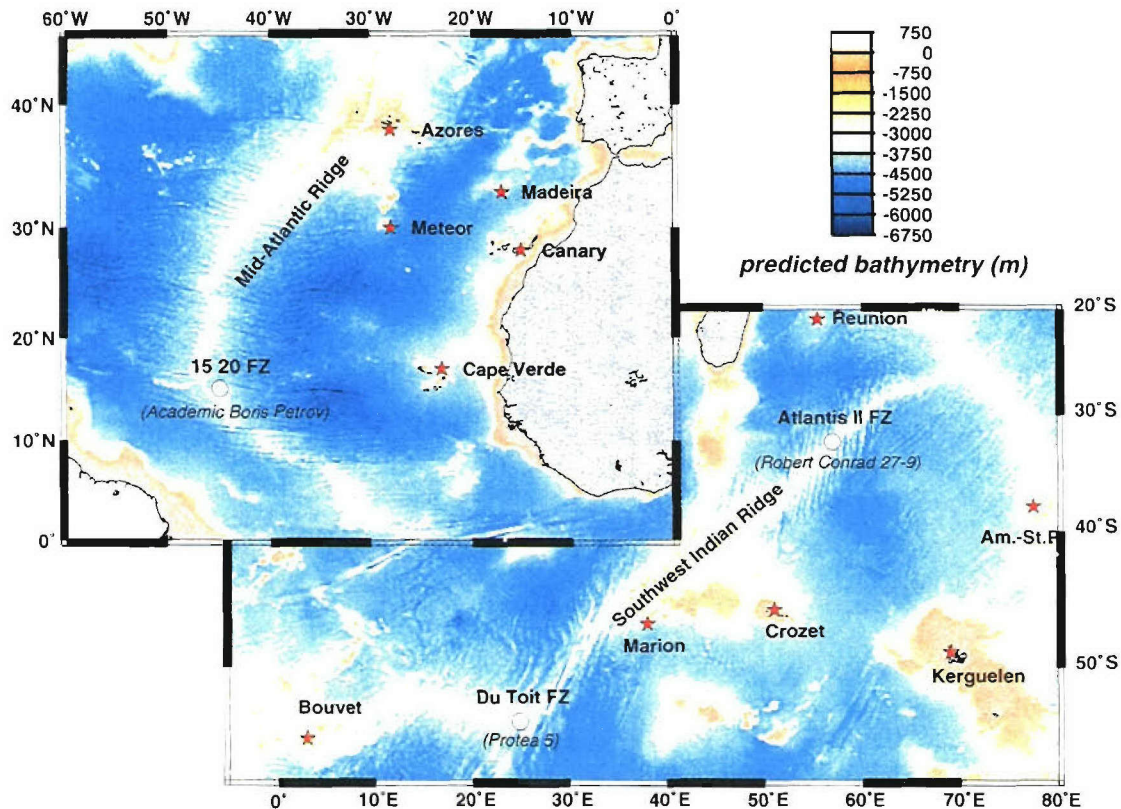


**Figure 1.** Predicted bathymetry [Smith and Sandwell, 1997] with abyssal peridotite sample locations denoted by white circles. Note the distance between sample locations and mantle plume locations (red stars). Associated cruise names are given in parentheses.

(1) what is the mineralogic heterogeneity of Os isotopes in the upper mantle and (2) what is the Os isotope signature of the depleted MORB mantle. The Re/Os system is useful for addressing questions concerning mantle evolution as, unlike the other long-lived radiogenic isotope systems, Os is compatible in mantle lithologies during melting and will tend to be enriched in residues. Because the parent, Re, is mildly incompatible in mantle lithologies, the residues of melting will have lowered Re/Os ratios, which over time will lead to unradiogenic Os isotope signatures in the residual peridotites. The Re/Os system provides a unique window into, and added constraints on, the mid-ocean ridge melting process; yet a great deal of uncertainty still exists.

[5] Presuming the seawater Os alteration problem can be solved, abyssal peridotites are ideal for addressing these questions. Whereas abyssal peridotite exposures were once thought to be limited to transform fracture zones, they are now known to be

quite widespread. Various studies have reported abyssal peridotites dredged from rift valleys [Karson and Winters, 1992; Aumento and Loubat, 1970; Meyer *et al.*, 1989; Mével *et al.*, 1991; Cannat *et al.*, 1992; Bougault *et al.*, 1993; Cannat *et al.*, 1995], transform faults on fast spreading ridges [Cannat *et al.*, 1990; Hebert *et al.*, 1983], propagating rifts in fast spreading environments [Gillis *et al.*, 1993; Francheteau *et al.*, 1990; Hekinian *et al.*, 1993; Dick and Natland, 1996], and peridotite massifs of large aerial extent on the ocean floor [Dick, 1989; Bonatti *et al.*, 1971; Engel and Fisher, 1975; Bougault *et al.*, 1993; Cannat and Casey, 1995].

## 2. Geology and Sample Description

[6] Our peridotite suite includes samples from the Atlantis II Fracture Zone (31°S, 57°E) and the Du Toit Fracture Zone (FZ) (53°S, 25.5°E), both part of the Southwest Indian Ridge, and samples from the



15°20' FZ (15.3°S, 46°W), on the Mid-Atlantic Ridge (Figure 1). Detailed studies of these abyssal peridotites and their respective locations are presented elsewhere [Dick *et al.*, 1991; Fisher *et al.*, 1986; Roest and Collette, 1986; Snow *et al.*, 1987; le Roex *et al.*, 1989; Grindlay *et al.*, 1998]. Samples from these fracture zones were chosen for study because they are situated between “normal” ridge segments far from any mantle plumes and thus escape the chemical influence of hot spot material. Although these three locations are all non-plume-influenced fracture zones, the spreading ridges upon which they are situated are variable (i.e., spreading rate). For example, the SWIR geochemistry is highly variable along its length from the Bouvet Triple Junction to the Indian Ocean Triple Junction. This may be a function of the changing spreading rates or reflective of heterogeneous mantle source regions. In this study the samples are grouped together as normal MORB peridotites, but it should be remembered that the isotopic and geochemical differences between fracture zone samples could be highly dependant on the spreading ridge characteristics and the underlying mantle lithologies.

[7] Our sample suite consists of harzburgites, lherzolites, and dunites, all of which have experienced varying degrees of serpentinization and weathering. The peridotites show a variety of textures and alteration stages. Rock color often indicates the degree of serpentinization and/or weathering: orangish-brown to tan coloring indicating moderate to high weathering of olivine to clay, while green and black colors indicate fresher, less weathered but usually highly serpentinized rocks. Petrographically, the peridotites show typical alteration features. Replacement of olivine, opx, and cpx is fairly widespread; a point count of sample RC 27-9-6-2 (lherzolite) reported by Snow and Dick [1995] puts the pre-alteration modal proportions at 48.2% olivine, 45.1% orthopyroxene, 6.1% clinopyroxene, 1.2% spinel, and 0.41% plagioclase. Primary olivine modal proportions in the rest of the harzburgites and lherzolites are generally >70% with orthopyroxene between 15 and 30% and clinopyroxene ranging from 0 to 11%. Protogranular textures dominate

the less altered peridotites, but little can be said concerning the primary textural relationships in the peridotites with high proportions of secondary minerals. Replacement of primary silicates is often accompanied by reddish-brown, Fe-oxidation minerals, and indicated by high proportions of serpentine (lizardite) and magnetite.

[8] Spinel is a common accessory mineral in abyssal peridotites, generally amounting to 0.25–1.0% in harzburgites and lherzolites. In dunites, spinel may be absent or, in rare cases, as much as 16% of the modal rock composition. The resistant nature of spinel results in the presence of fresh to moderately altered grains in peridotites that have otherwise undergone significant serpentinization. Sample RC27-9 6-2 has been shown to contain a significant amount of sulfide, present as interstitial grains, inclusions in pyroxene, and separate grains within alteration veins [Lee, 1997]. Petrographic investigation of the other peridotites found scattered sulfides (>1  $\mu\text{m}$ ) occasionally occurring within silicate hosts and along pyroxene exsolution lamellae. In a few thin sections there exist sulfide grains up to  $\sim 60 \mu\text{m}$ , often times associated with multiple smaller sulfide globules. The lack of visible sulfides in some samples containing high concentrations of osmium indicates that the bulk of the osmium must be contained in “ultra-trace phase” sulfide micro-inclusions [Shirey and Walker, 1998] within spinel.

### 3. Sample Preparation and Leaching

#### 3.1. Whole Rock

[9] From each peridotite, we crushed 150–200 g of rock to centimeter-sized chips using a steel jaw crusher. Careful inspection of the sample for shards of steel was conducted prior to further crushing. In a later group of whole rock samples, we tested a new method of rock pulverization called “electric pulse disintegration.” In this technique the sample chips sit in a water bath, which is charged with rapid electric pulses from a high-voltage power source. The sample is virtually exploded, which occurs preferentially along grain boundaries. As a result, individual undamaged mineral grains can be recovered. This method proved satisfactory as a prepow-



dering step and will be used in future sample preparation, thereby eliminating the threat of metal contamination. (Note that the whole rock sample ABP 16-71-22 was measured using both crushing techniques, and the Os compositions are nearly identical, indicating no detectable metal contamination from the jaw crusher.) After thorough inspection, the sample was powdered using an agate puck grinder. The powdered whole rock sample (1.5 g) was spiked with an in-house mixed spike enriched in  $^{99}\text{Ru}$ ,  $^{105}\text{Pd}$ ,  $^{190}\text{Os}$ ,  $^{191}\text{Ir}$ , and  $^{198}\text{Pt}$ . The sample and spike mixture was mechanically mixed and left overnight in a covered ceramic crucible at 40°C. The mixture was then combined with 3.6 g of flux, consisting of 0.20 grams of sulfur, 0.40 grams of nickel, and 3.0 grams of Na-borate; 1:2:15 flux proportions. Whole rock crucibles were fused at 1020°C for 1.5 hours. Complete tracer/sample equilibration is obtained during fusion and can be monitored during sparging. A detailed description of NiS fire assay is given in *Ravizza and Pyle [1997]*. Sample chemistry for ICP-MS sparging is briefly described in sections 3.3 and 4.2 and in detail by *Hassler et al. [2000]*.

[10] We selected whole rock sample RC27-9-34-84 to test for potential low-temperature Os degassing prior to fusion. We placed 1.5 g of sample powder in a ceramic crucible in the furnace at 400°C for 5 hours. The sample was cooled and then spiked before proceeding with the presparging chemistry as described in section 4.2.

### 3.2. Spinel

[11] The whole rock peridotite (150–200 g) was crushed to chip size and then placed in a disc mill and ground to <1 mm. From microprobe analysis we know that alteration rinds of “ferrite-chromite” and/or magnetite exist on and within the spinel and are due to serpentinization and low-temperature weathering. This secondary component is formed in the presence of radiogenic seawater Os, thus we used a two-step technique to ensure removal of as much of this seawater-compromised component as possible. Through continued crushing, using a steel diamond mortar, to <500  $\mu\text{m}$ , we were able to expose most of the altered spinel surfaces. Samples were inspected under the microscope for steel shards, which were

subsequently removed by hand. Thorough decanting removed the finest size fraction in preparation for heavy liquid separation. The sample was poured into a glass separation column with methylene iodide (specific gravity = 3.32). The heavy mineral separate was dominated by spinel (~70–80% on average), with some olivine and clinopyroxene. Both mineral fractions were thoroughly rinsed with acetone and dried. The spinel-rich fraction was then separated further into a magnetic and nonmagnetic fraction using a hand magnet. Both magnetic and nonmagnetic fractions were purified by extensive handpicking of silicate phases under a microscope. Prior to leaching, the samples were 85–99% pure spinel. Much of the remaining silicate was not easily separated mechanically because it existed interstitially with spinel.

[12] Mineral separates were then leached (section 3.3) and powdered under acetone, using an agate mortar. The sample powders were weighed in a ceramic crucible and then spiked with one of two tracers, both enriched in varying proportions of  $^{99}\text{Ru}$ ,  $^{105}\text{Pd}$ ,  $^{190}\text{Os}$ ,  $^{191}\text{Ir}$ , and  $^{198}\text{Pt}$ . Sample/spike mixtures were left on the hotplate overnight at 40°C to dry. Added to each sample in the following proportions 8:2:1 were 2.0 grams Na-borate, 0.5 grams nickel, and 0.25 grams sulfur. Each crucible was then placed in the oven for 1.5 hours at 1020°C. The nickel sulfide beads were weighed to evaluate fusion sample recovery (60–70% on average), followed by sparging chemistry as explained in section 4.2.

### 3.3. Leaching

[13] Each Cr-spinel fraction (magnetic and nonmagnetic) was leached prior to powdering under acetone. The following three solutions comprised the leaching sequence: (1) 6.2 N HCl, (2) 70% concentrated HF, 15% 6.2 N HCl, 15% concentrated  $\text{HNO}_3$ , and (3) concentrated HCl. Up to 250 mg of sample was placed in 1–2 mL of 6.2 N HCl at room temperature in a sealed, 4 mL Teflon vial. After 1 hour, the HCl was pipetted away, and the sample was rinsed with ultrapure water and dried. To the beaker 1–2 mL of HF/HCl/ $\text{HNO}_3$  solution was added and sealed, then placed on a hotplate at 100°C for 5 hours. (Note that the samples with

high Ca content, likely present as interstitial clinopyroxene, formed CaF during this step. This precipitate appeared as a thin white layer on the spinel. To deal with CaF precipitation we completely dried down the HF/HCl/HNO<sub>3</sub> solution, allowing fluorine to fume off, thereby breaking down the CaF. Samples that did not precipitate CaF had the HF/HCl/HNO<sub>3</sub> solution pipetted away and were rinsed with ultrapure water and dried. The final step used 1–2 mL of concentrated HCl. The beaker was sealed and sonicated for 45 min at room temperature. The HCl was pipetted away, and the sample was thoroughly rinsed with ultrapure water and dried.

[14] Sample RC 27-9-34-84m (previously measured  $^{187}\text{Os}/^{188}\text{Os} = 0.1289$ ) was subjected to a particularly rigorous leaching sequence to evaluate the affects of extensive leaching. The sample was leached with the same solutions, but the length of each leaching step was increased. Step 1, which involved the 6.2 N solution, was stretched from 1 hour to 3 days. Step 2, with the HF/HCl/HNO<sub>3</sub> solution, was lengthened from 5 hours to 20 hours at 100°C. Step 3 was increased from 45 min to 1 hour of sonication, and an additional hour in the beaker was added as well.

### 3.4. Leachates

[15] We carefully separated spinel leachate solutions for direct ICP-MS sparging. From each spinel leach we pipetted/decanted the leachate into a 4 mL Teflon beaker. To dilute the platinum group element (PGE) concentrations of the solution, 1 mL of ultra-pure water was added. The leachates were split in half, with the second split set aside for future PGE spiking and ICP-MS sparging to determine Os concentration. To each of the HCl leachates (both 6.2 N and concentrate) a drop of ethanol was added to maintain a reducing environment. The HCl leachates were dried down and then put back into solution with concentrate HNO<sub>3</sub> and transferred into a 24 mL screw cap beaker. The diluted (1 mL ultrapure water) HF/HCl/HNO<sub>3</sub> leachates were transferred to a 24 mL Teflon beaker and sealed tightly with Teflon tape to limit loss of oxidized Os. Just prior to sparging, the leachates were chilled on ice,

further diluted with ultrapure water, and sparged directly into the ICP-MS.

## 4. Analytical Methods

### 4.1. Mineral Data

[16] Spinel and sulfide chemistry was determined using the JOEL JXA-733 Superprobe at the MIT Electron Microprobe Facility. Multiple spinel and sulfide grains from selected samples were analyzed at 15 kV accelerating voltage and a probe current of 10 nA. The spot size was held constant at 10 microns, and the counting time per element was 10–40 s. Count times during sulfide analysis were generally 40 s, except for S at 120 s. Analyses were calibrated using synthetic standards. The data were reduced with the CITZAF program [Armstrong, 1995] using the atomic number correction of Duncumb and Reed, Heinrich's tabulation of mass absorption coefficients, and the fluorescence correction of Reed.

### 4.2. Sparging

[17] The NiS beads from the whole rock and Cr-spinel fusions were dissolved in 6.2 N HCl at ~150°C and filtered through a 0.45  $\mu\text{m}$  cellulose filter. The filter paper was then dissolved in 1–2 mL concentrated HNO<sub>3</sub>, in a 24 mL Teflon screw-cap beaker at room temperature. Oxidation of Os to OsO<sub>4</sub> was achieved by placing the tightly sealed beaker on a hotplate at 100°C the night prior to sparging. Before preparing the solution for sparging, it was chilled on ice for at least 1 hour. The acid solution was then diluted ~10-fold with ultrapure water and a screw cap with inflow and outflow tubes was placed on the beaker. This cap allowed argon to bubble through the solution, via perforated tubing, thereby carrying the volatile OsO<sub>4</sub> into the torch for analysis. See Hassler *et al.* [2000] for a detailed description of ICP-MS sparging method.

[18] Osmium composition and concentration was obtained by sparging [Hassler *et al.*, 2000] of volatile OsO<sub>4</sub> into our Finnigan Element Magnetic Sector ICP-MS. Argon sample gas flow rates were variable to optimize ion beam intensity but averaged around 1.35 L/min. Each analysis consisted of 30 runs with 100 passes (analysis time is 7 min).

Notes: Representative microprobe analyses have been recalculated by stoichiometry based on the method of Bence and Albee [1969].  $RFeO = Mg \cdot 100 / (Mg + Fe^{2+})$ ,  $Cr\# = Cr \cdot 100 / (Cr + Al)$ ,  $Fe^{3+}\# = Fe^{3+} \cdot 100 / (Cr + Al + Fe^{3+})$ .  
<sup>a</sup> Lower case letter indicates specific spinel crystal. Upper case letters indicate type of analysis: C = averaged core analyses (usually 5 points), R = rim analyses (10–30  $\mu m$  from crystal edge), IP = inclusion within plagioclase.

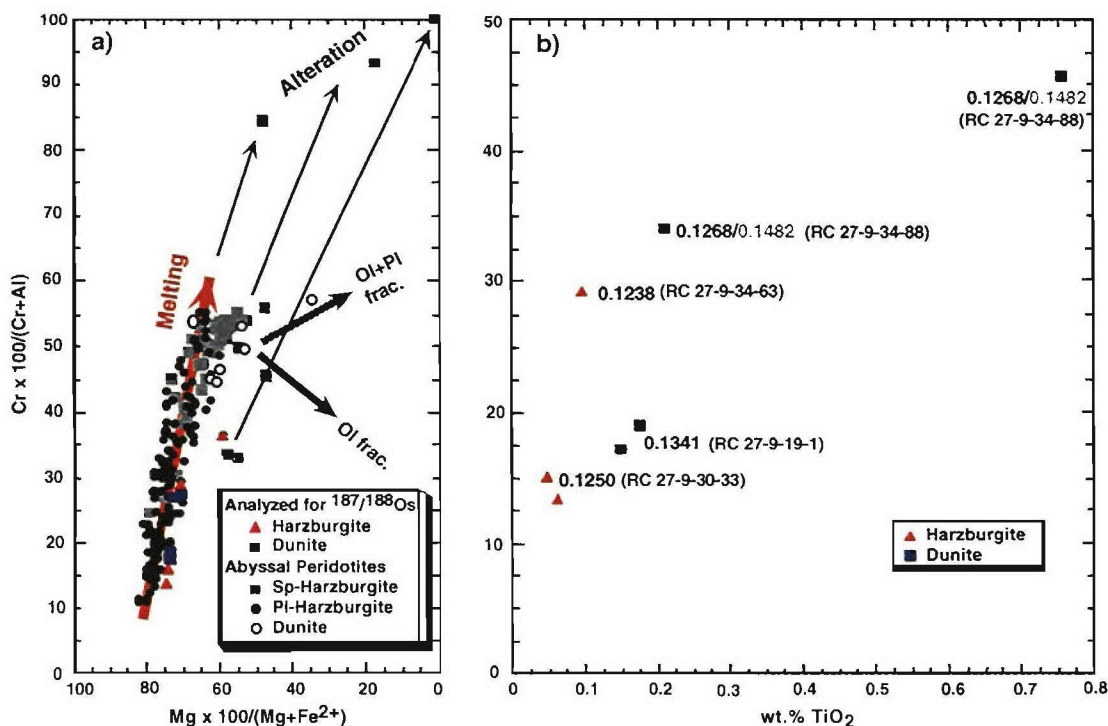


**Figure 2.** Cr-spinel compositions for Atlantis II FZ peridotites (H. Dick, personal communication, 2001). (a) Cr-spinel Cr # versus Mg # for harzburgites and dunites analyzed for <sup>187</sup>Os/<sup>188</sup>Os (this study) compared with the entire Atlantis II FZ peridotite suite. Harzburgites (red triangles) generally have low Cr # and high Mg #, which is indicative of low degrees of melting, relative to dunites (blue squares) with variable but on average higher Cr # and lower Mg #. (b) Cr-spinel Cr # versus TiO<sub>2</sub> with <sup>187</sup>Os/<sup>188</sup>Os values showing a general correlation of low degree of melting rocks (harzburgites) with the least radiogenic Os compositions and melt-reacted rocks (dunites) with more radiogenic Os compositions. Os values in black text are magnetic Cr-spinel and values in gray text are nonmagnetic Cr-spinel.

We report the following Os sparging standards on ICP-MS: 80 pg standard <sup>187</sup>Os/<sup>188</sup>Os = 0.17439 ± 0.56% (1 SD, *n* = 4), 400 pg standard <sup>187</sup>Os/<sup>188</sup>Os = 0.17432 ± 0.55% (1 SD, *n* = 24), 1.25 ng standard <sup>187</sup>Os/<sup>188</sup>Os = 0.17399 ± 0.29% (1 SD, *n* = 42). The whole rock fusion blank measured during sparging session had <sup>187</sup>Os/<sup>188</sup>Os ratio of 0.2364 ± 0.0104 and a concentration of 0.93 ± 0.01 pg/g and the Cr-spinel blank had <sup>187</sup>Os/<sup>188</sup>Os = 0.1392 ± 0.0061 with a concentration of 7.36 ± 0.22 pg/g. These blanks were used to calculate the “% blank correction” listed in Table 3.

## 5. Results

### 5.1. Mineralogical and Petrographic Analysis

[19] Electron microprobe analysis of selected spinel grains showed a large compositional range

in mineral chemistry, covering nearly the entire solid-solution face of the spinel prism between Cr-spinel-hercynite-magnetite. Specific phases included Al-Cr-spinel and Mg-Al-Cr-spinel to more Fe-rich picotite and pleonaste, and even altered “Ferrit-Chromite,” originally recognized by *Spangenberg* [1943] as an alteration product of Cr-spinel. Because of the variability in spinel composition, we will henceforth use the term Cr-spinel to represent the range in spinel solid-solution compositions shown in Table 1, unless specifically stated. Bulk crystal average Mg # and Cr # (Mg # = molecular Mg × 100/(Mg + Fe<sup>2+</sup>); Cr # = molecular Cr × 100/(Cr + Al); Fe<sub>2</sub>O<sub>3</sub> was obtained by stoichiometric recalculation from FeO) ranged from 47.6 to 74.7 and 13.8 to 84.3, respectively (Figure 2). The extremely high Cr # range is a result of ferrit-chromite dominated grains and/or magnetite rims in one or two samples.



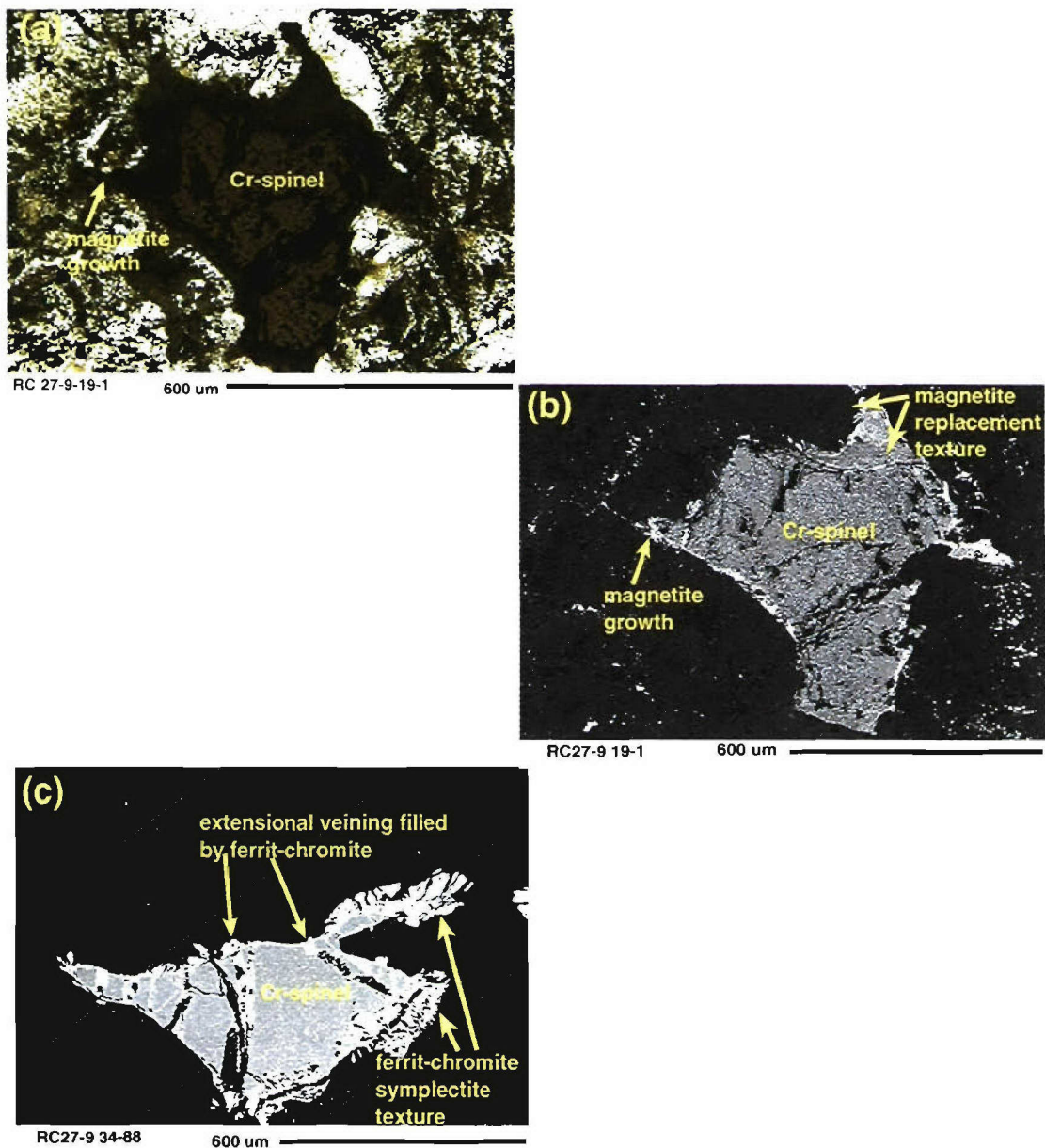


**Figure 3.** Photomicrographs of Cr-spinel contained in abyssal peridotite. (a) Polarized light image of Cr-spinel. Translucent dark brown Cr-spinel (Al-rich) is surrounded by various silicate minerals and Fe-oxides, most of which are secondary clay minerals, serpentine, and magnetite. Backscattered electron photomicrographs of slightly altered (b) and moderately altered (c) Cr-spinel. Note also the difference in composition (Table 1) of the metamorphic overprinting (highly reflective rim phase). Cr-spinel “RC27-9 19-1” is dominated by magnetite rather than ferrit-chromite, relative to Cr-spinel “RC27-9 34-88,” which contains primarily ferrit-chromite.

[20] Petrographic analysis under plain polarized light (Figure 3a) depicts a typical, nearly opaque to translucent brown Cr-spinel “RC27-9 19-1-b-C,” within various secondary silicate phases.

A variety of crystal habits exist in the peridotites, but generally the Cr-spinels are anhedral to subhedral with scalloped edges, often accompanied by holly-leaf and/or symplectite texture. Figure



**Table 2.** Sulfide Microprobe Data

Sample	RC 27-9 34-40a	RC 27-9 34-40b	RC 27-9 34-40c	RC 27-9 34-58a
Host mineral	Cpx	Cpx	Cpx	Interstitial
$n^a$	4	1	1	2
Fe	33.67	32.66	29.45	33.21
Co	0.3290	0.3508	0.5333	0.6530
Ni	27.48	32.37	34.85	30.44
Cu	3.16	1.30	0.18	0.14
Zn	0.1909	0.2360	0.2136	0.1831
S	35.03	32.43	33.60	34.80
Total	99.86	99.34	98.83	99.41

<sup>a</sup>Samples with  $n > 1$  (where  $n$  is number of spot analyses per sulfide grain) are averaged compositions.

3b is a backscattered electron image of Figure 3a (RC27-9 19-1-b-C from Table 1), a subhedral to angular, interstitial Al-Fe-Cr-spinel. Replacement of primary silicate phases was pervasive, yet because of the resistant nature of Cr-spinel, its primary interstitial igneous shape was well preserved. The interior of the grain appears to be unaltered, with only minor fractures and little magnetite. Microprobe analysis of the rim (RC27-9 19-1-b-R), the highly reflective portion of the grain, found the composition to be magnetite. Anomalous fine-grained zones (top and bottom of grain) may represent relict pyroxene, which has been permeated by highly reflective magnetite, or possibly exsolution of a Cr-Fe<sup>3+</sup>-rich composition from the Al-rich core. In the same area, a rather interesting transition zone or alteration front exists between the fine-grained silicate-magnetite mixture and the massive Cr-spinel. Magnetite is fairly thin on most edges, although a few sections seem to have well-developed rinds resulting from metamorphic overprinting of Cr-spinel. Other areas (right and left edges) have a distinctive needle-like growth texture, signifying new magnetite crystal-growth, rather than replacement. Overall, this Cr-spinel has very little ferrit-chromite or magnetite and thus would appear to have experienced limited serpentinization or alteration.

[21] The second backscattered electron photomicrograph (Figure 3c) shows a slightly more iron-rich Al-Fe-Cr-spinel "RC27-9 34-88-a-C". This Cr-spinel is angular and interstitial in nature and has much more veining. Analysis "RC27-9 34-88-a-R" was taken along the grain's highly reflective

rim and is compositionally different than the rim analysis in Figure 3b. The high amount of Cr<sub>2</sub>O<sub>3</sub> even in the highly reflective rim material indicates a ferrit-chromite composition rather than magnetite, which formed as Cr-spinel underwent moderate to low-temperature serpentinization (<500°C). Reflective ferrit-chromite laths delineate multiple extensional veins, which also contain secondary silicate minerals. The ferrit-chromite growth pattern within the veins and also in the upper right corner of the grain is illustrative of symplectite texture. Despite the presence of grain boundaries with little to no ferrit-chromite, this Cr-spinel, based on the proportion of metamorphic overprinting and hence the proportion of magnetite plus ferrit-chromite, is likely to have a more radiogenic Os signature.

[22] Preliminary petrographic and electron microprobe analysis (Table 2) of sulfide within these peridotites gave compositions similar to those measured by Lee [1997] in sample RC27-9 6-2. The petrographic occurrence of sulfide was three-fold: (1) sulfide hosted by silicates, either in the interior of the crystal or along exsolution lamellae, (2) sulfide hosted by spinel, dominantly as micro-sulfides (< 1  $\mu$ m), and 3) sulfide interstitially between silicates. Microsulfides within spinel are not represented in Table 2 owing to the difficulty associated with locating and analyzing a grain at the micron scale. The dominant sulfide phase is pentlandite, from the Fe-Ni-S system. Interestingly, the amount of Cu in the sulfides is highly variable, indicating the possibility of exsolution of chalcopyrite. There is also petrographic evidence of pyr-



**Table 3.** Osmium Sparging Data

Cruise	Dredge-Sample	Latitude, deg	Longitude, deg	Rock Type	Analysis <sup>a</sup>	Os Concentration (ppb)	<sup>187</sup> Os/ <sup>188</sup> Os	2σ	% Blank Correction <sup>b</sup>
Robert Conrad 27-9	6-2	S 31.9	E 57.2	Plagioclase	whole rock	2.72	0.1275	0.0007	0.18
	19-1	S 32.1	E 57.1	Lherzolite	sulfide		0.1278	0.0029	
				Dunite	whole rock	0.27	0.1496	0.0027	1.84
	30-33	S 32.8	E 57.1	Harzburgite	whole rock	0.63	0.1333	0.0118	0.35
					nonmagnetic chromite	2.20	0.1539	0.0022	5.21
					nonmagnetic chromite	8.50	0.1341	0.0035	0.27
					whole rock	1.19	0.1303	0.0010	0.42
	34-63	S 33.0	E 57.0	Harzburgite	whole rock (leached)	0.91	0.1322	0.0007	0.62
					nonmagnetic chromite	1.16	0.1250	0.0017	1.97
					whole rock	0.20	0.1582	0.0028	2.44
	34-84	S 33.0	E 57.0	Dunite	whole rock	1.09	0.1311	0.0006	0.21
					magnetic chromite	9.10	0.1238	0.0010	0.39
					nonmagnetic chromite	NA	0.1241	0.0020	0.13
					whole rock	0.45	0.1458	0.0010	1.10
	34-88	S 33.0	E 57.0	Dunite	whole rock2	0.12	0.1725	0.0055	1.87
					magnetic chromite	19.01	0.1288	0.0007	1.24
					magnetic chromite	127.27	0.1287	0.0005	0.02
					magnetic chromite	165.99	0.1289	0.0007	0.01
	34-88	S 33.0	E 57.0	Dunite	magnetic chromite <sup>c</sup>	104.27	0.1291	0.0005	0.01
					nonmagnetic chromite	0.57	0.1328	0.0058	7.18
Protea 5	10-127	S 53	E 25.5	Dunite	whole rock	0.91	0.1582	0.0029	0.55
					whole rock	1.52	0.1375	0.0030	0.15
					magnetic chromite	5.06	0.1259	0.0012	3.70
					magnetic chromite	26.10	0.1268	0.0012	0.09
	10-186	S 53	E 25.5	Dunite	nonmagnetic chromite	0.94	0.1238	0.0106	2.31
					nonmagnetic chromite	0.57	0.1482	0.0061	1.36
					whole rock	2.64	0.1268	0.0009	0.19
					magnetic chromite (NTIMS)	5.55	0.1363	0.0019	3.70
	16-71-22	N 15.3	W 46	Dunite	magnetic chromite	1.50	0.1326	0.0024	3.48
					whole rock	1.27	0.1326	0.0010	0.39
Academic Boris Petrov	16-77-120	N 15.3	W 46	Dunite	magnetic chromite (NTIMS)	8.74	0.1459	0.0009	0.30
					magnetic chromite	19.87	0.1371	0.0005	0.09
					nonmagnetic chromite	1.49	0.1327	0.0013	0.78
					whole rock	2.10	0.1183	0.0003	0.24
	16-77-120	N 15.3	W 46	Dunite	whole rock	2.17	0.1189	0.0004	0.10
					magnetic chromite (NTIMS) <sup>d</sup>	38.35	0.1224	0.0004	0.03
					magnetic chromite (NTIMS)	6.00	0.1241	0.0016	0.20
					magnetic chromite	1.38	0.1291	0.0011	1.17
	16-77-120	N 15.3	W 46	Dunite	whole rock	3.91	0.1385	0.0039	0.13
					whole rock	2.26	0.1263	0.0005	0.10
					magnetic chromite (NTIMS)	2.41	0.1207	0.0036	1.37

Table 3. (continued)

Cruise	Dredge-Sample	Latitude, deg	Longitude, deg	Rock Type	Analysis <sup>a</sup>	Os Concentration (ppb)	<sup>187</sup> Os/ <sup>188</sup> Os	2σ	% Blank Correction <sup>b</sup>
<b>Leachates<sup>c</sup></b>									
Robert Conrad	34-84	S 33.0	E 57.0		magnetic chromite		0.1289	0.0007	
					6.2N HCl		0.3816	0.0142	
					HF/HCl/HNO <sub>3</sub>		0.1296	0.0006	
					conc. HCl (sonication)		0.1840	0.0093	
Protea 5	10-127	S 53	E 25.5		magnetic chromite		0.1326	0.0024	
					6.2N HCl		0.1279	0.0004	
					HF/HCl/HNO <sub>3</sub>		0.1267	0.0011	
					conc. HCl (sonication)		0.1499	0.0020	
	10-186	S 53	E 25.5		magnetic chromite		0.1371	0.0005	
					6.2N HCl		0.1348	0.0013	
					HF/HCl/HNO <sub>3</sub>		0.1305	0.0006	
					conc. HCl (sonication)		0.1350	0.0032	
	10-186	S 53	E 25.5		nonmagnetic chromite		0.1327	0.0013	
					6.2N HCl		0.1390	0.0027	
					HF/HCl/HNO <sub>3</sub>		0.1379	0.0015	
					conc. HCl (sonication)		0.1504	0.0059	

<sup>a</sup> Os analyses conducted on ICP-MS via argon sparging method, unless otherwise indicated.

<sup>b</sup> Percent blank correction refers to the amount of Os contributed by all sources other than sample.

<sup>c</sup> Magnetic fraction subjected to extensive leaching steps (refer to text).

<sup>d</sup> Unleached chromite grains.

<sup>e</sup> Each of the four samples show the leached chromite <sup>187</sup>Os/<sup>188</sup>Os, as well as Os compositions of the three separate sequential leaches. Detailed description of procedure in text.

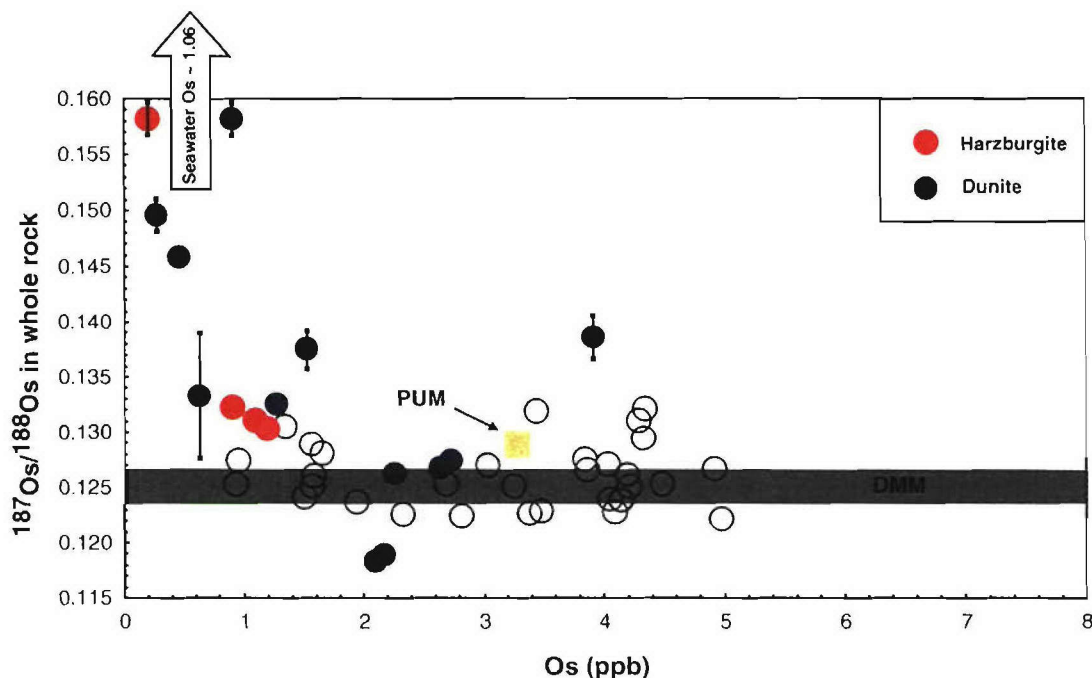


**Figure 4.** Global whole rock abyssal peridotite database from this study (filled circles) and Roy-Barman and Allègre [1994]; Martin [1991]; Snow and Reisberg [1995]; Brandon *et al.* [2000] (open circles). Harzburgite symbols (red circles) represent duplicate analyses from samples “30–33” and “34–63”. Primitive upper mantle (PUM) estimate from Morgan [1986], McDonough and Sun [1995], and Meisel *et al.* [1996]. Depleted MORB mantle (DMM) field taken from Snow and Reisberg [1995]. Seawater  $^{187}\text{Os}/^{188}\text{Os}$  from Ravizza *et al.* [1996] and Sharma *et al.* [1997]. Error bars are  $\pm 1\sigma$ ; those data points without error bars have errors less than the symbol size.

rotite exsolution. Two of the analyses in Table 2 are average compositions from multiple spot measurements within a grain. Unfortunately, no sulfide grains were located and successfully analyzed in samples also measured for Os.

## 5.2. Osmium Isotopes

[23] ICP-MS analysis of 10 abyssal peridotites gave whole rock  $^{187}\text{Os}/^{188}\text{Os}$  between 0.1268 and 0.1582. Whole rock Os concentrations vary from 0.25–3.0 ppb. Osmium isotopic compositions, concentrations, and corresponding precisions for each sample are listed in Table 3;  $^{187}\text{Os}/^{188}\text{Os}$  is plotted versus Os concentration in Figure 4. Osmium isotopic compositions for magnetic Cr-spinel fractions ranged between 0.1238 and 0.1371, with concentrations ranging from 1.50 ppb up to 166 ppb. Nonmagnetic Cr-spinel fractions showed a similar compositional range but extended to more radiogenic values (0.1539). Concentrations varied

from 0.57 to 8.50 ppb. Some early measurements of osmium in Cr-spinel were done by negative thermal ionization mass-spectrometry (NTIMS), as indicated in Table 3, and used different sample preparation and sample chemistry [Hart and Ravizza, 1996]. Most of the samples analyzed using both techniques show similar Os compositions and concentrations, with no apparent systematic differences between NTIMS and ICP-MS techniques.

[24] Abundant sulfide from sample RC 27-9-6-2 allowed direct osmium measurement on a sulfide separate. Owing to the high variation of Os content in sulfides, the sulfide powder was not spiked because we did not want to compromise the Os isotopic measurement by under or over-spiking. The  $^{187}\text{Os}/^{188}\text{Os}$  for the sulfide was 0.1278 (the corresponding whole rock from this study gave  $^{187}\text{Os}/^{188}\text{Os} = 0.1275$ ).

[25] A duplicate whole rock powder from “RC 27-9-34-84” was heated to 400°C prior to spiking to

assess the potential for low-temperature Os degassing. The subsample is reported in Table 3 as “Whole Rock 2” indicating that the concentration was significantly lowered by this preheating (from 0.45 to 0.12 ppb). The  $^{187}\text{Os}/^{188}\text{Os}$  ratio is much more radiogenic (0.1725) compared to the initial whole rock measurement (0.1458), suggesting loss of Os from dominantly unradiogenic sites.

[26] We also separated and measured leachates from selected samples. Osmium isotopic compositions from the sequential leachates were highly heterogeneous (Table 3). For example, Cr-spinel separate RC 27-9-34-84m has an  $^{187}\text{Os}/^{188}\text{Os} = 0.1289$ , a 6.2 N leachate  $^{187}\text{Os}/^{188}\text{Os} = 0.3816$ , a HF/HCl/HNO<sub>3</sub> leachate  $^{187}\text{Os}/^{188}\text{Os} = 0.1296$ , and a Conc. leachate  $^{187}\text{Os}/^{188}\text{Os} = 0.1840$ .

## 6. Discussion

### 6.1. Whole Rock Osmium

[27] The whole rock osmium isotopic data (Table 3) overlaps the published whole rock abyssal peridotite database and enlarges it by nearly 40% (Figure 4). About half of the data points plot at values more radiogenic than the estimated primitive upper mantle (PUM) composition of  $0.129 \pm 0.0009$  [Meisel *et al.*, 1996]; about half plot below PUM, within the proposed range of the present-day depleted MORB mantle (DMM) composition ( $0.125 \pm 0.0014$ ) [Snow and Reisberg, 1995]. Hattori and Hart [1991] derived a similar value (0.1248) from analysis of Os-rich minerals in ophiolites and peridotite massifs of various ages. A single anomalously low whole rock value (ABP 16-71-22) of 0.1183 is well below primitive upper mantle and is thought to be the least radiogenic abyssal peridotite whole rock measurement published.

[28] It should be noted that this estimated value for primitive upper mantle differs slightly from the chondritic reference composition. Meisel *et al.* [1996] stated that PUM represents the modern Os composition of the bulk upper mantle that would have evolved from the late accretionary period to present assuming no modification of Re/Os. The modern “chondritic” Os composition (0.127) is

derived from ordinary chondrites ( $^{187}\text{Os}/^{188}\text{Os} = 0.1286 \pm 0.0010$  and carbonaceous chondrites ( $^{187}\text{Os}/^{188}\text{Os} = 0.1258 \pm 0.0005$ ) [Meisel *et al.*, 1996]. The incompatible behavior of Re versus the compatible behavior of Os during silicate mantle melting should produce residual peridotites that are less radiogenic and have higher Os concentrations than bulk earth. This is not the case for a large portion of the global whole rock data set. The scatter seen in Figure 4 includes our whole rock measurements and extends to very radiogenic compositions with decreasing concentration. Many of the abyssal peridotites have more radiogenic compositions and lower concentrations than primitive upper mantle.

[29] Snow and Reisberg [1995] proposed that low-temperature seafloor alteration of abyssal peridotites produces elevated  $^{187}\text{Os}/^{188}\text{Os}$  values in some whole rocks. As indicated in Figure 4, the present-day seawater Os composition ( $^{187}\text{Os}/^{188}\text{Os} \sim 1.06$ ) is significantly more radiogenic than PUM, suggesting that, even at water/rock ratios of  $10^4$ , alteration of peridotite involving seawater could compromise the existing mantle Os signature [Martin, 1991; Roy-Barman and Allègre, 1994; Snow, 1993]. This does not mean that measurement of whole rock abyssal peridotites may not occasionally yield  $^{187}\text{Os}/^{188}\text{Os}$  similar to or less radiogenic than PUM. However, knowing that abyssal peridotites are pervasively altered over a range of temperatures by serpentinization and/or weathering and considering the compositional heterogeneity displayed in Figure 4, we interpret the scatter of data to indicate that  $^{187}\text{Os}/^{188}\text{Os}$  whole rock values are largely compromised by seawater interaction. The tendency for Os concentrations to be lower than PUM may suggest oxidation and removal of Os-rich sulfide during serpentinization and weathering.

### 6.2. Small-Scale Os Isotope Heterogeneity

[30] A longstanding issue in mantle geochemistry is the determination of the scale of chemical heterogeneity within the mantle. This is not easily addressed here because of the lack of understanding concerning the behavior of the Re-Os system during mantle melting. Hart and Ravizza [1996] addressed the issue of the distribution of Os in



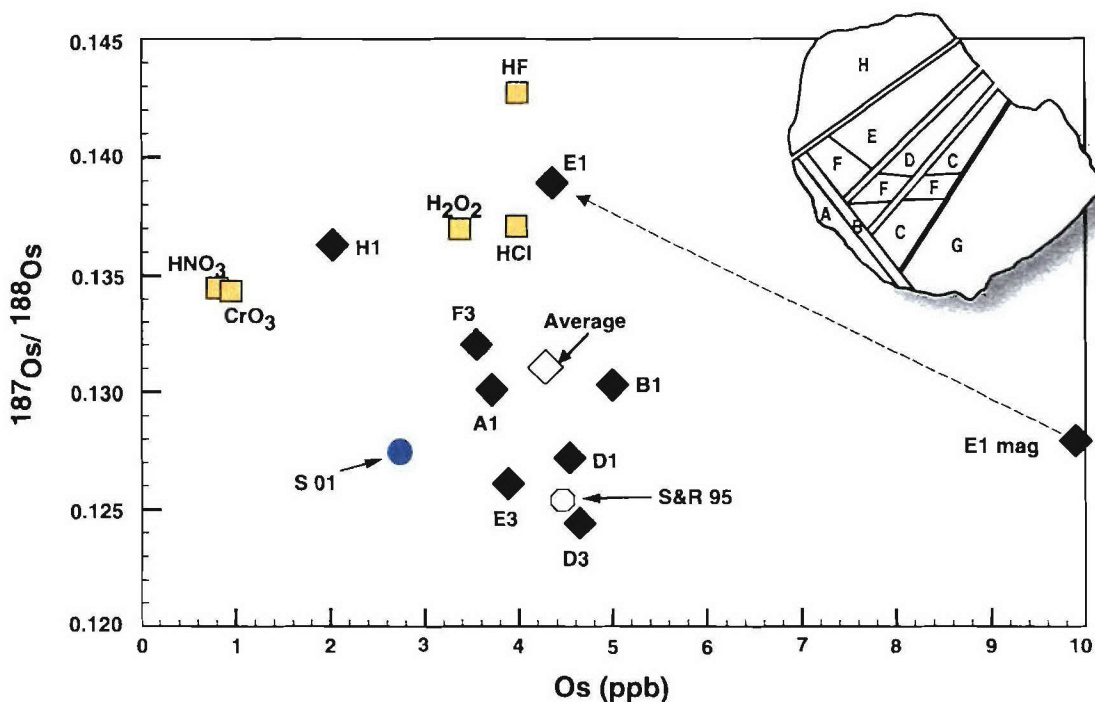


**Figure 5.** Re-Os isotope systematics of whole rock sub-samples (filled diamonds) from a single dredged abyssal peridotite boulder (RC27-9-6-2) show heterogeneity similar to that of the global whole rock database in Figure 4. Filled squares represent leached residues from sub-sample H and illustrate the possibility of radiogenic seawater contamination. Subsample E1 is connected by a dotted line to a separated magnetic spinel fraction (E1 mag). Sample numbers (e.g., F3) denote various slices of each subsample. The inset shows the locations of the sub-samples. A different part of this boulder, S&R95 (above), was sampled and reported by *Snow and Reisberg* [1995]. This study's whole rock measurement of RC27-9-6-2 ("S 01" blue circle) falls midway between the other whole rock compositions. Standard error for all data except "S 01" is given in *Lee* [1997]. Standard error for "S 01" is smaller than the symbol.

mantle phases by measuring Os compositions and concentrations in carefully separated phases from a Kilbourne Hole lherzolite xenolith. They found the Os content in sulfide to be 4.11 ppm. Their results were similar to those of *Morgan and Baedeker* [1983], who reported Os contents in Kilbourne Hole lherzolite sulfide particles ranging from 3.5 to 11 ppm Os. The other phases measured by *Hart and Ravizza* [1996] (olivine, clinopyroxene, orthopyroxene, and spinel) were found to have Os contents of 36, 200, 60, 36 ppt, respectively. This confirms the notion that the vast majority of the Os budget lies within the various sulfide phases present in mantle lithologies. It is important to note that the low Os concentration reported by *Hart and Ravizza* [1996] for spinel relative to silicates is surely due to a greater proportion of sulfide inclusions

in the pyroxenes. In the present study, however, the Os budget is dominated by spinel, which is similar to other work done on Kilbourne Hole xenoliths [*Burton et al.*, 1999] and other mantle lithologies [*Walker et al.*, 1996].

[31] In an effort to understand the nature of the phases hosting Os in abyssal peridotites and evaluate the potential for seawater contamination, we have incorporated data [*Lee*, 1997] from a detailed study of the least serpentinized sample (RC27-9-6-2) from the study of *Snow and Reisberg* [1995] (this sample was dredged from the east wall of the Atlantis II fracture zone). The boulder was divided into a number of sub-sections, as illustrated in Figure 5 [*Lee*, 1997], and each section was analyzed for osmium composition and concentration. In addition, a magnetic size fraction was analyzed from sub-

sample E1. Also, subsample powder H1 was leached by a variety of reagents, which were analyzed to assess the impact of seawater contamination.

[32] Sample RC 27-9-6-2 is somewhat unique in that it contains a 1 cm vein of diopside with a thin zone of dunite around it. In the matrix, there is both an abundance of sulfide and accessory biotite, andesine feldspar, apatite, and relict Fe-Ti oxides. These later minerals are all interpreted as owing to impregnation of the host peridotite by late melts associated with emplacement and crystallization of the vein. On the basis of the Nd isotope data, both the whole rock and the vein are in the range of typical Indian Ocean N-MORB mantle. The bulk sample  $^{143}\text{Nd}/^{144}\text{Nd}$  is 0.512965, Cpx separated from the bulk sample is 0.512994 [Snow *et al.*, 1994], and Cpx separated from the vein is 0.513091 [Lee, 1997].

[33] The Os isotopic heterogeneity of this single sample is enormous and spans almost the total range of the global abyssal peridotite data set shown in Figure 4. Interestingly, we measured a separate whole rock sample for Os isotopic composition and our value of 0.1275 is almost exactly the mean of the two previous whole rock measurements; Snow and Reisberg's [1995] at 0.1255 and Lee's [1997] average at 0.1310. The leached residues increase in Os concentration when silicates are dissolved (HF and HCl) and decrease when sulfides are dissolved ( $\text{HNO}_3$  and  $\text{CrO}_3$ ), suggesting that Os is dominantly hosted by the sulfide. Some of the leachates had Os ratios up to 0.1573, strongly implicating seawater as the source of the observed small-scale heterogeneity in this dredge boulder. However, the Os isotopic ratios do not bear any simple relationship to the exposed surfaces of the dredge boulder (Figure 5); the highest (*E*) and lowest (*D*) segments are both interior samples, suggesting the seawater introduction of Os took place under moderate to high-*T* conditions at depth, before the peridotite was exposed to weathering.

[34] Lee [1997] also studied and electron-probed virtually every sulfide occurrence in two selected areas of this rock, covering an area of almost 60  $\text{cm}^2$ . Sulfides occurred in three types: (1) tiny individual inclusions and curvi-planar arrays of

inclusions, dominantly hosted in Cpx; (2) larger interstitial sulfide grains on grain boundaries between silicates, and (3) larger irregular grains in mesh-textured serpentine surrounding relict olivine "islands." The sulfides are predominantly pyrrhotite, pentlandite, and chalcopyrite, with minor bornite, marcasite, heazlewoodite, millerite, polydymite, and rare pyrite. Most represent exsolution from the sulfur-poor end of the monosulfide solid solution. There is no correlation between sulfide minerals and textural type (i.e., pyrrhotite-pentlandite are common in all three textures). It is likely that all textural types were recrystallized and altered at moderately high temperature during serpentinization, with only the bornite and millerite bearing witness to lower temperature alteration (<200°C). There is no obvious correlation between sulfide texture or abundance and the Os isotopic composition (though the sulfide survey did not cover the entire slab surface). We suggest that the Ni-Fe-rich sulfides "scavenge" Os from circulating seawater, during serpentinization. This would be consistent with the low closure temperature recently reported for Os diffusion in pyrrhotite [Brenan *et al.*, 2000]. On the basis of their data, pyrrhotite grains of 100-micron diameter will equilibrate in 10,000 years at 380°C or in only 100 years at 470°C. Interstitial sulfides will thus readily equilibrate with circulating seawater at modest levels in the oceanic crust. Only sulfides encapsulated in silicates or chromites can be expected to retain primary Os signatures. The distribution of sulfide, the local water/rock ratio, and the effective "scavenging" of Os would almost certainly lead to isotopic "patchiness" and small-scale variability.

[35] It may also be possible that some of the osmium isotopic heterogeneity is primary, due in part to magmatic impregnation during formation of the diopside vein, as minor isotopic heterogeneity is evident in the Nd isotopes. Brandon *et al.* [2000] reported significant Os isotopic heterogeneity in drilled samples from a single section of abyssal peridotite from the Kane Fracture Zone. Samples within 80 cm of each other were as much as 8% different in  $^{187}\text{Os}/^{188}\text{Os}$ ; Brandon *et al.* [2000] argued that this heterogeneity was

primary and mantle-derived. It is difficult to rationalize this claim with the low closure temperatures reported by *Brenan et al.* [2000]. For a mantle upwelling rate under a ridge of 30 km/million years, the adiabatic cooling rate is  $\sim 10^\circ\text{C}/\text{million years}$ . Even large 1 mm sulfide grains in such a mantle domain will have closure temperatures for Os of only  $400^\circ\text{C}$ . Long-term preservation of isotopic heterogeneity in the convecting upper mantle seems highly unlikely on the length scales involved in the *Brandon et al.* [2000] sample suite. Furthermore, the correlation of  $^{187}\text{Os}/^{188}\text{Os}$  with Pt/Os ratio, which they put forward as prime evidence for the primary nature of the heterogeneity, could easily be produced by interaction of sulfides with seawater, as seawater has both high  $^{187}\text{Os}/^{188}\text{Os}$  and a high Pt/Os ratio. Open system behavior of sulfides with respect to Os has also been documented in a suite of peridotitic xenoliths [*Handler et al.*, 1999]. Further understanding of these complex processes will require microbeam Os isotope analysis of sulfides [*Alard et al.*, 2000].

### 6.3. Regional Os Heterogeneity

[36] One of the main assumptions made here is that serpentinization/alteration of abyssal peridotites results in elevated osmium isotopic compositions due to interaction with seawater. It is evident from Figure 4 that less-altered abyssal peridotites can be carefully selected and analyzed which yield whole rock  $^{187}\text{Os}/^{188}\text{Os}$  values less than or equal to primitive upper mantle. The explanation for the heterogeneity in  $^{187}\text{Os}/^{188}\text{Os}$  is then attributed to a variably enriched and depleted mantle source. However, the question then becomes, is it possible to recover the mantle osmium signature from a common serpentinized abyssal peridotite. We present rather compelling evidence illustrating that Os isotopic heterogeneity in abyssal peridotite whole rock measurements is the result of a radiogenic seawater Os component and not solely due to inherent mantle heterogeneity.

[37] This is especially true at the Atlantis II Fracture Zone, where it has been shown by *Snow* [1993] that the MORB mantle is typical N-

MORB. Sr, Nd, and Pb isotopic compositions from multiple abyssal basalts, taken along the Atlantis II FZ, show very homogeneous N-MORB-like signatures. This is quite important considering that a large portion of the SWIR, dominantly between Bouvet and Marion, displays significant variation in basalt Sr, Nd, and Pb isotope systematics. The Du Toit Fracture Zone, to the west of Marion, has been characterized by both N-MORB and E-MORB type basalts [*Le Roex*, 1989], and thus our case for alteration-induced Os isotopic heterogeneity for samples from this fracture zone is not as strong. Similarly, the isotopic systematics at  $15^\circ 20'$  FZ are complex and suggest that some primary mantle heterogeneity may underlie the dominant seawater alteration signal. On the basis of the anomalously low  $^{187}\text{Os}/^{188}\text{Os}$  values we report for the two  $15^\circ 20'$  FZ samples, it is apparent that there is significant complexity associated with the melting dynamics, and it has previously been suggested that sub-continental lithospheric lithologies within the upper mantle may play a role in the anomalous isotopic signatures [*Esperanca*, 1999].

[38] Recent PGE and Os isotopic work by *Blusztajn et al.* [2000] on gabbros drilled at the Atlantis II Fracture Zone lend further support for the presence of an alteration—induced radiogenic seawater Os component. Os isotopic compositions in the gabbros range from 0.140 to 0.467 and correlate with Rb/Cs, suggesting that seawater alteration affected the Os isotopic system. The effect of serpentinization on abyssal peridotite Os compositions can also be seen when comparing harzburgites to dunites from the Atlantis II FZ. One potential explanation for the rough correlation seen in Figure 2b could be that dunite is serpentinized and weathered more readily than harzburgite and thus interacts with a larger volume of radiogenic seawater Os. Because of the lesser proportion of olivine in harzburgite and hence greater proportion of more resistant pyroxene, the Os-hosting sulfides contained within Cr-spinel and pyroxene may be less affected by seawater interaction than sulfide found in dunite. Whether this difference in peridotite lithology would lead to a difference in Os isotopic composition is clearly speculative and



needs further attention. Another potential explanation is related to the variable melting dynamics associated with harzburgites versus dunites and the differing spinel mineralogy between these two lithologies.

#### 6.4. Cr-Spinel and Serpentinization

[39] As mantle melting progresses, the chrome content in residual spinel increases, while the magnesium content decreases, owing to the effect of Cr on the partitioning of Fe-Mg between olivine and spinel [Irvine, 1965]. This produces the apparently contradictory result of an inverse correlation between abyssal peridotite spinel Mg # and Cr # [Dick *et al.*, 1984]. It follows that dunites, products of melt focusing [Kelemen *et al.*, 2000], should generally have higher Cr # than the enclosing peridotitic residues of melting (Figure 2). Hybrid peridotites, melt impregnated and late melt-reacted rocks, are frequently characterized by the presence of plagioclase and spinel compositions with  $\text{TiO}_2 > 0.15\%$  [Allan and Dick, 1996] (Figure 2b). Spinel from harzburgite sample RC27-9-30-33 has low Cr # and high Mg #, suggesting a lower degree of melting and thus a less depleted residual peridotite. As long as the dunites are products of harzburgite melting, the two lithologies should have similar Cr-spinel  $^{187}\text{Os}/^{188}\text{Os}$  ratios. Although we have limited data to base a comparison on, we do see a difference in  $^{187}\text{Os}/^{188}\text{Os}$  values of harzburgite versus dunite.

[40] Serpentinization of abyssal peridotite commonly occurs at crustal temperatures as high as 500°C, continuing until near-extrusion on the seafloor. As the most resistant mantle phase, Cr-spinel preserves original isotopic and trace element signatures as the abyssal peridotite undergoes serpentinization and low-temperature seafloor weathering. In an extensive study, which looked at alteration of Cr-spinel in serpentinites, Burkhard [1993] found the composition of the spinel to control the degree of spinel alteration. Cr-spinel which is rich in Cr and  $\text{Fe}^{2+}$  is much more susceptible to alteration than Cr-spinel rich in Al and Mg. This suggests that dunitic spinel with high Cr #'s may tend have more radiogenic Os compositions than harzburgitic spinel. On the basis of this alteration argument,

the spinel compositions from the dunites, which have higher Cr #,  $\text{Fe}^{3+}$  #, and  $\text{TiO}_2$ , typical of rocks that have reacted with MORB-like melts, should have more radiogenic  $^{187}\text{Os}/^{188}\text{Os}$  compositions than the harzburgitic spinels. This is evident in Figure 2b, as Cr-spinel samples RC 27-9-30-33 and RC 27-9-34-63 have Cr #'s comparable to moderately depleted harzburgite and are two of the least radiogenic spinels. This may also be explained by melt transport through the dunites. More radiogenic Os compositions in dunites resulting from melt-interaction infer that more radiogenic source lithologies are melting and these melts are reacting with the dunites. In order to verify this possible petrogenetic relationship, Os from a much larger number of harzburgite and dunite spinels from a single ridge segment or fracture zone need to be studied.

#### 6.5. Cr-Spinel Osmium

[41] The separated and leached Cr-spinels from each of the abyssal peridotites show a similar heterogeneity in  $^{187}\text{Os}/^{188}\text{Os}$  to the whole rock compositions (Figures 4 and 6). Upon first glance, this would tend to indicate that we have not succeeded in removing any of the heterogeneity attributed to seawater alteration. If we consider all of the Cr-spinels together, this may be the case, but it is interesting to note the difference in Os composition between the various Cr-spinel fractions. The magnetic Cr-spinels display a much smaller range in  $^{187}\text{Os}/^{188}\text{Os}$  than nonmagnetic Cr-spinels and, except for a single non-magnetic Cr-spinel, have much higher Os concentrations. In fact, all but one of the magnetic Cr-spinels have a greater Os concentration than PUM, while the majority of the nonmagnetic Cr-spinels have concentrations below PUM. This division between magnetic and nonmagnetic fractions in Os isotope space stands to illustrate a number of potential differences. The variation in Os concentration, especially with nonmagnetic Cr-spinel dominantly below PUM, suggests a distinct difference in sulfide abundance between the spinel fractions, possibly coupled with variable leaching effectiveness. It would appear as though the nonmagnetic Cr-spinels have less Os due to lower abundances

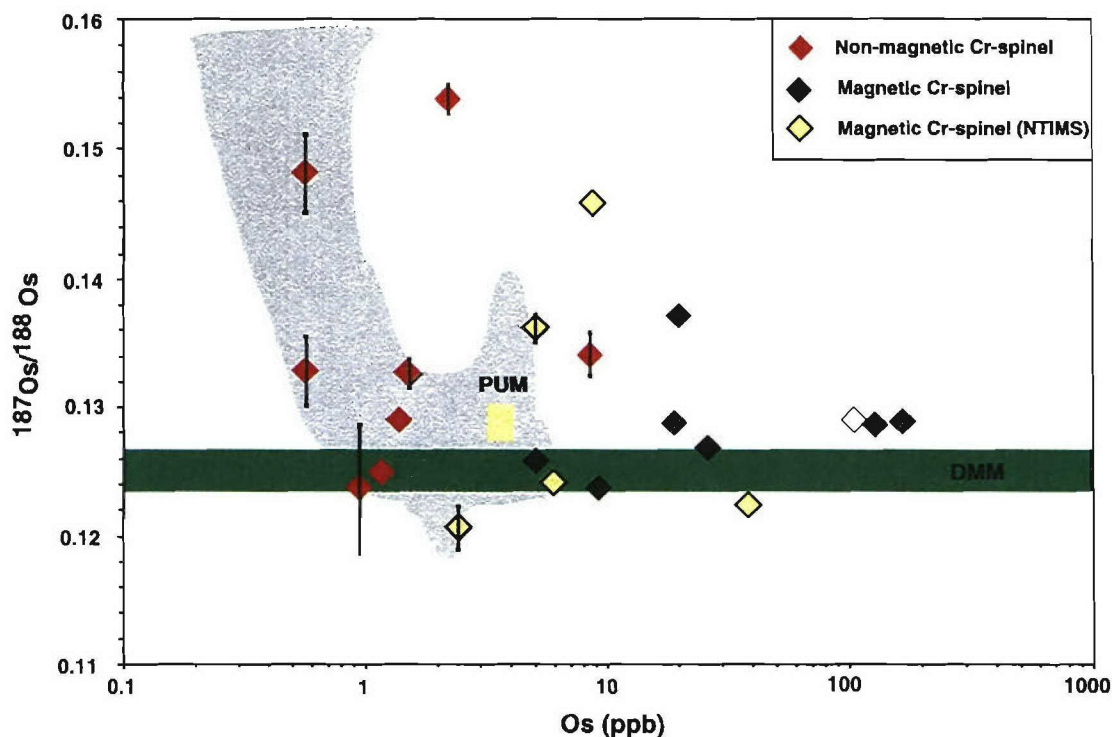


**Figure 6.** Cr-spinel Os composition versus concentration data. Reference fields are the same as in Figure 4. Whole rock Os data from Figure 4 is represented by the gray field. Note the difference from Figure 4 concentration axis (log scale versus linear scale). Magnetic Cr-spinels have distinctly higher concentrations than nonmagnetic Cr-spinels and a much smaller range in  $^{187}\text{Os}/^{188}\text{Os}$ . Open diamond represents extensively leached magnetic Cr-spinel. Error bars are  $\pm 1\sigma$ ; those data points without error bars have errors less than the symbol size.

of sulfide. However, this has not been petrographically verified.

[42] Alternatively, it may reflect a difference in sulfide occurrence. Magnetic Cr-spinels have more sulfide inclusions that are not affected by leaching, whereas nonmagnetic Cr-spinels have higher amounts of interstitial sulfide that lose Os during leaching. Furthermore, this variation in sulfide occurrence could also explain the range in Os composition seen in the nonmagnetic Cr-spinels versus the magnetic Cr-spinels. The non-magnetic fraction in many cases includes a small (<20%), but potentially influential, proportion of interstitial Cr-spinel/silicate grains. These multiphase grains failed to separate along true grain boundaries during mechanical separation. Highly altered (secondary) silicate phases could add additional radiogenic Os, thereby further compromising some of these Cr-spinels. Despite rigorous

leaching (HF/ HCl /HNO<sub>3</sub>), it seems that the removal of silicates may not be as effective as removal of Fe-oxides. Regardless of the differences between magnetic and nonmagnetic spinels, on the whole, both fractions have less radiogenic  $^{187}\text{Os}/^{188}\text{Os}$  values than their associated whole rock osmium compositions.

[43] To further verify that seawater alteration is responsible for most of the radiogenic Os isotopic heterogeneity, we conducted a crude mass balance experiment by collecting sequential leachates from each of the three acid-cleaning steps and measuring the Os composition and concentration stripped from three Cr-spinel samples. Results show that the Os compositions of the leachates for each sample are highly variable (Table 3). Sample "PROT 5 10-186nm" and "RC 27-9-34-84m" have Cr-spinel compositions that are less radiogenic than any of their three associated leachates,



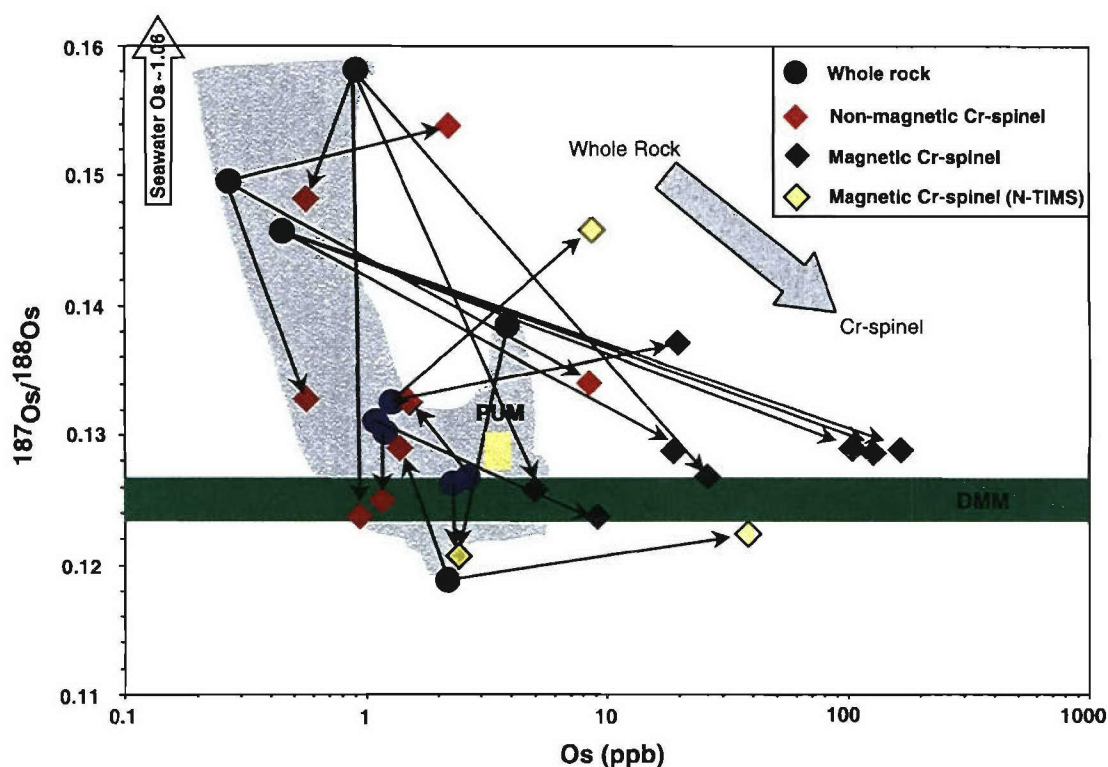


**Figure 7.** Os composition versus concentration for abyssal peridotite whole rock and Cr-spinel pairs. Arrows connect whole rock data points with Cr-spinel data points from identical peridotite. The large gray arrow depicts the dominant trend from radiogenic seawater-compromised whole rocks to less radiogenic Cr-spinels having higher concentrations. Reference fields the same as Figure 6. Standard deviations are plotted on Figures 4 and 6 and listed in Table 2.

indicating that leaching is removing a more radiogenic seawater component. For example, leached spinel “10–186nm” has an  $^{187}\text{Os}/^{188}\text{Os}$  of 0.1327, with corresponding 6.2 N HCl, HF/ HCl /HNO<sub>3</sub>, and conc. HCl leachate  $^{187}\text{Os}/^{188}\text{Os}$  values of 0.1390, 0.1379, and 0.1504, respectively. This clearly shows that a radiogenic seawater Os component is present in both the silicate phases (leached by the HF/ HCl /HNO<sub>3</sub> solution) and the Fe-oxide alteration phases (leached by HCl). This relationship between leachates and Cr-spinel did not hold for all samples, possibly due to loss of volatile OsO<sub>4</sub> during separation of leachates.

## 6.6. Cr-Spinel Versus Whole Rock Osmium

[44] The pervasive serpentinization and low-temperature seawater alteration make whole rock Os measurements of abyssal peridotites difficult to interpret when attempting to characterize the

present-day Os composition of DMM. *Snow and Reisberg* [1995] showed that some of the heterogeneity in the existing abyssal peridotite Os data is the result of a seawater alteration component. They propose a present-day oceanic mantle composition of 0.125 (green band in Figures 4, 6, and 7), based on a combination of carefully selected data from the literature and their measured values. We take a different approach to the same problem and propose that measurements made on separated and carefully treated Cr-spinels from abyssal peridotites will result in Os compositions reflecting the upper mantle Os signature.

[45] This relationship between whole rock and Cr-spinel is evident in Figure 7. The dominant trend, delineated by arrows going from whole rock compositions to Cr-spinel compositions, is from radiogenic Os compositions at low Os concentrations to less radiogenic compositions at higher concentra-

tions. This is precisely the trend that would be expected if a radiogenic seawater Os component were removed from a Cr-spinel with an unradiogenic Os signature. Several arrows show different trends, with Cr-spinel compositions more radiogenic than the whole rocks from which they were separated. Cr-spinel is not going to universally protect all sulfide-hosted Os signatures, as some highly fractured or veined grains will incur pervasive seawater alteration that is not easily removed by our leaching technique.

[46] Furthermore, while less than half of all Cr-spinels studied here are within the proposed DMM field (Figure 6), the majority is less radiogenic than PUM. On the basis of Re-Os systematics during melting, the depleted mantle composition should be less radiogenic than primitive upper mantle; even those samples that do plot at  $^{187}\text{Os}/^{188}\text{Os}$  values higher than PUM are less radiogenic than their corresponding whole rock compositions. So, although the Cr-spinel Os compositions do not distinctly define the present-day composition of DMM, they do provide a more tightly constrained range for the depleted MORB source. This range may continue to shrink as further refinements of the Cr-spinel technique emerge, and subsequently the actual DMM Os signature can be better defined. The uncertainty in the Os composition of the "normal" depleted MORB source is not only a function of the small quantity of data available but also the complicated Os isotopic interpretation required of whole rock abyssal peridotite analyses.

## 7. Conclusions

[47] Although isotopic evidence has shown specific fracture zones along the SWIR and MAR (i.e., Du Toit F.Z.) to have heterogeneous mantle source regions, this study documents that much of the Os isotopic heterogeneity seen in N-MORB residual mantle is due to an alteration-induced radiogenic seawater Os component. Therefore, in many cases, interpretation of the upper mantle isotopic signature can be obscured. In order to circumvent this problem, we separated resistant Cr-spinel from a number of abyssal peridotites and carefully treated them to remove the seawater

alteration component. ICP-MS sparging of the Cr-spinel solutions has produced Os compositions which still show heterogeneity, but which define two different populations. Nonmagnetic Cr-spinels have Os concentrations generally equal to or less than PUM and compositions spanning a range similar to the whole rock values. Magnetic Cr-spinels have higher concentrations than PUM and compositions generally equal to or less radiogenic than PUM, thereby illustrating that Cr-spinel can preserve a DMM-like Os signature. Despite the heterogeneity in the nonmagnetic Cr-spinel fraction, both fractions, when compared to their corresponding whole rock  $^{187}\text{Os}/^{188}\text{Os}$  values, dominantly have less radiogenic  $^{187}\text{Os}/^{188}\text{Os}$ . Not only does this trend, from radiogenic whole rocks to less radiogenic Cr-spinels, illustrate that the primary depleted upper mantle Os signature is obtainable, but it further constrains the Os isotopic signature for DMM.

[48] It is also interesting to note that Cr-spinels from the two harzburgites included in this study have two of the lowest  $^{187}\text{Os}/^{188}\text{Os}$  ratios and  $\text{TiO}_2$  contents, consistent with the idea that the melt-reacted rocks (dunites) would have more radiogenic  $^{187}\text{Os}/^{188}\text{Os}$  and high  $\text{TiO}_2$ . This leaves open the possibility that the melts from which the dunites formed were not in equilibrium with the ambient mantle. However, the data set is neither large enough nor sufficiently refined to demonstrate this as fact, and further work is needed to address this issue in more detail. We have, however, shown that the radiogenic seawater Os component, which compromises the isotopic signature of most abyssal peridotites, can be removed, allowing more straightforward interpretation of the Os signature. This then provides the means to define, albeit still quite vaguely, the Os isotopic signature of N-MORB depleted upper mantle.

## Acknowledgments

This work was supported by NSF-EAR 9804891, NSF-OCE9416620, and NSF-OCE0096634. We thank Parker Hackett for conducting Cr-spinel separations during early phases of this work. Larry Ball at the WHOI ICP-MS facility has been extremely helpful, and we thank him for his patience and flexibility during Os sparging. Thanks is also extended to Neel

Chatterjee in the MIT Electron Microprobe Facility for his help. Insightful discussions with Greg Ravizza and continual help in the lab from Tracy Abbruzzese were much appreciated. We would also like to thank Doug Pyle and Alan Brandon for their thoughtful and extremely helpful reviews and comments.

## References

- Alard, O., W. L. Griffin, J. P. Lorand, S. E. Jackson, and S. Y. O'Reilly, Non-chondritic distribution of the highly siderophile elements in mantle sulphides, *Nature*, **407**, 891–894, 2000.
- Allan, J. F., and H. J. B. Dick, Cr-rich spinel as a tracer for melt migration and melt-wall rock interaction in the mantle: Hess Deep, Leg 147, *Proc. Ocean Drill. Program Sci. Results*, **147**, 157–172, 1996.
- Armstrong, J. T., CITZAF - A package for correction programs for the quantitative electron microbeam x-ray analysis of thick polished materials, thin-films and particles, *Microbeam Anal.*, **4**, 177–200, 1995.
- Aumento, F., and H. Loubat, The Mid-Atlantic Ridge Near 45°N, XVI, Serpentinized Ultramafic Intrusions, *Can. J. Earth Sci.*, **8**, 631–663, 1970.
- Bence, A. E., and A. L. Albee, Empirical correction factors for the electron microanalysis of silicates and oxides, *J. Geol.*, **76**, 382–403, 1968.
- Blusztajn, J., S. R. Hart, G. Ravizza, and H. J. B. Dick, Platinum-group elements and Os isotopic characteristics of the lower oceanic crust, *Chem. Geol.*, **168**, 113–122, 2000.
- Bonatti, E., J. Honnorez, and G. Ferrara, Peridotite-gabbro-basalt complex from the equatorial Mid-Atlantic Ridge, *Philos. Trans. R. Soc. London Ser. A*, **268**, 385–402, 1971.
- Bougault, H., J.-L. Charlou, Y. Fouquet, H. D. Needham, N. Vaslet, P. Appriou, P. J. Baptiste, P. A. Rona, L. Dimitriev, and S. Silantiev, Fast and slow spreading ridges: Structure and hydrothermal activity, ultramafic topographic highs and CH<sub>4</sub> output, *J. Geophys. Res.*, **98**, 9643–9651, 1993.
- Brandon, A. D., J. E. Snow, R. J. Walker, J. W. Morgan, and T. D. Mock, <sup>190</sup>Pt-<sup>186</sup>Os and <sup>187</sup>Re-<sup>187</sup>Os systematics of abyssal peridotites, *Earth Planet. Sci. Lett.*, **177**, 319–335, 2000.
- Brenan, J. M., D. J. Cherniak, and L. A. Rose, Diffusion of osmium in pyrrhotite and pyrite; Implications for closure of the Re-Os isotopic system, *Earth Planet. Sci. Lett.*, **180**, 399–413, 2000.
- Burkhard, D. J. M., Accessory chromium spinels: Their coexistence and alteration in serpentinites, *Geochim. Cosmochim. Acta.*, **57**, 1297–1306, 1993.
- Burton, K. W., P. Schiano, J.-L. Birck, and C. J. Allègre, Osmium isotope disequilibrium between mantle minerals in a spinel-lherzolite, *Earth Planet. Sci. Lett.*, **172**, 311–322, 1999.
- Cannat, M., and J. Casey, An ultramafic uplift at the Mid-Atlantic Ridge: Successive stages of magmatism in serpentinized peridotites from the 15N region, in *Mantle Rocks in Oceanic Ridges and Ophiolites*, edited by R. Vissers, and A. Nicolas, pp. 5–34, Kluwer Acad., Norwell, Mass., 1995.
- Cannat, M., D. Bideau, and R. Hébert, Serpentinized peridotites and gabbros in the Mid-Atlantic ridge axial valley at 15°37'N and 16°52'N, *Earth Planet. Sci. Lett.*, **109**, 87–106, 1990.
- Cannat, M., D. Bideau, and H. Bougault, Serpentinized peridotites and gabbros in the Mid-Atlantic ridge axial valley at 15°37'N and 16°52'N, *Earth Planet. Sci. Lett.*, **109**, 87–106, 1992.
- Cannat, M., C. Mével, M. Maia, C. Deplus, C. Durand, P. Gente, P. Agrinier, A. Belarouchi, G. Dubuisson, and E. Humler, Thin crust, ultramafic exposures, and rugged faulting patterns at the Mid-Atlantic Ridge (22°–24°N), *Geology*, **23**, 49–52, 1995.
- Dick, H. J. B., Abyssal peridotites, very slow spreading ridges and ocean ridge magmatism, *Geol. Soc. Spec. Publ.*, **42**, 71–105, 1989.
- Dick, H. J. B., and T. Bullen, Chromian spinel as a petrogenetic indicator in abyssal and alpine-type peridotites and spatially associated lavas, *Contrib. Mineral. Petrol.*, **86**, 54–76, 1984.
- Dick, H. J. B., and J. H. Natland, Late stage melt evolution and transport in the shallow mantle beneath the East Pacific Rise, *Proc. Ocean Drill. Program Sci. Results*, **147**, 103–134, 1996.
- Dick, H. J. B., R. L. Fisher, and W. B. Bryan, Mineralogic variability of the uppermost mantle along mid-ocean ridges, *Earth Plan. Sci. Lett.*, **69**, 88–106, 1984.
- Dick, H. J. B., H. Schouten, P. S. Meyer, D. G. Gallo, H. Bergh, R. Tyce, P. Patriat, K. T. M. Johnson, J. Snow, and A. Fisher, Tectonic evolution of the Atlantis ii fracture zone, *Proc. Ocean Drill. Program Sci. Results*, **118**, 359–398, 1991.
- Engel, C. G., and R. L. Fisher, Granitic to ultramafic rock complexes of the Indian Ocean ridge system, western Indian Ocean, *Geol. Soc. Am. Bull.*, **86**, 1553–1578, 1975.
- Esperanca, S., S. E. Sichel, M. F. Horan, R. J. Walker, T. Juteau, and R. Hekinian, Some abyssal peridotites are old!, in Ninth V. M. Goldschmidt Conference [CD-ROM], Lunar and Planet. Inst., Houston, Tex., 1999.
- Fisher, R. L., H. J. B. Dick, J. H. Natland, and P. S. Meyer, Mafic/ultramafic suites of the slowly spreading Southwest Indian Ridge: PROTEA exploration of the Antarctic Plate boundary, 24°E–47°E, *Ophiolite*, **11**, 147–178, 1986.
- Francheteau, J., R. Armijo, J. L. Cheminée, R. Hekinian, P. F. Lonsdale, and N. Blum, 1 Ma East Pacific Rise oceanic crust and uppermost mantle exposed by rifting in Hess Deep (equatorial Pacific Ocean), *Earth Planet. Sci. Lett.*, **101**, 281–295, 1990.
- Gillis, K., C. Mevel, and J. Allan, *Ocean Drilling Program: Leg 147 Initial Report*, Ocean Drilling Program, College Station, Tex., 1993.
- Grindlay, N. R., J. A. Madsen, C. Rommevaux-Jestin, and J. Sclater, A different pattern of ridge segmentation and mantle Bouguer gravity anomalies along the ultra-slow spreading Southwest Indian Ridge, *Earth Plan. Sci. Lett.*, **161**, 243–253, 1998.
- Handler, M. R., V. C. Bennett, and G. Dreibus, Evidence from correlated Ir/Os and Cu/S for late-stage Os mobility in peridotite xenoliths: Implications for Re-Os systematics, *Geology*, **27**, 75–78, 1999.



- Hart, S. R., and G. E. Ravizza, Os partitioning between phases in lherzolite and basalt, in *Earth Processes: Reading the Isotopic Code*, *Geophys. Monogr. Ser.*, vol. 95, edited by A. Basu, and S. R. Hart, pp. 123–134, AGU, Washington, D.C., 1996.
- Hassler, D. R., B. Peucker-Ehrenbrink, and G. E. Ravizza, Rapid determination of Os isotopic composition by sparging  $\text{OsO}_4$  into a magnetic-sector ICP-MS, *Chem. Geol.*, **166**, 1–14, 2000.
- Hattori, K., and S. R. Hart, Osmium isotope ratios of platinum-group minerals associated with ultramafic intrusions: Os-isotopic evolution of the oceanic mantle, *Earth Plan. Sci. Lett.*, **107**, 499–514, 1991.
- Ilebert, R., D. Bideau, and R. Hekinian, Ultramafic and mafic rocks from the Garrett Transform Fault near  $13^{\circ}20'S$  on the East Pacific Rise: Igneous petrology, *Earth Planet. Sci. Lett.*, **65**, 107–125, 1983.
- Hekinian, R., D. Bideau, J. Francheteau, J. L. Cheminee, R. Armijo, P. Lonsdale, and N. Blum, Petrology of the East Pacific Rise crust and upper mantle exposed in the Hess Deep (eastern equatorial Pacific), *J. Geophys. Res.*, **98**, 8069–8094, 1993.
- Irvine, T. N., Chromian spinel as a petrogenetic indicator, Part I, Theory, *Can. J. Earth Sci.*, **2**, 648–671, 1965.
- Johnson, K. T. M., H. J. B. Dick, and N. Shimizu, Melting in the upper oceanic mantle: an ion microprobe study of diopsides in abyssal peridotites, *J. Geophys. Res.*, **95**, 2661–2678, 1990.
- Karson, J. A., and A. T. Winters, Along-axis variations in tectonic extension and accommodation zones in the MARK Area, Mid-Atlantic Ridge  $23^{\circ}$  N latitude, *Geol. Soc. Spec. Publ.*, **60**, 107–116, 1992.
- Kelemen, P. B., M. Braun, and G. Hirth, Spatial distribution of melt conduits in the mantle beneath oceanic spreading ridges: Observations from the Ingalls and Oman ophiolites, *Geochem., Geophys., Geosyst.*, **1**(Article), 1999GC000012 [8266 words], 2000. (Available at <http://www.g-cubed.org>)
- Lee, K. L., Petrologic and geochemical studies of an abyssal peridotite from the Atlantis II Fracture Zone, M.S. Thesis, Mass. Inst. Technol./Woods Hole Oceanogr. Inst. Joint Program, Woods Hole, Mass., 1997.
- le Roex, A. P., H. J. B. Dick, and R. L. Fisher, Petrology and geochemistry of MORB from  $25^{\circ}E$  to  $46^{\circ}E$  along the Southwest Indian Ridge: Evidence for contrasting styles of mantle enrichment, *J. Petrol.*, **30**, 947–986, 1989.
- Marcantonio, F., A. Zindler, L. Reisberg, and E. A. Mathez, Re-Os isotopic systematics in chromitites from the Stillwater Complex, Montana, USA, *Geochim. Cosmochim. Acta.*, **57**, 4029–4037, 1993.
- Martin, C. E., Os isotopic characteristics of mantle derived rocks, *Geochim. Cosmochim. Acta.*, **55**, 1421–1434, 1991.
- McDonough, W. F., and S. S. Sun, The composition of the Earth, in *Chemical Evolution of the Mantle*, edited by W. F. McDonough, N. T. Arndt, and S. Shirey, *Chem. Geol.*, **120**(3–4), 223–253, 1995.
- Meisel, T., R. J. Walker, and J. W. Morgan, The osmium isotopic composition of the Earth's primitive upper mantle, *Nature*, **383**, 517–520, 1996.
- Meisel, T., F. Melcher, P. Tomascak, C. Dingeldey, and F. Koller, Re-Os isotopes in orogenic peridotite massifs in the Eastern Alps, Austria, *Chem. Geol.*, **143**, 217–229, 1997.
- Mével, C. C., P. Gente, E. Marion, J. M. Auzende, and J. A. Karson, Emplacement of deep crustal and mantle rocks on the west wall of the MARK area (Mid-Atlantic Ridge,  $23^{\circ}N$ ), *Tectonophysics*, **190**, 31–53, 1991.
- Meyer, P. S., H. J. B. Dick, and G. Thompson, Cumulate gabbros from the Southwest Indian Ridge,  $54^{\circ}S$ – $7^{\circ}16'E$ : Implications for magmatic processes at a slow spreading ridge, *Contrib. Mineral. Petrol.*, **103**, 44–63, 1989.
- Morgan, J. W., Ultramafic xenoliths: Clues to Earth's late accretionary history, *J. Geophys. Res.*, **91**, 12,375–12,387, 1986.
- Morgan, J. W., and P. A. Baedeker, Elemental composition of sulfide particles from an Ultramafic Xenolith and the siderophile elements content of the upper mantle, *Proc. Lunar Planet. Sci. Conf.*, **14th**, Part 2, *J. Geophys. Res.*, **89**, B513–B514, 1983.
- Ravizza, G., and D. Pyle, PGE and Os isotopic analyses of single sample aliquots with NiS fire assay preconcentration, *Chem. Geol.*, **141**, 251–268, 1997.
- Ravizza, G., C. E. Martin, C. R. German, and G. Thompson, Os isotopes as tracers in seafloor hydrothermal systems: Metalliferous deposits from the TAG hydrothermal area,  $26^{\circ}N$  Mid-Atlantic Ridge, *Earth Planet. Sci. Lett.*, **138**, 105–119, 1996.
- Roest, W. R., and B. J. Collette, The Fifteen Twenty fracture zone and the North American-South American plate boundary: Oceanic fracture zones, *J. Geol. Soc. London*, **143**(5), 833–843, 1986.
- Roy-Barman, M., and C. J. Allègre,  $^{187}\text{Os}/^{188}\text{Os}$  ratios of mid-ocean ridge basalts and abyssal peridotites, *Geochim. Cosmochim. Acta.*, **58**, 5043–5054, 1994.
- Roy-Barman, M., G. J. Wasserburg, D. A. Papanastassiou, and M. Chaussidon, Osmium isotopic compositions and Re-Os concentrations in sulfide globules from basaltic glasses, *Earth Plan. Sci. Lett.*, **154**, 331–347, 1998.
- Schiano, P., J.-L. Birck, and C.-J. Allègre, Osmium-strontium-neodymium-lead isotopic covariations in mid-ocean ridge basalt glasses and the heterogeneity of the upper mantle, *Earth Planet. Sci. Lett.*, **150**, 363–379, 1997.
- Sharma, M., D. A. Papanastassiou, and G. J. Wasserburg, The concentration and isotopic composition of osmium in the oceans, *Geochim. Cosmochim. Acta.*, **61**, 3287–3299, 1997.
- Shirey, S. B., and R. J. Walker, The Re-Os isotopic system in cosmochemistry and high-temperature geochemistry, *Annu. Rev. Earth Planet. Sci.*, **26**, 423–500, 1998.
- Smith, W. H. F., and D. T. Sandwell, Global sea floor topography from satellite altimetry and ship depth soundings, *Science*, **277**, 1956–1962, 1997.
- Snow, J. E., The isotope geochemistry of abyssal peridotites and related rocks, Ph.D. Thesis, Mass. Inst. Technol. and Woods Hole Oceanogr. Inst., Woods Hole, Mass., 1993.
- Snow, J. E., and H. J. B. Dick, Pervasive magnesium loss by

- marine weathering of peridotite, *Geochim. Cosmochim. Acta.*, **59**, 4219–4235, 1995.
- Snow, J. E., and L. Reisberg, Os isotopic systematics of the MORB mantle: results from altered abyssal peridotites, *Earth Plan. Sci. Lett.*, **133**, 411–421, 1995.
- Snow, J., H. J. B. Dick, and S. R. Hart, Preliminary results from a transform volcano, Atlantis II Fracture Zone, Southwest Indian Ridge, *Eos, Trans. AGU*, **68**, 408, 1987.
- Snow, J. E., S. R. Hart, and H. J. B. Dick, Nd and Sr isotope evidence linking mid-ocean-ridge basalts and abyssal peridotites, *Nature*, **371**, 57–60, 1994.
- Spangenberg, K., Die chromitlagerstätte von Tampadel am Zobten, *Zeitschr. Prakt. Geol.*, **5**, 13–25, 1943.
- Walker, R. J., E. Hanski, J. Vuollo, and J. Liipo, The Os isotopic composition of Proterozoic upper mantle: Evidence for chondritic upper mantle from the Outkumpu Ophiolite, Finland, *Earth Plan. Sci. Lett.*, **141**, 161–173, 1996.



## *Chapter 6. Summary*

This thesis presents a detailed look at the basalt geochemistry of one of Earth's few examples of ultraslow-spreading crustal accretion. Ultraslow-spreading ridges comprise ~20,000 km of the ~55,000 km global ridge system [Solomon, 1989], but until recently have been little studied. The overall goal of this investigation was to use the geology, geophysics, and a full suite of geochemical data including, major element, trace element, heavy-isotope, He isotopic, and U-series disequilibrium data to assess the influence of spreading geometry and upwelling rate on mantle melting and ultimately the composition of erupted mid-ocean ridge basalts. We conclude that the composition of MORB between 9°-25°E on the Southwest Indian Ridge is highly heterogeneous, ranging from LREE and isotopically enriched to depleted basalts. These heterogeneous compositions reflect the competing influences of source and process. The along-axis trends and correlations further suggest the importance of process, as a function of upwelling rate and lithospheric thickness, over source on the oblique supersegment versus the orthogonal supersegment.

Detailed bathymetry and closely spaced dredging from 9° and 25° E on the Southwest Indian Ridge has revealed many unique 1<sup>st</sup> order observations. In Chapter 2 we define four individual tectonomagmatic provinces using high-resolution bathymetry; gravity data, geologic information, and major element basalt chemistry: 1) the orthogonal supersegment, 2) the Narrowgate segment, 3) the amagmatic accretionary segments, and 4) Joseph Mayes Seamount. Distinct differences between these provinces in spreading geometry, rift valley morphology, ridge segmentation, relative crustal thickness, and basalt chemistry leads to the development of a melting model to account for the along-axis compositional variations. Along-axis chemical variability of Fe<sub>8</sub>, Na<sub>8</sub>, Mg#, and particularly (K/Ti)<sub>8</sub> cannot be easily explained by conventional passive upwelling models that rely on partial melting to varying degrees of a homogeneous peridotite source. Alternatively, we propose a tectonomagmatic melting model based on, 1) partial melting of a two-lithology source consisting of enriched eclogite within depleted peridotite, 2) focused melt flow to volcanically robust segments as a function of inferred upwelling rate and lithospheric thickness, and 3) variable melt-rock reaction and depletion within the local mantle column. The model illustrates that basalt compositions generated in an environment of highly variable upwelling rates, lithospheric thickness, and melt focusing, as seen on the oblique supersegment are dominated by "process" rather than "source". On the other hand, MORB generation on the orthogonal supersegment where the above parameters are generally constant is dominated by "source".

In Chapter 3, we report a full trace element suite of data along with Sr, Nd, Pb, Hf, and He isotopic compositions, to better define the MORB mantle source and thereby better constrain the model developed in Chapter 2. Sr, Nd, Pb, and Hf isotopic measurements on glasses from 9°-25°E are highly variable, indicating a MORB source that is isotopically heterogeneous. Isotopes and incompatible element ratios display highly

systematic trends on the orthogonal supersegment reflecting a progressively stronger garnet signature from east to west. Locally systematic variations along the oblique supersegment farther to the west show an even larger influence of residual garnet melting, specifically at the Narrowgate segment and to lesser extents at Joseph Mayes Seamount and the amagmatic accretionary segments. Incompatible element modeling of LREE depleted peridotite melting sufficiently explains the N-MORB compositions seen along much of the orthogonal supersegment and parts of the amagmatic accretionary segments. Melting of garnet lherzolite can explain much of the variation observed within the E-MORBs from both supersegments, but this modeling requires degrees of melting near or less than 1%, which is not consistent with inferred crustal thicknesses at Joseph Mayes Seamount or the Narrowgate segment of 9 km and 7 km, respectively. A number of incompatible element signatures including  $(\text{Nb/Ta})_n > 1$ ,  $(\text{Hf/Sm})_n < 1$ , inverse abundance correlations between LREE and HREE, and low Sc contents with high Sm/Yb are all consistent with melting of an eclogitic lithology consisting of 75% cpx and 25% garnet. Melting of eclogite to varying degrees generates incompatible element compositions that serve as the LREE enriched end-member melt that when mixed in variable proportions with LREE depleted peridotite melt can explain the full range of E-MORB compositions, especially the Narrowgate segment lavas. Thus, along the orthogonal supersegment moderate degrees of partial melting of  $\sim 6\%$  effectively sample a bulk mantle source that is progressively enriched in radiogenic isotopes and LREE from east to west, thereby reflecting a systematic variation in the amount of eclogite veining within the peridotite source. Meanwhile on the oblique supersegment suppression of mantle melting to low degrees combined with enhanced melt focusing towards robust segments means that the bulk source, which likely contains up to 5% eclogite veins, is not uniformly sampled and thus “process” rather than “source” dominates melt chemistry. The effects of “process” are reflected by the LREE and radiogenic isotope enriched lavas from the Narrowgate segment, Joseph Mayes Seamount, and some amagmatic accretionary lavas where the proportion of eclogite melt to peridotite melt is larger than on the orthogonal supersegment. This indicates the sensitivity of MORB chemistry to melting process and source variations at spreading rates  $< 20$  mm/yr.

The data we present in Chapter 4 provide new insight into the processes involved in lithospheric accretion, particularly at the poorly understood ultraslow-spreading end-member environment. The presence of U-Th and Th-Ra disequilibrium in lavas erupted from the ultraslow-spreading Southwest Indian Ridge between  $9^\circ$ - $25^\circ\text{E}$ , illustrates that relatively young lavas are resurfacing much of the rift valley, even along amagmatic accretionary segments that are generally deprived of melt and have large areas of mantle peridotite emplaced at the seafloor. The measurement of U-Th disequilibrium in 10 or 12 basalts places a limit of  $< 300$  ka on the eruption age of lavas. These eruption age constraints show lavas to be younger than the predicted age of the ocean crust they sit on, based on symmetric spreading from the rift axis at 7 mm/yr. Therefore, U-Th disequilibrium indicates anomalously young lavas erupted across the rift valley floor and upon the rift valley walls. Th-Ra disequilibrium measured in 3 samples lowers the age limits on each to  $< 8$  ka, indicating remarkably young glass within an ultraslow-spreading

rift valley. That young, off-axis volcanism is occurring on both fast and ultraslow-spreading ridges suggests, 1) that crustal accretion at any rate occurs farther from the axis of rifting and volcanism than previously recognized and 2) that further investigation of viable mechanisms for off-axis volcanism need to be explored.

( $^{230}\text{Th}/^{238}\text{U}$ ) activity ratios for the 12 glasses display a large range, from  $^{230}\text{Th}$  excess of 26% to  $^{238}\text{U}$  excess of 4%. N-MORBs show a range of ( $^{230}\text{Th}/^{238}\text{U}$ ) from 1.02 – 1.15, while E-MORBs range between 0.96 – 1.05, with a single lava at 1.26. Systematic correlation of ( $^{230}\text{Th}/^{238}\text{U}$ ) with ( $\text{La}/\text{Sm}$ )<sub>n</sub> and  $^{87}\text{Sr}/^{86}\text{Sr}$  on the orthogonal supersegment supports the idea that MORB generation is largely controlled by source composition. However, ( $^{230}\text{Th}/^{238}\text{U}$ ) is inversely correlated with ( $\text{La}/\text{Sm}$ )<sub>n</sub> and  $^{87}\text{Sr}/^{86}\text{Sr}$  on the oblique supersegment. The decoupling of U-Th disequilibrium from long-lived isotopic indicators of source, suggest strongly that MORB chemistry (including U-Th disequilibrium) is dominated by “process”. We also observe that addition of the Southwest Indian Ridge U-series data to the global MORB dataset does not fall on the global trend for ( $^{230}\text{Th}/^{238}\text{U}$ ) vs. axial depth or slope of disequilibria trend vs. half spreading rate. The inconsistency of this dataset with the global MORB dataset indicates the important role that “process” plays during generation of MORB chemistry, and suggests that interpretation of U-Th-Ra disequilibrium measurements need to consider variations in melting process, as related to tectonic environment, as well as source heterogeneity.

Chapter 5 of the thesis investigates the composition of the MORB source in a bit different way. Instead of using basalt chemistry to look backwards, we use the residues of mid-ocean ridge melting, abyssal peridotites, to constrain the composition of depleted upper mantle. Specifically we attempt to determine the Os isotopic composition of DMM. Although isotopic evidence has shown specific fracture zones along the SWIR and MAR (i.e., Du Toit F.Z.) to have heterogeneous mantle source regions, this study documents that much of the Os isotopic heterogeneity seen in N-MORB residual mantle is due to an alteration-induced radiogenic seawater Os component. In order to circumvent this problem, we separated resistant Cr-spinel from a number of abyssal peridotites and carefully treated them to remove the seawater alteration component. ICP-MS sparging of the Cr-spinel solutions has produced Os compositions which still show heterogeneity, but which define two different populations. Despite the heterogeneity in the nonmagnetic Cr-spinel fraction, both fractions, when compared to their corresponding whole rock  $^{187}\text{Os}/^{188}\text{Os}$  values, dominantly have less radiogenic  $^{187}\text{Os}/^{188}\text{Os}$ . Not only does this trend, from radiogenic whole rocks to less radiogenic Cr-spinels, illustrate that the primary depleted upper mantle Os signature is obtainable, but it further constrains the Os isotopic signature for DMM. We have, however, shown that the radiogenic seawater Os component, which compromises the isotopic signature of most abyssal peridotites, can be removed, allowing more straightforward interpretation of the Os signature. This then provides the means to define, albeit still quite vaguely, the Os isotopic signature of N-MORB depleted upper mantle.

## References

- Solomon, S. (1989), Just how do ocean ridges vary? Characteristics and populating statistics of ocean ridges., in *Drilling the Oceanic Lower Crust and Mantle.*, JOI/USSAC Workshop Report, edited by H. J. B. Dick, pp. 73-74, Woods Hole Oceanographic Institution, Woods Hole, MA.

<b>REPORT DOCUMENTATION PAGE</b>	<b>1. REPORT NO.</b> MIT/WHOI 2006-02	<b>2.</b>	<b>3. Recipient's Accession No.</b>
<b>4. Title and Subtitle</b> The Influence of Ridge Geometry at the Ultraslow-Spreading Southwest Indian Ridge (9°-25°E): Basalt Composition Sensitivity to Variations in Source and Process			<b>5. Report Date</b> February 2006
<b>7. Author(s)</b> Jared Jeffrey Standish			<b>6.</b>
<b>9. Performing Organization Name and Address</b> MIT/WHOI Joint Program in Oceanography/Applied Ocean Science & Engineering			<b>8. Performing Organization Rept. No.</b>
<b>12. Sponsoring Organization Name and Address</b> National Science Foundation			<b>10. Project/Task/Work Unit No.</b> MIT/WHOI 2006-02
			<b>11. Contract(C) or Grant(G) No.</b> (C) OCE 9907630; (C) OCE 0137325; (G) EAR 9804891; (G) OCE 9416620;
<b>15. Supplementary Notes</b> This thesis should be cited as: Jared Jeffrey Standish, 2006. The Influence of Ridge Geometry at the Ultraslow-Spreading Southwest Indian Ridge (9°-25°E): Basalt Composition Sensitivity to Variations in Source and Process. Ph.D. Thesis. MIT/WHOI, 2006-02.			<b>13. Type of Report &amp; Period Covered</b> Ph.D. Thesis
			<b>14.</b>
<b>16. Abstract (Limit: 200 words)</b> Between 9°-25° E on the ultraslow-spreading Southwest Indian Ridge lie two sharply contrasting supersegments. One 630 km long supersegment erupts N-MORB that is progressively enriched in incompatible element concentrations from east to west. The second 400 km long supersegment contains three separate volcanic centers erupting E-MORB and connected by long amagmatic accretionary segments, where mantle is emplaced directly to the seafloor with only scattered N-MORB and E-MORB erupted. Rather than a major break in mantle composition at the discontinuity between the supersegments, this sharp contrast in geometry, physiography, and chemistry reflects "source" versus "process" dominated generation of basalt. Robust along-axis correlation of ridge characteristics (i.e. morphology, upwelling rate, lithospheric thickness), basalt chemistry, and crustal thickness (estimated from gravity) provides a unique opportunity to compare the influence of spreading geometry and rate on MORB generation. What had not been well established until now is the importance of melting processes rather than source at spreading rates < 20 mm/yr. Along the orthogonally spreading supersegment (14 mm/yr) moderate degrees of partial melting effectively sample the bulk mantle source, while on the obliquely spreading supersegment (7-14 mm/yr) suppression of mantle melting to low degrees means that the bulk source is not uniformly sampled, and thus "process" rather than "source" dominates melt chemistry.			
<b>17. Document Analysis</b> <b>a. Descriptors</b> ultraslow-spreading MORB segmentation  <b>b. Identifiers/Open-Ended Terms</b>   <b>c. COSATI Field/Group</b>			
<b>18. Availability Statement</b> Approved for publication; distribution unlimited.		<b>19. Security Class (This Report)</b> UNCLASSIFIED	<b>21. No. of Pages</b> 286
		<b>20. Security Class (This Page)</b>	<b>22. Price</b>